



**REZEKNE HIGHER EDUCATION  
INSTITUTION  
FACULTY OF ENGINEERING**

ISSN 2256-070X

**ENVIRONMENT. TECHNOLOGY.  
RESOURCES**

Proceedings of the 10<sup>th</sup> International Scientific and Practical Conference  
June 18-20, 2015

**VOLUME I**



**HOCHSCHULE  
MITTWEIDA**  
UNIVERSITY OF  
APPLIED SCIENCES



**Hochschule für Angewandte  
Wissenschaften Hamburg**  
*Hamburg University of Applied Sciences*



Vides aizsardzības un  
reģionālās attīstības  
ministrija

**JADE HOCHSCHULE**  
Wilhelmshaven Oldenburg Emden



**MASOC**  
Metālapstrādes un mašīnbūves  
rūpniecības asociācija



Rezekne  
2015

**ENVIRONMENT. TECHNOLOGY. RESOURCES:** Proceedings of the 10<sup>th</sup> International Scientific and Practical Conference June 18-20, 2015. *Volume I*. Rēzekne: Rēzeknes Augstskola, 2015. p 240.

*Recommended for publication by the Scientific Council of Rēzekne Augstskola on June, 3<sup>rd</sup>, 2015.*

*Regular scientific collected papers include reports of the 10th International Scientific Practical Conference "Environment.Technology.Resources." The themes of the papers reflect the modern dynamic changes in the complex interplay between humanity and nature. The results of the studies included in the collected papers, show that environmental science changes its vector from a passive nature protection and environmental decontamination to an active prevention of sources of the negative effects through using the latest solutions in technologies, mechanics, computer sciences, rationalising the complex use of resources, including at the same time natural, as well as technogenic energy and material resources.*

*Three volumes of collected papers represent the research in environmental protection, biology and ecological farming, energy, materials science, mechanics, metalworking, laser technologies, mathematical modelling, electrical engineering, environmental economics and management, computer technologies and modelling socio-technical systems, intellectual decision support systems, environmental education and sustainable development processes.*

*The author of the paper takes responsibility for the content of the paper.*

### **Conference Organizing Committee:**

#### **Chairman:**

Dr.habil.geol. Gotfrids Noviks - Latvia, Rezekne Higher Education Institution

#### **Co - Chairman:**

Dr.sc.ing. Edmunds Teirumnieks - Latvia, Rezekne Higher Education Institution

#### **Members:**

Dr.habil.sc.ing. Dagnija Blumberga - Latvia, Riga Technical University

Dr.habil.dat. Juris Borzovs - Latvia, University of Latvia

Dr. Xiao Chen - China, Hefei University

Dr.-Ing. Dr. h.c. Horst Exner - Germany, Mittweida University of Applied sciences

Dr.sc.ing. Egils Ginters - Latvia, Vidzeme University of Applied Sciences

Dr.sc.ing. Peteris Grabusts - Latvia, Rezekne Higher Education Institution

DSc. Dimitar Grekov – Bulgaria, Agricultural University - Plovdiv

Dr.habil.sc.ing. Janis Grundspenkis - Latvia, Riga Technical University

DSc. Raycho Ilarionov - Bulgaria, Technical University of Gabrovo

DSc. Hristo Ivanov Beloov - Bulgaria, “Angel Kanchev” University of Ruse

Dr.habil.chem. Maris Klavins - Latvia, University of Latvia

Dr. Linas Kliucininkas - Lithuania, Kaunas University of Technology

Dr.sc.ing. Eriks Kronbergs - Latvia, Latvia University of Agriculture

Dr. Walter Leal - Germany, Hamburg University of Applied Sciences

PhD Eng. Valeri Markov Mladenov – Bulgaria, Technical University of Sofia

Dr.sc.ing. Andris Martinovs - Latvia, Rezekne Higher Education Institution

Dr.sc.ing. Vladislav Morozov - Russia, Geophysical Centre of the Russian Academy of Sciences

Dr.geogr. Olgerts Nikodemus - Latvia, University of Latvia

Dr.habil.sc.ing. Igor Plokhov - Russia, Pskov State University

Vilnis Rantins - Latvia, Chairman of the Management Board of the Association of Mechanical Engineering and Metalworking Industries

Dr.sc.ing. Artis Teilans - Latvia, Rezekne Higher Education Institution

Tekn. Dr., Dr.eng. h.c. Ralejs Tepfers - Sweden, Chalmers University of Technology

Dr.-Ing. Josef Timmerberg - Germany, Jade University of Applied Sciences

Dr.sc.ing. Olegs Uzga - Rebrovs - Latvia, Rezekne Higher Education Institution

PhD Pepo Yordanov – Bulgaria, Technical University of Sofia Branch Plovdiv

Dr. Juri-Rivaldo Pastarus - Estonia, Tallinn University of Technology

#### **Reviewers:**

Dr.sc.ing. Ludmila Aleksejeva - Latvia, Riga Technical University

Dr.sc.ing. Janis Andersons - Latvia, University of Latvia

PhD Andres Annuk - Estonia, Estonian University of Life Sciences

Dr.habil.sc.ing. Dagnija Blumberga - Latvia, Riga Technical University

Dr.sc.ing. Vitalijs Bolsakovs - Latvia, Riga Technical University

Dr.habil.sc.comp. Juris Borzovs - Latvia, University of Latvia

Dr. Rene Brunsch - Germany, Apromace Data Systems GmbH

Dr.sc.ing. Edgars Cubars - Latvia, Rural Support Service

Dr. Kevin Curran - Northern Ireland, University of Ulster

Dr.eng. Hristina Deneva - Bulgaria, Technical University of Gabrovo

Dr.eng. Margarita Deneva - Bulgaria, Technical University of Sofia

PhD Vitalij Denisov – Lithuania, Klaipeda University

Dr. Maija Dimitrivo - Bulgaria, Agricultural University - Plovdiv

Dr.oec. Sandra Ezmale - Latvia, Rezekne Higher Education Institution

Dr.sc.ing. Ainars Galins - Latvia, Latvia University of Agriculture

Dr.sc.ing. Egils Ginters - Latvia, Vidzeme University of Applied Sciences

Dr.sc.ing. Vladimirs Gonca - Latvia, Riga Technical University

Dr.sc.ing. Aleksandrs Gorbunovs - Latvia, Riga Technical University

Dr.sc.ing. Peteris Grabusts - Latvia, Rezekne Higher Education Institution

Dr.sc.ing. Julija Gusca - Latvia, Riga Technical University

Dr.sc.comp. Anita Jansone - Latvia, Liepaja University

Dr.agr. Imants Jansons - Latvia, Latvia University of Agriculture

Dr.sc.ing. Aivars Kakitis - Latvia, Latvia University of Agriculture

Dr.paed. Ilmars Kangro - Latvia, Rezekne Higher Education Institution

PhD Atis Kapenieks - Latvia, Riga Technical University

Dr.paed. Aivars Kaupuzs - Latvia, Rezekne Higher Education Institution

Dr. Lars Kempt - Germany, Technical University Chemnitz

Dr.habil.chem. Maris Klavins - Latvia, University of Latvia

Dr.sc.ing. Olga Kononova - Latvia, Riga Technical University

Dr.biol. Georgs Kornilovs - Latvia, Institute of Food Safety, Animal Health and Environment BIOR

Dr. Sveta Kostadinova - Bulgaria, Agricultural University - Plovdiv

Dr.sc.ing. Eriks Kronbergs - Latvia, Latvia University of Agriculture

Dr. Hilmi Kuşçu - Turkey, Trakya University  
Dr.sc.ing. Lyubomir Lazov - Latvia, Rezekne Higher Education Institution  
Dr.sc.ing. Andris Martinovs - Latvia, Rezekne Higher Education Institution  
PhD Gilberto Marzano - Italy, Ecoinstitute Friuli Venezia Giulia  
Dr.biol. Anna Mezaka - Latvia, Rezekne Higher Education Institution  
Dr.sc.ing. Liana Napalkova - Spain, Universitat Autònoma de Barcelona  
Dr.geogr. Olgerts Nikodemus - Latvia, University of Latvia  
Dr.habil.geol. Gotfrids Noviks - Latvia, Rezekne Higher Education Institution  
Dr.sc.ing. Imants Nulle - Latvia, Latvia University of Agriculture  
Dr.habil.sc.ing. Igor Plokhov - Russia, Pskov State University  
Dr.geol. Janis Prols - Latvia, SIA "Geo Consultants"  
Dr.sc.ing. Francesco Romagnoli - Latvia, Riga Technical University  
Dr.sc.ing. Andrejs Romanovs - Latvia, Riga Technical University  
Dr.habil.phys. Vladimir Solovyev - Russia, Pskov State University  
Dr. Kiril Stoyanov - Bulgaria, Agricultural University - Plovdiv  
Dr.sc.ing. Egils Stalidzans - Latvia, Latvia University of Agriculture  
Dr.sc.ing. Vita Strazdina - Latvia, Institute of Food Safety, Animal Health and Environment BIOR  
Dr.paed., Mg.sc.ing. Aina Strode - Latvia, Rezekne Higher Education Institution  
Dr.sc.ing. Artis Teilans - Latvia, Rezekne Higher Education Institution  
Dr.sc.ing. Edmunds Teirumnieks - Latvia, Rezekne Higher Education Institution  
Dr.sc.ing. Janis Tenteris - United States of America, EIS Group  
Tekn. Dr., Dr.eng.h.c. Ralejs Tefers - Sweden, Chalmers University of Technology  
Dr.-Ing. Josef Timmerberg - Germany, Jade University of Applied Sciences  
Dr.biol. Rasma Tretjakova - Latvia, Rezekne Higher Education Institution  
Dr.paed. Svetlana Usca - Latvia, Rezekne Higher Education Institution  
Dr.sc.ing. Olegs Uzga-Rebrovs - Latvia, Rezekne Higher Education Institution  
Dr.chem. Sarma Valtere - Latvia, Riga Technical University  
Dr.habil.sc.ing. Ivars Veidenbergs - Latvia, Riga Technical University  
Dr. habil.sc.ing. Janis Viba - Latvia, Riga Technical University  
Dr.sc.ing. Vladimir Visipkov - United Kingdom, CLS Services  
Dr. Ivan Yanchev - Bulgaria, Agricultural University - Plovdiv

#### **Editorial Board:**

Dr.sc.ing. Janis Andersons - Latvia, University of Latvia  
Dr.sc.ing. Andra Blumberga - Latvia, Riga Technical University  
Dr.habil.sc.ing. Dagnija Blumberga - Latvia, Riga Technical University  
Dr.habil.dat. Juris Borzovs - Latvia, University of Latvia  
Dr.-Ing. Dr. h.c. Horst Exner - Germany, Mittweida University of Applied sciences  
Dr.sc.ing. Ainars Galins - Latvia, Latvia University of Agriculture  
Dr.sc.ing. Egils Ginters - Latvia, Vidzeme University of Applied Sciences  
Dr.sc.ing. Peteris Grabusts - Latvia, Rezekne Higher Education Institution  
Dr.sc.ing. Vladimirs Gonca - Latvia, Riga Technical University  
Dr.habil.sc.ing. Janis Grundspenkis - Latvia, Riga Technical University  
DSc. Hristo Ivanov Beloev - Bulgaria, "Angel Kanchev" University of Ruse  
Dr.sc.ing. Aivars Kakitis - Latvia, Latvia University of Agriculture  
Dr.paed. Ilmars Kangro - Latvia, Rezekne Higher Education Institution  
Dr.habil.chem. Maris Klavins - Latvia, University of Latvia  
Dr. Linas Kliucininkas - Lithuania, Kaunas University of Technology  
Dr.sc.ing. Olga Kononova - Latvia, Riga Technical University  
Dr.sc.ing. Lyubomir Lazov - Latvia, Rezekne Higher Education Institution  
Dr. Walter Leal - Germany, Hamburg University of Applied Sciences  
Dr.sc.ing. Andris Martinovs - Latvia, Rezekne Higher Education Institution  
Dr.sc.ing. Vladislav Morozov - Russia, Geophysical Centre of the Russian Academy of Sciences  
Dr.habil.geol. Gotfrids Noviks - Latvia, Rezekne Higher Education Institution  
Dr.sc.ing. Imants Nulle - Latvia, Latvia University of Agriculture  
Dr. Juri-Rivaldo Pastarus - Estonia, Tallinn University of Technology  
Dr.habil.phys. Vladimir Solovyev - Russia, Pskov State University  
Dr.sc.ing. Artis Teilans - Latvia, Rezekne Higher Education Institution  
Dr.sc.ing. Edmunds Teirumnieks - Latvia, Rezekne Higher Education Institution  
Dr.sc.ing. Janis Tenteris - United States of America, EIS Group  
Tekn. Dr., Dr.eng. h.c. Ralejs Tefers - Sweden, Chalmers University of Technology  
Dr.biol. Rasma Tretjakova - Latvia, Rezekne Higher Education Institution  
Dr. habil.sc.ing. Janis Viba - Latvia, Riga Technical University  
Dr.sc.ing. Vladimir Visipkov - United Kingdom, CLS Services

#### **Steering Committee:**

Mg.chem. Erika Teirumnieka - Latvia, Rezekne Higher Education Institution  
Mg.sc.env. Sintija Augule - Latvia, Rezekne Higher Education Institution  
Mg.chem. Inese Bernane - Latvia, Rezekne Higher Education Institution



**ENGINEERING SCIENCES  
AND PRODUCTION  
TECHNOLOGIES**



## CONTENT

<b>Andzs M., Tupciauskas R., Veveris A., Gravitis J.</b>	IMPACT OF WOOD FRACTION, MOISTURE AND STEAM EXPLOSION ON THE DEVELOPMENT OF AN INNOVATIVE INSULATION MATERIAL	11
<b>Bulaha N.</b>	ANALYSIS OF SERVICE PROPERTIES OF CYLINDRICALLY GROUND SURFACES, USING STANDARD ISO 25178-2:2012 SURFACE TEXTURE PARAMETERS	16
<b>Bumanis G., Toropovs N., Dembovska L., Bajare D., Korjakins A.</b>	THE EFFECT OF HEAT TREATMENT ON THE PROPERTIES OF ULTRA HIGH STRENGTH CONCRETE	22
<b>Dušenkova I., Kusiņa I., Mālers J., Bērziņa-Cimdiņa L.</b>	APPLICATION OF LATVIAN ILLITE CLAYS IN COSMETIC PRODUCTS WITH SUN PROTECTION ABILITY	28
<b>Fedotov I., Tikhonov V., Veselkov E., Seletskaya N.</b>	THE COMPARATIVE ANALYSIS OF ENERGETIC CHARACTERISTICS OF VARIABLE-FREQUENCY ELECTRIC DRIVES WITH DIRECT TORQUE CONTROL	33
<b>Frolovs Ģ., Rocēns K., Šliseris J.</b>	COMPARISON OF A LOAD BEARING CAPACITY FOR COMPOSITE SANDWICH PLYWOOD PLATES	39
<b>Gonca V., Polukoshko S., Lavendelis E.</b>	DISSIPATIVE AND DAMPING PROPERTIES OF MULTI-LAYERED RUBBER-METAL VIBRATION ABSORBER	46
<b>Khitrov A., Khitrov A.</b>	INVESTIGATION OF PERMANENT MAGNET SYNCHRONOUS MACHINE WITH RECUPERATION BLOCK	53
<b>Kirilovs E., Krūklīte L., Kukle S., Zelča Z.</b>	NANOLEVEL FINISHING FOR VENEERED PRODUCTS	56
<b>Kirilovs E., Kukle S., Beļakova D., Borodiņecs A., Ruciņš Ā., Stramkale V.</b>	THERMAL CONDUCTIVITY OF HEMP BASED BOARDS	61
<b>Konevtsov V., Poletaev I., Verteshev S.</b>	DISCRETE AUTOMATIC SCHEMES FOR ASC TP	67

<b>Korjakins A., Radina L., Bajare D.</b>	FABRICATION OF POROUS CERAMICS AS CLAY/GLASS COMPOSITE	72
<b>Korovkin V.</b>	NUMERICAL SIMULATION OF THE RECONSTRUCTION BANK-PROTECTION TYPE GRILLAGE ON CANALS AND RIVERS OF ST. PETERSBURG	78
<b>Kozyreva O. I., Plokhov I. V., Guraviev Y. N., Savraev I. E., Ilyin A. V.</b>	THE REGIONS OF PARAMETRIC INSTABILITY OF BRUSH-CONTACT DEVICE ELECTROMAGNETIC CIRCUIT IN UNSTABLE WORKING CONDITIONS	84
<b>Kroics K.</b>	SIMULATION BASED ANALYSIS OF DIGITALLY CONTROLLED 4-PHASE DC- DC CONVERTER WITH COUPLED INDUCTORS	89
<b>Lazov L., Deneva H., Narica P.</b>	A TASK FOR LASER CUTTING OF LAMELLAE WITH TRULASER 1030	96
<b>Lazov L., Deneva H., Narica P.</b>	FACTORS INFLUENCING THE COLOR LASER MARKING	102
<b>Lazov L., Deneva H., Narica P.</b>	LASER MARKING METHODS	108
<b>Leitans A., Boiko I., Lungevics J, Mironovs V.</b>	THE INFLUENCE OF THE TECHNOLOGICAL PROCESS ON THE SURFACE QUALITY AND TRIBOLOGICAL PROPERTIES OF POWDER DETAILS	116
<b>Leitans A., Lungevics J.</b>	MATHEMATICAL MODEL OF FRICTION COEFFICIENT DETERMINATION FOR LUBRICATED SURFACES	121
<b>Lengerov A.</b>	ADAPTIVE CONTROL OF THE INDENTATION MADE BY THE DRILLING TOOL	125
<b>Loginov S., Domracheva Y., Smirnov V., Fedorov D.</b>	RESEARCH OF RADIAL FORCES AND TORQUE OF BEARINGLESS SYNCHRONOUS MACHINE	128
<b>Macanovskis A., Krasnikovs A., Kononova O., Harjkova G., Yevstignejevs V.</b>	MECHANICAL PROPERTIES OF GLASS FIBER COMPOSITES REINFORCED BY TEXTILE FABRIC	133
<b>Martinovs A., Timmerberg J., Tretjakova R., Beckmann P., Popa V., Wagner R.</b>	MECHANICAL AND ELECTRICAL PROPERTIES OF THE SOLID SAPROPEL	139



<b>Mashkov P., Teirumnieks E., Gyoch B., Beloev H., Pencheva T., Kandilarov R.</b>	DESIGN OF LED LAMP WITH SPECIAL SPECTRAL CHARACTERISTICS	147
<b>Mironovs V., Treijs J., Teirumnieks E.</b>	RESEARCH OF OIL PRODUCT SORPTION PROCESSES BY FERROMAGNETIC SORBENTS	153
<b>Nikiforov I., Maltsev P., Ivanov V., Barsuk I.</b>	EXPLANATION OF THE EXPRESS METHOD OF THE DETERMINATION OF STEEL GRADE BY SPARK	157
<b>Noviks G.</b>	PHYSICO-TECHNICAL APPROACH TO DESIGN OF COMPOSITES FROM MINERAL AND POLYMER TECHNOGENIC RESOURCES	162
<b>Nikolskiy S., Pertseva O.</b>	ACCELERATED METHOD FOR THE DETERMINATION OF FREEZE-THAW RESISTANCE OF CONCRETE	170
<b>Pleiksnis S., Sinka M., Sahmenko G.</b>	EXPERIMENTAL JUSTIFICATION FOR SAPROPEL AND HEMP SHIVES USE AS A THERMAL INSULATION IN LATVIA	175
<b>Plovov I., Ilyin A., Kozyreva O., Savraev I.</b>	THE SIMULATION MODEL OF SLIDING CONTACT WITH THREE DEGREES OF FREEDOM AND DISTRIBUTED PARAMETERS OF THE TRANSITION LAYER	182
<b>Rubene S., Vilnitis M., Noviks J.</b>	IMPACT OF DENSITY AND SPECIAL FEATURES OF MANUFACTURING PROCESS ON DRYING OF AUTOCLAVED AERATED CONCRETE MASONRY BLOCKS	186
<b>Šahmenko G., Krasnikovs A., Lukašenoks A., Eiduks M.</b>	ULTRA HIGH PERFORMANCE CONCRETE REINFORCED WITH SHORT STEEL AND CARBON FIBERS	193
<b>Sele L., Bajare D., Bumanis G., Dembovska L.</b>	ALKALI ACTIVATED BINDERS BASED ON METAKAOLIN	200
<b>Sprince A., Pakrastinsh L., Baskers B., Gaile L.</b>	CRACK DEVELOPMENT RESEARCH IN EXTRA FINE AGGREGATE CEMENT COMPOSITES	205
<b>Stuklis A., Serdjuks D., Goremikins V.</b>	MATERIALS CONSUMPTION DECREASE FOR LONG-SPAN PRESTRESSED CABLE ROOF	209

<b>Stunda-Zujeva A., Stepanova V., Bērziņa-Cimdiņa L.</b>	EFFECT OF SPRAY DRYER SETTINGS ON THE MORPHOLOGY OF ILLITE CLAY GRANULES	216
<b>Tretjakova R., Grebeža J., Martinovs A.</b>	RESEARCH INTO BIOLOGICAL CHARACTERISTICS OF DRIED SAPROPEL	223
<b>Vanin A. I., Solovyev V. G.</b>	LASER EFFECT ON SPHERICAL NANOPARTICLES WITH THIN SURFACE LAYER	228
<b>Veisman V. L., Romanov S. G., Solovyev V. G., Yanikov M. V.</b>	OPTICAL PROPERTIES OF NANOSTRUCTURED SILVER EMBEDDED BY ELECTRO-THERMO-DIFFUSION IN OPAL PHOTONIC CRYSTAL	230
<b>Veļičko J., Gaile L.</b>	OVERVIEW OF TUNED LIQUID DAMPERS AND POSSIBLE WAYS OF OSCILLATION DAMPING PROPERTIES IMPROVEMENT	233

# Impact of wood fraction, moisture and steam explosion on the development of an innovative insulation material

Martins Andzs, Ramunas Tupciauskas, Andris Veveris, Janis Gravitis

Latvian State Institute of Wood Chemistry, Laboratory of Eco-Efficient Conversion of Biomass I,  
Dzerbenes street 27, Riga, LV-1006, Latvia.

**Abstract.** The study shows development of an innovative bulk heat insulation material from grey alder (*Alnus incana* L. Moench) chips and birch (*Betula pendula*, *Betula verrucosa*) flakes as residues of plywood production. The research is actual for the plywood production companies and for producers that process grey alder chips to make an innovative products with high added value. Chips and flakes eco-efficient converted to fibrous mass by steam explosion (SE) technology at temperatures (T) of 200 to 235 °C and time interval of 0 to 5 min. Application of SE technology to obtain fibrous insulating material is in the news at a global level and has not been studied previously. The bulk density of raw and SE materials determined using standardised method specified in LVS EN 15103: 2010. The bulk density of SE materials studied depending on the raw material fraction and moisture as well as depending on the SE conditions. The lowest bulk density (53 kg m<sup>-3</sup>) achieved SE material of grey alder chips with 12% of raw moisture processed at T 235 °C for 1 min. This is the optimal result, which reveals the industrial competitiveness of bulk heat insulation materials and indicate the justification for the further examination.

**Keywords:** grey alder, birch flakes, steam explosion, bulk density, bulk heat insulation.

## I INTRODUCTION

Alder as the fourth most Latvian widespread tree species is still not used in sufficient quantities. In forests, near the pine and spruce basic wood species, grows huge resource of grey alder that count of 40 million cubic meters (m<sup>3</sup>) or 6.1% of the total Latvian forest yield [1] Therefore, grey alder species retains the potential for use in materials with high added value. By contrast, the production of plywood forms a considerable amount of so-called veneer flaps which are predominantly burned for energy purposes [2]. Currently, Latvia implements „Technology platform vision 2030 of Latvian forestry and forest-based industry”, which one of the objectives is the innovative development and application increase of Latvian major tree species and wood products [3]. In response to the technological platform the research of the above-mentioned raw materials is sustainable based.

Traditionally, to convert wood chips to pulp, defibrators and rafinators are used. In nowadays, steam explosion (SE) pretreatment is one of the most promising technologies for biomass processing [4].

SE is the thermal hydrolysis process by which saturated steam acts on the biomass in a closed reactor a certain time (up to 10 min) at a certain

temperature (160-250 °C). After the time exceeds the reactor is opened and the biomass is exploded to the receiver due to rapid pressure reduction. Wood fibres after SE are a modified hierarchical assembly of its main ingredients – cellulose, hemicellulose and lignin (Fig. 1).



Fig. 1. Wood cell changes after SE processing [5].

During the research is intended to develop the optimal bulk heat insulation material from grey alder wood chips and veneer flaps, with the use in building structures. The article shows the study, the purpose of which is to provide the impact of raw material fraction, moisture and SE treatment on the bulk density of the pretreated material. The tasks of the study are to develop and implement a sample treatment scheme by selecting the sample different

fraction, moisture and SE modes, as well as to determine the sample optimal (lower) bulk density.

## II MATERIALS AND METHODS

To implement targets of the research the processing scheme has been developed (Fig. 2). Grey alder wood is obtained from the sample squares of Latvian State Forestry Research Institute „Silava”. Birch flaps is obtained from the plywood production company's “Latvijas Finieris”. The grey alder wood is crashed by a “Bruks” (Sweden) wood chipping machine, debarked and then one part cracked by a “Retsch” (Germany) appliance to particles (AP) characterised by sieve holes of 10 mm in diameter. The grey alder chips (AC) and birch flaps (BF) fractionated by sieve with holes of 20 mm in diameter. Finally, all raw materials conditioned to equilibrium moisture content (MC) that was achieved  $6 \pm 1\%$  after one week and to 12% of MC. The MC of raw materials controlled using the device Precisa XM120.

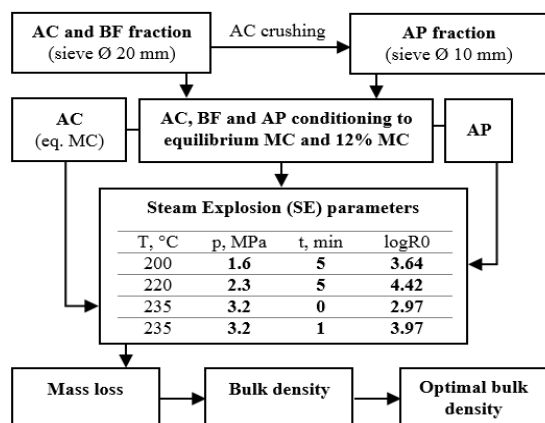


Fig. 2. Research scheme of grey alder chips (AC), particles (AP) and birch flaps (BF).

The bulk density ( $D_{ar}$ ,  $\text{kg m}^{-3}$ ) of conditioned raw materials determined using a standardized method [3] at cylindrical metal container of 0.5 litres ( $V$ ,  $\text{m}^3$ ) and calculated by equation (1):

$$D_{ar} = \frac{(m_2 - m_1)}{V}, \quad (1)$$

where  $m_1$  – the mass of the empty container in kg;  $m_2$  – the mass of the sample filled container in kg.

Prepared raw materials processed in the laboratory scale batch SE unit (Fig. 3), which allows to change the processing parameters: time, temperature and pressure. Empirically, conditions of the SE can be characterised by a single treatment severity index ( $R_0$ ) comprising temperature ( $T$ ) and time ( $t$ ) [7]:

$$R_0 = t \cdot \exp\left(\frac{T-100}{14.75}\right). \quad (2)$$

The same pretreatment quality could be achieved combining the process temperature and time [6]. Therefore, the temperature range was chosen from 200°C to 235°C and time of exposure to high pressure at current temperature from 0 min to 5 min. The time of 0 min there means that the sample was exploded to receiver immediately after the current pressure was achieved.

SE pretreatment parameters for used raw samples are shown in Table 1. In order to reduce the number of samples, the AP samples with MC of equilibrium and 12% processed with single SE mode at  $T$  200 °C,  $t$  5 min (Fig. 2, Table 1). While one of AC samples with only equilibrium MC processed with single SE mode at  $T$  235 °C and steam-exploded immediately after the high pressure achieved (Fig. 2, Table 1).

TABLE 1

SE TREATMENT PARAMETERS OF RAW SAMPLES

Sample	Fraction (sieve Ø, mm)	MC (before SE)	T, °C	p, Mpa	t, min	logR <sub>0</sub>
BF_W12_R3.97	20	12	235	3.2	1	3.97
BF_W5_R3.97	20	5	235	3.2	1	3.97
BF_W12_R4.23	20	12	220	2.3	5	4.23
BF_W5_R4.23	20	5	220	2.3	5	4.23
BF_W5_R3.64	20	5	200	1.6	5	3.64
AC_W7_R2.97	20	7	235	3.2	0	2.97
AC_W12_R3.97	20	12	235	3.2	1	3.97
AC_W6_R3.97	20	6	235	3.2	1	3.97
AC_W12_R4.23	20	12	220	2.3	5	4.23
AC_W6_R4.23	20	6	220	2.3	5	4.23
AC_W12_R3.64	20	12	200	1.6	5	3.64
AC_W6_R3.64	20	6	200	1.6	5	3.64
AP_W7_R3.64	10	6	200	1.6	5	3.64
AP_W12_R3.64	10	12	200	1.6	5	3.64

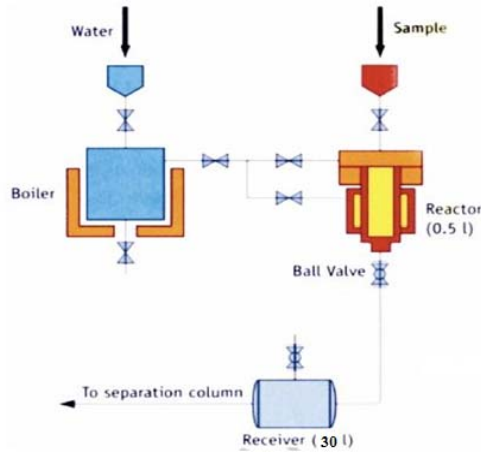


Fig. 3. Scheme of the laboratory scale SE device.

In order to assess the impact of SE regimes used the pretreated materials were collected and it's oven dry mass calculated. Mass loss ( $M_{loss}$ ) of the SE materials calculated according to equation (3):

$$M_{loss} = 100 - \frac{(m_2 \times 100)}{m_1}, \quad (3)$$

where  $m_1$  and  $m_2$  – is the oven dry mass of raw sample and pretreated one, respectively.

The influence of samples factors and comparison of it's the mean values are analysed by one-way ANOVA at the confidence level  $\alpha = 0.05$ .

### III RESULTS AND DISCUSSION

As it is known a certain part of biomass volatiles out during SE. This part is defined as mass loss and contains degraded hemicelluloses [6, 8]. Mass loss of

pretreated samples mostly depends on severity of the SE process and it indicates tight correlation approving the statement that increasing the severity index  $R_0$  by one unit the mass loss increases by almost 9% (Fig. 4). The mass loss variation at  $\log R_0$  3.64, 3.97 and 4.27 depends on moisture content of the raw materials and slightly decreases with the increasing moisture content from 6% to 11% (Tupciauskas et al. 2012). The last statement matches also the studies of other authors those declare that the optimal moisture is within range of 10–15% [9]. While fraction and species of the raw materials show no significant impact on the mass loss.

The bulk density of all raw materials varies in range between 154 and 172  $\text{kg m}^{-3}$  and the difference is not significant in spite of different fraction, moisture and species (Fig. 5).

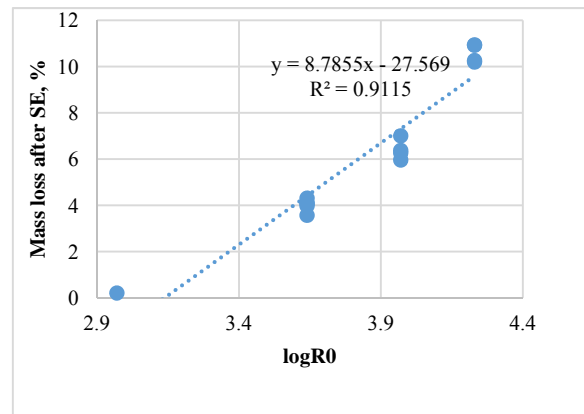


Fig. 4. Mass loss of the samples after SE depending on severity index ( $\log R_0$ )

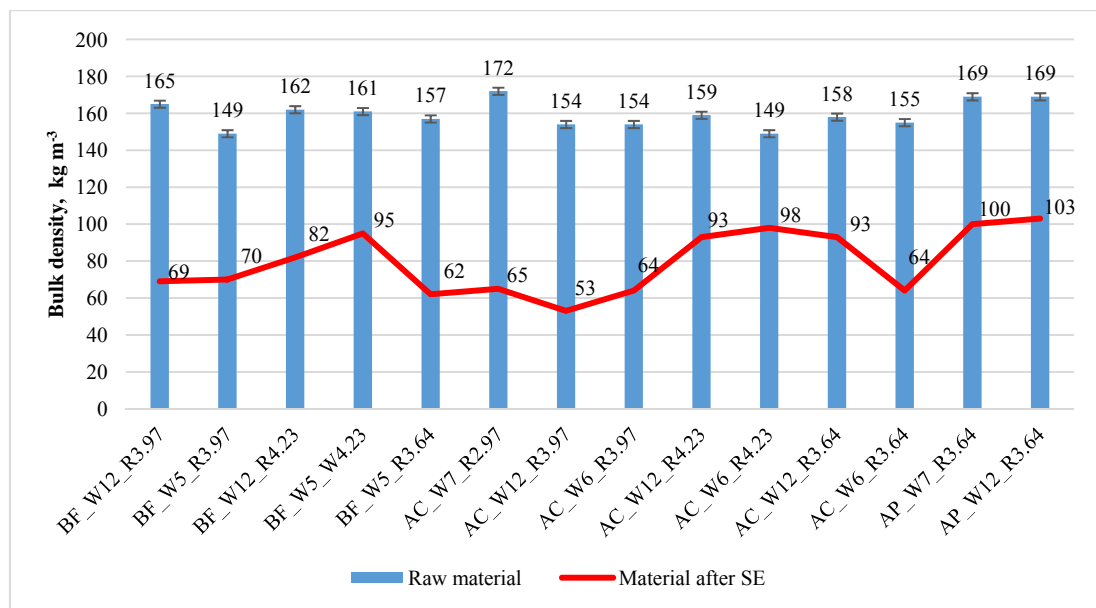


Fig. 5. Bulk density of all samples before and after the processing of SE.



Fig. 6. Visual appearance of the bulk samples: A – raw AC, B – AC\_W7\_R2.97; C – AP\_W12\_R3.64; D – AC\_W12\_R4.23.

The bulk density of the pretreated materials variate in range between 62 and 103 kg m<sup>-3</sup>. The bulk density of all raw materials varies in range between 154 and 172 kg m<sup>-3</sup> and the difference is not significant as in the case of raw materials (Fig. 5). The lowest bulk density achieved by sample from raw alder chips pretreated at T 235°C and 1 min, however the samples from birch flaps also demonstrate good enough results (Fig. 5). The pretreated samples of raw grey alder particles achieved higher bulk density indicating unsatisfactory results. The bulk density of the pretreated samples have a tendency to increase with increasing severity index as also noted by Tupciauskas et al. [10].

The bulk density of the pretreated materials decreased in average at 50% due to the effect of SE. However, the pretreated materials are not homogenous because of including single fibres and fibre bundles as well (Fig. 6).

#### IV CONCLUSION

Processing of grey alder chips and birch flaps there are obtained inhomogeneous fibrous mass that consist of fibres and fibre bundles.

SE optimal conditions under which the samples obtained with the lowest bulk density are T 235°C, p 3.2 MPa and t 0–1 min.

In spite of different parameters some samples pretreated under logR0 4 (PF\_W5\_R3.64, AC\_W7\_R2.97, AC\_W12\_R3.97, AC\_W6\_R3.97, AC\_W6\_R3.64) achieved optimum bulk density (under 65 kg m<sup>-3</sup>) that is comparable with other bulk heat insulation analogues. This is the optimal result, which reveals the industrial competitiveness of bulk

heat insulation materials and indicate the justification for the further examination.

#### V ACKNOWLEDGMENTS

The studies were implemented under the National Research Programme at Latvian State Institute of wood chemistry, Project No. 3. “Biomaterials and Bioproducts with extensive use of forest resources” 2014 – 2017.

#### VI REFERENCES

- [1] Latvian Central Statistical Bureau, January 2015 [Online] Available: <http://www.csb.gov.lv/dati/koku-sugas-latvijasz-mezos-30236.html> [Accessed: January 15, 2015]
- [2] Latvian State Environmental Service B permit environmental pollution. SIA VEREMS RSEZ file: April 2012 [Online] [http://C:/Users/User/Downloads/b-rsez-verems-re12ib0006%20\(1\).pdf](http://C:/Users/User/Downloads/b-rsez-verems-re12ib0006%20(1).pdf) [Accessed: January 15, 2015]
- [3] Latvian Academy of science “Home page” March 2006. [Online] Available: <http://www.lza.lv/ZV/zv062000.htm#6> [Accessed: March 20, 2015]
- [4] Wolfgang Stelte, Danish Technolgy institute, Report SE method, Available: <file:///C:/Users/User/Downloads/RK%20report%20steam%20explosion.pdf> [Accessed January 16, 2015]
- [5] March 2006. [Online] Available <http://www.hrs-heatexchangers.com/en/applications/biofuels/bioethanol/default.aspx> [Accessed January 16, 2015]
- [6] Гравитис, Я. А. 1987. Теоретические и прикладные аспекты метода взрывного автогидролиза растительной биомассы. Обзор. Химия древесины, 5:3 – 21.
- [7] Overend, R.P., Chornet, E. Fractionation of Lignocellulosics by steam aqueous pretreatments. Philos. Trans. R. Soc. Lond. Ser. A-Math. Phys. Eng. Sci., 1987. 321(1561):523-536.
- [8] Веверис, А. Г., Эринш, П. П., Калейне, Д. А., Полманис, А.Г., Веверис, Г.П., Кузмане, Г.В. 1990. Высокотемпературный автогидролиз древесины. 1. Сопоставление поведения древесины основных пород Латвийской ССР. Химия древесины, 3: 89 – 95.
- [9] Abolins, J., Gravitis, J. 2007. Biomass conversion to transportation fuels, combustibles and nano-materials by steam explosion. Latvian J. Phys. Techn. Sci., 4: 29 – 39.

[10]Tupciauskas, R., Veveris, A., Belkova, L., Gravitis, J. and Tuherm, H. 2012. Grey alder pretreatment by steam explosion for self adhesive composites. In: A. Baltrušaitis and K. Ukvalbergiene (eds.) *Proceedings of the 8<sup>th</sup> Meeting of the*

*Northern European Network for Wood Science and Engineering (WSE)*, 13-14 September, Kaunas, Lithuania. Kaunas University of Technology: Technologija, 214–220.

# **Analysis of service properties of cylindrically ground surfaces, using standard ISO 25178-2:2012 surface texture parameters**

**Natalija Bulaha**

*Riga Technical University, Institute of Mechanical engineering,  
Address: Ezermalas street 6k, Riga, LV-1006, Latvia.*

**Abstract.** At present surface roughness is one of the main indications of component quality. During the operation mainly the outer layer of the component is exposed to external action, and depending on the roughness structure conclusions can be drawn about the service properties of the surface. Because cylindrical grinding today is rather widely used and precise method of treatment of bodies of revolution in the field of mechanical engineering the given paper pays attention to the surfaces treated on cylindrical grinding machines, and more exactly to their roughness, determining the possible use of the given surfaces. For the analyses of the roughness parameters the ISO standard ISO 25178-2:2012 “Geometrical product specifications (GPS) - Surface texture: Areal - Part 2: Terms, definitions and surface texture parameters” was used, in which there were determined the texture parameters of the surface. Contrary to other standards, such as ISO 4287, ISO 13565 the new standard allowed to assess real surface properties, since in the given case the surface is being viewed in three-dimension space. During the research three cylindrically ground samples treated at different cutting conditions were chosen. By the help of modern measuring equipment Taylor Hobson Talysurf Intra 50 the topography of the given samples was taken in order to obtain and compare the roughness parameters and for the purpose of setting relation between the cutting regime and roughness parameters, and determining mathematical model of cylindrically ground samples. As a result of research it was stated that the given type of surfaces is characterized by irregular roughness, that is location of micro-peaks regarding their height and shape are irregular and also the correlation function of cylindrically ground surfaces is rapidly diminishing, but the density distribution of ordinates is close to normal. Based on the above feature of surface roughness such service properties as wear resistance, retention of lubricants and coatings (adhesion) and provision of required contact area were determined.

**Keywords:** Surface roughness, topography, cylindrical grinding, exploitative characteristics.

## I INTRODUCTION

Nowadays the volume of industrial production dramatically increases, due to the modernization of machine tools and equipment and thus enhance of their operational efficiency.

As it is known quality of manufactured details depends on technological factors, which to a greater or lesser extent affect the machining accuracy, and is characterized by a tolerance in size, shape, location and surface roughness. Particular interest is caused by the surface roughness, which helps to determine the service properties of machine components.

The present paper deals with the topography and parameters of surfaces treated on cylindrical grinding machines, and striking representatives are cylindrical and conic surfaces of components of type “shaft” and also internal surfaces. The given type of treatments is

rather modern and sufficiently precise and therefore the determination of features of roughness of cylindrically grinded surfaces will help improve the service properties of machine components.

Exploitative properties of surfaces include mainly wear resistance, retention of lubricants and coatings and also provision of contact area, which is particularly important when choosing fit and ensuring hermeticity. All the above properties can be determined theoretically and practically using roughness parameters measured on special “profilograph - profilometer” type equipment.

The given paper for the surface analyses uses relatively new Standard ISO 25178-2:2012 [1], comprising 6 groups of texture parameters of surface: height, functional, spatial, hybrid, functions/related and miscellaneous parameters. In the given standard,



as compared with others the roughness parameters allow to assess the actual properties of the surface, since their determination is carried out in three dimensional medium.

The following paragraphs will consider an experiment on the determination of roughness parameters of three cylindrically grinded surfaces and give analyses of their exploitation characteristics.

## II CYLINDRICALLY GROUND SAMPLES AND MEASUREMENT METHODS

For topography analyses of cylindrically grinded surfaces there were chosen surfaces No.1, 5, 8 (Fig.1) of Rugotest 105 sample (company L.C.A.-C.E.A.). Sample's material – corrosion resistant nickel treated on a cylindrical grinding machine at different feed rate; the sample being made according to ISO 2632 standard.

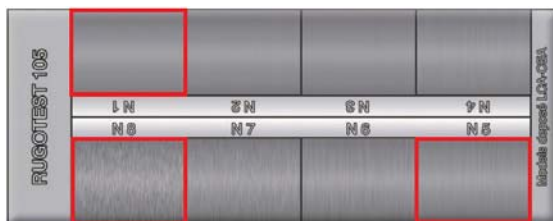


Fig.1. Cylindrically grinded sample Rugotest 105

The roughness of surfaces of the given sample was measured using modern profilograph - profilometer Taylor Hobson Talysurf Intra 50 (Fig.2), equipped with a stylus with a needle, drive, a table, a unit of electronic system to collect information and a computer necessary for data processing. The resolving power of the given roughness indicator is 16nm for the 1mm range. The roughness measurement principle is based on the movement of the probe-needle along the examined surface, whereas the needle prints down the profile of the roughness [2].



Fig.2. Measurement device Taylor Hobson Talysurf Intra 50

Because the profilograph - profilometer is equipped with 3D measurement system, which ensures movement of the table with the sample and measuring

needle along three axes, to get a surface topography is a very simple task for this device.

For the determination of 3D roughness of the surface special software: TalyMap expert (3.2.0.Version) was used for the input of needed parameters and  $\mu$ ltra – for the processing of surface topography.

## III EXPERIMENT ON ROUGHNESS MEASUREMENT

Prior to carrying out experiment it was necessary to clean the surface from oil and dirt using alcoholic solution. Then the sample was placed and fixed on the measurement table and the measurement needle was attached to it to ensure an initial contact. The pressing force of the needle was set according to the software data. Further in the software TalyMap expert the needed measurement conditions were chosen, which are shown in Table 1.

Table 1  
Set conditions of measurement of roughness parameters in TalyMap expert software

Parameter	Value
Number of points (Y)	150
Data length (Y)	2 mm
Number of points (X)	150
Data length (X)	2 mm
Measurement Speed	0,5mm/s

When experiment was finished, initial topographies of all three surfaces were obtained. The term “initial” means that given topographies do not provide a possibility to determine actual values of roughness parameters. For this purpose it is necessary to process the obtained data [3], [4], separating from the initial topography the form and waviness, which are the result of wrong cutting regimes, vibrations during the operations and other factors. Additionally before filtration it is necessary to carry out leveling of the surface, because when sample is fixed on the table it is impossible to ensure a full contact area, and thus the measuring needle will not be situated towards the sample's surface at the right angle (Fig.3).

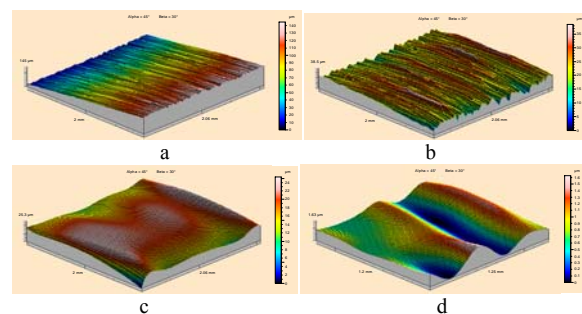


Fig.3. Surface topography filtration  
a – initial topography, b – topography after leveling, c – separated form of the surface, d – separated waviness of the surface

After the surface filtration the actual roughness was obtained, what is shown in Fig.4. The surface roughness after cylindrical grinding has parallel situated scratches caused by abrasive grains. Fig.4 shows that roughness has a definite orientation, which demonstrates non-isotropy of surface, which influences the surface strength.

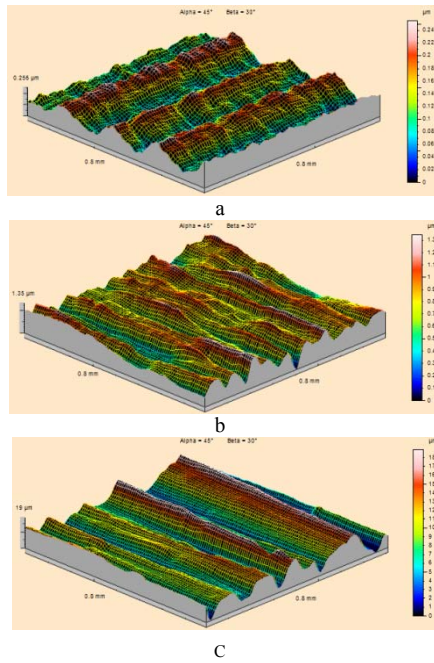


Fig.4. Roughness of surfaces No.1 (a), No.5 (b), No.8 (c)

Additionally there were determined the correlation function of roughness of cylindrically grinded samples, which indicates a connection between the process points [5], and also the density distribution of ordinates of the surface. The correlation functions of all three surfaces are diminishing with damped oscillations and the distribution density is close to normal and corresponds to Gaussian distribution law (Fig.5).

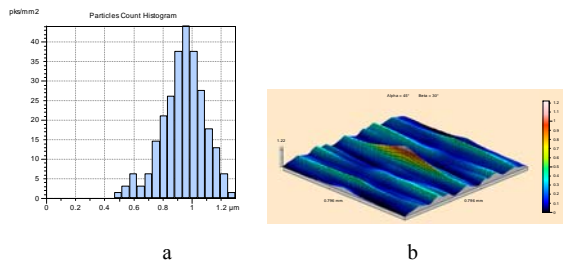


Fig.5. Correlation function of roughness (a) and density distribution of ordinates (b)

Further on in this paper there were determined roughness parameters of surfaces under research. For this purpose in μltra software it was necessary to choose the function “parameters”, isolating previously the filtered topography. The obtained values differ

from each other, what can be explained by varying of cutting conditions. Table 2 presents roughness parameters needed for the analyses.

Further in the paper the obtained roughness parameters will be examined more in details in order to determine the service properties of surfaces and relation between roughness parameters and cutting condition.

Table 2  
Roughness parameters of surfaces №1, №5, №8

Parameter	№1	№5	№8	Unit
<i>3D parameters</i>				
Sa	0.04	0.155	3,25	μm
Spk	0.0135	0.129	2.91	μm
Sk	0.0718	0.326	5.71	μm
Svk	0.0154	0.137	1.9	μm
Ssk	0.252	-0.38	0.322	-
Str	0.1211	0.0909	0.0983	-
Vmp	0.0000211	0.000109	0.00165	mm <sup>3</sup> /mm <sup>2</sup>
Vm	0.000132	0.000789	0.00917	mm <sup>3</sup> /mm <sup>2</sup>
Vv	0.000116	0.000553	0.00966	mm <sup>3</sup> /mm <sup>2</sup>
Vvc	0.0000662	0.00021	0.00541	mm <sup>3</sup> /mm <sup>2</sup>
Vvv	0.0000325	0.0000267	0.000316	mm <sup>3</sup> /mm <sup>2</sup>
Sdr	0.000196	0.00708	1.55	%
Sz	0.2	1.11	16.5	μm
Sku	2.06	3.25	2.41	-
Smr1	5.83	11.7	11.4	%
Smr2	95.3	88.7	85.7	%
<i>2D parameters</i>				
RSm1	0.055	0.062	0.064	mm
RSm2	0.041	0.057	0.071	mm

#### IV ANALYSES OF ROUGHNESS PARAMETERS OF CYLINDRICALLY GRINDED SURFACES

Roughness parameters of cylindrically grinded surfaces were divided into several groups, depending on the service properties of surfaces.

For the determination of surfaces’ wear resistance it is useful to use parameters *Sa*, *Str*, *Ssk*, *Smr1* and *Smr2*. According to reference [6], the surface wear is characterized by mean arithmetic height of the surface, the roughness steps in the direction of X and Y axes, anisotropy coefficient and relation of nominal and actual area of the surface. And besides, the bigger are the surface irregularities (*Sa*) the weaker is their resistance to deformation. In its turn the bigger are roughness steps values the greater area the protrusions will have, so under load they will be less exposed to shocks and deformations.

Table 2 shows that that sample No.1 has the least roughness and roughness step, which is connected with the reduced longitudinal feed rate of component.

However asymmetry of roughness should also be taken into consideration, because it determines the distribution of load along peaks. Thus using parameter  $Ssk$  it is possible to determine the general shape of roughness peaks.

The surfaces No.1 and No.8 have positive values of parameter  $Ssk$ , i.e. roughness micro-peaks have sharp form and are stress concentrators. At negative values of parameter  $Ssk$  peaks form flat micro-tops, so the load distribution area becomes larger.

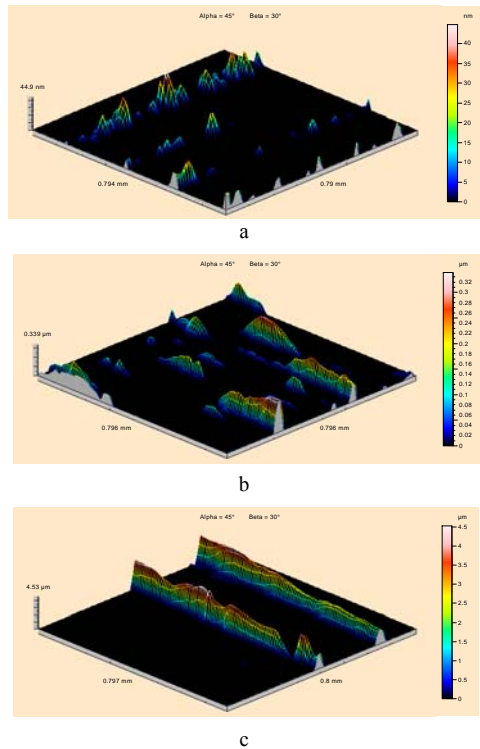


Fig.6. Volume of separated material of surfaces No.1 (a), No.5 (b), No.8 (c) during the running-in operation

Fig.6 shows a part of roughness, which will be rapidly separated from the surface during running-in - initial stage of component exploitation. Values of parameter  $Vmp$  show the volume of the separated material, which is the biggest for the surface No.8. Possible meaning of wear can be determined also by the help of parameter  $Spk$ , which shows the height of the most pronounced micro-peaks.

Additionally it is needed to determine the contact area of surface. Generally, it is simpler to examine contact of rough surface with perfectly smooth (completely hard). In the initial stage of exploitation of component the surface contact takes place at definite points. But in the course of wear of the surface the contact area is increasing and after the run-in stage the surface roughness can have the following look (Fig.7).

The area of bearing surface can be expressed in per cents using parameter  $Smr1$ , which for the surface

No.1 is twice smaller than for No.5 and No.8. Thus it can be concluded that bigger values of roughness  $Sa$  testify more intensive wear, which practically is not affected by height distribution of roughness peaks.

Further in this work it was analyzed the ability of surface to retain lubricants, which mainly depends on hollows depth.

Understanding of the ability of surface to retain oils is given by parameters  $Vv$ ,  $Vvc$  and  $Vvv$ , which help to determine the void volume of roughness prior to exploitation, after the running-in stage and after the period of normal wear.

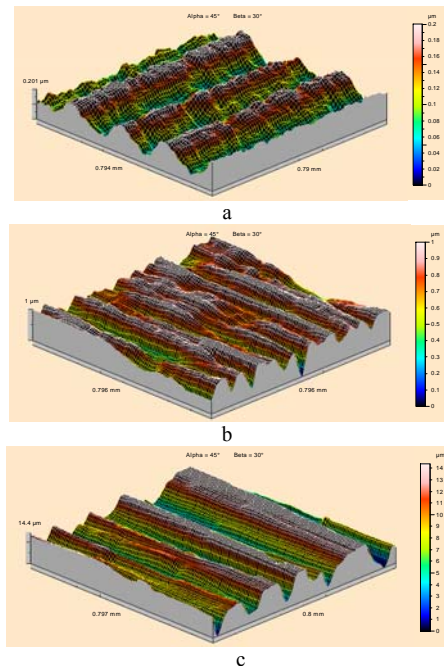


Fig.7. Roughness of surfaces No.1 (a), No.5 (b), No.8 (c) after running-in stage

The growth of height of micro-peaks as compared with optimum values increases wear, which is more intensive even at relatively low service loads, because on the tops of micro-peaks it is appeared a high specific pressure, which causes rupture of oil-film wedge and cutting off of micro-peaks. As a result the friction character changes, clearance becomes bigger, what brings to lubricants free extrusion and dynamic load formation. Due to the fact that the oil-film wedge task is to accommodate the substantial load, the oil shall be all the time evenly distributed between the surface irregularities.

The size of hollows of all three samples after run-in operation is reduced about twice. But the void volume of samples with higher roughness is considerably bigger. Yet this tendency was not observed while normal wear stage, during which values of hollows of surfaces No.1 and No.5 became practically similar. So it can be concluded that surfaces with explicit roughness possess an ability to retain lubrication.

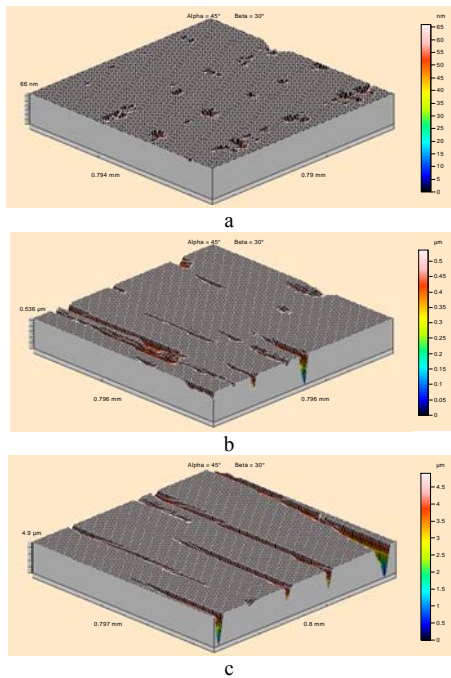


Fig.8. Roughness of surfaces No. 1(a), No.5 (b), No.8 (c) after intensive wear

Regarding to adhesion of coating it should be noted that the advantage of rough surface is the increase of area for the formation of adhesion connections, because the large surface area of substrate provides a greater number of links. For this purpose, it is important to know the value of the parameter  $Sa$ , which gives a notion of the arithmetic average height of roughness and surface smoothness. To understand how great is contact area of deposited coating, it is important to know the value of parameter  $Sdr$ , which is showing relations between nominal surface (without roughness) and actual surface. The bigger the area of actual surface compared to nominal, the more connections will be formed between the substrate and deposited coating.

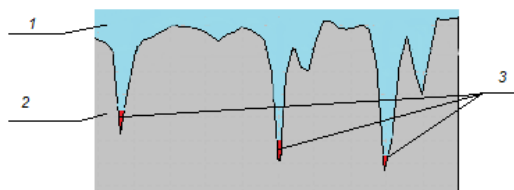


Fig.9. Formation of air pocket.  
1 – coating, 2 – substrate, 3 – air pocket [7]

Because area of substrate surface depends on the character of roughness, it is necessary that surface has deep valleys. Yet there is a risk of air capturing [7]. Air capturing can considerably reduce the efficient volume for sticking as a result connections will be weakened. (Fig.9.). Therefore to allow adhesive to flow into these valleys their form should be rounded as possible. The distribution of

surface roughness height is characterized by parameter  $Sku$ , which values, less than 3, indicate that surface has no sharp peaks.

Parameter  $Sdr$  of surfaces No.1 and No.5 has very small values, only at a considerable increase of roughness the necessary surface area can be ensured for retaining coatings. Values of parameter  $Svk$  indicates that surface No.3 has rather deep hollows but this does not ensure good adhesion, since hollows have sharp form, what is indicated by the values of parameter  $Sku$ . All three samples have the same problem.

## V CONCLUSION

In the course of research mathematical model of cylindrically ground surfaces was determined, including diminishing correlation function and distribution density of ordinates of the surface, which corresponds to normal distribution law.

Roughness of the surface by the increase of the longitudinal feed rate becomes more explicit and the values of mean arithmetical height of roughness are increasing respectively. The given relation affects negatively the wear resistance of the surface however the values of volume of voids to retain lubricant can be sufficient.

It should also be noted that roughness ensures a larger area for its adhesion with a coating, but there is risk of emerging air pocket because of the sharp shape of valleys. With the growth of roughness the average step of roughness is also increasing, what positively affects the distribution of load while surfaces contacting.

## VI ACKNOWLEDGMENTS

This work has been supported by the European Social Fund within the project “Support for the implementation of doctoral studies at Riga Technical University”.



## VII REFERENCES

- [1] ISO 25178-2:2012, Geometrical product specifications (GPS) - Surface texture: Areal - Part 2: Terms, definitions and surface texture parameters.
- [2] Taylor Hobson Ltd. “Form Talysurf Intra”, Taylor Hobson Precision, 2013. – 12 p.
- [3] K.J.Stout, P.J.Sullivan, W.P.Dong, E.Mainsah, N.Luo, T.Mathia, H.Zahouani, *Development of Methods for the Characterisation of Roughness in Three Dimensions*, ECSCE-EEC-AEC, Brussels - Luxemburg, 1993. – 359 p.
- [4] A.N.Tabenkin., S.B.Tarasov, S.N.Stepanov, *Roughness, waviness, profile*, SPb: Politeh. un., 2007- 136 p.
- [5] J.Rudzitis, *Contact mechanics of surfaces, part I*. RTU, Riga, 2007. – 193p.

- [6] J.Rudzitis, *Contact mechanics of surfaces, part II*. RTU, Riga, 2007. – 213p.      [7] N.Filipova, *Surface texture parameters application, studying plane grinded surfaces*. Master's work, RTU, 2014. – 79 p.

# The Effect of Heat Treatment on the Properties of Ultra High Strength Concrete

**Girts Bumanis, Nikolajs Toropovs, Laura Dembovska, Diana Bajare, Aleksandrs Korjakins**  
*Riga Technical University, Faculty of Civil Engineering, Department of Building Materials and Products. Address: Azenes Street 16, Riga, LV-1658, Latvia*

**Abstract.** The influence of heat treatment during curing process of ultra high strength concrete (UHSC) was researched. Four different heat treatment temperatures ranging from 50 to 200°C were studied and compared to the reference temperature regime (20°C). Two series of heat treatment were applied: (a) at the early age of UHSC (3 days) and (b) after 27 days of standard curing regime in water at 20°C. Concrete compressive strength was tested at the early age (4 days) and at the age of 28 days. The water absorption and water penetration under pressure were tested for heat treated and untreated UHSC specimens. SEM and XRD investigations of the studied samples were performed. UHSC with the strength of 123 MPa at the age of 28 days was tested at the standard curing conditions. Results indicate that early age curing at elevated temperature increases early compressive strength from 123 to 189% while at the age of 28 days the compressive strength was only 95 to 117% from reference and depends on the heat treatment regime. The heat treatment of UHSC at the age of 27 days was beneficial with regard to the strength development. Heat-treated UHSC provided compressive strength gain from 112 to 124% from reference. The water absorption for all UHSC specimens was from 2.6 to 3.2 wt.% and it was not affected by the heat treatment. The calcite was detected with XRD in heat treated UHSC samples which indicates the carbonization of Portlandite. This could explain the strength gain of heat-treated samples and the reason for slow compressive strength increase in the case of early heat treatment application. SEM images reveal dense structure and unreacted silica fume particles. The early heat treatment initiated high early strength but the strength of concrete reduced at the age of 28 days comparing to the early strength; therefore late heat application was beneficial for strength gain of the UHSC.

**Keywords:** curing conditions, heat treatment, ultra high performance concrete.

## I INTRODUCTION

In the concrete industry ultra high strength concrete (UHSC) is a result of logical evolution process of traditional concrete and high strength concrete (HSC). UHSC is characterised with high binder content and reduced aggregate size and water to cement (or cement paste) ratio below 0.25 which allows obtaining material without capillary porosity. The compressive strength of UHSC exceeds 150 MPa [1]. To obtain UHSC effective micro and nano fillers such as pozzolans or supplementary cementitious materials have to be used. Incorporation of the above mentioned fillers which contain amorphous SiO<sub>2</sub> additives (i.e. micro and nano silica) in the mixture composition of concrete reduces the amount of Portlandite Ca(OH)<sub>2</sub> and CaCO<sub>3</sub> due to the pozzolanic reaction in hardened cement paste; therefore the amount of C-S-H increases which promotes strength gain of concrete [2]. Also SiO<sub>2</sub> and Al<sub>2</sub>O<sub>3</sub> rich additives like zeolites can increase the amount of the C-S-H gel in concrete and

reduce Portlandite by almost 50% at the concrete age of 3 and 28 days [3]. Pozzolanic reactions are slow thus for favourable reactions in UHSC heat treatment can be applied and the potential of supplementary cementitious materials containing high amount of amorphous SiO<sub>2</sub> can be used in the concrete cured at elevated temperatures. Fine glass (<25 μm) incorporated in concrete provides significant pozzolanic reactions in elevated temperatures even at early age [4]. The heat treatment of cement matrix leads to mineral composition change in the structure. Increased temperature during hardening intensifies the formation of CAH<sub>10</sub> and C<sub>2</sub>AH<sub>8</sub> at the temperature 60 and 80°C, while at 110°C there is dense C<sub>3</sub>AH<sub>6</sub> structure observed [5].

Gallucci concluded that concrete cured at elevated temperatures up to 60 °C provides lower final strength caused by the C-S-H packing in nanoscale due to lose of bound water; therefore cement paste is coarser and more porous [6]. Derabla and Benmalek has published a research where self-compacting concrete with 50

MPa strength has been heat treated at 60°C for 24 h. This approach turned out to be cost effective in early age of concrete while in long term the compressive strength loss was observed comparing to reference concrete [7].

Yan and Cui have reported that HSC cured at elevated temperatures restrains the compressive strength development, if only Portland cement is used in mixture composition, while using pozzolanic materials the compressive strength of concrete increases two times at early age and continues to grow in long term [8]. Other research has tested effect of elevated temperature to high volume fly ash concrete and it was concluded that exposure to elevated temperature up to 300°C increased the compressive strength of concrete while treatment at higher temperature decreased the strength of concrete [9], [10].

There are negative aspects which must be considered in order to apply heat treatment to the UHSC. In some cases significant damages of surfaces were observed for specimens cured at elevated temperatures. It is explained by excessive deformation of the exposed surface layer of concrete [11]. This can cause microcracking of the surface; therefore reduction of mechanical properties and durability of concrete can be observed.

Another problem of HSC exposure to elevated temperatures is related to explosive spalling, when sudden and destructive breaking of surface layer occurs during heating of concrete [12]. This problem has been associated with dense structure of the HSC and UHSC and this leads to low permeability of the material. The evaporation of free water from the structure of such concrete is limited, which builds up inner pressure, and when the tensile strength of concrete is reached, the spalling of concrete surface destroys the structure of the material. The pore pressure begins at 105°C, which corresponds to the water evaporation temperature, and the peak of pressure is reached at 220°C, when either explosive spalling occurs or pore pressure attenuates [13]. This is important finding for understanding the properties of UHCP. It is recommended not to exceed curing temperature above 200°C to avoid the potential pressure building up to critical and reduce the risk of explosive spalling.

In current research two series of heat treatment regimes in curing processes of UHCP were investigated and 200°C was selected as the highest heat treatment temperature.

## II MATERIALS AND METHODS

Ultra high strength concrete (UHSC) mixture design was created using CEM I 42.5 N with Blaine fineness of 3787 cm<sup>2</sup>/g. The maximal grain size of

UHSC filler was 2.5 mm. Four fractions of fine sands were used: 0.3/2.5 mm, 0/1.0 mm, 0/0.3 mm and quartz powder to ensure compact structure of the UHCP. Elkem silica fume grade 971 (Fig. 1) and NanoSilica 999 (Fig. 2) were used as microfillers.

The mixture composition of UHSC is given in Table 1. The amount of cement was 800 kg/m<sup>3</sup>, the W/C was 0.25, and water to cement paste (cement and silica fumes) ratio W/(C+P) was 0.22. To ensure workability of such low W/C UHCP mixture superplasticizer Sikament 56 was used (2.5% from weight of cement). Micro silica fume was added 12.5% from the mass of cement (100 kg/m<sup>3</sup>) and nanosilica – 2.5% (20 kg/m<sup>3</sup>) respectively.

The mixing procedure of UHCP was the following: all dry components except NanoSilica were mixed together for 90 s to obtain homogenous mixture of dry components.

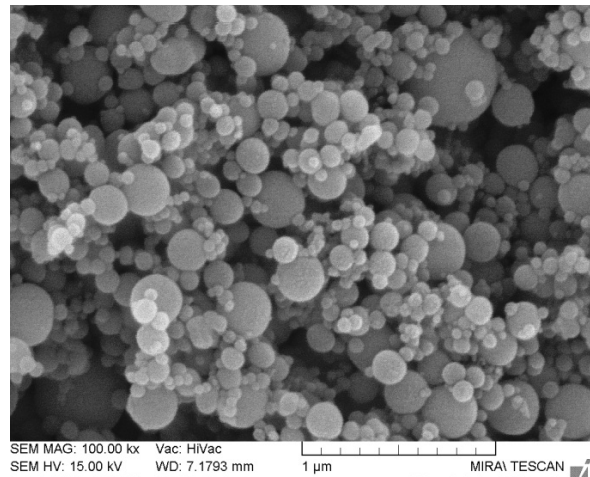


Fig. 1. Scanning electron microscope image of Elkem micro silica fume grade 971.

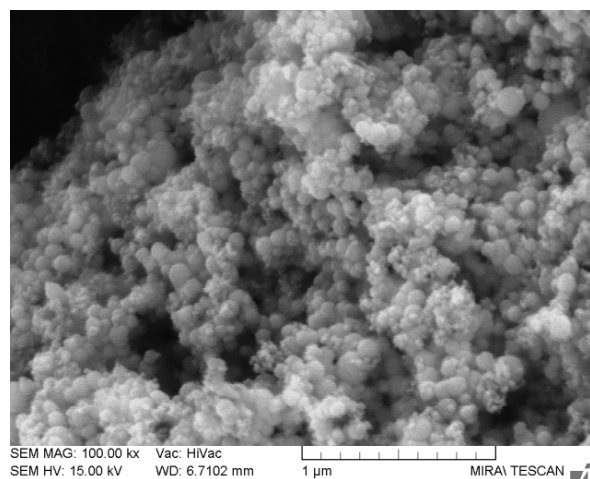


Fig. 2. Scanning electron microscope image of Elkem nano silica fume NanoSilica 999.

Then NanoSilica as water suspension (with ratio 1:2) and 75% of water were added to the mixture of dry components and mixed together for 120 s. In the last stage superplasticizer with the rest of water (25%) were added and mixed until homogenous and workable mixture was obtained. The total mixing time of UHCP was 6 minutes. 3 batches were prepared with 7 l of UHCP in each batch. The UHCP was cast in 18 cubical moulds with dimensions 5x5x5 cm, 4 cubical moulds with dimensions 10x10x10 cm and 9 prismatic moulds with dimension of 4x4x16 cm. After casting of UHCP in moulds samples were vibrated for 10 s.

Table I  
Mixture composition of UHCP

Mixture composition	kg/m <sup>3</sup>
Cement CEM I 42,5 N	800
Sand 0.3/2.5 mm	510
Sand 0/1.0 mm	480
Sand 0/0.3 mm	100
Quartz powder	100
Micro silica fume	100
Nano silica fume	20
Superplasticizer	20
Water	200
W/C	0.25
W/(C+P)	0.22

Samples were remoulded after 3 days of hardening and cured at standard conditions in water ( $\pm 20^{\circ}\text{C}$ ) or early heat treatment regime was applied. Four heat treatment conditions at temperature 50, 100, 150 and 200°C were tested for UHCP. The heat treatment was applied after remoulding the samples (on 3<sup>rd</sup> day) or at the age of 27 days after standard curing conditions (Table 2). The temperature increase during heating was 10 °C/min, samples were treated at the maximal temperature for 4 h and then cooled to room temperature.

Table II  
Heat treatment regimes applied to UHCP

Sample ID	Concrete age, d	Heat treatment, °C
Ref	-	-
HT3-50	3	50
HT3-100	3	100
HT3-150	3	150
HT3-200	3	200
HT27-50	27	50
HT27-100	27	100
HT27-150	27	150
HT27-200	27	200

The compressive strength of concrete was tested according to LVS EN 12390-3. Compressive strength was determined for the specimens sized 50x50x50 mm. Depth of penetration of water was tested according to LVS EN 12390-8. Concrete specimens with dimensions 100x100x100 mm were tested under pressure of 500 KPa for 72+2 h. Water absorption was determined according to EN 1097-6. Scanning electron microscope (SEM) (Tescan Mira/LMU) was used for microstructural research and the mineralogical composition was determined with XRD (PAN analytical X'Pert PRO).

### III RESULTS AND DISCUSSION

The density of obtained UHSC was 2.32 g/cm<sup>3</sup> and after heat treatment at temperature 200°C it decreased to 2.25 g/cm<sup>3</sup> which can be attributed to the evaporation of free water from the structure of UHSC. The SEM image of microstructure for reference sample (Ref) is given in Fig. 3 and for HT3-200 in Fig. 4. In both images dense microstructure of specimens was observed and the unreacted silica fume particles were detected. The significant difference of microstructure after heat treatment cannot be observed by SEM images; however, microstructure of the heat treated samples looks more porous compared to the reference sample. It could be explain by dehydration of C-S-H gel during heat application.

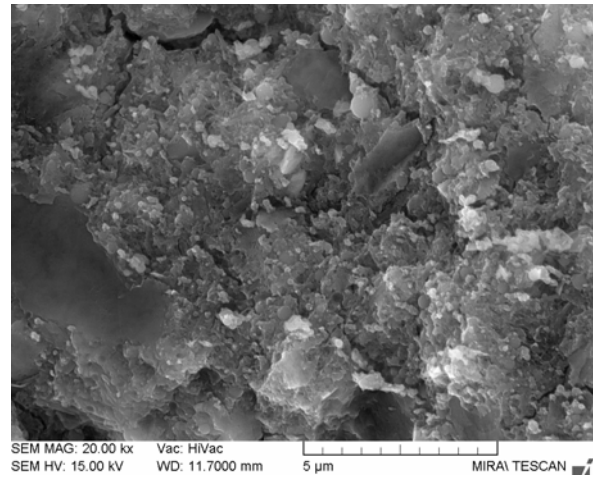


Fig. 3. The microstructure of UHSC cured at standard conditions at the age of 4 days (Ref).



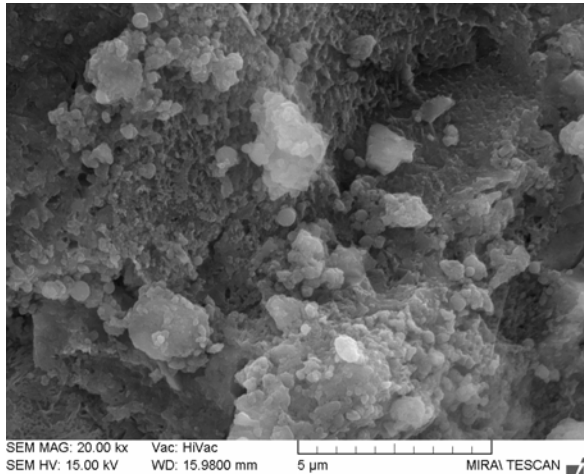


Fig. 4. The microstructure of UHSC cured at 200 °C for 4 h at the age of 4 days (HT3-200).

The results of compressive strength are given in Table 3. The early heat treatment of UHSC was beneficial for early compressive strength. The compressive strength for reference (Ref) UHSC was 77 MPa at the age of 4 days. The heat treatment even at 50°C for 4 hours increased the compressive strength up to 95 MPa but significant strength gain was observed for UHSC treated at temperature 100°C (130 MPa).

The heat treatment at early age in the temperature above 100°C – 143 MPa (150°C) and 145 MPa (200°C) was less effective. However, the early heat treatment did not provide further compressive strength increase during ageing of the concrete. At the age of 28 days compressive strength of reference increased to 123 MPa while for HT3-50 the decrease of compressive strength to only 117 MPa was observed-. HT3-100 provided almost the same compressive strength as Ref at the age of 28 days (124 MPa) while samples cured at 150 and 200°C (HT3-150 and HT3-200) provided compressive strength increase to 137 and 144 MPa respectively.

Table III  
Compressive strength results of UHSC

Sample ID	Compressive strength, MPa		Strength index, %	
	4 <sup>th</sup> day	28 <sup>th</sup> day	4 <sup>th</sup> day	28 <sup>th</sup> day
Ref	77	123	100	100
HT3-50	95	117	119	95
HT3-100	130	124	141	101
HT3-150	143	137	146	110
HT3-200	145	144	147	115
HT27-50	-	138	-	111
HT27-100	-	144	-	115
HT27-150	-	150	-	118
HT27-200	-	153	-	120

The heat treatment for UHSC at the age of 27 days was beneficial to the compressive strength increase for all heat treatment regimes. The compressive strength of samples treated at temperature 200 °C in age of 27 days increased up to 153 MPa comparing to the reference samples (123 MPa). This indicates the importance of initial water curing at standard conditions of UHSC and understanding the necessity for heat treatment at proper age of the concrete. The strength index increased to 111 to 120% compared to the reference by applying heat treatment at the UHSC aged 27 days

The relative strength increase of UHSC related to the heat treatment temperature and the age of UHSC, when heat treatment was applied, is given in Fig 5. The initial compressive strength increase at the age of 4 days was significant (119%) even at the heat treatment at 50 °C, while the strength at 28 days decreased to 95% comparing to the reference. The compressive strength increase at the age of 28 days for samples, which were heat treated at the age of 27 days, was almost linear and strength increase was observed for every sample treated in elevated temperature.

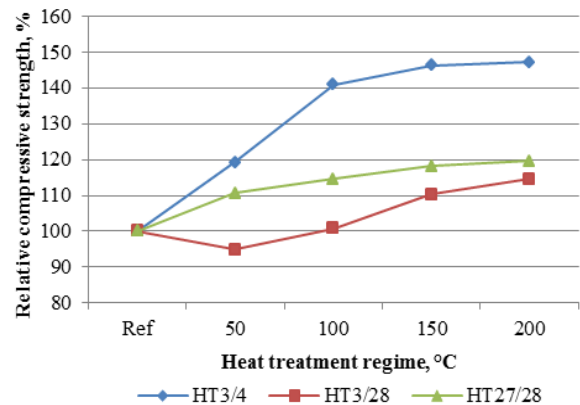


Fig. 5. Relative strength index of heat treated UHSC samples comparing to reference samples with standard curing regime.

The water absorption of UHSC was from 2.2 to 3.5%, and it was not affected by the heat treatment regime. The water penetration under pressure of 5 Bar was not detected for untreated UHSC at the age of 28 days (0 mm) while for heat treated samples HT3-200 the water penetration was 3 mm in average and up to 8 mm in some parts. This could be explained by the crack pattern of UHSC which appeared after heat treatment and thermal stresses, induced by the increased temperature and drying conditions, and was clearly seen after water penetration test (Fig 6).



Fig. 6. The microcrack pattern of split UHSC sample cured at 200 °C for 4 h (HT3-200).

The XRD patterns of reference and HT3-200 are given in Fig. 7 and Fig. 8. The results indicate that UHSC cured at standard conditions has quartz (Q), larnite (L) and plagioclase (P) minerals, while in heat treated sample calcite (C) has been detected, which could indicate the carbonization of free portlandite ( $\text{Ca}(\text{OH})_2$ ) and therefore possibly increases the early age strength of UHCP. The reduction of portlandite could restrict the pozzolanic reaction; therefore long term strength gain is limited for heat treated samples.

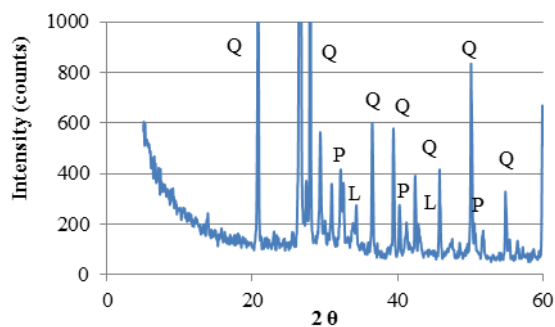


Fig. 7. XRD pattern of UHSC cured at standard conditions (Ref) at the age of 28 days.

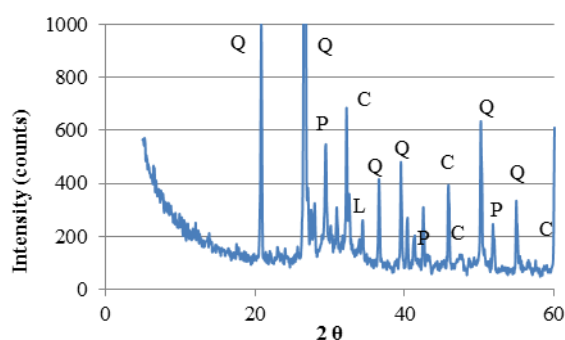


Fig. 8. XRD pattern of UHSC cured at 200 °C for 4 h (HT3-200) at the age of 28 days.

#### IV CONCLUSIONS

It was concluded that the early heat treatment at the temperatures ranging from 50 to 200°C is effective to gain early age strength of UHSC, while in the long term curing in temperature from 50 to 100°C was not effective and strength reduction was observed

comparing to UHSC cured in standard conditions. Early heat treatment was effective in temperature range from 150 to 200°C, when compressive strength at 28 days increased from 110 to 115% comparing with reference concrete. The heat treatment of UHSC at the age of 27 days increased its compressive strength from 111 to 120%, and was beneficial with all heat treatment regimes. The heat treatment caused microcrack pattern of UHSC which reduced resistance to water penetration under pressure. In the mineralogical composition of UHSC after heat treatment calcite  $\text{CaCO}_3$  was detected, which indicates the carbonization of free  $\text{Ca}(\text{OH})_2$  and is one of reasons for early age strength gain of UHSC.

#### V ACKNOWLEDGMENT

The research leading to these results has received the funding from the Latvian state research programme under grant agreement „INNOVATIVE MATERIALS AND SMART TECHNOLOGIES FOR ENVIRONMENTAL SAFETY, IMATEH”.

#### VI REFERENCES

- [1] B. Graybeal, “UHPC Making Strides - Vol. 72 · No. 4 - Public Roads,” 2009. [Online]. Available: <http://www.fhwa.dot.gov/publications/publicroads/09janfeb/03.cfm>. [Accessed: 24-Mar-2015].
- [2] D. Vaičiukyniene, V. Vaitkevičius, A. Kantautas, and V. Sasnauskas, “Effect of AIF<sub>3</sub> Production Waste on the Properties of Hardened Cement Paste,” *Mater. Sci.*, vol. 18, no. 2, pp. 187–191, Jun. 2012.
- [3] D. Vaičiukyniene, G. Skipkiunas, M. Daukšys, and V. Sasnauskas, “Cement hydration with zeolite-based additive,” *Chemija*, vol. 24, no. 4, pp. 271–278, 2013.
- [4] M. Mirzahosseini and K. A. Riding, “Effect of curing temperature and glass type on the pozzolanic reactivity of glass powder,” *Cem. Concr. Res.*, vol. 58, pp. 103–111, Apr. 2014.
- [5] I. Demidova-Buizine and I. Pundiene, “Effect of Amount of Deflocculant on Change in Physicomechanical Properties of Medium-Cement Heat-Resistant Concretes During Drying and Heat Treatment,” *Refract. Ind. Ceram.*, vol. 55, no. 2, pp. 121–127, Aug. 2014.
- [6] E. Gallucci, X. Zhang, and K. L. Scrivener, “Effect of temperature on the microstructure of calcium silicate hydrate (C-S-H),” *Cem. Concr. Res.*, vol. 53, pp. 185–195, Nov. 2013.
- [7] R. Derabla and M. L. Benmalek, “Characterization of heat-treated self-compacting concrete containing mineral admixtures at early age and in the long term,” *Constr. Build. Mater.*, vol. 66, pp. 787–794, Sep. 2014.
- [8] P. Yan and Q. Cui, “Effects of curing regimes on strength development of high-strength concrete,” *Kuei Suan Jen Hsueh Pao/Journal Chinese Ceram. Soc.*, vol. 43, no. 2, pp. 133–137, 2015.
- [9] M. S. Khan and H. Abbas, “Effect of elevated temperature on the behavior of high volume fly ash concrete,” *KSCE J. Civ. Eng.*, Dec. 2014.
- [10] K. N. Vishwanath Prof., S. Narayana Dr., and V. Bindiganavile Dr., “Influence of sustained elevated temperature on fly ash concrete,” *Indian Concr. J.*, vol. 88, no. 1, pp. 26–32, 2014.
- [11] A. Omran, Z. He, and G. Long, “Heat damage of steam curing on the surface layer of concrete,” *Mag. Concr. Res.*, vol. 64, no. 11, pp. 995–1004, Nov. 2012.

- [12] L. Phan and N. Carino, "Effects of test conditions and mixture proportions on behavior of high-strength concrete exposed to high temperatures," *ACI Mater. J.*, vol. 99, no. 1, pp. 54–66, 2002.
- [13] L. T. Phan, "Pore pressure and explosive spalling in concrete," *Mater. Struct.*, vol. 41, no. 10, pp. 1623–1632, 2008.

# **Application of Latvian illite clays in cosmetic products with sun protection ability**

**Inga Dušenkova, Iveta Kusiņa, Juris Mālers, Līga Bērziņa-Cimdiņa**  
*Rīga Technical University, Faculty of Material Science and Applied Chemistry,  
Institute of General Chemical Engineering.  
Address: Valdena street 3, Rīga, LV-1048, Latvia.*

**Abstract.** Recent research shows that clay minerals can be used in sunscreens as UV filters instead of inorganic and organic compounds, which can cause unexpected photo-catalytic effect and damage the skin surface and can be absorbed into the skin and cause allergic reactions. In this study UV transmittance of suspensions containing clay fraction (mostly illite) and 50% glycerol/water solution was measured. Samples without chemical treatment, with removed carbonates and iron containing minerals (oxides and hydroxides) were analyzed.

Results showed that the chemical treatment decreased UV protection ability. The highest increase of UV transmittance was observed for samples after removal of iron containing minerals. UV transmittance decreased by 10-14% when the concentration of clay fraction in the suspension was increased from 20 to 30 mass%. Samples with the highest concentration of iron oxide showed also the highest UV protection ability.

**Keywords:** carbonates, illite clays, iron compounds, purification, UV transmittance.

## I INTRODUCTION

UV radiation has both positive and negative effects on human skin. The positive effect is vitamin D synthesis in the skin, but overexposure to UV radiation can cause sunburn, premature skin aging and skin cancer. There are three types of UV radiation: UV-A (320-400 nm) causes sunburn and skin aging, UV-B (280-320 nm) may cause DNA damage and skin cancer and UV-C (200-280 nm) is the most dangerous, but it is generally absorbed by the ozone layer [1, 2].

Sunscreens can contain both organic and inorganic compounds as UV filters. TiO<sub>2</sub> and ZnO are the most used inorganic compounds, but they can cause an unexpected photo-catalytic effect and damage the skin. The inorganic UV filters are also called physical filters, because their mode of action is based on scattering, reflecting and/or absorbing the sun's radiation [3]. The organic UV filters are usually aromatic compounds with a carbonyl group – salicylates, cinnamates, benzophenones and others. They are called chemical filters due to the chemical changes in their molecules that protect the skin from solar radiation. These compounds can be absorbed into the skin and cause allergic reactions [2, 4].

One of the potential candidate as natural UV filters in sunscreens are clay minerals, due to their positive impact on human health and chemical inertness. Recent research shows that clay minerals have UV protection ability due to their high specific surface area, therefore providing effective coverage of skin surface. The magnitude of UV protection depends on the clay mineralogical composition [1, 5].

The presence of carbonates can cause alkaline media, therefore reducing the efficiency of clay mineral separation from non-clay minerals [6] and can be irritating to the skin [7]. The presence of iron oxides and hydroxides (iron containing minerals) also reduce the efficiency of clay mineral purification [6] and in most cases gives the colour to clays [8]. After the removal of these iron containing minerals the clay samples become lighter in colour (from light greenish gray to white), therefore expanding their application possibilities, because in cosmetics colour is an essential property.

The sun protection ability is characterized by the sun protection factor (SPF) - a ratio of the least amount of solar energy (UV radiation) required to produce sunburn on sunscreen protected skin to the amount of solar energy required to produce sunburn on unprotected skin [1]. The SPF value depends on the applied amount of the sunscreen – the sun protection

ability increases by increasing the applied amount [9]. It is recommended to use sunscreen products with an SPF of 15 or higher [1].

The aim of this study was to determine UV protection ability of Latvian illite clays and to evaluate their possible application in sunscreens and other cosmetic products as UV filters.

## II MATERIALS AND METHODS

### Materials

Clay samples with different mineralogical composition (Table 1) from four sites in Latvia were used. Laža (La) and Prometejs (Pr) clays are from Quaternary period, Pavāri (Pa) clays are from Devonian period, but Iecava (Ie) clays are from dolomite deposits, were they are as by-product after the purification of dolomite. Sample fraction < 63 μm was used, obtained by wet sieving.

Table 1  
Mineralogical composition (mass%) of untreated clays with fraction < 63 μm (± stdev)

Mineral phase	Ie	Pr	La	Pa
Illite	51 ± 3	51 ± 2	34 ± 2	35 ± 3
Kaolinite	-	9 ± 1	11 ± 1	4 ± 2
Chlorite	-	-	8 ± 2	-
Quartz	11 ± 1	14 ± 1	13 ± 1	54 ± 2
Feldspar	26 ± 2	10 ± 1	16 ± 1	7 ± 2
Dolomite	4 ± 1	9 ± 1	5 ± 1	-
Calcite	-	7 ± 1	8 ± 1	-
Muscovite	8 ± 2	-	5 ± 2	-

To evaluate the sun protection ability, commercial sunscreens with SPF 15, 30 and 50 were used. All sunscreens contained TiO<sub>2</sub> and ZnO.

### Purification methods

1M hydrochloric acid solution was used to dissolve carbonates. During the dissolution process the suspensions were stirred and the pH was kept above 4.5 in order to avoid damaging the structure of clay minerals [6]. When the pH was ~ 5 and stayed constant, the suspensions were centrifuged and all clay samples were washed with distilled water several times, until the electrical conductivity of supernatant liquid was < 100 μS/cm. Then clay fraction < 2 μm was obtained by centrifugation. These clay samples were referred to as -HCl, for example La-HCl.

Before the removal of iron oxides and hydroxides, all samples were treated with HCl in order to dissolve the carbonates. Dry clay samples (10 g) were mixed with 40 ml of 0.3 M sodium citrate and 5 ml of 1 M sodium bicarbonate solutions. Suspensions were

heated to 75-80°C, 1 g of sodium dithionite was added to each and then mixed for 30 minutes [10]. The colour of suspensions turned blue-green. All suspensions were washed twice with 1M NaCl and then with distilled water, until electrical conductivity of the supernatant liquid was < 100 μS/cm. Then clay fraction < 2 μm was obtained by centrifugation. All treated samples were referred to as -D, for example, La-D.

### Preparation of suspensions

Dry samples were mixed with necessary amount of 50% (mass/mass) glycerol/water solutions to obtain suspensions with 20 and 30 mass% of clay fraction. All suspensions were homogenized with disperser T18 Ultra Turrax and matured in locked containers for 2 weeks.

### Characterization of the samples

Determination of chemical composition was conducted with scanning electron microscopy energy-dispersive X-ray spectroscopy SEM-EDS (Tescan, Mira/LMU). The loss on ignition (LOI) was obtained after heating in 1000°C for 4 h.

The sun protection ability of clay fraction/glycerol suspensions was determined by measuring UV transmittance from 290 to 400 nm. UV-VIS spectrophotometer Evolution 300 was used. A small drop of the suspension was applied on 2 mm thick quartz glass and spread evenly on the whole glass surface (3.14 cm<sup>2</sup>) with finger, until the sample mass was 0.45 ± 0.01 mg. After 20 minutes UV transmittance was measured in 5 different places. Three parallel measurements were made for each sample and the average result with standard deviation (stdev) was used. The SPF values are calculated from the obtained data using equation (1):

$$SPF_{invitro} = \frac{\sum_{290}^{400} E_{\lambda} \cdot S_{\lambda}}{\sum_{290}^{400} E_{\lambda} \cdot S_{\lambda} \cdot T_{\lambda}} \quad (1)$$

where  $E_{\lambda}$  is the erythema action spectrum,  $S_{\lambda}$  is the solar spectral irradiance,  $T_{\lambda}$  is the spectral transmittance of the sample [9].

## III RESULTS AND DISCUSSION

### Sample characteristics

The changes in the colour of samples (Table 2) indicated the removal of iron containing minerals. The brown colour of La and Pr samples indicated the presence of goethite and hematite [8], the light gray colour of sample Ie – small amounts of pyrite, but the light beige colour (pinkish white in Munsell colour scale) of sample Pa indicated low content of iron containing minerals and organic matter [11]. After the removal of iron containing minerals, La-D and Pr-D samples were light gray, Ie-D sample – greenish gray,

but Pa-D sample – grayish white (white in Munsell colour scale). Because Ie and Pa samples were not brown, the removal of iron containing minerals was proved by the changes in chemical composition, as shown in Table 3.

After the removal of iron containing minerals the amount of iron has decreased by 10% in sample Ie-D, by 22% in sample La-D, by 19% in sample Pr-D and by 3% in sample Pa-D (see Table 3). Because  $\text{Fe}^{2+}$  and  $\text{Fe}^{3+}$  ions can be found in the octahedral sheet of clay mineral structure [12], the rest of iron can be from the structure of clay minerals. The amount of calcium ions also have significantly decreased, due to the removal of carbonates.

Table 2  
Colour based on Munsell colour system before and after removal of iron containing minerals

Samples	Colour	Colour code
Pa	Pinkish white	7.5YR 8/2
Pa-D	White	7.5YR 8/1
Ie	Light gray	5Y 7/1
Ie-D	Light greenish gray	10BG 7/1
La	Light brown	7.5YR 6/4
L-D	Light gray	2.5Y 7/1
Pr	Light reddish brown	5YR 6/4
Pr-D	Light gray	2.5Y 7/1

Table 3

Chemical composition (mass%) of clay fraction < 2  $\mu\text{m}$  before and after removal of iron containing minerals ( $\pm$  stdev)

Sample	$\text{SiO}_2$	$\text{Al}_2\text{O}_3$	$\text{Fe}_2\text{O}_3$	CaO	MgO	$\text{K}_2\text{O}$	$\text{TiO}_2$	$\text{Na}_2\text{O}$	LOI
Ie	49.6 $\pm$ 1.0	18.5 $\pm$ 0.2	9.0 $\pm$ 0.5	3.9 $\pm$ 0.8	4.3 $\pm$ 0.4	7.1 $\pm$ 0.3	1.0 $\pm$ 0.3	0.3 $\pm$ 0.1	6.8 $\pm$ 0.1
Ie-D	52.2 $\pm$ 1.0	19.8 $\pm$ 0.4	8.1 $\pm$ 0.3	0.7 $\pm$ 0.1	4.1 $\pm$ 0.2	8.0 $\pm$ 0.1	1.2 $\pm$ 0.3	0.6 $\pm$ 0.1	5.7 $\pm$ 0.1
Pr	47.3 $\pm$ 1.0	20.4 $\pm$ 1.4	9.7 $\pm$ 0.2	4.2 $\pm$ 0.2	3.7 $\pm$ 0.3	5.2 $\pm$ 0.3	0.6 $\pm$ 0.2	0.6 $\pm$ 0.2	9.1 $\pm$ 0.1
Pr-D	53.6 $\pm$ 0.7	21.8 $\pm$ 1.0	7.9 $\pm$ 0.7	0.6 $\pm$ 0.4	3.3 $\pm$ 0.2	5.1 $\pm$ 0.2	0.4 $\pm$ 0.4	1.4 $\pm$ 0.1	6.2 $\pm$ 0.3
La	46.7 $\pm$ 1.1	21.6 $\pm$ 0.8	8.9 $\pm$ 0.4	3.4 $\pm$ 0.3	3.5 $\pm$ 0.2	5.1 $\pm$ 0.2	1.0 $\pm$ 0.1	0.9 $\pm$ 0.1	8.9 $\pm$ 0.1
La-D	53.8 $\pm$ 0.9	21.8 $\pm$ 0.2	6.9 $\pm$ 0.4	0.5 $\pm$ 0.1	3.3 $\pm$ 0.3	5.4 $\pm$ 0.2	1.0 $\pm$ 0.4	1.3 $\pm$ 0.2	6.5 $\pm$ 0.1
Pa	56.2 $\pm$ 1.0	24.3 $\pm$ 0.3	7.4 $\pm$ 0.7	0.6 $\pm$ 0.2	2.1 $\pm$ 0.2	5.3 $\pm$ 0.3	1.5 $\pm$ 0.1	0.1 $\pm$ 0.2	2.5 $\pm$ 0.1
Pa-D	54.1 $\pm$ 0.9	24.6 $\pm$ 0.7	7.2 $\pm$ 0.3	0.5 $\pm$ 0.1	2.0 $\pm$ 0.2	5.0 $\pm$ 0.2	1.3 $\pm$ 0.1	0.3 $\pm$ 0.1	5.0 $\pm$ 0.1

#### Purification influence

Samples with untreated clay fraction showed the lowest UV transmittance (Fig.1), therefore these samples have higher UV-protection ability than those after removal of carbonates and iron containing minerals. The most significant increase in UV transmittance showed samples after removal of iron containing minerals – approximately 12-18% higher than for untreated samples. Hoang-Minh et al. research [1] obtained similar results after the treatment with sodium dithionite and explained it with the absence of  $\text{Fe}^{3+}$  ions. They stated and proved that UV-protection ability is closely related to the presence of iron containing minerals. For example, hematite ( $\text{Fe}_2\text{O}_3$ ) contains  $\text{Fe}^{3+}$  bonded to  $\text{O}^{2-}$ , where the electron configuration of  $\text{Fe}^{3+}$  is characterized by an empty orbital (4s), so that inner electrons can absorb the energy and move from the 3d orbital to the 4s orbital with a higher energy level.  $\text{TiO}_2$  particles (specifically  $\text{Ti}^{4+}$  ions) have the same UV absorption mechanism. The octahedral sheet in the structure of clay minerals also can contain  $\text{Fe}^{3+}$  ions that have an

electron configuration with an empty orbital, and thus it should theoretically absorb photons. This assumption was shown experimentally by Chen et al. [13] where the absorption intensity in the UV-C range was directly correlated to structural octahedral contents of  $\text{Fe}^{3+}$  in smectite clays. Similar correlation was demonstrated also in clays containing mostly nontronite [1].

#### Influence of clay fraction concentration

As the concentration of clay fraction was increased by 10 mass% (from 20 to 30 mass%), UV transmittance decreased by 12-14% for sample Ie, 11% for sample La, 10% for sample Pr and 12% for sample Pa. Based on the decrease of UV transmittance, the SPF values slightly increased: by 35% for sample Ie, by 27% for samples La and Pr, and only by 16% for sample Pa (see Table 4). Sample Pa showed the highest UV transmittance due to the lowest content of iron containing minerals.

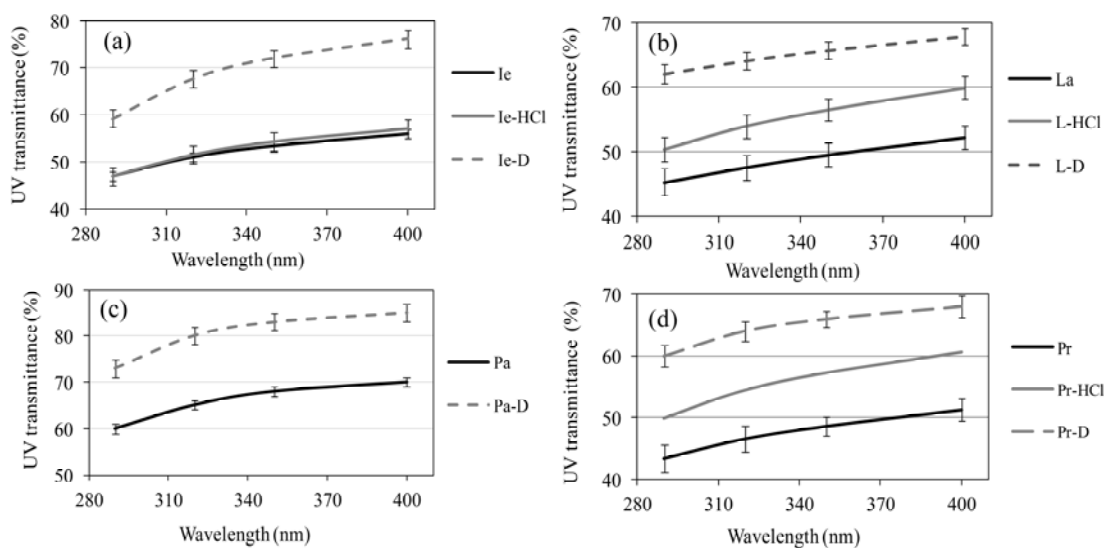


Fig.1. Influence of the used treatment on UV transmittance of Iecava (a), Laža (b), Pavāri (c) and Prometejs (d) clay samples with solid concentration 20 mass%.

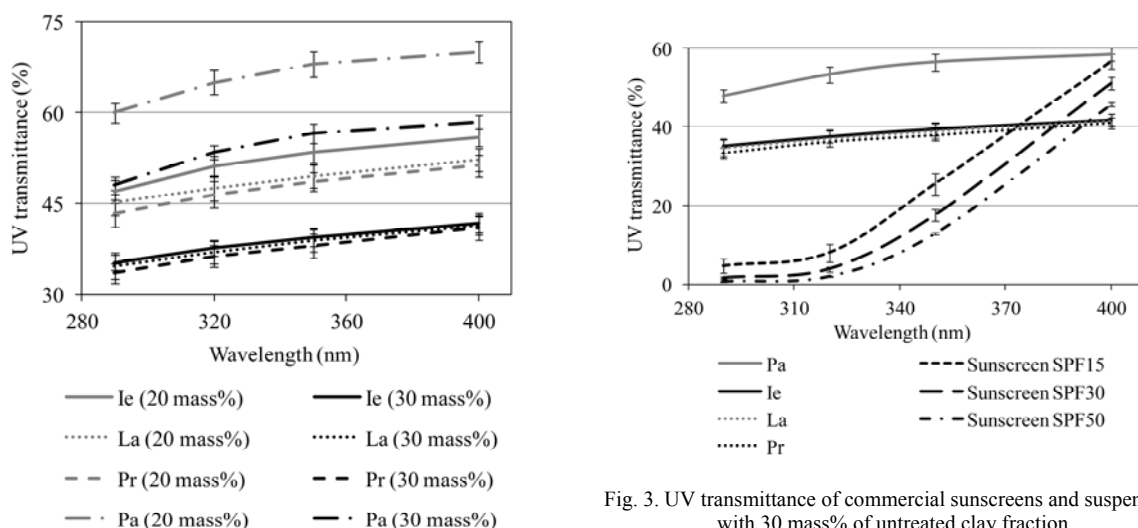


Fig. 2. Influence of clay fraction concentration in the suspension on UV transmittance.

The commercial sunscreens containing TiO<sub>2</sub> and ZnO showed more intensive UV protection abilities in all UV-B and in the beginning of UV-A range (see Fig.3), therefore they also have much higher SPF values – 15, 30 and 50. Pastes and creams containing TiO<sub>2</sub> and ZnO for application as sunscreens tends to be white on the skin, which is unacceptable for cosmetic use, therefore occasionally iron oxide pigments are added to improve the appearance of the product [4]. Because most of the clays in Latvia are brown, they can be used as pigment in sunscreens of tonal creams. At the same time the addition of clay fraction would increase the SPF of the product, thereby decreasing the necessary amount of synthetic UV filters to obtain certain SPF value.

Fig. 3. UV transmittance of commercial sunscreens and suspensions with 30 mass% of untreated clay fraction.

#### IV CONCLUSION

Illite containing clay fraction samples from Latvian clays showed the ability to partially absorb UV radiation. The influence of the removal of carbonates

Table 4  
SPF of untreated clay fraction suspensions in glycerol solution

Sample	Concentration of clay fraction, mass%	SPF ± stdev
Ie	20	2,0 ± 0,1
	30	2,7 ± 0,1
La	20	2,2 ± 0,1
	30	2,8 ± 0,2
Pr	20	2,2 ± 0,1
	30	2,8 ± 0,1
Pa	20	1,6 ± 0,1
	30	1,9 ± 0,1

and iron containing minerals was negative – UV transmittance increased, therefore UV protection properties decreased. From these results it can be concluded, that it is useful to use clay minerals with high content of iron compounds in sunscreens. Despite the relatively low SFP values of clay samples, illite containing clay minerals can be used in sunscreens with low SPF values as one of the UV filters, at the same time giving a light brown colour.

#### V ACKNOWLEDGMENTS

This work has been supported by the National Research Program of Latvia 2014-2017 within the project No.4.4. (Y8099) „Zemes dziļu resursu izpēte dabisko izejvielu dažādošanai un jaunu tehnoloģiju izstrādei (GEO)” (in English - Investigation of underground resources to obtain different natural raw materials and to develop new technologies (GEO)).

#### VI REFERENCES

- [1] Hoang-Minh T., Le T.L., Kasbohm J., Giere R. UV-protection characteristics of some clays. *Applied Clay Science*, 48, 2010, pp. 349.-357.
- [2] El-Boury S., Couteau C., Boulande L., et al. Effect of the combination of organic and inorganic filters on the Sun Protection Factor (SPF) determined by in vitro method// *Int. J. Pharm.* – 2007. – Vol.340. – 1.-5. p.
- [3] Smijs T.G., Pavel S. Titanium dioxide and zinc oxide nanoparticles in sunscreens: focus on their safety and effectiveness. *Nanotechnology, Science and Applications*, 4, 2011, pp. 95.-112.
- [4] Serpone N., Dondi D., Albini A. Inorganic and organic UV filters: Their role and efficiency in sunscreens and sun care products. *Inorganica Chimica Acta*, 360, 2007, pp. 794.-802.
- [5] Hoang-Minh T., Le T.L., Kasbohm J., Giere R. Substituting non-natural agents in UV protection cream by a mixture of clay with *Ganoderma pfeifferi* extract. *Applied Clay Science*, 53, 2011, pp. 66-72.
- [6] Carrado K.A., Decerreau A., Petit S. Synthetic clay minerals and purification of natural clays. *Handbook of Clay Science*, 2006, pp. 115.-139.
- [7] Matike D.M.E., Ekosse G.I.E., Ngole V.M. Physico-chemical properties of clayey soils used traditionally for cosmetics in Eastern Cape, South Africa. *International Journal of the Physical Sciences*, 2011, 33, pp. 7557 – 7566.
- [8] Reeves G.M., Sims I., Cripps J.C. The composition of clay materials. *Clay Materials Used in Construction*, 2006, pp. 13-27.
- [9] Couteau C., Paparis E., El-Bourry-Alami S., Coiffard L.J.M. Influence on SPF of the quantity of sunscreen product applied. *International Journal of Pharmaceutics*, 2012, 437, pp. 250-252.
- [10] Mehra O.P., Jackson M.L. Iron oxide removal from soils and clays by a dithionite-citrate system buffered with sodium bicarbonate. *Clays and Clay Minerals*, 7, 1960, pp. 317.-327.
- [11] Merriman R.J., Highley D.E., Cameron D.G. Definition and characteristics of very-fine grained sedimentary rocks: clay, mudstone, shale and slate. 2003, pp. 22.
- [12] Brigatti M.F., Galan E., Theng B.K.G. Structures and mineralogy of clay minerals. *Handbook of Clay Science*, 2006, pp. 19-86.
- [13] Chen Y., Shaked D., Banin A. The role of structural iron(III) in the UV absorption by smectites. *Clay Minerals*, 1979, 14, pp. 93-102.



# **The comparative analysis of energetic characteristics of variable-frequency electric drives with direct torque control**

**Ilya Fedotov<sup>1</sup>, Vyacheslav Tikhonov<sup>2</sup>, Evgeniy Veselkov<sup>3</sup>, Nina Seletskaya<sup>4</sup>**  
*<sup>1,2,3</sup> Pskov State University, Electrical Engineering Faculty,  
Department of drive and automation systems,  
<sup>4</sup> Pskov State University, Foreign Languages Faculty,  
Department of Foreign Languages for the technical and economic faculties.  
Address: Russian Federation, 180760, Pskov, Lenin Square, 2.*

**Abstract.** The simulation models of variable-frequency electric drives with direct torque control were built in MATLAB / Simulink simulation environment. These models are shown and described in the article. A number of energetic characteristics of the electric drives being investigated are considered. The calculations of these characteristics were made on the computer models and the comparative analysis of the values obtained is given.

**Keywords:** simulation, direct torque control, vector control, harmonic spectrum, total harmonic distortion (THD), coefficient of losses increasing.

## **I INTRODUCTION**

Nowadays variable-frequency electric drives, with induction motors powered by static frequency converters are widely used. The most common frequency converters in use nowadays are indirect frequency converters including a rectifier with a filter and an inverter and having an intermediate DC link. The form of the inverter output voltage feeding the stator windings of the induction motor is different from the sine wave one. Under the nonsinusoidal voltage the harmonic spectrum, which can include high-order harmonics with sufficiently big magnitudes, appears [1]. Voltage waveform distortion results in a nonsinusoidal current waveform and causes the increase of losses in the induction motor. These factors reduce the induction motor energy efficiency [2, 3]. When the induction motor is powered by the frequency converter its efficiency coefficient is lower by 2 – 3% on the average, and the power coefficient – by 5% in comparison to the mains supply with the voltage sine waveform [4]. The increasing pulsations of the induction motor electromagnetic torque, which appear mainly at low frequencies and small inertia, cause problems of electromechanical compatibility of the motor and the converter.

## **II SYSTEMS OF DIRECT TORQUE CONTROL: OVERVIEW, SIMULATION MODELS.**

In up-to-date frequency converters various control strategies can be implemented. The most convenient control systems are vector systems of direct torque control. They are: vector control (VC), in which the torque is controlled while the rotor flux linkage is maintained with digital controllers for main coordinates (rotor flux linkage, d-axis and q-axis stator currents, speed), and direct torque control (DTC) wherein torque control is performed by stator flux linkage adjustment by means of relay controllers for flux linkage and torque [5].

The main theoretical statements, concerning the development of these systems and control principles being used, were shown in [6]. The simulation model of DTC system built in MATLAB / Simulink simulation environment (Fig. 1) and the principle of work of that model were also described in that article.

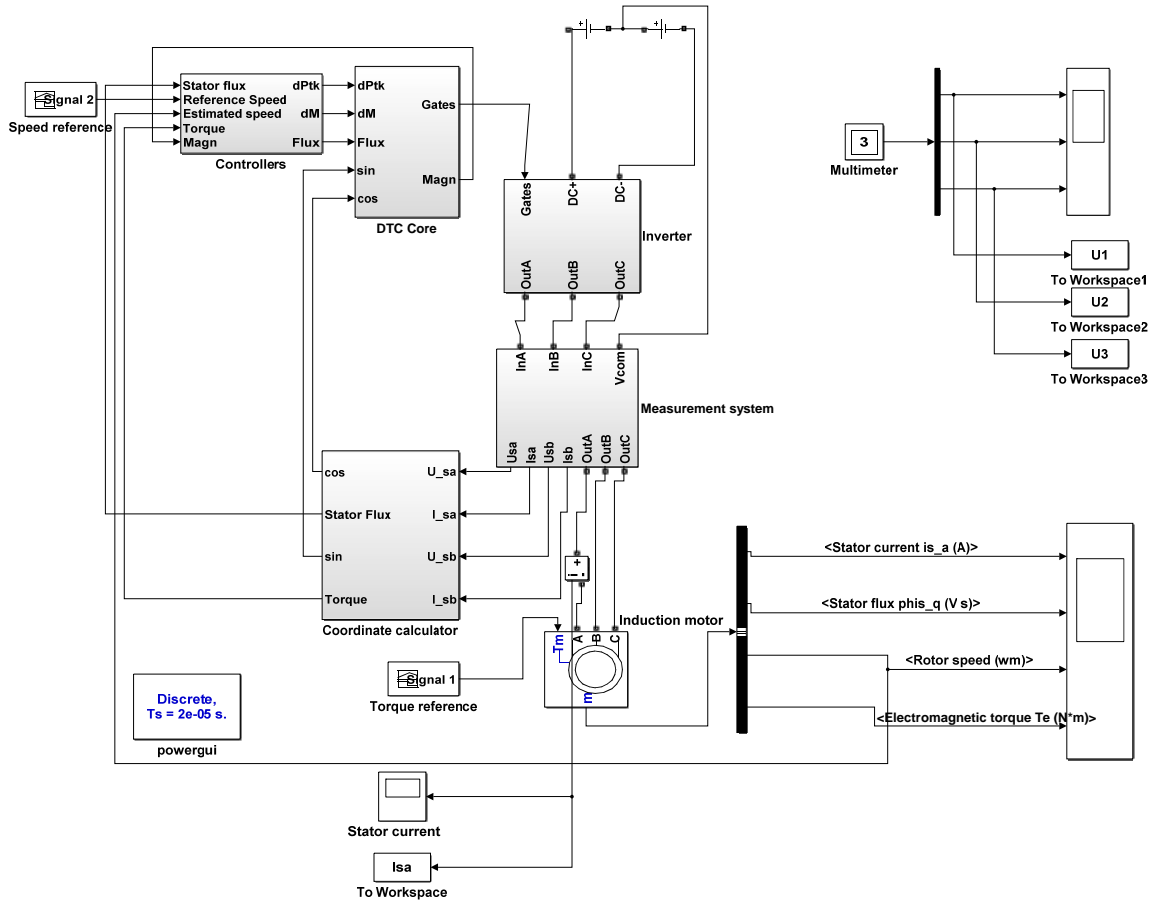


Fig. 1. Simulation model of DTC system.

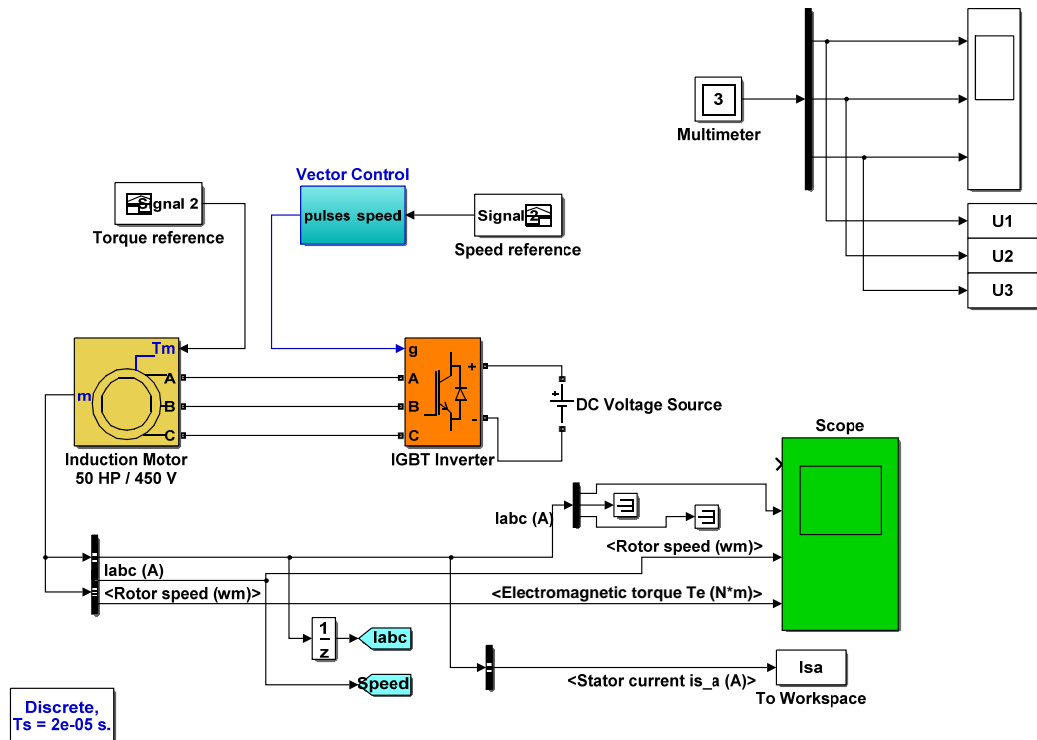


Fig. 2. Simulation model of VC system.

The simulation model of system with VC built in MATLAB / Simulink is shown in Fig. 2. Inverter (IGBT Inverter) switch control is performed via the subsystem *Vector Control* by using the PI speed controller and relay current controller. The speed reference signal and signal from the current sensors positioned in the stator circuit of the induction motor are used as input signals of this subsystem. The logical signal, specifying the combination of turned-on inverter IGBT-modules, is an output signal of the subsystem.

### III MAIN CHARACTERISTICS OF THE ENERGY EFFICIENCY OF THE SYSTEMS WITH DIRECT TORQUE CONTROL.

The above-mentioned models are analyzed in this article from the point of view of energetic characteristics. One of the most important quality factors is known to be a total harmonic distortion of voltage  $K_U$  and current  $K_I$  [7]. The higher the values of these coefficients the more are constant and variable losses in the motors. High-order harmonics in the supplying voltage cause the additional heating of motors because of an increased eddy current and hysteresis losses and, as a sequence, an intensified insulation deterioration, which can result in a premature failure of the machine, if this circumstance is not taken into the account [8, 9].

The level of an impact of each harmonic on the voltage and current waveform quantitatively can be evaluated by the harmonics coefficient  $k_v$  [10]:

$$k_{v(U,I)} = \frac{U(I)_v}{U(I)_1} \cdot 100\%,$$

where  $U(I)_v$  - the RMS value of voltage (current) of the  $v^{\text{th}}$  harmonic;

$U(I)_1$  - the RMS value of voltage (current) of the 1<sup>st</sup> harmonic.

The level of the distortion of voltage (current) waveform due to the total impact of all harmonics is evaluated by means of voltage (current) total harmonic distortion (THD) [11]:

$$k_{U(I)} = \frac{\sqrt{\sum_{v=2}^m U(I)_v^2}}{U(I)_1} \cdot 100\%, \quad (1)$$

where  $m$  is number of the highest harmonic being considered.

One more characteristic used for evaluation of energy efficiency of induction motors powered by frequency converters is a coefficient of total losses increasing  $K_{total}$  what is the ratio between the losses in the motor when it is powered by pulse voltage and when it is powered by sine voltage [12]. The expression for this coefficient includes two components – the coefficient of electrical losses increasing  $K_{el}$  and the coefficient of iron losses increasing  $K_{ir}$ , which are calculated as follows [4]:

$$K_{el} = 1 + K_{sc}^2 \sum_{v=3}^{\infty} \left[ \frac{1}{v} \left( \frac{U_v}{U_1} \right)^2 \right],$$

$$K_{ir} = 1 + K_{HOHC} \sum_{v=3}^{\infty} \left[ \frac{1}{v^{0,7}} \left( \frac{U_v}{U_1} \right)^2 \right], \quad (2)$$

where  $K_{sc}$  is starting current-to-rated current ratio of the motor,  $K_{HOHC} = (2 \div 3)$  is the coefficient of magnetic losses increasing due to high-order harmonic components of the induction motor.

For induction motors of general purpose industrial version electrical losses are in the average 60% of total losses and iron losses are 25%. Taking it into consideration we can calculate  $K_{total}$  as follows [4]:

$$K_{total} = 1 + 0,6 \cdot \hat{E}_{el} + 0,25 \cdot \hat{E}_{ir}. \quad (3)$$

Analyzing energetic characteristics of variable-frequency electric drives controlled according to the above-mentioned control laws can be done, based on the stator current and voltage waveforms, obtained from the computer simulation.

### IV SIMULATION RESULTS

Investigated were two operating modes: no-load mode ( $M_{LOAD} = 0$ ) and the operating mode with  $M_{LOAD} = 0,5 \cdot \hat{I}_{RATED}$ . As a result of the simulation stator current and frequency converter output voltage waveforms were obtained. These waveforms are shown in Fig. 3–6.

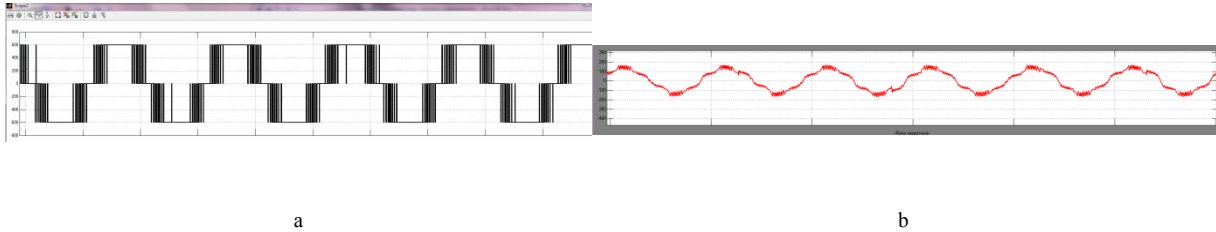


Fig. 3. Waveforms of frequency converter output voltage (a) and stator current (b) in the system with vector control ( $M_{LOAD} = 0$ ).

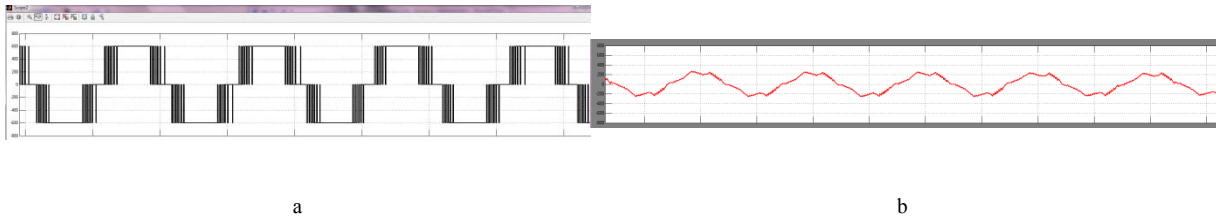


Fig. 4. Waveforms of frequency converter output voltage (a) and stator current (b) in the system with vector control ( $M_{LOAD} = 0,5 \cdot \dot{I}_{RATED}$ ).

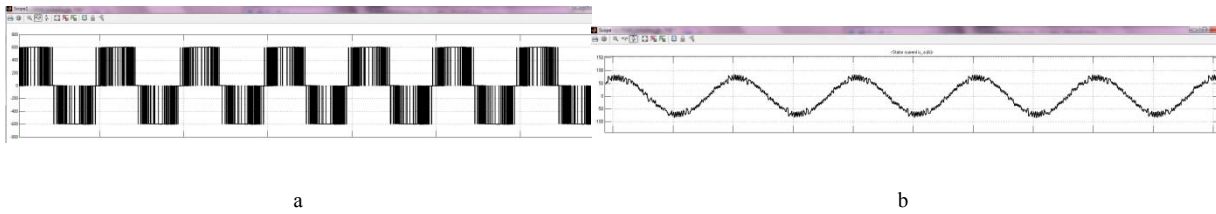


Fig. 5. Waveforms of frequency converter output voltage (a) and stator current (b) in the system with DTC ( $M_{LOAD} = 0$ ).

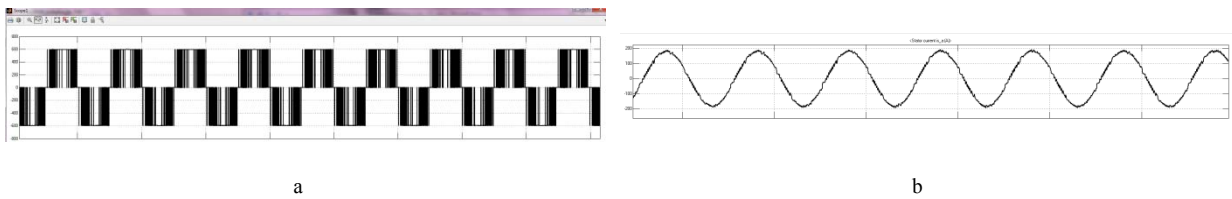


Fig. 6. Waveforms of frequency converter output voltage (a) and stator current (b) in the system with DTC ( $M_{LOAD} = 0,5 \cdot \dot{I}_{RATED}$ ).

To analyze the harmonic spectrum of the waveforms obtained the MATLAB / Simulink standard tool – FFT Analysis, which performs the Fourier series expansion of the initial waveforms, is used.

As the results of the simulation done for the waveforms being under consideration, the harmonic spectra up to the 49-th harmonic were obtained. These results are shown in Table I.

TABLE I.  
THE HARMONIC SPECTRA OF SIGNALS ( $m = 49$ ).

Harmonic order	VC				DTC			
	$M_{LOAD} = 0$		$M_{LOAD} = 0,5 \cdot \dot{I}_{RATED}$		$M_{LOAD} = 0$		$M_{LOAD} = 0,5 \cdot \dot{I}_{RATED}$	
	$U, V$	$I, A$	$U, V$	$I, A$	$U, V$	$I, A$	$U, V$	$I, A$
1	446,2	94,68	452	160,3	409,7	50,95	415,2	129
3	4,15	0,97	2,58	2,64	1,07	0,42	1,33	0,67
5	17,54	10,8	34,58	21,99	4,47	1,09	3,16	1,02
7	12,14	4,52	10,49	6,22	4,06	0,67	7,68	1,51
9	3,21	0,86	3,8	1,22	0,45	0,18	6,89	0,74
11	8,79	1,92	18,89	4,81	7,78	0,77	8,93	1,08

Harmonic order	VC				DTC			
	$M_{LOAD} = 0$		$M_{LOAD} = 0,5 \cdot \dot{i}_{RATED}$		$M_{LOAD} = 0$		$M_{LOAD} = 0,5 \cdot \dot{i}_{RATED}$	
	$U, V$	$I, A$	$U, V$	$I, A$	$U, V$	$I, A$	$U, V$	$I, A$
13	7,81	1,19	18,35	3,48	8,23	0,77	7,22	0,55
15	18,56	0,37	5,24	1,09	2,46	0,16	1,83	0,25
17	1,65	0,66	5,74	0,5	9,55	0,93	5,56	0,94
19	5,89	0,38	10,49	1,33	7,7	1,04	9,47	0,52
21	3,79	0,33	5,02	0,82	5,78	0,36	6,19	0,3
23	5,35	0,27	13,33	1,89	16,96	1,38	13,12	1,25
25	6,11	0,95	11,16	0,95	10,65	0,33	6,98	0,46
27	4,91	0,44	2,17	0,63	2,74	0,31	15,49	0,62
29	5,89	0,4	8,99	0,93	16,67	1,01	21,38	0,72
31	14,99	1,69	18,94	1,86	5,9	0,22	4,82	0,05
33	2,59	0,45	2,67	0,75	8,93	0,29	12,21	0,52
35	7,94	0,77	16	1,3	14,5	0,79	27,61	0,71
37	19,45	1,57	6,64	0,37	19,42	0,63	17,06	0,68
39	8,43	0,39	2,98	0,21	12,05	0,42	17,52	0,58
41	4,15	0,59	18,94	1,47	17,78	0,36	27,15	0,88
43	5,13	0,05	24,59	1,47	29,87	1,01	22,59	0,99
45	14,86	0,57	4,97	0,77	14,71	0,26	11,13	0,4
47	20,21	0,84	19,21	1,38	9,91	0,2	3,11	0,27
49	38,02	2,94	21,47	0,64	4,51	0,34	17,56	0,63

The numerical values of THDs for the voltage and current waveforms in the systems being considered, obtained after calculation using the formula (1), are shown in Table II.

Table II.  
THE VALUES OF THD.

VC				DTC			
$M_{LOAD} = 0$		$M_{LOAD} = 0,5 \cdot \dot{i}_{RATED}$		$M_{LOAD} = 0$		$M_{LOAD} = 0,5 \cdot \dot{i}_{RATED}$	
$k_U, \%$	$k_I, \%$	$k_U, \%$	$k_I, \%$	$k_U, \%$	$k_I, \%$	$k_U, \%$	$k_I, \%$
14,18	13,4	15,79	15,13	14,3	6,4	16,25	2,87

For the systems being considered the calculated values of the coefficient of electrical losses increasing  $K_{el}$  and the coefficient of iron losses increasing  $K_{ir}$  are obtained by using the formulae (2). These values are shown in Table III.

Table III.  
THE VALUES OF  $K_{el}$  AND  $K_{ir}$ .

	VC		DTC	
	$M_{LOAD} = 0$	$M_{LOAD} = 0,5 \cdot \dot{i}_{RATED}$	$M_{LOAD} = 0$	$M_{LOAD} = 0,5 \cdot \dot{i}_{RATED}$
$K_{el}$	1,048	1,097	1,033	1,043

	VC		DTC	
	$M_{LOAD} = 0$	$M_{LOAD} = 0,5 \cdot \dot{i}_{RATED}$	$M_{LOAD} = 0$	$M_{LOAD} = 0,5 \cdot \dot{i}_{RATED}$
$K_{el}$	1,048	1,097	1,033	1,043
$K_{ir}$	1,0056	1,0097	1,0046	1,0059

Based on the  $K_{el}$  and  $K_{ir}$ , the values of coefficient of total losses increasing  $K_{total}$  were calculated by using the formula (3). The results obtained are shown in Table IV.

Table IV.  
THE VALUES OF  $K_{total}$ .

	VC		DTC	
	$M_{LOAD} = 0$	$M_{LOAD} = 0,5 \cdot \dot{i}_{RATED}$	$M_{LOAD} = 0$	$M_{LOAD} = 0,5 \cdot \dot{i}_{RATED}$
$K_{total}$	1,03	1,06	1,021	1,027

## V CONCLUSIONS

Relying on the results obtained the following conclusions can be made:

1. The values of THD for the voltage waveform are nearly constant for both systems

considered and are slightly dependent on the load torque; they lie in the range of (14÷17)% .

2. The simulation shows that the values of THD for the current waveform in the no-load mode for the DTC system (6,49%) nearly are as small as twice then the corresponding values for the VC system (13,4%), and in the on-load mode the values reduces to the 2,87%, what makes the system energetically efficient.

3. The values of  $K_{el}$  and  $K_{ir}$ , obtained after simulating DTC system, are smaller than those for the VC system, and as a sequence, the coefficient of total losses increasing is also smaller.

Further research contemplates more detailed investigation of main operating modes of variable frequency electric drives with direct torque control. This research is going to be carried out by means both simulation and full-scale experiments using the test stand [13].

## VI APPENDIX

The test machine is a three phase 50 Hz induction machine having the following parameters as shown in Table V.

TABLE V.  
PARAMETERS OF THE TESTED INDUCTION MACHINE

Parameter	Parameter value
Power rating, $P_{rated}$	180 kW
Rated voltage, $V_{rated}$	450 V
Rated current, $I_{rated}$	276 A
Pole pair, $p$	2
Torque rating, $M_{rated}$	1150 N·m
Stator resistance, $R_s$	0,02 $\Omega$
Leakage stator inductive reactance, $x_s$	0,00967 $\Omega$
Rotor resistance, $R_r$	0,00859 $\Omega$
Leakage rotor inductive reactance, $x_r$	0,0962 $\Omega$
Magnetizing inductive reactance, $x_m$	2,6 $\Omega$
Inertia, $J$	3,2 kg·m <sup>2</sup>

## VII REFERENCES

- Браславский И.Я. Энергосберегающий асинхронный электропривод: учеб. Пособие для студ. Высш. Уч. Заведений / И.Я. Браславский, З.Ш. Ишматов, В.Н. Поляков; под ред. И.Я. Браславского. – М.: Издательский центр «Академия», 2004. – 256 с.
- Филлюшов Ю.П. Энергоэффективное управление асинхронной машиной. Электротехника, №6, 2014. – С. 57–65.
- Казаков Ю.Б. Энергоэффективность работы двигателей и трансформаторов при конструктивных и режимных вариациях: учебное пособие для вузов / Ю. Б. Казаков. – М.: Издательский дом МЭИ, 2013. – 152 с.: ил.
- Водозов А.М., Королёв Т.В. Система оценки энергетических параметров электроприводов переменного тока. Труды VII Международной (XVIII Всероссийской) научно-технической конференции по автоматизированному электроприводу: ФГБОУ ВПО «Ивановский государственный энергетический университет имени В.И. Ленина». – Иваново, 2012. – С. 96–101.
- I. Takahashi, T. Noguchi. A New Quick-Response and High-Efficiency Control Strategy of an Induction Motor. IEEE Transactions on Industry Applications. Vol. IA-22, No. 5, PP. 820 – 827. September / October, 1986.
- I.M. Fedotov, V.I. Tikhonov. «Simulation of traction electric drive with vector systems of direct torque control». Environment. Technology. Recourses. Proceedings of the 9th International Scientific and Practical Conference June 20–22, 2013 Volume II. – pp. 106–111.
- Осадчук Ю.Г., Козакевич И.А., Зиненко А.Н. «Исследование энергетических характеристик частотно-регулируемых электроприводов» // Вісник КТУ. – 2008. – Вип. 20. – С. 126–130.
- Вольдек А.И. Электрические машины: учеб. для студентов высших технических учебных заведений. – 3-е изд., перераб. – Л.: Энергия, 1978. – 832 с.
- Арилага Дж., Брэдли Д., Боджер П. Гармоники в электрических системах. – М.: Энергоатомиздат, 1990. – 320 с.
- Иньков Ю.М., Фадейкин Т.Н., Бредихина Я.А. «Потери мощности в асинхронных тяговых двигателях перспективного электроподвижного состава». Электротехника, №8, 2014. – С. 44–47.
- В.М. Зырянов, Н.А. Митрофанов, Ю.Б. Соколовский. «Исследование гармонического состава напряжения преобразователя частоты». Вестник ИГЭУ, Вып. 1, 2015. – С. 1–6.
- Ю.Б. Казаков, А.Р. Колганов, Н.К. Швецов. Энергоэффективность асинхронного двигателя при частотном управлении с широтно-импульсной модуляцией напряжения. Труды VIII Международной (XIX Всероссийской) конференции по автоматизированному электроприводу АЭП-2014: в 2 т. / отв. за выпуск И.В. Гуляев. – Саранск : Изд-во Мордов. ун-та, 2014. – Т. 1, с. 74–78.
- И.М. Федотов, А.А. Хитров. «Structure designing of test stand for investigation of variable frequency electric drives». Cilvēks. Vide. Tehnoloģijas: 16 starptautiskās student zinātniski praktiskās konferences rakstu krājums 2012. gada. 25. aprīlis. – pp. 448–452.

# Comparison of a load bearing capacity for composite sandwich plywood plates

Ģirts Frolovs, Kārlis Rocēns, Jānis Šliseris

Faculty of Building and Civil Engineering, Riga Technical University,  
Kalku st. 1, Riga, LV-1001, Latvia

**Abstract.** This article shows numerical investigations of composite sandwich plywood plates with birch plywood faces and a core of straight and curved plywood honeycomb-type ribs in comparison to standard plywood plates and other core type plates.

This shape of core ribs provides several improvements for these plates in manufacturing process as well as mechanical properties.

The influence of core element shapes on stiffness in longitudinal direction of a plate is insignificant although it is possible to vary with stiffness in transverse direction of these plates by changing form of plate's ribs. The results are describable as specific strength or stiffness (stiffness to mass or strength to mass ratio etc.) in both directions.

The various results depending on chosen variables (according to strength-stiffness criteria) plywood composite macrostructure is obtained for one span plate with uniformly distributed loading. The results show that it is possible to reduce material consumption causing reduction in stiffness but in general increasing stiffness to weight ratio for about 30% or even more if it is possible to increase height of a plate more than maximum standard plywood plate.

All thicknesses of elements are chosen according to plywood supplier assortment.

A various thicknesses of plywood sheets (0/90/0+90/0·n) are taken for straight ribs as well as various plates coverings for waved part of ribs the 3 layer plywood was taken (90/0/90) or (0/90/0) due to simplification of manufacturing process.

For all parts of plate were Birch plywood plates used, as well as reference plywood were Standard Birch plywood plates chosen.

**Keywords:** Composite plywood plates, sandwich structures.

## I INTRODUCTION

It is actual as much as possible to use renewable resources and one of these is wood. Although they are environment friendly materials by increasing demand we should plan how we could save even more materials by using them rationally where they are used in greater amounts.

The consumption of wood products is increasing last few decades although the sawn wood production is decreasing [1]. The wood based panels become more significant in constructions as well as other wood based structural elements. Plywood is one of the most common wood based secondary (transformed) used materials and its consumption (and production) is increasing over past decades especially in area of Asia [2], [3].

Although the use of material in plywood structure is improved some problem still remains. The normal stresses in middle part through plate's thickness are low (Fig. 1) so the material is not rationally used. It is possible to reduce material in middle layer of a plate to make traditional "sandwich" core material. The

faces' materials have the main influence on plates stiffness while the core material to the shear properties.

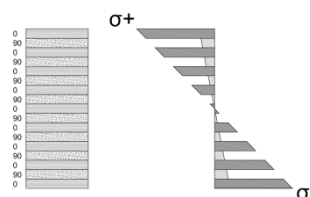


Fig. 1. Distribution of stresses in plywood in cross section (methodology of calculations according to LVS ENV 14272)

We cannot reduce this material unreasonable due to shear stresses that should take the middle part of a plate, like it is in "traditional" sandwich structures (Fig. 2).

If the plates are subjected to bending it is not allowable to unreasonable reduction of material as the shear stresses ( $\tau$ ) increases.

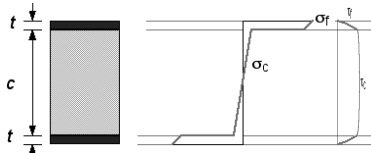


Fig. 2. Stress distribution in sandwich structures (faces with high stiffness and core with low stiffness) [4]

It is experienced that the bearing capacity for all parts (faces and core) is solved in previous research by using different materials or cross sections for each part of a plate. Although the problem with serviceability limit state still remains (it is the determinant for these plates) as it is taken for this research main problem to be solved.

## II RESEARCH OBJECT

In recent doctoral thesis [5] [6] the idea of honeycomb-type sandwich plates are already provided, but with low level depth of detail. And used plates are complicated for manufacturing of curved hollow ribs. So the new type of plates [7] [8] is provided with thin curved rib parts and multiple thicknesses for straight rib parts and faces of plates. (Fig. 3) These plates require more complicated manufacturing since there are different layers to assembly, but this process should be mechanized to make it simpler, efficient and safer. Thereby for high amount of manufacturing these plates could be established in building, mechanical and furniture engineering.

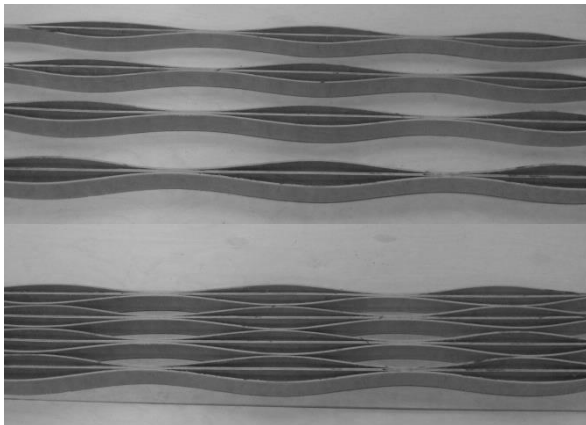


Fig. 3. Assembly of composite plywood plate with cell-type core. Bottom only one face layer shown.

The main advantages for such plates are ability to save material and energy due to improved stiffness properties, improved stability, increased shear strength and simplified technology comparing to plates with straight rib core.

The influence of geometrical parameters was previously investigated [9] so in this paper the case study was presented.

The most influence of stiffness has the height of a plate ( $h$ ), so it was chosen as one of changeable parameters to see the plate's properties at various heights.

All these problems could be reduced by using such plates with previously mentioned new type of core layer.

The geometry of ribs allows to improve properties in other direction (transversal to the longitudinal direction) of a plate when we the deflection of both directions of a plate should be improved.

## III RESEARCH METHODOLOGY

These plates could be compared to standard plywood plates as they can carry load in longitudinal and transversal directions and they provide good properties in both directions. The dominant for this type plates is the serviceability limit state therefore it is taken as a major problem in this paper.

For the case study the plate with dimensions of 2.1 m span in longitudinal direction and 1.1 m span in transversal direction was chosen. Although it is proved that dimensions and other geometrical parameters make influence on plate's stiffness and specific stiffness [9].

The research is based on bending behavior of these plates. Main results will show the comparison of stiffness, specific stiffness (stiffness-to-Weight) or load bearing capacity of these plates.

For large displacements non-linear calculations are required but they are not described here. The maximal service load was calculated to assume that

The plates were loaded with uniformly distributed load which is the most common loading type. For calculation and extrapolation the load with intensity of 1 kN/m<sup>2</sup> was used.

As the height of the plate is considerable larger than the span of a plate the influence of shear deformation is not separated from bending deformation.

### A. Used symbols for research

Table I

The mainly used symbols

	Symbol	Units
Span of a plate	L	m
Width of a plate	B	m
Height of a plate	$h_{plate}$	m
Service Load	SL	kN; kN/m <sup>2</sup> ;
Ultimate Load	UL	kN; kN/m <sup>2</sup> ;
Dead Weight	DW	kg

### B. Stiffness in longitudinal direction

For these plates most common limitation is 1/200 of a span, so all the serviceability loads and conditions were calculated with this limitation. And the different



plates compared with achieved results for this limitation.

As it was proved earlier [9] the influence on stiffness and specific stiffness in longitudinal direction is not dependent on width of a plate.

C. Stresses

Bending stresses were analyzed in three parts of a plate. Longitudinal stresses in faces of a plate ( $\sigma_i$ ;  $\sigma_t$ ), longitudinal stresses in all parts of a rib.

The factors for determination of design plywood bending strength are taken according to EN 1995-1-1 [10] with the characteristic values from Riga ply supplier catalogue [11]

$$f_{m,d} = \frac{k_{mod}}{\gamma_M} f_{m,k}$$

$k_{mod}$  – is a modification factor taking into account the effect of the duration of load and moisture content (for plywood in 1 or 2 class - 0.6)

$\gamma_M$  – is the partial factor for a material property (for plywood - 1,2)

$f_{m,k}$  – is the characteristic value of bending load-carrying capacity; (for 3 ply 4mm plywood - 52 MPa in tension)

D. Used material and FEM data

Material properties applied for birch plywood of one ply sheet Fig. 4 [12] are summarized in Table 1. It is assumed that the ply has the same properties as sawn wood material.



Fig. 4. Three principal axes of wood with respect to grain direction and growth rings. (x – longitudinal; y – tangential; z – radial) [13]

As these plates could be used as interior and exterior elements they should provide water-resistant properties according to EN 636 and EN 314 Class 2 (for internal use as structural component in humid conditions) the same class 2 according to EN 1995-1-1 [10].

The index at E shows the property in corresponding direction, for the Poisson’s ratio the first index shows the extension direction as the second shows contraction’s direction.

Plywood stacking sequence has been modelled assuming that each layer is perpendicular to the upper and lower one, as plywood consists of an odd number of plies. In this paper three layers plywood was taken for all parts of a plate with total thickness of one plywood sheet of 4.0 mm. It has been assumed that

each ply has same thickness of 1.27 mm and transversal isotropic material properties (see Table II.). For waved ribs constant thickness was taken and various thickness of straight rib, from 3 layer to 15 layer according to standard birch plywood (Latvijas Finieris 2005).

Table II  
Properties of birch wood

	Symbol	Value
Modulus of elasticity in longitudinal direction [GPa]	$E_x$	16.4
Modulus of elasticity in tangential direction [GPa]	$E_y$	0.68
Modulus of elasticity radial direction [GPa]	$E_z$	0.68
Poisson ratio xy	$\mu_{xy}$	0.04
Poisson ratio yz	$\mu_{yz}$	0.81
Poisson ratio xz	$\mu_{xz}$	0.043
Shear modulus in xy plane [GPa]	$G_{xy}$	0.89
Shear modulus in yz plane [GPa]	$G_{xz}$	0.23
Shear modulus in xz plane [GPa]	$G_{yz}$	1.54
Density [kg/m <sup>3</sup> ]	$\rho$	715

Three types of ribbed plates were analyzed and compared to standard plywood and to plates with straight ribs [14]. With only straight ribs (Fig. 5 A); straight ribs and curved ribs (Fig. 5 B); and only with curved ribs (Fig. 5 C); For direction of curved ribs orientation same direction as the plates longitudinal direction was taken (||) or transversal to plates longitudinal direction but in direction of plates height ( $\perp$ ). For the symbols the first index shows the type of the rib (whether or not with straight rib part) while the second index shows the orientation of curved rib part. the detailed explanation is summarized in Table III.

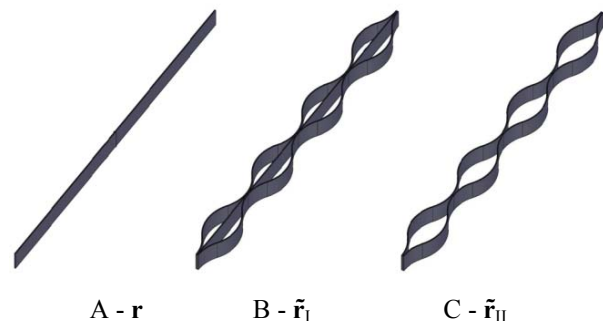


Fig. 5. Three types of ribs analyzed (A – flat rib; B – flat and curved rib; C – only curved rib)

Table III  
Symbols of plates

	Reference in Fig. 5 Fig. 8	Symbol
Standard plywood		<b>PW</b>
Only straight ribs*	A	<b>r</b>
Straight ribs* and waved ribs* (outer layers fiber direction same as panel and rib longitudinal direction)	B	$\tilde{r}_{I,\parallel}$
Straight ribs* and waved ribs* (outer layers fiber direction transversal to panel and rib longitudinal direction)	B	$\tilde{r}_{I,\perp}$
Only waved ribs* (outer layers fiber direction transversal to panel and rib longitudinal direction)	C	$\tilde{r}_{II,\parallel}$
Only waved ribs* (outer layers fiber direction same as panel and rib longitudinal direction)	C	$\tilde{r}_{II,\perp}$

\* Thickness for each rib part 4mm

IV RESULTS

In this paper the both limit states are analyzed although as mentioned before for such type structures in the mostly cases the decisive is the serviceability limit state so the main results were achieved for it. The results were obtained for one span plate

For comparison specific values (bearing capacity to weight) were used so the influence is dependent not only from mechanical properties but also from dead weight changes (Fig. 6) If we compare only the dead weight, it is seen that material consumption for increasing plate's height similar for ribbed plates (about 15%) while for plywood it increases for about 67 % when the height is increased from 3 cm to 5 cm.

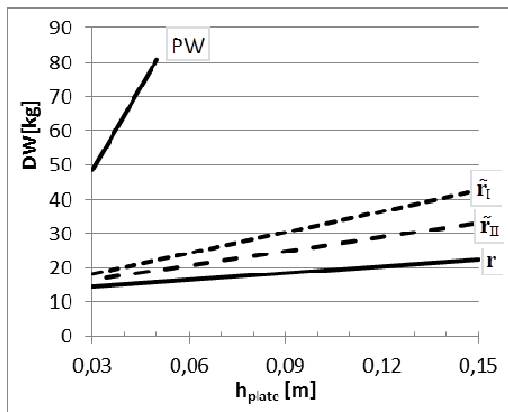


Fig. 6. Dead Weight (DW) comparison for different type of plates. (Symbolical meaning see Table III).

A. Serviceability limit state

For these plates most common limitation is 1/200 of a span, so all the calculations were done at this level and was assumed that material is loaded in linear stage of a material. The results show that Service Load

is increased for the I type of plates as there is more material in core layer Fig. 7.

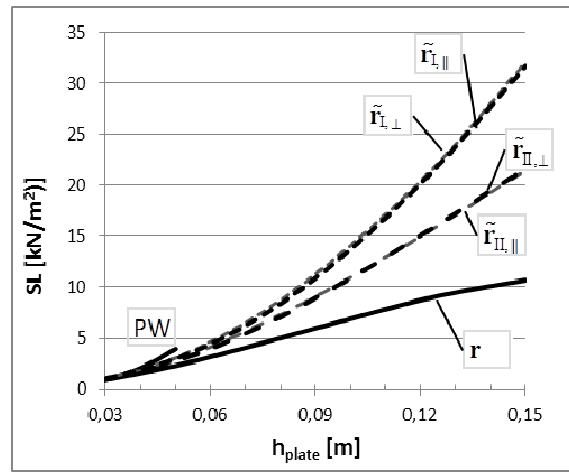


Fig. 7. Maximal Service Load (SL) for different type of plates. (Symbolical meaning see Table III).

Although by comparing Service Load to dead weight results show similar properties.

These results were summarized in Fig. 9 for each height that was analysed. It is seen that by lower height of a plate the straight ribs has larger specific stiffness as the  $SL_{max}/DW$  is larger. Although by increasing height of a plate the advantages of cell type plates becomes more significant.

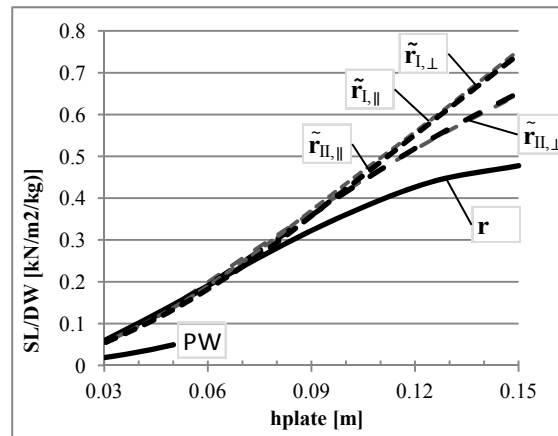


Fig. 8. Maximal Service Load (SL) to Dead weight (DW) for different type of plates. (Symbolical meaning see Table III).

By comparing plywood and ribbed structures it is achieved that dead weight decreases for 70% in average while the stiffness decreases for 30 % in average. So it was analysed 35 mm plate and compared to 35mm plywood. And as a result it was achieved that for achieving the stiffness that has the 35 mm we should increase height of a plate to 45mm Fig. 10 and Fig. 11.

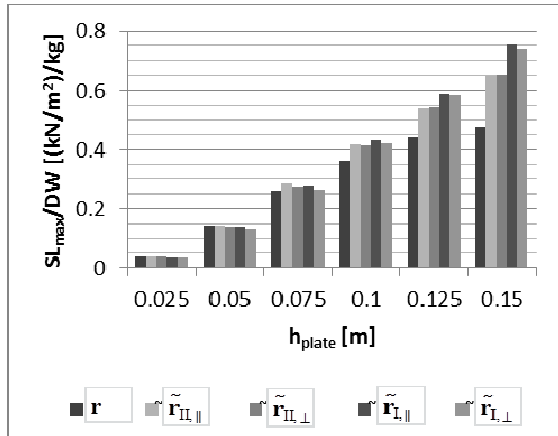


Fig. 9. Maximal Service Load (SL) to Dead weight (DW) for different type of plates. (Symbolical meaning see Table III).

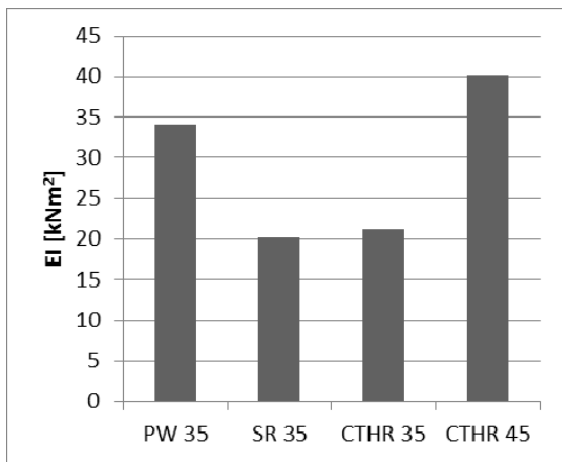


Fig. 10. Comparison of stiffness for different plates. (Symbolical meaning see Table III).

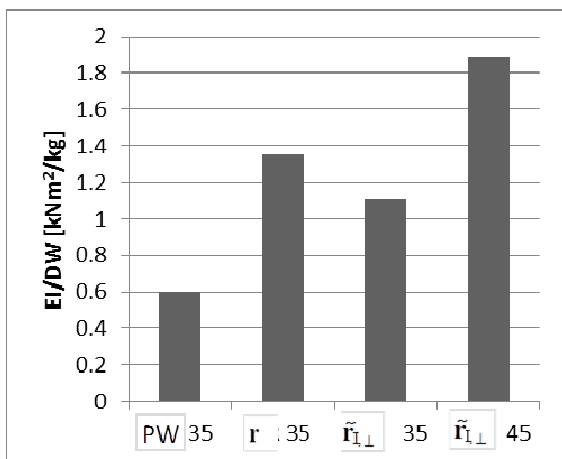


Fig. 11. Comparison of stiffness-to-mass ratio for different plates. (Symbolical meaning see Table III).

Comparing cell-type ribs to straight ribs provides easier technology and resists to local deformations that occurs with thin faces of plate.

*B. Ultimate limit state*

For the comparison of stresses for the same plate dimensions normal stresses in plate's faces were analyzed.

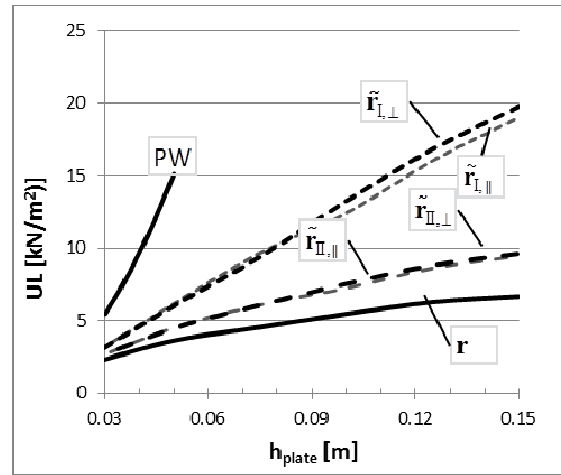


Fig. 12. Maximal Ultimate Load (UL) for different type of plates. (Symbolical meaning see Table III).

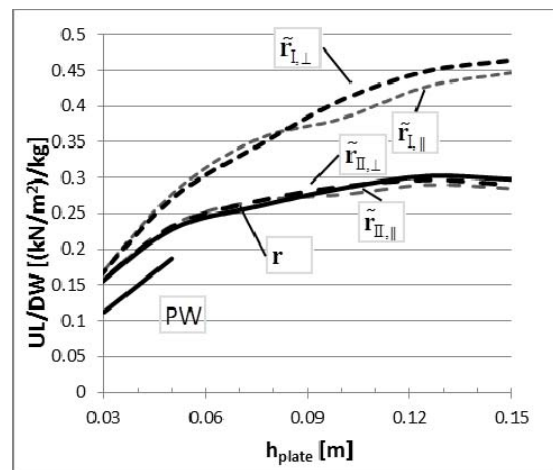


Fig. 13. Maximal Ultimate Load (UL) to mass for different type of plates. (Symbolical meaning see Table III).

We can see that also for Ultimate load the highest strength from ribbed plates show I type plates (Fig. 12) only plywood shows highest strength. That still remains for the UL/DW ratio only here Standard plywood shows the lowest ratio comparing to other plates Fig. 13.

By increasing height of a plate more than 10 cm 1/200 the shear stresses and deformation should be taken into account as they become more determinant. Therefore by increasing plates height the orientation of waved ribs' outer layers transversal to plates longitudinal axis are more sufficient, although it reaches maximum at some point where the increase of plate's covering is needed due to overloaded plate's skins.

The stress-deformation plot is seen in Fig. 14. It is seen that straight ribs show the highest stress-deformation ratio.

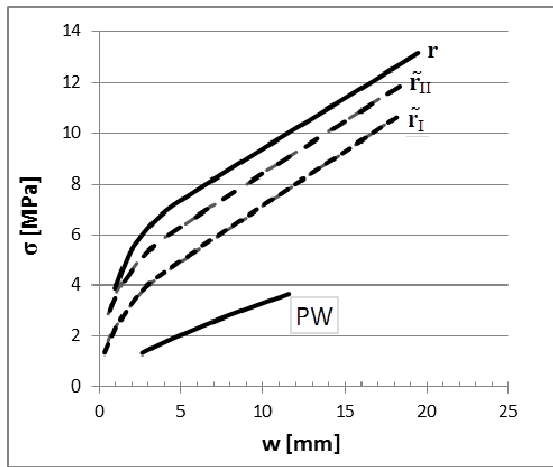


Fig. 14. Stress-deformation plots for different type of plates. (Symbolical meaning see Table III).

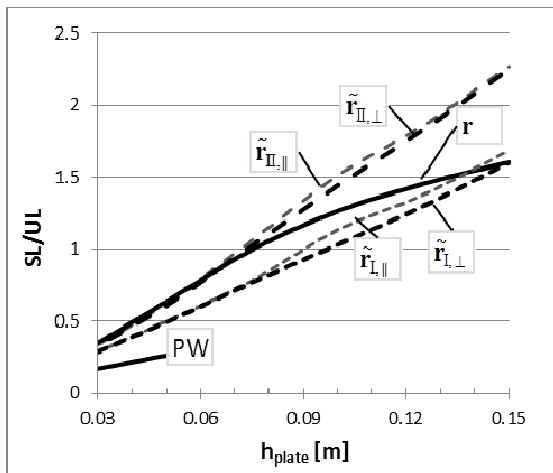


Fig. 15. Service Load-to-Ultimate Load ratio depending on the Height of a plate (Symbolical meaning see Table III).

In Fig. 15 we can see how much is used material in comparing both limit states (SL and UL). It is seen that it is different for different type of plates. For plates with straight ribs up to plate's height  $h_{plate}$  7cm it is similar to II type plates but by increasing the height more we achieve that the determinant becomes the Ultimate Limit State becomes determinant for design. The similar trend could be seen for I type of plates although this point where the Ultimate Limit State becomes determinant is at larger plate's height.

By using this chart it is possible to optimize and choose geometrical parameters of the plate for required load to fill the maximum load conditions in both limit state SL/UL ratio equal to 1. Where it is needed could be varied by thickness of plate's faces or the straight rib.

## V FUTURE RESERACH

A physical tests should be done for such plates and improved technology of gluing process that provides possibility to ensure pressure 5-15 kg/cm<sup>2</sup> (70-150 psi) like it is used for glued wood structures [15].

The bending properties in transversal direction should be detailed analyzed as they can show more advantages to plates with only straight ribs.

The use of other materials could be considered at some parts of a plate.

## VI CONCLUSIONS

By using such plates it is possible to equal the bearing capacity for Ultimate limit state and Serviceability limit state so that the material is used for the same level in both of the Limit states.

Provided type of plates shows improved bending properties that allows to decrease material consumption for 70% at 30% of stiffness decrease that gives possibility to increase stiffness-to-weight ratio for up to 100% by keeping all requirements.

Where it is possible to increase plate's height for 30% the improvement in stiffness reaches up to 100% and keep increasing by even more increase of height.

## VII ACKNOWLEDGEMENT

The research leading to these results has received the funding from Latvia state research programme under grant agreement „INNOVATIVE MATERIALS AND SMART TECHNOLOGIES FOR ENVIRONMENTAL SAFETY, IMATEH”.

## VIII REFERENCES

- [1] E. Pepke, «Global Wood Markets: Consumption, Production and Trade,» [Tiešsaiste]. Available: <http://www.unece.org/fileadmin/DAM/timber/mis/presentations/PepkeGlobalWoodMkts050510.pdf>. [Piekļūts 15 March 2015].
- [2] «Vital Forest Graphics,» 2009. [Tiešsaiste]. Available: [http://www.unep.org/vitalforest/Report/VFG\\_full\\_report.pdf](http://www.unep.org/vitalforest/Report/VFG_full_report.pdf). [Piekļūts 15 March 2015].
- [3] «Production of Wood-based Panels,» [Tiešsaiste]. Available: [http://eippcb.jrc.ec.europa.eu/reference/BREF/WBP\\_online.pdf](http://eippcb.jrc.ec.europa.eu/reference/BREF/WBP_online.pdf). [Piekļūts 15 March 2015].
- [4] «Strength of Sandwich Structures,» [Tiešsaiste]. Available: <http://www.mse.mtu.edu/~drjohn/my4150/sandwich/sp2.html>. [Piekļūts 27 02 2015].
- [5] J. Sliseris, «Non-traditional wood composite structural elements and their analysis methods,» %1 *Doctoral Thesis*, Riga, Latvia, Riga Technical Univeristy, 2013.
- [6] S. W. Kavermann, «Mechanical properties of lightweight sandwich panels with corrugated plywood core,» %1 *Doctoral Thesis*, Auckland, New Zealand, The University of Auckland, 2013.

- [7] K. Rocens, J. Sliseris un G. Verdins, «Multilayer composite with cellular ribbed structure based on wood materials». Latvia, Riga Patents 14519, 2. April 2012.
- [8] J. Sliseris un K. Rocens, «Optimal design of composite plate with discrete varying stiffness», *Composite Structures*, sēj. 98, pp. 15-23, 2013.
- [9] G. Frolovs, K. Rocens un J. Sliseris, «Experimental investigations of composite plywood plates with vertically placed wavy ribs», Kaunas, Lithuania, 2014.
- [10] EN 1995-1-1: Design of timber structures.
- [11] Plywood handbook, Riga: Latvijas Finieris, 2005.
- [12] L. Pereligin, B. Ugolev, П. (Л.М. un У. Б.Н.), Лесная промышленность, Wood Science (In Russian). — 288 p., 1971, p. 288.
- [13] Wood Handbook Wood as an Engineering Material, Madison, Wisconsin USA: Forest Products Laboratory, 1999.
- [14] E. Labans un K. Kalnīnsh, «Experimental validation of the stiffness optimisation for plywood sandwich panels with rib-stiffened core», *Wood Research Slovak Forest Products Research Inst.*, sēj. 59, nr. 5, pp. 793-802, 2014.
- [15] T. G. Williamson, APA Engineered Wood Handbook, USA: McGraw-Hill, 2002.

# Dissipative and Damping Properties of Multi-layered Rubber-Metal Vibration Absorber

Vladimirs Gonca<sup>1</sup>, Svetlana Polukoshko<sup>2</sup>, Egons Lavendelis<sup>1</sup>

<sup>1</sup>Riga Technical University, Institute of Mechanics.

Address: 6, Ezermalas str, LV-460, Riga, Latvia

<sup>2</sup>Ventspils University College, Engineering Research Institute "VSRC".

Address: 101a, Inženieru str, LV-3601, Ventspils, Latvia

**Abstract.** Rubber and rubber-metal (RM) elements are successfully used as bearing, joints, compensating devices, vibration and shock absorbers in civil engineering and machine building because of rubber and rubberlike materials (elastomers) have a capability of absorbing input energy much better than other construction materials. The elastic properties of rubber in such supports allows reverse backward to its original position under dynamic load action. Along with the instantaneous elastic deformation these materials exhibit a retarded elastic deformation, viscous flow (creep) and relaxation. The mechanical properties of rubber which are necessary for the optimal design of antivibration devices are next: bulk modulus of compression, dynamic and static shear modulus, energy dissipation factor. To describe the relationship between the compressive (or shear) stress  $\sigma(t)$  and strain  $\varepsilon(t)$  the creep and relaxation kernel, taking into account the viscoelastic properties of the rubber, is used. The kernels proposed by A. Rzhantsin, Y. Rabotnov, M. Koltunov give satisfactory results for the mechanical properties of rubber in the mean frequency domain ( $10^{-3} < \omega < 10^3 \text{ s}^{-1}$ ). In this paper for the accounting of dissipative properties of the rubber Rabotnov's kernel is used, the energy loss during one oscillation period is calculated. The flat-type RM absorber with kinematic excitation, which lower base oscillates harmonically is considered, oscillation parameters of the upper base on which the protected object is placed, are calculated. Damping properties are expressed by the ratio of the amplitude of the forced oscillations of the upper base (and object) to the amplitude of driving lower base.

**Keywords:** vibration damping, relaxation kernel, dynamic shear and compression moduli, rubber-metal package.

## I INTRODUCTION

Nowadays under conditions of intensification of production processes, increasing of the equipment capacity and high-speed vehicles creation the question of preventing the harmful effects of vibration requires special attention. In the most cases it is necessary to provide of shock and vibration protection devices at the design stage [1] – [5].

Elastomers (rubber and rubber-like materials) are the most suitable material for anti-vibration devices due to its adhesive characteristics, the ability to acquire a predetermined shape at press processing after curing, high elasticity and high internal damping. The elastic properties of rubber characterized by a large difference between bulk and shear moduli ( $K/G$  ratio reaches  $500 \div 5000$ ) [3], [6] – [10]. The high elasticity of rubbers allows them to withstand the large elongation without breaking. Consequently, the rubber has a greater capacity to store energy per unit volume compared with other materials.

Rubber and rubber-metal parts (rubber and metal connected by vulcanization or gluing) are used as elastic supports of vehicle and machinery and are designed to reduce the dynamic loads of the working machines on their foundations or floors of buildings or for the protection of equipment and devices from bumps, shock and vibration loading operating on their base. The packages of thin-layered rubber-metal elements (rubber layer width/height ratio  $> 20$ ) are also successfully used. Thin-layered rubber-metal elements (TRME) - essentially anisotropic elastic element made of rubber (or other elastomeric) and metal (or hard plastic) assembled in a package of two or more layers having a high load capacity (more than 30 MPa in the normal to layer direction) and higher compliance (50 ... 200% from relative deformation) in the transverse direction [9] – [13].

Rubber is a material that has a clearly defined relaxation properties, so its mechanical properties strongly depend on the time of application of external loads, that is, the mode of deformation [10], [14] –

[18]. If the duration of the force causing a deformation equal to the time of relaxation processes in the rubber, the elastic deformation is fully manifested, and this mode of deformation will correspond to well-defined modulus of rubber.

When rate of deforming load application increases modulus of elasticity will be changing, and its magnitude will be more than elastic modulus for the mode with full implementation of the elastic process.

Since many rubber-metal products serve as elastic links experience an impulsive load, alternating-sign load, periodical and non-periodical high-frequency load, it is necessary to take into account the characteristics of the mechanical properties of rubber under dynamic loads [9] – [13].

In this paper the vibration absorber operating under uniaxial deformation (compression or shear) is considered. In Fig. 1 the scheme of mounting of this device are shown: RM absorber with flat layers (cylindrical or prismatic form) is placed between protected object and base. Rubber layers 1 are reinforced by perfectly rigid undeformable plates 2, which is cured on to the elastomers by vulcanizing.

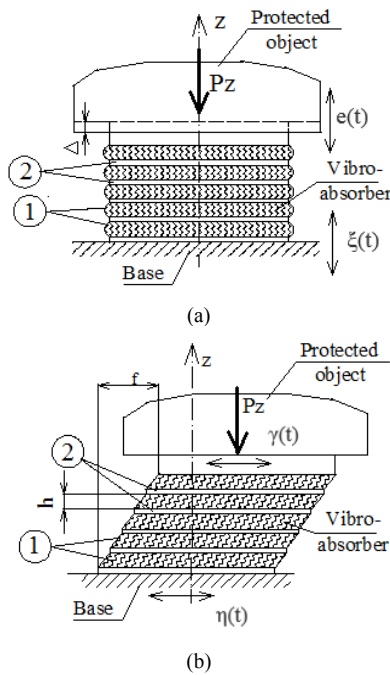


Fig. 1. Scheme of the installed absorbers: (a) anti-vertical vibrations, (b) anti-horizontal vibrations; 1-rubber layers of height  $h$ , 2 –metal layer.

The aim of this work is to determine the dependence of this absorber dissipative and damping properties on the viscoelastic behaviour of elastomer, on the forced vibration frequency and natural frequency of the system for the model with one degree of freedom (ODF) under the action of harmonic excitation. Mass of isolator is not taken into account because of its smallness. The damping properties are determined by the ratio of the amplitude of the upper plate forced

oscillations to the amplitude of the forcing oscillation of lower plate. Dissipative properties of vibroabsorber are estimated by the energy loss during one period of oscillation. Such approach allows to appoint the dimensions of antivibration devices at design stage.

## II MATERIALS AND METHODS

### Visco-elastic properties in rubber model

In the mechanical properties of rubber a set of features manifest itself: alongside with the instantaneous elastic deformation these materials exhibit retarding elastic deformation, viscous flow (creep) and relaxation. For the description of the elastic and dissipative processes for the most materials a combination of two types of mechanical elements, elastic and viscous, may be used. Elastic element is controlled by Hooke's law, viscous - by Newton's law of flow. Connections of them in series or in parallel joint (Maxwell model or Kelvin-Voigt model) approximately describes the visco-elastic behaviour of the material [17] – [19].

The most common relationship between stress and strain may be expressed by means of integral equations of relaxation and creep. In this case accounting of the time factor influence is reduced to solving systems of integro-differential equations. Methods of solving such systems are very diverse, the most widely used methods based on the use of integral transforms, especially Laplace and Fourier transforms, and also integral operators Volterra's type [13].

In the case of axial deformation for weakly filled rubbers and small deformation ( $\epsilon \leq 20\%$ ), when the linear dependence between stress and strain exists, the dependence is valid:

$$\sigma(t) = E_t \epsilon(t),$$

where  $E_t$  - time operator, which does not depend on  $\sigma$  and  $\epsilon$  and reflects the viscoelastic behaviour of system.

This dependence may be written in the form of an integral equation of Volterra:

$$\sigma(t) = E_0 \left[ \epsilon(t) - \int_0^t R(t-\tau) \epsilon(\tau) d\tau \right] \quad (1)$$

where:  $E_0$  - instantaneous compressive modulus (or  $G_0$  - instantaneous shear modulus), which specifies the instantaneous stiffness in the classical sense;  $R(t-\tau)$  - relaxation kernel describing the viscoelastic properties of the rubber. The presence of relaxation kernel determines the dissipative properties of rubber.

Using Fourier – images transform of  $\sigma(\omega)$ ,  $\epsilon(\omega)$  and  $R(\omega)$ , equation (1) may be written as:

$$\sigma(\omega) = E_0 (1 - R(\omega)) \epsilon(\omega) = E(\omega) \epsilon(\omega) \quad (2)$$

where  $E(\omega)$  - dynamic compression modulus of elasticity (it may be also  $G(\omega)$  - shear modulus).

$$\sigma(\omega) = \int_{-\infty}^{\infty} \sigma(t) e^{-i\omega t} dt,$$

analogically for  $\varepsilon(\omega)$ ,  $R(\omega)$ .

The elastic compressive modulus  $E(\omega)$  expressed as complex modulus is:

$$E(\omega) = E'(\omega) + iE''(\omega).$$

Splitting  $E_0(1-R(\omega))$  in (2) into real and imaginary parts we obtain:

$$\begin{aligned} E'(\omega) &= E_0 \operatorname{Re}(1 - R(\omega)), \\ E''(\omega) &= -E_0 \operatorname{Im} R(\omega). \end{aligned} \quad (3)$$

Let's denote

$$\begin{aligned} \operatorname{Re}(1 - R(\omega)) &= B_1(\omega), \\ -\operatorname{Im} R(\omega) &= B_2(\omega), \end{aligned}$$

and rewrite the elastic complex modulus  $E(\omega)$  as:

$$E(\omega) = E_0 B_1(\omega) + iE_0 B_2(\omega).$$

Proposed by A. Rzhantsin, Y. Rabotnov and M. Koltunov kernels are in most common use. These kernels allow satisfactory describing the mechanical properties of rubber in the medium frequency range  $10^{-3} < \omega < 10^3 \text{ s}^{-1}$ . In this work the Rabotnov's kernel is considered, which represents fractional exponential function  $R(t - \tau) = \mathcal{O}_\alpha(-\beta, t - \tau)$ :

$$R(t - \tau) = (1 - \tau)^\alpha \sum_{n=0}^{\infty} \frac{(-\beta)^n (t - \tau)^{n(1-\alpha)}}{\Gamma[(n+1)(1+\alpha)]}, \quad (4)$$

where  $\Gamma$  - gamma-function,  $-1 < \alpha < 0$ ,  $\beta > 0$ .

In this equation  $\alpha$  - parameter of fractionality, expressed in terms of the maximum value of the spectrum of relaxation times and modulus defect,  $\beta$  - rheological characteristics of rubber equal to:

$$\beta = t_0^{-1-\alpha},$$

where  $t_0$  - generalized relaxation time.

Rheological parameters are tabulated for many types rubbers.

Fourier image for Rabotnov's kernel is:

$$R(\omega) = \frac{1}{(i\omega)^{(1+\alpha)} + \beta}. \quad (5)$$

Taking into account (3) real and imaginary parts we obtain from (5):

$$\begin{aligned} B_1(\omega) &= \frac{\omega^{1+\alpha} \cos \delta + \beta}{\omega^{2(1+\alpha)} + 2\omega^{1+\alpha} \beta \cos \delta + \beta^2}, \\ B_2(\omega) &= \frac{\omega^{1+\alpha} \sin \delta}{\omega^{2(1+\alpha)} + 2\omega^{1+\alpha} \beta \cos \delta + \beta^2}, \end{aligned} \quad (6)$$

$$\delta = \frac{\pi}{2}(1 + \alpha).$$

The coefficients  $B_1$  and  $B_2$  are the Fourier cosine transform and sinus transform of the fractional exponential function (4):

$$\begin{aligned} B_1 &= \int_0^{\infty} R(z) \cos(\omega z) dz, \\ B_2 &= \int_0^{\infty} R(z) \sin(\omega z) dz. \end{aligned}$$

If the deformation of the elastomer is harmonic, equation (1) may be written as:

$$\sigma(t) = E_1 \varepsilon_0 \sin(\omega t) \quad (7)$$

$$\begin{aligned} \sigma(t) &= E_0 \varepsilon_0 \left[ \sin(\omega t) - \int_{-\infty}^t R(t - \tau) \sin(\omega \tau) d\tau \right] = \\ &= E_0 \varepsilon_0 [(1 - B_1) \sin(\omega t) + B_2 \cos(\omega t)] \end{aligned}$$

The coefficients  $B_1$  and  $B_2$  are the same for compression and shear deformation. In the case of share:

$$G'(\omega) = G_0 B_1(\omega) \text{ and } G''(\omega) = G_0 B_2(\omega).$$

In this case stress is calculated by the same way.

#### Model of damping system with one degree of freedom

Most clearly it is possible to estimate the dynamic properties of the RME in the frame of the simplified one-degree-of-freedom model, which allows to obtain explicit analytical dependences for dissipation and damping characteristics of RME. Such model, presented in Fig.1, is considered below. Protected object is represented as a point mass, vibration isolator is placed between the protected object and the vibrating base with kinematic excitation in accordance with time dependence of  $\zeta(t)$ . The time dependence of the movement of the protected object is  $e(t)$ .

Since  $\zeta$  and  $e$  are defined in the inertial system, the relative motion of the object and base will be equal to  $\zeta(t) - e(t)$ , and the deformation of compression of the elastomer layers with total thickness  $h_x$  is equal to:



$$\varepsilon(t) = \frac{\xi(t) - e(t)}{h_z} \quad (8)$$

Let function  $\xi(t)$  is periodic with amplitude  $\xi_0$ :

$$\xi(t) = \xi_0 \sin(\omega t) \quad (9)$$

Since the system is linear, for the harmonic input function (e. g. deformation) all caused by its output processes (e. g. stress) will also be harmonic functions with the same frequency. Then it is natural to assume that function  $e(t)$  will be as follows:

$$e(t) = e_0 \sin(\omega t + \varphi) \quad (10)$$

where  $e_0$  - amplitude vibrations of steady-state vibrations of mass,  $\varphi$  - angle of lag.

The force imposed on the object with mass  $m$  from the

TRM support is equal to:

$$F = A\sigma(t),$$

where  $A$  - area of the upper face of the vibration.

The equation of motion of mass  $m$  in the  $z$  direction is:

$$m\ddot{e}(t) = -A\sigma(t).$$

Let us find the mass displacement depending on the viscoelastic properties of the rubber.

Taking into account (1) we have:

$$m\ddot{e}(t) = -AE_0 \left[ \varepsilon(t) - \int_{-\infty}^t R(t-\tau)\varepsilon(\tau)d\tau \right] \quad (11)$$

Let denote the natural frequency of vibrating mass as  $\omega_0$ , taking into account (8):

$$\omega_0 = \sqrt{\frac{AE_0}{h_z m}} \quad (12)$$

Substituting (8), (9) and (10) into (11) and taking into account (12) we received the equation of the object motion in the form:

$$\ddot{e}(t) - \omega_0^2 \left[ (\xi(t) - e(t)) - \int_{-\infty}^t R(t-\tau)(\xi(\tau) - e(\tau))d\tau \right] = 0$$

or:

$$\ddot{e}(t) + \omega_0^2 e_0 \sin(\omega t + \varphi) - \omega_0^2 \xi_0 \sin(\omega t) - \omega_0^2 \left[ \int_{-\infty}^t R(t-\tau)(\xi_0 \sin(\omega \tau) - e_0 \sin(\omega \tau + \varphi))d\tau \right] = 0 \quad (13)$$

For harmonic deformation taking into account linear independency of the functions  $\sin(\omega t)$  and

$\cos(\omega t)$ , using the property  $R(t-\tau) = 0$  if  $t < \tau$ , the system of the equations is obtained from (13):

$$\begin{vmatrix} \cos(\varphi) & -\sin(\varphi) \\ \sin(\varphi) & \cos(\varphi) \end{vmatrix} \begin{vmatrix} (1-B_1(\omega)) - \frac{\omega^2}{\omega_0^2} \\ B_2(\omega) \end{vmatrix} = \frac{\xi_0}{e_0} \begin{vmatrix} (1-B_1(\omega)) \\ B_2(\omega) \end{vmatrix} \quad (14)$$

From system (14) we can define the amplitude of the forced vibration  $e_0$  of mass and the angle of lag  $\varphi$ :

$$\frac{e_0}{\xi_0}(\omega) = \frac{B_1^2 - 2B_1 + B_2^2 + 1}{\sqrt{(B_2 b^2)^2 + (B_1^2 + B_1 b^2 - 2B_1 + B_2^2 - b^2 + 1)^2}} \quad (15)$$

$$\varphi(\omega) = \arctan \frac{-B_2 b^2}{B_1^2 + B_1 b^2 - 2B_1 + B_2^2 - b^2 + 1} \quad (16)$$

$$b = \frac{\omega}{\omega_0}.$$

In (15) and (16)  $B_1=B_1(\omega)$ ,  $B_2=B_2(\omega)$  are the functions of excitation frequency and calculated in accordance with (6).

#### Dissipative properties of rubber elements

The expression (1) is the generalized Hooke's law, here  $E_0$  defines the instantaneous stiffness of rubber in classic sense, but relaxation kernel defines the dissipative properties of rubber. Further we can calculate the work of compressive (or shear) stress per unit volume during the all-time of the existence of deformations  $\varepsilon(t)$ .

$$A = \int_{-\infty}^{\infty} \sigma(t)d\varepsilon(t) = \int_{-\infty}^{\infty} \sigma(t)\dot{\varepsilon}(t)dt \quad (17)$$

Expressing  $\sigma(t)$  and  $\varepsilon(t)$  in terms of Fourier components we receive:

$$\int_{-\infty}^{\infty} \sigma(t)\dot{\varepsilon}(t)dt = \frac{1}{4\pi^2} \int_{-\infty}^{\infty} dt \int_{-\infty}^{\infty} E(\omega) e^{i\omega t} d\omega \int_{-\infty}^{\infty} i\omega \varepsilon(\omega) e^{i\omega t} d\omega,$$

after transformation:

$$A = \int_{-\infty}^{\infty} \sigma(t)d\varepsilon(t) = \int_{-\infty}^{\infty} \omega E''(\omega) |\varepsilon(\omega)|^2 d\omega.$$

It is seen that  $\omega E''(\omega)$  defines the density of the energy dissipation due to viscoelastic rheology of rubber. This expression may be used for the estimation of the volume density of energy release. Generally speaking, at an orbitally point of time it is impossible to divide dissipative loss and elastic energy, saved in the RM

support. For the harmonic loading the loss of energy during the period of vibration may be calculated as:

$$U_T(\omega) = \pi m \omega_0^2 B_2 b^4 \frac{\xi_0^2}{B_2^2 + [1 - B_1 - b^2]^2}, \quad b = \frac{\omega}{\omega_0}. \quad (18)$$

Energy loss depends on natural frequency  $\omega_0$ , excitation frequency  $\omega$ , vibration amplitude  $\xi_0$  of the base, as well as  $B_1$  and  $B_2$  coefficients. It is necessary to take into account, that  $\omega_0$  in turn depends on vibrating mass.

This expression is necessary for attenuation factor definition, if vibration motion of the object is describe approximately, for example, by viscoelastic Maxwell model.

### III RESULTS AND DISCUSSION

The results of the calculation of damping properties of RM elements in accordance with above algorithm and equations are given below. Numerical examples was solved with help of Mathcad program.

In Fig. 2 plots of dependence the amplitudes ratio on excitation frequency for natural frequencies  $\omega_0 = 1, 5, 10, 15, 20 \text{ s}^{-1}$  for low-filled rubber 2959 ( $\alpha = -0.6$  and factor  $\beta = 1.062$ ) are presented.

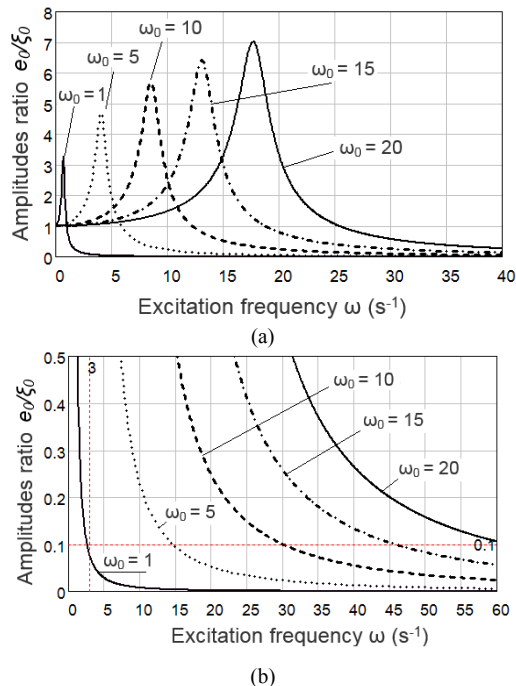


Fig. 2. Plots of dependence the amplitude ratio on excitation frequency for different natural frequencies  $\omega_0$  and factor  $\beta = 1.062$ . (a) – full-scale plots, (b) – lower part of plots.

From Fig. 2 (b) we can see that under the excitation frequency  $\omega = 3, 15, 30, 45$  and  $60 \text{ s}^{-1}$  the amplitude of the forced vibration of the objects becomes in 10 times smaller for natural frequencies  $\omega_0 = 1, 5, 10, 15$  and  $20 \text{ s}^{-1}$  respectively. This confirm the well-known fact

from vibration protection theory. From this graphs it is seen that RM absorber diminishes the vibration action on the object if it's natural frequency much less than forcing frequency.

Plots of dependence the lag angle  $\varphi$  on excitation frequency for different natural frequencies  $\omega_0$  are presented in Fig. 3; factor  $\beta = 1.062, \alpha = -0.6$ .

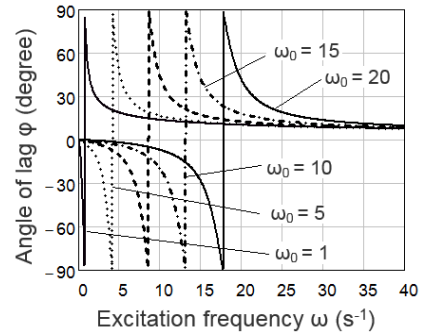


Fig. 3. Plots of dependence the lag angle  $\varphi$  on excitation frequency for different natural frequencies  $\omega_0$ , factor  $\beta = 1.062, \alpha = -0.6$ .

In Fig. 4 (a), (b) plots of dependence the amplitudes ratio on factor  $\beta$  for different rubbers for natural frequencies  $\omega_0 = 5 \text{ s}^{-1}$  (a)  $\omega_0 = 20 \text{ s}^{-1}$  (b) are shown. For all rubber  $\alpha = -0.6$ .

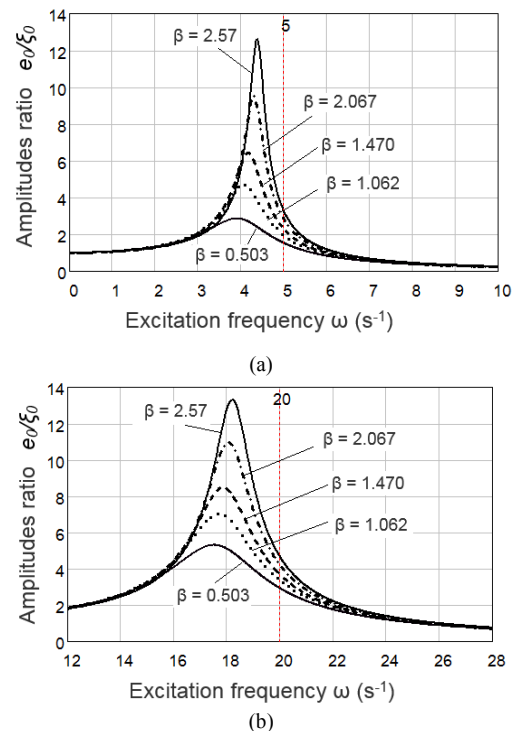


Fig. 4. Plots of dependence the amplitude ratio on excitation frequency for rubbers with  $\alpha = -0.6$  and different  $\beta$  factor: (a) for natural frequency  $\omega_0 = 5 \text{ s}^{-1}$ , (b) for natural frequency  $\omega_0 = 20 \text{ s}^{-1}$ .

Energy loss according to (18) is studied for RM absorbers with excitation amplitude  $\xi_0 = 0.5\text{mm}$ , factors  $\beta = 1.062$  and  $\alpha = -0.6$ . Plots in Fig. 5 shows the dependence of energy loss per period  $U_T$  on excitation frequency for mass 200 kg and 400 kg

( $\omega_0 = 14.09 \text{ s}^{-1}$  and  $9.96 \text{ s}^{-1}$  respectively).

Reinforced RM absorber of the cylindrical form with rubber part radius  $r = 18 \text{ mm}$  and total rubber height  $h_\Sigma = 40 \text{ mm}$  is applied,  $E_0 = 1.56 \cdot 10^6 \text{ N/m}^2$ .

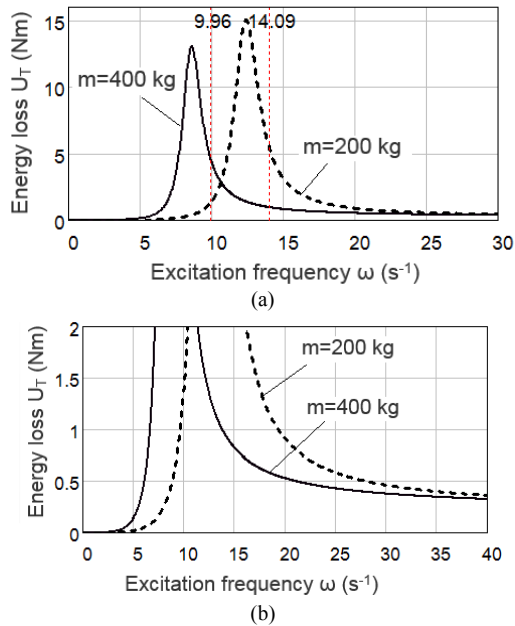


Fig. 5. Plots of dependence energy loss per period  $U_T$  on excitation frequency: (a) for mass 200kg ( $\omega_0 = 14.09 \text{ s}^{-1}$ ); (b) for mass 400 kg ( $\omega_0 = 9.96 \text{ s}^{-1}$ ).

It is seen from the plots that the energy loss per period is identical for different mass if excitation frequency is equal to the natural frequency.

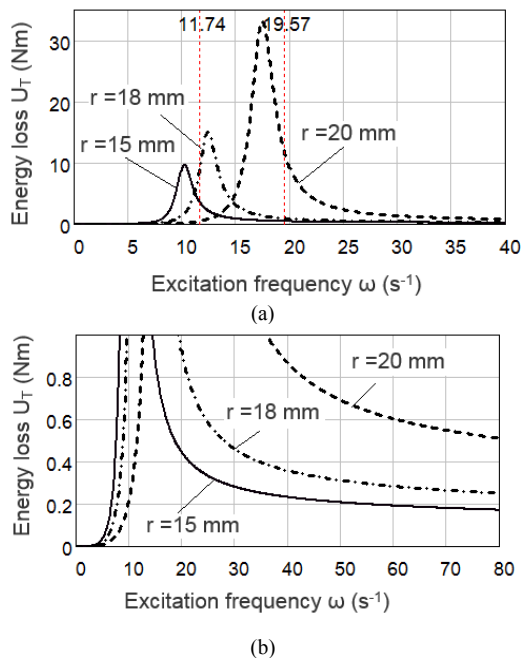


Fig. 6. Plots of dependence energy loss per period  $U_T$  on excitation frequency for mass 200 kg. and natural frequencies  $\omega_0 = 11.74 \text{ s}^{-1}$ ,  $14.09 \text{ s}^{-1}$  and  $19.57 \text{ s}^{-1}$ .

In Fig. 6 plots of the dependence of energy loss per period  $U_T$  on excitation frequency for mass 200 kg are presented for RM absorbers with  $h_\Sigma = 40 \text{ mm}$ , radii 15, 18 and 25 mm (natural frequency  $\omega_0 = 11.74 \text{ s}^{-1}$ ,  $14.09 \text{ s}^{-1}$  and  $9.96 \text{ s}^{-1}$  respectively).

Loss of energy more distinguishes in the post-resonance zone; absorbers with radius 20 mm deposits the energy twice as large than absorber with  $r=18 \text{ mm}$ .

#### IV CONCLUSIONS

This paper presents the procedure of the estimation of damping and dissipative properties of rubber-metal absorber devices for ODF system under harmonic excitation. Definition of damping properties is fulfilled for one degree-of-freedom system with kinematic excitation. Damping properties are expressed by the ratio of the amplitude of the forced oscillations of the upper base with the object to the amplitude of the forcing lower base oscillations. The dissipative properties are expressed by the energy loss per period of oscillation. The flat layer rubber – metal absorber of cylindrical form is calculated as the examples. Numerical examples was solved with help of Mathcad -15 program. The fulfilled calculations confirm the known fact of the theory of vibration protection: if the natural frequency of the object is three times lower than the frequency of the forcing oscillations, the forced oscillation amplitude is attenuated approximately in ten times.

It can be concluded that the proposed approach is suitable for dimensioning of RM absorber on the design stage depending on the prevented object mass, its operating mode and taking into account physical – Experimental study of the dissipative and damping properties of rubber-metal vibration absorber will be the next step of the current research work mechanical properties of the elastomeric layers.

#### V REFERENCES

- [1] J. M. Kelly and D. A. Konstantinidas, *Mechanics of Rubber Bearings for Seismic and Vibration Isolation*. UK: John Wiley & Sons, 2011.
- [2] A. N. Gent, *Engineering with Rubber: How to Design Rubber Components*. Munich: Carl Hanser Verlag, 2011.
- [3] J. T. Bauman, *Fatigue, Stress and Strain of Rubber Components: Guide for Design Engineers*. Munich: Carl Hanser Verlag, 2008.
- [4] D. Konstantinidis, J. M. Kelly, *Advances in Low-Cost Seismic Isolation with Rubber: Proceedings of the 10th National Conference in Earthquake Engineering*, July 21-25, 2014, Earthquake Engineering Research Institute, Anchorage, AK, 2014.
- [5] Lihua Zou, Kai Huang, Yu Rao, Ran Guo, Zhixu Xu, "Research on isolation property of prestressed thick rubber bearings". *JVE Journal of Vibroengineering*, March 2013, Volume 15, Issue 1. pp. 383-394.
- [6] V. A. Lepetov, *Rubber technical products*. Moscow: Chemistry, 1972. (In Russian)
- [7] V. T. Lyapunov, E. E. Lavendel and S. A. Shlyapochnikov, *Rubber vibration isolators. Handbook*. Russia, Leningrad: Sudostrojenie, 1988. 216 p. (In Russian).

- [8] S. I. Dimnikov, *Design of Rubber Elements of Structures*. Latvia, Riga: Zinatne, 1991. (in Russian)
- [9] E. E. Lavendel, *Design of Rubber Products*. Moscow: Mashinostroenie, 1976. (in Russian)
- [10] V. M. Malkov, *Mechanics of Multi-layered Elastomeric Structures*. St.-Petersburg, Russia: St.-Petersburg University Press, 1998. (in Russian)
- [11] N. S. Gusyatsinskaya, *Application of Thin Layer Rubber-Metal Elements in Machine-Tools and Other Engines*. Moscow: Mashinostroenie, 1978. (In Russian).
- [12] N. N. Frolov, S. J. Moldovanov and S. B. Lozovoy, *Mechanics of Thin Rubber Elements* (monograph). Kuban State Technological University, Krasnodar: Publishing House "Jug", 2011. (in Russian).
- [13] N. A. Leykand, E. E. Lavendel and V. A. Hrichikova, "Calculation of Compression Rigidity of Thin-layer Rubber-Metal Elements." In book: *Problems of Dynamics and Strength*, Issue 38, pp. 57-63, Riga, 1981. (in Russian)
- [14] T. O. Ormonbekov and U. T. Begaliev, *Use of Thin Rubber-Metal Elements in Earthquake Protection of Buildings, Engineering Constructions and Equipments*. Kyrgyzstan, Bishkek: Ilim, 1996.
- [15] A. R. Bhuiyan, A. F. M. S. Amin, T. Hossain, Y. Okui. "Nonlinear viscosity law for rate-dependent response of high damping rubber: FE implementation and verification." *Constitutive Models for Rubber V* – Boukamel, Lairinandrasana, Meo & Verrou (eds), Taylor & Francis Group, London, 2008, pp. 279 - 284.
- [16] A. S. Kravchuk, A. I. Kravchuk, "Simulation on creep by hereditary theory in a simple model of constant thickness deformed coating" *Electronic scientific journal "Apriori. Series: natural and technical sciences"*. no 2, 2014. Available: <http://apriori-journal.ru/seria2/2-2014/Kravchuk-Kravchuk.pdf>
- [17] V. N. Poturaev and V. I. Dyrda, *Rubber Machine Elements*. Moscow: Mashinostroenie, 1977.
- [18] A. R. Bhuiyan, Y. Okui, H. Mitamura, T. Imaic, "A Rheology Model of High Damping Rubber Bearings for Seismic Analysis: Identification of nonlinear viscosity", *International Journal of Solids and Structures*, 46, pp. 1778 – 1792, 2009. Available: <http://www.sciencedirect.com/science/article/pii/S0020768309000298>
- [19] A. F. M. S. Amin, M. S. Alam and Y. Okui, "Measurement of Lateral Deformation in Natural and High Damping Rubbers in Large Deformation Uniaxial Tests". *Journal of Testing and Evaluation*, Vol. 31, no 6, pp. 524-532, Nov. 2003, Available: <http://www.saifulamin.info/publication/journals/j4.pdf>

# Investigation of permanent magnet synchronous machine with recuperation block

Andrei Khitrov, Alexander Khitrov

Pskov State University, Electro mechanic Faculty.

Address: Russian Federation, Pskov, Lenin square, 2

**Abstract.** permanent magnet synchronous machines (motors) (PMSM) are getting increasingly involved in electrical engineering and electric power sector. The possible application for PMSM is autonomous decentralized low-power source which requires electric starter-generator.

Structure designing electric starter-generator for the autonomous cogeneration plant based on the rotary-vane external combustion vehicle (RVECE) is mostly consists of designing electric energy generating system. But the designing and investigating system starting operating modes is also of interest.

The paper considers structures of the starter-generator for autonomous low-power sources based on RVECE, the test stand composition and the experiment results.

**Keywords:** permanent magnet synchronous machine, recuperation block, autonomous electrical supply system, starter-generator set, test stand.

## I INTRODUCCION

Despite their comparatively high cost permanent magnet synchronous machines (motors) (PMSM) are getting increasingly involved in electrical engineering and electric power sector. Because of the top energetic characteristics among modern electromechanical converters PMSM are used both in low-speed high-accuracy motion control systems (brushless DC motors – BLDC) and in very high-speed systems having a primary filed of application covering gas turbine generators, compressor drives, expansion machines and electromechanic energy storages [1,2].

The possible application for PMSM is autonomous decentralized low-power source which requires electric starter-generator. Aspects of structure designing electric starter-generator for the autonomous cogeneration plant based on the rotary-vane external combustion engine (as well as the features and advantages of this type of engines) were considered in [3,4].

Fig. 1 shows the diagram of electrical energy generating using intermediate DC link (power factor corrector (DC/DC) 2) and two bidirectional blocks such as active front end (AFE) converter 1 and inverter 3 along with the corresponding control systems 4, 5, 6 [5].

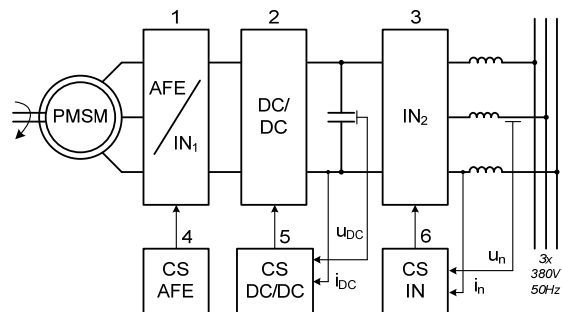


Fig. 1. The diagram of the autonomous generator plant with PMSM.

The referenced paper [3] contains the results of modeling and experiments in generator mode of the plant while investigation of system starting operating modes is also of interest.

## II PERMANENT-MAGNET SYNCHRONOUS MOTOR SYSTEM STARTING

It is expected that the start of the plant can be performed both from the network and from accumulator battery (battery start is the only option for autonomous work). The structures of converters applying for starting are shown in fig. 2. DC/DC converter can be switched off in the case of network start or the option of start from 48 V battery or can be

used to increase the battery voltage and to feed to the DC link.

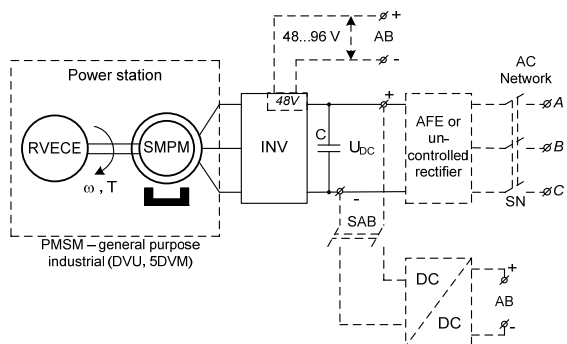


Fig. 2. The structure of the electrical subsystem of the autonomous power supply system based on rotary-vane external combustion engine.

The department of electric drive and automatics of Pskov State University has the test stand for the investigation of PMSM systems [6,7]. It was designed for the experiments with general purpose PMSM both in the motor mode and the generator mode. The test stand is embedded in the learning process for specialization «Electric drive, energy efficiency and autonomous energetics» in the courses «Mobile power supply plants and generating sets» and «Permanent magnet synchronous machines in electrical engineering and electric power sector».

Fig.3 shows the structure of the test bench. The set connections shown allow to carry out experiments with recuperation block while varying the load for PMSM.

The set includes:

- recuperation block (RB) ЭПВ-Р (ООО «ЧАЭЗ-ЭЛПИИ» Chelyabinsk), two connected to it frequency converters: inverter ACSM (ABB product) having vector control system and direct torque control system (DTC) and inverter Unidrive (Control Techniques product) operating in vector pulse-width modulation mode of the base vectors,

- three electromechanical converters: PMSM of DVU2M type, induction motor of 4A series having two shafts and PMSM of 9C type (ABB product) composing the complete electric drive together with the converter ACSM, equipped with encoder (EN).

Testing mode is selected by circuit breakers FM1-FM3. The experiments were performed to research the processes of start, reverse and load step in the PMSM system when powered from a three-phase AC voltage with recuperation block and without it.

Fig. 4 shows plots of starting and load rising when powered from a three-phase network without using recuperation block with the following agreed notations:

- 1 – curve of speed changing,
- 2 – curve of current changing,

- 3 – curve of mechanical torque changing (the torque is measured as a percentage of the rated value),
- 4 – curve of DC link voltage changing.

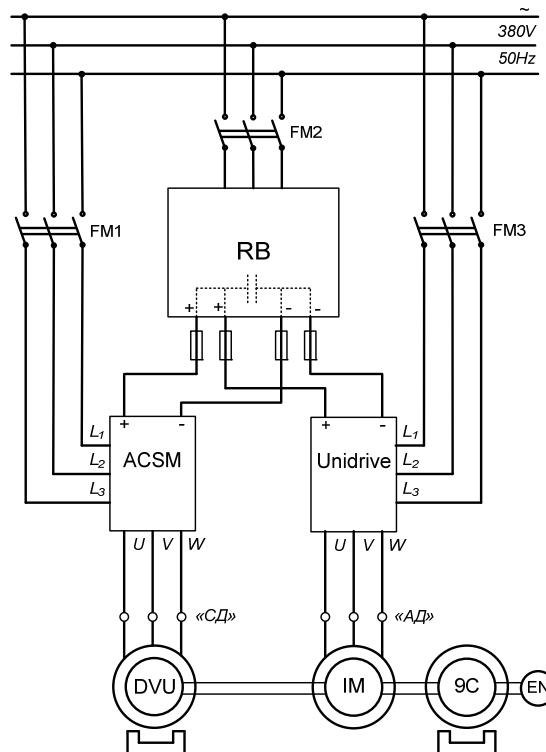


Fig. 3. The test stand structure.

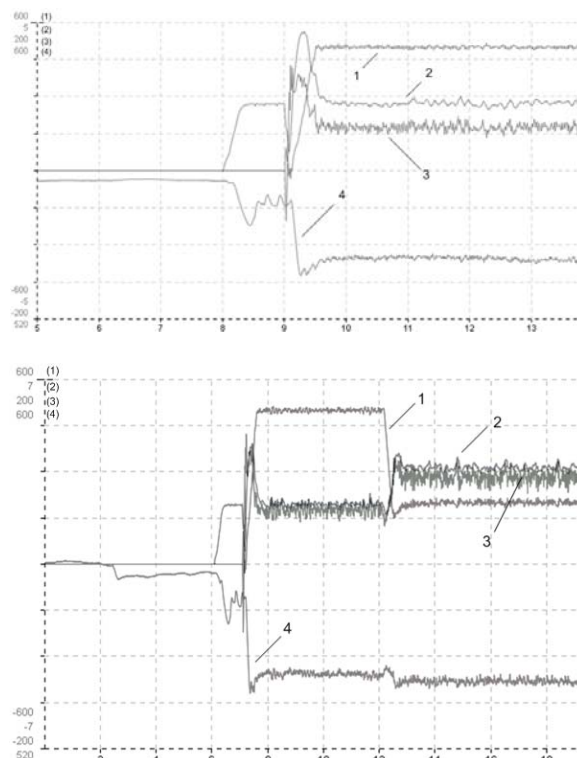


Fig. 4. PMSM modes without RB

Fig.5 shows plots of starting and load rising when powered from a three-phase network using recuperation block and the same notations as notations for fig.4.

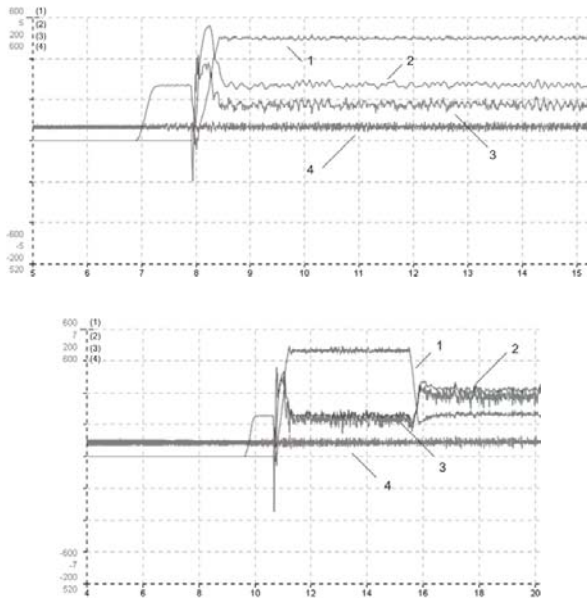


Fig 5. PMSM modes with RB.

The plots shown are obtained by using ABB Drive Studio software.

### III CONCLUSION

The results of the investigations allow to draw several conclusions:

- creation of experimental sets (test stands) for permanent magnet synchronous and induction motors modes investigations is recommended to be build using recuperation blocks (AFE converters): that allows to expand dynamic modes research when using visualization tools (software oscilloscope) of modern frequency converters;
- setting recuperation block instead of uncontrolled rectifier on the input of the inverter allows to improve electromagnetic capability (EMC) with a power network and to optimize electromagnetic transients on the DC link at starting and reversing frequency-controlled electric drives;
- when PMSM is used as the generator for the set with variable-speed engine (occurring in non-constant PMSM shaft speed), the electric energy generation system should be built as shown in the diagram in fig.1;

- researches shown that for creating low-power generating systems (10-20 kW) based on PMSM in autonomous power sets (cogeneration plants) it is necessary to develop the inverter (DC/AC) having input DC voltage 48-100 V, having built-in semiconductor DC/DC «transformer» (power factor corrector) and forming output three-phase AC voltage of industrial frequency.

### IV REFERENCES

- [1]. Шумов Ю.Н., Сафонов А.С. Сверхскоростные и ультраскоростные синхронные машины с возбуждением от постоянных магнитов (обзор зарубежных публикаций). *Электричество* №3, 2014.
- [2]. Аракелян А.К., Афанасьев А.А. Вентильные электрические машины в системах регулируемых электроприводов: Учебное пособие для вузов: В 2 т. Т.2.- М.:Высш.шк.,2006.-518с.
- [3]. Khitrov A.I., Khitrov A.A. Electrical subsystem of the low power cogeneration plant with low-speed vehicle. *Environment. Technology. Resources. Proceeding of the 9th International Scientific and Practical Conference, 2013. Volume II. Rezekne. p.119-123.*
- [4]. Перминов А. Л., Хитров А. А., Хитров А. И. Мехатронная система «магнитоэлектрический синхронный двигатель - активный выпрямитель» для автономной системы электроснабжения на базе роторно-лопастной машины с внешним подводом тепла. Труды VII Международной (VIII Всероссийской) конференции по автоматизированному электроприводу АЭП-2012: ФГБОУВПО "Ивановский государственный энергетический университет им. Ленина". - Иваново, 2012. - 708 с. с. 330-335
- [5]. Хитров А.И., Хитров А.А. Система управления электрической частью автономной когенерационной установки малой мощности с использованием твердотельных реле. Сборник статей Международной научно-практической конференции. Уфа: РИЦ БашГУ, 2014 – 244 с.
- [6]. Хитров А.И., Федотов И.М., Хитров А.А. Экспериментальный стенд для исследования режимов работы асинхронных и вентильных двигателей современных электроприводов. *Известия ТулГУ. Технические науки. Выпуск 3. ч.4, 2010. 262 с.*
- [7]. Федотов И.М., Хитров А.А. Structure designing of test stand for investigation of variable frequency electric drives. *Cilvēks. Vide. Tehnoloģijas: 16 starptautiskās studentu zinātniski praktiskās konferences rakstu krājums 2012. gada 25. aprīlis. Rēzekne: 2012. – 464 lpp. p. 448-452.*
- [8]. Харитонов С. А. Электромагнитные процессы в системах генерирования электрической энергии для автономных объектов. – Новосибирск: Изд-во НГТУ, 2011. – 536с.
- [9]. Мелешин В.И., Овчинников Д.А. Управление транзисторными преобразователями электроэнергии. М. Техносфера, 2011. - 576 с.
- [10]. Плохов И.В., Донченко М.А., Лукьянов Ю.Н. Энергоэффективная автономная энергоустановка нового поколения. Доклад на международной конференции «Инновационные технологии 2009». М.:Иннотехэкспо, 2009.

# Nanolevel Finishing for Veneered Products

Edgars Kirilovs, Laura Krūklīte, Silvija Kukle, Zane Zelča  
Riga Technical University  
Address: Azenes street 18, Riga, LV-1048, Latvia.

**Abstract.** Wood veneer is mainly used for interior decoration applications in many different segments. It's ideal for residential projects, hotel projects, offices giving to the any interior a unique look and feel. In addition, veneer is also processed to create a variety of products such as veneer parquet, flexible veneer sheets, wood veneer boards, wood veneer wallpaper, etc. From the other side, veneered surfaces will always to a greater or lesser degree change color, particular upon exposure to natural and artificial light. The degree of color change will depend on such factors as the species chosen, the coating type used and intensity and period of the exposure to light. In addition, conventional finishes have a tendency to yellow with age which can have quite dramatic effects on the original color of the selected timber. To minimize these effects new finishes have to be developed. In the paper new, invisible nanolevel coating for veneer finish based on the sol-gel process is offered. It is known that the sol-gel technique is an established industrial process for the generation of colloidal nanoparticles from liquid phase, which has been further developed in last years for the production of advanced coatings. It is well adapted for oxide nanoparticles and composites synthesis. The main advantages of sol-gel techniques are comparable low processing temperatures offering unique opportunities for access to organic and inorganic materials. The sol synthesis and application technology as well protective properties of coating will be discussed.

**Keywords:** Wood veneer, advanced coatings, sol-gel technique, organic materials.

## I INTRODUCTION

### *Birch wood microscopy*

Veneer is the finest use of timber, because it is real timber.

The benefits of its use are:

- the natural variations of timber means each project is individual as choice from the vast array of species, colors and textures are available; even from the same specie veneers differ in grain, color, texture and markings;
- they are pleasant and friendly to the touch;
- adds prestige and style to the furniture and joinery;
- veneer can be molded to fit any shape and adhered to a different substrates to give all the versatility of solid timber; various types of substrates can be used for the production of veneered panels and furniture, such as solid timber, particle boards, medium density fiber boards, plywood, block boards, and hardboards;
- veneer is highly efficient use of timber as one cubic meter of log could produce around 1000 square meters of veneer;
- veneer is sustainable use of forest resources. [1]

The main sources of veneers are hardwoods with the more complicated anatomy compared to softwoods and as consequence more complicated wood structure.

Veneer quality is a factor in construction and industrial plywood based on visually observable

characteristics. Knots, decay, splits, insect holes, surface roughness, number of surface repairs, and other defects are considered. Veneer species and characteristics are also a major factor in categorization of hardwood and decorative plywood.

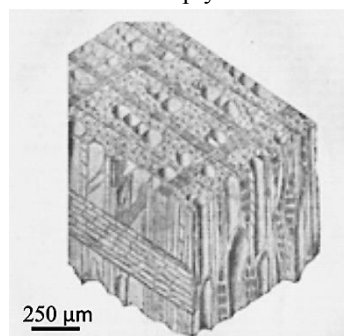


Figure 1. Anatomical features of birch [2]

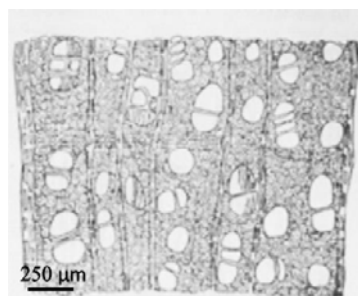


Figure 2. Birch cross section [2]



However, when observing the microstructure of a hardwood sample in practice it is normally only easy to see the vessels, fibres and parenchyma cells, since the tracheids are very few in number.

The hardwood axial system is composed of vessel elements in various sizes and arrangements, and of axial parenchyma in various patterns and abundance (Fig.1). As in softwoods, rays comprise the radial system and are composed of ray parenchyma cells, but hardwoods show greater variety in cell sizes and shapes. Vessel elements are stacked one on top of the other to form vessels. On the transverse section, vessels appear as large openings and are often referred to as pores (Fig. 1 and 2). Vessel diameters may be small (<30 µm) or quite large (>300 µm), but typically range from 50 to 200 µm. They are much shorter than tracheid's and range from 100 to 1,200 µm.[2]

If all the vessels are the same size and more or less scattered throughout the growth ring, the wood is diffuse-porous. If the early wood vessels are much larger than the latewood vessels, the wood is ring-porous. Diffuse-porous species woods maple and birch have two main types of growth rings and one intermediate form. In diffuse-porous woods, vessels either do not markedly differ in size and distribution from the earlywood to the latewood, or the change in size and distribution is gradual and no clear distinction between earlywood and latewood can be found (Fig. 2). Vessels can also be arranged in a tangential or oblique arrangement in a radial arrangement, in clusters, or in many combinations of these types. In addition, individual vessels may occur alone (solitary arrangement) or in pairs (Fig. 2), or radial multiples of up to five or more vessels in a row. Where vessel elements come in contact with each other tangentially, intervessel or intervascular bordered pits ranging in size from 2 to >16 µm in height are formed (Fig.3).

Hardwoods have a wide variety of axial parenchyma patterns. Paratracheal parenchyma is associated with the vessels, and further divided into vasicentric (surrounding the vessels), aliform (surrounding the vessel and with wing-like extensions), and confluent (several connecting patches of paratracheal parenchyma sometimes forming a band).

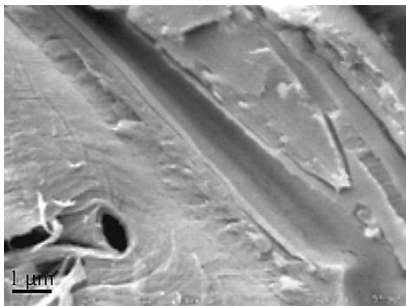


Figure 3. Exposed channel of hardwood showing pit [3]

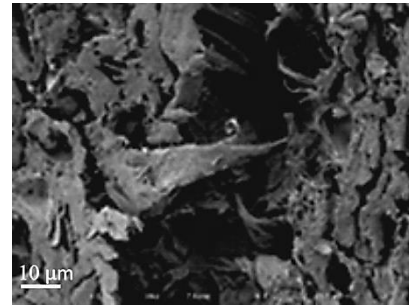


Figure 4. Hardwood microstructure [3]

Apotracheal parenchyma is not associated with the vessels and is divided into diffuse (scattered), diffuse-in-aggregate short bands and banded, whether at the beginning or end of the growth ring or within a growth ring. Each specie has a particular pattern of axial parenchyma, which is more or less consistent from specimen to specimen, and these cell patterns are important in wood identification. The rays in hardwoods are structurally more diverse than those found in softwoods. Most species have rays that are more than one cell wide. In oak and hard maple, the rays are two-sized, uniseriate and more than eight cells wide. Such hardwood anatomy specifics and differences between species lead to a very complicated and uneven veneer surface microstructure (Fig. 4). Small holes are typically created when the wood cells shrink during the drying process at the mill. Cracks can also occur when a veneer loses too much moisture (or loses moisture too quickly). When this happens, internal stresses become so strong that the wood cells shrink, lose elasticity, and then separate from each other. These types of splits are more challenging to repair. The success rate for repairing this type of crack depends on several factors. It is difficult to select the highest quality logs, because many internal defects such as gum veins, rot and insect damages are difficult to detect from the log outside. Probably the most critical aspect of preparation for finishing is the moisture content of veneered products. Equilibrium moisture content of veneer are approximately 10 to 12%. High moisture content is difficult to detect visually so prevention is a key.

#### *Birch wood veneer surface modification*

One of the different new approaches and possibly one of the most promising for surface modification of materials is the sol-gel technology. Probably this technology offering possibilities to tailor surface properties to a certain extent and to combine different functionalities in a single material was one of the most important developments in material sciences during the last decades. At the same time the application of sols can be carried out with the techniques commonly used in finishing processes such as immersion or sprinkling following by thermal processing.

Colloid solutions of nano sized oxides particles in aqueous or organic solvents or in their mixtures (nanosols) today become more and more popular. Due to the high surface area of the small particles the nanosols are metastable and during coating process the particles will aggregate as well as condense, initiated by evaporation of solvent in result of thermal treatment. Process result in dense three-dimensional networks leading in coatings which exhibit new functions.[4]

In comparison with many other materials such as ceramics or metals, wood products possess low thermal resistance. The conditions for the treatment and the sol composition have to be adapted to the particular demands of material. As chemical structure of such natural fibres as flax and hemp are close to the chemical structure of hardwoods, the sol synthesized for cotton and lignocellulosic fiber textiles surface modification are used. Obtained by this sol modified textile surfaces had presented excellent protection from ultraviolet radiation, antimicrobial activity and water repellency. All mentioned properties are important to improve protection of veneered surfaces in outdoor and indoor applications.[5]

Some stains, notably dye stains can fade if subjected to long term ultra violet light; if wooden surface is not protected, destruction of lignin could be caused by UV radiation.

Under direct sunlight fading, bleaching or color changes of veneered surfaces may occur. Excessive hot sunshine may dry the veneer surface more quickly than substrate thereby causing appearance of small surface checks parallel to the grain and possible damage of the coating. Treated with the sol surface will become more protected due to the restricted water vapor transmittance.

It is well known that all chemical substances and alcohols should be removed immediately from all veneered surfaces to avoid their damages. Water repellency property doesn't allow liquid to penetrate into surface and make it easy-to-clean.

Antimicrobial properties are necessary in a wide range of uses such as furniture of public and hospital premises, kitchen, dining room and bathroom furniture, outdoor constructions and furniture etc.

In Latvia work with implementation of modern waste management system was started in middle nineties of the 20th century. Up to date the system is sufficiently well developed, especially in landfill field. Until year 2012 in Latvia it is planned to be build 10-12 municipal solid waste sanitary landfills.

## II MATERIALS AND METHODS

### *Sol-gel method*

The veneer samples were modified in the prepared sols with and without Zinc acetate dehydrate, acetone pretreatment and SiO<sub>2</sub>. Sols were synthesized using silica alkoxide tetraethylortosilicate, ethanol and water

added to perform the hydrolysis and condensation, and hydrofluoric acid used as a catalyst. Zinc acetate dehydrate was used as the modifier of the sol-gel system. After the treatments, the samples were dried in an oven with the following thermal post-treatment, low temperature thermal treatment the drying and thermal post-treatment were combined [5].

Veneer is treated with acetic anhydride 1,5 h 24C 80% aqueous solution, then pressed for 2 min in 50 °C and loaded till is completely dry not to damage.

### *Adhesion theory and wetting parameters*

Several adhesion mechanisms or theories have been proposed and applied in the adhesion science and technology field [6]. This work involves the wetting (or adsorption) theory, which by far is the most applied concept for evaluation of theoretical secondary (non-covalent) bonding, for example hydrogen bonding, i.e. interfacial forces relevant mainly for adhesion and gluing technology. Wetting phenomena can be defined as "macroscopic manifestations of molecular interactions between liquids and solids in direct contact at the interface between them" [7]. Surface free energy, contact angles and work of adhesion are some parameters that define the wettability of materials.

Four basic types of birch wood veneer specimens with dimensions of 100x100x0.6 mm and 15x15x0.6 mm were prepared: reference samples of unmodified wood, and four types of modified wood samples, i.e. 1) modified with silica sol and two different regimes of thermal post-treatment 120 °C and 140 °C, 2) modified with Zn diacetate sol and two different regimes of thermal post-treatment 120 °C and 140 °C.

Figure 5 illustrates an equilibrium state of a drop of liquid surrounded by a gas at a solid surface. This is the fundamental basis for the Young's equation (1) and is expressed as:

$$\gamma_{LG} \cos\theta = \gamma_{SG} - \gamma_{SL} \quad (1)$$

where  $\theta$  is the liquid-solid-air contact angle,  $\gamma_{LG}$  and  $\gamma_{SG}$  are the surface free energies of the liquid (L) and the solid (S), respectively, exposed to a gas (G), and  $\gamma_{SL}$  is the solid-liquid interfacial free energy.[5]

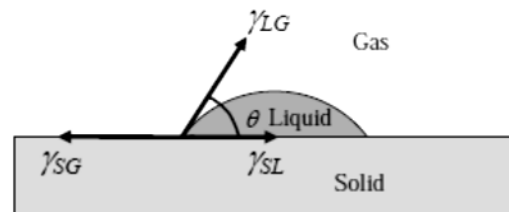


Figure 5. Equilibrium state of a drop of liquid surrounded by a gas on a solid surface.

### Atomic Force Microscope

Atomic Force Microscope (AFM) is relatively new technique used for the surface characterization. In AFM, one scans the sample surface with a sharp probe or tip, situated at the apex of a flexible cantilever that is often a diving board or V-shaped, usually made of silicon. The AFM utilizes a piezoelectric scanner that moves the sample in 3 dimensions by a subnanometer amount when a voltage is applied. To form an image, the tip is brought close to the sample and raster-scanned over the surface, causing the cantilever to be deflected due to probe-sample interactions. A line-by-line image of the sample is formed as a result of this deflection, which is itself detected using laser light reflected off the back surface of the cantilever onto a position-sensitive photodiode detector.[8]

AFM was applied to investigate the morphology of veneer. Height was scanned using silicone probe. Cantilever was 125 μm long and height at 15-20 μm. Test operated in Tapping mode, image size 50x50 μm with Scan Rate 0,1 Hz. Probe nominal tip radius, Spring constants and free resonance frequencies were 3,75 μm, 40 N/m and 300 kHz. The reference voltage was set to 2.6±0,2 V, a level that provided clear images.

### III RESULTS AND DISCUSSION

A popular chemical treatment method esterification usually involves reactions with organic acids or anhydrides. In acetylation process hydroxyl groups of hemicelluloses and lignin react with acetic anhydride, forming esters (Fig.6).

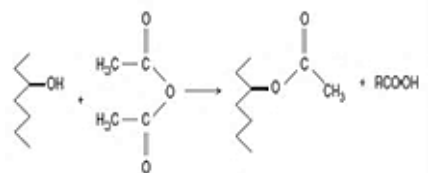


Figure 6. Esterification process

The obtained hydrophobic nature of the fibres is more compatible with non-polar polymers used as matrix. It is reported that treatment with acetic anhydride improve the adhesion and compatibility between the two phases of composite. In addition to this, better performance is acquired such as lower moisture absorption, higher wettability and improved mechanical properties and dimensional stability. Also, these chemical treatments improve the thermal and thermo-oxidative stability of the composite materials, by increasing their oxidation temperature (Fig. 7; 8).

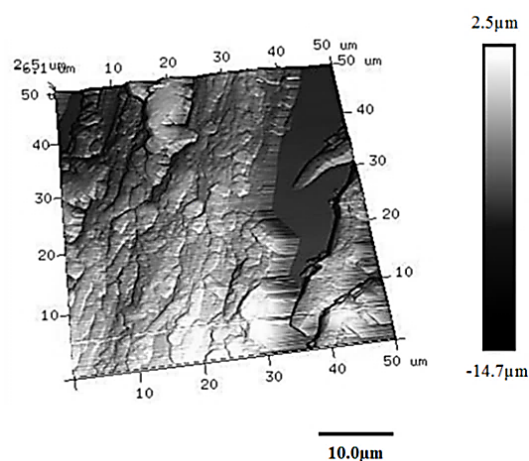


Figure 7. Sanded veneer processed with acetic anhydride, 3D surface

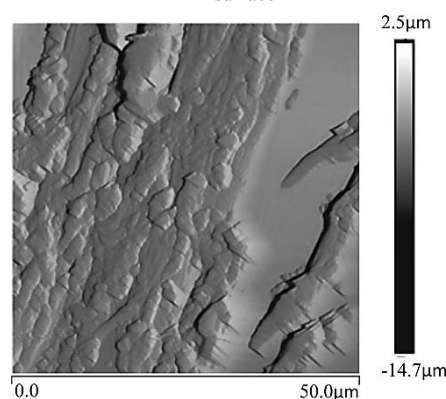


Figure 8. Sanded veneer processed with acetic anhydride, 2D surface

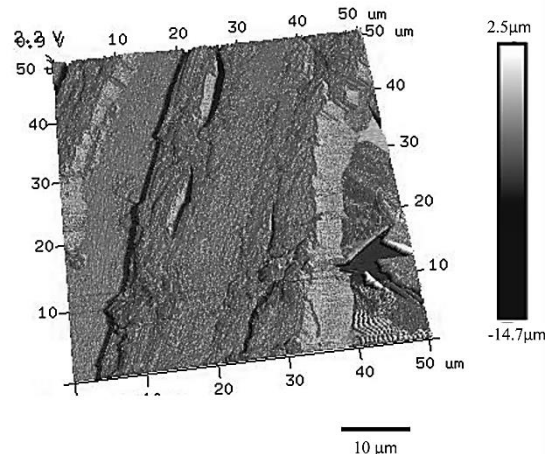


Figure 9. Sanded veneer processed with SiO<sub>2</sub>, 3D surface

Figure 9 shows the sliced birch veneer sample that is treated with SiO<sub>2</sub> solution using the sol-gel method. Before soaking the sample in SiO<sub>2</sub> liquid, it was twice sanded. Among the sanding there was done wetting and drying. Although the material was wetted between the sanding, after soaking it in SiO<sub>2</sub>, there was a

material irregularity of the surface, which can be explained by fibre lift up. This is also reflected in Figure 9.

Figure 10 shows birch veneer sample prior to processing, and Figure 11 shows a sample after treatment with Zn diacetate. After treatment of the sample there is observed terrain flattening that could be explained by the fact that the slightest relief wells are completed with Zn diacetate nano particles. Zn has effected the material so coloring it darker. The coating also reduces the presence of water absorption, and the drop is formed on the surface.

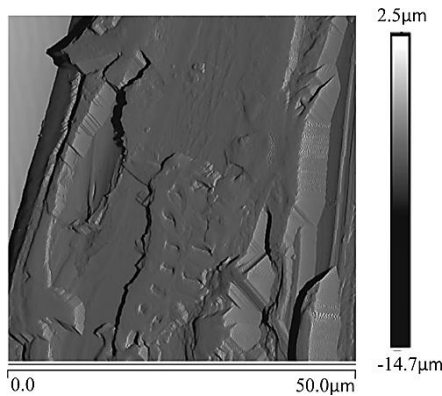


Figure 10. Unmodified veneer sample

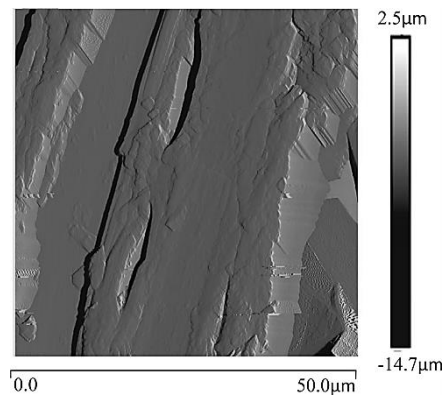


Figure 11. Modified sample by Zn acetate sol

Figure 12 shows that on the untreated surface drop smoothest over the surface, while Figure 13 shows that due to the Zn treatment diacetate drop retains its shape. There is formed a surface coating that reduces water absorption ability of the material. Further

research is needed to determine the surface protective sustainability.



Figure 12. Unmodified veneer sample

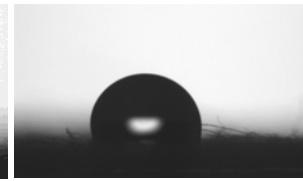


Figure 13. Modified veneer sample by Zn acetate sol

#### IV CONCLUSION

Regardless in which sol-gel liquid the veneer was soaked, the treatment improved resistance to water uptake. The sol-gel process formed a thin film of acetic anhydride, SiO<sub>2</sub> and Zn diacetate. Sample processing using acetic anhydride, requires two to four hours to achieve a sample size stability. But using silicon and zinc liquid, it requires 10 to 15 minutes. Further research is needed to determine the surface protective sustainability against various external influences and in premises with high moisture content.

#### V REFERENCES

- [1] MacGregor J. Preparing and applying decorative wood veneers and inlays to substrates, Forest and wood products research and development corporation, 2004, pp 80.
- [2] Forest Products Laboratory, Wood Handbook -- Wood as an Engineering Material [author's book] Michael C. Characteristics and Availability of Commercially Important Woods. Madison: Department of Agriculture, Forest Service, Forest Products Laboratory, 2010.
- [3] Shmulsky R., Jones D. Forest Products and Wood Science. Wiley-Blackwell. 2011, pp 496.
- [4] Sumo Sakka E. Handbook of Sol-Gel Science and Technology: Processing, Characterization and Applications, Springer, 2004, pp 1980.
- [5] Vihodceva S. Extension of the Range of Textile Modified at Nano-Level. Latvia: Institute of design technology, Department of material technology and design, 2014. Doctoral Thesis.
- [6] Schultz, J. and Nardin M., Theories and mechanisms of adhesion. In: Adhesion Promotion Techniques, Technological Applications. Eds. Mittal, K.L., Pizzi, A. Marcel Dekker Inc. 1999. pp. 1–26., ISBN 9780824702397
- [7] Berg, J. C. Role of Acid-Base Interactions in Wetting and Related Phenomena. Wettability. Ed. Berg, J.C. Marcel Dekker, 1993. New York. pp. 75–148, ISBN
- [8] Leite F.L., Mattoso L. H. The Atomic Force Spectroscopy as a Tool to Investigate Surface Forces: Basic Principles and Applications. Formatex.2007. pp 747-757.

# Thermal Conductivity of Hemp Based Boards

Edgars Kirilovs<sup>1</sup>, Silvija Kukle<sup>2</sup>, Dana Beļakova<sup>3</sup>, Anatolijs Borodinecs<sup>4</sup>, Ādolfs Ruciņš<sup>5</sup>,  
Veneranda Stramkale<sup>6</sup>

<sup>1,2,3,4</sup> Riga Technical University, <sup>5</sup>Research Institute of Agricultural Machinery, <sup>6</sup>Agriculture Science  
Center of Latgale

**Abstract.** Energy and raw material costs, an increase in environmental pollution, greenhouse gas emissions, global warming, depletion of fossil raw materials stimulate to seek and study alternatives to the synthetic fibers and products made of them for full or partial replacement. Renewable raw materials, including natural fiber sources, are the future of storage resources with a variety of positive effects on both the planet ecosystem and the living and working environment, and the energy consumption of delivering the required functionality. One of the most important energy-saving types is to reduce energy consumption in buildings by insulating them.

For Latvian conditions suitable crops are historically grown flax and hemp. Within the framework of the studies, hemp stems are being used. Hemp compared with flax, are less suffering from diseases and less damaged by pests, so hemp cultivation is practically free from use of chemical pesticides and herbicides reducing the risk to the ecosystem.

One of the most frequently mentioned industrial hemp raw materials positive qualities are their very wide use, practically all plant parts can be used in production of different products. This work explores the possibilities and technologies within the Latvian grown hemp stems to work into board materials with insulation capability.

Hemp fibers/shives mix boards can fulfill the main function of insulation materials, i.e., to reduce the transmission of heat, because they have a porous structure and low density. Material thermal insulation properties affect physical and structural properties of compounds. Cost effective particles board samples from chopped hemp stems with three types of adhesives and different thicknesses were produced and their thermal conductivity evaluated. The technologies applied and test results will be discussed in the paper.

**Keywords:** Hemp stems, insulation materials, particle boards, thermal conductivity.

## I INTRODUCTION

Insulating materials are used in public and private buildings, refrigerators, in insulating the electrical cables and in many other applications. Following the technology developments a range of new insulation materials are studied and technologies created. Around the world researches are carried out trying to find a thermal insulation material with excellent heat resistance, which at the same time also would be environmentally friendly, inexpensive, durable, easy to produce and use.

Flax and hemp bast fibres were applied for the insulation between the wood for centuries, but exactly in the last decades several types of insulation in form of roll materials are preferred instead of synthetic insulation. Despite the historical past, flax and hemp are often treated as a new material in heat insulation area. The contemporary studies of thermal qualities of bast fibres confirm their ability to compete with traditional insulation materials.

One of the reasons for usage is the higher price of bast fibres insulation in comparison with the price

of wide used mineral wool. On the other hand, environmental performance of natural fibres insulation as low energy consumption for their production from annually renewable resources, CO<sub>2</sub> neutrality during the life cycle, the positive effect on the indoor air and potential for processing secondary raw material are positive, but not always supporting arguments.

This study presents experimental work done to produce thermal insulation materials from hemp stems harvested and chopped on the field with the following preservation like a silage [1; 2; 3; 4; 5]. Hemp plant particles are created the porous layer rich in air. Attention is attached to the thermal and acoustic qualities of this material, as well as its ability to regulate the moisture inside the building - absorbing and/or releasing moisture in the air. Thermal conductivity determination and analysis of insulating properties of hemp particle boards with different thicknesses using as binders Phenol formaldehyde (PF) – Tembec 340 and Urea-formaldehyde (UF) – Kleberit 871.0 resins are discussed.

## II MATERIALS AND METHODS

### *The sequence of hemp board making, binder usage and board thickness base*

According to Leibniz-Institute for Agricultural Engineering Potsdam-Born (ATB) developed technology harvested and chopped whole hemp plants (seeds, leaves, fibres, shives) are wet preserved under anaerobic conditions [2]. The resulting acidity of the raw material is pH = 4.6 to 5.0. Dry and preserved component weight ratio is 1: 3; there is taken 2/3 preserved component and 1/3 dry component that are mixed manually. In order to obtain a homogeneous mixture of hemp structure, sewing is done. Raw material that is stored for 14 days and used to manufacture the boards; binders Phenol formaldehyde (PF) – Tembec 340 and Urea-formaldehyde (UF) – Kleberit 871.0 resins in amount  $10 \text{ g kg}^{-1}$  of mixture dry mass are used as the binders. To ensure optimal moisture the preserved material is mixed with dry hemp straw and processed with an extruder. Mixed and drayed material is divided into 5 kg units and it is mixed with glue and fleece is formed. The resulting fleece is pressed in the heated press to 130 degrees with holding time 1900 seconds fewer than 100 bar pressure (Table 1). Pressing resulted in the board with dimensions  $300 \times 300 \text{ mm}$  (Figure 1) and different thickness sample which were tested according ISO 8301:1991[6] standard. The thermal insulation were manufactured in cooperation with Research Institute of Agricultural Machinery and tested with Riga Technical University Faculty of Civil Engineering with the thermal flow meter Laser Comp FOX 600.

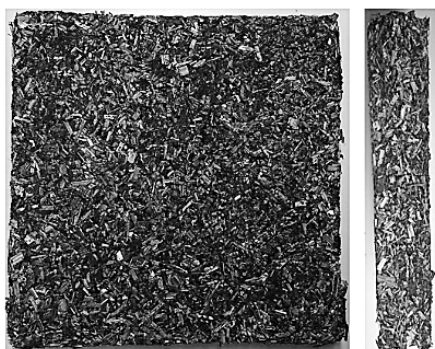


Fig.1. Board sample

Before starting the pressing (Figure 2) the upper and lower termplates surfaces of the pressing chamber are heated to a temperature (T) and the moisture extraction is turned between pressing times ( $t_1$ ) to ( $t_5$ ). Pressing mode consists of five cycles (Table 1), each cycle consists of pressing time and the distance between the termplates. In the first cycle the fleece material is pressed to a thickness ( $H_1$ ) and kept ( $t_1$ ) time. In the second cycle press is temporarily

relieved for time ( $t_2$ ) to remove the molded plates accumulated wet steam. In the third cycle the fleece material is compressed to a thickness ( $H_3$ ) and kept ( $t_3$ ) time. In the fourth cycle the press is relieved for time ( $t_4$ ). In the fifth cycle the fleece material is compressed to a thickness ( $H_5$ ) and kept ( $t_5$ ) time. In the last cycle the steam from the molded plates is released most intensive, so after pressing ( $t_5$ ) is continued 15 minutes moisture extraction.

Table 1.  
Pressing mode

T, C°	Pressing mode							
	1.stage		2.stage		3.stage		5.stage	
	H <sub>1</sub> , cm	t <sub>1</sub> , sec	t <sub>2</sub> , sec.	H <sub>3</sub> , cm	t <sub>3</sub> , sec.	t <sub>4</sub> , sec	H <sub>5</sub> , cm	t <sub>5</sub> , sec.
130	20	30	20	11	30	20	10	1800
130	10	30	20	0.55	30	20	0.5	1800
130	0.64	30	20	0.35	30	20	0.32	1800
130	0.48	30	20	0.26	30	20	0.24	1800



Fig.2. The technology of board pressing

Using PF binder the material's humidity must be in the ranges of 6 to 12%; if the moisture content is higher, partial or full curl is possible. To ensure that the glue hardens fast enough, pressing temperature must be maintained within the range of 140 to 150 °C. The pressing temperature can be technologically downgraded if the glue is mixed with hardener [7]. Using UF resin adhesive has a number of very good aspects: the low price, it is non-flammable, with bright colors and a very fast vulcanization. As negative features can be mentioned fact that the adhesive bond

is not water resistant and formaldehyde can be released from the adhesive. [8]

Temperature is a very important factor that determines not only urea and formaldehyde reaction rate, but also the properties of the final product. If condensation occurs at temperatures lower than 60 °C, the result is low molecular weight compounds in water with poor adhesive properties. The reaction temperature of urea-formaldehyde resin extraction process is usually higher than 75 °C. With the amount of hardener can be adjusted both key settings: holding time and the time of using glue.[9]

The humidity of the glued material should not exceed 10 ± 2%. If the material humidity is higher, the connection strength is severely weakening. [10, 11]

#### Determination of the thermal conductivity coefficient using heat flow meter

Thermal conductivity is semi static process. In the calculations the temperature gradient is assumed constant. It is very difficult to accurately determine the thermal conductivity coefficient, because as soon there is change in temperature changes also the temperature gradient.

The thermal conductivity coefficient measuring equipment FOX600 is based on stationary heat flow generation, which passes through the samples of a specific thickness perpendicular to the largest sides.



Fig. 3. Thermal conductivity measuring equipment FOX600 in RTU Faculty of Civil Engineering

Thermal conductivity measuring equipment FOX600 (Figure 3) technical data:

- Thermal conductivity range 0.01-0.2 W/(m\*K);
- Accuracy 1%;
- Maximum temperature of hot plate (at 18°C cooling water temperature) 65 °C
- Maximum temperature of cold plate (at 18°C cooling water temperature) -10 °C
- Temperature control stability ±0.03 °C
- Thickness measurement precision ± 0.025 mm

Measured sample dimension:

- Maximum sample size 610 x 610 mm

- Minimum sample size 300 x 300 mm
- Maximum sample thickness 203 mm
- Actual measuring area 254 x 254 mm

Facility FOX600 heat flow meter operating principle has been established on Fourier -Bio one dimensional law. French mathematician and physicist Jean Baptiste Joseph Fourier and the French physicist and astronomer Jean-Baptiste Biot in 1822 created the law isotropic thermal conductivity environments. Fourier -Bio law links environmental temperature gradient with heat flux densities (1):

$$q = -\lambda \frac{dT}{dx} \frac{W}{m^2} \quad (1)$$

where: q – heat flux (heat quantity per unit time emitted through the isothermal surface with an area (S) through the sample,  $\frac{W}{m^2}$ ;

$\lambda$  – its thermal conductivity,  $\frac{W}{m \cdot K}$ ;

$\frac{dT}{dx}$  - temperature on the isothermal flat surface,  $\frac{K}{m}$ .

The heat emitted from warmer to colder material surfaces of the heat flux by body particle interaction. This contributes to body temperature equalization. Transferred heat amount- heat flux density is proportional to the temperature gradient, it is evaluated by the coefficient of thermal conductivity  $\lambda$ .

The temperature gradient can be determined by measurements of difference between temperatures of the hot and cold plates (2):

$$\Delta T = T_{hot} - T_{cold}, K \quad (2)$$

where:  $T_{hot}$  – hot plate temperature, K;

$T_{cold}$  – cold plate temperature, K.

Average temperature gradient (3):

$$\frac{dT}{dx} = \frac{-\Delta T}{\Delta x}, \frac{K}{m} \quad (3)$$

where:  $\Delta T$  – the difference between the hot and cold plate temperature, K;

$\Delta x$  – sample thickness, m.

Before starting tests (by FOX600), the heat flow meter instrument must be calibrated using some certified sample (standard) having reliable known values of thermal conductivity  $\lambda_{cal}(T)$ .

Electric signal from the transducer Q ( $\mu V$ ) is proportional to the heat flux q (4):

$$q = \lambda_{cal}(T_{cal}) * \frac{\Delta T_{cal}}{\Delta x_{cal}} = S_{cal}(T_{cal}) * Q, \frac{W}{m^2} \quad (4)$$

Where:  $S_{cal}(T)$  – calibration factor;

Q – electric signal from the transducer,  $\mu V$ .

In order to obtain temperature dependent calibration is divided  $S_{cal}(T)$  in parts. The calibration factor is measured in  $\frac{W}{m^2 \cdot \mu V}$  or  $\frac{W}{m^2 \cdot mV}$ . Each of the two converters has its own temperature, and the calibration factors need to shift converter actual temperatures. The calibration factor' two separate sets have been measured during calibration.

The calibration factors  $S_{cal}(T)$  are the instrument's characteristics. They are used for thermal conductivity calculation during the test run (5):

$$\lambda_{test} = S_{cal}(T_{cal}) * Q * \frac{\Delta x_{test}}{\Delta T_{test}}, \frac{W}{m \cdot K} \quad (5)$$

As each plate has its own temperature the calibration factors should be calculated for plate's actual temperature. Average of two thermal conductivity values is also the final result of thermal conductivity test.

Determination of heat diffusivity (6):

$$a = \frac{\lambda}{C_p * \rho}, \frac{m^2}{s} \quad (6)$$

where:  $C_p * \rho$  – volumetric heat capacity,  $\frac{J}{kg \cdot K}$ ;

$C_p$  – heat capacity in constant pressure,  $\frac{J}{kg \cdot K}$ ;

$\rho$  – density,  $\frac{kg}{m^3}$ .

Thermal diffusivity coefficient's typical range for thermal insulation materials is approximately (4-7)  $10^{-7} \frac{m^2}{s}$ .

Fourier number (a dimensionless heat of similarity parameter that can be used in studying the problem of flow) can be determined (7):

$$F_0 = \frac{a * t}{(\frac{\Delta x}{2})^2} \quad (7)$$

where:  $a$  – temperature conductivity coefficient (physical value which characterizes the substance temperature changes (smoothing) the speed of unbalanced thermal processes) (8):

$$a = \frac{\lambda}{\rho * c}, \frac{m^2}{s} \quad (8)$$

where:  $\lambda$  – its thermal conductivity,  $\frac{W}{m \cdot K}$ ;

$\rho$  – density,  $\frac{kg}{m^3}$

$c$  – heat capacity in constant pressure,  $\frac{J}{kg \cdot K}$

$t$  – external conditions of the characteristic time, s;

$(\frac{\Delta x}{2})^2$  – characterized by body size,  $m^2$ .

The Fourier figure for FOX600 heat flow meter instruments constitutes -16 per hour 1 inch (25.4 mm) thick sample. Experiment showed that average value

of two heat flow meters signals reaches equilibrium several times faster than their individual values. Therefore the duration of tests is shorter, because the value of thermal conductivity is calculated using the average value of the signal.

### III RESULTS AND DISCUSSION

#### Thermal conductivity coefficient $\lambda$ measurements of different thickness and density hemp boards

During the experiment there were obtained four sample variants with the arithmetical average thicknesses of 24, 32, 50 and 100 mm and the corresponding density of 243, 252 and 316 +/- 38 kg/m<sup>3</sup>. Figure 4 shows that an increase in the thickness of the sample with UF binder in the range of 23 to 100 mm thermal conductivity of 0 °C side linearly increases in the range of 0.051 to 0.063 that is by 22.6% that is a large ratio. Changes under considered frequent intervals are showed by equation (9):

$$Y_{UF1} = 0.0475 + 0.0015X_b \quad (9)$$

where:  $X_b$  - sample thickness, mm;  
determination coefficient 0.99

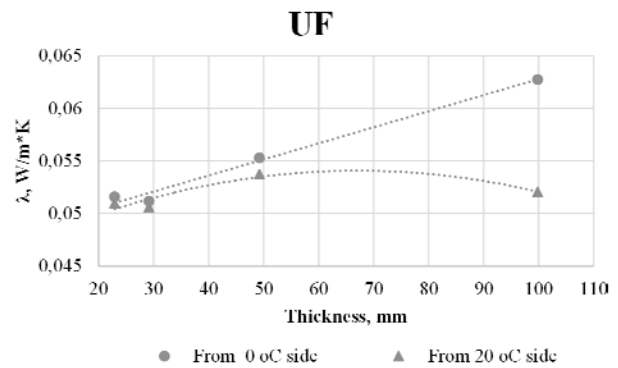


Fig. 4. The thermal conductivity of hemp fiber / shive insulation material with UF binder depending on the thickness of the sample

By contrast, the same coefficient of thermal conductivity of the sample at 20 °C side varies nonlinearly in a narrower area, reflecting the change in the nature of equation (10) second-degree polynomial form. Overall, the viewed sample thermal conductivity coefficient changes from 20 °C side can be regarded as a minor, as the maximum observed differences are within the error limits (not more than 2.9%). Also, the coefficient of determination 0.83 shows that the thickness effect only partly has caused thermal conductivity coefficient changes.

$$Y_{UF2} = 0.0457 + 0.0025X_b - 0.0002X_b^2 \quad (10)$$



Two times sieved by PF glue-related hemp fiber / shive insulation boards sample insulation coefficient varies nonlinearly in both tests from 0 °C side, and from 20 °C side (equations 11 and 12). In Figure 5 we can see that if the sample thickness changes in the range of 28 to 53 mm then thermal conductivity coefficients practically do not depend on whether the scale is from 0 °C or 20 °C side, as well as changes in thickness in the mentioned range have not effected the thermal conductivity coefficient values. However, reaching a thickness of 95 mm thermal conductivity coefficient values are increasing in both measurements, as well substantially are increasing differences in  $\lambda$  measurements: measured from 20 °C side the resulting coefficient by 21% in exceeds the one from 0 °C side resulting thermal conductivity coefficient presenting the opposite trend compared with UF adhesive material identified trends.

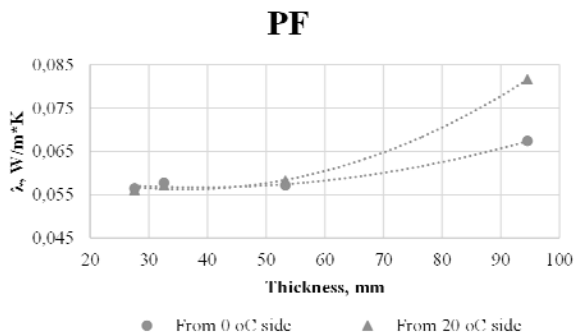


Fig 5. The thermal conductivity of hemp fiber / shive insulation material with PF binder depending on the thickness of the sample

$$Y_{PF1}=0.0618 -0.0026X_{b1}+0.0003X_{b12} \quad (11)$$

$$Y_{PF2}=0.0658-0.0053X_{b1}+0.0007X_{b12} \quad (12)$$

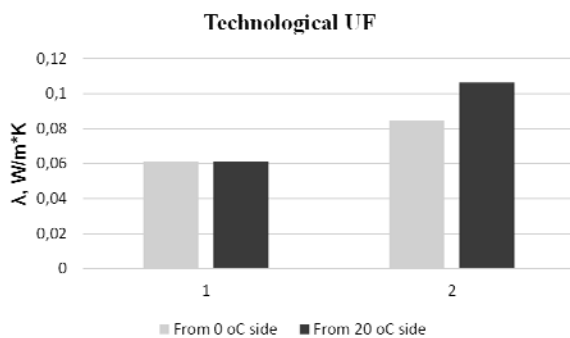


Fig. 6. The thermal conductivity coefficients of hemp fiber/shive fastened with technological UF glue. 1 - thickness 42.6 mm; 2 - thickness 104.2 mm

Comparing the graphs in Figure 6 shows that the small thickness sample values of the coefficient of thermal conductivity do not depend on what temperature is made the measurement, but by increase in thickness increases both the reference temperature

and the effect of thickness. In the experiment by increasing thickness of 2.44 times the thermal conductivity coefficient increases 1.38 times from 0 °C side and 1.74 times from 20 °C side.

#### IV CONCLUSION

Although it is often considered that the thermal conductivity does not depend on the thickness of the material, a number of research results have showed that increasing the thickness ratio  $\lambda$  becomes dependent on the thickness [12; 13]. At the same time, depending on the material and the structure of its constituent components originating, acquiring technology and binders used the link may be stronger or weaker. We cannot exclude also the impact of tested methods.

Comparing the obtained board thermal conductivity of some materials traditionally used (mineral wool from 0.033- 0.055, hardwood 0.16, softwood timber 0.12, wool felt 0.07, wood fiber insulation boards 0.04- 0.06), and taking into account that for materials with a thermal potential is deemed to be, the thermal conductivity coefficient  $\lambda$  in the range of 0.16 to 0.035 [14].

From hemp straw chips with a relatively simple process obtained board sample corresponds to the thermal conductivity of insulation materials required. Developing a prototype technology it will be possible to reduce the thermal conductivity precisely dosing binder consumption and dissipation.

#### V ACKNOWLEDGMENTS

This research is co-financed by the ESF within the project „Development of innovative technologies for the accumulation and production of heating and cooling”, project implementation agreement No. 2013/0064/1DP/1.1.1.2.0/13/APIA/VIAA/050.

#### VI REFERENCES

- [1] Pecenka R., Furl C., Radosavljevic L. Processing of Wet Preserved Hemp to Fibre Boards in a Pilot Plant. Saskatoon, : SaskFlax, 2008. p. 75- 80. ISBN 978-0-9809664-0-4.
- [2] Idler C., Pecenka R. Ensiling- a new practice for preservation of hemp. Gauta Instituto, 2007. p. 40-48. Vol. 39. ISSN 1392-1134.
- [3] Idler C., u.c., Wet Processing of Hemp: An Overview. London: Taylor & Francis, 2011. p. 59-80. Vol. 8. ISSN 1544-0478.
- [4] Kirilovs E., Gusovius H-J., Kukle S. Inovative MDF board material for furniture from hemp. Zadar: University of Zagreb Faculty of Textile Technology, 2012. p. 1641-1646. ISBN 978-953-7105-47-1.
- [5] Kirilovs E., Kukle S., Gusovius H-J., „Wet-preserved hemp fibreboard properties improvement with veneering” Submitted for publication in conference: 4TH International advances in applied physic and materials science congress & exhibition, Oludeniz, Turkey, April 23-27, 2014
- [6] ISO 8301:1991. Thermal insulation; Determination of steady-state thermal resistance and related properties; Heat flow meter apparatus.

- [7] Atta-Obeng E. Characterization of Phenol Formaldehyde Adhesive and Adhesive-Wood Particle Composites Reinforced with Microcrystalline Cellulose// Doctoral Thesis. - Auburn: Auburn University, 2011.
- [8] Нуч В. Деревообработка. - Москва: Техносфера, 2008. стр. 129-143. ISBN: 978-5-94836-139-0
- [9] Conner H. Urea-formaldehyde adhesive resins. [book author] Salamone J-C. Polymeric materials encyclopedia. USA: CRC Press, 1996, p. 8497-8501.
- [10] Gierenz G.,Karmann W. Adhesives and Adhesives tapes. - Germany: Wiley-vch Verlag GmbH, 2001. p. 58-64. ISBN 3-527-30110-0.
- [11] Pizzi A., Mittal K.L. Handbook of Adhesive technology. - New York: CRC Press; 2 edition, 2003. ISBN 1-40-8247-0986-1.
- [12] Kirilovs E. *Efficient Use of Annually Renewable Raw Materials for Production of Fiber Boards and Composites*. Latvia : Institute of design technology, Department of material technology and design, 2013. Doctoral Thesis.
- [13] Freivalde L. *Technology Impact on Hemp Fiber Insulation Material Properties*. Latvia : Institute of design technology, Department of material technology and design, 2014. Doctoral Thesis.
- [14] Thermal Conductivity of some common Materials. [Online] Available from <http://www.engineeringtoolbox.com>.

# Discrete automatic schemes for ASC TP

Vladimir Konevtsov, Igor Poletaev, Sergey Verteshev  
FSG-fEIHPЕ «Pskov State University», Faculty of Informatics.  
Adress: pl. Lenin, 2, Pskov, 180000, Russia.

**Abstract.** The article given shows functional possibilities of creating discrete automatic schemes in CAD of digital automatic control system (CAD of digital ACS), in complex of Software Design of System of the Digital Control (Complex SDSDC) for automated system of control of technological processes (ASC TP). Possibilities of complex SDSDC for implementing combination and sequential control compared with requirements of international standard IEC 61131-3:2003 (Part 3: Programming languages) are estimated.

**Keywords:** comparator of vectors of logical signals, flip-flop, shift register, counter of clock periods, recognition of the front of a logical signal, vote function, decoder, coder, transformer of bit sequence in a vector of logical signals and visa versa, index register, timer, multiplexer, signal generator.

## I INTRODUCTION

For designing blocking systems, protection of technological equipment from overloading, technological mode control (included start and stop modes, switching under usual conditions and abnormal ones) discrete automatic schemes are used. These are realized by technical means according standard IEC 61131-1:2003 (Part 1: General information) programmable logic controllers (PLC). For mathematical description of these means system of calculation of expressions-Boolean algebra is taken [10, 14]. Logical control units are classified as combinational (having no built-in memory- automat without memory) and sequential ones (automat with memory). According to this classification one can differ units of single clock period (combinational) and multi clock period (sequential) control [1, 3, 5-7].

## II ARCHITECTURE OF DISCRETE AUTOMATIC DEVICES

Any logical variable and function of binary logic is defined on multiple values {0, 1} or {false, true}. The function of binary logic can be single-place, two-place and multi place. Functions of repeat  $Y = X$ , negation  $Y = \bar{X}$ , constant-false  $Y = 0$ , constant-true  $Y = 1$  belong to single placed functions. For two independent variables one can get 16 different functions [10, 14], which can be equivalently expressed through NOT function and conjunction function (AND) or through NOT function and disjunction function (OR). Along with these functions the function of addition on mod-

ule two is used (XOR). These four functions are defined in the set of operations of expression calculation modules of complex SDSDC [8, 9, 13, 18, 19]. These are basic functions for implementation of discrete automatic schemes to perform memorizing, storing, counting, analyzing, comparing logical signals and vectors of logical signals. These devices are flip-flops, registers, counters, decoders, coders, commutators, comparators of circuit computer technology [10, 14] etc. Standardized functional modules of complex SDSDC are defined by analysis mathematical methods of control theory [8]. Comparative evaluation of features of complex SDSDC [13] and functional requirements IEC 61131-3 [16] is given in the table I [4, 12, 15, 17, 20].

Comparing vectors of logical signals (for example, finding a state of tens and hundreds discrete performing mechanisms on the state of end switchers in ASC TP) can be carried out more conveniently with comparator [14]:

$$Y_i = \begin{cases} X_i & \text{if } f=0 & \text{reiteration} \\ \bar{X}_i & \text{if } f=1 & \text{negation} \\ X_i \oplus Z_i & \text{if } f=2 & \text{exclusiving OR,} \\ X_i \wedge Z_i & \text{if } f=3 & \text{conjunction} \\ X_i \vee Z_i & \text{if } f=4 & \text{disjunction} \end{cases} \quad (1)$$

where  $i = 1, 2, \dots, n$ ;  $n$  – is a signal vector dimension,  $f$  – is a parameter of choice of operation,  $X_i, Z_i$  – are components of vectors of dimension  $n$ .

TABLE I  
COMPARATIVE EVALUATION OF FEATURES OF COMPLEX SDSDC

Groups of discrete automatic modules	Complex SDSDC	IEC 61131-3
Comparators of vectors of logical signals	+	-
Flip-flops	+	+
Shift registers	+	-
Counter of clock periods	+	+
Recognition of the front of logical signals	+	+
Vote functions	+	-
Decoders	+	-
Coders	+	-
Transformer of bit sequence in a vector of logical signals	+	-
Transformer of vector of logical signals in a bit sequences	+	-
Index registers	+	-
Timers (TP-Pulse, TON-ON delay, TOF-OFF delay)	+	+
Multiplexers	+	-
Signals generators	+	-

Note to the table I: (+) is presence, (-) is absence of standardized module group.

For storage of values of one signal of a logical look the RS and SR triggers [6] having two stable conditions in case of reset or set [10] (bistable elements) are used.

These flip-flops have a reset input R, a set input S, an input of a state and an inverse output of a state. For storing a vector from n logical signals one can define a «packet» RS flip-flops (this packaging is used by manufacturing integrated circuits [11]) and at programming it can be done very simply: at n = 1 flip-flop is (becomes) usual [10]:

$$Q_i(k) = \begin{cases} 0 & \text{if } R_i=1 \\ 1 & \text{if } S_i=1 \\ Q_i(k-1) & \text{else} \end{cases}, \quad (2)$$

$$Y_i(k) = \overline{Q_i(k)},$$

where  $i=1,2,\dots,n$ ; n – is the number of flip-flops in «the packet». The signals having close inertance, i.e. having the same rate of change are included in «the packet» of logical signals. If the vector of logical signals is to contain signals of different inertance then the time required to process the scheme to have a block of this functional module is defined by the signal with the highest rate of changing its value. At the output of a flip-flop state with the reset priority when  $R=S=1$  at the same clock period the value of the signal always equal to 0. At the output of a flip-flop state with the set priority when  $R = S = 1$  at the same clock period the value of the signal always equal to:

$$Q_i(k) = \begin{cases} 1 & \text{if } S_i=1 \\ 0 & \text{if } R_i=1 \\ Q_i(k-1) & \text{else} \end{cases}, \quad (3)$$

$$Y_i(k) = \overline{Q_i(k)},$$

where  $i=1,2,\dots,n$ ; n – is the number of flip-flops in «the packet». In the classical definition of RS and SR flip-flops the memory at the state input in a previous clock period is not accessible, this is an inner connection of a module, it is destroyed if power is switched off. In definitions of complex SDSDC this connection is accessible for an system engineer, and the memory at the input state in the previous clock period can be stored when power is switched off.

For storing signals of different types multi place registers are used («cells» of memory), they are registers of different action: series input-series output, series input-parallel output, parallel input- parallel output, parallel input-series output. In systems with memory (fixing the trend of pre-abnormal situation, correcting devices of high order, identification and imitation of systems etc.) registers with multi-value memory are used. These registers are referred to as shift registers [2, 8]:

$$\left. \begin{aligned} Z_2 &= \begin{cases} 1 & \text{if } (q \geq N) \wedge (Z_0 = 0) \\ 0 & \text{if } (q < N) \vee (Z_0 = 1); \end{cases} \\ q &= \begin{cases} q_0 + 1 & \text{if } (q < N) \wedge (Z_1 = 1) \wedge (Z_0 = 0) \\ N & \text{if } (q \geq N) \wedge (Z_0 = 0) \\ 0 & \text{if } Z_0 = 1; \end{cases} \\ Y_k &= \begin{cases} X_k & \text{if } (Z_1 = 1) \wedge (Z_0 = 0) \\ X_{k-1} & \text{if } (Z_1 = 0) \wedge (Z_0 = 0) \\ 0 & \text{if } Z_0 = 1; \end{cases} \end{aligned} \right\}, \quad (4)$$

where  $k=1,2,\dots,N$ ;  $N$  – is the length of the trend;  $q_0$  – is the initial length of the trend;  $Z_0$  – is the reset of the register;  $Z_1$  – is the shift of the register;  $q$  – is the current length of the register;  $X(k), X(k-1), \dots, X(k-N)$  – are values of the variable at the clock periods  $(k-1), (k-2), \dots, (k-N)$ ;  $y(k), Y(k-1), \dots, Y(k-N)$  – is the content of the register.

Counters differ by the way of counting (direct, reverse), by representing in notation system (binary, decimal), by the way of count controlling (synchronous, asynchronous). The counter («the packet» counter) performs a relative count of time, that is count in clock periods of control scheme. The signals having close inertance, that is having the same rate of changing are included into «the packet» if signals of different inertance are to be connected to «the packet» of counters then the time required to process the scheme containing blocks of this functional module is defined by the signal of the highest rate of changing its values:

$$\left. \begin{aligned} Z_i &= \begin{cases} 1 & \text{if } TZ_i = TT_i \\ 0 & \text{else} \end{cases} \\ Y_i &= \begin{cases} TH_i & \text{if } C_i = 1 \\ TT_i + 1 & \text{if } TT_i < TZ_i \\ TT_i - 1 & \text{if } TT_i > TZ_i \\ TZ_i & \text{if } TT_i = TZ_i, \end{cases} \end{aligned} \right\} \quad (5)$$

where  $C_i$  – is the reset of the counter;  $i=1,2,\dots,n$ ;  $n$  – is the number of counters in «the packet»;  $TH_i$  – is the initial value of the counter  $i$  at resetting;  $TZ_i$  – is the task of the counter  $i$ ;  $TT_i$  – is the current value of the counter  $i$ ;  $Z_i=1$  – means counter is filled.

The analysis of changing logical signal (recognition of the front) is carried out by logical elements called signal front definer. Front definer differ by the character of changing logical signal: rising front:

$$\left. \begin{aligned} Q_i &= \begin{cases} 1 & \text{if } (X_i(k-1)=0) \wedge (X_i(k)=1) \\ 0 & \text{else}; \end{cases} \\ Y_i &= X_i(k); \\ q_i &= \overline{Q_i}, \\ \text{where } i &= 1, 2, \dots, n \end{aligned} \right\}, \quad (6)$$

where  $n$  – is the number of definer in «the packet»;  $X_i(k)$  – is the value of the signal being analyzed in the current clock period  $kT$ ;  $X_i(k-1)$  – is the value of the signal being analyzed in the previous clock period  $(k-1)T$ ;  $Y_i$  – is the memory of the signal being analyzed;  $q_i$  – is absence of rising front, falling front:

$$\left. \begin{aligned} Q_i &= \begin{cases} 1 & \text{if } (X_i(k-1)=1) \wedge (X_i(k)=0) \\ 0 & \text{else}; \end{cases} \\ Y_i &= X_i(k) \\ q_i &= \overline{Q_i}, \\ \text{where } i &= 1, 2, \dots, n \end{aligned} \right\}, \quad (7)$$

where  $n$  – is the number of definer in «the packet»;  $X_i(k)$  – is the value of the signal being analyzed in the current clock period  $kT$ ;  $X_i(k-1)$  – is the value of the signal being analyzed in the previous clock period  $(k-1)T$ ;  $Y_i$  – is the memory of the signal being analysed;  $q_i$  – is absence of falling front, (either) front:

$$\left. \begin{aligned} Q_i &= \begin{cases} 1 & \text{if } X_i(k-1) \neq X_i(k) \\ 0 & \text{else} \end{cases} \\ Y_i &= X_i(k) \\ q_i &= \overline{Q_i} \\ \text{where } i &= 1, 2, \dots, n \end{aligned} \right\} \quad (8).$$

where  $n$  – is the number of definer in «the packet»;  $X_i(k)$  – is the value of the signal being analyzed in the current clock period  $kT$ ;  $X_i(k-1)$  – is the value of the signal being analyzed in the previous clock period  $(k-1)T$ ;  $Y_i$  – is the memory of the signal being analyzed;  $q_i$  – is absence of front.

The signals having close inertance, that is having the same rate of changing are also included into «the packet» of logical signals. If the vector of logical signals is to contain signals of different inertance, then the time required to process the scheme containing the block of this module is defined by the signal of the highest rate of values. The definers of the front are also given in a «packet» form. At the time of changing signals at «packet» outputs corresponding logical values of signals appear during the time equal to one period of scheme processing if the signal change rate at the corresponding inputs isn't greater than that one at starting the control scheme.

Processing logical signals as arguments of multi place functions can be performed by means of so called vote function in schemes of recognition and correction of mistakes when information is transformed:

$$Y = \begin{cases} 1 & \text{if } \sum(X_1, X_2, \dots, X_n) \geq m \\ 0 & \text{else} \end{cases}, \quad (9)$$

where  $n$  – is the number of logical variables,  $m$  – quorum of vote system.

The dependence (9) defines the vote function conjunctively (majoritarian element) for any combination of logical signals from  $n$  by  $m$ . When  $n = m$  the expression (9) corresponds to multi place conjunction, when  $m = 1$  the expression (9) corresponds to multi place disjunction, when  $n = m = 1$  the expression (9) corresponds to the function of repeat.

There are many different code converters. At designing sequential schemes, end automats, digital computers coders and decoders (these modules are also absent as standard ones according to IEC 61131-3) are especially important. The number of states of end automat corresponds to the number of inputs of coder and the number of outputs of a decoder [10, 14]. The function of a decoder is to transform any number of notation system  $X$  with base  $B$  from  $N$  positions, in the vector of logical signals having a dimension  $m = B^N$ . The signal at the output of the decoder  $Y_j$  with number  $j = X$  is always equal to logical 1,  $1 \leq j \leq m$ , and values of the signals at other outputs  $Y_j$  with numbers  $j \neq X$  being always equal to logical 0:

$$Y_j = \begin{cases} 1 & \text{if } j = X \\ 0 & \text{for all } j \neq X, \end{cases} \quad (10)$$

where  $j = 1, 2, \dots, m$ ,  $1 \leq X \leq m$ .

Coder performs the operation being opposite that of decoder, that is it transforms the logical input vector  $X_1, X_2, \dots, X_m$  of dimension  $m$  into number  $j$  belonging to that input  $X_j$  which has a logical value equal 0. All inputs of a decoder but that one, which shows the current number of object state, must have zero values of signals:

$$Y = \begin{cases} 1 & \text{if } n \neq m \\ 0 & \text{else,} \end{cases} \quad (11)$$

$$m = \begin{cases} i & \text{for } X_i = 1 \text{ and all } X_j = 0, j \neq i \\ n & \text{else,} \end{cases} \quad (12)$$

When being put in discrete signals are grouped in bytes, like real numbers, which later are used as logical signals. To get separate signals, not grouped into bytes the module of transforming sequence of real

numbers into digit-by-digit position code, where each digit takes one byte is used.

When discrete signals are put out from outputs of combinatorial or sequential schemes it is necessary to transform the vector of logical signals into signals packed into bytes. For this purpose the module of transforming the vector of logical signals into a sequence of real numbers is used.

If signals on the vector  $X_1, X_2, \dots, X_n$  can take arbitrary logical values, then the inputs with logical 1's can be «marked», that is can be indexed by dependence (indication register):

$$\left. \begin{aligned} q &= \sum(X_1, X_2, \dots, X_n) \\ Y_j &= i \cdot X_i \text{ for all } X_i \neq 0, \end{aligned} \right\} \quad (13)$$

where  $q$  – is the number of inputs with value of the signal equal to 1,  $X_i, j = 1, 2, \dots, q$

Indication register is a function of coding with variable number of outputs. This module can be used for example for numbering inputs having value of signals equal to 1 (for example, numbering performing mechanisms whose state deviates from the norm). If values of signals at all  $n$  inputs are equal to 1 then the dependence will give the following values of outputs:  $q = n, Y_1 = 1, Y_2 = 2, \dots, Y_n = n$ . If values at all inputs are 0, then  $q = 0$ , and outputs  $Y_j$  don't exist.

All variable connections in control system are performed by means of commutators. There are commutators of input signals (multiplexers or reading commutators), commutators of output signals (demultiplexers or distributors or writing commutators) and matrix commutators (multiplexers-demultiplexers or read/write commutators) [14]:

$$Y_i = (AC + EN + \{NV - 1\}NE + i), \quad m = 1 \quad (14)$$

$$(AC + EN + \{NV - 1\}NE + i) = X_i, \quad m = 0 \quad (15)$$

where  $i = 1, 2, \dots, NE$ ;  $m = 1$  reading;  $m = 0$  writing;  $m$  – instruction to read/write;  $AC$  – the address of the signal;  $EN$  – number of the element;  $NV$  – number of the vector;  $NE$  – a number of elements. The function of a multiplexer we'll get by replacing  $m = 1$  in the expression (14), and the function of a demultiplexer by replacing  $m = 0$  in the expression (15). Each of the values being switched  $X_1, X_2, \dots, X_{NE}, Y_1, Y_2, \dots, Y_{NE}$  may be a separate value of the signal (scalar) or a vector of values of a signal of a definite dimension and kind.

The sequence of low frequency impulses (getting signals of frequency 0,5 Hz; 1 Hz; 2 Hz;... for the

synthesis of control schemes and warning) can be got by means of signal generators.

$$Y_i = \left. \begin{array}{l} C(k) = \bar{C}(k-1); \\ C(k) \text{ at } X_i = 1, i=1, 2, \dots, KK, \\ 0 \text{ else,} \end{array} \right\} \quad (16)$$

where  $kk$  – is the number of periodic pulse channels,  $C(k)$  – is the state of outputs at the moment  $kT$ ;  $C(k-1)$  – is the state of outputs at the moment  $(k-1)T$ ;  $X_i$  – is the state of pulses at input start/stop generation;  $Y_i$  – is the state of pulses at outputs.

Thus, discrete automatic devices can be implemented by programming according to formulae (1)-(16)

### III CONCLUSION

Program implementation of main discrete automatic devices in complex SDSDC provides its universality at designing digital ACS. Such approach to the creation of industrial control systems allows to expend the set of standardized groups of discrete automatic modules without any essential expenses in comparison with the functional requirements of IEC 61131-3. The complex SDSDC as a design tool of digital ACS, is oriented not on professional programmers, but on engineers i.e. specialists in automation and remote control. The offered approach to the program implementation of discrete automatic devices allows to use the technique accepted at developing hardware systems. For example, the technique of developing and mounting control and regulation systems on the basis of pneumatics, hydraulics, electrical mechanics and discrete automatic devices based on chips of different scale integration.

### IV REFERENCES

- [1] Айзерман М.А., Гусев Л.А., Розоноэр Л.И. Логика. Автоматы. Алгоритмы.- М.: Государственное издательство физико-математической литературы, 1963, с. 556.
- [2] Антонью А. Цифровые фильтры: анализ и проектирование.- М.: Радио и связь, 1983, с. 320.
- [3] Баранов С.И. Синтез микропрограммных автоматов.- М.: Энергия, 1974, с. 216.
- [4] Виши Г. Стандартные программы вычислительных машин для обработки данных. - М.: ВЦП, 1973, перевод № Ц-16684, с. 45.
- [5] Гаврилов М.А., Девятков В.В., Пупырев Е.И. Логическое проектирование дискретных автоматов.- М.: Наука, 1977, с. 252.
- [6] Горбатов В.А., Кафаров В.В., Павлов П.Г. Логическое управление технологическими процессами.- М.: Энергия, 1978, с. 272.
- [7] Горбатов В.А., Крылов А.В., Федоров Н.В. САПР систем логического управления. М.: Энергоатомиздат, 1988, с. 230.
- [8] Конеvцов В.А. САПР цифровых САУ. Концепция: Монография. Издание третье, дополненное и исправленное: Псков: Псковский государственный университет, 2013. – с. 317.
- [9] Конеvцов В.А., Казаченко А.П., Литвинова Л.М., Бунин А.Б. Модифицированные средства цифрового управления.- М.: Информприбор, Каталог Государственной Системы Приборов СССР, 1987, том 4, вып. 10, 11, 12, с. 112.
- [10] Лехин С.Н. Схемотехника ЭВМ.– СПб.: БХВ – Петербург, 2010, 661с.
- [11] Микросхемы интегральные. Серии K1500...KP1531. Справочник.- С-Петербург, Издательство РНИИ «Электронстандарт», 1993, с.130.
- [12] John Karl-Heinz, Tiegelkamp Michael SPS–Programmierung mit IEC 61131-3. - Springer – Verlag Berlin Heidelberg 4. Auflage, 2009, s.402.
- [13] Konevtsov V.A., Verteshev S.M., Poletaev I.A. Eigenschaften von Complex SDSDC // European Science and Technology: 7th International scientific conference. Germany, Munich 2014, Vol.1, p. 493-497.
- [14] Seifart M. Digitale Schaltungen.- Berlin, VEB Verlag Technik, 1986, s. 560.
- [15] Seitz M. Speicherprogrammierbare Steuerungen für die Fabrik- und Prozessautomation.- Fachbuchverlag Leipzig im Carl Hanser Verlag, 3. Auflage, 2012, s. 277.
- [16] Speicherprogrammierbare Steuerungen. Teil 3: Programmiersprachen (IEC 61131-3:2003). Deutsche Fassung EN 61131-3:2003.
- [17] Tröster F. Steuerungs- und Regelungstechnik für Ingenieure.- Oldenburg Verlag München, 3. Auflage, s. 562.
- [18] Verteshev S.M., Konevtsov V.A., Poletaev I.A. Methods of Software Developing of Complex SDSDC // European Science and Technology: 4th International scientific conference. Germany, Munich 2013, p. 377-380.
- [19] Verteshev S.M., Konevtsov V.A., Poletaev I.A. Softwaremittel der Projektierung von Systemen der digitalen Steuerung // European Science and Technology: 5th International scientific conference. Germany, Munich 2013, Vol. I, p. 501-504.
- [20] Wellenreuter G., Zastrow D. Automatisierung mit SPS. Theorie und Praxis.- Vieweg + Teubner, 5. Auflage, 2011, s.870.

# **Fabrication of porous ceramics as clay/glass composite**

**Aleksandrs Korjamins, Liga Radina, Diana Bajare,**

*Riga Technical University, Department of Building Materials and Products*

*Address: Kalku 1, Riga, LV-1658, Latvia.*

**Abstract.** Nowadays porous ceramics are widely researched, becoming an increasingly marketable material in the world, mainly due to the wide possibilities of usage in different technical and technology industries. Porous ceramics are successfully used in the filtration and has a high potential of usage also in the production of heat insulation materials thus obtaining the material which combine high resistance that can compete with other heat insulation and constructive materials.

Article reports a study of porous ceramics, which are produced using foamglass pellets as melting fillers, despite the fact that these additives are not frequently used as filler in traditional ceramic materials. The basis of this method is mixing fire resistant material with hard and melting substance.

For the production of porous ceramics clay, hard filler, water and various sized foamglass pellets were used, thus allowing to determine optimal size of melting filler and thereby ensuring the necessary physical and mechanical properties of the obtained porous ceramic samples and required amount, size and division of pores. Compressive strength tests were performed, as well as density and water absorption of the samples was determined.

Obtained results of the study shows that ceramic materials, obtained within the research, have great potential of application for load-bearing constructions as constructive building materials, as well as insulation materials. Production of porous ceramics materials, where foamglass pellets are used as melting filler, allows to produce more effective ceramics, creating high added value for the final product.

**Keywords:** ecological materials, insulation material, porous ceramics, clay matrix.

## **I INTRODUCTION**

Clay science has emerged after a few millennia of clay use and a century-long accumulation of written information about clays and clay minerals. There are two main features that evoke interest in clays: (1) their common availability, and (2) their extraordinary properties. Clays and clay minerals represent the youngest members of the family of minerals in the Earth's crust, being formed from different parent rocks under variable conditions [1].

Clay allows us to obtain contemporary ceramics, which have more attractive properties compared to metals and polymers, making them useful for specific applications [2], thanks to which it is modern material which can be successfully used from materials of ceramics up to social life, construction and other traditional products of ceramics up to the present time miniature computers, television, cars, planes and spacecraft and other modern technique developments. Current general civilization progress is not conceivable without ceramics [3]. And current material science cannot be imagined without the porous ceramic.

Methods of porous ceramics production are widely studied regarding attaining filtrating ceramics, since this material can be successfully used for the purification of different liquids and gasiform products. Within this subclass, those information and research results allow to apply the knowledge to production of heat-insulation materials because ceramic heat-insulation materials, characterized by high priority, can also be obtained in several ways: using contents of monofraction raw materials, foam formation method, using burn-out additive method and forming of pores in a chemical way.

Within this research, burn-out additive method is used. The basis of this method is mixing fire-resistant material - clay with hard and melting substances – chamotte and foamglass pellets, which have not been used as filler in traditional ceramic materials till now.

There are numerous patents on foamglass pellet production dating back to the 1930s. Foamglass was originally manufactured from a specially formulated glass composition, using virgin glass only. Currently, there are number of foamglass production plants that are using up to 98% post-consumer waste glass in their production. The basic principle of foam glass manufacture is to generate a gas in glass at a

*ISSN 1691-5402*

*© Rezekne Higher Education Institution (Rēzeknes Augstskola), Rezekne 2015*

*DOI: <http://dx.doi.org/10.17770/etr2015vol1.201>*



temperature between 700°C to 900°C. The gas expands thus producing a structure of cells to form a porous body.

Advantages of foamglass are lower transport costs, wide availability. Also foamglass pellets are non-toxic [4].

This study allows us to use unusual filler for production of porous ceramics and compare the obtained results with the properties of the materials, where the traditional fillers were used.

For instance sawdust is traditionally burnable filler used for production of the porous ceramics. It is widely researched both in Latvia by obtaining samples with a strength of 10 MPa to 12 MPa in a density up to 1.5 g/cm<sup>3</sup>, by using 25 % woodchip and burning the clay in a 950 – 960 °C temperature [5]. The leading Russian scientific centers have developed porous clay ceramic, with compression strength up to 17 MPa [6]. Moreover, mentioned centre's research was conducted to develop a new ceramic based high efficiency heat insulation material with low volume mass of 200-500 kg/m<sup>3</sup> at a processing temperature of 840-960 °C. However, this material exhibited insufficient strength to be used in load-bearing walls [7]. In order to solve the ceramic material strength increase issue, it is being suggested to use e.g. nanotechnologies, thus forming ceramic solid matter nano-crystals. [8].

Besides, nanoscale ceramic powders offer the possibility of manufacturing dense ceramics at low sintering temperature [9].

## II MATERIALS AND METHODS

Carbonized clay with volume mass – 1600 kg/m<sup>3</sup> and humidity level of 24%, as well as ground chamotte and water were used for sample preparation, where the various sized foamglass pellets are used as melting filler.

The properties of foamglass pellets are given in Table 1 and the chemical structure of carbonized clay is shown in Table 2.

TABLE 1. PROPERTIES OF FOAMGLASS PELLETS

Designation	Grain size, mm	
	0-4	4-8
Bulk density, kg/m <sup>3</sup>	265	150
Volume density, kg/m <sup>3</sup>	270	270
Exploitation regime, °C	from -250 to +650	

TABLE 2. CHEMICAL COMPOSITION OF CLAY

Component	SiO <sub>2</sub>	Al <sub>2</sub> O <sub>3</sub>	Fe <sub>2</sub> O <sub>3</sub>	MgO	Na <sub>2</sub> O	MnO
Amount, %	49.5	13.04	5.14	3.68	0.63	0.071
Component	K <sub>2</sub> O	P <sub>2</sub> O <sub>5</sub>	TiO <sub>2</sub>	CaO	Cr <sub>2</sub> O <sub>3</sub>	SO <sub>3</sub>
Amount, %	3.64	0.138	0.757	8.69	0.008	0.05

Proportion of dry clay, chamotte and water used in present research varied, changing the amount of chamotte, as well as changing the grain size and amount of foamglass pellets in order to obtain the

porous ceramic samples with better mechanical properties.

When making porous ceramics using foamglass pellets as melting filler, components of dry mixture were dosed according to mass, where dried, milled clay was 38 – 69%, water – 25-37% but foamglass pellets 6-31%.

Mould at the size 5x5 cm for sides was used for preparation of the samples.

During the research great attention has been paid to the chemical and mineralogical composition of the carbonized clay, therefore quartz, which reduces the technological characteristics – complicates sintering process, reduces strength and, in certain cases, frost resistance of the samples, has been not used in production of porous ceramics. Quartz also worsens the plasticity of ceramic mass, but reduces the shrinkage of the samples after drying and burning.

Whereas CaO and MgO (see Table 2) existing in the clay composition promote sintering of ceramics mass and advancing formation of pores.

### Experimental procedure

In the beginning, clay was dried in the drying oven and ground in RETSCH PM 400 mill for 30 minutes in dry condition. All of the required components were dosed in the required amount and mixed in dry condition, gradually adding water till the sufficiently homogenous mixture for sample making is obtained.

Samples were dried using BINDER FED drying-case at 70°C temperature for 48 hours and afterwards burnt gradually increasing temperature. Within the range of temperature 0°C up to 150°C, samples were kept for 3 hours for the vaporization of excessive water, thus eliminating cracks in the porous ceramic samples. Temperature in the range from 150-800°C was increased with rate 5°C/min or 130 min in total to ensure that melting process of foamglass pellets is not too fast, but in the range from 800-1090°C - rate was 2°C/min or 145 min in total. At the maximal temperature 1090°C, samples were kept for 2 hours in order to completely burn all of them (see Fig.1). After burning samples were refrigerated for 48 hours by gradual decrease of temperature from 1090°C to 20°C.

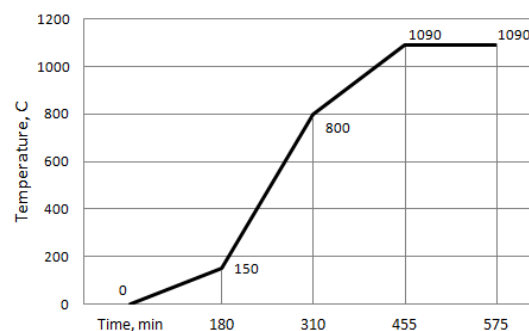


Fig. 1. Sample burning graph

Water absorption, volumetric mass, compressive strength, as well as an efficiency coefficient  $C_E$  has been defined for the obtained porous ceramic samples, using the following equation:

$$C_E = Rcs/\rho_{cs} \cdot 100$$

Where  $Rcs$  – Compressive strength, MPa.  
 $\rho_{cs}$  – Volume density,  $kg/m^3$

### III RESULTS AND DISCUSSION

The goal of this research is to obtain a porous ceramic materials with definite volume density and compressive strength characteristics, so achieving a material that could be used for load-bearing constructions as constructive building material, as well as insulation material.

To achieve the goal of the research, it was necessary to select the composition of formation mixture, drying and burning regimes, as well as determine the mechanical and structural parameters of ceramic samples, selecting the best possible composition of the drying/burning regimes and composition.

Volumetric mass of samples where foamglass pellets with grain size of 4-8 mm were used as the melting filler, varied from  $861.71 kg/m^3$ , if the amount of filler is 18%, to  $1178.34 kg/m^3$ , if the amount of filler is 6% (Fig. 2).

While the volumetric mass of samples where foamglass pellets with grain size of 0-4 mm were used, varied from  $1094.03 kg/m^3$ , if the amount of filler is 20%, to  $1472.01 kg/m^3$ , if the amount of filler is 35% (Fig. 2).

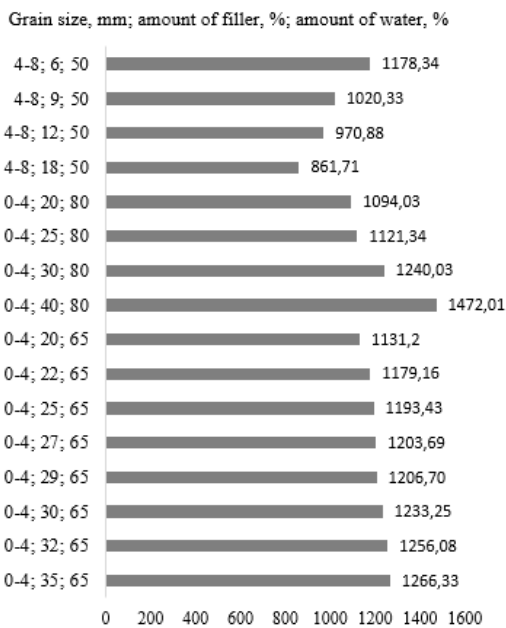


Fig. 2. Average volumetric mass of the samples with grain size of 0-4 mm and 4-8 mm

For the preparation of samples, using 0-4 mm foamglass pellets, the necessary water amount was higher (65-80% comparing to the amount of dried clay) in comparison to samples where the grain size of foamglass pellets was 4-8 mm, in order to ensure a better consistency of the mixture and increase the amount of melting filler.

Despite the fact, that samples, where the smaller filler (0-4 mm) was used, were with higher volume density, usage of smaller grain size made it possible to avoid the formation of cracks in the material after the drying and burning of samples.

Shrinkage of the samples was measured after their drying and after burning. For samples with foamglass grain size of 4-8 mm was from 2.22% up to 8.78%. Highest shrinkage was observed at the freater amount of filler.

Shrinkage of samples with foamglass grain size of 0-4 mm was from 3.27% up to 15.02%, increasing if the amount of filler is higher.

Shrinkage after the burning of samples, where the foamglass pellets with grain size of 4-8 mm were used, was from 3.33 to 11.56%, but for samples with foamglass grain size of 0-4% - 15.27-28.12%; in both cases the least shrinkage was observed for the samples smaller content of the melting filler.

Compressive strength was determined for all the samples, the resulting values for the samples with foamglass grain size of 4-8 mm can be seen in Fig.3, whereas resulting values for the samples with grain size of 0-4 mm are summarized in Fig.4.

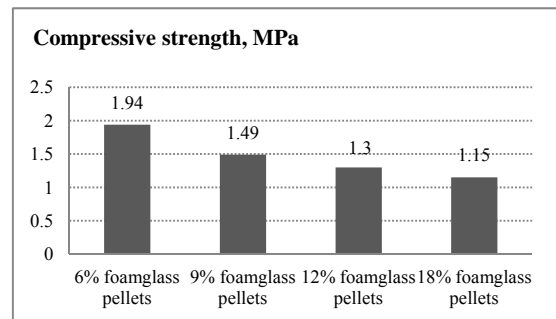


Fig. 3. Compressive strength of the samples, where the grain size of foamglass pellets is 4-8 mm

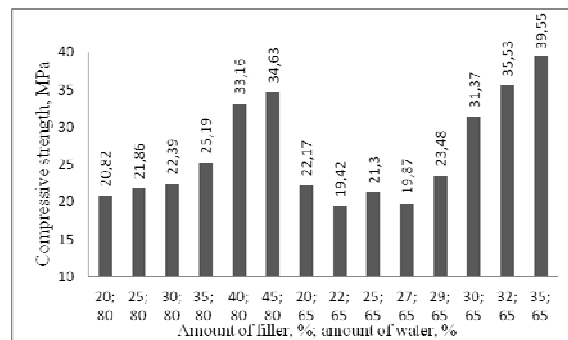


Fig. 4. Compressive strength of the samples, where the grain size of foamglass pellets is 0-4 mm

Greatest compressive strength – 39.55 MPa has been stated for the samples with 65% of water, where 35% of foamglass pellets with grain size of 0-4 mm were used as a melting filler. For the samples with the foamglass grain size of 0-4 mm and 80% water amount the greatest compressive strength, using 45% of filler, reached 34.63 MPa. Greatest compressive strength in both cases was observed for samples with highest content of foamglass pellets.

In samples where foamglass pellets with grain size 4-8 mm were used the compressive strength is in range from 1.15 MPa to 1.94 MPa by respective increase upon decreasing of the amount of melting filler.

Water absorption of the samples, where the grain size of melting filler is 0-4 mm or 4-8 mm was obtained during the research it is summarized in Table 3.

TABLE 3. WATER ABSORPTION OF THE SAMPLES

Grain size of filler, mm	Amount of filler, %	Amount of water, %	Water absorption, %
4-8	6	50	10.21
4-8	9	50	9.55
4-8	12	50	9.11
4-8	18	50	8.33
0-4	20	80	6.52
0-4	25	80	4.53
0-4	30	80	3.51
0-4	40	80	2.70
0-4	20	65	6.78
0-4	22	65	5.71
0-4	25	65	5.70
0-4	27	65	4.53
0-4	29	65	4.48
0-4	30	65	4.09
0-4	32	65	3.72
0-4	35	65	2.65

Obtained data demonstrates that the greatest water absorption – 10.21% is for the samples with filler grain size of 4-8 mm and the amount of filler – 6%.

Water absorption of samples, where the grain size of filler is 0-4 mm varies from 2.65% for samples with 65% of water and 35% of filler to 6.78% for samples with 65% of water and 20% of foamglass pellets.

For grain size of 0-4 mm and 4-8 mm the greater water absorption is recognized for the samples with smaller content of the melting filler.

Efficiency (as a proportion between the compressive strength and volume density) has been defined (Table 4) for the obtained porous ceramic samples in order to better characterization of the interdependence of the material properties. Samples with the 4-8 mm foamglass pellets are 10.31 – 24.00 times less effective comparing to samples where the grain size of foamglass pellets is 0-4 mm, reaching from 0.13 – 0.16 of efficiency.

TABLE 4. EFFICIENCY OF THE SAMPLES

Grain size of filler, mm	Amount of filler, %	Amount of water, %	Volum. mass, kg/m <sup>3</sup>	Compr. strength, MPa	Efficiency,
4-8	6	50	1178.34	1.94	0.16
4-8	9	50	1020.33	1.49	0.15
4-8	12	50	970.88	1.30	0.14
4-8	18	50	861.71	1.15	0.13
0-4	20	80	1094.03	20.82	1.90
0-4	25	80	1121.34	21.86	1.95
0-4	30	80	1240.03	22.39	1.81
0-4	40	80	1472.01	33.16	2.25
0-4	20	65	1131.20	22.17	1.96
0-4	22	65	1179.16	19.42	1.65
0-4	25	65	1193.43	21.30	1.78
0-4	27	65	1203.69	19.87	1.65
0-4	29	65	1206.70	23.48	1.95
0-4	30	65	1233.25	31.37	2.54
0-4	32	65	1256.08	35.53	2.83
0-4	35	65	1266.33	39.55	3.12

Maximal efficiency of the samples is 3.12, if the amount of filler is 35% and the amount of water is 65%. It can be seen that highest efficiency is observed at greater amount of filler and lower amount of water.

Macropores and micropores can be seen within the structure of porous ceramic sample, where melting filler grain size was 0-4 mm. Pores, acquired by melting of foamglass pellets, have regular form and pores measuring 0.2 – 1.5mm as they are shown in Fig. 5.

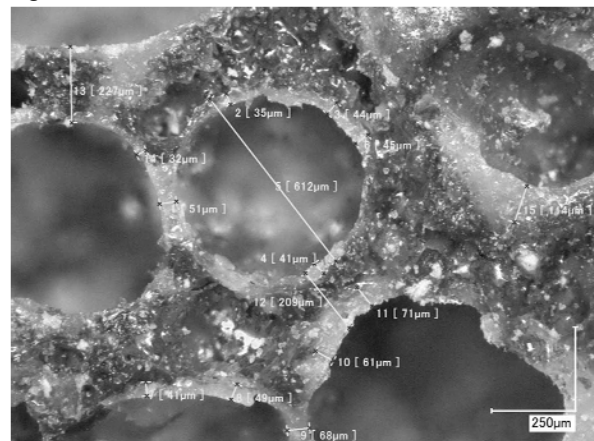


Fig. 5. Micrography of porous ceramic, where the grain size of melting filler was 0-4 mm.

It can be seen in micrography, that after the melting of foamglass pellets, 0.04 – 0.11 mm thick glass layer is formed around the pores, providing samples with higher compressive strength and lower water absorption.

### Discussion

During the research the acquisition of porous ceramics was practically demonstrated by using foamglass pellets with different grain size as the melting filler upon changing the amount of it and obtaining the material with various physical and mechanical features.

Volumetric mass of porous ceramic samples can be easily regulated by changing the amount and type of foamglass pellets, if the amount of water is kept at the same level, as well as changing the necessary amount of water. With the lower amount of water, plasticity of the mixture decreases and it is more difficult to get homogeneous mixture as well as to work it in the moulds, though besides the decrease of plasticity we must also consider the increase of compressive strength and efficiency, therefore recognition and acquisition of optimal proportion between the mentioned parameters plays essential role, thus ensuring the acquisition of optimal material.

Obtained results of the research testify that porous ceramics, obtained within this research, have a great potential of application for load-bearing constructions.

Decreasing of water absorption with increasing amount of melting filler – foamglass pellets in ceramics may be explained by decreasing permeability of the materials for water due to covering inner surface of voids by glass (Fig. 5). It means that the obtained material should improve the thermal insulation properties by saving breathing possibility.

In line with the conducted research, the addition of foamglass pellets as a melting filler improves the strength of the obtained samples, however, it reduces the temperature necessary for burning as well as the amount of clay required, thus enabling to save a natural resources through effective recycling of the glass waste.

With the use of mentioned porous ceramic production method, heat insulation elements of various forms (depends on moulds) and sizes may be obtained, controlling the size and amount of pores in the material.

The following investigation will be devoted to developing more effective material by controlling thermal conductivity properties.

### IV CONCLUSION

Within the research samples of porous ceramics were developed upon application of melting fillers with various grain size, stating the shrinkage (after the artificial drying and burning), volumetric mass, water absorption, compressive strength and efficiency (as a ratio between compressive strength and volumetric mass) of the acquired samples.

Following results were obtained for the samples, where the grain size of the melting filler was 4-8 mm: volumetric mass - 861.71 kg/m<sup>3</sup>, if the amount of filler is 18%, to 1178.34 kg/m<sup>3</sup>, if the amount of filler is

6%; shrinkage after drying - from 2.22% up to 8.78% and the highest shrinkage was recognized at the greater amount of filler; shrinkage after burning - from 3.33 to 11.56%, compressive strength – 1.15 to 1.94 MPa, water absorption – 8.33 – 10.21% and efficiency – 0.13-0.16.

While for the samples, where the grain size of the melting filler was 0-4 mm volumetric mass varied from 1094,03 kg/m<sup>3</sup>, if the amount of filler is 20%, to 1472,01 kg/m<sup>3</sup>, if the amount of filler is 35% , shrinkage after drying - from 3.27% up to 15.02%, increasing if the amount of filler is higher, shrinkage after burning - 15.27-28.12%; compressive strength – 19.42 MPa to 39,55 MPa, which has been stated for the samples with 65% of water, where 35% of foamglass pellets were used as a melting filler. For the samples with 80% water amount the greatest compressive strength, using 45% of filler, reached 34.63 MPa. Highest compressive strength in both cases was observed for samples with highest content of foamglass pellets. Water absorption of the samples - from 2.65% for samples with 65% of water and 35% of filler to 6.78% for samples with 65% of water and 20% of foamglass pellets. Efficiency – 1.65 – 3.12%, where greatest efficiency is observed at greater amount of filler and lower amount of water.

By comparing the features of the obtained materials we can see that samples, where the grain size of melting filler is 0-4 mm have better compressive strength, efficiency and water absorption indicators, but samples, where the grain size of filler is 4-8 mm – lower volumetric mass. It can be seen, that, despite the decrease of the mixture plasticity, the usage of smaller amount of water – 65% instead of 80%, guarantees better properties of the material, as well as reduces the amount of melting filler, which we can use, therefore for the acquisition of necessary features of the material, in the following researches it is essential to find the optimal amount of filler and water.

Production of porous ceramics materials where foamglass pellets are used as the melting filler, allows us to create more effective ceramics, using waste glass and creating high added value for the final product.

### V ACKNOWLEDGMENTS

The financial support of the Latvian Council of Science, project Nr.12.0412 is acknowledged.

### VI REFERENCES

- [1] F. Bergaya, B.K.G. Theng, G. Lagaly, *Handbook of clay science*. Amsterdam, The Netherlands: Elsevier Academic Press, 2006, p. 19.
- [2] G. Sedmale, *Keramika. Ķīmija un tehnoloģija*. Rīga, RTU izdevniecība, 2010, pp. 224-225.
- [3] S. El-Haggar, *Sustainable industrial design and waste management*. Burlington, MA: Elsevier Academic Press, 2007, pp. 175-177.
- [4] D. Munz, T. Fett, *Ceramics. Mechanical Properties, Failure Behaviour, Materials Selection*. Springer – Verlag Berlin Heidelberg New York, 1999, pp. 1-2.

- [5] G. Sedmale, A. Cimmers, .U. Sedmalis, *Charasteristics of illite clay and compositions for porous building ceramics production*. Instiute of Silicate Materials, Riga Technical University, Chemine Technologija Vol. 2. 2009, p.51.
- [6] A. Salahov, L. Tagirov, R. SalahovaV. Parfenov, N. Ljadov, *Поры и прочностные характеристики строительных материалов*. Строительные материалы, Vol. 12. 2011, pp. 25-27.
- [7] М. Атамчан, *Технология получения теплоизоляционного материала на основе легкоплавких глин*. Строительные материалы, Vol. 8. 2009, pp.68-69.
- [8] A. Salahov, A. Livada, R. Salahova, *Нанотехнология – гарантия заданных свойств керамических материалов*. Строительные материалы, Vol 4. 2008, pp. 27-29. Vile M.A., Wieder R.K. and Novak M. Mobility of Pb in Sphagnum-derived peat. *Biochemistry* 45. 1999, pp. 35-52.
- [9] K. A. Khalil, *Advanced Sintering of Nano-Ceramic Materials*. Ceramic Materials – Progress in Modern Ceramics, InTech. 2012, p.66.

# Numerical simulation of the reconstruction bank-protection type grillage on canals and rivers of St. Petersburg

Vladimir Korovkin

*St. Petersburg State Polytechnical University, 195251, St. Petersburg, Russian Federation*

**Abstract.** Reconstruction of urban waterfronts in St. Petersburg, built in the beginning of the last century, is relevant. In the technical literature and departmental document each type of mooring hydraulic structure has its own method of calculation. Shown the practical implementation of engineering universal method of calculating berthing quays. The proposed generalized model piles in the soil, which under the action of horizontal load rotates as a rigid body and at the same time bends as a flexible rod. Kind of movement depends on the flexural rigidity of the piles and stiffness of the soil. The position of the elastic line of the pile depends on the nature of the upper sealing. The stiffness of soil from the entire cycle, the load on the piles is determined from the curve the load– displacement

**Keywords:** city quay, coefficient of soil stiffness, generalized model of the piles, low pile grillage, pile foundation.

## I INTRODUCTION

Embankments of the city St. Petersburg are many of kilometers designs in the form of pile foundation, built at the beginning of the last century. Restoration of the historic appearance of buildings and structures of the city requires the preservation and renovation of the specified type of finishing off the coast and canals.

Refinement calculation reconstruction bank protection in the form of low-pile raft foundation is the actual problem



Fig. 1. Winter Canal with a bridge hanging over him and Arch.

## II DESCRIPTION OF THE OBJECT OF STUDY

The object of study is the construction in the form of a low piles raft foundation in the ground. Figure 1 presented on the coast canal to St. Petersburg using shore protection structure in the form of low-pile raft foundation.

Arch of two bank protection combines two buildings – the Old Hermitage, built Y. Felten in 1771 – 1787, respectively, and the Hermitage Theatre, built by Giacomo Quarenghi in 1783–1787 years. City boardwalk, preserving the building is of rubble concrete grillage on wooden piles. Obviously, this is a beautiful architecture, but still associated in the public mind with the "Queen of Spades" and not so much of Pushkin as Tchaikovsky must be maintained forever.

In modern cities in a dense housing is becoming increasingly urgent problem of high-rise buildings, requiring load transfer to the deeper layers of soil base. A number of cities, including St. Petersburg, with its numerous channels, have complex conditions for the construction of modern buildings and urban waterfronts, due to the presence of a thick layer (15-20 m) of weak clay soils. It makes use of pile foundation.

Enhancing the relevance of this topic is due to the rapid growth of the number of storeys of buildings, including the installation of pile foundation. In relation to the city waterfront of St. Petersburg practical interest as the reconstruction of existing embankment rivers and canals so and the construction is of concrete grillage on piles.

### III THE AIM OF THE WORK

In the technical literature [1, 2, 3] and in the departmental normative documents [4, 5], each type of ports hydraulic structure has its own method of calculation. When translating the manual is based on a significant portion of the computers calculation is made on the terms and assumptions that were laid in the era of the lack of computers [6- 8].

To simplify the understanding of the mechanism of interaction of structural elements with the ground and maximize the use of computers was proposed in 2002, the engineering universal method of calculation, which can be applied to any structure mooring quay [9] and with utilization in the work [10,11].

The essence of the calculation is that any mooring quay consists of separate elements – joist of different stiffness from perfectly flexible (anchor rod) up to absolutely rigid ( rigid rigel).

Condition rod interaction with other elements of the mooring quay can be various. They include different types of supports and the subgrade. Specific combination of rods connected to each other as a condition of joint deformation of structural elements so and the structure itself whole, each of which has different forms of interaction between them. This approach unifies computational methods and thus eliminates the need of some simplifications adopted in exist in calculation.

For example, bolverk is a system from fixed by a flexible rod and of two vertical rods.

Wall – a balk of finite stiffness, with the top support and in the lower part, respectively – in the ground. Anchor rod – flexible rod which leans on the sandy soil. Anchor wall – balk finite stiffness, which is located in a homogeneous or inhomogeneous ground.

The purpose of this paper is the practical implementation of engineering universal method of calculation of mooring quays in relation to the urban waterfront as a low pile raft foundation so and the possibility of using the method in the pile foundations of the high-rise buildings. Assesses the impact of the assumptions used in the departmental document.

### IV REVIEW OF THE LITERATURE

N. Gersevanov first gave a general solution to the problem of calculating pile of the embankments grillage type, treating them as a frame on the racks with fixed sealing up (1913). He received three canonical equations of method deformation, taking the unknowns displacement vertical, horizontal and rotate of the structure. The solution of the equations allowed us to obtain all forces in the piles.

Russian scientists B. Lozovskiy, F. Dimentberg, V. Khristophorov et al. proposed graphics solutions. Methods of calculation, developed N. Vyunshem, C. Nekkentvedom are special cases of solutions N. Gersevanov. These decisions involve the transfer

of the coordinate in the elastic center, which reduced the number of canonical equations of deformation.

V. Skuratov and N. Shaposhnikov offered calculation flexible pile grillage. Pile design with an elastic fastening regarded as an ordinary multi-span frame with elastic supports, in which each node has an independent vertical displacement and rotation, and also are common to all nodes of the frame horizontal movement.

Approximate methods of calculating these structures proposed by V. Skuratov, F. Dimentbergom, N. Smorodinskii, S. Antonov and others used before the advent of computers. In order to simplify the calculations used different assumptions, which do not give a correct picture of the construction work and creates significant errors in the effort elements.

The author of this article proposed an approximate calculation of a pile structures irrespective of the hardness of the top structure, the development of ideas N. Smorodinskii (1949).The calculation uses the method of separation of design elements and their subsequent gluing and the superposition of loads..

Method N. Gersevanov in relation to low grillage used in regulatory guidance on the design of pile foundations and as adopted by the coefficient of subgrade serves the secondary purpose for finding the estimated depth of seal piles [12].

In recent years, associated with the calculation of pilegrillage, typically use a classic design scheme [13]. Works of foreign scientists, devoted to the calculation of piled embankments [14 – 17].

Significant progress has been made in recent years in methods of calculation, design and construction of pile foundations. New or improved methods of analysis and design of pile foundations designed, based on extensive experience with the use of piles in various soil conditions. Method of calculation of pile foundations under the first and second limiting conditions has important theoretical and practical importance.

Work in the field of soil mechanics scientists B. Berezantseva, M. Goldstein, M. Gorbunov-Posadowa, B. Dolmatova, N. Tsytoovich and many others provided a basis for improvement of the methods of calculation of piles. Systematization of research results and improvement of methods of calculation of piles foundations performed V. A. Barbashov, A. A. Bartholomay , G. I. Glushkov, V. N. Golubkov, A. A. Meadows, etc.

However, in many cases, the projects pile foundations are with large stock, reducing the economic efficiency of the use of piles, indicating the need for further improvement of methods of their calculation.

### V THE MECHANISM OF PILE FOUNDATION WITH GROUND

The author proposed a generic model of the behavior of piles in the ground. Pile under horizontal load action rotates as a rigid balk and simultaneously bends

as a flexible rod. The offset of the top of the pile is the sum of:

$$\Delta = \Delta_1 + \Delta_2 \quad (1)$$

where  $\Delta_1$  is the displacement of the piles from turning;  $\Delta_2$  – displacement piles from bending. The amount of movement depends on the ratio of flexural stiffness of the piles and deformation characteristics of the soil (stiffness) (Fig. 2, a). Experiments A. H. Zarkhi (1954), shows which increase the flexibility of the wall causes an increase in jet pressure of the soil in the upper layers, more passive pressure (Fig. 2, b).

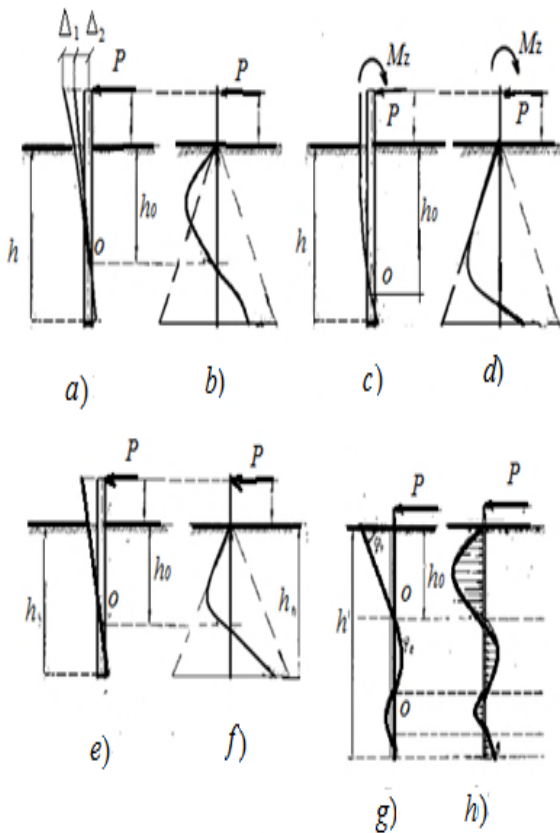


Fig. 2. Generalized model of behavior of the piles in the ground. a, b) The position of the elastic line and curve of earth pressure on the pile of finite stiffness from the force P; c, d) Also from the force P and moment Mz; e, f) Too from force P in a rigid piles; g, h) Too from the force P in a flexible piles.

The rigel creates in the piles bending moment in the sealing. The position of the piles in the depends on the stiffness of the beams, piles and soil. (Fig. 1c). For example, short rigid piles, embedded in the ground can be displaced parallel to the axis under the action of horizontal load. In another case, they are rotated relative to the zero point changing the sign of the plot of pressure on the pile. (Fig. 2 (d)).

If you change the bending stiffness of the piles in the limit  $\infty > EI > 0$  and consequently – the stiffness of soil from  $0 < K_{xy} < \infty$  behavior of piles in the soil

varies from rigid (Fig. 2, e, f) to flexible piles (Fig. 2, g, h).

In the interests of practical range rigidity of the rigel, piles and the soil there are a large number of options that have different meanings efforts in piles. In the interests of practical range rigidity of the rigel, piles and the soil there are a large number of options that have different meanings efforts in piles.

Classic calculation of piles constructions of the N. Gersevanov, using rigid fixation of the piles in the ground without regard to its stiffness, can be viewed as a individual case, when  $K_{x,y} = \infty$  in the sealing,

Experimental studies show that from the action of the horizontal force is short piles rotates as a rigid body with respect to the zero point  $h_0$  of rotation. Distance  $h_0$  from this point to the surface is about 0,7 h (Fig. 2, e). Flexible piles gets wavy bending, and the first zero point for approaching them to the surface (Fig. 2, g). Hard short piles considered in relation to the depth of driving h to the diameter d of up to 10 - 12. Flexible long piles considered respectively with a ratio of more than 10 [18].

Analysis and generalization of results of experimental studies allowed to develop and propose to use in practice engineering calculation method of pile foundation, reflecting the basic laws of their interaction with the soil foundation established of the empirically [19].

## VI SOLUTION OF THE PROBLEM

Pile grillage can be viewed as a system of a finite number different rods, which linked as joint deformations of structural elements so and deformations the structure as a whole.

Rigel – the rigid balk, which leans on the pile foundation. This balk loaded as external loads, so and internal forces from impact of the pile foundation.

Pile foundation is a system of balks of different rigidity, rigidly fixed embedded in the rigel, and immersed in the soil foundation. Settlement scheme uses of the frame construction with different stiffness crossbar and uprights. The nature of the work structures in the soil is determined by the stiffness characteristics of the rigel, uprights and ground. Additionally taken into account the beneficial effect of between the pile space, which is ignored in the standard method of calculation..

*Deformation characteristics of soil.* In port hydraulic engineering calculations of constructions interacting with the ground, early was performed only with regard to the first limiting condition. Experiments have shown that not accounting for the deformation characteristics of the soil when you interact with it design distorts the calculation scheme structures.

The software system using continuum model more accurately reflects the actual behavior of the soil under load. However, they are not sufficiently adapted to the calculation of berthing waterworks, due to not taking into account many factors in their work. In the prac-



tice the calculation of berthing waterworks are use over a simple model Fuss-Winkler using coefficient of subgrade resistance.

Theory analysis of structures lying on the ground with a deformed one and two coefficients of subgrade resistance was developed in the works of A. Dinnik, P. Pasternak, A. Krylov, N. Snitko, V. Vlasov and many others. Among foreign scientists engaged in this task H. Westergaard, H. Bufler, H. Lieb, G. Meier [20], Y. Cheung, O. Zienkiewicz [21], C. Desai, J. Christian [22] and others.

Using in calculations a variable coefficient of subgrade resistance (soil stiffness coefficient) better reflects the operation of the foundation. It is sufficient to choose the law of variation coefficient of subgrade resistance, which provides the desired character of rainfall. However, there are some difficulties, because for this purpose it is necessary to solve the problem in the theory of elasticity. Then select the desired ratio, that makes no sense. The coefficient of stiffness are devoted studies of B. Kositsin (1963), V. Lishak (1964), S. Rivkin (1969), V. Fedorovsk (2000) and others.

Using the program «CROSS» successive approximation procedure applied to foundations can more accurately determine the stiffness coefficient of soil [23]. «CROSS» program is part of the package SCAD Office and provides independent work, and the exchange of data with the integrated strength analysis of structures Structure CAD (SCAD) [24]. The above procedure of successive approximations, in our opinion, is acceptable at low loads to the foundation. Since there is no law changes the stiffness of soil from the full load cycle and is not considered a redistribution of the contact pressure from the edge of the plasticity region.

Author represented the mechanical model of the combined stiffness of the soil (subgrade resistance) for pile foundation. The model has the elastic body Hooke (H) and of the plastic body of the Saint-Venant (SV), besides include structural element (S), which taking of the different degrees of hardening or softening the soil. The model on Fig. 3, what similarly the model adopted for the foundation [25].

Quantity springs in the model are located on a lateral surface of the pile. The number of turns of the springs depends on the depth of the active zone of the soil (Fig. 3,a). The spring resists compression more or less of elastic, when a small external loads. The load increases to the limiting value and changes of the value resistance to compression of springs due from the structural element (S). This leads to a nonlinear plot reactive pressure of the soil. The nature of changes in the relative deformation characteristics of the resistance of the soil on the pile from the load shown in Fig. 3, b.

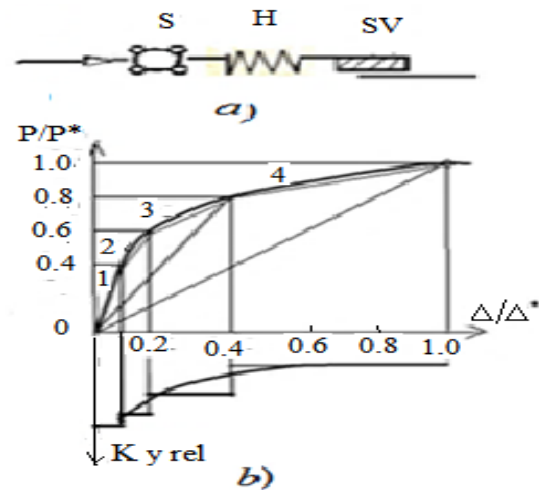


Fig. 3. a) Mechanical model of the combined stiffness of soil, taking into account the structural element. b) Schedule changes in the relative stiffness from the dimensionless curve deformation.

Piles divide the height by the number of plots. Each plot corresponds of the interval on the relative curve deformation depending on the load (Fig. 3 b, top). In the Interval of the curve determines the relative stiffness of the soil  $K_{u,rel}$  (Fig. 3 b, bottom).

Values of force  $P$  and deformation piles  $\Delta$  allow you to find the coefficient of stiffness of the soil depending on the load.

**Example.** To calculate the reconstructed waterfront on the canal Griboyedov in St. Petersburg.

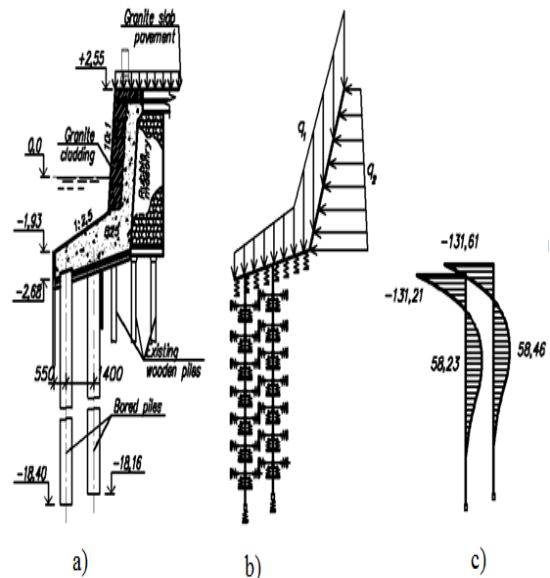


Fig. 4. a) Cross-section of piles grillage. b) Design scheme. c) Bending moment of the diagram in piles.

**Initial data.** The old quay in the form of hard rubble concrete masonry grillage rests on three rows of wooden piles. The new hard grillage with variable cross-section of reinforced concrete on the pile foun-

dition of two rows of 0.6 m diameter bored piles. Step across the line cordon of piles 2.35 m, respectively, and along the cordon 1.4 m.

The strength characteristics of soils are shown in Fig. 3 and the deformation characteristics respectively, taken from [11]. In calculating the existing wooden piles in a margin of safety facilities not taken into account. Results of the comparison of calculations are given in table 1.

Table 1.  
Results of calculations<sup>1</sup>

Name	Calculati for a SNP [11].	Calcula- tion for a generic method	Program " Plaxis"
Bending moment in the topic sealing of the first piles, [kNm]	-135.23	-131.21	-129.43
Bending moment at the topic sealing of the second pile, [kNm]	-135.23	-131.61	-129.50
Bending moment in the span of the first pile, [kNm]	-	58.23	51.54
Bending moment in the span of the second pile, [kNm]	-	58.46	51.9
The effort in the first pile, [kN]	-470.0	-417.92	- 410.34
The effort in the second pile, [kN]	64.16	12.02	9.08
Horizontal displacement of the top, [mm]	-	4.87	6.16

1.The calculation was performed by student A. Melentev.

## VII ANALYSIS OF THE CALCULATION RESULTS

Stiffness of characteristics soil, interacting with the piles, and increased flexural rigidity of the piles changed the designs scheme, featured SNP [11]. In particular the moment of fix the bottom of the piles is not apparent. Efforts in piles obtained as in the generic method, using SCAD, so and in Plaxis, were less than in the calculation of the SNP. This had resulted from accounting stiffness characteristics of the soil, interacting with piles.

Comparative calculations of the promenade with various values of the stiffness characteristics of the soil, shows that in the case of flexible piles and dense soil settlement efforts more or less comparable with the calculation SNP 2.02.03-85. In other conditions

the computational scheme used in the normative document may not be manifest that, as shown by calculations using the deformation characteristics of the soil, leads to distortion of the forces in piles.

## VIII CONCLUSIONS

1. In the current technical literature and regulations, each type of port hydraulic engineering has its own method of calculation. In first N. Gersevanov was given a general solution to the problem of calculation grillage type of the pile embankments. Treating them as a frame construction with absolutely rigid grillage on racks with rigid bottom seal.
2. Shows the mechanical model of coefficient soil stiffness based on structural element.
3. Shows the method of determining the stiffness of the soil from load on the curve deformation..
4. Shows the practical implementation of the proposed above engineering universal calculation method berthing quays in the low of pile grillage, using the program SCAD. In calculating the deformation characteristics used in the form of horizontal and vertical coefficients stiffness of the soil.
5. Comparative calculations of the promenade with various values of the stiffness characteristics of the soil, shows that in the case of flexible piles and dense soil settlement efforts more or less comparable with the calculation SNP 2.02.03-85. In other conditions the computational scheme used in the normative document may not be manifest that, as shown by calculations using the deformation characteristics of the soil, leads to distortion of the forces in piles.
6. When calculating the structures using a model coefficient bed, special attention should be paid to the reliability of the characteristics of the soil on which depend essentially on efforts and deformation in structural elements. Meanwhile, their values recommended in Rules, have a fairly wide range of values and require adjustments.

## IX REFERENCES

- [1] G.N. Smirnov, V.V. Aristarkhov, S.N. Levichev, A.G. Sidorov, E.A. Korchagin. Ports and port facilities. Ed. DIA, Moscow, 2003, 463 p.
- [2] P.I. Yakovlev, A.P. Tyurin, Y.A. Fortucel. Port hydraulic structures. Ed. Transport, Moscow, 1990320 p.
- [3] P.P. Kulmach, V. Filippenok, N.G. Zaritovskiy. Marine hydraulic structures. Ch. II, Mooring, offshore and shore protection structures. LVVISU, Leningrad, 1991, 391 p
- [4] Design of the mooring quays, CH-RF 54.1-85 MRF RSFSR, Moscow, 1991, 247 p.
- [5] Instruction on designing marine berthing and shore protection structures. RD 31.31.55.93, MMF, Moscow,1996.
- [6] PLAXIS. Plaxis v. 8.2. Finite Element Code for soil and rock analyses. Netherlands, 2002.
- [7] Program GEO5 for design and analysis of retaining. Armagrandi and gravitational structures. Certificate of conformity No ROSS CZ.SP.N, Moscow, 2012.

- [8] Program Cluster, version 1, Engineering and consulting centre for Foundation. Moscow, 2005.
- [9] V. S. Korovkin. Universal method of calculating berthing quays. The first scientific-practical conference Sea and river ports of Russia, Moscow, 2002, 103-105 pp.
- [10] T. Dang, V. Korovkin. Engineering kinematic theory of ground contact pressure in the annexto the hydraulic port facilities. *Advanced Materials Research*, Vols. 945-949, 2014, pp. 541-548.
- [11] A. Melentev, V. Korovkin. Calculation of Retaining Walls with Anchoring at Different Levels. *Applied Mechanics and Materials*, 725-726, 2015, pp. 185-189.
- [12] SP 24.13330.2011. Pile foundations. The updated version of SNP 2.02.03-85. Moscow, 2011.
- [13] A.Y. Budin. City and harbourquays Ed. Polytechnic, St. Petersburg, 2014, 418 p.
- [14] CUR-publication 166. Damwand constructies. | ISBN 90 376 063 8 | CUR, Gouda, the Netherlands, 4th issue, 2005.
- [15] J. Grabe. Sheet Piling Handbook Design. Thyssen Krupp GfT, Bautechnik GmbH HSP HOESCH Spundwandand Profil GmbH, Hamburg, 2008.
- [16] Design Manual. Steel Sheet Piling United States. Steel Updated and reprinted by U. S. Department of Transportation. FHWA with permission, 1984.
- [17] A Handbook of Quay Walls. CURCentre for Civil Engineering Research, Havenbedrijf Rotterdam NV, Gemeentewerken Rotterdam. Published by Taylor & Francis, the Netherlands ISBN: 978-0-415-36439-3, .2005.
- [18] N. K. Snitko. Static and dynamic pressure of the soil. Stroiizdat, Leningrad, 207, 1970.
- [19] V.S. Korovkin. Calculation exploited berthing facilities with regard to reologicheskikh properties of the base and the harsh climatic conditions of the continental shelf. Ed. SPbGPU, Sankt-Peterburg, 2013. 88 p.
- [20] H. Buffler, H. Lieb, G. Meier. Frictionless contact between an elastic stamp and elastic foundation. *Ing. Arch.*, Bd. 52, No.1/2, 1982.
- [21] Y.K. Cheung, O.C. Zienkiewicz. Plate and tank on elastic foundation. An application of finite element method *Intern. J. Solid structural*, vol. 1, No. 4, 1965.
- [22] C.S. Desai, J.T. Christian Numerical methods in geotechnical engineering. McGraw-Hill. Inc., 1977.
- [23] E. H. Krikunov, A. C. Perelmuter, M. A. Perelmuter, , A. I. Sementsov. Fedorov Century, CROSS-program for determining the coefficients of the bed *Magazine of foundation, foundations and soil mechanics*, 2002.
- [24] N. I. Vatin, U.P. Wash. Joint settlement building and shallow foundations in SCAD. Methodical instructions, St. Petersburg, 2007.
- [25] V. S. Korovkin Engineering kinematic theory, the contact pressure of the soil in the application to the calculation of certain types of foundations *Magazine of civil Engineering*, 6, 2013, 39-49p.

# The regions of parametric instability of brush-contact device electromagnetic circuit in unstable working conditions

O. I. Kozyreva, I. V. Plokhov, Y. N. Guraviev, I. E. Savraev, A. V. Ilyin  
Pskov State University, Electro mechanic Faculty.  
Address: Russian Federation, Pskov, Lenin square, 2

**Abstract.** The method to determine parametric instability regions of the electromagnetic circuit of the secluded brush contact of brush-contact device with using the oscillation equation Mathieu II order for a dissipative system with one degree of freedom is developed. Recommendations on the selection of the parameters of the external damping device to eliminate the instability of electromagnetic waves in unstable working conditions brush-contact device are given.

**Keywords:** brush-contact device, sliding electrical contact, zone of parametric instability, damping device.

## I INTRODUCTION

Energy turbine generators have a constructive unit, called brush-contact device (BCD) or subassembly of the sliding electrical contact (SSEC). Reliability of the turbine generator is determined, including, reliable operation of this device. On the brush are acting significant dynamic forces that lead to mechanical disturbances and interruption current [1, 2]. Also in the electrical circuits BCD arise electromagnetic resonance phenomena caused by the parametric modulation of the transition resistance and capacitance in the contact zone [3–6]. Described effect may cause increased brush-sparking, wear of contact parts, ring fire [7–10]. One of the important ways to reduce brush-sparking is the elimination of parametric resonance processes in electromagnetic circuits. To do this, we need to explore the regions of parametric instability of the oscillating system and to set appropriate limits on the functional parameters of the node [11–15]. We also will define characteristics of the external damping device to eliminate the instability of electromagnetic oscillations in unstable working conditions brush-contact device. These problems are important, since their decision will increase the reliability of BCD and of turbine generator as a whole.

In this paper the problem of constructing the regions of parametric instability of the electromagnetic vibrating system BCD of turbine

generator is solved analytically. Also, a technique of selecting the parameters for the brush-contact device test stand is shown.

## II MATERIALS AND METHODS

Complete replacement scheme SSEC of the turbine generator is shown in Figure 1.

In this scheme:

$L_{b1}, L_{b2}, \dots, L_{bn}; R_{b1}, R_{b2}, \dots, R_{bn}$  are the inductance and the electrical resistance of the secluded brush contact at the first slip ring;

$L'_{b1}, L'_{b2}, \dots, L'_{bn}; R'_{b1}, R'_{b2}, \dots, R'_{bn}$  are the inductance and the electrical resistance of the secluded brush contact at the second slip ring;

$C_{r1}, C_{r2}, \dots, C_{rn}; R_{r1}, R_{r2}, \dots, R_{rn}$  are the transition capacitance and the resistance of the secluded brush contact at the first slip ring (variables parameters);  
 $C'_{r1}, C'_{r2}, \dots, C'_{rn}; R'_{r1}, R'_{r2}, \dots, R'_{rn}$  are the transition capacitance and the resistance of the secluded brush contact at the second slip ring (variables parameters);

$L_{rv1}, R_{rv1}$  are the inductance and the electrical resistance of the rotor winding;

$L_{es}, R_{es}, E_{es}$  are the inductance, the electrical resistance and the electromotive force of energy supply of drive winding of the turbine generator;

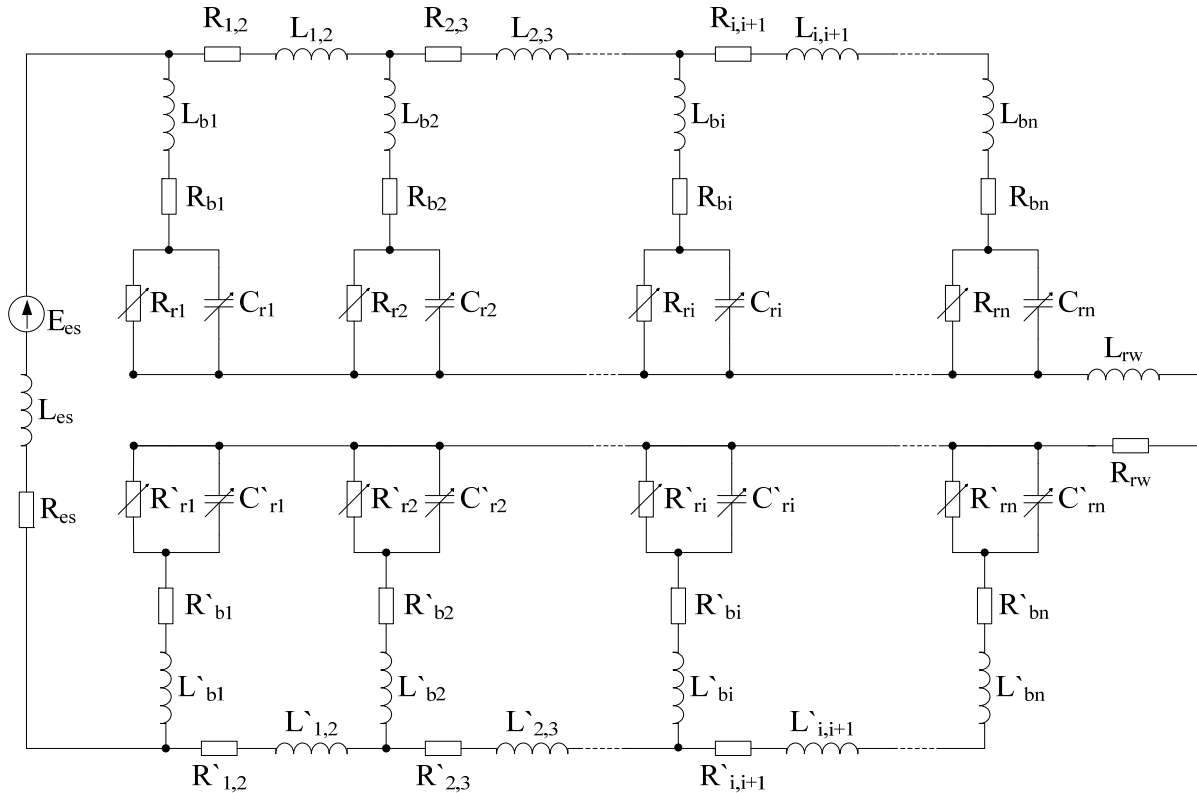


Fig. 1. The replacement scheme SSEC of the turbine generator.

$L_{1,2}, L_{2,3}, \dots, L_{i,i+1}; R_{1,2}, R_{2,3}, \dots, R_{i,i+1}$  are the inductance and the electrical resistance between the two secluded brush contacts at the first slip ring;  
 $L'_{1,2}, L'_{2,3}, \dots, L'_{i,i+1}; R'_{1,2}, R'_{2,3}, \dots, R'_{i,i+1}$  are the inductance and the electrical resistance between the two secluded brush contacts at the second slip ring;  
 $L'_{1,2}, L'_{2,3}, \dots, L'_{i,i+1}; R'_{1,2}, R'_{2,3}, \dots, R'_{i,i+1}$  – the inductance and the electrical resistance between the two secluded brush contacts at the second slip ring.

Consider the electrical processes in the electric circuit of the secluded brush contact. Equivalent circuit is shown in Figure 2.

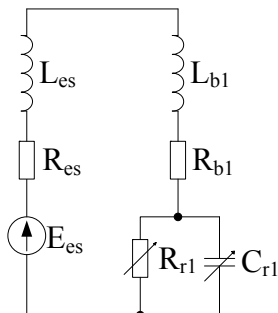


Fig. 2. Equivalent circuit of the secluded brush contact.

The operator expression for the electric resistance in this circuit is presented:

$$Z_1(p) = Lp + R + \frac{R_{r1}}{1 + R_{r1}C_{r1}p}$$

Then, the operator equation of the circuit is evident:

$$LR_{r1}C_{r1}p^2 + (L + RR_{r1}C_{r1})p + (R + R_{r1})I_1 = (1 + R_{r1}C_{r1}p)E_v$$

where

$$R = R_{b1} + R_{es}, L = L_{b1} + L_{es}$$

Linear differential equation II order with periodic coefficients is obtained by inverse Laplace transform. Voltage of winding excitation is given constant  $E_{es} = const$ :

$$I'' + \left( \frac{R}{L} + \frac{1}{R_{r1}C_{r1}} \right) I' + \left( \frac{1}{LC_{r1}} \right) \left( 1 + \frac{R}{R_{r1}} \right) I = \left( \frac{1}{LR_{r1}C_{r1}} \right) E_{es} \tag{1}$$

The research of the stability of the electromagnetic system, being described by the equation (1) is considered below.

The differential equation of the following form

$$A(t) \frac{d^2q}{dt^2} + B(t) \frac{dq}{dt} + C(t) = 0$$

generally describes the parametric vibrations of a linear system. The

coefficients in this equation are dependent on parameters, that characterize the properties of parametric action. For certain values of the parameters, the solution may be unstable. A set of points form in the space of parameters regions of dynamic instability [11, 16, 17]. If the variable parameters are frequency of periodic parametric action, then the most interesting is the frequency ratio, called parametric resonance [11–17].

In this variant, oscillating motions are external parameters impact on the system. Vibrations are transmitted to the brush from the contact surface of the rotating collector ring. They entail periodic oscillations of the resistance and the capacitance of transition layer of the sliding contact [3, 4, 9, 10]. If depth of modulation parameters of the transition layer is high, then the system may be in the region of parametric resonance (brush-sparking, ring fire).

To find the parametric resonances of the system, we will plot the boundary of instability, using oscillation equation Mathieu II order for a dissipative system with one degree of freedom [11].

Equation Mathieu has the form:

$$I'' + 2\varepsilon I' + \omega_0^2(1 + 2\mu \cos \omega t)I = 0 \quad (2)$$

Lead the equation (1) to the form of the Mathieu equation (2). Assign  $R = const, L = const$ . We assume that the transition capacitance  $C_{r1}$  and the transition resistance  $R_{r1}$  of the secluded brush contact vary harmonically with the frequency  $\omega$ , amplitude  $a_r, a_c$  and constant component  $R_0, C_0$  [3–5]:

$$R_{r1}(t) = R_0(1 \pm \varepsilon_R \cos \omega t);$$

$$C_{r1}(t) = C_0(1 \pm \varepsilon_C \cos \omega t),$$

where  $\varepsilon_R = a_R/R_0, \varepsilon_C = a_C/C_0$  are the parameters of the modulation depth  $\varepsilon_R, \varepsilon_C \ll 0$ .

Approximately find the coefficients for the Mathieu equation [11, 16, 17]:

$\omega_0$  is the natural frequency of electromagnetic oscillations in this circuit,

$$\omega_0^2 = \frac{1}{LC_0}(1 + R/R_0);$$

$\mu$  is the total modulation depth of the oscillating circuit (excitation coefficient),

$$2\mu = \varepsilon_C + \varepsilon_R \frac{R}{R + R_0};$$

$\varepsilon$  is the damping parameter of electromagnetic oscillations (dissipation),

$$2\varepsilon = \frac{R}{L} + \frac{1}{R_0 C_0};$$

$\omega$  is the frequency of parametric action (frequency of vibrations).

Plot the boundary of instability for the dissipative system on in the plane  $\mu, \eta = \omega/2\omega_0$ . For calculation boundaries of instability are taken the following formulas. For the first instability region (basic parametric resonance):

$$\omega \approx 2\omega_0 \sqrt{1 \pm \sqrt{\mu^2 - (v/\pi)^2}};$$

For the second instability region:

$$\omega \approx \omega_0 \sqrt{1 - \mu^2 \pm \sqrt{\mu^4 - (1 - \mu^2)(v/\pi)^2}},$$

where  $v = 2\pi\varepsilon/\omega_0$  – decrement of free oscillations.

### III RESULTS AND DISCUSSION

For calculations the parameters of the brush-contact device test stand are taken (Tables 1) [18–20].

Tables 1

The parameters of the test stand				
$R_{sv}, \Omega$	$L_{sv}, \text{mH}$	$R_{b1}, \text{m}\Omega$	$L_{b1}, \text{nH}$	$\varepsilon_R, \varepsilon_C$
1.3	0.3	0.8	75	0.5

Calculations for several values  $R_0, C_0$  are given in Tables 2:

Tables 2

Calculations data				
$C_0, \text{nF}$	$R_0, \Omega$	$\omega_0, \text{rad/s}$	$\varepsilon$	$v$
200	40	1.31E+05	5.21E+04	2.507
200	70	1.30E+05	3.79E+04	1.827
200	90	1.30E+05	3.00E+04	1.447
200	200	1.30E+05	1.47E+04	0.712

According to the calculations we plot graphs in Fig. 3

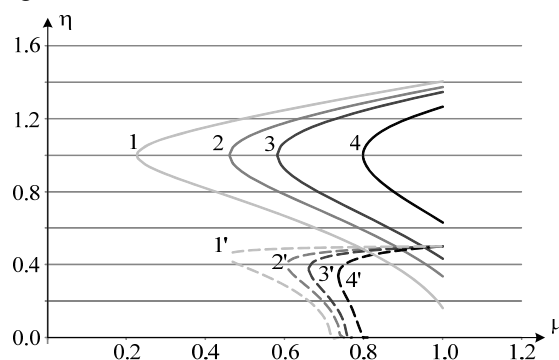


Fig. 3. The instability regions for equivalent circuit of the brush-contact device test stand:

1 and 1' are the boundaries of the first and the second instability regions,  $R_0 = 200 \Omega$ ; 2 and 2' are the boundaries of the first and the second instability regions,  $R_0 = 90 \Omega$ ; 3 and 3' are the boundaries of the first and the second instability regions,  $R_0 = 70 \Omega$ ; 4 and 4' are the boundaries of the first and the second instability regions,  $R_0 = 40 \Omega$ .

As can be seen from the graphs, the instability region appears at a sufficiently high resistance value  $R_0$ . With the growth of  $R_0$ , the boundaries of the instability regions shift toward lower values of the modulation.

A similar calculation for several values of the transition capacitance  $C_0$  shows that there is an inverse relationship: at the growth of  $C_0$ , the boundaries of the instability regions shift toward high values of the modulation.

Analysing the instability regions with value of the modulation factor calculated by the formula (4), we can see whether the processes of circuit stability.

Calculated modulation factor for the circuit  $\mu = 0.256$ . Thus, EM circuit gets into the region of parametric resonance when  $R_0 = 180\Omega$ , Fig 4.

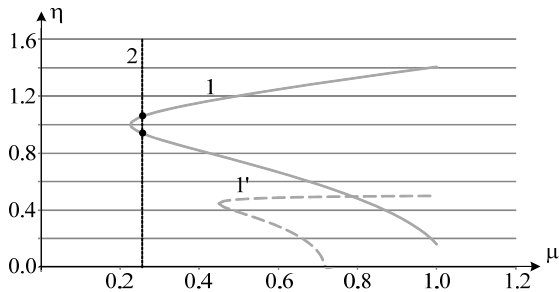


Fig. 4. The instability regions for the equivalent circuit of the brush-contact device test stand: 1 and 1\* are the boundaries of the first and the second instability regions,  $R_0 = 200\Omega$ ; 2 is the line  $\mu = 0.256$ .

According to Fig.4 define the values of the decrement of free oscillations  $\nu = 2\pi\varepsilon/\omega_0$ , in which the circuit will be unstable.

Tables 3

Values determined from Figure 4			
	$\eta$	$\omega$ , rad/s	f, kHz
start value	1.0577	2.74E+05	43.6
final value	0.9387	2.43E+05	38.69

So, if the frequency of external vibrations will be in the range from 43.6 kHz to 38.69 kHz investigated circuit will be unstable.

Thus, we have found the possible regions of parametric instability with the frequency of vibrations  $\omega$  for the electromagnetic circuit of secluded brush contact, for given values of the total modulation depth  $\mu$ , of the natural frequency of electromagnetic oscillations  $\omega_0$  and of the dissipation  $\varepsilon$ .

To exclude the parametric resonance should be avoided working condition in which mean values of transition capacitance and resistance of sliding contact exceeds allowed value.

Whenever it is impossible we propose the introduction in the electromagnetic circuit the external damping device [21]. Its main element is the additional capacitor installed between the working brush and the slip ring.

The equivalent circuit and the calculations of EM circuit with the additional capacitor for the secluded brush contact are presented.

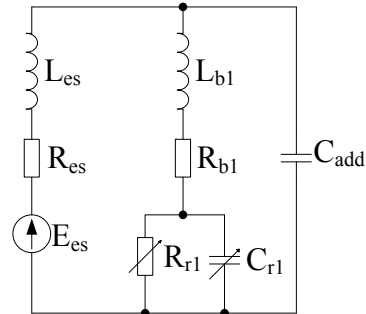


Fig. 5. The equivalent circuit of the secluded brush contact with the additional capacitor.

For this circuit the linear differential equation II order with periodic coefficients in the form of the Mathieu equation (2) is offered:

$$I'' + \left( \frac{R_{es}}{L_{es}} + 1/R_{r1} (C_{r1} + C_{add}) \right) I' + \left( 1/L_{es} (C_{r1} + C_{add}) \right) \left( 1 + R_{es}/R_{r1} \right) I = \left( 1/L_{es} R_{r1} (C_{r1} + C_{add}) \right) E_{es},$$

Where

$$R_{es} = R, L_{es} = L.$$

The coefficients for the Mathieu equation are evident:

$$\omega_0^2 = \frac{1}{L(C_{r1} + C_{add})} (1 + R_{es}/R_{r1});$$

$$2\varepsilon = \frac{R_{es}}{L_{es}} + \frac{1}{R_{r1} (C_{r1} + C_{add})}.$$

The parameters of the brush-contact device test stand with the additional capacitor  $C_{add}$  for the plot instability regions are given in Tables 1, 5 [18–20].

Tables 4

The parameters of test stand				
$R_{sv}, \Omega$	$L_{sv}, \text{mH}$	$R_{b1}, \text{m}\Omega$	$L_{b1}, \text{nH}$	$\varepsilon_R, \varepsilon_C$
1.3	0.3	0.8	75	0.5

According to the calculations we plot graphs in Fig. 5.

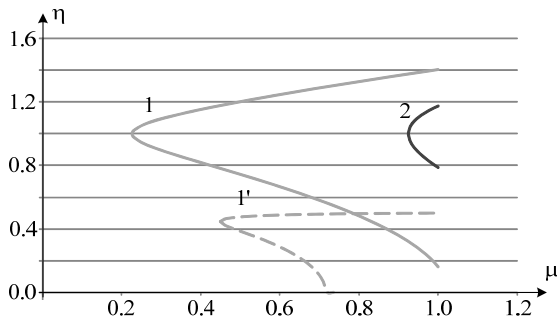


Fig. 5. The instability regions for the equivalent circuit of brush-contact device test stand with the additional capacitor: 1 and 1' are the boundaries of the first and the second instability regions,  $R_0 = 200 \Omega$ ; 2 is the boundary of the first instability region for the test stand with the additional capacitor  $C_{add}$ .

As can be seen from the graphs when we add the additional capacitor the boundary of instability region shifts toward higher values of the modulation.

Calculated modulation factor for the circuit  $\mu = 0.256$ . Thus, circuit with the additional capacitor is not gets into a region of parametric resonance. By increasing the value of additional capacitor, the instability regions completely disappear.

#### IV CONCLUSION

In electrical circuits brush-contact device arise electromagnetic resonance effects, which may cause increased brush-sparking and wear, as well as a ring fire. This occurs when the frequency of parametric mechanical modulation of the transition resistance and the transition capacitance of sliding contact coincides with natural oscillations of EM circuit of brush-contact device.

We have developed the method to determine parametric instability regions of the electromagnetic circuit of the secluded brush contact of brush-contact device, leaning upon the following parameters:

- the frequency of parametric action (frequency of modulation of parameters of transition layer)  $\omega$ ;
- the total modulation depth of the oscillating circuit of transition capacitance and resistance in the contact zone  $\mu$ ;
- the natural frequency of electromagnetic oscillations in circuit of the secluded brush contact,  $\omega_0$ ;
- the damping parameter of electromagnetic oscillations  $\varepsilon$ .

Recommendations on the selection of the parameters of the external damping device to

eliminate the instability of electromagnetic oscillations in unstable working conditions brush-contact device are given.

#### V REFERENCES

- [1] Механика скользящего контакта / В.И.Нэллин, Н.Я.Богатырев, Л.В.Ложкин и др. – М.:Транспорт. 1966.
- [2] Кончиц В.В., Мешков В.В., Мышкин В.В. Триботехника электрических контактов. Минск: Наука и техника. 1986.
- [3] Плохов И. В. Комплексная диагностика и прогнозирование технического состояния узлов скользящего токосъема турбогенераторов. Диссертация доктора технических наук. – СПб: СПбГПУ, 2001.
- [4] Плохов И. В. Модель динамики токопередачи через скользящий контакт // Электротехника. – М., 2005. – №2. – С. 28–33
- [5] Ильин А. В., Плохов И. В., Козырева О. И. Моделирование процессов электрофрикционного взаимодействия в узлах скользящего токосъема. // Научно-технический вестник Поволжья. – Казань: Научно-технический вестник Поволжья, 2013. – №4. – С. 166–173
- [6] Ильин А. В., Плохов И. В., Козырева О. И. Моделирование микрорельефа поверхностей контактирующих деталей. // Научно-технический вестник Поволжья. – Казань: Научно-технический вестник Поволжья, 2013. – №5. – С. 180–183
- [7] Holm P. Theory of the sparking during communication on dynames // IEEE Transactions on Power Apparatus and System. – 1962. – No. 63. – P. 588–590.
- [8] Хольм Р. Электрические контакты. – М.: Иностранная литература, 1961.
- [9] Greenwood J.A. Constriction resistance and the real area of contact. – British Journal off appl. Physics. 1966. V.17. P.1621-1631.
- [10] Yip F.C., Venart J.E.S. Surface topography effects in the estimation of thermal and electrical contact resistance. – In: Proc. Inst. Mech. Eng., 1968. V. 182. Pt. 3K. P. 81.
- [11] Вибрации в технике, т.1, М.: «Машиностроение», 1978 г., с. 121.
- [12] Мандельштам Л. И. Лекции по теории колебаний, М., 1972.
- [13] Мандельштам Л. И. Основы теории колебаний, 2 изд., М., 1988.
- [14] Рабинович М. И., Трубецков Д. И. Введение в теорию колебаний и волн, М., 1984.
- [15] Мэттьюс Дж., Уокер Р. Математические методы в физике. Пер. с англ., М., Атомиздат, 1972, 392 с.
- [16] Паровик Р.И. Диаграммы Стретта-Айнса для обобщенного уравнения матье. Вестник КРАУНЦ. Физ.-мат. науки. – 2012. – № 1(4). – С. 29-30 – ISSN 2079-6641.
- [17] McLachlan, N. W., Theory and Application of Mathieu Functions, Clarendon Press, Oxford, 1947.
- [18] Лившиц П.С. Справочник по щеткам электрических машин. М.:Энергоатомиздат. 1983.
- [19] Веселовский В. С. Угольные и графитовые конструкционные материалы, М., 1966.
- [20] Шулёпов С. В., Физика углеграфитовых материалов, М., 1972.
- [21] Устройство для уменьшения искрообразования в узле скользящего токосъема / Плохов И.В., Ильин А.В., Исаков А.Н., Козырева О.И. // Патент на полезную модель RU132630, опубл. 2013.09.20.



# Simulation Based Analysis of Digitally Controlled 4-phase DC-DC Converter with Coupled Inductors

Kaspars Kroics

Institute of Physical Energetics, Laboratory of Power electronics.  
Address: Aizkraukles street 21, Riga, Latvia, e-mail: kaselt@inbox.lv.

**Abstract.** Interleaved converters are used in many different conversion systems involving various topologies and are related to different fields of application due its advantages over single-phase converters. Such advantages include reduced current in switching devices and passive elements, reduced output current ripple, and so on. Reductions in size and costs of magnetic components and inductors current ripple can be achieved by an integration of magnetics. In this paper application of 2-phase coupled inductor designed in convenient way by using commercially manufactured coil formers and ferrite cores is analyzed to developed 4-phase interleaved DC-DC converter. Different structures of the coupled inductor for 4 phases is studied. The steady state phase and output current ripple in buck mode of the interleaving magnetic integrated bidirectional DC-DC converter is simulated. The necessary count of inductors for selected topology are manufactured and placed on the PCB board.

**Keywords:** DC-DC power converters, multiphase switching converters, integrated magnetic, bi-directional converter, digital control.

## I INTRODUCTION

Switching power converters have become more and more important in industry today. Interfacing the energy sources and storage devices such as fuel cells, batteries and supercapacitors requires several DC-DC conversion functions. In many applications such as photovoltaic arrays, fuel cells, wind generators high efficiency, small size DC-DC converter are required as an interface between the voltage source and the output loads, which operates at different voltage level.

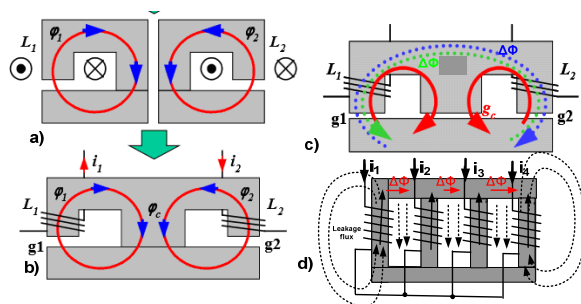


Fig. 1. Magnetic integration principle: a) single inductors; b) paralleled cores sharing a part of the core; c) increasing the coupling with gap in the central leg; d) multiphase magnetic integration

Single phase DC-DC converters have limitations in high current applications due to the redundant power loss in inductor and high inductor ripple current. The

standard multiphase interleaved design avoids this problem because it achieves output current ripple cancelation. In the recent years energy transfer among phases by means of magnetic coupling has been used in multiphase converters [1-7]. Advantages of magnetic integration is improved dynamic behavior, size and losses of magnetic components and reduction of MOSFET stresses.

The geometric definition of the integrated cores can be done looking at the general principle of paralleling magnetic circuits (Fig. 1.). In Fig. 1a, two separate inductors with single gapped core is shown. The winding produces a magnetic flux through the magnetic circuit as shown by the arrows. In Fig. 1b, the cores of the inductors of different phases are split together, sharing a central leg. As magnetic resistance of the central leg is low, only a small part of magnetic flux goes through the other winding. If air gap in central leg is introduced (Fig. 1c) then AC component of flux ( $\Delta\Phi$ ) goes through second winding and acts like a transformer reducing per-phase current ripple. The central leg have lower flux level and therefore the size of magnetic component can be reduced. If interleaved converter has many phases (Fig. 1d) then output current ripple is eliminated by interleaving and small inductance is necessary therefore magnetic leg for DC magnetic flux can be removed.

Most of the prior scientific papers about coupling in multiphase converters is based on monolithic inter phase transformers similar to Fig. 1d. Such a transformer allows transferring energy among phases but for this transformer using of non standard cores is necessary. In this paper application of 2-phase coupled inductor designed in convenient way by using commercially manufactured coil formers and ferrite cores is analyzed to developed 4-phase interleaved DC-DC converter.

## II MULTIPHASE INTERLEAVED CONVERTER APPROACH

Interleaving control schemes are widely used in converter applications [8-12]. Merits of such control methods are reduction of input/output current and volume of the converter, increase in the processed power capacity of converters.

First look at the single phase converter. Current ripple of such a converter describes well known expression:

$$\Delta I_{one\_phase} = \frac{(1-D) \cdot V_{IN} DT}{L} \quad (1)$$

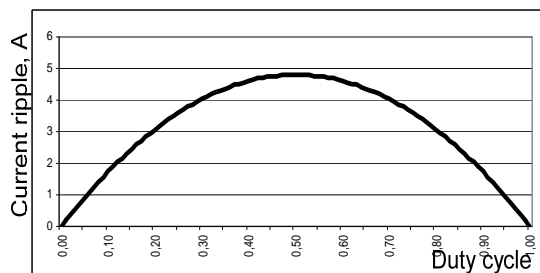


Fig. 2. Output current ripple of the single phase converter

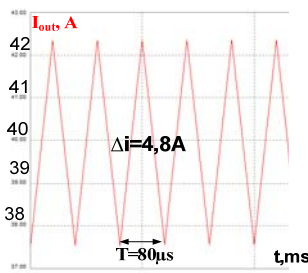


Fig. 3. Current of the single phase converter by D=0,5

By using of the Eq. 1 can be drawn curve shown in Fig. 2. Can be seen that maximum current ripple is when duty cycle is equal to 0,5. The particular curve is designed assuming that  $V_{IN}=120$  V,  $L=500$  μH and switching frequency of 12,5 kHz. Fig. 3 shows form of the current with maximum ripple by duty cycle equal to 0,5. These curves will be used further to

compare single phase solution with interleaved and interleaved with coupled inductor ones. The interleaving technique allows reducing of the output current ripple, reduction factor can be calculated as follows:

$$\frac{\Delta I_{multiphase}}{\Delta I_{one\_phase}} = \frac{N \cdot (D - \frac{m}{N}) \cdot (\frac{m+1}{N} - D)}{D \cdot (1-D)} \quad (2)$$

where D - duty cycle, N - number of phases and  $m=floor(N \cdot D)$  is the maximum integer that does not exceed  $N \cdot D$  [14].

By using of the Eq. 2 can be drawn curve for particular four phase case shown in Fig. 4. By splitting together curve represented in Fig. 2 in relative units and calculated by Eq. 2 can be obtained viewable picture (Fig. 5) that allows comparing how interleaving allows to reduce output current ripple.

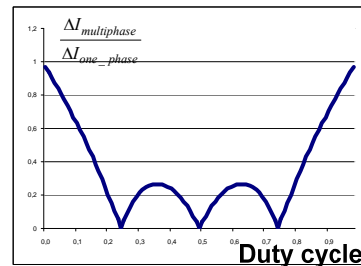


Fig. 4. Reduction factor of output current ripple of the four phase converter

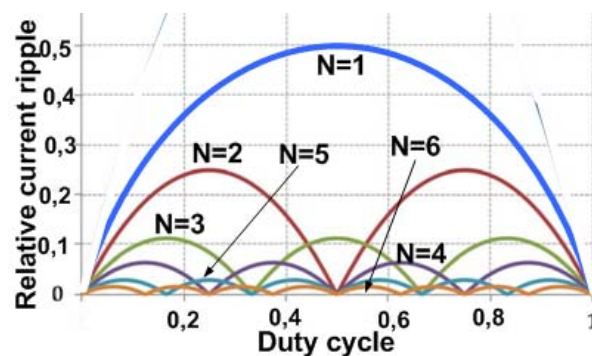


Fig. 5. Normalized output current ripple of the interleaved converter

Fig. 5 [13] shows the normalized output current ripple according to number of phases (N) and duty cycle. It shows that by using interleaved structure current ripple can be significantly reduced. As can be seen from Fig. 5 interleaving of four phases reduces output current ripples in wide range therefore 4 phase boost converter structure is selected. Multiphase interleaved approach employing phase-shifted pulse width modulation (PWM) to control MOSFETs, it is often used in designs where paralleling of

semiconductor devices is required. The phases are kept independent by using discrete inductors in each phase. Feature of the independent phase approach is the ability to turn-off the individual phases when the output power decreases, this allows maximization of the efficiency in each operating point.

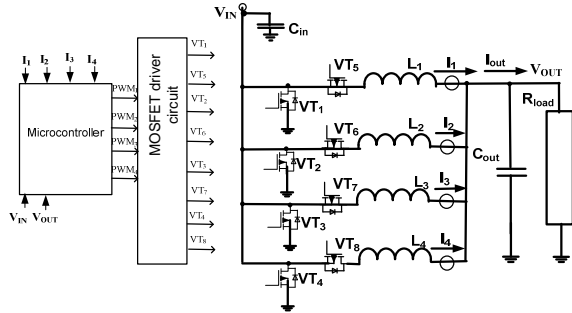


Fig. 6. The schematics of the interleaved DC-DC converter in buck mode with the uncoupled inductors

The prospective DC/DC converter will be provided for supercapacitor based energy storage system. Fig. 6 shows the structure of this bidirectional DC-DC converter. The transistors VT1 to VT8 is controlled by pulse width modulation. Each parallel pair of switches turns ON with shifting of 90 degrees. The switching frequency of the converter will be around 12,5 kHz. To control this DC/DC converter digital control will be used. Digital controllers of the previous era had bandwidth problems. In the recent years the situation has changed significantly. The speed and functionality performance of the microcontrollers has improved. They are also available at a much lower cost. The advantage of the digital controller is that it is programmable and offers more functionality to the system compared to the analog controllers. Novel control algorithms and methods with digital control can be realized. Such converter can be used for many other application, it can be modified as only buck or boost converter because synchronous rectification has better efficiency than diodes.

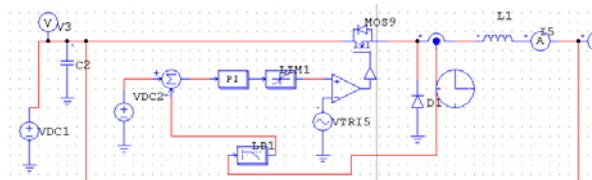


Fig. 7. The schematics of PSIM model for one phase of the interleaved DC-DC converter

For assessment of pulsation of current in for phase interleaved DC-DC converter PSIM model is used. Fig. 7. shows schematics of PSIM model for one phase of the converter. It consists of 120 V DC voltage source (VDC1), MOSFET transistor (MOS9), diode (D1), inductance  $L_1=0,5$  mH, PI regulator which regulates average phase current equal to 10 A.

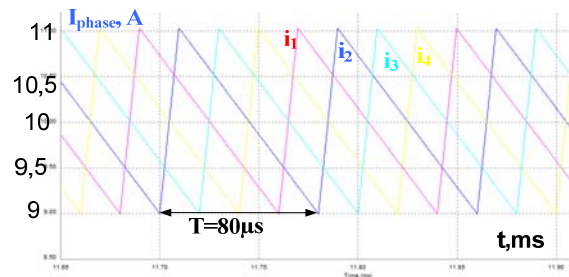


Fig. 8. Per-phase current in interleaved 4-phase DC-DC converter,  $D=0,125$

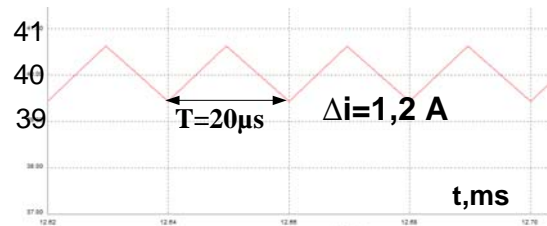


Fig. 9. Output current in interleaved 4-phase DC-DC converter,  $D=0,125$

Fig 8 and 9 shows results of the simulation by the duty cycle equal to 0,125 while then output current ripple is the biggest (Fig. 5). As can be seen from figures pulsation of phase current is more significant than pulsation of output current. Ripple of output current is reduced at least 4 times and is less than 3 percent of the output current. Whereas per-phase current ripple stays high, it can be described by expression as follows:

$$\Delta I_{phase\_uncoupled} = \frac{(V_{IN} - V_{out})DT}{L} = \frac{(1-D)V_{IN}DT}{L} \quad (3)$$

Eq. 3 matches with Eg.1 consequently Fig. 2 describes per-phase current ripple to. As follows from Fig. 2 the largest current ripple is when duty cycle is equal to 0,5. Let us examine this case more detail by mean of simulation.

As can be seen from Fig. 9 pulsation of phase current (4,8 A) is almost 50 percent of the total per-phase current (10 A) and is much more larger than pulsation of output current (1,2 A). So big current ripple leads to increased losses in inductor and MOSFET transistors therefore interleaved converter with coupled inductor is useful because the significant advantage of interleaved converter with coupled inductor is that the ripple in one winding can be dumped to another winding and per-phase current ripple can be reduced.

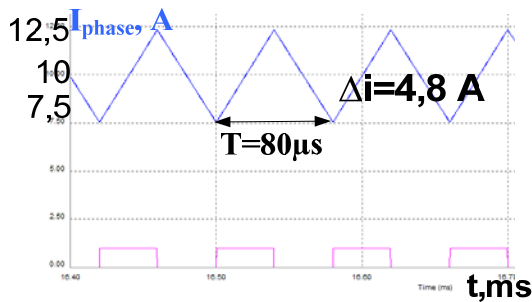


Fig. 9. Per-phase current in interleaved 4-phase DC-DC converter, D=0,5

### III PROPOSED COUPLED INDUCTOR

The interleaving structure has more inductors than the single phase converter. The two individual inductors of the two interleaving channels can be integrated on a single magnetic core to reduce component size, per phase current ripple. The structure of the proposed integrated inductor is shown in Fig. 10. The both windings of the inductors is built on the central leg of the E core. Although in literature [1] is proposed to place windings of the inductor on the wing legs thereby obtaining higher leakage inductance, it is not available commercially manufactured coil formers for such a case. In this paper proposed inductor can be wound on ETD coil former in a convenient way. Figure 11 shows practical implementation of the coupled inductor of two phases. Winding of the one phase (2) and winding of the second phase (3) are separated by isolating material (1) and are placed on the coil former (4). The winding machine (5) can be used to build such an inductor.

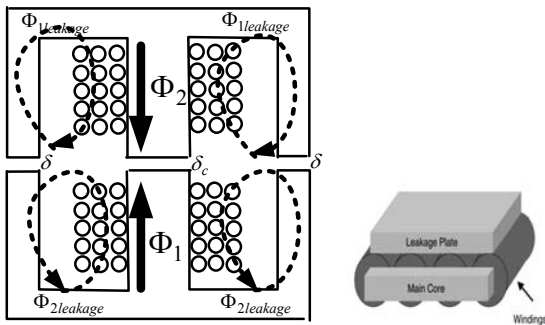


Fig. 10. Core structure of the coupled inductor and similar solution from [14]

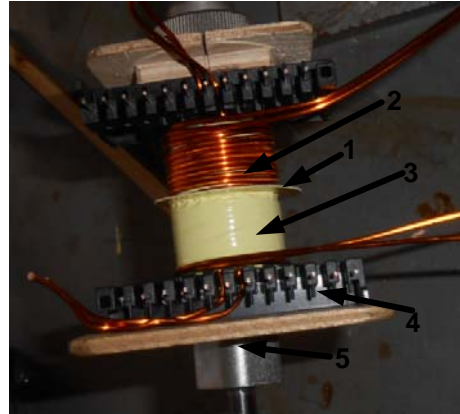


Fig. 11. Practical design of the coupled inductor

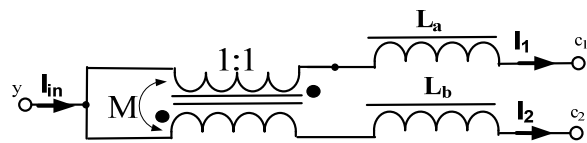


Fig. 12. Equivalent circuit of inversely coupled inductors

The equivalent circuit of a two-phase coupled inductor is shown in Fig. 12. The mutual inductance  $M$  represents the coupling between the two inductors. The voltages across the two inductors ( $v_{yc1}$ ,  $v_{yc2}$ ) are related to the currents through them ( $i_1$ ,  $i_2$ ) as follows:

$$v_{yc1} = (L_a + M) \frac{di_1}{dt} - M \frac{di_2}{dt}, \quad (4)$$

$$v_{yc2} = -M \frac{di_1}{dt} + (L_b + M) \frac{di_2}{dt}. \quad (5)$$

Assuming that both inductors have the same inductance  $L_a=L_b=L_{leakage}$ ,  $L=M+L_{leakage}$  and by rearranging the equations (4) and (5):

$$\frac{di_2}{dt} = \frac{v_{yc2}}{L} + \frac{M}{L} \frac{di_1}{dt} \quad (6)$$

As follows from equations 6 per phase current ripple of other phase affect first phase and in such a way current ripple of each phase can be reduced.

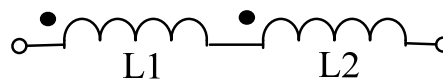


Fig. 13. Measuring of inductance

It is difficult to calculate precise value of inductance and coupling coefficient therefore easier is measure this values and change parameters of the inductor (air gaps, winding count) to achieve desired values. To measure coupling coefficient both

windings must be connect in series and measured total inductance of this connection (Fig. 13). This inductance can be expressed as follows.

$$L_{total} = L_1 + L_2 + 2M . \quad (7)$$

If both of inductances is equal ( $L_1=L_2=L$ ) then mutual inductance can be expressed as:

$$M = \frac{L_{total} - 2L}{2} . \quad (8)$$

Coupling coefficient is equal to:

$$k = \frac{M}{L} . \quad (9)$$

#### IV SIMULATION AND ANALYSIS

There are several implementation methods to build multiphase converter from two winding coupled inductor. The rule to generate a valid structure is that all the transformer lines must form at least a single line that includes all phases. Leakage inductance of all windings connected in the same phase can be considered as a single phase inductance that can help to filter the output voltage produced by the ideal transformer.

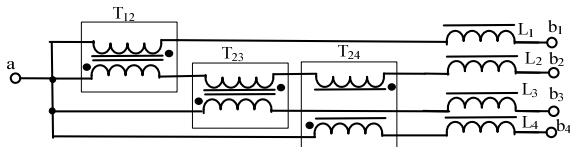


Fig. 14. Centralized structure of the coupled inductor for 4 phases

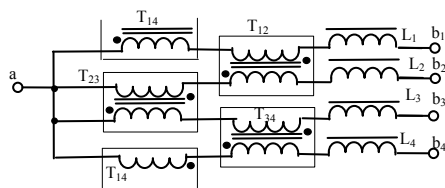


Fig. 15. Closed chain structure of the coupled inductor for 4 phases

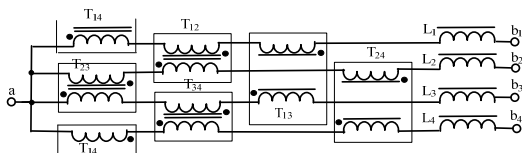


Fig. 16. Full matrix structure of the coupled inductor for 4 phases

Fig. 14, 15, 16 shows different structures to build 4-phase interleaved converter with coupled inductor. In design of the proposed structures important are the

number of transformers and volt-seconds applied to the transformer. The volt-seconds applied to the windings of the transformers reflects the way of transferring energy. If the energy is transferred more than once (centralized and closed chain structure), the higher the total losses of the transformer structure. From this point of view the best structure is full matrix but this structure needs more transformers therefore magnetic structure will be expensive with bigger volume. Centralized and closed chain structure have the same count of coupled inductors but centralized structure is not symmetrical so inductance of second phase will be larger and it leads to non symmetrical current in this phase therefore for closed chain structure is selected as most appropriate for particular case.

To assess the per-phase and output current ripple PSIM simulation of closed chain structure of coupled inductors with parameters equal to the developed inductor. In PSIM software is special element that simulates coupled inductor, they are connected in closed chain structure (Fig. 15) to simulate 4-phase interleaved DC-DC converter.

To view on integrated magnetic impression on current ripple reduction objectively magnetic flux must be taking in to account. As can be seen in Fig. 10 through ferrite core flows magnetic flux that is generated by the current difference  $i_1-i_2$  and DC component of current which creates leakage flux. Assuming the worst case when both currents of coupled inductor is in opposite phase then  $i_1-i_2=2\Delta I_1$ . Taking this into account can be written equation for flux density B:

$$B = \frac{L(1-k) \cdot I_{IN-DC} / 4}{NA_c} + \frac{2\Delta I_1 L}{NA_c} , \quad (10)$$

where N - number of turns;  $A_c$  - core cross sectional area.

As can be seen from Eq. 10 flux density through core can be significantly reduced if coupling coefficient is equal to 1, but increasing of coupling coefficient leads to the significant current ripple of output current therefore must be find some compromise between current ripple and flux density.

As for the core materials ferrite is used maximum flux density is set to 0,35 T. If separate inductors is used then 5mm air gap it is necessary to avoid saturation, by winding count 50 and the inductance is equal to 500 uH. If  $k=1$  then  $M=L=5,6$  mH, very small air gap is necessary but additional inductor is required to stay in the continues conduction mode and reduce output current ripple, the current regulator must be very advanced as current misbalance leads to saturation of the core of the transformer. In this case to avoid this problems coupling coefficient equal to 0,85 is selected with inductance of 400  $\mu$ H.

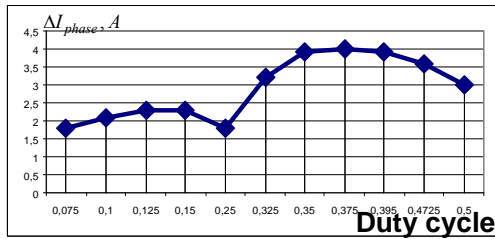


Fig. 17. Per-phase current ripple in 4-phase converter with coupled inductors

Per-phase current ripple of 4-phase interleaved DC-DC converter with coupled inductors in cyclic cascade (Fig. 17) is less than in case with uncoupled inductors (Fig. 2). This curve is designed by simulation of the converter by different duty cycles, for example as displayed in Fig. 18. The form of the current is changing by different duty cycles.

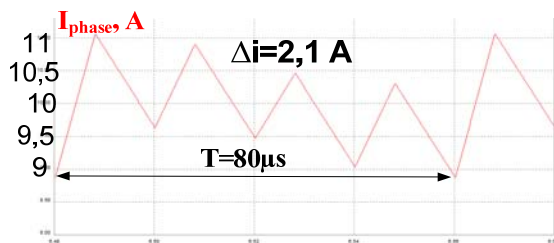


Fig. 28. Per-phase current ripple in 4-phase converter with coupled inductors, D=0,1

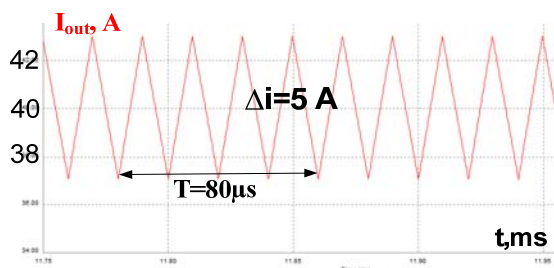


Fig. 19. Output current ripple in 4-phase converter with coupled inductors, D=0,125 (max output current ripple)

Output core ripple in case of coupled inductor (Fig. 19) is higher than if uncoupled inductor is used (Fig. 9) and in particular converter is close to the one phase case (Fig. 2). Nevertheless, proposed structure allows reducing this current ripples by adding additional inductor in each phase or in the output branch to achieve desirable level of pulsations of output current.

## V EXPERIMENTAL PROTOTYPE

Four coupled inductors is made, they are placed on the board and connected in closed chain structure. It is necessary to complement with DSP, current sensors, MOSFET driver and so on to develop an operating interleaved DC-DC converter. Inductor is wound on ETD59 coil former, its structure is shown in

Fig. 3. The central air gap and air gaps of outer legs is selected equal to  $\delta = \delta_c = 0,5$  mm, count of windings is 30, the measured inductance is  $L = 400 \mu\text{H}$ , coupling coefficient  $k = 0,85$ . In each phase there is two inductors in series.

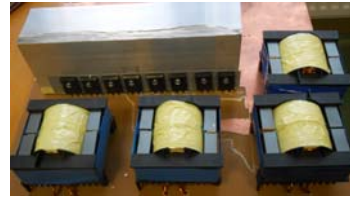


Fig. 20. Experimental prototype

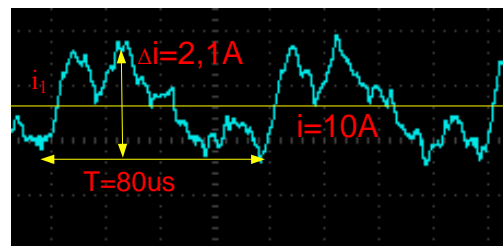


Fig. 21. Phase current, D=0,1

Fig. 21 shows per-phase current of the experimental prototype, it is similar to the Fig. 18. This means that the simulation results are correct.

## VI CONCLUSIONS

In this paper application of 2-phase coupled inductor designed in convenient way by using commercially manufactured coil formers and ferrite cores is analyzed to developed 4-phase interleaved DC-DC converter. The implementation approaches, operational principles and benefits are analyzed in detail based on simulation.

One of the main advantages of interleaved converters over single-phase converters is reduced output current ripple but per-phase current ripple remains large. Reductions this current ripple can be achieved by an integration of magnetics. Therefore original structure of two phase coupled inductor is proposed, it has constant inductance but moderate by air gap coupling coefficient, it can be designed by using traditional ETD core former.

Different structures of the coupled inductor for 4 phases DC-DC converter is studied and the closed chain structure is selected as the optimal solution. The phase and output current ripple in buck mode of the interleaving magnetic integrated converter is simulated. Simulation shows that per-phase ripple can be significantly reduced but output current ripple becomes a little bigger. If it is necessary, output current ripple can be reduced by using additional inductor.

## VII ACKNOWLEDGMENTS

This research work has been supported by Latvian Council of Science (Project Nr. 673/2014).

## VIII REFERENCES

- [1] Pit-Leong W., Peng X., Yang P. Performance improvements of interleaving VRMs with coupling inductors, *IEEE Trans. Power Electronics*, Vol. 16, No. 4, 2001, pp. 499-507.
- [2] Wong P. Performance Improvement Of Multi-Channel Interleaving Voltage Regulator Modules With Integrated Coupling Inductors, Ph.D. dissertation, Dept. Electr.Comput. Eng., Virginia Tech, Blacksburg, 2001.
- [3] Zakis J., Husev O., Strzelecki R. Feasibility study of inductor coupling in three-level neutral-point-clamped quasi-Z-source DC/AC converter, *Electric Power Quality and Supply Reliability Conference*, 2014, pp. 273 - 276.
- [4] Zhu G., Wang K. Modeling and design considerations of coupled inductor converters, *Applied Power Electronics Conference and Exposition (APEC)*, 2010., pp.7-13.
- [5] Lee P., Lee Y., Cheng D., Liu X. Steady-state analysis of an interleaved boost converter with coupled inductors, *Industrial Electronics, IEEE Transactions on* , vol.47, no.4, 2000., pp.787-795.
- [6] Santhos A., et al. Analysis of coupled inductors for low-ripple fast-response buck converter. *IEICE transactions on fundamentals of electronics, communications and computer sciences* vol. 92, no.2, 2009., pp. 451-455.
- [7] Zumel P., et al. Tight magnetic coupling in multiphase interleaved converters based on simple transformers. *Applied Power Electronics Conference and Exposition*, 2005. *APEC 2005. Twentieth Annual IEEE. Vol. 1.*, 2005., pp. 385 - 391.
- [8] Ashur A. S., Thorn, R. Modeling and Simulation of Automotive Interleaved Buck Converter. *Universities Power Engineering Conference*, 2009, pp. 1-6.
- [9] Chunliu C., Chenghua W. Research of an Interleaved Boost Converter with four Interleaved Boost Convert Cells. *Microelectronics & Electronics*, 2009, pp. 396-399.
- [10] Jin K., Yang M., Ruan X., Xu M., Three-Level Bidirectional Converter for Fuel-Cell/Battery Hybrid Power System. *IEEE Trans. on Industrial Electronics*, Vol. 57, No. 6, Jun. 2010, pp. 1976-1986.
- [11] Carpita M., De Vivo M., Gavin S. A Bidirectional DC/DC interleaved converter for supercapacitor applications. *Education and Research Conference (EDERC)*, 2012., pp.149,153.
- [12] Grbović P., Delarue P., Le Moigne P., Bartholomeus P. A Bidirectional Three-Level DC-DC Converter for the Ultracapacitor Applications. *IEEE Transactions on* , Vol.57., No.10., 2010., pp. 3415-3430.
- [13] Taylor R. PowerLab Notes: When to choose multiphase [online] [16.05.2014.]. Available at: <http://goo.gl/KVfusd>.
- [14] Zimnik M. Multiphase buck converters [online] [12.02.2015.]. Available at: <http://www.powerguru.org/multiphase-buck-converters/>.

# A task for laser cutting of lamellae with TruLaser 1030

Lyubomir Lazov, Hristina Deneva, Pavels Narica

Rezeknes Augstskola, Faculty of Engineering, Institute of Regional Studies (REGI),  
Address: Atbrivosanas aleja 90, Rezekne, LV-4601, Latvia.

**Abstract.** The growing development of manufacturing, automotive, aerospace and other sectors in the industry generates the necessity to continuously expanding on modifications of electrical machinery and equipments which are used in them, as well as to improve their performance and reliability. The report presents some results from a study to the process of laser cutting through melting on lamellae for rotor and stator packages by using the laser system TruLaser 1030. Some functional dependencies are offered between physical quantities describing the cutting process by melting and technological parameters aimed providing the quality requirements. With a software TruTops to optimize the cutting out are shown the results of studies to determine the technological working time for cutting of a concrete stator lamella.

**Keywords:** laser technology, laser cutting, electrical steel.

## I INTRODUCTION

To contemporary production of new and special motors in small series for modern electric cars stay a task to find a new technological solution for cutting of lamellae by Si-sheet metal for stator and rotor packages (fig. 1) [1]. Requirements are: the information by the designer quickly and flexibly to be carries over to the production equipment with which is created and tested new samples.

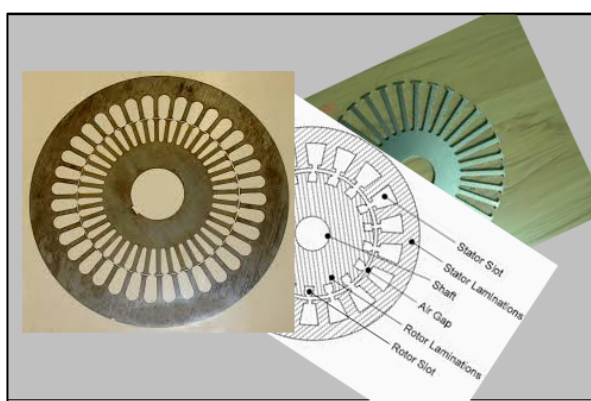


Fig. 1. Lamellae with different geometry

Such possibility provides the laser technology for contour cutting. Extensive specific studies are necessary to make for the deployment of such innovative task. In recent years, a new generation (disk and fiber) lasers appeared [2,3,4]. Laser

technique and technology are priority aspects in the industrial production of the 21st century due to many unique and specific features that these lasers have. They are very efficient for solving the tasks, as well as they provide high performance and flexibility of the cutting process.

Advantages [5] offered by the innovative laser technology for cutting of sheet material in the automotive industry, are:

- very high reliability;
- there is no tool wear – no mechanical action of the process;
- high speed;
- flexibility and changeovers;
- processing of lamellae with complex configuration because of the possibility of the laser radiation to transported by fiber and finely to focus in small work spot;
- a rapid implementation at new constructive solutions, shortening the time of execution (from creating a new drawing to cutting of lamella with new sizes and shapes) ; there is no necessity of production a new punching tool, as it stands in conventional technology;
- reducing the tooling costs;
- reducing the setup times of the technological system;
- lower production costs and higher productivity;
- high accuracy of the obtained dimensions;
- good quality (no burrs, a small HAZ, etc.).



Laser technological process is due to the thermal effect of electromagnetic laser energy absorbed from the surface of the material. As indicators for quality to substance treatment are presented in the functional dependence from: the laser parameters (power density, pulse repetition rate, etc.), the parameters of the process (speed of displacement to the laser radiation; physical and chemically properties of the material [5].

### II CHOICE OF APPROPRIATE LASER SYSTEM

A suitable choice of laser source is necessary to make at solving any particular task. As for each specific cutting process must be noted:

- characteristics of the laser system (power  $P$  of laser radiation, cutting speed  $v$ , wavelength  $\lambda$ , operation mode of the laser source, focal length  $f$  of focusing system, type and pressure  $p$  of the gas, shape and diameter of gas nozzle  $dG$ , etc.);
- specifics of interaction of laser radiation with the substance (a choice of an appropriate method for cutting – by melting and/or evaporation).

For example, the parameters of the laser radiation have to:

- be stable through the entire time of the treatment process;
- correspond at selected method used in the technological process, as well as at the kind and composition of the material, its thickness, the surface quality and the complexity of the contour;
- be able to manage and follow during the work.

It is a matter of fact that the choice of a suitable laser system for each concrete technological process is a complex issue.

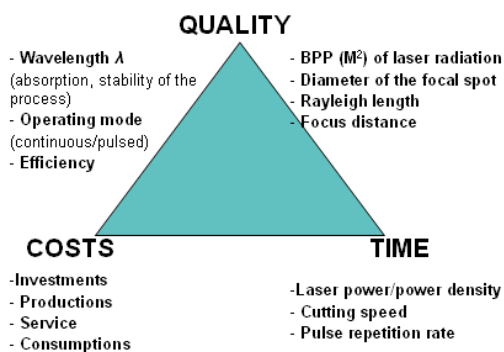


Fig. 2. Important considerations that should be taken into report the choice of laser system for cutting of lamellae

Along with a number of technological factors that should be taken into account, it is necessary to be analyzed and economical ones too (fig. 2):

- investment and production costs;
- efficiency and productivity, etc.

Eventually, the quality of production and its economical efficiency are determined by the correct

and optimal selection of these factors and considerations that should be well noted and analyzed.

The aim of the present study is:

1. Conducting of experimental studies in order to give working intervals of the basic technological parameters for the qualitative cutting of lamellae with technological system TruLaser 1030 and disk laser TruDisk 2001 – its wavelength is  $\lambda = 1,03 \mu m$  and power  $P$  up to 2 000 W.
2. Cutting of a specific lamella on a sheet material of electric metal steel with TruTops program under real conditions.

### III METHODS

In practice, dependent on the laser type, kind of the materials and the requirements of the production itself, there are well known four methods of laser cutting.

They are different both, in the essence and the character of the ongoing physical process, as well as in their capabilities and specific purpose.

#### *Sublimation laser cutting*

Removing the material from the lamella by laser cutting through sublimation is performed by direct evaporation of the substance from the area of impact [6]. Higher power densities are required – about  $(10^{11} \div 10^{12}) W/m^2$ , in order to realize this cutting process. Basically high power fiber lasers are used. In a single scan of the laser beam along the contour depth of cut in the material is several tens of micrometers.

Several scans along the same contour should be done to realize this method when cutting thicker materials. Although in our case the task is cutting of lamellas with thickness 0,35 mm and 0,50 mm, this method is not preferred – the results are in good quality, but the cost of technological equipment is quite high as compared with that of disk lasers.

#### *Oxygen laser cutting*

In this cutting method simultaneously with the laser radiation, oxygen is served in the treatment zone through a nozzle [7, 8].

There occurs an exothermic reaction of combustion with the release of a large amount of heat, as opposed to the previous method. Heat energy and the energy of laser radiation assisted melting of the material and ultimately accelerated the cutting process, so it is used for the processing of significantly thicker steel sheets. That allows passing the method of oxygen laser cutting with lower power densities (about  $10^9 W/m^2$ ). Disadvantages of the method: treatment zone and HAZ are considerably larger comparing to conventional methods. And in the case of the task the method is also unsuitable.

**Laser cutting with water jet**

The specificity of the method is that the laser beam enters along the axis of a thin water jet into the treatment area [9]. In the water jet the beam has total internal reflection as in a fiber. Subsidiary reagent is no added in the processing zone as it could lead to objectionable impacts on the surface treatment of the material – the electrical steel. An additional specialized aggregate needs to be included in order to provide a water pressure up to 500 bar and a flow rate  $V = (5 \div 75)$  ml/min.

**Laser cutting by melting**

In laser cutting by melting in the processing area are reached temperatures higher than the melting temperature  $T \geq T_m$  of a given material.

The formed melt is discharged from the cutting zone as the influence of steam raising pressure and the gaseous stream – for example nitrogen gas under pressure up to 24 bar [10]. In our experiments the technological system TruLaser 1030 with a built-in disc laser TruDisk 2001 provides output power up to 2000 W sufficient to realize the laser cutting process by melting. Technological parameters and characteristics of the system are referred to in our previous publications [11, 12].

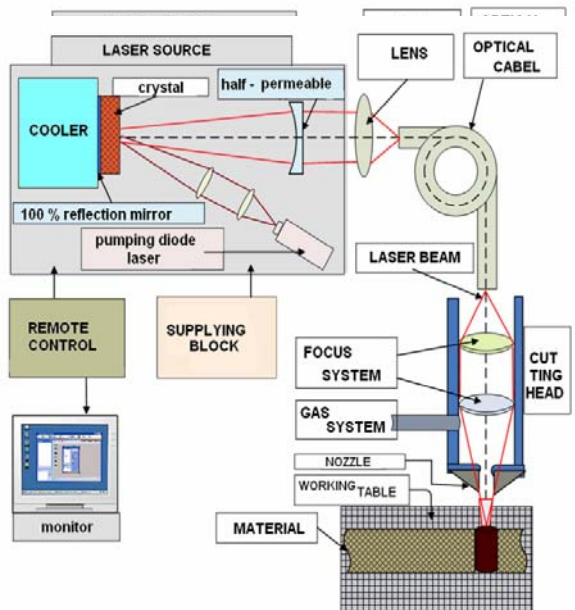


Fig. 3. Principle schema for a laser cutting system

A principle schema for a technological laser system is shown on fig. 3. In it are included the following basic modules:

- laser source TruDisk 2001 of Trupmf company [1];
- supply block (26 kVA); remote system; cooler system;
- working table;
- cutting head for moving along x, y and z axis;

- an optical cable for laser beam transporting to the working table;
- focusing system;
- auxiliary gas supply system – nitrogen.

**IV RESULTS AND DISCUSSION**

According to the chosen method, experiments to determine the optimal operating ranges of technological parameters ( $P$ ,  $v$ ,  $\Delta f$  and  $p$ ) are carried out as well as analyze their affects on the width  $b$  and the cutting quality on samples from electrical steel sheet M250-35A and M530-50A [13, 14].

An essential part of the experiments was oriented to study the impact of the technological parameters (laser power  $P$ , cutting speed  $v$  and gas pressure  $p$ ) on  $\alpha$  – the angle of divergence on the wall of the cut (fig. 4).

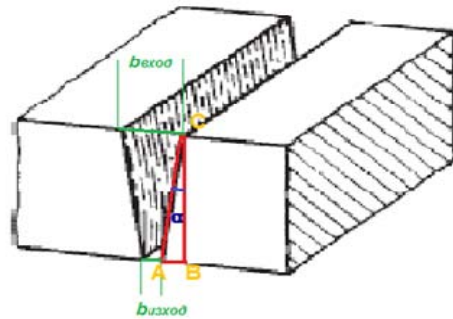


Fig. 4. An angle  $\alpha$  defining deviation from parallelisms of the walls through cutting

Changing the power  $P$  of laser radiation in the range of 400 W to 2 000 W at the cutting speed  $v = 14$  m/min on samples of steel sheet with 0,35 mm thickness leads to change  $\Delta\alpha \sim 1,4^\circ$  (fig. 5).

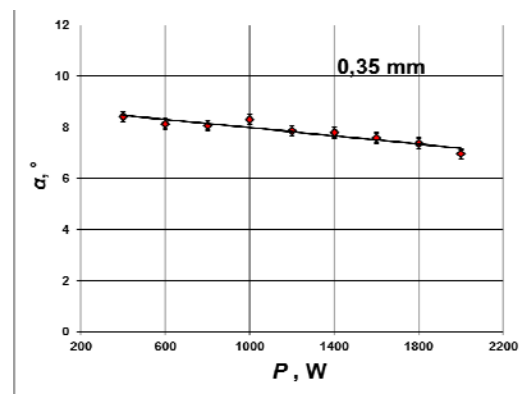


Fig. 5. A chart of dependence  $\alpha = \alpha(P)$  at cutting speed  $v = 14$  m/min on samples of M250-35A

Similar graphs of the relation  $\alpha = \alpha(P)$  were obtained when cutting specimens M530-50A at speeds  $v = (4, 8, 20)$  m/min.

To study the relationship  $\alpha = \alpha(v)$  the cutting speed is varied in the range  $v = (20 \pm 60)$  m/min,

respectively at constant power  $P = (500, 1\ 000, 2\ 000)$  W and pressure  $p$  of the working gas.

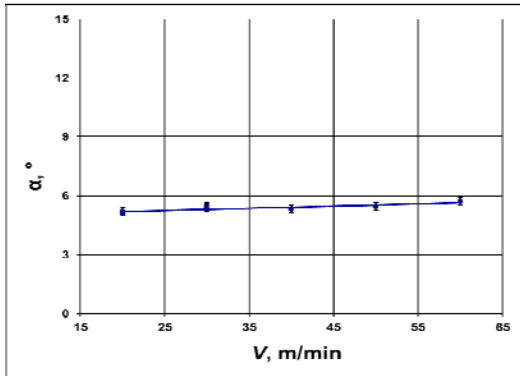


Fig. 6. A graph of experimental dependence  $\alpha = \alpha(v)$  for samples of M530-50A at power  $P = 2\ 000$  W

In the studied diapason of speeds the alteration of inclination angle  $\alpha$  is very small  $\Delta\alpha = 0,5^\circ$  (fig.6).

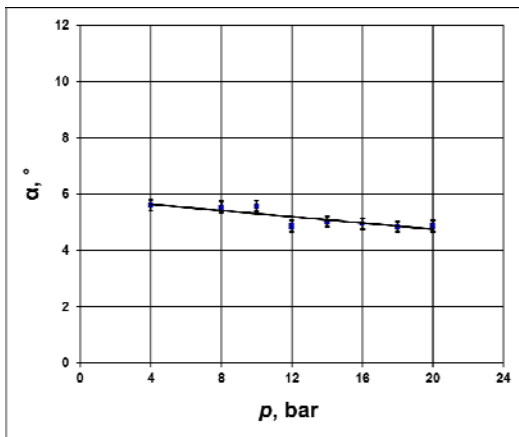


Fig. 7. A graph of experimental relationship  $\alpha = \alpha(p)$  when cutting the samples of M530-50A; the power  $P = 2\ 000$  W and speed  $v = 50$  m/min are constant

The pressure of auxiliary gas-nitrogen is varied in the range  $p = (4 \div 20)$  bar with step  $\Delta p = 2$  bar when studying the dependence  $\alpha = \alpha(p)$ , in the set of experiments (fig. 7). The obtained results indicate that in the interval from 4 bar to 20 bar as the variable  $\Delta\alpha$  is  $\sim 1^\circ$  for samples with thickness 0,35 mm and 0,50 mm.

The relationships  $b = b(P)$  and  $b = b(v)$  for sheet electrical steel M250-35A and M530-50A, are studied in a series of experiments with a special developed methodology. Results are described in detail at our papers [11, 12]. Analysis shows that the amendment of power  $P$  and speed  $v$  does not substantially alter the geometry of the cut (the width  $b$  of upper and lower surface of the lamella).

For example: The rapidity, with which is being amended width of the cut as the entrance  $\Delta b_{\text{enter}}$  and the exit  $\Delta b_{\text{exit}}$  in function of power  $P = (400 \div 2000)$

W, has many small values, respectively: at the entrance  $\Delta b_{\text{enter}} / \Delta P = 0,0081 \mu\text{m}/\text{W}$ ; at the exit  $\Delta b_{\text{exit}} / \Delta P = 0,0061 \mu\text{m}/\text{W}$  (fig. 8).

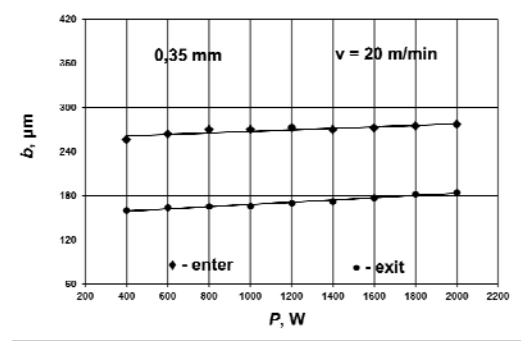


Fig.8. Experimental dependences  $b_{\text{enter}} = b_{\text{enter}}(P)$  and  $b_{\text{exit}} = b_{\text{exit}}(P)$  at cutting with speed  $v = 20$  m/min

It is not established significant change of the cutting width  $b$  on the entrance and exit when altered the cutting speed  $v$  in the range  $(20 \div 60)$  m/min. Average values of cutting width in the studied range of speeds are as follows: M250-35A –  $b_{\text{enter}} = (262 \pm 5)\mu\text{m}$ ;  $b_{\text{exit}} = (173 \pm 5)\mu\text{m}$ ; за M530-50A –  $b_{\text{enter}} = (273 \pm 5)\mu\text{m}$ ;  $b_{\text{exit}} = (168 \pm 5)\mu\text{m}$  (fig. 9).

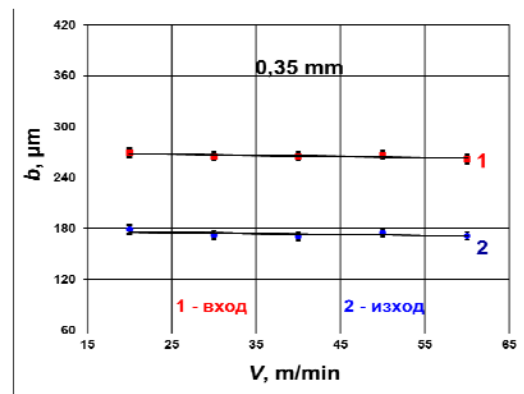


Fig. 9 Graphics of experimental relationships  $b_{\text{enter}} = b_{\text{enter}}(v)$  and  $b_{\text{exit}} = b_{\text{exit}}(v)$  at constant power  $P = 1000$  W

Cutting quality in studied experiment series are evaluated by using optic observations of the treatment areas.

Operating intervals for the studied technological parameters  $P$  and  $v$  are defined when cutting of lamellas with good quality:

- Laser power  $P = (1\ 000 \text{ W} \div 1\ 400 \text{ W})$  at constant speed  $v = 20$  m/min (fig. 10);
- Cutting speed  $v = (20 \div 30)$  m/min and power  $P = 1\ 000$  W; as well as  $v = (20 \div 50)$  m/min and power  $P = 2\ 000$  W (fig. 11).

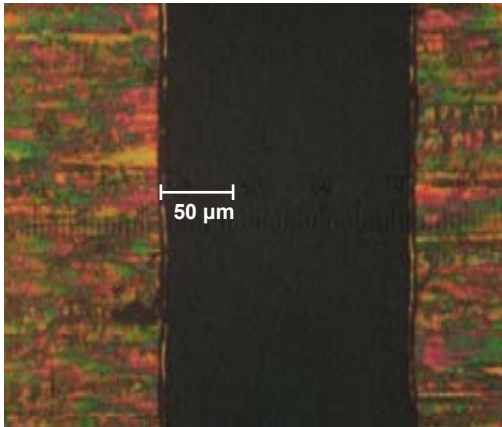


Fig. 10. A cutting section at  $P = 1\ 200\ \text{W}$  and  $v = 20\ \text{m/min}$  on samples of width  $0,50\ \text{mm}$

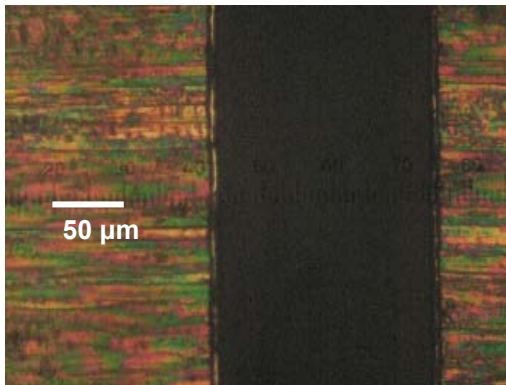


Fig. 11 A section of cut at  $P = 1\ 000\ \text{W}$  and  $v = 20\ \text{m/min}$  of samples with  $0,35\ \text{mm}$

### Program control of the process

An optimization for specific cutting is done by software TruTops when using preliminary engineering theoretical and experimental results in the examination of the cutting process through melt of stator lamella.

Nowadays the program management of the laser processes has been developing very fast. A software controls the movement of the focal spot on a given path to the working surface, as well as adjusts the power of laser radiation and gas supplies. Measured values are recognized by special sensors that controlled the laser process.

The optimization of the laser power and cutting speed during the laser process is one of the biggest challenges to managing the laser processes. For example the laser power and cutting speed have to decrease when there is a motion on complicated contour. In some cases on complex contours the laser beam must be switched off for a split second and then be switched on again. At that time the cutting head must be moved with high speed over the material surface from a one point to a new position. A set of programs for process control in the laser technological system are created for optimization of the cutting.

Programs automatically calculated the best path on which the laser beam has to move as the sequence of scan individual elements (lamellas) in cutting is given, as well as the starting position for cutting each element. The program should be taken into account these values of speeds that are suitable for cutting of curves and angles. This is a comprehensive strategy which must be well thought out and planned.

Control command module of the technological system consists of three groups with included information data:

A) constructive design – a special design of the lamella is drawn in CAD module which is written in the specific track under GEO format;

B) parameters of the sheet material – the geometry of sheet material ( $4\ 000 \times 1\ 000 \times 0,50$ ), its thickness and type, surface condition (in our case the varnish holding is type C), optimization function for cutting (cropping as much as possible details with minimal waste), route (fig. 12), etc.;

B) laser technological parameters of the cutting process: power  $P$ , W; speed  $v$ , m/min; focal length  $f$ , mm; focus position  $\Delta f$ , mm; pressure  $p$ , bar; auxiliary gas (nitrogen), etc.

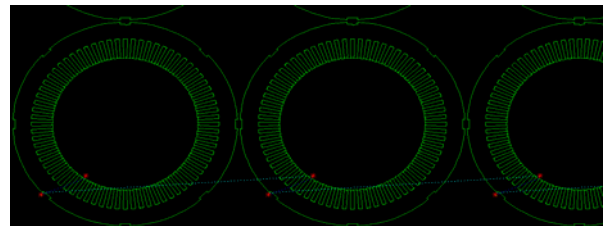


Fig. 12 A cutting route of as stator lamella

29,02 min is the measured time for cutting of 36 stator lamellas with smooth and pure edges and 45,24 min – for 58 lamellas (fig. 13).

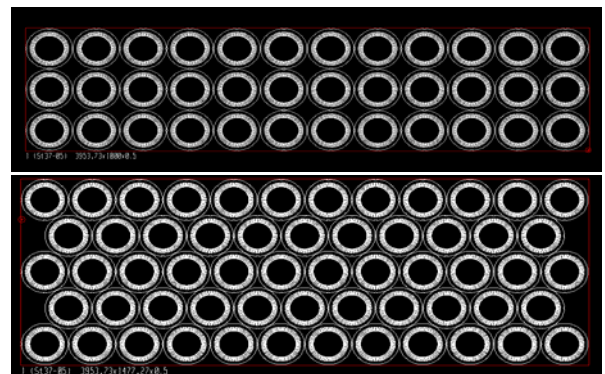


Fig. 13 Optimization cutting of sheet material for 36 and 58 stator lamellae

Based on final results, technological tables are prepared using TruTops software. The technological tables consist of database. They are made for every

kind of material according to its thickness. The optimal values of laser parameters for the particular technological process as laser power, cutting speed, the type and contour size, focal length, etc., are included in these tables. Any technological table has a separate number and previously is inserted in the machine databases. It could be queried and updated at any time. Only an individual technological table is taken when the process is programmed by the operator. During the process the machine management automatically takes the necessary values from the table.

Using these data, the machine operator can quickly reach the optimal working parameters for the quality cutting of lamellas by electrical steel.

#### V CONCLUSION

Implementation of the method of laser cutting of thin materials from electrical steel for achieving higher quality in manufacturing process of electric motors is a cause for increasing in the competitiveness of SMSs in Bulgaria and Latvia.

The positive economic and social effect by the introduction of such innovative laser technologies has been connected not only with increasing of the production, but also they created new technological areas, opened new horizons and thereby a large number of jobs; as it leads to improve quality and increase the competitiveness of the products on world markets; intellectualization of the engineering work, resulting in improved working conditions, while increasing the educational level of working staff and

ultimately increases the standard of living in countries applying innovative solutions and procedures.

#### VI REFERENCES

- [1] G. Pasquarella, Innovation als Antrieb Stator- und Rotorpakete für Elektrische mMaschinen Prototypen und Vorserien., LCD LaserCut AG
- [2] T. Himmer, Hochwertig Schneiden mit CO<sub>2</sub> und Feiberlasern, Blech Inform 3/2007 pp 50-53
- [3] L. Matthias, T. Himmer, Remote-Schneiden mit dem Faserlaser ermöglicht hohe Konturgeschwindigkeiten, <http://www.maschinenmarkt.vogel.de/themenkanale/produktion/trenntechnik/articles/146592/>
- [4] Fraunhofer-Institut, IWS demonstriert Vorteile beim Laser-Remote-Schneiden, Lasys 2008 <http://www.blechnet.com/themen/zulieferungen/articles/105024/>
- [5] Deneva H., A Study on Laser Cutting Process of Lamellae for Rotor and Stator Packages. Dissertation 2014, TU - Gabrovo, pp.160
- [6] Sublimation cutting, Trumpf-laser <http://www.us.trumpf.com/en/products/laser-technology/solutions/applications/laser-cutting/sublimation-cutting.html>
- [7] Schuöcker, D. Handbook of the EuroLaser Academy, Chapman&Hall, London, 1998, ISBN 0412819201.
- [8] Вейко, В. П. Технологические лазеры и лазерное излучение, Санкт-Петербург, ИТМО, 2007, 52с
- [9] Mai, T. A., B. Ric, Laser-Microjet: das ideale Werkzeug für Präzisionsmikrobearbeitung.pdf, Oktober 2005, [www.synova.ch](http://www.synova.ch)
- [10] LCD LaserCut AG, Laserschneiden und Paketieren von dünnen Blechen bis 0.1mm <http://www.lcd-lasercut.ch/>
- [11] Lazov, L., H. Deneva. Investigation of Cutting Width from Laser Power and Velocity. IJETCAS, Issue 4, Vol 1, 2 & 3, March – May, 2013, ISSN 2279-0047
- [12] Lazov, L., H. Deneva. Investigation on the Influence of the Process Parameters Power and Velocity to Laser Cutting of Lamellae. Bulgarian National Conference on Physics, Plovdiv 10-12.10.2014 (in the press)
- [13] <http://www.splav-kharkov.com/main.php>
- [14] Ленгеров, А., Г. Николчева, П. Даскалов. Изследване на режимите на рязане при обработка на детайли с наварени повърхнини, 10 Международна научно-техническа конференция АМО, 27-29 юни 2010, стр.146.

# Factors influencing the color laser marking

**Lyubomir Lazov, Hristina Deneva, Pavels Narica**

*Rezeknes Augstskola, Faculty of Engineering, Institute of Regional Studies (REGI).*

*Address: Atbrivosanas aleja 90, Rezekne, LV-4601, Latvia.*

**Abstract.** In recent years, conventional techniques of marking on some parts of different work pieces, as well as on packages with color printing are increasingly being displaced by laser color marking. Colored marking of stainless steel could be realized by the process annealing. The advantages offered by the new technology are in greater accuracy, speed, flexibility and high amount of recorded information per unit area (bar and matrix codes). In the report are discussed and analyzed the factors influencing on the specific to the process of laser color marking at the products of CrNi steel. The study was conducted using a commercially available industrial pulsed fiber laser. Presents the results of the measurements and analysis of the influence of laser process parameters on the color contrasting obtained. In this case, the relevant parameter, the field of high frequencies and low pulse energy were examined. The present thesis describes studies a properties of the laser radiation, such as, pulse width, average power, the intensity and beam diameter.

**Keywords:** laser, marking, color lettering of stainless steel.

## I INTRODUCTION

Modern solid-state Q-switched lasers generate a powerful pulses with a repetition rate of tens of kHz. The average radiation power value of tens of watts, provides  $P \sim 10^8 \text{ W / cm}^2$  power density in the area of processing. This allows to use solid-state lasers for marking metals, refractory alloys and steels, hard ceramics in various industries. The laser marking is a modification of the material surface. It causes local heating, melting and partial evaporation of the material in the limited spot size field.

The most common method for color marking on metal surfaces are termoprinting, emulsion coating, powder coating or electrolytic oxidation techniques. The disadvantages of these methods can be noted that during operation they have a low degree of durability, color fading over time, etc. The method of electrolytic oxidation does not allow simultaneous labeling with several colors on the surface.

Mechanism of coloring marking on plastic materials is based on major four principles: bubbling; condensation; carbonization; chemical change.

Laser color marking on metals appeared about 15 years ago. Compared to other methods, laser color marking is the fastest and cheapest way of color marking on metal surface. But it have not found wide application in practice. The reason can be found in quite complicated implementation, time-consuming and not quite often repeatable results.

The two main problems that researchers must solve at this stage is reproducibility and process stability. Often, experimentally determined parameters required

to obtain a specific color on one system, do not give a positive result for other systems, even very similar to the same model. In the literature are articles that describes this process, but there is still a lack of information about what extent and which of the process parameters have an impact on the reproducibility of the created colors.

## II LASER COLORING MARKING PRINCIPLE

To be successful conditions for the emergence color marking, there are several parameters to be optimized for all solid-state lasers used for marking: frequency and pulse width, power density, the layout of the intensity over the cross-section of the beam, etc. It is known that for lasers such as lamp-pumped, the optimal frequency range for labeling metals is 2-5 kHz, and the use of such frequencies in Fiber laser are impossible. If, try to compare different modes of laser marking systems at the same power, we will not get correct result, as the time and energy characteristics of the pulses are different, not mentioning the significant differences of the spatial characteristics of radiation.

Colour marking can be obtained with diode and lamp-pumped lasers. However, this effect is not stable ("floating") and difficult to reproduce. Constancy integrated zone temperature laser action is probably necessary condition Table 1, but for the better effect of color marking specific conditions are required that are related to the spatio-temporal characteristics of the laser radiation and its stability. It is these conditions














are fulfilled in Fiber-lasers that successfully determined the possibility of color coding.

In the literature are mentioned two methods for color laser marking on metal surfaces:

- The first utilizes a laser as a heat source, which covers metal surface with transparent or semitransparent oxide film. [1, 2, 3, 4, 5]. Illuminating surface with white light, radiation is reflected from the upper and lower oxide layer. As a result, the phenomenon of interference (superposition) of the reflected rays turns light effect, which is perceived by sight. The thickness of the oxide layer [6] and are determined by the coefficient of the refractive index into color spectrum.

TABLE 1.

PROCESS OF HEAT TREATING (TEMPERING) OF STAINLESS STEEL

Color visually	Color	Temperature °C
	white yellow	200
	straw yellow	220
	golden yellow	230
	yellow brown	240
	brownish red	250
	red	260
	magenta	270
	violet	280
	dark blue	290
	cornflower blue	300
	light blue	320
	bluegrey	340
	gray	360

- Second method, colors on the surface of various metals are created by the laser-induced periodic surface structures (LIPSS), known as “laser-induced ripples,” by the femtoor and picosecond lasers [7, 8] (fig.1).

At the moment, there is an increasing trend to look for scientific and engineering and technological solutions to improve the capabilities of these technologies and related systems for color marking. Today, for commercial marking there are available laser systems with stable parameters. For a real implementation of this method in the industry identification of process control parameters and articulation of scientifically-based physical representations are needed.

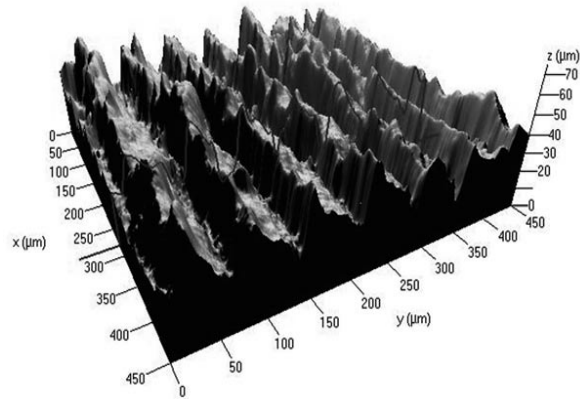


Fig. 1. 3-D image of laser induced periodic surface structures (LIPSS) on material LSM

### III EXPERIMENT DETAILS

The study was conducted on industrial laser marking system „DFL Ventus Marker II “ Firma ACI (fig.2) Yb: Fiber laser wavelength  $\lambda = 1062 \text{ nm}$ , with average output power  $P = 20 \text{ W}$ , pulse peak power  $P_{imax} = 12\text{kW}$ , beam quality factor  $M^2 = 1,32$ , pulse duration  $\tau$  - variable, pulse frequency  $\nu = 1\text{-}1000\text{kHz}$ .



Fig. 2. Laser marking system „DFL Ventus Marker II “ Firma ACI

For a deviation of the laser beam is used in the scanner system. The galvanometric mirrors deviate (deflected) the beam and the F-Theta lens (LINOS type 4401-305-000-21) with a 160 mm focal length focused the laser beam ( $X, Y$ -axes) on working surface. The beam diameter at the focal point was approximately  $61 \mu\text{m}$ . One an adjustable ( $Z$ -axis) table used to placed to the marking samples. An external distance sensor allowed the displacement of the sample in the  $Z$ -axis to be measured with an accuracy of  $10 \mu\text{m}$ . A block diagram of the experimental is shown in Fig. 3.

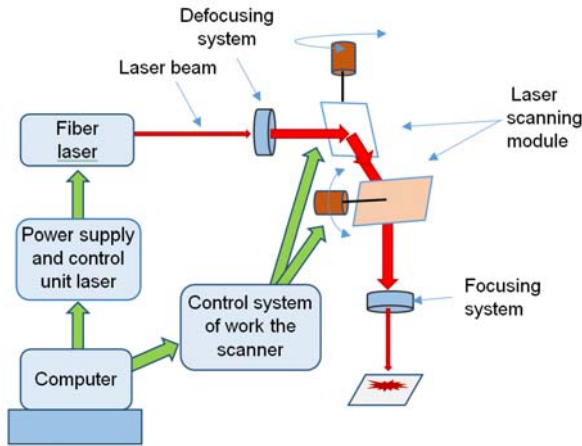


Fig. 3. Block diagram of the experimental system

Tests were carried out on plates made of the most commonly used type of stainless steel alloys. The chemical composition of the samples 12X18H10T is (71% Fe; 0,12% C; 18% Cr; 10% Ni, 2% Mn, 0,8% Si,...) [9][10].

The samples of stainless steel with dimensions of 100 × 100 mm and thickness of 1 mm. Before the experiment, the plates were washed with isopropyl alcohol in an ultrasonic cleaner. The samples were marked in atmospheric air.

The tested plates contained up to 81 fields with dimensions of 6 × 6 mm and about 1 mm interval between successive rows and columns. Each tested field corresponded to a different set of process parameters (laser fluence). The tests were conducted for the experimentally determined range of parameters (presented in Table 2).

TABLE 2.

PARAMETERS SELECTED FOR TESTING OF LASER COLOR MARKING

Average laser power	$P$ [W]	10–64 in steps of 5
Speed of scanning	$V$ [mm/s]	10–633 in steps of 78
Pulse repetition rate	$PRR$ [kHz]	395
Hatching	$h$ [μm]	10

Due to the vast number of parameters, experiments were designed in a manner to keep several parameters constant while adjusting the others and thus establishing the effect of the processing parameters individually.

A test fields be filled by the method of the raster marking (the principle of sequential line scanning) (fig.4) with an option for variable pitch  $d_y = 10 \mu\text{m}$ . At diameter of work spot  $62 \mu\text{m}$  any line would overlap about 83%.

Working ranges for power and processing speed were selected from preliminary experiments. The speed range of 50 to 650 mm/s was selected for

research from available scanner speeds (10 - 2000 mm/s). The average power working range of 5 W to 13 W was selected accordingly. The frequency was changed in a range of 100 kHz to 715 kHz with a corresponding pulse width. The Table 3 are presented the data for puls frequency  $\nu$ , puls duration  $\tau$ , puls energy  $E_i$  which were conducted experimental studies.

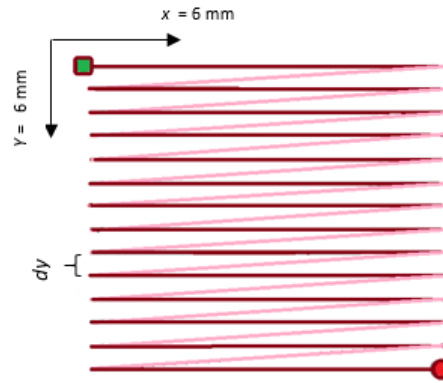


Fig. 4. The method of the raster marking

TABLE 3.

SUMMARIZED DATA FOR PULS FREQUENCY, PULS DURATION AND PULS ENERGY USED IN THE EXPERIMENT

$\nu$ , kHz	$\tau$ , ns	$E_i$ , μJ
20	320	1000
25	221	800
32	144	630
41	100	490
76	36	260
123	20	160
215	13	90
500	5	40
715	3	30

In order to optimize the laser coloring process can adjust the pulse width, repetition rate, average power and scanning velocity. Further, the combinations of these parameters produce different pulse energies and peak powers. The peak power  $P_{imax}$  during a square pulse can be calculated by

$$P_{imax} = P / \tau \nu \tag{1}$$

$$P_{imax} = E_p / \tau \tag{2}$$

in which  $P$  is the average power [W],

$\tau$  - the pulse width [s],

$\nu$  - the pulse repetition rate [Hz],

$E_p$  - the pulse energy [J].

The pulse energy can be calculated by

$$E_p = P / \nu \tag{3}$$



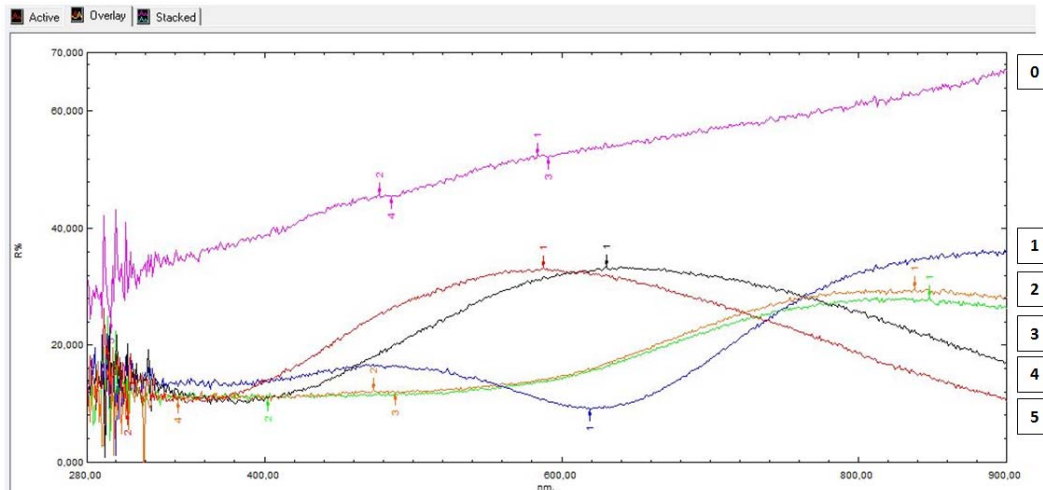


Fig. 5. Cpectograms of the 4 sample processed with different regimes

Objective change of color was carried under various technological processing modes with a help of spectrophotometer “Shimadzu MCP-2200 UV-Vis-NIR”. The measurements (was taken) were realized in the wavelength range from 300 nm to 900 nm. The spectrograms of 4 of the examined samples can be seen on fig. 5. Regimes for their treatment are listed in Table 3.

TABLE 4.  
THE SAMPLES AND REGIMES OF PROCESSING

No.	graphics	P, %	v, kHz	$\tau$ , ns	v, mm/s	d, $\mu$ m	h, $\mu$ m	color
0								Unprocessed surface
1		26	395	7	88	62	10	Cornflower blue
2		36	395	7	244	62	10	Violet
3		36	395	7	244	62	10	Violet
4		45	395	7	477	62	10	Straw yellow
5		50	395	7	633	62	10	Pale green

The software used to control the spectrometer enables operation on several color spaces. For colorimetric identification, one of the most useful color spaces, the CIE  $L^*a^*b^*$ , was used. It enables color difference to be easily evaluated. CIE  $L^*a^*b^*$  (CIELAB) is the most complete[citation needed] color space specified by the International Commission on Illumination (French Commission internationale de l'éclairage). It describes all the colors visible to the human eye and was created to serve as a device-independent model to be used as a reference. In the Lab color space is separated from the value of the lightness values of chromatic color component (hue, saturation). The three coordinates of CIELAB represent the lightness of the color ( $L^* = 0$  yields black and  $L^* = 100$  indicates diffuse white; specular white may be higher), its position between

red/magenta and green ( $a^*$ , negative values indicate green while positive values indicate magenta) and its position between yellow and blue ( $b^*$ , negative values indicate blue and positive values indicate yellow).

Its unit vector is approximately identical to the color resolution of the human eye.

#### IV RESULTS

Parameters  $\nu$  (frequency) and  $\tau$  (pulse width) provide intensive effect of radiation to the material while minimizing its overall warming.

Strict coincidence in naming colors and in fixing temperatures is not observed. After all, qualitative assessment of color is purely subjective task. Above all, duration of heating has significant impact on getting one heat tint (temper) color or another. The color of iron turning blue at temperature much lower than the one expected to be necessary to cause even straw yellow coloration can be caused by a more or less lengthy processing. Similarly, the straw yellow coating on iron-steel products can be caused by holding the latter for necessary number of minutes at temperature several tens of degrees lower than than indicated in Table 1 ( $220^\circ$ ).

Oxide films depending on their thickness on metals are commonly subdivided into thin (invisible) with a thickness of 40 nm, medium (visible as heat tint) with a thickness of 40-500 nm, and thick (visible) with a thickness of more than 500 nm.

As seen by research findings (fig.6) certain integral heating characteristic which takes into account the sample surface temperature  $T(N_x)$  generated by theaction of pulses train and total heating time  $t_{x,y}$  must be the parameter which characterizes the formation of oxide films with different structures and colors. This resembles Bunsen-Roscoe law (in photochemistry): amount of product of photochemical reaction is determined by total amount of energy of

incident radiation, i.e., product of power of radiation and time of action, or generalized parameter - exposure (amount of lighting). In addition, photochemical effect does not change for various values of generalized parameter.

The made a series of experiments at  $\nu = 215$  kHz;  $\tau = 13$ ns and  $\nu = 715$  kHz;  $\tau = 3$ ns have shown that each color corresponds to a value of an integral temperature which is in narrow range for wide change of mode parameters (power, speed, pulse frequency and width) fig. 7a,b.

According our results of experiments the specific form of chosen function for laser coloring is well described by the semiempirical temperature-time combination the function F.

$$F = T(N_x) \cdot t_{x,y} \quad (4)$$

where  $t_{x,y}$  is the action time,  $T(N_x)$ - the temperature of metal surface.

The action time  $t_{x,y}$  can be calculated on the basis of the following formula

$$t_{x,y} = N_x \cdot N_y \tau = \frac{d^2 \nu \tau N}{\nu} \quad (5)$$

where  $N_x, N_y$  are the amounts of pulses in the focus region taking into account the overlap on  $x$  and  $y$  axes,  $\nu$  is the scanning speed,  $d$  - diameter of working spot, mm,  $N$  is the resolution (lines by 1 mm)

The temperature of metal surface  $T(N_x)$  upon laser irradiation with the series of  $N_x$  pulses the following formula can be attained [11]

$$T(N_x) = \frac{2q_0(1-R)\sqrt{a}}{k\sqrt{\pi}} \sum_{n=0}^{N_x} \left[ \sqrt{\frac{n+\nu\tau}{\nu}} + \sqrt{\frac{n}{\nu}} \right] + T_0 \quad (6)$$

where  $q_0$  is the density of radiation power;  $\tau$  - the pulse duration;  $\nu$  - the repetition rate;  $T_0$  - the initial sample temperature;  $R$  - the reflectivity on  $\lambda = 1,06$   $\mu$ m;  $k$  - the material thermal conduction;  $a$  is the material thermal diffusivity.

Research suggested that change of the parameter of function  $F$  characterizes the order of occurrence of colors upon the laser coloring, which is also confirmed by other authors [12].

According to thermodynamic calculations in research, the most probable is formation of compounds of iron and chromium with oxygen in the process of interaction between steel and atmosphere during laser heating, as the magnitude of the Gibbs energy in temperature range of (298-1000)K is significantly lower than needed for compounds with nitrogen, carbon or water. According to results of calculations, multicomponent film with phase composition of  $Fe_2O_3, CrO_2, NiO$  is formed in the atmosphere while heating surface of stainless steel up to 700 K.

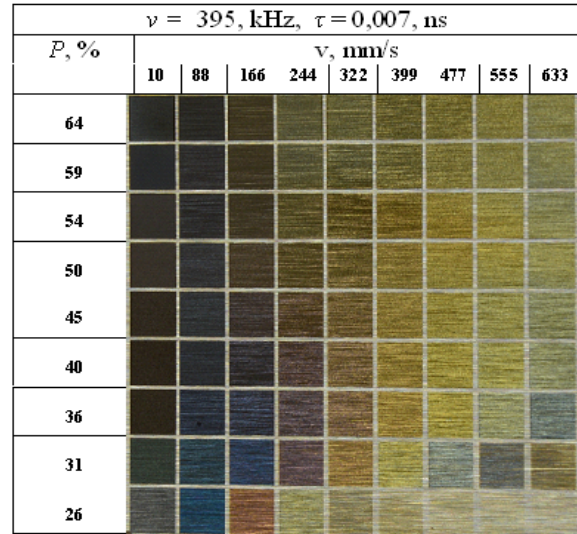


Fig. 6. The influence of average power  $P$  and scanning speed  $\nu$  of the sample on the color marking,  $\nu = 395$  kHz,  $\tau = 7 \cdot 10^{-9}$  s

TABLE 5.  
THE SAMPLES AND REGIMES OF PROCESSING

Elements	Weight %			
	Metal 12X18H10T	Metal 12X18H10T surface of the test sample		
	GOST 5632-72 (EN - 1.4878)	Unprocessed surface	Treated surface 50%	Treated surface 26%
O oxygen	--	--	5,70	9,05
Cr chrome	17,0 - 19,0	19,16	15,68	17,33
Fe iron	Basic	70,87	69,44	64,40
Ni nickel	9,0 - 11,0	7,72	7,77	7,86
Mn manganese	< 2,0	2,25	1,41	1,37
Si silicon	< 0,8			

This fact is confirmed in our experimental results. From the components of the atmosphere we found only oxygen during energy-dispersive X-ray spectroscopy analysis with scanning electron microscope (SEM) TESCAN-VEGA LMU II. Investigation of thin films structure was performed on x-ray diffractometer SmartLab RIGAKU with  $Cu-K\alpha$  radiation ( $\lambda = 1,543$  Å) operated at an acceleration voltage of 40 kV and an emission current of 150 mA. Bragg - Brentano focusing optic wavelength with a primary monochromator was used.

Mass fraction  $\omega(X)$  of each component of stainless steel for an unprocessed surface of stainless steel as well as for colored films after laser heating up to certain temperature is shown in the Table 5.

Frequency 215 kHz, pulse width 0,013μs									
P, %	v, mm/s								
	313	356	400	444	487	530	574	608	616
45									
44									
44									
43									
42									
41									
40									
40									
39									

a)

Frequency 715 kHz, pulse width 0,003μs									
P, %	v, mm/s								
	43	60	76	93	110	126	143	160	176
32									
31									
30									
29									
28									
28									
27									
26									
26									

b)

Fig. 7. The influence of average power  $P$  and scanning speed  $v$  of the color marking:

- a)  $v = 215 \text{ kHz}, \tau = 13 \cdot 10^{-9} \text{ s}$
- b)  $v = 715 \text{ kHz}, \tau = 7 \cdot 10^{-9} \text{ s}$

## V CONCLUSION

The research of interaction of nanosecond duration laser radiation with surface of stainless steel was conducted in this work. As a result, empirical tables of dependencies between colors formed by engraving and laser radiation parameters with help of which it is possible to program obtaining quite complex colored images were set up for given stainless steel specimens.

The research of phase composition of surface and its structure confirmed presence of oxide films and showed that quite complex periodic surface structure and layers of various thickness form by virtue of pulsed nature of radiation caused by exposure. In order to ascertain this complex process there is a need for further research with application of other types of lasers and other technological parameters.

The technology of laser color marking of metal surfaces which allows to change their optical properties in visible range can be applied in metal coloring when obtaining a durable high resolution image is needed with help of contactless effect on material (advertising business, jewelry production, machine manufacturing). It can also be used successfully as a mean of protection against corrosion.

## VI VI. REFERENCES

- [1] A. Pérez del Pino, P. Serra, J.L. Morenza, Oxidation of titanium through Nd:YAG laser irradiation. Appl. Surf. Sci. 197–198, 887–890 (2002)
- [2] S. O'Hana, A.J. Pinkerton, K. Shoba, A.W. Gale, L. Li, Laser surface colouring of titanium for contemporary jewellery. Surf. Eng. 24, 147–153 (2008)
- [3] Á. Perez del Pino, J.M. Fernandez-Pradas, P. Serra, J.L. Morenza, Coloring of titanium through laser oxidation: comparative study with anodizing. Surf. Coat. Technol. 187, 106–112 (2004)
- [4] Z.L. Li, H.Y. Zheng, K.M. Teh, Y.C. Liu, G.C. Lim, H.L. Seng, N.L. Yakovlev, Analysis of oxide formation induced by UV laser coloration of stainless steel. Appl. Surf. Sci. 256, 1731–1734 (2009)
- [5] A.J. Anto'nczak, D. Koco'n, M. Nowak, P. Koziol, K.M. Abramski, Laser-induced colour marking—Sensitivity 16. L. Baufay, F.A. Houle, R.J. Wilson, Optical self-regulation during laser-induced oxidation of copper. J. Appl. Phys. 61, 4640 (1987)
- [6] S. Fujimoto, K. Tsujino, T. Shibata, Growth and properties of Cr-rich thick and porous oxide films on Type 304 stainless steel formed by square wave potential pulse polarisation. Electrochim. Acta 47, 543–551 (2001)
- [7] A.Y. Vorobyev, C. Guo, Colorizing metals with femtosecond laser pulses. Appl. Phys. Lett. 92, 041914 (2008)
- [8] E.B. Barmina, E. Stratakis, C. Fotakis, G.A. Shafeev, Generation of nanostructures on metals by laser ablation in liquids: new results. Quantum Electron. 40, 1012 (2010)
- [9] www.inoxstory.ru/ask.html
- [10] Гост 5632-72, издательство стандартов, Москва, www.docload.ru/Basesdoc/3/3936/index.htm
- [11] Шахно Е. А. Аналитические методы исследования и разработки лазерных микро- и нанотехнологий. Методические рекомендации по выполнению курсовых проектов и само-стоятельных работ студентов. – СПб: СПбГУ ИТМО, 2008 18
- [12] Вейко В. П., Горный С. Г., Одинцова Г. В. и др. Формирование многоцветного изображения при лазерном окислении металлов. – Изв. вузов. Приборостроение, 2011, т.54, №2, с.47–53

# Laser Marking Methods

Lyubomir Lazov, Hristina Deneva, Pavels Narica

Rezeknes Augstskola, Faculty of Engineering, Institute of Regional Studies (REGI).

Address: Atbrivosanas aleja 90, Rezekne, LV-4601, Latvia.

**Abstract.** Different methods for laser marking are systematized and discussed in the paper. Today in the practice there are many different methods that could be used to realise high quality on the workpiece of various materials with various shapes. Some materials could be marked only by marking or engraving without special requirements and difficulty, while for other materials one can choose the concrete method about the kind of material, marking type, and the specific needs of the production process and the geometry of detail. This makes it necessary to know, to summarise and systematize in a database all methods for particular lasers and materials, in order to quickly and flexibly respond to the specific needs of each customer by the manufactories on marking systems. The report studies the specific opportunities and fields of applications of different methods for marking with laser.

**Keywords:** laser marking, methods.

## I INTRODUCTION

In recent years the process of laser marking is used to perform automated reading of information plotted on a given part and written as alphanumeric or coded as bar and matrix codes of individual components or products [1, 2, 3, 4]. The marked parts and details containing coded information which can be read automatically enable them to be monitored during the manufacturing process and throughout the supply chain (fig. 1). It is ideal when looking for service parts and repairs or putting in a claim, as well as being able to contribute to accountability and ensuring guarantee.

In many branches of industry the method of „Direct Marking on the Product” (DPM) is used to allow identification of the final industrial product. Ordinarily, the usage of DPM is preferred over other methods such as labeling of products. However, the physical characteristics and makeup of the part can also result in marking issues for manufacturers.

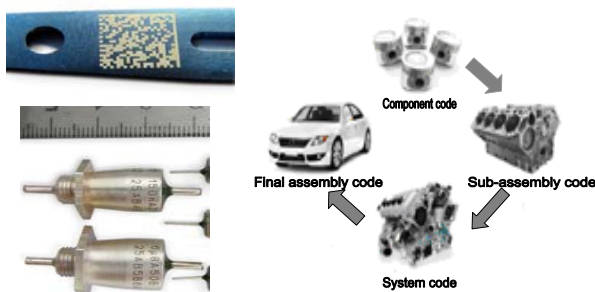


Fig. 1. Laser marking of parts with different codes

Today in automotive and aerospace industries, mechanical engineering, etc., the most common technologies used for DPM are laser marking, continuous ink jet printing, dot peening and electrochemical etching [5, 6]. When selecting one of these marking technologies it is necessary to focus on the type of material, the flexibility of the process, the financial cost, the process speed, the productivity and ability to automate the process of marking. In making a decision on the marking of some product except the choosing type of code and its content, it is also important to evaluate and select the best marking method – view table 1 and table 2.

TABLE 1

A COMPARISON BETWEEN THE DIFFERENT TECHNOLOGIES AND MATERIALS SUITABLE FOR MARKING

	Type of method	Ease of integration	Investment	Flexibility	Abrasion resistance	Mobility	Thermal or chemical stress
Electrochemical etching	contact	low	low	low	high	high	yes
Dot peening	contact	average	low	average	high	high	no
Continuous ink jet	non-contact	high	average	average	low	high	no
Laser	non-contact	high	high	high	high	low	yes

TABLE 2

A COMPARATIVE ANALYSIS BETWEEN MARKING TECHNOLOGIES BASED ON SEVERAL FACTORS

	Steel	Cu	Ti	Al	Fe	Mg	Ceramic	Glass	Plastic
Electrochemical etching	●	●	●	●	●	●			
Dot peening	●	●		●	●				●
Continuous ink jet	●	●	●	●	●	●	●	●	●
Laser	●	●	●	●	●	●	●	●	●

## II LASER MARKING

The process of laser marking is one of the most widespread industrial applications of lasers. It can be implemented through different physical processes by interaction of laser beam with the substrate – fig. 2. Different types of lasers and optical delivery systems for transportations, focus locked, and deviation of the beam are used by laser marking systems to mark metals, ceramics, glass, plastics, leather, wood and other different kinds of materials. Laser marking is mostly in the form of an alphanumeric and 2D Data Matrix code affixed on the surface of the product, containing some information about the date of manufacture, serial number etc. [7, 8, 9, 10].



Fig. 2. Physical processes in laser marking on metals

Laser marking compared with traditional techniques for marking has not only a higher quality and flexibility of the process, but also it allows the introduction of automation and integration within production process. The main advantages of various types of laser techniques for marking are [2, 11]:

- durable process;
- non-contact technology;
- precise beam focusing;
- high speed machining;
- high contrast and quality of the treatment;
- high productivity and low operation cost;
- good accessibility, even if the surface is irregularly shaped;
- easy automation and integration in the manufacturing process;
- prompt localization of laser energy to the workpiece;
- high reproducibility;
- environmental technology.

Depending on the absorbed energy and the reaction time thermal processing is distinguished from cold treatment (UV).

Photons with high energy (UV) can realize the so-called "cold treatment", as well as they may cause

some cuts in the material by breaking the chemical bonds within the organic material, or separate a given material in some parts, without having a thermal process in the treatment zone. Laser marking by "cold processing" is a specific process that implements material removal without causing any thermal effect of the areas around cuts, i.e., no thermal damage or heat deformation, etc. effect. For example, in the industrial electronics using an excimer laser a material may be removed by a thin layer deposited on a backing of semiconductor matter.

The thermal method is based on the absorption of electromagnetic energy of the laser radiation from the sample surface and its transformation into thermal energy. The temperature in the treatment zone is increased and it is possible to realize physical processes such as heating, melting, vaporization, etc. in the area of the marking. As a result of the interaction marking can be achieved by layers deposited on the base material as well as the surface. The thermal laser processing for marking is divided into two groups - laser marking and laser engraving:

*Laser marking?*

"Laser marking" means a marking or labeling of details and materials with a laser beam. In this respect, there are various processes of implementation, such as removing of substance, coloring, annealing, foaming, etc. Depending on the material and requirement for the quality, each of these procedures has its own advantages and disadvantages.

*Laser engraving?*

During laser engraving, the surface of the workpiece is melted and evaporated. Therefore, the laser beam removes the material. So the result obtained on the surface is the "engraving".

## III TYPES OF LASER MARKING

There are several ways of the realization of laser marking on the surface of products: Raster Marking, Vector Marking and Marking using a Mask.

### A. Raster Marking

The principle is similar to a dot matrix printer, with the particularity that here the working tool is the laser beam (fig. 3). The raster marking is primarily used in cases where it is necessary to affix mainly textual information at high speed. Rarely, it is used for drawing images (photos/logos), i.e., where there is no need for high quality and high volume of information.

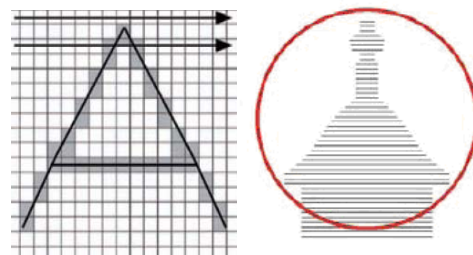


Fig. 3. Raster marking

### B. Vector Marking

This is the most widespread method of laser marking. This is the most flexible method for marking with which various applications almost anywhere in the industry that require making of numerical codes, bar codes, 2D codes, logos and almost any other kind of a desirable marking can be realized. The beam is focused onto the workpiece via an optical system (lenses and mirrors), whose management is controlled by a sophisticated computer program. Using special software, a computer controls mirrors of the galvanometer. The marking is made by directing the beam in directions x and y onto the working area (fig. 4). The beam deflection method can transmit a high density of information. The position of the laser beam and its focus can be changed in order to implement exactly the preset image without distortions or deviations. In accordance to the needs of the user, the new image is started easily by the software and the passing to marking can take away only some seconds. The most commonly used lasers for this method are in continuous mode.

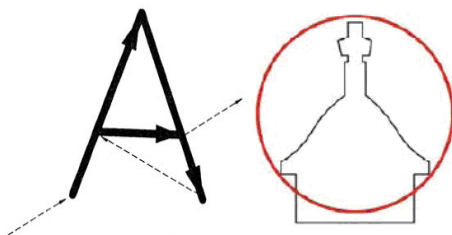


Fig. 4 Vector marking

Methods a) and b) can be implemented successfully as well as systems of plotter and such incorporating scanner fig. 5.

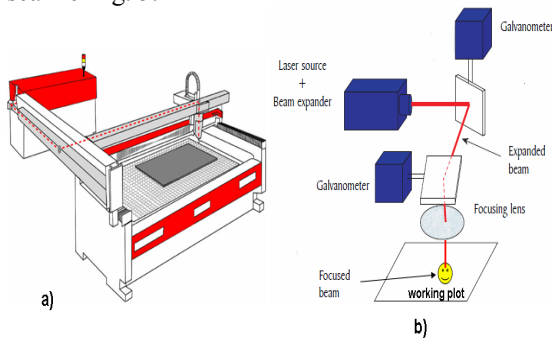


Fig.5. a) plotter system b) scanner system

### A. Projection Marking Using a Mask

A laser beam passes through a mask (template). The beam is designed by an optical system on the working area – fig. 6. The method allows the mask to be used repeatedly, thereby the processing parameters are not changed. Receiving time of the image is very short because it works in pulsed mode of the laser. Disadvantage of the projection method is that for each new task a new mask has to be prepared, i.e., lacking flexibility; more time and resources to make new

mask are necessary; time lost on another selection of appropriate technological parameters.

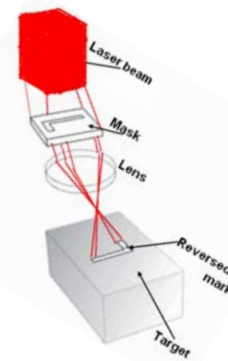


Fig. 6. Projection marking

Comparing the three marking types, it is concluded that:

- **marking speed:** the projection method for marking using mask is the highest-speed – per second up to several tens of marks. This is due to the fact that marking is made in pulse mode as the duration of laser pulses is within the range of microsecond  $\mu s$  to nanosecond  $ns$ . During the marking it is not necessary to stop the movement of the specimen.
- **working area:** A) and B) methods provide significantly bigger working area of the marking. By mask marking the marking area is very small because the diameter of beam spot is with limited sizes, as well as the energy per pulse on the mask is restricted, too.
- **flexibility:** for the projection method to produce each new mark a new mask is required. The production of a mask requires a lot of time. Therefore, the projection method is more suitable for manufacturing of large series without any change in the patterns. In beam deflected marking, the patterns are produced by software. Thus, it is highly flexible to change patterns.
- **investment cost:** investments for the realization of the methods A) and B) are higher, as the system for scanning and deflection of the beam is more expensive.

## IV MARKING METHODS IN LASER MARKING TECHNOLOGIES

The marking processes include one or a combination of the following:

- forming a channel with a smallish depth into the material by evaporation;
- a modification of the surface by melting and a subsequent solidification;
- changing the colors in the material;
- physical modification of the layers piled on the material surface;
- etc.

### REMOVING THE SURFACE LAYER

During the impact, the laser beam removes the coatings previously insisted onto the substrate (fig. 7). As a result, contrast is obtained between the substrate and the colors of the coating. Most often used materials to be plotted onto the surface are: special foils, films, laminates, anodized aluminum or coating of other metals.

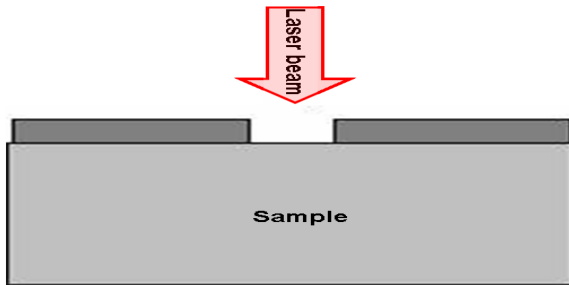


Fig. 7. A schema of removing the surface layer

### LASER ENGRAVING

For implementation of laser engraving it is necessary for material to absorb a larger amount of energy in the zone of the processing than when implementing laser marking. Removal of material by evaporation occurs in the process. With this method, engraved channel is obtained in the specimen (fig. 8) similar to that which arises as a marking in the method of the electrochemical etching. The main advantage of this laser marking method is that it can be done at high speed. Although this method appears to be the most vigorous laser marking technique, it can not be seen coloring the treatment zone as a result of the interaction. Like laser etching, direct laser engraving can be easily determined by touch or low power microscope (10X) magnification. Laser engraving is not recommended for use on parts with thickness less than 2,5 mm.

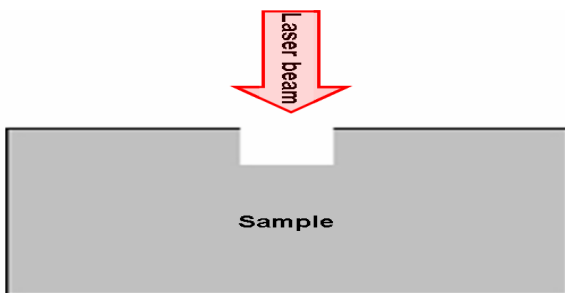


Fig. 8. A scheme of formation of a channel in the material under the action of laser radiation

### LASER THERMAL BONDING

Laser thermal bonding is a process realized by an additional material which under the heat influence generated from laser impact is coupled with the base material (fig. 9). Fine glass powder or crushed metal oxides mixed with inorganic pigments or a liquid carrier (typically water) are primarily used as additive

materials. The pigment can be applied by brush or sprayed directly onto the surface.

When using laser bonding, it is possible to transfer the coating to be implemented with a pad printer, a screen printer or a roller. For this process adhesive tape with plotting on the additional material is often used.

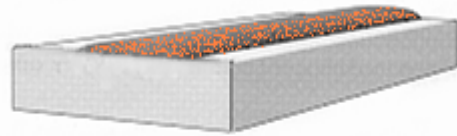


Fig.9. Material fused on a surface using the laser thermal bonding process

### LASER SURFACE MODIFICATION

Laser surface modification by melting and diffusion is done by some material preliminarily deposited onto the surface (fig. 10). As a result of the impact a new alloy with other physical and mechanical properties (e.g. corrosion-resistant and rubbing (wear)) is generated. The coating materials can be applied with a brush or sprayed with an atomizer onto the surface, as the process is realized after the drying of the layer. Unmarked areas of the coating subsequently are washed with water or a special cleaning agent. The marking symbol may be located directly in the untreated surface or on the laser treatment area. The process is well done on the surfaces of carbon steel and aluminum alloys.

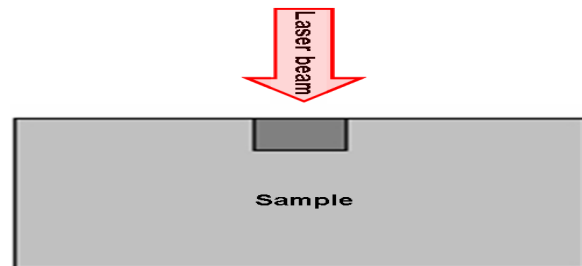


Fig. 10. A scheme of laser modifying the material

### LASER INDUCED VAPOR DEPOSITION (LIVD)

Laser induced vapor deposition is a patent pending process that is used to apply for identification markings, heating and defrosting strips, antennas, circuitry, and sun shields of gauzy materials. This is achieved by vaporizing material from a marking zone under a transparent part using the heat generated from a laser. The gaseous vapors and droplets resulting from the heat make condense on the cooler surface to form a hard uniform coating that is applied in a prescribed pattern. The process is carried out under normal conditions without a need for high heat or seal gas. The marking materials (most metals) used to produce machine-readable symbols can be formulated

to be read using optical readers and sensing devices like X-ray, thermal imaging, ultrasound, magneto-optic, radar, capacitance, or other similar sensing means.

The LIVD processes will provide another sure way to apply machine-readable marking to aerospace parts. Details of these advanced processes will be reported in updates to the future.

#### ANNEALING MARKING / LASER COLORING

Color laser marking is a special kind of laser etching for metals. The energy absorbed in the impact zone of the laser beam leads to a process of oxidation on the material surface.

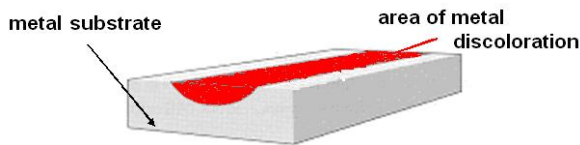


Fig.11. Marking of a surface using the laser coloring process

The process is used to change the color of metallic substrate material without burning, melting, or vaporizing the irradiated material. This is done using a laser beam with low power that moves slowly across the surface at a given speed as a result of which the marking area is changed (fig. 11). In this laser marking method a high-quality, high-contrast marking is obtained that does not destroy the surface of the specimen. A colored laser marking penetrates in deep surface roughness and allows the process to be implemented at levels of unevenness to 12,7  $\mu\text{m}$ . Laser color marking causes less damage to the surface in comparison with other methods and does not lead to corrosion of the surface and therefore it can be used for the marking of some stainless steel. These effects can be minimized or eliminated by careful selection of the parameters of the laser marking. This method of marking cannot be removed by rubbing the surface with fingers and can be successfully seen at a magnification less than ten (10X).

#### LASER ETCHING

The method of laser etching is similar to that of the laser coloring excluding that energy absorbed by the surface is sufficient here to implement the process of melting in the work area. The advantage of using this technique is that the marking process can be implemented at high speed since it is not realized to a great depth in the preparation of the colored image. Excellent results can be obtained at the depths of penetration less than 25  $\mu\text{m}$ . This technique, however, should not be used in some cases for metals because the cracks resulting from the cooling of the melt may be disseminated on surface of the basic material that can prove critical for a safe exploitation of certain details. These cracks can be extended into the material, by subjecting it to repeated cycles of

heating/cooling. In such modes of operation of this method, the details to the marking are not preferable.

#### GAS ASSISTED LASER ETCH (GALE)

Laser marking that takes place in a normal environment often has no better contrast, i.e., the difference between the engraved mark and background of the substrate is not large. This often makes it necessary to increase the time for marking (impact) and also may result in the limitation of the various materials that can be marked. Laser etching (GALE) is a technique that uses an auxiliary gas, i.e., the marking is carried out in the presence of an appropriate gas environment, thereby improving the contrast and increasing readability. The mark is done at lower values of laser power, i.e., marking on the material is realized with minimal laser treatment. GALE method achieves this through the use of an auxiliary gas that reacts with the material under the laser impact. A mark is prepared which is a different color from the background – fig. 12. The auxiliary gases might be reductive, oxidizing or even inert, such as their choice being dependent upon the target material. Contrasting surface results were achieved through optimization of the parameters of the laser source, the gas and the material.

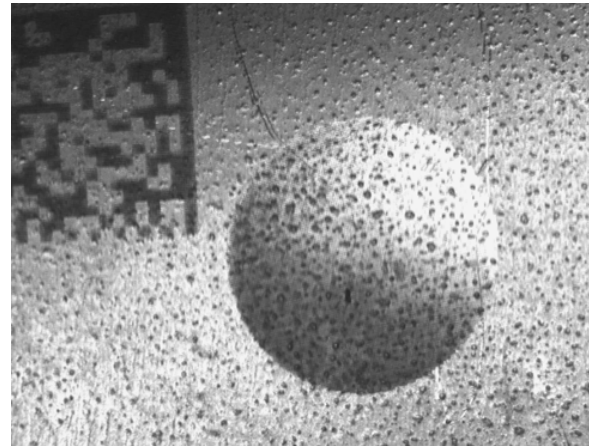


Fig. 12. View of gas auxiliary laser etch coating under magnification (Note that surface protrusions are left intact after marking) - Tests performed at the University of Tennessee Space Institute, B. H. Goethert Parkway, Tullahoma, TN 373888

## V LASERS FOR THE MARKING PROCESS

Technological schema of a system for laser marking is shown in fig. 13.

In the process various types of lasers can be used in systems [12] – see table 3. The most popular laser sources that are used in the marking technological systems are: Nd:YAG lamp-pumped lasers, which produce a light in the near infrared area at a wavelength of 1064 nm [13], and CO<sub>2</sub> lasers - at the wavelength 10600 nm.

The wavelength of Nd:YAG lasers – 1064 nm is absorbed more easily by a vast range of materials.



CO<sub>2</sub> lasers are economically advantageous for marking on condition that their wavelengths are being absorbed by the treated materials.

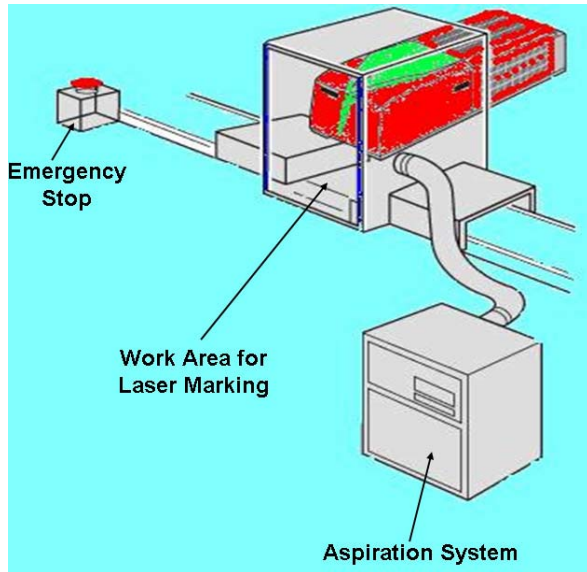


Fig. 13. A general view of the technological system for laser marking

TABLE 3

SOME LASER SOURCES USED IN THE TECHNOLOGICAL SYSTEMS FOR MARKING AND ENGRAVING

Type of laser	Wavelength $\lambda$ , nm	Power $P$ , W
CO <sub>2</sub>	10600	10÷200 W 6J/pulse when marking
Nd:YAG	1060	25÷10 W, 0.20 J/pulse when marking
Doubled Nd:YAG	532	1-3 W
Excimer	175-483	max 2 J/pulse when marking
Fiber	1062-1064	10 – 20 W
Disc	1062-1064	20-70 W

Excimer lasers also are successfully used in the laser marking [14,15]. Among all types of lasers, they shall ensure the highest resolution of the mark. But, these types of lasers are rarely used due to the low productivity of the process and the very high cost of the laser equipment. Recently, diode-pumped fiber and disc lasers have appeared, which are also successfully used for the marking process. These lasers offer high beam quality, excellent stability of the frequency, and long maintenance intervals (typically every 12,000 to 15,000 hours without service).

For any particular application of laser marking many factors should be taken into account [16,17,18,19,20,21]:

- power density  $q_s$ ;
- wavelength  $\lambda$ ;
- time of impact  $t_{proc}$ ;

- material properties;
  - thermal conductivity  $k$
  - specific heat capacity  $c$
  - melting temperature  $T_m$
  - vaporisation temperature  $T_v$
  - reflectivity  $R$  / absorptivity  $A$  for the concrete

material, wavelength and temperature.

Power density  $q_s$  is determined by the amount of power  $P$  generated by the laser divided by the area of focused beam.

$$q_s = \frac{4P}{\pi d^2}, \quad P = P_p \tau \nu$$

- where:  $P_p$  is pulsed power,  
 $\tau$  – duration of time,  
 $\nu$  – pulse frequency,  
 $d$  – diameter of working spot.

Wavelength, beam divergence and quality of optics become important factors in determining how small a focused beam can be on the work surface.

$$d_0 = M^2 \frac{4\lambda f}{\pi D}$$

- where:  $f$  is the focal length,  
 $D$  – beam diameter,  
 $M^2$  – a parameter defining the quality of the beam

(for fiber laser  $M^2 = 1.1$ , for disk laser -  $M^2 = 1.2$ , i.e., these lasers have almost perfect quality of radiation, for Nd:YAG laser –  $M^2 = 1.5 \div 2$ , for CO<sub>2</sub>-lasers –  $M^2 = 1.5 \div 2$ , for diode lasers –  $M^2 = 10 \div 20$ ).

The time of the impact of the laser beam on the material also has a significant influence on the quality of marking and the penetration depth (fig. 14).

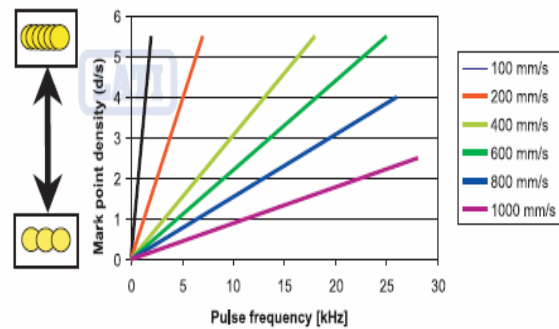


Fig. 14. Mark-point density vs. pulse rate at various beam velocities [22].

Sometimes, the pulse duration is a key factor when choosing a laser which can be used for carrying out a certain marking.

The reflectivity or absorptivity depends on the kind of the material, surface state (i.e. smooth or rugged, polish or oxidized), the wavelength of the laser radiation and the surface temperature. In general, metals absorb a larger percentage of the incident laser power of Nd:YAG lasers ( $\lambda = 1064$  nm) than that of CO<sub>2</sub> laser ( $\lambda = 10600$  nm). On the other hand, non-

metals such as wood, paper, leather, plastics, glass, etc. absorb the wavelength of the CO<sub>2</sub> lasers better. Some materials, such as silicon successfully absorbs energy from the both lasers. Laser marking is a complex technological process. For its implementation it is necessary to select the appropriate laser.

To evaluate the correct choice of a system for realizing a specific laser marking the following factors should be taken into account:

- a system for transportation of laser radiation;
- laser specification;
- system control and software;
- ergonomics - ease of operation;
- recommendations for the manufacturer;
- service guarantee and maintenance;
- the cost.

The laser specifications of different types of lasers are different. For CW lasers, the basic positions that should be required in a specification are: wavelength, average laser power, output power stability, quality factors of the beam and Q-switch mode (maximum pulse repetition rate, minimum pulse duration, laser peak power).

For pulsed lasers, the specifications should include: wavelength, average power of the laser, maximum peak power, maximum energy per pulse, pulse repetition rate, pulse duration, frequency stability, and quality of the beam.

There are many types of optical delivery systems. For mask marking processes, the systems can include: beam expander, homogeniser, CCD camera and monitor or/and microscope, and project lens. The project lens, together with the beam size entering it, determines how big a mark can be obtained per pulse. For beam deflected marking system, the system may include beam expander, CCD camera and monitor or/and microscope, scanner, fiber optics, and lens. The lens is very important in determining focused spot size, marking field, minimum marked-line width and power density on the workpiece.

The scanner together with the marking software determines the scanning speed.

Control systems and software for different laser marking systems are very different. The control system can involve feeding of the workpiece, control for switching the beam on/off, as well as interfaces for computers, laser source, stage, and protection/alarm systems. The marking software must be easy to introduce into the consumer system and provide convenient and easy interaction.

## VI CONCLUSIONS

An increasing number of companies is interested in industrial applications of laser technology, primarily in mechanical engineering, automotive and electronics. More and more new products that were made using the laser as one of the most important tools in their production have appeared in the strongly

competitive global market. Industrial laser applications, mainly for cutting, welding and marking are well established techniques.

Currently, among the different types of material processing that use laser, laser marking is one of those that found the highest prevalence. It provides a high quality of marking compared to traditional methods.

Nowadays, lasers are effective as tools for marking and engraving, as well as their application is predominate in marking of plastics, metals, alloys, silicon, ceramics. Laser technology meets the requirements for speed, quality, flexibility and price. Some of these qualities are impossible to implement with traditional technologies.

The need to process materials that have special characteristics as well as the implementation of the processes of marking in new fields of industry require the development and the production of new technological systems that will meet these requirements. The progress in the laser equipment and technology provides users with a wide range of new options for marking at a rapid pace. At present, several new lasers are under development; their appearance will result in lower investment and operating costs and will improve the quality of product marking. There are new green lasers being developed for marking special products such as silicon wafers, without damaging the base material, and lasers emitting in the blue and violet ranges of the electromagnetic waves, such that it would be possible to significantly reduce the amount of marking sign with their assistance. This leads to a continuous development in the sector of laser marking.

## VII REFERENCES

- [1] Валиулин А., С.Горный, Ю.Гречко, М.Патров, К.Юдин, В.Юревич, Лазерная маркировка материалов, Научно-технический журнал Фотоника, выпуск № 3/2007, с.16-22
- [2] Schüböcker D. Handbook of the EuroLaser Academy, CHAPMAN&HALL, London, 1998
- [3] Danotre, N, N. B., Harimkar, S. P.: Laser Fabrication and Machining of Materials, Springer, New York, USA, 2008.
- [4] Steen, W. M.: Laser Material Processing. Springer-Verlag, New York Berlin Heidelberg, 1991
- [5] Mihaela NISTORAN-BOTIS, Dinu GUBENCU, Glass etching, Proceedings of the 3rd International Conference RaDMI 2003, 19-23 September 2003, Herceg Novi, Serbia and Montenegro
- [6] N. N.: Elektroerosive Bearbeitung - Begriffe, Verfahren, Anwendung. VDI-Richtlinie VDI 3400. Verein Deutscher Ingenieure, Düsseldorf. Artikel: DK 621.9.048.4 (083.132). Jahrgang 06/1975
- [7] Григорьянц А.Г., Шиганов И.Н., Мисюрлов А.И., Технологические процессы лазерной обработки, – М., Издательство МГТУ им. Н.Э. Баумана, 2006
- [8] Горный С.Г., Емельченков И.Р. Лазерная маркировка. В кн.: Лазерная технология и ее применение в металлообработке. – Л.: ЛДНТИ, 1990, с.42–47.
- [9] J. QI, K.L. WANG, Y.M. ZHU, A study on the marking process of stainless steel. Material Processing Technology, 139, 2003, p. 273-273 Vol.
- [10] Lazov L., and others., Optimization of the Process of Laser Marking of Products Made of Tool Steel, Metallofizika I

- Noveishie Tekhnologii, 2012, ISSN 10241809 Vol. 34, №8, pp 1125-1131
- [11] Wolf E. Flexibel und genau, Wolf Productionssysteme, Prooductionic, 4/2006
- [12] Горный С.Г., Юдин К.В. – Индустрия, 2006, №1(43), с.20–21.
- [13] Wang, W; Wang, L.; Guo, N.; The research and development of a Nd:YAG laser engraving system, SPIE vol. 2888, p. 207-212 (1996)
- [14] K. CALLEWAERT s.a., Excimer laser induced patterning of polymeric surface. Applied Surface Science, Vol. 209, 2003, p. 55-62.
- [15] N.N, Single Mode Fiber Lasers for Industrial and Scientific Applications. 2008, IPG Photonics Corporation
- [16] T.W, NG, S.C. YEO, Aesthetic laser marking assessment. Optics and Laser Technology, Vol. 32, 2000, p, 187–191
- [17] D.R. ALEXANDRE, M.S. KHLIF, Laser marking using organo-metallic films. Optic and Laser in Engineering, Vol. 2, 1996, p. 55–70.
- [18] Горный С.Г., Емельченков И.Р. Лазерная маркировка. В кн.: Лазерная технология и ее применение в металлообработке. – Л.: ЛДНТП, 1990, с.42–47.
- [19] L. Lasov, Atanasov A., Angelov N., Investigation of the role of certain factors affecting the contrast in laser marking, Journal of the Academy of Sciences and arts of the Republic of Srpska, Contemporary Materials, II -1, 2011, S, 13-17
- [20] Lazov L., Stojanova P., Die Rolle der optischen und thermischen Eigenschaften des Targets bei Lasermaterialbearbeitung, Journal of Applied Sciences Mittweida 2000, ISSN 1437-7624 N 14, Band K Lasertechnik S. 192-200
- [21] Lazov L., N. Angelov, Investigation of the Impact of the Number of Repetitions and the Defocus on the Contrast of Laser Markings for Products Made of Tool Steel, Metallofizika I Noveishie Tekhnologii, 2012, ISSN 10241809 Vol. 34, №7, pp 1003-1011
- [22] Laser Marking, High Performance Thermoplastics LATI, printed by C&I Italy, 2008 S.5

# The Influence of the Technological Process on the Surface Quality and Tribological Properties of Powder Details

Armands Leitans<sup>1</sup>, Irina Boiko<sup>1</sup>, Janis Lungevics<sup>1</sup>, Viktors Mironovs<sup>2</sup>

<sup>1</sup>Riga Technical University, Faculty of Transport and Mechanical Engineering, Institute of Mechanical Engineering, Address: Ezermalas 6k, Riga, LV-1006, Latvia

<sup>2</sup>Riga Technical university, Faculty of Civil Engineering, Scientific Laboratory of Powder Materials, Azenes 16/20, LV-1048, Riga, Latvia

**Abstract.** Nowadays the materials made by methods of powder metallurgy are widely used for producing details of the heavy-duty friction pair. Due to high reliability and effective combination of mechanical and tribological properties such materials are usually used in transport industry, for example for gear assemblies of different kinds of automobiles, brake system of high speed trains, aircrafts etc. There are many variations of powder materials, but for friction pairs the iron based antifriction materials, for example Fe-C-Cu, Fe-P, Fe-Cu-Sn, Fe-Cu-Sn-Pb-MoS<sub>2</sub>, Fe-C-Cu-Ni-Mo and others are successfully used. In recent years, the requirements for antifriction materials are raised highly because of more intensive freight traffic and speed of vehicles. On the other hand, the demand of more inexpensive materials and effective using of natural resources is the issue of the day.

The aim of this paper is to offer the new low-cost metal powder material based on Fe-C compound with content of Ni and Mo up to 0.3%. The influence of the parameters of technological process (pressing and sintering) on physical properties (porosity, density), mechanical properties (hardness) as well as on 2D roughness and 3D texture parameters was studied and is presented in this paper as well. The "Taylor Hobson Ltd" 3D measurement system has been used in metrological study. The analysis of the influence of the technological process on the surface roughness parameters is given. The tribological properties (friction coefficient) were evaluated using "ball-on-disk" testing without lubrication. The analysis of achieved results is prove the appropriateness of using of new low-alloy metal powder material on the iron base for producing details of friction pair. One of the possible applications - bushes for braking systems of railway rolling stock. Using offered material allows reducing the product cost in complex with acceptable wear resistance and durability.

**Keywords:** materials testing, surface roughness, friction.

## I INTRODUCTION

Powder Metallurgy (PM) is a materials processing technology to create new materials and parts by diffusing different metal powders as raw ingredients through the sintering process after mixing and compacting. PM has grown with the expansion of various industries since middle of 20th century. Nowadays, over 90% PM products including details of the heavy-duty friction pairs like automotive braking systems are used in the transportation market of all kinds (air, ground and water transport) [1].

Modern tribomaterials consist of composites made by PM with metallic matrix from iron, copper or aluminum reinforced with a) friction components (as oxides: Al<sub>2</sub>O<sub>3</sub>, ZrO<sub>2</sub>, SiO<sub>2</sub>, carbide: TiC, SiC, B<sub>4</sub>C, nitrides: TiN, Si<sub>3</sub>N<sub>4</sub>) with role of friction and improving of the wear resistance and b) lubrication components (graphite, molybdenum disulfide, etc.), with the role of increasing material resistance to

gripping and for wear reduction of disc (rotor) brake [2]. Iron and copper have been used extensively for various tribological applications [1] - [3]. The copper and iron-based antifriction materials are most often fabricated using PM technique due to its many advantages such as the elimination of solidification induced chemical segregation and structural defects often accompanied with melting and solidification processes. The ease in mixing of different powders leads to the possibility for developing new composite materials with special physical and mechanical properties that are otherwise difficult to manufacture [3].

In the recent years iron-based sintered bearings production was considerably increased at the expense of the copper-based ones, due to the low cost and availability of the iron powders as well as their higher strength [4], [5]. It should be mentioned here, that mixtures of iron and copper powder have a twofold

benefits: 1) copper melts at 1094°C, i.e. below sintering temperature, and rapidly infiltrates the pore system of the compact from where it diffuses relatively easily into the iron powder particles; 2) copper is dissolvable in  $\gamma$ -iron (austenite) up to approx. 9 wt.-%, but only up to 0,4 wt.-% in  $\alpha$ -iron (ferrite); consequently, iron-copper alloys can be precipitation-hardened by low-temperature annealing after sintering – and actually do so to a certain extent already on passing the cooling zone of the sintering furnace [6].

Good results were achieved by adding nickel and molybdenum, but the costs of such elements rise rapidly in recent years [1]. In some cases the cost of expensive alloying elements can be avoided and micro-alloying can be applied. In micro-alloying the amount of additive usually is from 0.1 to 5%. Some authors assumed that dispersed additives have great potential for microalloying and nanoalloying [1], [7], [8]. Thus, the introduction of nanopowders of copper or copper-iron ligature into a powder iron-based material has led to an increase in strength, hardness, density, and to reduce in sintering temperature [8].

The demand of more inexpensive antifriction materials and effective using of natural resources is the issue of the day. The aim of this paper is to offer the new low-cost metal powder material based on Fe-C compound with content of Ni and Mo up to 0.3%.

It is known that the quality of contact surfaces together with dimensional tolerance and properties of powder parts are very important for tribological applications [9] - [11]. Surface condition of powder parts on the different stages of producing is the important factor that influences on the exploitation properties and running ability of product. The investigation of the influence of the technological process (pressing and sintering) on surface quality and tribological properties of powder parts produced from new micro-alloyed powder material was done for proving the possibility of using such material for producing the details for the friction pairs.

## II MATERIALS AND METHODS

The view of fragments of powder parts after different stages of production (two-side compacting and following sintering) is shown on Fig. 1.

For investigation the following powder mixture (from powders produced by „Höganäs AB”, Sweden) was used (mass %): Fe 96.5%, Ni 0.22%, Cu 2.27%, Mo 0.28%, S 0.04%, P 0.01%, C 0.6%, Kennolube (graphite lubricant) 0.7%. The main properties of offered low-alloy metal powder material are the following: apparent density 3.15 g/cm<sup>3</sup>; flow 40 sec/50g; compressibility 6.80 g/cm<sup>3</sup>. Powder parts (Fig. 1) were produced by the following steps: 1) two-side compacting was carried out on the hydraulic press in the closed die at pressure up to 600 MPa;

2) sintering was realised in the endogas atmosphere at the temperature 1120°C, retention time 40 min.



Fig.1. Fragments and view of powder parts after compacting (H1) and following sintering (S2): outer diameter 25 (45) mm, inner diameter 11 (29) mm, length 22 (31) mm correspondingly.

After compacting the porosity of powder parts was up to 23 %, density – up to 6.9 g/cm<sup>3</sup>. Sintered density of the parts was up to 7.1 g/cm<sup>3</sup>, porosity 20%, tensile strength 300 MPa, hardness HV10 98÷100. Methodology for the investigation of the properties of powder parts which was used in our investigation is given in [12].

For metrological study of surface quality of the powder parts on the different stages of producing (after compacting and after compacting and sintering) the “Taylor Hobson Ltd” 3D measurement system was used. This system allows roughness and waviness filtration out of measured (primary surface) that gives better understanding of surface structure and manufacturing process as well it can be used for creating surface 3D photo simulation images etc. 2D and 3D measurements with stylus instrument were achieved by basic “stepping” method (Fig. 2) and data processing by computer [13].

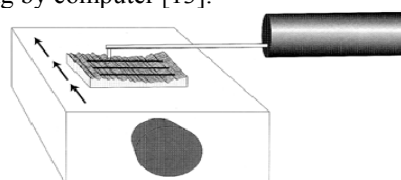


Fig.2. Principal scheme of basic “stepping” method used by stylus systems [13].

Tribological study was done using tribometer made by “CSM Instruments” (Switzerland), besides testing conforms to the following standards DIN 50324 “Tribology; testing of friction and wear model test for sliding friction of solids (ball-on-disc system)”, ASTM G99 “Standard test method for wear testing with a pin-on-disk apparatus” and ASTM G133 “Standard test method for linear reciprocating Ball-on-flat sliding wear”. The friction coefficient was evaluated using “ball-on-disk” testing without lubrication, when the tested example was used as a disc, but a high-strength steel ball was used as a counter-body. The principal scheme of testing is

shown on Fig. 3. Experimental settings are shown in Table I.

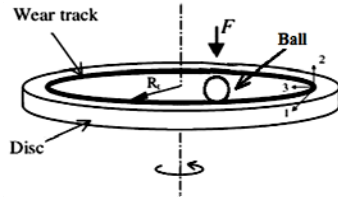


Fig.3. Principal scheme of ball-on-disk testing: F is the normal force applied on the ball, R is the radius of the wear track.

TABLE I  
EXPERIMENTAL SETTINGS

Testing parameters:	Value/type of testing parameters:
Force	3 N
Measurement period	20 s
Linear velocity	0.05 m/s
Radius of ball's contact	3 mm
Distance	1 m
Diameter of the ball	6 mm
Material of the ball	100Cr6 (DIN EN ISO 683-17)
Material of the sample	H1, S2
Liquid for surface cleaning	Alcohol solution
Atmosphere	Air
Temperature	21°C (room)
Moisture	46% (room)

### III RESULTS AND DISCUSSION

The influence of the technological process on the surface quality and tribological properties of powder parts, produced from new low-cost metal powder material, was investigated by measurement and comparison of the average 2D roughness parameters and 3D (surface) texture parameters of powder parts after compacting and following sintering and by measurement and analysis of the friction coefficient as well.

#### A. 2D roughness parameters

The 2D amplitude roughness parameters (according to ISO 4287 “Surface texture: Profile method - Terms, definitions and surface texture parameters”) Ra - arithmetic mean roughness and Rz - maximum height of profile were measured. Comparison of 2D amplitude roughness parameters of powder parts on the different stages of producing is given in Table II. As shown the Ra and Rz values increases after sintering.

Some researches assume, that surface texture metrology gives a better understanding of the surface in its functional state since in practical applications surface roughness of the machine parts behaves as a 3D object [14] - [17].

TABLE II  
COMPARISON OF 2D AMPLITUDE ROUGHNESS PARAMETERS

Powder parts after:	Ra, $\mu\text{m}$	Rz, $\mu\text{m}$
compacting	1.56	7.76
sintering	2.37	11.2

#### B. 3D texture parameters

Achieved 3D surface images of the powder parts after compacting and following sintering are given on Fig. 4 and Fig. 5 respectively. The following 3D texture parameters (according to EN ISO 25178-2 “Surface texture: Areal - Part 2: Terms, definitions

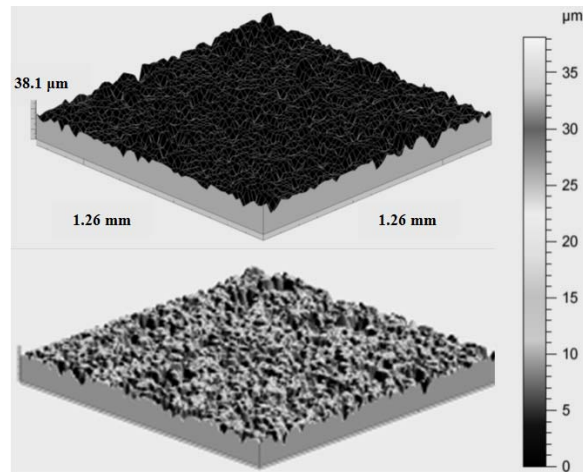


Fig.4. View of the 3D surface image and photo simulation of the powder part after compacting.

and surface texture parameters” and [13]) were measured and analyzed: 1) amplitude parameters: Sa, Ssk; 2) spatial parameter: Str, 3) functional (material volume) parameter: Vmc, 4) hybrid parameter: Sfd. Such choice of texture parameters is based on its essence and significance for friction surfaces of the powder parts:

- Sa - arithmetic mean of the deviations from the mean plane, represent an overall measure of the texture comprising the surface;
- Ssk - skewness of the scale-limited surface, represents the degree of symmetry of the surface heights about the mean plane;
- Str - texture aspect ratio of the surface, measures the isotropy of surface;
- Vmc - core material volume of the scale-limited surface, indicate a measure of the material forming the surface between various heights;
- Sfd - fractal dimension of the surface (complexity of the surface), smaller value specifies the more periodical surface (different from the random surface).

Comparison of the mentioned 3D texture parameters of powder parts after compacting and following sintering is given in Table III.

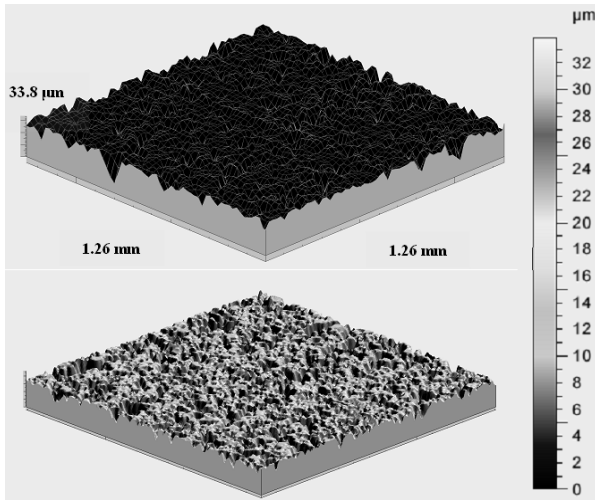


Fig.5. View of the 3D surface image and photo simulation of the powder part after sintering.

TABLE III  
COMPARISON OF 3D TEXTURE PARAMETERS

Powder parts after:	Sa, μm	Ssk	Str	Vmc, mm <sup>3</sup> /mm <sup>2</sup>	Sfd
compacting	3.06	-1.39	0.706	0.0174	2.57
sintering	2.65	-1.56	0.766	0.0187	2.56

As distinct from 2D amplitude roughness parameters the 3D texture amplitude parameter Sa decreases after sintering. As was mentioned earlier it could be explained by more adequate measurement results using surface texture metrology. The high values of the hybrid parameter Sfd (close to 3 - maximum value of Sfd) partially confirm such hypothesis: deterministic-chaotic surface like surface of porous powder material after compacting and sintering cannot be adequately characterized by standard 2D roughness parameters.

An important point is that the surface after sintering is more isotropic since the value of parameter Str is closer to 1 (maximal value of Str). The reason for these changes of surface condition could be argued by shrinkage of powder material during sintering. So in future we can use measurement results not only for evaluation of details quality, but for prediction of shrinkage and consequently for pressing equipment design and choosing of sintering regimes.

The highest value of functional parameter Vmc prove the better bearing ability of surface after sintering due to greater core material volume in contact during normal exploitation time (after wear-in).

On the other hand the negatives values of amplitude parameter Ssk - surface after compacting and following sintering is characterized by negative skeweness - confirm good lubricant retention ability.

We can assume that the values of 3D texture parameters, especially for surface of powder part after sintering, open up wide possibilities of using new low-alloyed powder material.

### C. Friction Coefficient

The friction coefficient as a function of time and length of friction path for compacted and sintered powder parts is shown in Fig. 6 and Fig. 7 respectively.

In both cases the stable curve of friction coefficient with relatively small fluctuation along length of friction path is observed. Average value of friction coefficient for compacted sample is  $\mu = 0.14$ , but for sintered sample  $\mu = 0.22$ .

After the testing of friction the visual examination of the surfaces of samples was done. As a result of visual examination it could be stated, that during testing the standard friction process occur, because no any trace of wear or plastic deformation of surface were founded out.

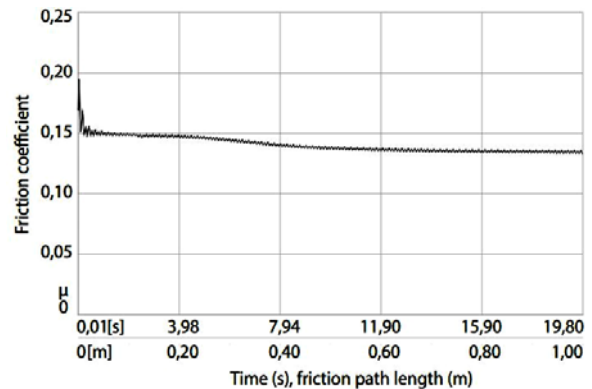


Fig.6 The friction coefficient as a function of time and length of friction path for compacted powder part.

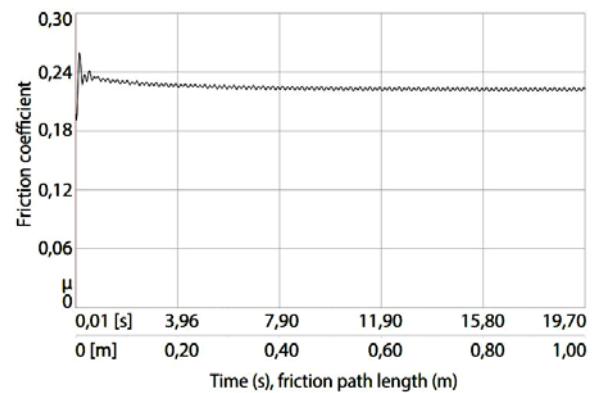


Fig.7 The friction coefficient as a function of time and length of friction path for sintered powder part.

#### IV CONCLUSIONS

The new low-cost metal powder material based on Fe-C compound with content of Ni and Mo up to 0.3% is offered. The powder details from this material could be produced by conventional PM technology consists of two-stage compacting and following sintering.

The complex testing of powder parts on the different stages of producing was done including evaluation of physical and mechanical properties (porosity, density and hardness), measurement and analysis of 2D roughness parameters, 3D texture parameters and friction coefficient as well.

It was hypothesized, that different character of changes of 2D and 3D amplitude parameters could be explained by the premise that the 3D metrology is more suitable for exploring deterministic-chaotic surfaces like surfaces of porous powder parts. Received values of 3D texture parameters show, that the surface of powder parts is isotropic with good lubricant retention ability and bearing ability. Appropriateness of using of new low-alloy metal powder material on the iron base for producing details of friction pair confirms the relatively small friction coefficient (after sintering 0.22) as well. One of the possible applications - bushes for braking systems of railway rolling stock. Using offered material allows reducing the product cost in complex with acceptable wear resistance and durability, which could be predicted taking into account favorable results of metrological and tribological studies.

#### V ACKNOWLEDGEMENT

This work has been supported by the Latvian Council of Science within the Project Nr. 110/2012 "Titanium compound wear-resistant nano-coatings in mechanical engineering". In this work the RTU student Pavels Stankevics was involved.

#### VI REFERENCES

- [1] T. Tsutsui, "Recent Technology of Powder Metallurgy and Applications," Hitachi Chemical Technical Report, No.54, 2012.
- [2] I. N. Popescu, V. Bratu, F. V. Anghelina and L. G. Toma, "The Effect of Wear Test Parameters on Tribological Characteristics of Aluminium Based Composites," The Scientific Bulletin of Valahia University - Materials and Mechanics, Nr. 6 (year 9), pp. 83-86, 2011.
- [3] S.-Z. Chen, J.-H. Chern Lin and C.-P. Ju, "Effect of Aluminum Content on Tribological Behavior of a Cu-Fe-C Based Friction Material Sliding against FC30 Cast Iron," *Materials Transactions*, vol. 44, No. 4, pp. 787-793, 2003.
- [4] C. Teisanu and S. Gheorghe, "Development of New PM Iron-Based Materials for Self-Lubricating Bearings," Hindawi Publishing Corporation, *Advances in Tribology*, 2011.
- [5] Z. Shi, P. Jian, P. Xue and D. Chen, "The Friction and Wear Characteristic of Iron-based Powder Metallurgy Materials in Scroll Compressor," *Proceedings of 21st International Compressor Engineering Conference at Purdue*, July 16-19, 2012, West Lafayette, Indiana, USA, West Lafayette: 2012.
- [6] "Sintered Iron-Based Materials," Höganäs PM-school, [Online]. Available: <http://riad.pk.edu.pl/~mnykiel/iim/KTM/> [Accessed: Nov. 11, 2014].
- [7] A. Ilyushchenko and V. Savich, "Powder Metallurgy in Belarus: Overview 2008-2013," *Proceedings of 8th International Scientific Conference "Materials, Environment, Technology MET-2013"*, June 19-20, 2013, Riga, Latvia, Riga: RTU. 2013.
- [8] F. A. Sadykov, N. P. Barykin, I. R. Aslanyan "Wear of copper and its alloys with submicrocrystalline structure," *Wear*, vol. 225-229, pp. 649-655, 1999.
- [9] J. W. Kaczmar, K. Granat, E. Grodzka and A. Kurzawa, "Tribological Properties of Cu Based Composite Materials Strengthened with Al<sub>2</sub>O<sub>3</sub> Particles," *Archives of Foundry Engineering*, vol.13, special issue 2, pp. 33-36, 2013.
- [10] C. Yang, "Role of Surface Roughness in Tribology: from Atomic to Macroscopic Scale," *Key Technologies Band*, Volume 7, 2008.
- [11] A. Y. Suh, A. A. Polycarpou and T. F. Conry, "Detailed Surface Roughness Characterization of Engineering Surfaces Undergoing Tribological Testing Leading to Scuffing," *Wear*, vol.255, pp. 556-558, Aug. 2003.
- [12] L. N. Dyachkova, L. F. Kerzhentseva and L. V. Markova, *Powder iron-based materials*, Minsk: Belaruskaya navuka, 2004.
- [13] "Exploring Surface Texture," Taylor Hobson Ltd., 4th Edition Leicester, 2003.
- [14] J. Petzing, J. Coupland and R. Leach, "The measurement of rough surface topography using coherence scanning interferometry," *Good practice guide*, No.116, National Physical Laboratory, Hampton Road, UK, 2010.
- [15] E.B. Las Casas, F.S. Bastos, G.C.D. Godoy, and V.T.L. Buono, "Enamel wear and surface roughness characterization using 3D profilometry," *Tribology International*, vol. 41, 2008.
- [16] O. Linins, J. Krizbergs and I. Boiko, "Wear Estimation using 3D Surface Roughness Parameters," *Key Engineering Materials, Engineering Materials and Tribology*, vol. 527, pp. 167-172, 2013.
- [17] A. Zawada-Tomkiewicz, "Analysis of surface roughness parameters achieved by hard turning with the use of PCBN tools," *Estonian Journal of Engineering*, vol. 17, pp. 88-99, 2011.



# Mathematical Model of Friction Coefficient Determination for Lubricated Surfaces

Armands Leitans, Janis Lungevics

Riga Technical University, Faculty of Transport and Mechanical Engineering, Institute of Mechanical Engineering, Ezermalas str. 6k Riga, LV-1006, Latvia

**Abstract.** This article reviews mathematical model for the determination of friction coefficient for sliding friction pair for lubricated surfaces in case of friction of boundary lubrication. The given case examines contact of an absolutely smooth ball and flat rough surface taking into consideration properties of the material, surface roughness parameters, as well as kinematic viscosity and density of lubricating material. The model refers to widely spread ball-on-disc type tribometer measurements for ball and plane contact.

**Keywords:** friction coefficient, boundary friction, sliding friction.

## I INTRODUCTION

This article examines a mathematical model for the determination of friction coefficient for sliding friction pairs of lubricated surfaces. In the particular model contact of absolutely smooth ball and flat rough surface is regarded as a friction pair taking into consideration mechanical properties of the material and surface roughness parameters, as well as kinematic viscosity and density of lubricating material. The model refers to widely spread ball-on-disc type tribometer measurements where ball is in the contact with plane. Specification of tribometer meets tribological measurement standard [1]. In the given case mathematical modelling of friction process is being carried out, which helps to describe theoretically the effect of additive to parameter influencing friction coefficient, the mathematical model is based on the experimental work described in the publication [2].

## II MATHEMATICAL MODEL OF FRICTION COEFFICIENT DETERMINATION FOR LUBRICATED SURFACES

Rotary moving parts, lubricated surface friction is shown by Strybeck curve [3] the character of which is given on Fig. 1. It shows a simplified version of the change of friction coefficient  $V_d$  depending on the Hersy Index  $\frac{V_d \cdot n}{q}$ , where  $V_d$  – dynamic viscosity of oil,  $n$  – speed of rotation,  $q$  – load per an area unit. The Strybeck curve is divided into three parts and each part characterises a separate friction mode:

- I – hydrodynamic friction,
- II – mixed friction,
- III – friction of boundary lubrication.

In mode I two hard surfaces are separated by an uninterrupted oil layer, where thickness of oil layer  $h$  is more than the height of surface roughness  $R_t$ .

Since in this case there is no direct contact between surfaces 1 and 3 it, can be regarded that there are no friction processes between surfaces. Part II of the curve that characterises mixed friction shows that only a part of load is received by oil layer and partly also by peaks of roughness of both surfaces. Thickness of oil film  $h$  is approximately similar to the height of surface roughness  $R_t$ .

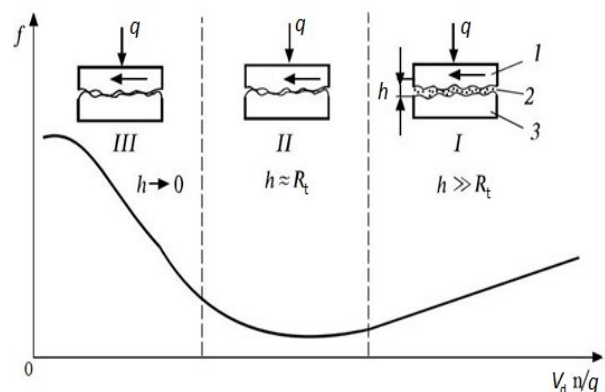


Fig. 1. Diagram of Strybeck curve and zones of lubrication modes ( $h$  - thickness of lubrication layer,  $R_t$  - height of roughness).

In case of part III of the curve, i.e. in case of boundary lubrication thickness of lubricating material being in contact turns very thin and load is fully received by surface roughness peaks that are covered with a thin oil layer.

Based on the parameters characterising the Strybeck curve we can write the respective friction coefficient formula:

$$f = \alpha \cdot \frac{V_d \cdot n}{q} \quad (1.1)$$

where  $V_d$  - dynamic viscosity;  
 $n$  - rotation speed;  
 $q$  - load per an area unit;  
 $\alpha$  - coefficient of correction determined experimentally;

In practice when determining viscosity of lubricating material at different temperatures the most often there is being used kinematic viscosity  $V_k$ , which is determined using the following formula:

$$V_k = \frac{V_d}{\rho} \quad (1.2)$$

where  $\rho$  - density of lubricating material;  
 $V_k$  - kinematic viscosity;

Thus the friction coefficient can be rewritten by the following formula.

$$f = \alpha \cdot \frac{V_k \cdot \rho \cdot n}{q} \quad (1.3)$$

Formula (1.3) shows that friction coefficient depends on kinematic viscosity  $V_k$ , density of lubricating material, rotation speed  $n$  and load  $q$ . Studying the effect of oil additive the only variable value is kinematic viscosity  $V_k$  because other parameters are characteristic quantities of experiment.

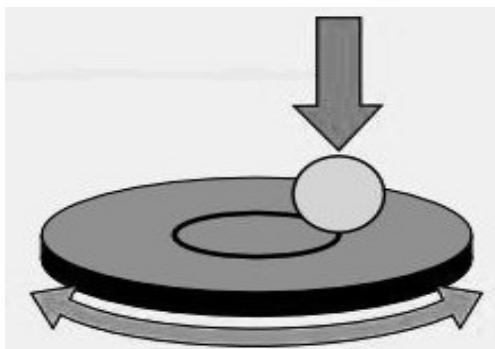


Fig.2. Contact diagram of friction surfaces according to tribometer.

The given paper envisages studying of the effect of oil additives by tribometer *CSM Instruments*, the design of which envisages contact of ball with a flat

surface, therefore it is necessary to study this contact (see Fig. 2). Formula (1.3) comprises parameter  $q$ , which can be determined applying the contact provisions of friction surfaces.

### III CONTACT OF ABSOLUTELY SMOOTH BALL AND FLAT ROUGH SURFACE

The surface contact theory envisages an area arising when solid body deforms rough surface [3];

$$\eta = \frac{A_r}{A_a}, \quad (1.4)$$

where  $A_r$  - actual contact area including roughness;  
 $A_a$  - nominal area to be determined according to component dimensions.

With flat components the nominal area is equal to nominal dimensions of contacting surfaces. The nominal area of ball in contact with a plane will be the area of side surface of ball settling that is in contact with material (Fig. 3)

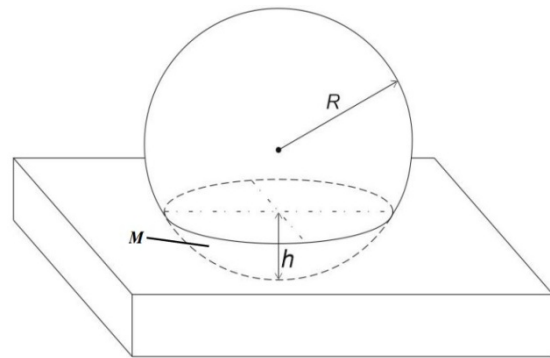


Fig.3 . Contact diagram of settled ball

According to [4] the side area of the ball  $M$  is equal to

$$M = 2\pi R h \quad (1.5)$$

where  $R$  - ball radius;  
 $h$  - height of the settled part;

In *CSM* tribometer a ball having a constant radius ( $R=3\text{mm}$ ) has contact with a rough flat surface. In the existing contact theory such characteristic dimensions of contact have not been established. Therefore we will replace ball - plane contact with the contact of two planes. For this pupose we use graphical simulation of contacts (Fig.4)

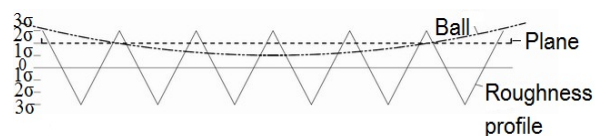


Fig. 4 Contact of ball with rough flat surface

This simulation compares the contact of ball with a rough flat surface if the top of the ball reaches the level of surface roughness  $1\sigma$  counted from the mid-line with the contact of a plane and rough surface, but plane during contact reaches level  $2\sigma$  counting from the mid-line.

The result shows that at the roughness parameter  $R_a = 0,12-0,18 \mu\text{m}$ , contact area of ball – rough plane differs from an ideal plane - rough plane contact not more than by 5%.

It should be noted that for the purpose of visuality Fig.4 gives a schematic picture of rough surface, yet simulation of actual contact includes actual character of roughness with correct roughness step parameters.

Since the surface roughness  $R_a$  of the experimental sample of the given paper satisfies this provision we can use formulas obtained in this work [5] in case of contact of two plate.

In case of an elastic contact, arising when tribometer's steel ball contacts with a flat disk load per an area unit  $q$  can be calculated according to formula;

$$q_{el} = k_q^{el} \frac{S_a}{R_{Sm1} \cdot \theta} F_1(\gamma), \quad (1.6)$$

where  $S_a$  – 3D surface roughness mean arithmetic deviation ;

$R_{Sm1}$  - surface roughness steps perpendicular to the direction of surface treatment (in general case);  
 $\theta$  – elastic contact constant.

$$\theta = \frac{1-\mu^2}{\pi E} \quad (1.7)$$

where  $\mu$  – Poisson's ratio of deformed material.

$E$  – elasticity modulus of deformed material.,

$k_q^{el}$  - coefficient considering surface roughness anisotropy;

$$k_q^{el} = \frac{2}{3} \sqrt[4]{\frac{\pi}{2} \cdot \frac{\pi}{K(e)} \left[ \frac{E(e)}{K(e)} \right]^{\frac{1}{2}} \cdot \frac{(1-e^2)^{-\frac{1}{8}}}{[1+(1-e^2)^{\frac{3}{4}}]^{\frac{1}{2}}}} \quad (1.8)$$

where  $e$  – eccentricity of contact area;

$K(e)$  and  $E(e)$  – elliptic integrals [4];

$$e^2 = 1 - c^{\frac{8}{3}}, \quad (1.9)$$

Value  $c$  is obtained from the relation of surface roughness steps;

$$c = \frac{R_{Sm1}}{R_{Sm2}} \quad (1.10)$$

$R_{Sm1}, R_{Sm2}$  – roughness steps perpendicular to and along treatment directions.

$F_1(\gamma)$  - tabulated function of parameter  $\gamma$  where;

$\gamma$  – deformation level counted from the mid - plane of roughness.

Since the load envisaged in the experiment on the sample is 3N (see 1.3), it can be predicted, that in the flat sample deformations, take place in the upper layers, i.e. deformation level  $\gamma \geq 2$ .

At  $\gamma \geq 2$ , according to [6]

$$F_1(\gamma) \leq \frac{1}{40\gamma} \leq \frac{1}{40 \cdot 2} \leq \frac{1}{80};$$

In the given case formula (1.6) is considerably simplified, because surfaces have isotropic roughness, where  $c=1$  and  $e=0$ , and value of coefficient  $k_q^{el}$  is  $k_q^{el} = 0,85$ .

Inserting the above values in formula (1.7)

$$q_{el} = 0,01 \frac{S_a}{R_{Sm} \cdot \theta} \quad (1.11)$$

Inserting formula (1.11) in the expression (1.4) we obtain the final formula for the calculation of friction coefficient:

$$f = 1,7 \cdot \alpha \frac{V_k \cdot \rho \cdot n \cdot R_{Sm} \cdot \theta}{S_a} \quad (1.12)$$

Values included in the formula (1.12) have the following measuring units:

$V_k$  - kinematic viscosity ( $\text{m}^2/\text{s}$ ),

$\rho$  – density ( $\text{kg}/\text{m}^3$ ),

$n$  – rotation speed (1/s),

$R_{Sm}$  – surface roughness step parameter ( $\mu\text{m}$ ),

$S_a$  - surface roughness ( $\mu\text{m}$ ),

$\theta$  – elastic contact constant ( $\text{Pa}^{-1}$ );

At the given measuring units we get non-dimensional value of friction coefficient  $f$ .

To compare the experiment with the theory we use formula (1.12). This formula includes non-dimensional coefficient a characterising sample friction in case when oil has no additives.

According to formula (1.12) we get the following expression:

$$\alpha = \frac{f \cdot S_a}{1,7 \cdot V_k \cdot \rho \cdot n \cdot R_{Sm} \cdot \theta} \quad (1.13)$$

#### IV CONCLUSIONS

The given mathematical model, can be used, for the comparison of results obtained during friction coefficient experiments with theoretical values. Taking into consideration the parameter of kinematic viscosity of lubricating material, at different concentrations of additives, determining viscosity experimentally. It can be concluded, from the model that influence of additives, can be strongly affected by the kinematic viscosity of lubricating material, which can affect the friction coefficient of lubricated friction pair.

V REFERENCES

- [1] ASTM G99 – 05 Standard Test Method for Wear Testing with Pin-on-Disc apparatus 2010.
- [2] *Leitans A, Springis G, Rudzitis J, Semjonovs J, Berezins G*, Determination of coefficient of friction for different oil additive concentrations in automotive oil , 10th International Conference Mechatronic Systems and Materials. Conference proceedings, Opole 2014
- [3] *George E. Totten, Simon C. Tung* Automotive lubricants and testing .
- [4] *Бронштейн И.Н., Семендяев К.А.* Справочник по математике для инженеров и учащихся вузов, 1981.
- [5] *Рудзитис Я.*, Контактная механика поверхностей 2ч, Рижский технический университет, 2007
- [6] *Konrads G.*, Mašīnu detaļu slīdes virsmu dilšana; Rīgas tehniskā universitāte , 2006.
- [7] *Kragelskiy I., Alisin V.* Tribology – Lubrication, Friction and Wear. MIR publishers Moscow, 2001

# Adaptive control of the indentation made by the drilling tool

Angel Lengerov

Technical University of Sofia, Branch Plovdiv, Faculty of Mechanical Engineering,  
 Address: Tsanko Diustabanov 25, Plovdiv, 4000, Bulgaria.

**Abstract.** The objective of this study is to determine the advisability of introducing adaptive control of the indentation made by the drilling tool depending on the structural characteristics of the processed part. In the cases when the adaptive control is economically advisable, the selection of the technological cycle and the speed of moving of the tool can be achieved by the implementation of the respective algorithm for optimization of the dimensions fed for drilling.

**Keywords:** engage, adaptive, tool, drilling.

## I INTRODUCTION

Metal cutting machine tools with numerical control (CNC) are intended to provide a solution to the occurred in the modern machine engineering contradictions between the requirements for flexibility and the high degree of automation. In order to increase their efficiency and widen the scope of their implementation, it is necessary to assess in full their technical potential for technological operation optimization. One of the areas of cost minimization of the technological operations is related to the reduction of the idle strokes runtime (auxiliary strokes) that are required and accompany the operating strokes (main strokes).

## II FORMULATION OF THE PROBLEM

The solution of this problem can be achieved by the introduction of adaptive control. The differences between the operating cycles of drilling holes with and without adaptive control are shown on Figure 1.

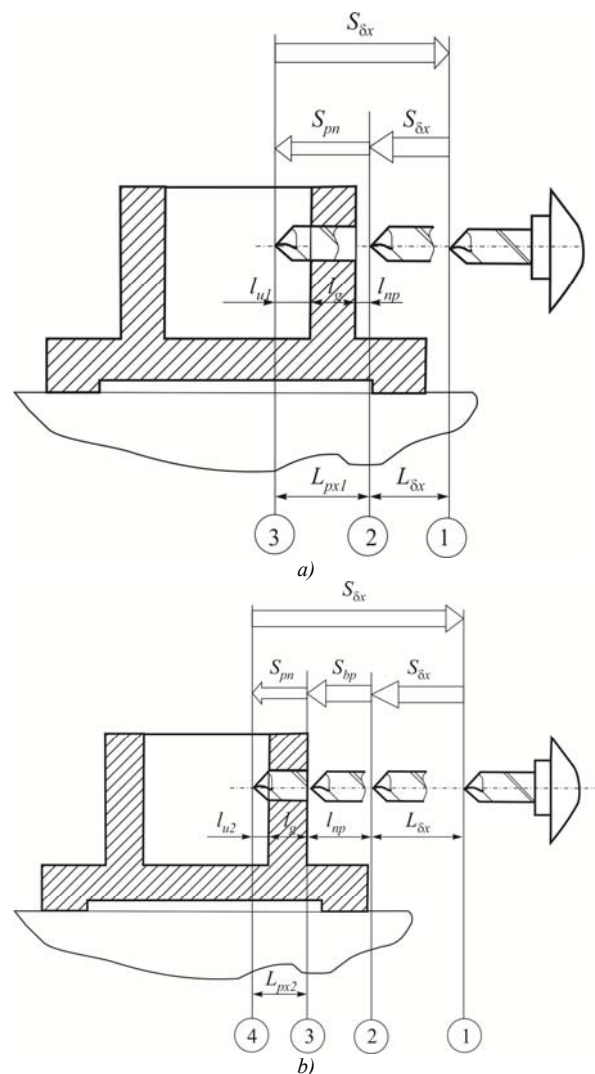


Fig. 1. Drilling operating cycle: a) without adaptive control;  
 b) with adaptive control

In the case of the standard CNC (without adaptive control) processing is carried out by a program that provides:

- quick movement of the tool from p. 1 to p. 2;
- operating feeding movement from p.2 to p.3 and quick tool retraction from p. 3 to p.1.

In this case, the operating feeding stroke is defined as:

$$(1) \quad L_{px1} = l_{np} + l_g + l_{u1}$$

Where  $L_{px1}$  is the length of the stroke in the case of drilling without adaptive control;

$l_{np}$  - the distance required for the safe tool cutting;

$l_g$  - the size of the processed surface;

$l_{u1}$  - the exit distance of the tool in the case without adaptive control.

With the application of the dedicated adaptive control program, the programmable tool leading is achieved at fast pace from p. 1 to p.2 and afterwards the forward leading of the tool with maximum allowed feeding, while taking into account its resilience. This movement continues until reaching p. 3 which is not set in the programme. It corresponds to the point where the tool contacts the work piece. The contact is registered by the adaptive control system which sends a signal for stopping the accelerated feeding and for switch on of the operating tool feeding. The movement of the operating feeding continues to p. 4 which similarly to p.3 is not set in the programme, but it is determined by the adaptive control system. It corresponds to the point at which the tool in fact has left the processed material of the work piece. After reaching p. 4 the adaptive control system gives a command for quick tool retraction from p. 4 to p. 1. In this case, the stroke is determined by the formula:

$$(2) \quad L_{px2} = l_g + l_{u2}$$

where  $L_{px2}$  is the stroke length in the adaptive control drilling;

$l_{u2}$  - exit length of the tool in the adaptive control drilling.

### III ANALYTICAL STUDY

The operating time cycle is expressed as follows:

$$(3) \quad T_1 = \frac{L_{\delta x}}{S_{\delta x}} + \frac{L_{px1}}{S_{pn}},$$

$$(4) \quad T_2 = \frac{L_{\delta x}}{S_{\delta x}} + \frac{L_{px2}}{S_{pn}} + \frac{l_{np}}{S_{bp}},$$

where  $L_{\delta x}$  is the distance of movement of the tool at rapid pace;

$S_{\delta x}$  - speed of rapid pace;

$S_{pn}$  - speed of movement of operating feeding;

$S_{bp}$  - speed of movement of rapid pitching-in.

The time reduction of the operating cycle with applied adaptive control is defined as:

$$(5) \quad \Delta T = T_1 - T_2.$$

After converting equations (1), (2), (3), (4) and substitution in equation (5), it looks as:

$$(6) \quad \Delta T = \frac{l_{u1} - l_{u2}}{S_{pn}} + \frac{l_{np}}{S_{pn}} \left( 1 - \frac{S_{pn}}{S_{bp}} \right).$$

If we assume that  $l_{u1} - l_{u2} = l_{up} = \omega_z$ , equation (6) is converted into

$$\Delta T = \frac{\omega_z}{S_{pn}} \left( 2 - \frac{S_{pn}}{S_{bp}} \right),$$

where  $\omega_z = \omega_{lb} + \omega_{lg}$  is the error of the linear dimensions of the work piece;

$\omega_{lb}$  - error of the dimensions of the supporting technological base to the end of the work piece;

$\omega_{lg}$  - error of the size of the processed surface.

The specific increase of the processing performance will be equal to:

$$(7) \quad \frac{\Delta T}{T} = \frac{2\omega_z}{l_g} \left( 1 - \frac{S_{pn}}{2S_{bp}} \right),$$

where  $T = \frac{l_g}{S_{pn}}$  is the cutting time.

If we denote  $\frac{\omega_z}{l_g} = k_1$  and  $\frac{S_{pn}}{S_{bp}} = k_2$ , the relationship (7) assumes the following form:

$$(8) \quad \frac{\Delta T}{T} = k_1 (2 - k_2).$$

On the grounds of (8) we assume the following:

1. With the increase of the pitch-in speed of the tool (reduction of  $k_2$ ) the adaptive control effect increases, which is expressed in higher processing efficiency.

2. The adaptive control effect depends considerably on the size of the processed surface. With the increase of this size (reduction of  $k_1$ ) the performance is reduced.

In order to achieve maximum effect of the adaptive control in specific working conditions, the speed of the feeding movement of pitching in  $S_{bp}$  has to be maximal, while taking into account the tool's resilience.

The maximum axial force that can withstand the drill when pitching into the processed surface is determined by [2] according to the following:

$$(9) \quad P_{kp} = \frac{2\pi^2 EJ_{\min}}{\left( 1 + \frac{J_{\min}}{J_{\max}} \right) l^2},$$

where  $J_{\min}$  and  $J_{\max}$  are respectively the smallest and the biggest inertia moment along the cross section of the drill.

$l$  - length of the taper drills.

The maximum allowed torque of the pitching drills

$$(10) \quad M_{kp} = W \tau_p$$

where  $\tau_p$  is the tangential pressure of destruction;

$W$  - the polar moment of resistance of the drill.

To determine the moment of inertia and resistance of the spiral drill with satisfactory accuracy, the following equation can be applied [2]:

$$J_{\min} = 0.0052d^4, \quad J_{\max} = 0.027d^4, \quad W = 0.047d^3,$$

where  $d$  is the external diameter of the drill in mm;

For spiral drill made of tool steel, it is experimentally found out that  $\tau_p = 620 \div 660 \text{ N/mm}^2$ .

Under these conditions formula (9) and (10) assume the form:

$$P_{kp} = 18 \cdot 10^3 d^4 / l^2, \quad M_{kp} = 29 \cdot d^3.$$

To determine the pitching-in feeding  $S_{bp}$  the empirical relations of the axial force can be used -  $P_0$  and the torque moment  $M$  when drilling. The order models of the following type are widespread:

$$P_o = C_p \cdot d^{q_p} \cdot S^{y_p} \cdot K_p, \quad M = C_m \cdot d^{q_m} \cdot S^{y_m} \cdot K_m,$$

where  $C_m$  and  $C_p$  are constants defining the type of the work piece and the tool. If  $P_0 = P_{kp}$ ,  $M = M_{kp}$ , we obtain two values of the pitching-in feeding:

$$S_{bp1} = \left( \frac{P_{kp}}{C_p \cdot d^{q_p} \cdot K_p} \right)^{\frac{1}{y_p}}, \quad S_{bp2} = \left( \frac{M_{kp}}{C_m \cdot d^{q_m} \cdot K_m} \right)^{\frac{1}{y_m}}.$$

The pitching-in feeding of the tool into the processed work piece in the drilling operation is defined finally by the limitations of the metal cutting machine.

$$S_{bp} = \min(S_{bp1}, S_{bp2}) \quad \text{when}$$

$$S_{\max} \geq \min(S_{bp1}, S_{bp2}) \geq S_{\min}$$

$$S_{bp} = S_{\max} \quad \text{when} \quad \min(S_{bp1}, S_{bp2}) > S_{\max},$$

where  $S_{\min}$  and  $S_{\max}$  are the minimum and maximum feeding that can be achieved by the metal cutting machine.

If  $\min(S_{bp1}, S_{bp2}) < S_{\min}$  the processing on this machine is impossible.

#### IV CONCLUSION

On the grounds of the present analytical study on the application of the adaptive control of the pitching-in of the drilling tool, we can conclude that the processing optimization in terms of time is possible only by defining the feeding of each separate drill of the toolset of the machine. This is done in the course of the preparation of the control programme for the machine with CNC. The computational operations can be done by the respective developed computer software.

#### V REFERENCES

- [1] Georgiev V., Lengerov, A. Adaptive control of the drilling process. AMTECH '95. Ruse, 1995, 6-15.
- [2] Filipov G.V. Cutting tools. Machine building, Saint Petersburg, 1984, 13-17.

# Research of Radial Forces and Torque of Bearingless Synchronous Machine

Sergei Loginov, Yulia Domracheva, Vadim Smirnov, Dmitriy Fedorov

*Pskov State University, Electrical Engineering,*

*Department of Electric Drive and Automation Systems.*

*Address: Lenin Square 2, Pskov, 180000, Russian Federation.*

**Abstract.** bearingless synchronous machine (BSM) is an electrical machine which rotor is suspended by electromagnetic forces (not ball bearings). It allows achieving ultra-high rotation speed and significantly extending area of electric drive application. Nowadays there are different variants of the machines with the structural design and the searching of optimal solution is going on.

The basic calculation parameters of bearingless machines are radial forces that can withstand the rotor from external load and torque produced on the shaft. This article describes the theoretical results based on a computer model that produces the finite element method and experimental study of the BSM prototype.

**Keywords:** bearingless electrical machine, active magnate bearing.

## I INTRODUCTION

Electrical machines with active magnetic bearings are used in high-speed motor drives [1]. Implementation of magnetic suspension started being possible by the development of the element base of radio components. As a result, that implementation of complex currents control laws in electrical machines became possible. It enabled the development of new designs of machines, without the difficulties which encountered in the past with limited processing speed signals.

Currently different versions of bearingless electrical machines are being developed, but at the same time each of them has advantages and disadvantages. One of the variants is bearingless electric machine with distributed windings [2,3,4,5,6].

In a bearingless motor gap magnetic field generates both torque and radial forces and it keeps the rotor in the centre. It is a result of electromagnetic field with the help of a drive and a suspension winding superposition [2,7,8]. For example motor has a stator with four and two magnetic poles windings and a cylindrical rotor. In figure 1a) is shown magnetic flux  $\Phi_{4a}$  from drive winding is shown.

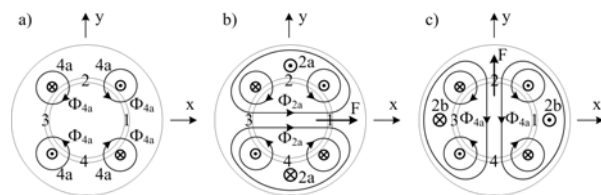


Fig. 1. Creating radial forces in BSM.

Fluxes create four poles in arias 1,2,3,4. Every pole creates magnetic force, total force equals zero in rotor center position. The principle of radial x-force creation is shown in figure 1b). Two poles winding 2a creates magnetic flux  $\Phi_{2a}$ . Magnetic induction increases in sector 1 as magnetic flux  $\Phi_{4a}$  and  $\Phi_{2a}$  which are summed, and decreases in sector 3 as magnetic flux  $\Phi_{4a}$  и  $\Phi_{2a}$ , are subtracted. So radial x-force appears. The force amplitude is controlled by current in 2a conductor. Force vector is controlled by current phase. In figure c1) the creation of radial y-force is shown. The principle of 3-phase motor operation is the same [2,9,10].

The basis of this principle allows us to create different types of bearingless motors, such as an induction motor [11], permanent magnet synchronous motor, synchronous reluctance motor, homopolar and hybrid motors [12], switched reluctance motor [13] and etc. Each type of motor has its advantages and disadvantages [14]. In this paper we are going to research on the bearingless synchronous inductor machines [15].



## II MATERIALS AND METHODS

The creation of an electromagnetic field, that allows hold the rotor in the center position and creates the desired torque are the main goals of control in bearingless machine. Due to the high cost of natural modeling, computer simulation is getting more and more common in the design and study of new devices. Currently there are many computer programs that allow simulate electromagnetic fields in the electrical machines (ANSYS, COMSOL, ELCUT, SolidWorks). Most of them use the finite element method for the analysis. Comparing computer simulation to the analytical description, the apparent advantage of the first one is a higher accuracy that helps to avoid many simplifications. It allows you to explore the model of almost any complexity. Naturally, we cannot speak about the reliability of a computer model of a complex technical device without experimental investigation.

In this paper we present a comparison of the results of computer simulation in the modeling environment FEMM and real modeling of bearingless synchronous machine module. Figure 2 shows a cross-sectional cut of a BSM module with a windings arrangement example.

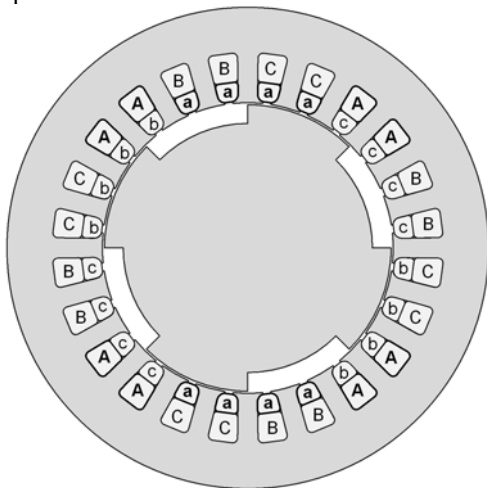


Fig. 2. Module of BSM (A, B, C – drive windings; a, b, c – suspension windings).

The rotor module has four poles, as well as one of the stator windings (we call it a drive winding). The second winding (suspension winding) has two poles. Axes of similar phases both of winding drive and suspension winding are the same. The volume occupied by the windings in the slots is determined by the required ratio of the radial force and torque module. The width of the rotor pole is 45 degrees.

The stator of induction motor 4A71B4 is the basis pattern. The stator has 24 slots and two three-phase distributed winding: 4-pole winding drive and 2-pole suspension winding. Winding drive is fundamental, the number of turns in a slot is 50, and the turn

number of the suspension windings is 35. The length of the rotor's active part is 74 mm.

Figure 3 shows the model modular unit of bearingless electrical machine in the FEMM.

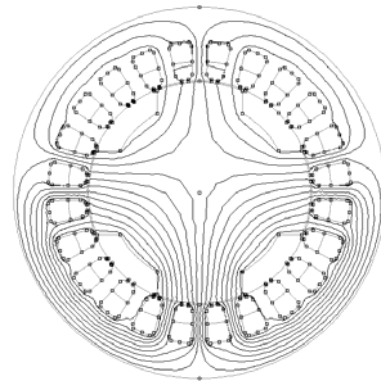


Fig. 3. The model in the FEMM.

The program allows calculating directly the torque and radial forces acting on the rotor.

To create a physical model the stator of the induction motor 4A71B4 was used. The scheme for radial forces research is shown in Figure 4. The rotor has a mechanical support to the ball bearing (point O). Assume that this hinge support and the rotor can rotate freely relatively to this point. The load application center of electromagnetic forces ( $F_{em}$ ) is the center of the stator (point  $O_1$ ).

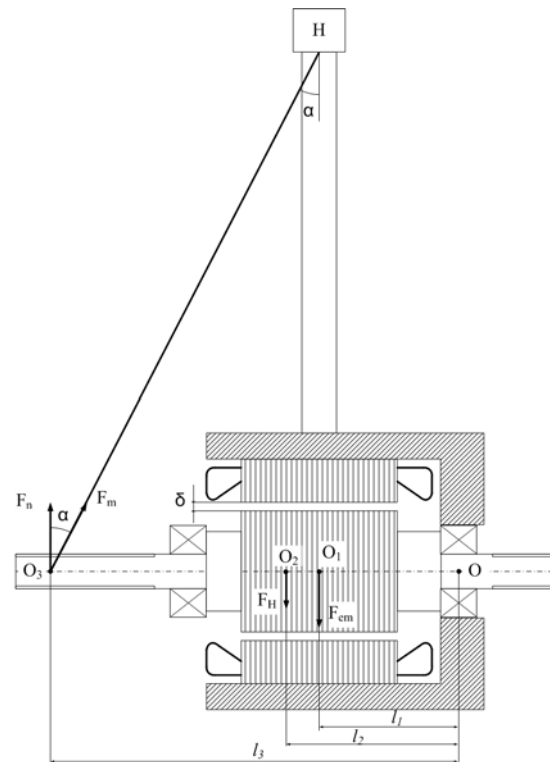


Fig. 4. Scheme for radial forces research .

The gravity application center ( $F_H$ ) is the rotor mass center - point  $O_2$ .  $O_3$  - point of balance force application  $F_m$ , which is measured by scales. Having known the force  $F_m$  and  $F_H$ ,  $F_{em}$  can be determined.

The moment equation, acting on the rotor relative to point  $O$  is (1):

$$F_{em} * l_1 + F_H * l_2 = F_n * l_3 \quad (1)$$

where  $F_n$  is defined as:  $F_n = F_m * \cos(\alpha)$

So,

$$F_{em} = (F_H * l_2 - F_m * \cos(\alpha) * l_3) / l_1 \quad (2)$$

To find the torque the second ball-bearing was set and the maximum force required to rotate the rotor was measured.

Currents in the drive and suspension windings are delivered from two three-phase inverters and they are measured by ammeters. Currents phases are selected such way that the resulting radial force is directed vertically downward.

### III RESULTS AND DISCUSSION

The research purpose is a comparison of the results of a computer simulation and an experiment. The main parameters are the torque and radial force.

During the experimental research only the maximum torque was measured. The torque in this type of machines depends on the angle of rotor rotation relative to the stator field, so the maximum moment angle was determined firstly. The dependence of the torque on the angle of rotor rotation were determined in the FEMM (Fig.5).

For leachate  $BOD_5$  is very low, varying from 8.1 to 18.9 mg/L, which is non-typical for young landfill leachate. The reason of this can be landfill management, where concentrate from

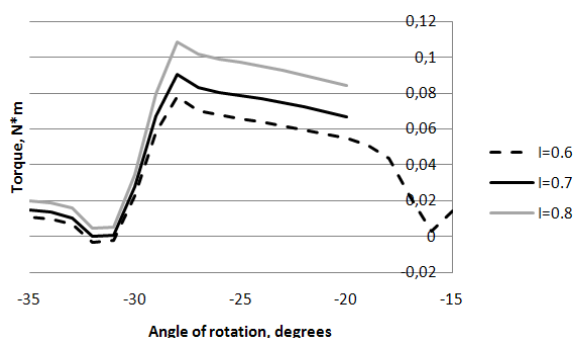


Fig. 5. Torque depending on the angle of rotor rotation 1)  $I_4=0.6$  A 2)  $I_4=0.7$  A 3)  $I_4=0.8$  A

These graphs are plotted for various values of the drive windings currents. As can be seen, the maximum torque angle does not depend on the value of current and is approximately 28 degrees. The reduction of the

date of 17 degrees is explained by the specific situation of the stator teeth from the rotor teeth. Reducing of this impact can be achieved by manufacturing a rotor with beveled slot. In experimental research was obtained the similar data. Thus, all the torque measurements were performed at the rotor rotation angle of 28 degrees.

Values obtained at a suspension windings currents  $I_2$  are 0 and the changes of drive windings currents  $I_4$  are shown in the figure 6.

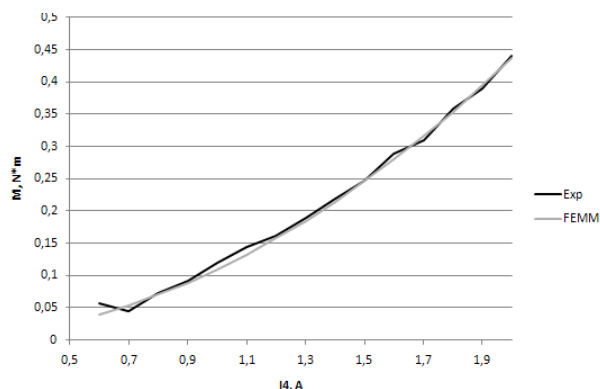


Fig. 6. Torque depending on the drive windings currents.

As can be seen, the results obtained by computer simulation (FEMM) almost completely agree with the experimental research results (Exp).

An important parameter in the bearingless machine is the impact of the suspension windings currents on torque. If this effect is large, the torque on the shaft changes at a constant current  $I_4$ , which has negative effect on the load. The research of these parameters is shown in the Figure 7.

Date Exp\_1 and FEMM\_1 is obtained for the drive windings currents  $I_4 = 1$ , Exp\_2 and FEMM\_2 for  $I_4 = 2$ A.

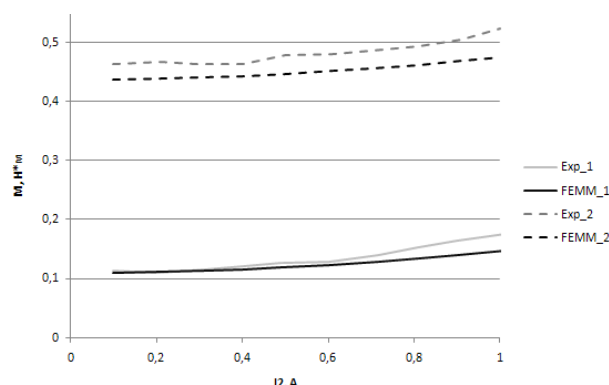


Fig. 7. Effect of the suspension windings currents on the torque.

The discrepancy between the results of computer simulations and experimental research is presented in Table 1.

TABLE 1.  
THE DISCREPANCY BETWEEN THE RESULTS OF COMPUTER SIMULATIONS AND EXPERIMENTAL RESEARCH

EXPERIMENT, N*M	FEMM, N*M	DISCREPANCY, %
0,462	0,437	5,34
0,467	0,439	6,13
0,462	0,440	4,72
0,463	0,443	4,39
0,478	0,446	6,56
0,480	0,451	6,12
0,486	0,455	6,24
0,493	0,461	6,47
0,504	0,468	7,11

As can be seen from the table, the difference does not exceed 8%. It can be explained by the assumptions made in the computer model: magnetostrictive saturation and magnetization of ferromagnetic materials are ignore.

Another important parameter for this research is the dependence of the radial forces from the windings currents. Previously it was said that the radial force is generated by magnetic fields superposition generated by the drive and suspension windings currents. Moreover, the radial force is controlled by the suspension windings currents. Therefore, the main thing is the confirmation of the dependence of the radial force of the suspension windings currents. The results obtained by computer simulation (FEMM) and experimental researches are presented in Figure 8.

The dependence of the radial forces from the drive windings currents is also important (Figure 9). Table 2 shows the discrepancy between the results of computer simulations and the experimental research.

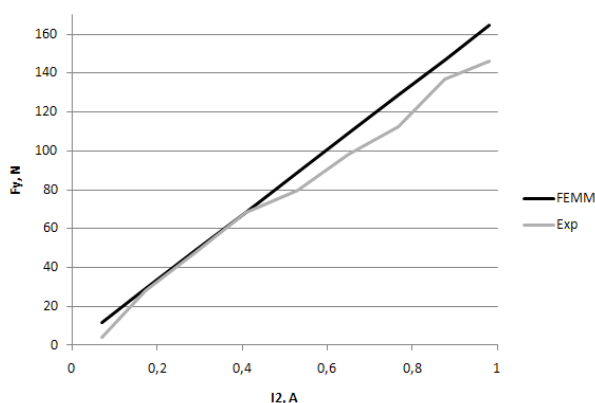


Fig. 8. The dependence of the radial forces on the suspension windings currents.

As seen in the table, the discrepancy does not exceed 15%. Such discrepancy can also be explained by the assumptions made in the computer model.

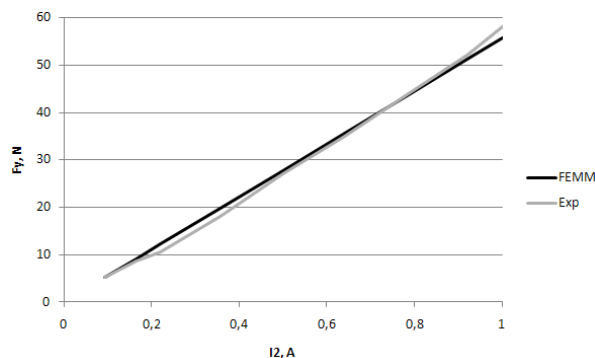


Fig. 9. The dependence of the radial forces on the drive windings currents.

TABLE 2.  
THE DISCREPANCY BETWEEN THE RESULTS OF COMPUTER SIMULATIONS AND THE EXPERIMENTAL RESEARCH

EXPERIMENT, N*M	FEMM, N*M	DISCREPANCY, %
28,25	29,01	-2,69
47,81	48,55	-1,55
68,45	68,47	-0,07
79,86	88,98	-11,41
98,33	108,9	-10,74
112,46	128,63	-14,38
136,91	146,62	-7,09
146,14	164,42	-12,5

#### IV CONCLUSION

The data obtained in the research demonstrate the adequate usage of the computer simulation technique. Thus, guaranteeing reliable results, computer simulations can be employed to investigate bearingless synchronous machine. Further research are going to be concentrated on the determination of the optimal design of the machine, the study of the dynamic characteristics, the synthesis of control laws and the development of the electronic control unit for BSM.

#### V ACKNOWLEDGMENTS

The authors would like to thank the Ministry of Education and Science of the Russian Federation for funding this research (Project 403 - "Development of the theory of the bearingless synchronous electric machine").

#### VI REFERENCES

- [1] Zhuravlyov Y.N. Active magnetic bearings: theort, design, application. St. Petersburg: Politechnica, 2003, pp. 12-25
- [2] A.Chiba, T.Fykao, O.Ichikawa, M.Oshima, M.Takemoto, D.G.Dorrell Magnetic Bearings and Bearingsless Drives. /ELSEVIER, pp. 127-135.
- [3] A. Chiba, M. A. Rahman and T. Fukao. Radial Force in a Bearingless Reluctance Motor. //IEEE Transactions on IA, 1991, No. 2, pp. 786-790.
- [4] A. Chiba, T. Deido, T. Fukao and M. A. Rahman. An Analysis of Bearingless AC Motors. //IEEE Transaction on Energy Conversion, Vol. 9, No. 1, 1994, pp. 61-68.

- [5] A. R. Husain, M. N. Ahmad Deterministic Models of an Active Magnetic Bearing System // Journal of Computers, 2007, No. 8, pp. 9-17
- [6] Chen, L. Hofmann, W. Performance Characteristics of one Novel Switched Reluctance Bearingless Motor Drive. // Proc. of Power Conversion Conference (PCC'07), 2007, pp. 608 – 613.
- [7] Katou T., Chiba A., Fukao T. Magnetic suspension force in an induction bearingless motor with a squirrel cage rotor. // Electrical Engineering in Japan, 2007, No. 3, pp. 77–87
- [8] Li Chen, Hofmann W. Design procedure of bearingless high-speed switched reluctance motors // Proc. of International Symposium on Power Electronics Electrical Drives Automation and Motion (SPEEDAM), 2010, pp. 1442 – 1447.
- [9] Neff M., Barletta N., Schoeb R., Bearingless Centrifugal Pump for Highly Pure Chemicals. //Proc. of 8-th International Symposium on Magnetic Bearings (ISMB 8), Mito, 2002, pp. 283-287.
- [10] Bartholet M., Silber S., Nussbaumer T., Kolar J., Performance investigation of two-, three- and four-phase bearingless slice motor configurations, in Power Electronics and Drive Systems. //Proc. of the 7th International Conference on Power Electronics and Drive Systems, Bangkok, 2007, pp. pp. 9-16.
- [11] Loginov S., Domracheva Y. The Model of Induction Bearingless Machine// Proc. of International Conference Low Voltage Electrical Machines, No. 102, 2009, pp. 78-80.
- [12] O. Ichikawa, A. Chiba and T. Fukao. Principles and Structures of Homopolar-Type Bearingless Motors. //Proc. of International Power Electronics Conference (IPEC), Tokyo, 2000, pp. 401-406.
- [13] Li Chen, Hofmann W. Design procedure of bearingless high-speed switched reluctance motors // Proc. of International Symposium on Power Electronics Electrical Drives Automation and Motion (SPEEDAM), 2010, pp. 1442 – 1447.
- [14] M. Ohsawa, S. Mori and T. Satoh. Study of the Induction type Bearingless Motor. //Proc. of 7-th International Symposium on Magnetic Bearings (ISMB 7), Zurich, 2000, pp. 389-394.
- [15] Domracheva Y., Loginov S. Simulation Technique of Synchronous Reluctance Bearingless Machine // Environment. Technology. Resources. Proceedings of the 9-th International Scientific and Practical Conference, 2013, pp. 101-105.

# **Mechanical Properties of Glass Fiber Composites Reinforced by Textile Fabric**

**Arturs Macanovskis, Andrejs Krasnikovs, Olga Kononova, Galina Harjkova,  
Vladislav Yevstignejevs**

*Riga Technical University, Institute of Mechanics, Riga, Latvia*

**Abstract.** Interest to structural application of textile reinforced polymer matrix composite materials (CM) is growing during last years. In different branches of machine building, aerospace, automotive and others industries we can find structural elements preferably be produced using such reinforcement. At the same time, such materials are exhibiting elastic and strength properties scatter. Present work is devoted to structural modeling of the composite material with textile (knitted) reinforcement having the goal to predict such materials strength and behavior under applied mechanical loads. In the framework of the present investigation, we observe yarn penetrated by a resin in a composite as a reinforcing “macro” fiber. Such “macro” fiber mechanical properties were measured experimentally, for this purpose was produced and was tested by tension until fracture fiber samples, having different length. Then was elaborated and was realized structural strength probabilistic model. In the textile geometry, was picked out repeating structural element – polymer matrix volume with two curved “macro” fiber’s chunks inside it. Complete composite material volume is possible to represent as a set of repeating structural elements. External loads application leads to disperse structural elements failure. Neighboring to ruptured elements are overloaded leading to higher probability to fail for them. Using FEM was modeled stress state in “macro” fibers inside CM. Then, was numerically obtained stress distribution in composite material, having different number of broken loops. Probabilities of different numbers of failed elements were calculated. Strength probability function, based on Weibull approach was obtained. CM samples were tested under tension and obtained results were compared with numerical modeling as well as were analyzed.

**Keywords:** Elastic properties, glass fiber, polymer matrix, yarn.

## I INTRODUCTION

Novel composite materials (CM) investigation and incorporation in different structural automotive, marine and aerospace applications is important nowadays. Some of such materials have non-traditional reinforcement. Polymer matrix composites, reinforced by textile fabric in many situations have simple fabrication technology and are exhibiting attractive mechanical properties, such as high wear and impact resistance, as well as high energy absorption. Woven fabric has threads running horizontally and vertically, in the case of knitted fabric, strands are forming loops. Knitted fabric has high shape forming ability, which allows it to be applied in a complex shape mould without forming folds. Such property is important in fabrication of composite material made sophisticated form structural elements. Elastic properties of a composite reinforced by knitted fabric are dependent on mechanical properties of the matrix and mechanical properties of the fibers as well as thread thickness, its degree of twist, geometrical size and form of the loops in the fabric and were numerically and experimentally investigated in [1-6]. At the same time strength

properties and damage accumulation in such materials during loading are investigated poor. Damage accumulation in mechanically loaded CM, reinforced by knitted fabric is stochastic process of single disperse yarn loops rupture, ruptured loops formation in clusters and clusters growth till final material rupture within structural element. If we want to model such process numerically we can observe yarn filled by polymer matrix as a “macro” fiber having elastic properties corresponding to curved unidirectional composite material and strength properties which can be obtained experimentally performing such unidirectional composite material testing. After that stresses in curved “macro” fiber loops can be calculated numerically using FEM approach. More overloaded crosssections of “macro” fiber loops in the material will fail. Performing stochastic procedure is possible to evaluate this process from the beginning till the final CM rupture. In such case studied materials have properties necessary for design and manufacturing.

## II UNIDIRECTIONAL MATERIAL EXPERIMENTAL INVESTIGATION

We observe yarn filled by polymer matrix as a “macro” fiber having elastic properties corresponding to curved unidirectional composite material. Strength properties of such CM will be evaluated stochastically using Weibull probabilistic distribution (1). Weibull probabilistic distribution

$$F(\sigma) = 1 - e^{-(\frac{\sigma}{\eta})^\beta} \quad (1)$$

$$\text{where: } \eta = (\frac{L_0}{L})^{\frac{1}{\beta}} * \sigma_0 \quad (2)$$

(1) will describe “macro” fiber probability to fail dependent on applied to the composite “macro” fiber stretching stress  $\sigma$  and its length  $L$ .  $\sigma_0, \beta, L_0$  are numerical constants. In the framework of our investigation, we are accepting that curved “macro” fiber in the composite can fail only by its rupture

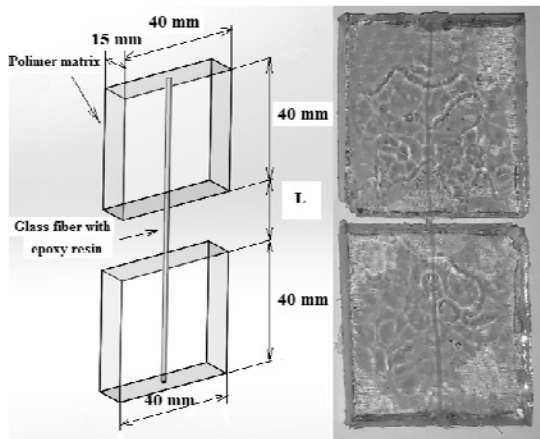


Fig. 1. Sample M2, where L – the length between the tabs in mm

under acting in its orthogonal to longitudinal fiber direction tensile stress. Traditional way of parameters  $\eta$  and  $\beta$  experimental evaluation is performing experimental tests with fibers having different length. For this purpose composite “macro” fiber samples having different span length were experimentally fabricated. For getting samples – were conducted following steps: a) into epoxy resin was poured catalyzer for gradual solidification; b) straight glass fiber yarns were easily stretched and were penetrated by epoxy resin. After solidification “macro” fibers were cutted in pieces for samples fabrication. Each “macro” fiber piece was precisely positioned going through two empty boxes with the size 40X40X15 mm as is shown in Fig. 1. Boxes were filled by a resin. After 2 days epoxy resin was hardened and samples were demoulded and tested by tension till rupture. Corresponding following samples were fabricated:

- 1) M2 – samples with a “macro” fiber length between tabs  $L=2$  mm;

- 2) M6 – samples with a “macro” fiber length between tabs  $L=6$  mm;
- 3) M10 – samples with a “macro” fiber length between tabs  $L=10$  mm;
- 4) M16 – samples with a “macro” fiber length between tabs  $L=16$  mm;
- 5) M26 – samples with a “macro” fiber length between tabs  $L=26$  mm;
- 6) M100 – samples with a “macro” fiber length between tabs  $L=100$  mm;
- 7) M800 – samples with a “macro” fiber length between tabs  $L=800$  mm;

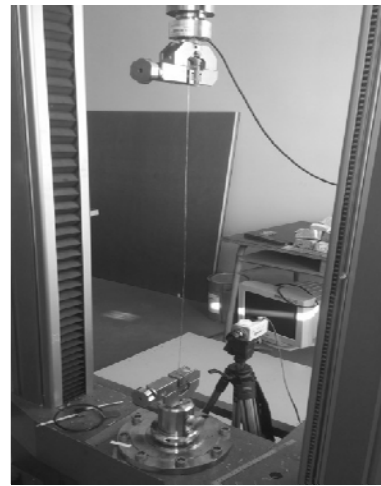


Fig. 2. The sample M800 is testing

Were produced five samples having each particular L length value between tabs. Samples were placed in a tensile testing machine grips (Fig. 2) and subjected to tension.

## III “MACRO” FIBER ELASTIC PROPERTIES

“Macro” fiber consists of glass fiber yarn penetrated by epoxy resin. At the beginning, dry glass fibers yarn without epoxy resin was mechanically investigated. Yarn was tested by tension for finding Young's modulus. The diameter of the glass fiber yarn was calculated by the following (3) [7]:

$$D = \frac{\sqrt{\frac{4}{\pi * \rho * k}}}{\sqrt{1000}} * \sqrt{Tex} \quad (3)$$

where: D – diameter of the yarn in mm;

Tex – is a unit of measuring the linear mass density of fibers, 300 g/km;

$\rho$  -the density of the glass fiber, 2.54 g/cm<sup>3</sup>

k – numerical coefficient, which describes how many fibers are in the yarn volume.

Experimental curve averaged over data obtained for five samples is shown in Fig. 3. Young's modulus for a glass fiber yarn without epoxy resin was obtained

$E = 71.9\text{GPa}$ . Then all prepared “macro” fiber samples having different

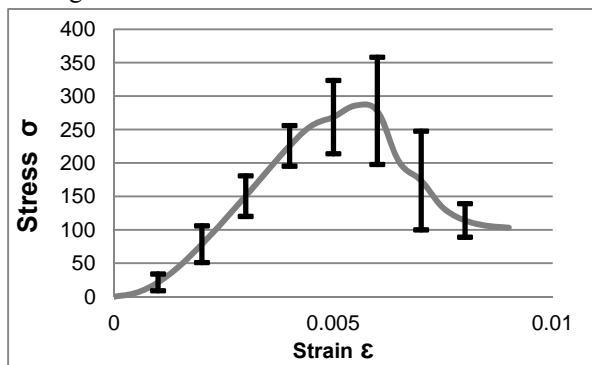


Fig. 3. Stress (MPa) –strain (averaged over five samples) curve for glass fiber yarn not contains epoxy resin

length were tested. During samples testing was observed following:

a) for some part of M2 samples fiber break was happened partially inside the clamps. Broken crosssection was inside polymer tabs;

b) for all samples M6, M10, M16, M26 и M100 “macro” fiber broken crosssection was located in the middle part of the sample away from the polymer tabs (Fig. 4);

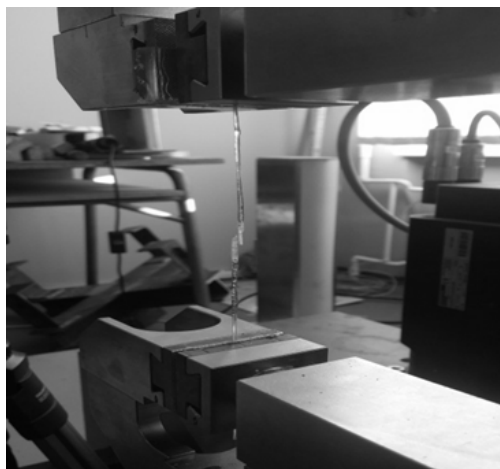


Fig. 4. Broken sample M100

c) for samples M800 “macro” fiber broken crosssection was located in the middle part of the sample. First break was initiated elastic wave which running from broken crosssection along the “macro” fiber in both directions was initiated secondary breaks, leading to sample separation in few pieces.

After testing for samples were received following graphs:

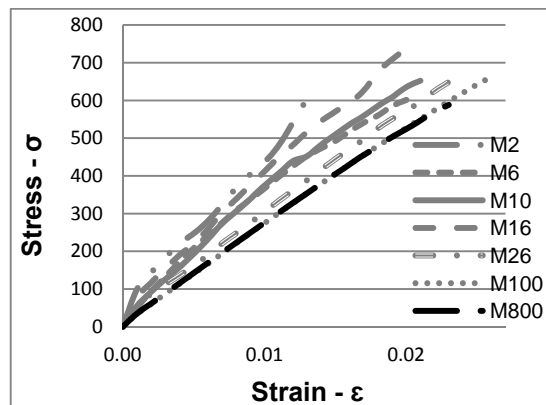


Fig. 5. Stress (MPa) – strain (each averaged over five samples) curves for all tested samples

From curves in the Fig. 5 were obtained Young's modulus of the “macro” fiber  $E_{average} = 32.4\text{GPa}$  – the average value over all experimentally obtained data. The average volumetric glass fibers content in our prepared samples was evaluated from the (4) and was  $V_f = 0.42$ .

$$V_f = \frac{E_m - E_{average}}{E_m - E_f} \quad (4)$$

where:  $E_m = 4\text{GP}$  – Young's modulus of the epoxy matrix,  $E_f = 71.9\text{GPa}$  – the average value of the Young's modulus of the glass fiber without epoxy resin, which was obtained in experiments stretching yarns without resin.

#### IV “MACRO” FIBER STOCHASTIC PROPERTIES

All length samples were tested till rupture. Strength properties dependence on samples length is shown in Fig. 6. From Fig. 6 were obtained following approximation function  $\ln(L) = -8.0033 \cdot \ln(\sigma) + 55.366$  and values  $\beta = 8.1443$  and  $A = 56.709$  in Weibull probabilistic function (1) and (2) describing glass fiber yarn impregnated by epoxy matrix strength distribution.

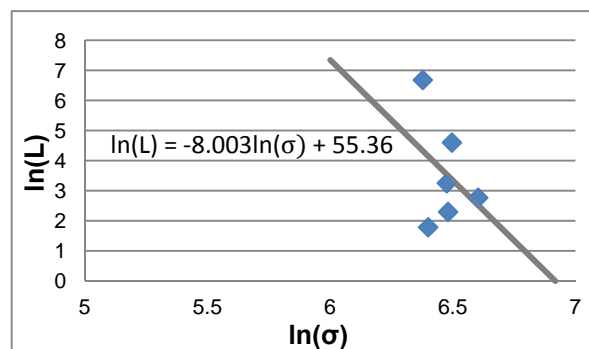


Fig. 6. Linear approximation of the samples strength dependence on length for “macro” fibers, were L is in mm and  $\sigma$  in MPa

## V DAMAGE ACCUMULATION IN THE COMPOSITE MATERIAL REINFORCED BY KNITTED FABRIC AND IT STRENGTH

Existing failure models are mostly based on the use of different phenomenological criteria [5,6,8]. Polymer matrix composite material reinforced by knitted fabric is forming repeatable structure of elements shown in Fig. 7. A repeating structural element - volume can be subtracted from the structure. Translation of the volume in four directions gives us composite plate. Such subtracted volume of looped fiber with surrounding matrix is shown in Fig. 8. In the case of such material loading, all translated repeatable volumes are loaded in the same way. The finite element method was used studying sequential failure of loops in a plate of composite material reinforced with knitted fabric. Loading of material will lead to distributed in CM volume "macro" fiber breaks within the loops. We suppose then if failure will happen it will happen in more heavily loaded crosssection of the loop. For this purpose more stretched crosssection within structural element was recognized (Fig. 9). Then according to applied external loads level, probabilities to find such single breaks dispersed in material were calculated according to (1), using obtained experimentally numerical constants. The broken crosssection within the loop is leading to overstress formation on crosssections within closest neighboring fibers (in neighboring repeating volumes). More heavily loaded crosssection of the fiber within neighboring to ruptured loop was recognized and probability to failure under overloads was obtained. In such way, probabilities to find in loaded CM plate single ruptured "macro" fibers crosssections, two neighboring broken crosssections in two neighboring "macro" fibers, three broken crosssections in three neighboring "macro" fibers were calculated and so on.

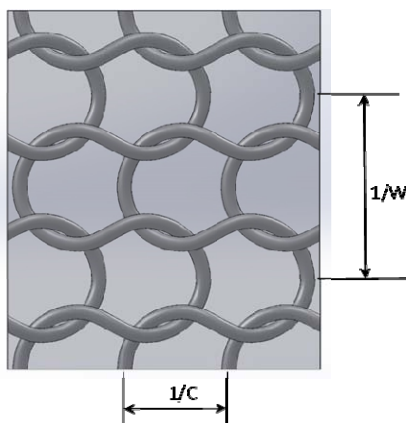


Fig. 7. Polymer matrix composite plate reinforced by glass fiber knitted fabric. Glass fiber yarn impregnated by epoxy matrix is observed as "macro" fiber

Thin knitted reinforcement in the composite is shown in Fig. 7. This structure is loaded with a tensile force in the horizontal direction. Investigated composite material plate sizes was  $12 \times 14 \times 2.43$  mm (width  $\times$  length  $\times$  thickness). Knitted geometric parameters were: number of loop columns per cm,  $W=1.43$  loop/cm, the number of rows per cm,  $C=2.5$  loop/cm. In order to simulate the thin knitted fabric geometry was used Leif-Glaskin model [1-4].

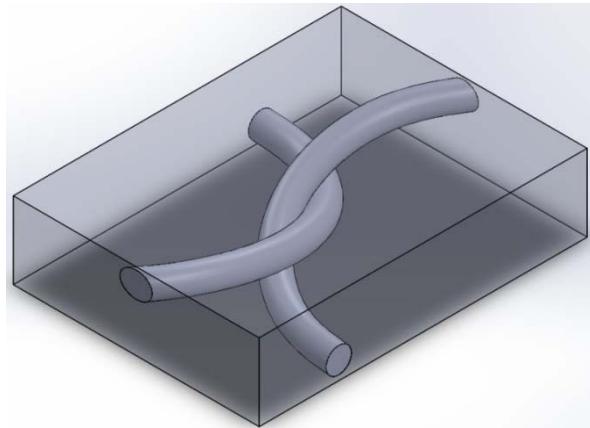


Fig. 8. Repeating structural element of the composite material [1-3]

Applied tensile stress in horizontal direction causes uneven tensile stress distribution along "macro" fiber orthogonal crosssections.

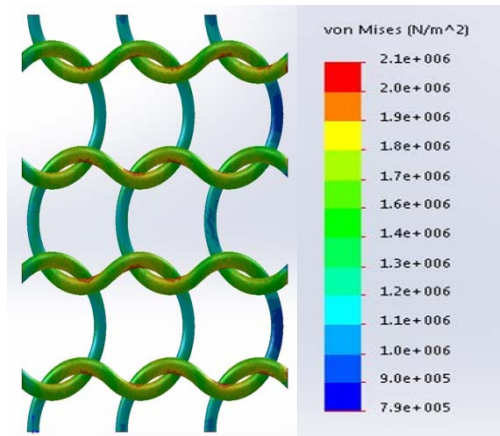


Fig. 9. Equivalent Mizes stress distribution in orthogonal crosssections of „macro” fibers in a case of CM stretching in horizontal direction by stress equal to 1 MPa (FEM solution)

Was supposed full contact between „macro” fibers and matrix. Was used FEM mesh, dependent on the curvature of the fiber. Finite element maximal size was 0.1675 mm. Were calculated stresses in situations of one broken crosssection, two broken crosssection, three broken crosssection and so on till 12. Stress distribution along unbroken fiber within the repeating element is show in Fig. 9 and Fig.10. The averaged (across crosssection of the "macro" fiber) overload



coefficients in more dangerously loaded neighboring fibers are shown in the table 1.

TABLE I

Number of ruptured crosssections	Normal stress in more heavily loaded neighboring crosssection, MPa
Material without broken crosssections	1.7640
1 broken crosssection	1.7660
2 broken crosssections	1.7680
3 broken crosssections	1.7700
4 broken crosssections	1.7710
5 broken crosssections	1.7714
6 broken crosssections	1.7732
7 broken crosssections	1.7750
8 broken crosssections	1.7768

Simulation of damage accumulation in the composite material having knitted reinforcement based on the assumption that it is a complex stochastic process, which begins with the single ruptured yarns accumulation in the material and is continuing to such single ruptures growth by other yarns failure on the border of the cluster of ruptured commonly located yarns. This process begins relatively slowly and turns to catastrophic development when the cluster growth. Model is not considering interaction between two adjacent clusters.

Let introduce the random value  $I(\sigma)$ :  $P\{I(\sigma) \geq i, \sigma > 0\}$ , it is the size of neighboring broken fibers crosssections. Cluster is reaching size of at least  $i$  adjacent broken yarns when the external tensile load is reaching value  $\sigma$ . In this case probability to find inside material clusters having size at least one broken "macro" fiber is equal to  $P(i \geq 1) = W(\sigma)$ . The probability of finding clusters, consisting of at least two broken adjacent "macro" fibers is equal to  $P(i \geq 2) = P(i \geq 1)W(\sigma_1)$ , the probability of finding clusters, consisting of at least three breaking adjacent "macro" fibers is  $P(i \geq 3) = P(i \geq 2)(1 - (1 - W(\sigma_2))^2)$ , the probability of finding clusters, consisting of at least four breaking adjacent "macro" fibers is  $P(i \geq 4) = P(i \geq 3)W(\sigma_3)$ .

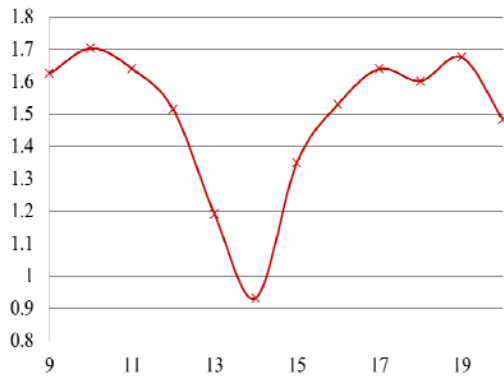


Fig. 10. The averaged overload coefficient distribution for (across crosssection of the "macro" fiber) tensile stress acting along the fiber within one repeating structural element

This process can be continued and probability of finding clusters, consisting of at least  $n$  breaking adjacent "macro" fibers can be calculated as  $P(i \geq n) = P(i \geq n-1)W(\sigma_{n-1})$ .

Above mentioned probabilistic model was realized and probabilities to find different size clusters of adjacently located broken fibers were obtained (Fig. 11). When size of the cluster is growing, probabilistic curves are linking forming one envelop curve, which is CM plate failure curve (probability to find in the plate cluster consisting of  $n \rightarrow \infty$  broken crosssections).

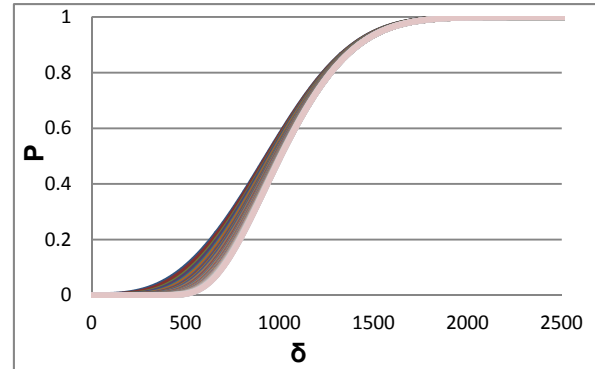


Fig. 11. Probabilities to obtained different size clusters consisting of broken adjacent "macro" fibers in loaded by tension CM plate

VI CONCLUSION

In the present work detailed failure process investigation in mechanically loaded CM plates reinforced by knitted fabric was realized. For this purpose experimentally were obtained micro composite material – single glass fiber yarn in epoxy resin, elastic and strength properties. Probabilistic numerical model was elaborated for structural damage accumulation evaluation. Model was realized and probability of CM plate reinforced by knitted glass fiber yarn was obtained.

VII REFERENCES

- [1] Ramakrishna, S and Hull, D., Tensile Behavior of Knitted Carbon-Fibre-Fabric/Epoxy Laminates, Composites Science and Technology, Vol. 50, 1994, pp.237-247.
- [2] A.Krasnikovs, O.Kononova, G.Harjkova, V.Zaharevskis and A.Galushchak „Mechanical Properties Characterization by Inverse Technique for Composite Reinforced by Knitted Fabric”, CD-Proceedings of ECCM15 – 15th European Conference on Composite Materials, Venice, Italy, 24-28 June 2012, 8 p.
- [3] Kononova, O., Krasnikovs, A., Harjkova, G., Zaļeskijs, J., Mačanovskis, E. Characterization of Mechanical Properties by Inverse Technique for Composite Reinforced by Knitted Fabric. Part 1. Material Modeling and Direct Experimental Evaluation of Mechanical Properties. Journal of Vibroengineering, 2012, Vol.14, Iss.2, pp.681-690.
- [4] Kononova, O., Krasnikovs, A., Dzelzītis, K., Harjkova, G., Vagele, A., Eiduks, M. Modelling and Experimental Verification of Mechanical Properties of Cotton Knitted Fabric Composites. Estonian Journal of Engineering, 2011, Vol.17, Iss.1, pp.39-50.
- [5] Ramakrishna, S., Cuong, N.K. and Hamada, H., Tensile Properties of Plain Weft Knitted Glass fiber Fabric Reinforced

- Epoxy Composites, *J. Reinf. Plast. & Comp.* Vol. 16, No 10, 1997, pp. 946-966.
- [6] Luo, Y.; Verpoest, I. Biaxial tension and ultimate deformation of knitted fabric reinforcements, *Compos. Part A: Appl. Sci. Manuf.* 2002, 33, 197–203.
- [7] Matusiak M and Sikorski K. Influence of the structure of woven fabrics on their thermal insulation properties. *Fibres Text East Eur* 2011; 19: 46–53.
- [8] Ramakrishna S., Fujita A., Cuong N.K., Hamada H. Tensile failure mechanisms of knitted glass fibre fabric reinforced epoxy composites. (Proc. Conf.) Fourth Japan International SAMPE Symposium, 25–28 September 1995. pp. 661–666.

# **Mechanical and electrical properties of the solid sapropel**

**Andris Martinovs<sup>1</sup>, Josef Timmerberg<sup>2</sup>, Rasma Tretjakova<sup>1</sup>, Paul Beckmann<sup>2</sup>,  
Valentina Popa<sup>1</sup>, Regina Wagner<sup>2</sup>**

<sup>1</sup> *Rēzeknes Augstskola, Faculty of Engineering,*

*Address: Atbrīvošanas aleja 115/K-4, Rēzekne, LV-4601, Latvia*

<sup>2</sup> *Jade University of Applied Sciences,*

*Address: Friedrich-Paffrath-Str. 101, 26389, Wilhelmshaven, Germany*

**Abstract.** In this paper are explored the mechanical (ultimate compression strength, ultimate strain, Young's modulus, hardness) and the electrical (relative permittivity, specific electrical resistance, quality factor, their dependence on the electric field frequency in the range till 1MHz) properties of the solid sapropel. For the researches are used samples from the solid, monolith sapropel (obtained in the drying process) and samples from the sapropel powder that are pressed with a different force; before the measurements, a part of these samples were heated. There is explored the dependence of the relative permittivity on temperature. Are explored the methods for the forming of the products from the solid sapropel powder.

**Keywords:** solid sapropel, mechanical properties, electrical properties, sapropel powder.

## I INTRODUCTION

Sapropel is a product of mechanical, physical, chemical, and biological transformations of the remnants of lacustrine plants and animals, as well as inorganic components of biogenic origin [1]. Process of creation of sapropel is reflected in works of many authors, for example [2], [3], [4], [5]. Sapropel is renewable natural resource. Overall resources of sapropel in Latvia are approximately 2 billion m<sup>3</sup>; layer of sapropel in hollows of lakes collects with speed 1-2mm per year; sapropel is used in agriculture, gardening, forest husbandry, animal husbandry, chemical industry, building, balneology and cosmetology; the amount of resources of sapropel and wide possibilities of using make it a national-scale strategic natural resource [5]. Lake sapropel production methods are reviewed in article [6]. In industrial scale in Latvia sapropel is used for production of soil enrichers by mixing it with peat. In small amounts it is used as a binder in building [7]. It is possible to use sapropel as modifying additive for binders in production of brown coal briquettes; dry lacustrine sapropel accelerate the oxidation processes and enhance adhesive coupling in the coal-binder system [1]. Admixing of sapropel enhance mechanical strength of brown coal briquettes; discovered increasing of adhesion strength of compounds of coal grains and goudron by using sapropel as modifying

additive [8]. Sapropel from which free water is separated is possible to use as natural sorbent [1]. In sapropel approximately 75% is organic matter; it determines biological activity, biochemical resistance, and adhesiveness of sapropel [1], [9]. According to [5] composition of organic matters in sapropel is 15-85%; composition and properties of various sapropel deposits are very different. Drugs derived out of sapropel can be used in veterinary medicine [10] as biostimulants [11] and as biologically active substances [12]. Sapropel is a good adsorbent; capacity for short residues is 70-75% [1]. Biological and chemical composition of sapropel layers in different depths can be used as biomarker, which gives information about changes of earth climate and geological conditions [13], [14]. Outlook would be using of this resource also in other national economy sectors so that brings maximally high added value. When the sapropel dries, it converts to a solid substance that is similar to stone. The solid sapropel – at present it is a new, in national economy almost unused material. It is necessary to know the mechanical, physical (thermal, electrical etc.), chemical and biological properties to find the maximal effective use of the solid sapropel. Researches of chemical properties of the sapropel were made by many authors, for example [4], [15], [16], [17]. Proved that the sapropel extracts have antibacterial properties and defined a positive correlation between the chemical composition and the biological activity

ISSN 1691-5402

© Rezekne Higher Education Institution (Rēzeknes Augstskola), Rezekne 2015

DOI: <http://dx.doi.org/10.17770/etr2015vol1.622>

of the sapropel [18]. A wide review of works of many authors about the classification, formation, chemical and biological properties see in [5]. The magnetic properties of the sapropel were researched in [19]. The thermal properties of the Black sea sapropel were researched in [20]; determined that depending on humidity (25- 72%) thermal conductivity is in the range 0.65- 1.25W/(m·K), specific heat capacity is 1580- 3260 J/(kg·K), density is 1150- 1900kg/m<sup>3</sup>. At the same time mechanical and electrical properties of the solid sapropel are less researched.

The aim of the work is to explore mechanical (ultimate compression strength, ultimate strain, Young's modulus, hardness) and electrical (relative permittivity, specific electrical resistance, quality factor) properties of the solid sapropel so that it would be possible to find the most effective further use of this material.

## II MATERIALS AND METHODS

For this research is used a sapropel that was gotten in Latvia, Rēzekne region, in the lake Ubogova (from depth) and in the Diunokļa bay of the lake Rušons (from the upper layer, 0.3-0.5m deep). The sapropel that was gathered before 1-3 months is filled into moulds and dried in the laboratory conditions (temperature 19-21°C, relative humidity 50-60%). To test the mechanical properties, are used cubic, monolith samples of the solid sapropel with polished surfaces and a dimension 11x11x11mm. For the testing electrical properties are used parallelepiped-form, monolith samples of the solid sapropel with polished surfaces and a dimension 11x11x4mm. The solid rest in the sapropel makes up about 8%. During the process of drying, there are several serious problems to form the samples of the solid sapropel – when this material become dry, it shrinks hard, cracks, crinkles, loses its form, consequently there are a lot of defective samples. So there is also used one another method to prepare the samples: particles of the solid sapropel are grinded into powder; this powder is to fill into cylindrical forming die (diameter 20mm) and to press with a constant force (3, 5, 8, 10, 15 tons); as a result we become cylindrical samples with a diameter 19.3mm, height about 21mm (to test the mechanical properties) and 5mm (to test the electrical properties). The size of the sapropel-powder-particles is not measured in the experiments.

To test the electrical properties is to apply silver-lacquer (Kemo N36BA L100 Electronic Conducting Silver) electrodes on two opposite sample-faces (with the largest surface area), with a thickness about 0.05mm.

There is performed a compression test for the samples with the universal tensile machine Zwick/Roell Z-150; compression rate – 10mm/min; temperature 20°C. Using the compression curves, we can determine the ultimate compressive strength,

strain and Young's modulus of the investigated material.

The electrical capacity of the samples for the DC case is determined with the Fluke 189 True RMS Multimeter. A sample of the solid sapropel (with a silver layer on the opposite faces) is inserted into a holder between steel electrodes that are connected with the multimeter. Then is measured the capacity  $C$  of the steel electrodes, among whom is placed the sapropel. After it, the sample of the sapropel is ejected from the holder; distance between the steel electrodes is equal with a thickness of the sample. Subsequently is measured the capacity  $C_0$  of the steel electrodes, among whom is air. If are given geometrical sizes of the samples- area of the silver electrode  $A$ , thickness of the sapropel-layer  $d$ , then the relative permittivity is:

$$\varepsilon = \frac{(C-C_0) \cdot d}{\varepsilon_0 \cdot A}, \quad (1)$$

where  $\varepsilon_0=8.85 \cdot 10^{-12}$ F/m- electric constant.

The electrical resistance  $R$  of the samples for the DC case is determined with the Megohmmetre Sefelec M1500P. The specific electrical resistance:

$$\rho = \frac{R \cdot A}{d}. \quad (2)$$

For the test of the electrical properties in the range from 20Hz to 1MHz is used the HP 4284A Precision LCR Meter; there is measured the conductance  $G$  and the susceptance  $B$  of the inspected samples. To calculate the relative permittivity and the specific electrical resistance are used equations (1), (2),

$$R = \frac{1}{G} \quad (3)$$

and

$$C = \frac{B}{2 \cdot \pi \cdot f}, \quad (4)$$

where  $f$ - frequency of the electric field.

The quality factor  $Q$  (that is inverse proportional to the dissipation factor) for a parallel tuned circuit is [21]:

$$Q = \frac{B}{G}. \quad (5)$$

For the researches of the electrical properties depending on temperature is used the oven Memmert UNE 400. The electrical parameters are determined in the range from 20 to 130°C; as a result are used average values obtained from the heating and the cooling processes.

## III RESULTS AND DISCUSSION

The compression curves of the solid, monolith sapropel from the lake Ubogova are given in Fig.1.

Hereof we see that the solid, monolith sapropel is a breakable material, during the elastic deformation compression (straight phases, where the Hooke's law is valid) remains almost intact until the rupture. The compression curves of the pressed (with strength 312MPa) sapropel-powder samples from the lake Ubogova see in Fig.2. The main mechanical properties of the solid sapropel during the compression are given in Table 1. A large scattering of the mechanical properties of the solid, monolith sapropel is related with problems during the sample preparation- in the drying process they shrinks hard, appear cracks, whose formation during the simple drying is not possible to exclude. The scattering of the mechanical properties of the solid, pressed sapropel can be explained by the fact that the granulometric

composition of the sample-forming powder was not constant.

The given experiments enable to compare the mechanical properties of the sapropel products, when they are obtained during the drying process and the powder pressing process. The strength of the sapropel-powder samples is more than two times lower than the strength of the samples that are obtained during the drying process. On the other hand, the pressed-powder samples have lower scattering of the mechanical properties than the samples that were dried. It means that during the powder-pressing process we can get products with the significantly more precise mechanical properties than using the method of drying.

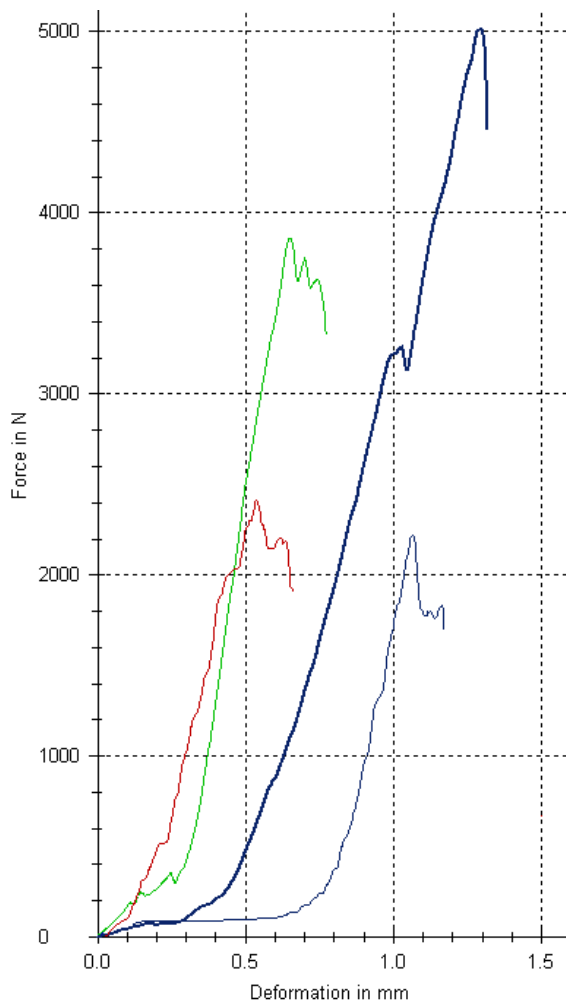


Fig.1. The compression curves of the sapropel samples (monolith cube 11x11x11mm) from the lake Ubogova.

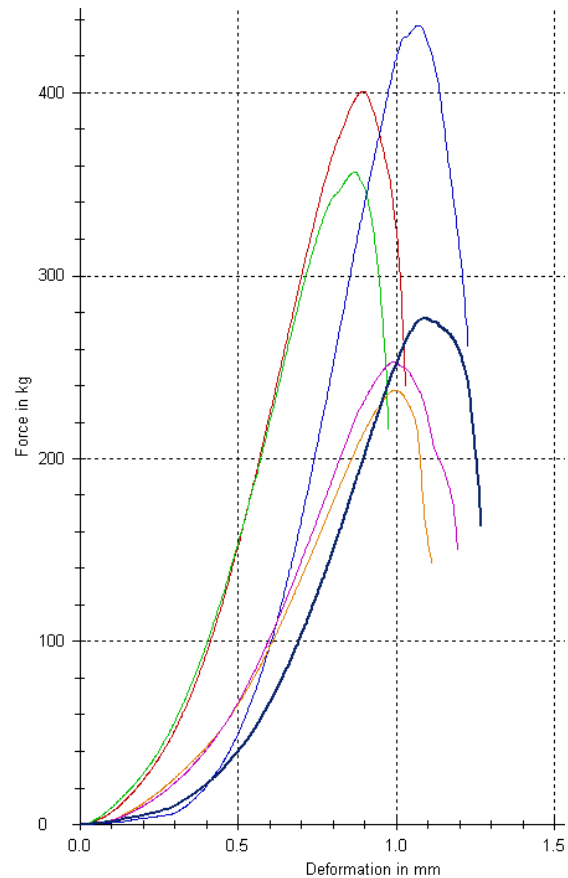


Fig.2. The compression curves of the pressed (with a strength 312MPa) sapropel-powder samples (cylinders: diameter 19.3mm, average height 21mm) from the lake Ubogova.

TABLE 1  
MECHANICAL PROPERTIES OF THE SOLID SAPROPEL FROM THE LAKE UBOGOVA AT 20°C.

	Solid, monolith sapropel	Pressed (312MPa) sapropel-powder
Ultimate compressive strength, MPa	28±15	11.3±2.8
Ultimate strain, %	4.0±2.6	3.51±0.39
Young's modulus, MPa	760±320	430±120
Hardness	<25 HRB	20 Shore C
Density, kg/m <sup>3</sup>	1260±80	-

One of the methods used by making products from metal powder is following: at first products are formed under compressive load, after it heated 30 – 90min at 0.6- 0.9 from the powder melting temperature, as a result there are forming stronger bonds between the powder particles, consequently increases the strength [22]. A similar approach is used also in the sapropel powder (although it is not a metal) case: the powder from the solid sapropel is to pour into cylindrical mould and to press applying the mechanical stress  $\sigma$ ; is gotten a cylindrical sapropel sample; this sample is to take out from the mould, to put into the oven and to heat 1 hour at 150°C (temperature is chosen following in order to avoid an ignition of the sapropel); after the cooling in air, the sample is to subject to the compression test. The ultimate compressive strength of the pressed sapropel-powder samples from the lake Ubogova with and without the heat treatment depending on the pressing strength  $\sigma$ , applied during the formation, is given in Fig.3, the ultimate strain  $\epsilon_{max}$  depending on  $\sigma$  see in Fig.4. From these figures, we see that the heat treatment after the formation worsens the mechanical properties of the sapropel products (if the sapropel powder is without admixtures).

The next researches in this area could be related to obtaining the relationships between the granulometric composition, pressure force, concentration of various admixtures (e.g. surfactants, low melting substances etc.), temperature and time during the formation and the heating processes and also for the mechanical properties of the sample- ultimate strength, ultimate strain, hardness. It would enable to improve the mechanical properties of the samples that are gotten using the powder pressing method. These researches would give a chance to create products from the solid sapropel, using the powder pressing method that is significantly simpler than the formation by the drying.

To research the electrical properties of the solid sapropel are used six different samples: 1, 2, 3 – monolith (obtained drying the sapropel) sapropel from the lake Ubogova, 4 – pressed (with a strength 250MPa) sapropel-powder from the lake Ubogova, 5 – pressed (with a strength 250MPa) sapropel-powder

from the Diunokļa bay, 6 – monolith sapropel from the Diunokļa bay.

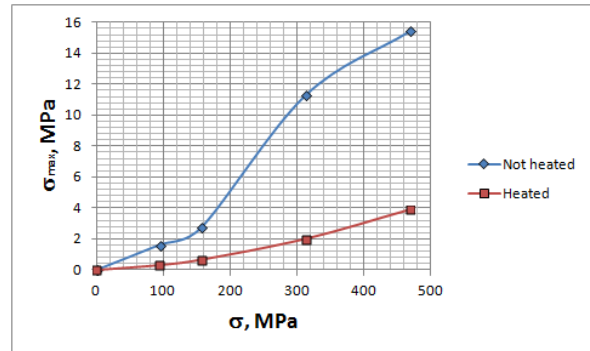


Fig.3. The ultimate compressive strength  $\sigma_{max}$  of the sapropel samples (cold-pressed sapropel powder) from the lake Ubogova depending on the pressing strength  $\sigma$  during the preparation of the samples; rhombus corresponds to the samples, which are not subjected to the heat treatment, squares- to samples that after the pressing were heated 1 hour at 150°C; measurement error of  $\sigma_{max}$  is 8.8%.

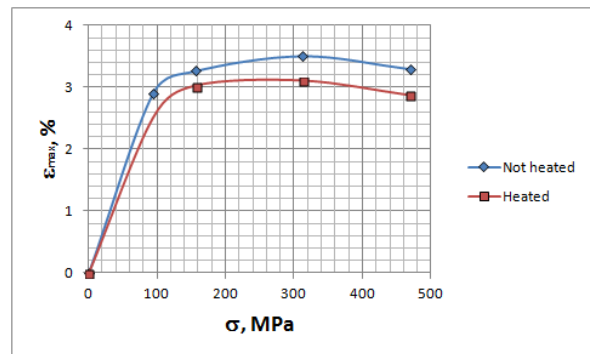


Fig.4. The ultimate strain  $\epsilon_{max}$  of the sapropel samples (cold-pressed sapropel powder) from the lake Ubogova depending on the pressing strength  $\sigma$  during the preparation of the samples; rhombus corresponds to the samples, which are not subjected to the heat treatment, squares- to the samples that after the pressing were heated 1 hour at 150°C; measurement error of  $\epsilon_{max}$  is 11%.

The electrical properties of the solid sapropel in the DC case at 20°C are given in Tab.2. As in the semiconductors  $\rho = 10^{-4} \dots 10^7 \Omega \cdot m$  [23], it means that the solid sapropel is an isolator (dielectric).

TABLE 2  
ELECTRICAL PROPERTIES OF THE SOLID SAPROPEL IN THE DC CASE AT THE TEMPERATURE T=20°C

	Lake Ubogova	Diunokļa bay
Solid, monolith sapropel		
Specific electrical resistance, $\Omega \cdot m$	$(4.3 \pm 2.1) \cdot 10^8$	$(4.0 \pm 3.2) \cdot 10^9$
Relative permittivity	7.4±3.0	16.6±3.0
Pressed (with a strength 250MPa) sapropel-powder		
Specific electrical resistance, $\Omega \cdot m$	$(6.9 \pm 4.8) \cdot 10^8$	$(4.9 \pm 3.3) \cdot 10^8$
Relative permittivity	9.3±3.0	7.7±3.0

The frequency curves of the solid sapropel for the specific electrical resistance are given in Fig.5, for the relative permittivity – in Fig.6, for the quality factor - in Fig.7. From the Fig.5 we see the general tendency - if the frequency  $f$  increases, the specific electrical resistance  $\rho$  decreases. In a dielectric exists not only an electron conduction mechanism (the current is transferred by the free electrons, the number of which is small in the dielectric) but also a polarization conduction mechanism: the electrons that are closely related to the crystal lattice cannot move from one atom to another but within the limits of the atom can shift in the direction of the electric field and polarize the atom [24]; when the frequency increases, the flow of these polarization-electrons becomes more intense in the direction of the electric field, the polarization-current becomes higher but the resistance - lower. An another explanation of this phenomenon could be the fact that in the case of the low frequencies the oxidation-reduction reactions have a high intensity, consequently decreases the concentration of the charged particles (dipoles, ions, electrons) near the electrodes that increases the resistance [25].

At the frequency 50Hz, the samples 1-5 have a local minimum of the specific electrical resistance, after which, in the frequency interval 50-100Hz, follows the 1.5-2.4-time increase of the specific electrical resistance. This could be explained that in the frequencies near 50Hz is observed a maximum of the resonance at some large, electrically charged molecular formations. From the Fig.5 is obvious that in the frequency range 20-100Hz the specific electrical resistance of the samples 1-5 is especially sensitive on the frequency.

From the relative permittivity  $\epsilon$ - frequency curve (see Fig.6) can be seen, if the frequency of the electric field increases, the relative permittivity decreases. An explanation is the decrease in a degree of the polarization of the ions and the dipoles, while the electric field frequency increases; at higher frequencies, the change of the position of the ions and the dipoles according to the electric field direction delays [Pavlov]. In addition, the relative permittivity has a local minimum in the frequency range 20-100Hz, where  $\epsilon$  is especially sensitive on the frequency.

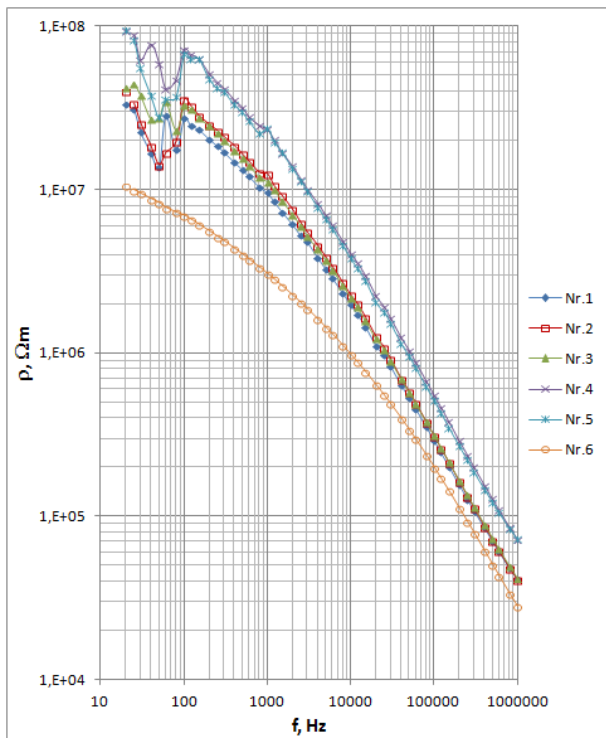


Fig.5. The specific electrical resistance of the solid sapropel depending on the frequency at 20°C

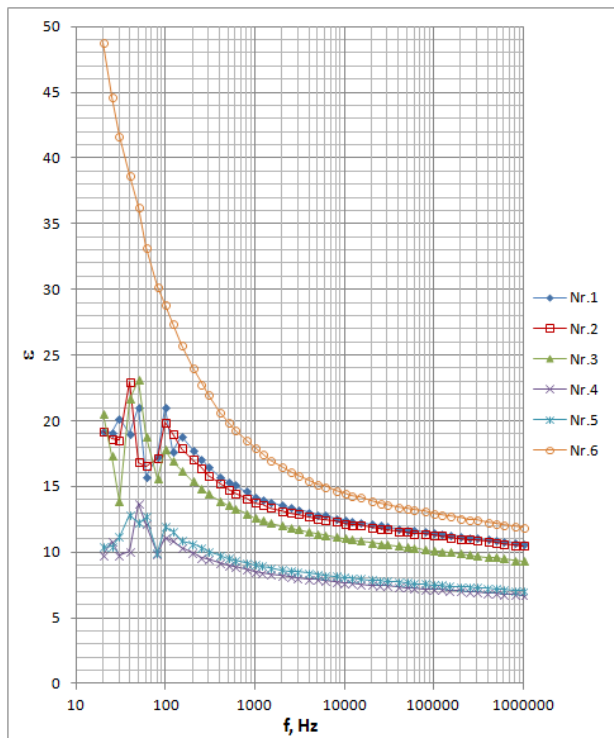


Fig.6. The relative permittivity of the solid sapropel depending on the frequency at 20°C

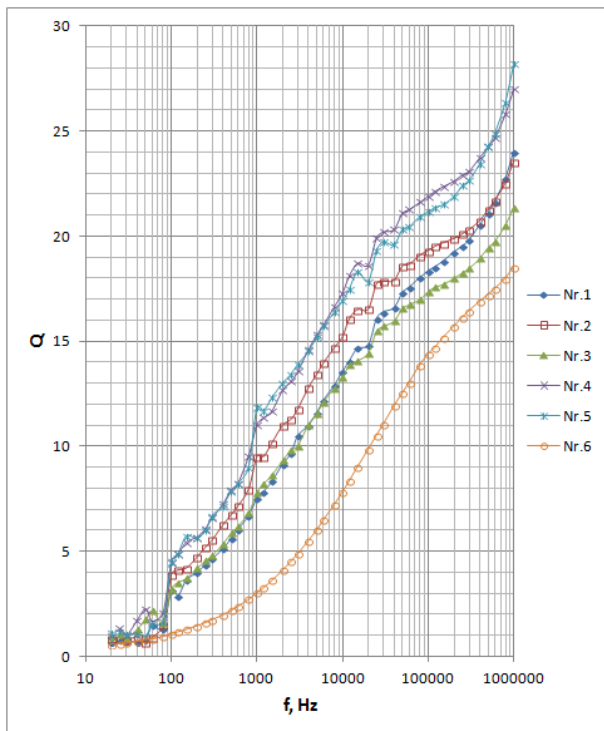


Fig. 7. The quality factor of the solid sapropel depending on the frequency at 20°C

If the relationships  $\rho=\rho(f)$  and  $\varepsilon=\varepsilon(f)$  are known, then the solid sapropel can be used in sensors to determine the frequency of the electric field. By measuring the electrical resistance or capacity of the sensor can be determined the frequency of the electrical field. Best of all is to use it in the frequency range, in which  $\rho$  and  $\varepsilon$  are especially dependent on  $f$ ; in this case – in the range 20-100Hz.

From the Fig.7 can be seen, if the frequency grows, the quality factor  $Q$  increases from 0.57-1.09 at the frequency 20Hz to 18-28 at the frequency 1MHz; the quality factor of the pressed-sapropel samples (4, 5) is higher; the local minimum of the quality factor is observed at frequencies 50-100Hz that can be explained by the significant decrease of the electrical resistance in this frequency range. From the relationships (1)- (5) we get:

$$Q = 2\pi\varepsilon_0 f \rho \varepsilon . \quad (6)$$

If the growth of  $f$  is faster than the reduction of  $\rho \cdot \varepsilon$ , where  $\rho=\rho(f)$  and  $\varepsilon=\varepsilon(f)$ , then, at the increasing frequency  $f$ , the quality factor  $Q$  must grow. It means that in the future materials from the solid sapropel could be used in electrical circuits (e.g. in condensers) with high (>1MHz) frequencies.

Is found that the relative permittivity of the solid sapropel during the increase of the temperature from 20 to 130°C grows (see Fig.8). The samples of the solid, monolith sapropel (1, 2, 3 and 6) have an increase of 11-16 times; the samples from the pressed

powder (4 and 5) – 1.7-3.8 times. An explanation is the existence of air pores in the samples from the pressed powder. In this research is found out that a change of the total capacity  $C_0$  (see relationship (1)) of sample-holder electrodes (air condenser) and supply-wires depending on the temperature is several times lower than a change of the capacity  $C$  of the sapropel condenser with the same dimension.

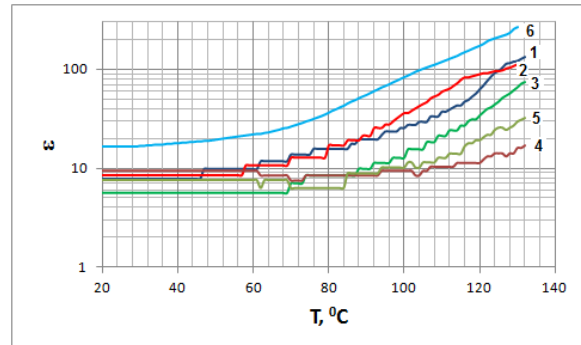


Fig.8. The relative permittivity of the solid sapropel (in the DC case) depending on the temperature; before that samples were not subjected to the heat treatment at the elevated temperature; measurement error  $\Delta\varepsilon=3$

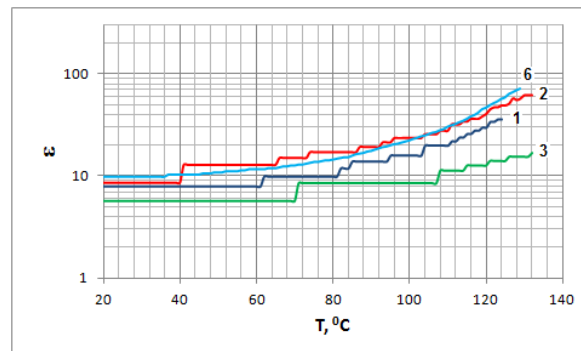


Fig.9. The relative permittivity of the solid sapropel (in the DC case) depending on the temperature; before that samples were subjected to the heat treatment- heated to 140°C and cooled in the oven to 20°C; measurement error  $\Delta\varepsilon=3$

Measurements of the relative permittivity depending on the temperature were repeated for the same samples (see Fig.9). Is determined that the growth of the relative permittivity of the samples, which has been heated before, depending on the temperature is decreased. An explanation could be related with two factors: 1) with the accelerated diffusion processes and the formation of stronger chemical bonds during the initial heating that complicates the polarization of the sapropel; 2) with the evaporation of the moisture and the volatile substances. This effect could be used in electronic and mechanical devices producing indicators (sapropel condensers) with a memory: if the device has been heated during the exploitation time, then the capacity of the condenser will be decreased; the value of the capacity could store the information about the heating-temperature and the heating-time. For this purpose we



must know the relationships between the capacity, heating-temperature and heating-time of each type of the indicators; the indicator must be located in a hermetic casing so that the effect of the air humidity would be excluded.

#### IV CONCLUSION

The solid, monolith sapropel has the ultimate compressive strength  $28 \pm 15$  MPa, ultimate strain  $4.0 \pm 2.6\%$ , Young's modulus  $760 \pm 320$  MPa, hardness  $HRB < 25$ , density  $1260 \pm 30$  kg/m<sup>3</sup>, specific electrical resistance  $2.2 \cdot 10^8 \Omega \cdot m - 7.2 \cdot 10^9 \Omega \cdot m$ , static relative permittivity 4.4- 19.6.

If the electric field frequency  $f$  in the range from 20 Hz to 1 MHz increases, then the specific electrical resistance  $\rho$  and the relative permittivity  $\varepsilon$  decrease but the quality factor  $Q$  grows. If the relationships  $\rho = \rho(f)$  and  $\varepsilon = \varepsilon(f)$  are known, then the solid sapropel can be used in the sensors to determine the electric field frequency, basing on the measurements of the electrical resistance or the capacity of the sensor.

If the temperature increases from 20 to 130 °C, then the relative permittivity of the solid, monolith sapropel grows 11-16 times, of the pressed sapropel powder - 1.7-3.8 times. If the solid sapropel is subjected to the heat treatment before the measurements (heated till 130 °C and cooled till 20 °C in the oven), then, after the repeated heating, its relative permittivity decreases: 0-1.7 times at 20 °C and 1.8-4.2 times at 130 °C. This effect could be used in indicators (sapropel condensers) with a memory; their capacity would store the information about emergency cases of the device during the exploitation time – heating-temperature and heating-time.

Forming of solid monolithic sapropel workpieces is problematic; technologically simpler is forming of workpieces under pressure out of sapropel powder. If cold pressing load for sapropel powder is 312 MPa, then ultimate compressive strength is  $11.3 \pm 2.8$  MPa that is more than 2 times lower than for monolithic sapropel. Heating of cold formed by pressing sapropel powder workpieces is not permitted (if powder is not modified, there are no surface active substances or admixtures in that), because of considerable decrease of strength. Further research can be concerned with modifying of sapropel powder particles, finding of surface active substances and admixtures, that increase strength of formed by pressure workpieces.

#### V ACKNOWLEDGMENTS

This work has been supported by Rēzeknes Augstskola and Jade University of Applied Sciences.

#### VI REFERENCES

- [1] **Nikolaeva L. A., Latyshev V. G., Burenina O. N.** Fuel Briquettes from Brown Coals of Yakutia. ISSN 0361-5219, Solid Fuel Chemistry, 2009, Vol. 43, No. 2, pp. 109–112.

- [2] **Rohling E.J.** (1994) Review and new aspects concerning the formation of eastern Mediterranean sapropels. *Mar. Geol.* 122, 1628.
- [3] **Rossignol-Strick M., Nesterhoff W., Olive P., and Vergnaud-Grazzini C.** After the deluge: Mediterranean stagnation and sapropel formation. *Nature* 295, 1982, p. 105-110.
- [4] **Hilde F. Passier.** Sulphur geochemistry and sapropel formation Syngenetic and diagenetic signals in eastern Mediterranean sediments. Mededelingen van de Faculteit Aardwetenschappen, Universiteit Utrecht, ISBN 90-5744-016-4, 1998, pp.154.
- [5] **Stankeveica K., Kļavins M.** Sapropelis un tā izmantošanas iespējas (Sapropel and Its Application Possibilities)// *Material Science and Applied Chemistry.* 2013 / 29, p.109-126. (in Latvian)
- [6] **Dement'ev V. A.** Removal of organic sediments from reservoirs and lakes and their processing// *Power Technology and Engineering;* Vol. 44, No. 4, 2010, p.289-292.
- [7] **Pleiksnis, S., Teirumnieka E.** Concrete containing sapropel and hemp sheaves for insulation of buildings. Latvijas Republikas patents: Nr. 14869, 20.11.2014. C04B18/18, C04B18/24, 20.06.2014.
- [8] **Черский И. Н., Давыдова Н. Н.** Проблемы рационального использования сапропелевых ресурсов// *Вестник Северо-Восточного научного центра ДВО РАН.* - 2009. - № 4. - С. 88-92. (in Russian)
- [9] **Kireicheva, L.V., Khokhlova, O.B.** Sapropeli: sostav, svoistva, primenenie (Sapropels: Composition, Properties, and Use), Moscow: Roma, 1998. (in Russian)
- [10] **Ядрихинский В. Ф., Перк А. А., Егорова М. С.** Применение препарата из сапропеля для лечения демодекоза собак// *Актуальные вопросы ветеринарной медицины.* - Новосибирск, 2003. - С. 71-72. (in Russian)
- [11] **Павлова П. А., Перк А. А., Егорова М. С.** Влияние биостимулятора из сапропеля на рост и развитие интродуцентов в условиях многолетней мерзлоты [Якутия]// *Фундаментальные и прикладные проблемы ботаники в начале XXI века: материалы Всерос. конф. (Петрозаводск, 22-27 сент. 2008 г.).* - Петрозаводск, 2008. - Ч. 6: Экологическая физиология и биохимия растений. Интродукция растений. - С. 291-294. (in Russian)
- [12] **Перк А. А.** Использование сапропелей криолитозоны в качестве источника получения биологически активных веществ гуминового ряда// *Перспективы фитобиотехнологии для улучшения качества жизни на Севере: материалы Междунар. конф. с элементами научной школы для молодежи, г. Якутск, Россия, 11-16 окт. 2010 г.- Якутск, 2010.* - С. 154-158. (in Russian)
- [13] **Rinna J., Warning B., Meyers P. A., Brumsack H.-J., Rullkötter J.** Combined organic and inorganic geochemical reconstruction of paleodepositional conditions of a Pliocene sapropel from the eastern Mediterranean Sea. *Geochimica et Cosmochimica Acta*, Vol. 66, No. 11, pp. 1969–1986, 2002.
- [14] **Edouard Bard, Gilles Delaygue, Frauke Rostek, Fabrizio Antonioli, Sergio Silenzi, Daniel P. Schrag.** Hydrological conditions over the western Mediterranean basin during the deposition of the cold Sapropel 6 (ca. 175 kyr BP). *Earth and Planetary Science Letters* 202 (2002) 481-494.
- [15] **Thomson J., Higgs N.C., Wilson T.R.S., Croudace I.W., de Lange G.J., and van Santvoort P.J.M.** (1995) Redistribution and geochemical behaviour of redox-sensitive elements around S1, the most recent eastern Mediterranean sapropel. *Geochim. Cosmochim. Acta* 59, 3487-3501.
- [16] **Angelidis M.O., Radakovitch O., Veron A., Aloupi M., Heussner S., Price B.** Anthropogenic metal contamination and sapropel imprints in deep Mediterranean sediments. *Marine Pollution Bulletin* 62 (2011) 1041–1052.
- [17] **Van Santvoort P.J.M., de Lange G.J., Thomson J., Cussen H., Wilson T.R.S., Krom M.D., Ströhle K.** (1996) Active post-depositional oxidation of the most recent sapropel (S1) in sediments of the eastern Mediterranean. *Geochim. Cosmochim. Acta* 60, 4007-4024.

- [18] **Галкина, И. С.** Сапропель Оренбургской области: биологическая активность и пути применения. Диссертации кандидата химических наук. (Galkina I.S. Sapropel Orenburg region: biological activity and ways of application; Dissertation of the candidate of chemical sciences) ВАК 05.17.07, Тула, 2003, с.221. (in Russian).
- [19] **Juan C. Larrasoana, Andrew P. Roberts, Joseph S. Stoner, Carl Richter, Rolf Wehausen.** A new proxy for bottom-water ventilation in the eastern Mediterranean based on diagenetically controlled magnetic properties of sapropel-bearing sediments. *Palaeogeography, Palaeoclimatology, Palaeoecology* 190, 2003, p.221-242.
- [20] **Petrinin G. I., Popov V. G., Soskov A. V.** Thermal Properties of the Bottom Sediments of the Black Sea// *Moscow University Physics Bulletin*, 2008, Vol. 63, No. 1, pp. 61–66.
- [21] HP 4284A Precision LCR meter. Operation manual. Hewlett Packard, 1998.
- [22] **Дальский А.М.** [и др.] Технология конструкционных материалов : учеб. для студентов машиностроит. Вузов, 6-е изд. Москва : Машиностроение, 2005. - 592 с. (in Russian)
- [23] **Siegfried Hunklinger:** Festkörperphysik. Oldenbourg Verlag, 2009, ISBN 978-3-486-59045-6, S. 378. (in Germany)
- [24] **Павлов П.В., Хохлов А.Ф.** Физика твердого тела// Москва: Высшая школа, 2000. (in Russian)
- [25] **Старцев А.Э., Ягубов З.Х.** Влияние удельной электропроводности бурового раствора на энергетические характеристики электромагнитного канала связи забойной телесистемы. *Электронный научный журнал «Нефтегазовое дело»*, 2011, No 3 (in Russian).

# **Design of LED Lamp with special spectral characteristics**

**Petko Mashkov<sup>1</sup>, Edmunds Teirumnieks<sup>2</sup>, Berkant Gyoch<sup>1</sup>, Hristo Beloev<sup>1</sup>,  
Tamara Pencheva<sup>1</sup>, Rostislav Kandilarov<sup>1</sup>**

<sup>1</sup>*University of Ruse.*

*Address: Studentska str. 8, Ruse, Bulgaria*

<sup>2</sup>*Rezeknes Augstskola, Faculty of Engineering,*

*Environmental Technology Transfer Contactpoint.*

*Address: Atbrivosanas aleja 115, Rezekne, LV-4601, Latvia.*

**Abstract.** The goal of this work is the design of LED lamp with adjustable spectral characteristics. The spectral power distribution (SPD) of the lamp can be adjusted to imitate the SPD of the daylight at noon and at evening. Noon light is “bluish” and stimulates cognitive abilities, work productivity and attention; sunlight at evening doesn’t inhibit melatonin production leading to improved sleep during the night and better health. Special combinations of LEDs with different spectral and power characteristics and proper control of the LEDs’ operation are used to achieve the required spectral characteristics of the lamp. Thermal management investigations are made at various ambient temperatures ranging from 20°C to 45°C and different current values through LEDs – up to their maximum values. They allow determining safety operating conditions for LEDs depending on the ambient conditions

**Keywords:** Power LEDs; LEDs’ thermal management.

## **I INTRODUCTION**

In 2012 the Scientific Committee on Emerging and Newly Identified Health Risks (an independent scientific committee under the European Commission) published the report “Health Effects of Artificial Light”. The report presented the possibilities for regulation of spectral characteristics of light sources to achieve better health, improved mood and work productivity. The interest in this topic has increased in the last couple of years. This is based on the possibilities to develop integrated energy efficient light sources which have variable spectral characteristics; can stimulate the cognitive abilities, work productivity and attention in factories and office buildings; change their light spectrum in the afternoon so it doesn’t inhibit melatonin production leading to improved sleep during the night.

When the sun is high in the sky, the spectral composition of the light is more intensive in the blue-violet part of the spectrum (correlated colour temperature CCT = 5500 ÷ 6500 K). It is known [1-15] that the radiation in that part of the spectrum (with maximum close to 440 nm – 480 nm) stimulates the production of cortisol and improves the cognitive abilities, work productivity, concentration, focus, and has positive effect on the mood. On the other hand light in this part of the spectrum inhibits production of

melatonin. Decrease in the production of this hormone leads to sleep problems and increases the risk of some cancers (breast cancer and others) [1-15].

During sunset sunlight passes through a thicker layer of air which leads to decrease of the intensity in the blue part of the spectrum and increase in the red-orange part. Light of this kind of spectral composition doesn’t inhibit melatonin production and the human body naturally prepares for rest and sleep.

The analysis of these facts leads to the conclusion that in order for artificial lightning to be beneficial for the health it needs to change its spectral composition in accordance with natural daylight.

The goals of this work are connected with design of LED lamp, proper for illumination a small room. The spectral characteristics of the lamp must be adjustable to imitate noon light (CCT = 5500 ÷ 6500 K) and sunlight at evening (CCT ~ 3000 K). The lamp’s operation control has to be easy and cheap.

## **II MATERIALS AND METHODS**

### *Choice of LEDs with proper spectral and power characteristics*

Meet specific design requirements of the lamp involves the use of LEDs with different spectral characteristics and different power. Our previous experience leads us to the use of LED module

Samsung (COB), SPHWTHDD 805WHV0ED [16] – Fig.1:



Fig. 1. Samsung LED, SPHWTHDD 805WHV0ED [16].

Its light output is 800 ÷ 900 lm at 460 mA and 1012 lm at 620 mA (junction temperature  $T_j = 25^\circ\text{C}$ ) at CCT 3000K [16]. Its use allows the fulfillment of the requirements for night lighting with a luminous flux of about 800 ÷ 850 lm.

To realize daylight with bluish light, which supports cognition, attention and working capacity is necessary to add LEDs with spectral characteristics with a maximum in the spectral region 440 ÷ 480 nm. After analyzing the properties of LEDs with appropriate features our choice is - LEDs XLamp XPCBLU – CREE Inc. Spectral characteristics of this type of LEDs are shown in Fig.2.

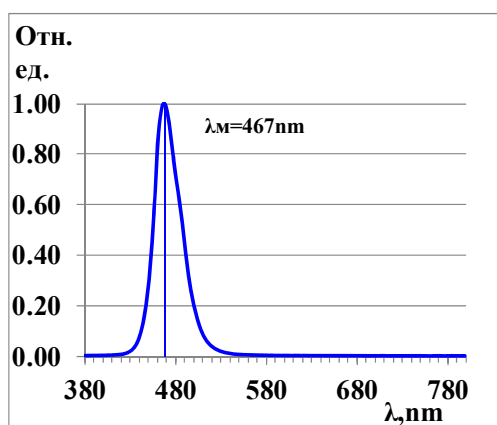


Fig. 2. Spectral characteristics of XPCBLU - CREE Inc.

Using LEDs' chromaticity (x, y in the 1931 CIE color space) and flux ( $\Phi = Y$ ) it is possible to calculate tristimulus values in color mixing, as follows [17]:

$$X = x \cdot (Y/y)$$

$$Y = Y$$

$$Z = (Y/y) \cdot (1-x-y). \quad (1)$$

$$Z_{\text{mix}} = Z_1 + Z_2 + Z_3 \quad (2)$$

$$X_{\text{mix}} = X_1 + X_2 + X_3$$

$$Y_{\text{mix}} = Y_1 + Y_2 + Y_3$$

$$x_{\text{mix}} = X_{\text{mix}} / (X_{\text{mix}} + Y_{\text{mix}} + Z_{\text{mix}})$$

$$y_{\text{mix}} = Y_{\text{mix}} / (X_{\text{mix}} + Y_{\text{mix}} + Z_{\text{mix}})$$

$$\Phi_{\text{mix}} = Y_1 + Y_2 + Y_3 \quad (3)$$

For various combinations of LEDs using the relationships (1) to (3) allow spectral characteristics' evaluation of the resultant radiation and to select the most appropriate combination. Calculations showed that using only blue LEDs satisfy the requirement for a sufficient intensity in the blue area (needed to stimulate the production of cortisol), but the luminous flux of the lamp is not of good quality, as it is far from the Planck's locus.

Theoretical calculations have shown that the optimal use of two blue and three green LEDs plus LED module Samsung allows achieving design goals. In this combination and selection of the magnitude of the current through the LEDs may produce appropriate spectral characteristics of the lamp - the luminous flux about 800 ÷ 850 lm and the color temperature of 5500 ÷ 6000 K. Green LEDs XLamp XPC – CREE Inc. are chosen.

All studies were further made in designed lamp are used: one LED module Samsung (Fig.1); two blue LEDs XPCBLU – CREE Inc. and three green LEDs XPCGRN – CREE Inc

#### Thermal managements' calculations

Usually for thermal managements calculations and junction temperature  $T_j$  estimations the thermal resistance model, described in [17], is used – Fig. 3.

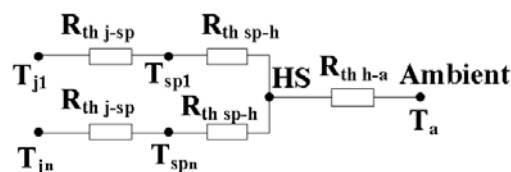


Fig. 3. Thermal resistance model for n XLamp LEDs.  $R_{\text{th j-sp}}$  - thermal resistance from junction to solder point;  $R_{\text{th sp-h}}$  - thermal resistance from solder point to heat sink;  $R_{\text{th h-a}}$  - thermal resistance from heat sink to ambient;  $T_{j1}$ ,  $T_{jn}$  and  $T_{sp1}$ ,  $T_{spn}$  are junction and solder point temperatures corresponding.

$$T_{j\text{MAX}} = T_{a\text{-max}} + (R_{\text{th j-sp}} + R_{\text{th sp-h}}) \cdot P_{\text{LED}} + R_{\text{th h-a}} \cdot P_{\text{tot}} \quad (4)$$

where:

$R_{\text{th h-a}}$  - thermal resistance from heat sink to ambient.

$P_{\text{LED}}$  is the power of one LED chip:

$$P_{\text{LED}} = I_F \cdot U_F; \quad (5)$$

$P_{\text{LEDS}} = I_F \cdot U_F = 0.46 \cdot 17 = 7.82 \text{ W}$ ; for Samsung LED module;

$P_{\text{LEDBLU}} = I_F \cdot U_F = 0.35 \cdot 3.3 = 1.16 \text{ W}$  for blue LED;

$P_{\text{LEDGRN}} = I_F \cdot U_F = 0.35 \cdot 3.4 = 1.19 \text{ W}$  for green LED;

$P_{\text{tot}}$  is the power of all LEDs:

$$P_{\text{tot}} = P_{\text{LEDS}} + 2 \cdot P_{\text{LEDBLU}} + 3 \cdot P_{\text{LEDGRN}} = 13.7 \text{ W};$$

For Samsung LED module  $R_{th\ j-sp} = 2.24^{\circ}C/W$ ;  $R_{th\ sp-h} = 0.4^{\circ}C/W$  [16];

For blue LED  $R_{th\ j-sp} = 12^{\circ}C/W$ ;  $R_{th\ sp-h} = 1^{\circ}C/W$ ;

For green LED  $R_{th\ j-sp} = 20^{\circ}C/W$ ;  $R_{th\ sp-h} = 1^{\circ}C/W$  [17].

The calculations made on the basis of equation (4) show that heat sink with thermal resistance  $R_{th\ h-a} = 1^{\circ}C/W$  is sufficient - even under the most heavy operating conditions (ambient temperature  $45^{\circ}C$  and maximum operating current) junction temperature  $T_{j\ MAX}$  of the LEDs does not exceed  $85^{\circ}C$  which is quite acceptable.

### III RESULTS AND DISCUSSION

#### Spectral characteristics of the lamp

Spectral characteristics are experimentally determined using measurements equipment of Stellar Net.

**1. First operating regime - spectral power distribution (SPD) of the lamp stimulates cognitive abilities, work productivity, concentration, focus, and has positive effect on the mood.**

In this case the spectral distribution of the radiation is characterized by a peak in the area  $440 \div 480\ nm$ . All LEDs are on, the size of the current through the blue and green LEDs is  $350\ mA$ ; by controlling the magnitude of the current through Samsung LED module correlated color temperature can be set between  $5000\ K$  and  $6000\ K$  – Fig. 5 – Fig. 8.

Depending on the selected mode of operation and ambient temperature the luminous flux is in the interval  $800 \div 850\ lm$ . As can be seen from Fig. 5, Fig. 7 and Fig. 8 the coordinates of the radiant flux is positioned close to the Plank's locus.

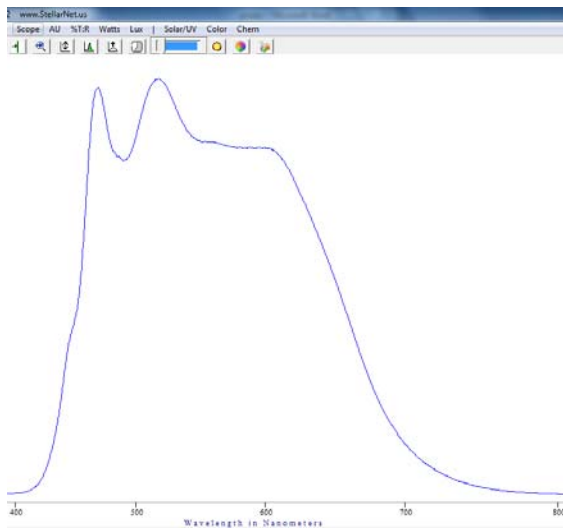


Fig. 4. Lamp's spectral characteristic. The current through the blue and green LEDs is  $350\ mA$ ; through Samsung LED module  $360\ mA$ .

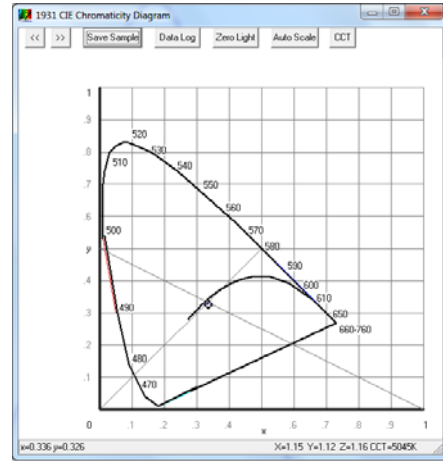


Fig. 5. Color temperature 5045K.

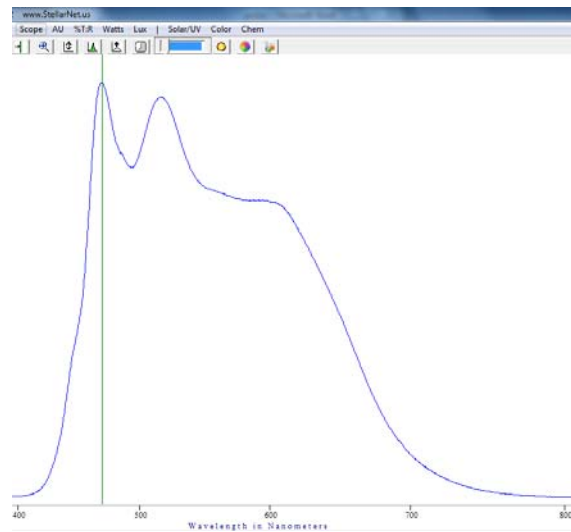


Fig. 6. Lamp's spectral characteristic. The current through the blue and green LEDs is  $350\ mA$ ; through Samsung LED module  $300\ mA$ .

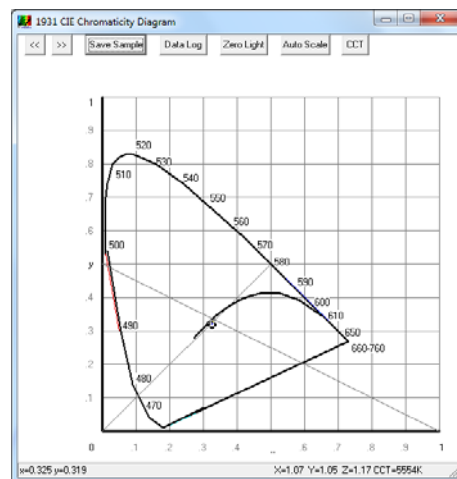


Fig. 7. Color temperature 5554K.

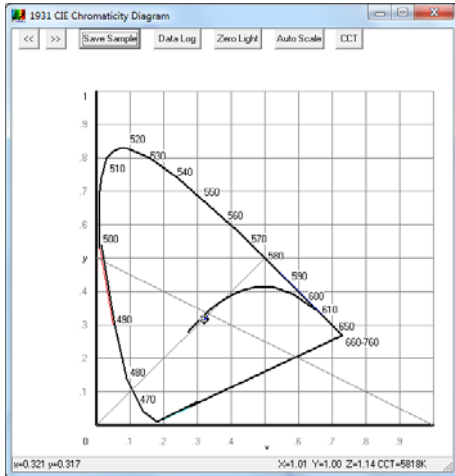


Fig. 8. Color temperature 5818K.

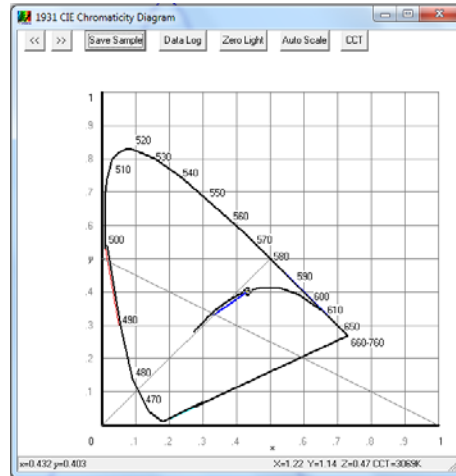


Fig. 10. Color temperature 3069K.

**2. Lamp's spectral power distribution (SPD) which doesn't inhibit melatonin production and the human body naturally prepares for rest and sleep.**

In this case only lights the Samsung LED module. To maintain the same luminous flux ( $800 \div 850$  lm) the current through the LED module is increased up to 500mA. In the spectral distribution of the light flux is absent intense blue component, which suppresses the production of melatonin – Fig. 9. The CCT of the luminous flux is about 3000K – Fig. 10. These features in the spectral distribution of the lamp's luminous flux makes it suitable for lighting in the second half of the day - late afternoon and evening, when the human body naturally prepares for rest and sleep.

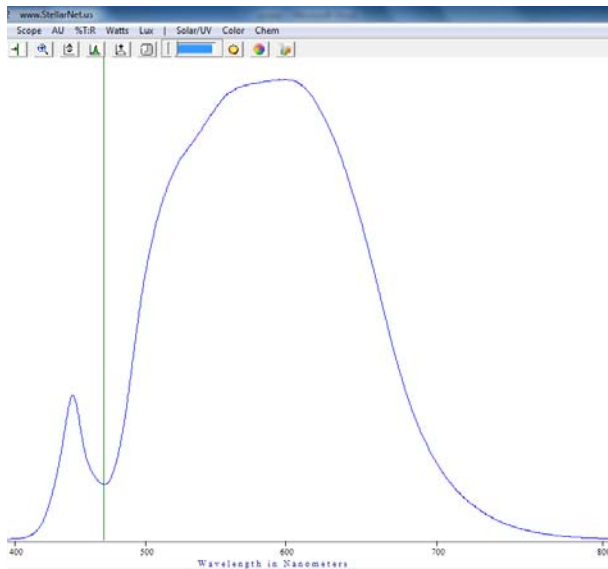


Fig. 9. Lamp's spectral characteristic. The current through the Samsung LED module is 500mA.

**LEDs' thermal management. Experimental investigations.**

Experiments are made in a thermal chamber where the temperature is kept at desirable values with the accuracy better than 0.5°C.

Solder point temperatures' distributions are measured using IR camera Therma Cam E300 – FLIR Systems; results are verified using standard measurement technique – by thermocouples.

At each value of solder points' temperatures  $T_{sp}$  the corresponding temperatures of the LEDs' junction are calculated in accordance with [17]:

$$T_j = T_{sp} + R_{th\ j-sp} * P_{LED}. \quad (6)$$

Results are presented below:

**1. First regime of operation – all LEDs are switched on; the currents' values through LEDs are: for Samsung module  $I_{Samsung} = 460$  mA; for green and blue LEDs  $I_{GRN} = I_{BLU} = 350$  mA.**

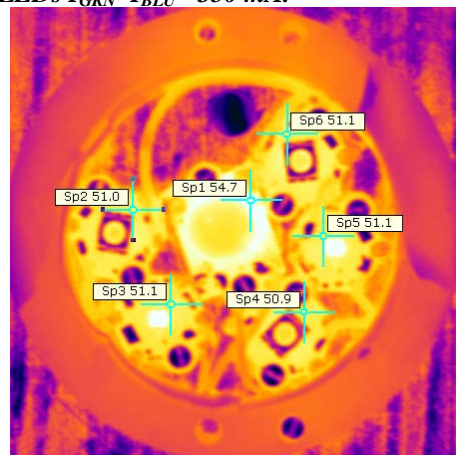


Fig. 11a. First regime of operation. IR photo of LED lamp. Sp – measured solder point temperatures. Ambient temperature  $T_a = 25^\circ\text{C}$ .

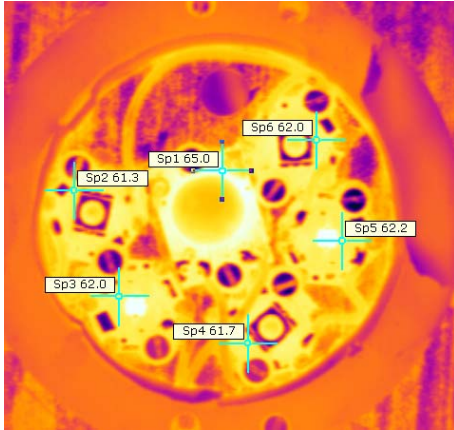


Fig. 11b. First regime of operation. IR photo of LED lamp. Sp – measured solder point temperatures. Ambient temperature  $T_a=45^\circ\text{C}$ .

In Fig. 12 ÷ Fig. 14 measured temperatures of solder points of LEDs and corresponding calculated junctions' temperatures at different temperatures of ambient air are presented.

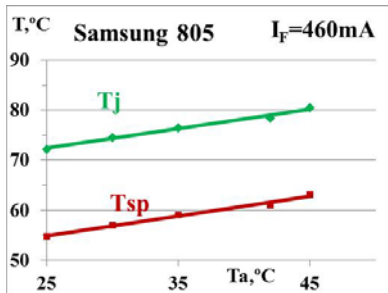


Fig. 12. Solder point's temperature  $T_{sp}$  and junction temperature  $T_j$  dependences on temperature of the ambient air  $T_a$  for the Samsung module;  $I_F = 460\text{ mA}$  – forward current through Samsung module.

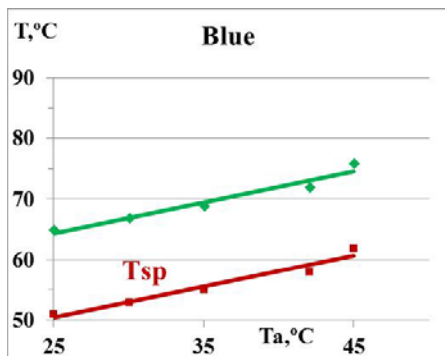


Fig. 13. Solder point's temperature  $T_{sp}$  and junction temperature  $T_j$  dependences on temperature of the ambient air  $T_a$  for the blue LEDs;  $I_F = 350\text{ mA}$  – forward current through blue LEDs.

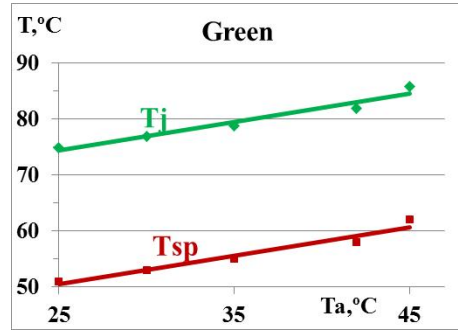


Fig. 14. Solder point's temperature  $T_{sp}$  and junction temperature  $T_j$  dependences on temperature of the ambient air  $T_a$  for the green LEDs;  $I_F = 350\text{ mA}$  – forward current through green LEDs.

**2. Second regime of operation – only Samsung LED module is switched on; the current through Samsung LED module is  $I_{Samsung} = 500\text{ mA}$ .**

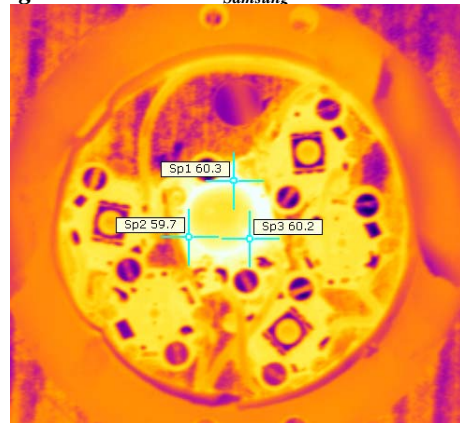


Fig. 15. Second regime of operation. IR photo of LED lamp. Sp – measured solder point temperatures. Ambient temperature  $T_a=42^\circ\text{C}$

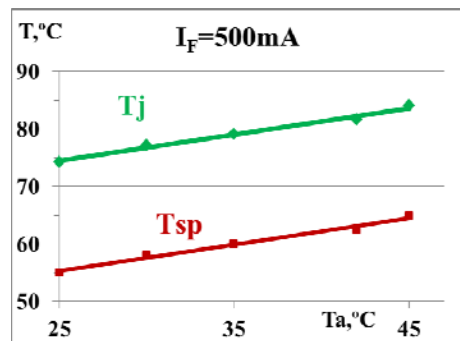


Fig. 16. Second regime of operation. Solder point's temperature  $T_{sp}$  and junction temperature  $T_j$  dependences on temperature of the ambient air  $T_a$  for the Samsung module;  $I_F = 500\text{ mA}$  – forward current through Samsung module.

As it can be seen from the Fig. 12, Fig. 13, Fig. 14 and Fig. 16 junction temperatures  $T_j$  for all types of LEDs don't exceed  $85^\circ\text{C}$ , which ensure safety working condition and long life of the designed lighting equipment.

#### IV CONCLUSION

LED lamp with special spectral characteristics is designed and produced. The spectral characteristics of the lamp contribute to the preservation of human health. The lamp can be used in two modes of operation: in the first mode (lighting during the day) spectral characteristics of the light stimulate the production of cortisol (and inhibits production of melatonin) in the human body and improves the cognitive abilities, work productivity, concentration, focus, and has positive effect on the mood; in the second regime (lighting in the evening) light's spectral characteristics doesn't inhibit melatonin production and the human body naturally prepares for rest and sleep. The transition between the two modes of operation can be performed quite simply - with a key or remote control.

#### V ACKNOWLEDGMENTS

The National Science Fund, Ministry of Education and Science of Bulgaria, is gratefully acknowledged for the financial support of research project DFNI – B02/2 12.12.2014 (Int. № FNI B 02/75).

#### VI REFERENCES

- [1] B. Ramos-Alvarado, B. Feng, G.P. Peterson, Comparison and optimization of single-phase liquid cooling devices for the heat dissipation of high-power LED arrays, *Applied Thermal Engineering*, 59, (2013), pp. 648-659
- [2] L. Bellia, A. Pedace, G. Barbato, Lighting in educational environments: An example of a complete analysis of the effects of daylight and electric light on occupants, *Building and Environment*, 68 (2013), pp. 50-65.
- [3] C. Cajochen, Alerting effects of light, *Sleep Medicine Reviews* (2007)11, pp.453–464.
- [4] L. S., R. Steiner, P. Blattner, P. Oelhafen, T. Gotz, C. Cajochen, Non-Visual Effects of Light on Melatonin, Alertness and Cognitive Performance: Can Blue-Enriched Light Keep Us Alert?, *Blue-Enriched Light, Alertness and Performance*, January 2011, Volume 6, Issue 1, e16429, pp.1-12.
- [5] Edwards L. and P. Torcellini, A Literature Review of the Effects of Natural Light on Building Occupants, U.S. Department of Energy Laboratory, 2002, p.58.
- [6] E. V., E. W. Gonzalez, D. A. Kratzer, D. L. McEachron, G. Yeutter, Auto-tuning Daylight with LEDs: Sustainable Lighting for Health and Wellbeing, ARCC 2013, The Visibility of Research Sustainability: Visualization Sustainability and Performance, pp.465-473.
- [7] Fisk W. J., Review of Health and Productivity Gains From Better IEQ, *Proceedings of Healthy Buildings 2000*, vol 4, pp 23-34.
- [8] V. Gabel, M. Maire, C. F. Reichert, S. L. Chellappa, C. Schmidt, V. Hommes, A. U. Viola and C. Cajochen, Effects of Artificial Dawn and Morning Blue Light on Daytime Cognitive Performance, Well-being, Cortisol and Melatonin Levels, *Chronobiology International*, Informa Healthcare USA, Inc (2013), pp.1–10.
- [9] Illuminating the Effects of Dynamic Lighting on Student Learning, Michael S. Mott - The University of Mississippi, Daniel H. Robinson -The University of Texas, Ashley Walden, Jodie Burnette & Angela S. Rutherford - The University of Mississippi
- [10] In-Tae Kim, An-Seop Choi, Jae-Weon Jeong, Precise control of a correlated color temperature tunable luminaire for a suitable luminous environment, *Building and Environment*, 57 (2012), pp. 302-312.
- [11] Ir.W. J. M. van Bommel and Ir. G. J. van den Beld, Lighting for work: visual and biological effects, April 2004, Philips Lighting, The Netherlands, 2004, p.20.
- [12] Ir.W.J.M. van Bommel, Ir. G.J. van den Beld, Ir. M.H.F. van Ooijen. Industrial lighting and productivity, Philips Lighting, The Netherlands, 2002, p.20.
- [13] Joseph A., The Impact of Light on Outcomes in Healthcare Settings, 2006 The Center for Health Design, p.14.
- [14] Knez I. Effects of colour of light on nonvisual psychological processes, *Journal of Environmental Psychology*, Volume 21, Issue 2, June 2001, pp. 201–208.
- [15] L. Bellia, F. Bisegna, G. Spada, Lighting in indoor environments: Visual and non-visual effects of light sources with different spectral power distributions, *Building and Environment*, 46, (2011), pp. 1984-1992.
- [16] [www.samsung.com](http://www.samsung.com)
- [17] [www.cree.com/xlamp](http://www.cree.com/xlamp)



# Research of Oil Product Sorption Processes by Ferromagnetic Sorbents

V. Mironovs<sup>1</sup>, J. Treijs<sup>1</sup>, E. Teirumnieks<sup>2</sup>

<sup>1</sup> Riga Technical University, Riga, Latvia,

<sup>2</sup> Rezekne Higher Education Institution, Rezekne, Latvia

**Abstract.** In paper, is given overview of sorbents with ferromagnetic particles. The series of newly designed composite sorbents SOMSOR, are described. Described experiment of oil spill collection from water surface, which comprises of sorbent spreading and collection. Oil sorption by capillary forces, is discussed. Concluded that use of ferromagnetic sorbents a promising direction in the field of water purification from light oil products since it allows expanding the scope of the used powder sorbents, to use the high-mechanized methods of collecting by means of magnetic and electromagnetic devices.

**Keywords:** oil spill collection, ferromagnetic sorbent, metal powder, composite sorbent, buoyancy.

## I INTRODUCTION

Possibilities for use of the disperse sorbents for collecting oils and other oil products (OPs) poured on a water surface and at the bottom of a reservoir, have been considered in many papers, including [1-3]. The sorbent which is used for collecting OPs poured in water, has to possess the following properties:

- to possess good sorption to OPs;
- to have low cost;
- to be non-toxic;
- good to be sprayed;
- to be reused;
- good to be grasped by mechanized means;
- easy to surrender OPs at the place of collecting.

High interest in the powder sprayed sorbents with magnetic properties (PSMS) is observed during the recent years. Works are conducted for creation and application of such sorbents at the Riga Technical University and the Rezekne Higher Education Institution in the course of several years [4-8]. Iron powders were generally used as initial materials for their preparation. For increase of efficiency of the processes of sorption and decrease in expenses, topical issues are related to use of the crushed rolling scale, and also to development and application of composite sorbents, et al. In this case also research of processes of sorption, removal of a collected sorbent with oil product (SOP), subsequent technologies of utilization and regeneration is very important.

## II SOME VARIETIES OF POWDER SORBENTS

### 2.1 Sorbents on the basis of rolling scale

Rolling scale (RS) of Liepaja metallurgical plant [4] was offered to be used as material for removal of OPs from water. Its advantages in this case: low cost since scale is a little-used technological residue of production; fast grindability to the state suitable for dispersion on a water surface; good magnetic properties and safety for environment.

For researches the rolling scale has been used, which is formed during production of the low-alloyed flint-manganese steel of the brands 35 GS, 25G2S, applied for production of construction fittings. Scale in steel-rolling production of the enterprise is collected by means of the crane supplied with an electromagnet and is stored.

Our researches have showed that scale with the minimum period of storage is appropriate to be used for production of a sorbent. It is established that the optimum size PO (the size of particles) has to be within 1-2 mm.

During studies it was also established that efficiency of sorption is increased by preliminary mixing of scale powder with OPs and the subsequent drying of mixture [6].

### 2.2 Sorbents based on iron powders

Powder materials on the basis of powders of iron ASC 100.29 (sprayed, used in production of constructional details to methods of powder metallurgy), MH 80.23 (restored spongy, used in the production of self-greased sliding bearings),

ISSN 1691-5402

M20/80-19 (with low content of carbon) and R-12 (with low content of hydrogen, used in production of frictional products) were used as a research material. All the powders are produced by Höganas AB company (Sweden). Also the powder CMS was used, which represents residue from filters. These materials were tested in a condition of delivery, as well as after processing in oil and subsequent ignition [7].

### 2.3 Composite sorbents

One of the composite sorbents (CS) on the basis of iron was offered earlier in [3]. Its feature is represented by especially small dispersion (5-10  $\mu\text{m}$ ). Such sorbent doesn't destroy the film of oil product, and modifies its properties. Its buoyancy increases, however fluidity sharply decreases. Due to this its spraying is made difficult. Efficiency of the method has appeared to be rather low since the modification process is slow, the size of lifting effort is small, and the sorbent cost is high.

We have developed the COMSOR type composite sorbents [8]. These represent mixes of iron fine dispersed powders with cenospheres (the waste formed when burning coal (Fig. 1). Use of modification of sorbents has succeeded to increase sorption ability of a sorbent by 2-5 times with its bulk mass of just 0.6-0.8 (in relation to earlier used dry sorbents on the basis of iron powders having the bulk mass of 1.4-1.8  $\text{g}/\text{cm}^3$ ).

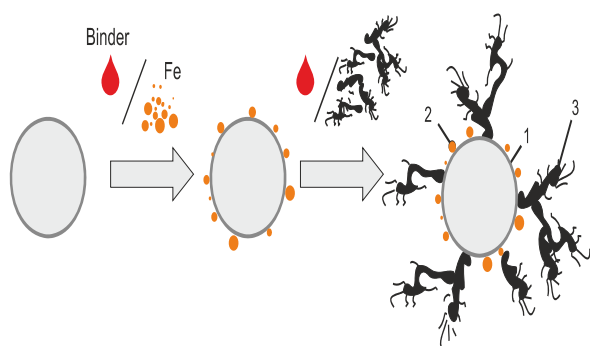


Fig.1. Scheme of creation of COMSOR composite sorbent

Important role for the process of sorption is played by a particle surface and its form (Fig. 2). The best results with regard to efficiency have appeared for the particles of a powder sorbent M20/80-19 (a) having highly branched surface, and at a composite sorbent Comsor M (c), differing for its small bulk weight and increased buoyancy.

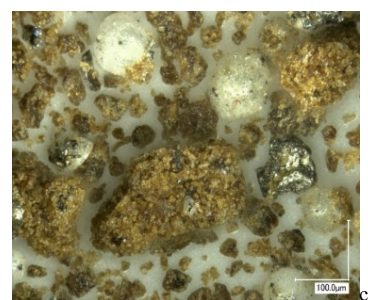
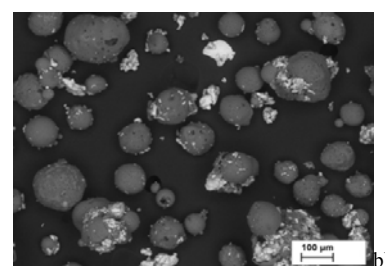
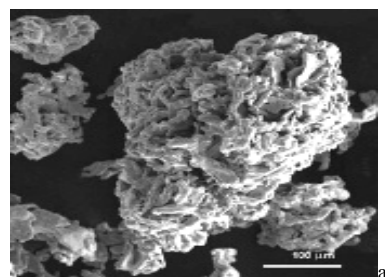
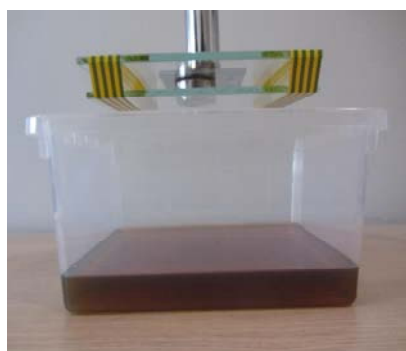


Fig. 2. Morphology of a particle surface of a powder sorbent M20/80-19 (a), composite sorbent Comsor A(b) and sorbent Comsor M (c).

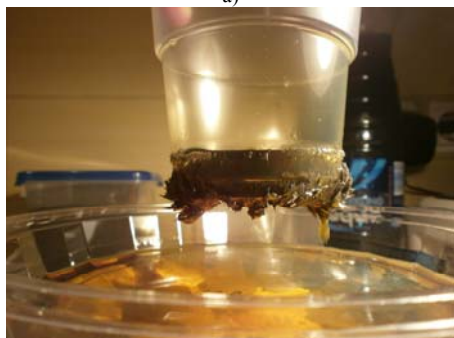
### III EQUIPMENT. EXPERIMENT METHODOLOGY

Experimental tests of the operation of sorbents are performed on the experimental installation made at the Rezekne Higher Education Institution (Latvia) (Fig. 3). Installation is equipped with highly effective permanent magnets FeNiB. It allows installation of magnets of various loading capacity and alteration of distance between the polluted water surface, and a magnet.

The experiment methodology has included the following stages: filling in non-magnetic capacity of water at the fixed height (not less than 30 mm); application on its surface of oil product (transmission oil TAD-17 with the specific weight of 0,8  $\text{g}/\text{cm}^3$ ); holding during 2-3 minutes for development of stable film, spraying of the set mass of powder on the film by means of a rotating disk [7]; removal of the collected oil product and carrying out further researches for assessment of sorption ability and thermogravimetric research.



a)



b)

Fig. 3. General view of the experimental equipment(a) and working process of sorption(b).

Previously bulk weight, the form and the size of particles of a sorbent, its fluidity, connecting ability concerning oil product, water absorption, buoyancy and possible energy consumption has been identified.

#### IV FEATURES OF THE SORPTION PROCESS

The powder sorbent on the basis of iron powder or PO has a branched surface of particles with rather high specific surface. Monitoring has showed that the process of sorption is taking place in manifestation of the coagulation, gravitation and infiltration phenomena. Fine dispersed material is evenly dispersed or sprayed on a quiet surface of a water-oil layer. In addition to that, the smaller the powder, the more even turns out a covering. Further due to magnetic interaction and adhesion, suspension coagulates in large globules, clearing considerable part of a surface from the oil product film (up to 50%). Accurately expressed clots (fig. 4) are formed from uniform layer of powder on the oil spot. They should be removed quickly enough as further under influence of the gravitational phenomena and infiltration of oil product in the pores of particles, the last fall to the bottom of a vessel (Fig. 5c). It occurs during 10-20 min.



Fig. 4. Stages for performance of experiment a) coagulation of OPs: b) raising of SOPs, c) falling of OPs to the bottom of a vessel

The water oil film approaches the surface of firm particle of a powder sorbent under some acute angle  $\theta$  (edge angle of wetting) characteristic for this couple liquid – solid body (Fig. 6). For improvement of process of sorption it is necessary to seek its reduction. It can be reached, for example, by means of preliminary processing of a powder sorbent in oil and its subsequent drying.

High importance on the process of sorption is rendered also by capillary phenomena in particles. Water oil liquid rises on capillaries of a porous particle until  $Ft$  gravity force operating on a liquid column in a capillary doesn't become equal to the module of surface tension forces (1)

$$Fn = \sigma 2\pi r \cos \theta, \quad (1)$$

where  $\sigma$  – coefficient of a superficial tension of a film.

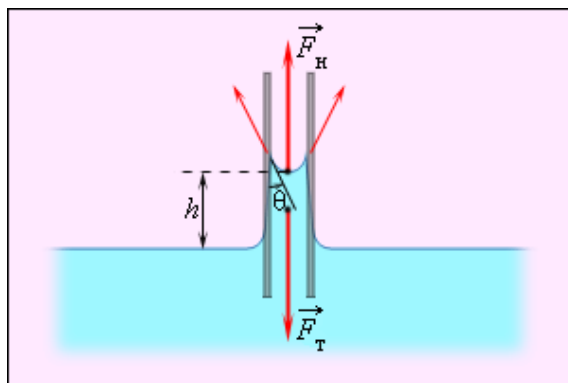


Fig. 5. The scheme of manifestation of capillary forces during sorption

Containment of collected oil product (SOPs) on a water oil surface is taking place not only due to forces of a superficial tension of the environment (in this case it is a water oil film), but also at the expense of air which is contained in the pores of particles of a sorbent.

The course of process to a large degree depends on dispersion of a powder sorbent, form of its particles, size of a specific surface, bulk weight, and also degree of dispersion and some other factors.

For removal of SOPs, force of a permanent magnet (or an electromagnet) is used, which necessary size depends from the gravity  $F_g$  and water oil film tension  $F_a$  (Fig. 6).

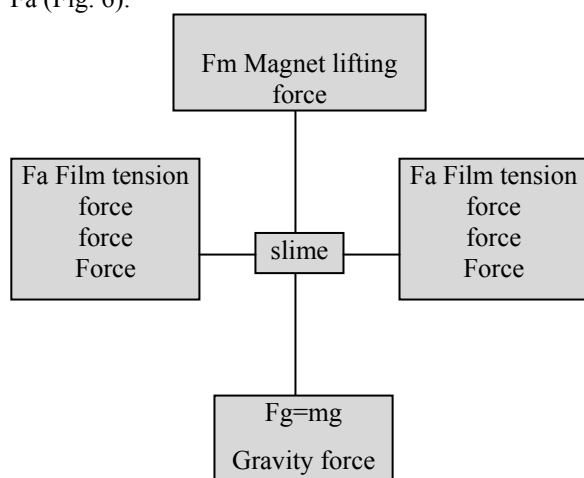


Fig. 6. The scheme of operation of forces in the course of magnetic sorption.

$F_g$  - Gravity force of slime (sorbent + oil product + water) depends on the weight and the specific weight of a sorbent, oil product and water.

For calculations of necessary lifting force it is possible to presume that the amount of water, contained in the sorbent pores, as up to 5-8%, and oil

absorption ability – up to 30% from the sorbent mass. The bulk weight of a sorbent on the basis of iron powders may be assumed as  $0.8 - 2 \text{ g/cm}^3$ , and sorbent layer thickness for removal of light oil products - not more than 1-3 mm. All this will allow determining the mass of a necessary sorbent.

At the moments of undulation of the water surface as a result of dispergating the water-oil emulsion, the content of water increases, which leads to increase in its apparent viscosity, and this, in its turn, increases power costs of sorption of such emulsion.

## V CONCLUSIONS

1. Use of ferromagnetic sorbents represents a perspective direction in the field of water purification from light oil products since it allows expanding the scope of the used powder sorbents, to use the high-mechanized methods of collecting by means of magnetic and electromagnetic devices.

2. Process of magnetic sorption has some pronounced stages: coagulation, infiltration, separation of a collected product from the water-oil surface, transportation and warehousing.

## VI REFERENCES

- [1] Pat. 4784773, U.S., MCI C 02 F 1/40. Petroleum product absorption method and apparatus. Sandberg Fr.H.
- [2] Orbell, JD, Dao, HV, Ngeh, LN, bigger, SW 2005, "Magnetic particle technology in environmental remediation and wildlife mental", Proceedings of the 9th Annual Environmental Postgraduate Conference, Hobart, Womack, 29 Nov- 2 December, 2005, pp. 1-7.
- [3] Azizov A.A., Alosmanov R.M., Bunyat-zade I.A., Magerramov A.M., Mamedov G.G. Magnetic sorbent to remove thin oil films // Environmental Problems of Chemistry and Chemical Technology (in Russian - Магнитный сорбент для удаления тонких нефтяных пленок // Экологические проблемы химии и химической технологии). 2010, V. 53, No. 4, pp. 114-117.
- [4] Shishkins, A., Mironovs, V., Lapkovskis, V., Treijs, J., and Korjakins, A. "Ferromagnetic Sorbents for collection and utilization of oil products," in Baltmattrib, Riga, Latvia, 2013, pp. 25-26.
- [5] Mironovs, V., Lapkovskis, V., Zemčenkova, V. Sorbent for collection of oil products (in Latvian - Sorbents naftas produktu savākšanai). LR patent LV 13927 B 20.08.2009, Int. Cl. B01J20/02.
- [6] Mironovs, V., Belovs, V., Zemčenkova, V. Equipment for collection of spilled oil products (in Latvian - Iekārta izlietu naftas produktu savākšanai). LR patent LV 13911 B 20.08.2009, Int. Cl. E02B15/04.
- [7] Shishkins, A., Mironovs V., Lapkovskis, V., Treijs, J., and Korjakins, A. "Ferromagnetic Sorbents for collection and utilization of oil products," in Baltmattrib, Riga, Latvia, 2013, pp. 25-26.
- [8] Shishkins, A., Mironovs, V., Treijs, J., Baroniņš, J. Sorbent with ferromagnetic properties. LR Patent application LV 14822 B, 20.06.2014.
- [9] Gorozhankina G.I., Pinchukova L.I. Sorbents for oil collection: comparative characteristics and special features of application. Pipeline Transportation of Oil (in Russian ). 2000. No. 4, pp. 12-17.

# **Explanation of the express method of the determination of steel grade by spark**

**Igor Nikiforov<sup>1</sup>, Pavel Maltsev<sup>1</sup>, Vladimir Ivanov<sup>1</sup>, Inna Barsuk<sup>2</sup>**

<sup>1</sup>*Pskov state university, Faculty of Mechanical and machine building,  
Department of Technology of machinebuilding.*

*Address: Lenin square 2, Pskov, 180000, Russian Federation*

<sup>2</sup>*Pskov state university, Faculty of Mechanical and machine  
building, Department of Theory of machinery and machines.*

*Address: Lenin square 2, Pskov, 180000, Russian Federation.*

**Abstract.** On the basis of physico-chemical theory of burning metal particles, the explanation known method of determining the grade of steel for the spark when it is grinding is performed. The features of formation of globules are reviewed and given them a brief description. The conditions for the formation of a spark in the processing of steels and alloys of various grades are researched.

**Keywords:** grinding, chips, spark, combustion, diffusion oxidation, globule, thermal defect.

## **I INTRODUCTION**

In the recent past, is widely used express method of determining the grade of steel by spark when grinding the sample [1]. This method is currently losing relevance, since many machine building plants has modern equipment for the chemical and spectral analysis. However, it is sometimes used, since it does not require expensive equipment, and if used properly, gives satisfactory results. Specified express method most in demand in the repair industry, at small plants.

Some of the steel, irons, hard alloys and non-ferrous metals shows in Table I, moreover therein the characteristic of the beam sparks when grinding is submitted [2]. As seen from the table, the hallmarks of sparks during grinding of various materials are color sparks (at the beginning - i.e. near the grinding wheel, and at the end of the flight); volume of the beam sparks; maximum length of the flight; amount of flashes in sparks beam and the nature of their demonstrations (in the form of a bifurcation, or in the form of the "stars" - when scatter of a small sparks in different directions is take place).

Analysis occurring physical and chemical processes that underlie the said express method can promotes to a more correct understanding of phenomena and processes existent in the grinding surfaces of workpieces. Since diffusion-oxidation processes occurring on the surface of the workpiece and during combustion of the chips are very similar and taking place at significant temperatures (up to 1500 ° C and above [3]). As a result, thermal defects

appear on the surface of workpieces: burns (visible and invisible), microcracks and phase transformation.

Clearly, the method of determination of steel grade and other metals by spark based on the specifics of burning metal chips after her removal from the area of grinding. The combustion process is primarily affected by: the initial temperature of the chips, the nature of its heat exchange with the environment, the diffusion-oxidation processes, the strength characteristics of the outer oxide layer and the value of the activation energy [4].

The exothermic oxidation reaction (with discharge of heat) is occur after the remove of the hot chips from the grinding zone. Metal is oxidized and if the temperature of surface of chips exceeds the melting temperature of the oxide film, then there is burning. In this case, the molten metal chips takes a spherical shape, formed the so-called globule. Simultaneously, the carbon, which presence in the steel, interacting with the oxygen forms carbon dioxide (CO<sub>2</sub>) and with an additional discharge of heat.

Moreover, presence of alloying elements in the steel, such as magnesium, aluminum, silicon, manganese, cobalt, nickel, etc., is affects the chips burning, due to the fact that they have a melting point lower than that of iron. It should be also pointed that the enthalpy of formation of oxides all of the alloying additives is negative, which leads to an additional increase of the chips temperature.

Purpose of this work - to explain express method of the determination of steel grade by spark.

*ISSN 1691-5402*

*© Rezekne Higher Education Institution (Rēzeknes Augstskola), Rezekne 2015*







*DOI: <http://dx.doi.org/10.17770/etr2015vol1.225>*

Achieving performed based on the micrographic analysis of the globules as a part of slurry. This method of analysis has allowed to interpret the impact of visual effects that occur during grinding of construction materials.

The studies will contribute to obtain new knowledge about the course of oxidative processes,

including occurring in areas of contact of single abrasive grains with the treated surface. Analogy between combustion chips and oxidation local area on the treated surface in this case is justified, since in both cases the processes takes place at high temperatures.

TABLE I  
IDENTIFICATION OF METALS IN GRINDING SPARK

Material	Color of stream		Beam sparks		Flash	
	Near wheel	Near end	Volume	Length, mm	Quantity of	Nature of
Wrought Iron	Straw	White	Large	1651	Very Few	Forked
1020 steel	White		Large	1778	Few	Forked
Carbon tool steel	White		(M)Large	1397	Very Many	Fine repeating
Gray Cast Iron	Red	Straw	Small	635	Many	Fine repeating
White Cast Iron	Red	Straw	Very small	508	Few	Fine repeating
Annealed Malleable cast	Red	Straw	Moderate (M)	762	Many	Fine repeating
High Speed steel	Red	Straw	Small	1524	Very Few	Forked
Manganese steel	White		(M)Large	1143	Many	Fine repeating
Stainless	Straw	White	Moderate (M)	1270	Many	Fine repeating
Tungsten Cr Die steel	Red	Straw	Small	889	Many	Fine repeating
Nitrided nitralloy	White		Large curved	1397	Moderate	Forked
Stellite	Orange		Very small	254	none	—
Cemented tungsten carbide	Light Orange		Extra small	50.8	none	—
Nickel	Orange		Very small	254	none	—
Copper, brass, aluminum	—		none	—	none	—
Examples of sparks						
Low Carbon	High Carbon	Gray Cast Iron		Nickel	Stainless Steel	Wrought Iron
						

## II MATERIALS AND METHODS

On the surface grinding machine 3G71 handled specially made a samles of various structural materials wide range of applications and physical-chemical properties.

Cutting speed in all cases was equal to 35 m / s. As an abrasive tool for grinding steel, alloys and non-ferrous metals was used grinding wheel of synthetic aluminum oxide white marks 24A, for grinding

cemented-carbide composition - silicon carbide black marks 53C.


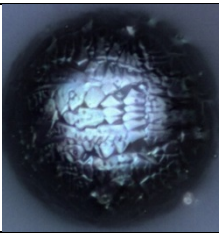
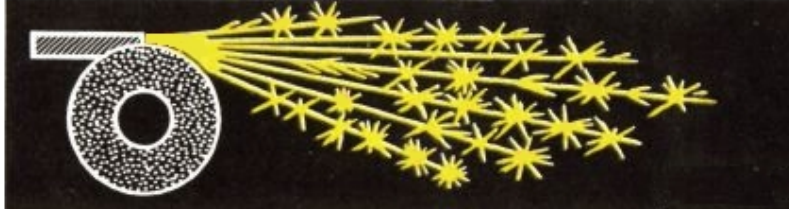
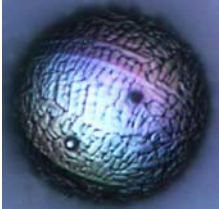


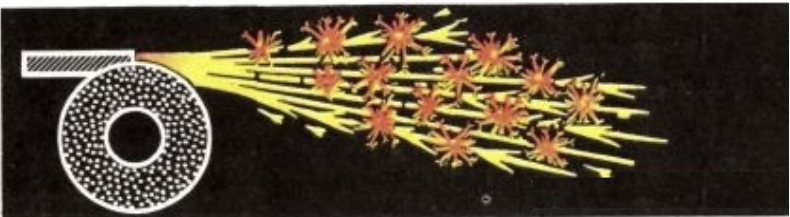
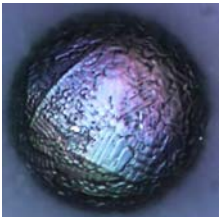

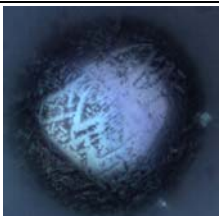

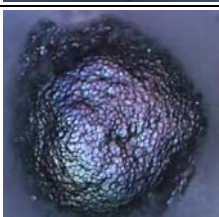
The slurry is collected through a sticky white tape, which installed in the removal zone of sparks, and studied by means of the microscope model Axiovert 40 MAT, designed for metallographic studies. Increase varied from 500<sup>x</sup> to 1000<sup>x</sup> (depending on the nature of the problem being solved and the best perception of the object of research). To solve the problem of small depth of field and produce

three-dimensional image used computer software Helicon Focus.

A large number of globules in the slurry composition were analyzed, including at different stages of combustion of the metal particles. Followed by a statistical analysis of the results of research.

Micrographic images globules obtained as a result of conducted research. The most typical of which are presented in Table II. There are shown the corresponding beams sparks resulting from the treatment of some materials [1].

TABLE II  
CONFORMITY OF BEAM SPARKS AND FORMED GLOBULES

Alloy	Beam sparks	Typical globule *
St20		
U12A		
40HFA		
SH15		
08H17T		
R6M5		



\*Note: there are many other variants

### III RESULTS AND DISCUSSION

Microscopic analysis of spherical particles composed of grinding slurry and comparison the results obtained with the basic thesis of the theory of

combustion and diffusion oxidation allowed to formulate the basic features of the formation of groups of globules, which are presented in Table III.

TABLE III  
MICROGRAPHIC ANALYSIS OF THE GLOBULES IN THE COMPOSITION OF THE SLURRY

Fig.	Material grade	The features of the forming of globules and their characteristics	Micrographs images of the final product
1	Steel 20GS2	Alloying elements is reinforced outer oxide shell and reduce its thermal conductivity. Superheated metal breaks out, forming a plurality of ragged holes and small globules. Result: globule with small holes (oxide) and a plurality of small globules (metal + oxide)	
2	Steel 20	Superheated metal breaks out through the hole. Result: globule with small dendritic structure (metal + oxide) and large globule with a dendritic structure (oxide).	
3	Steel A11R3M3F2	Tungsten oxide forms a solid surface. Metal boils and deforms the outer shell (metal + oxide). At rupture of the shall forms a globule with a thick wall (oxide).	
4	Cemented-carbide composition T5K10 и TN20	Slight burning. Globules solid and small size. Present globule heterogeneous due to the presence of the carbide phase.	

Volume of sparks beam is directly dependent on the quantity of burning metal and carbon dioxide. The more carbon in the alloy is, the higher the temperature of the chips, the more carbon dioxide, the more sparks. Alloying elements (manganese, silicon, chromium, etc.) produce on globules surface oxide film with a low thermal conductivity. This leads to a decrease the oxidation reaction (combustion) and reduce the volume of sparks beam. However, the oxygen continues to diffuse through the liquid oxide layer, which can lead to overheating of the metal

inside. As a result, it is break out through the outer layer.

Alloying elements lead to hardening of the oxide layer in addition to reducing thermal conductivity of the outer shell [5]. The quantity of holes through which superheated metal break out depends on the strength of the outer layer (Table. III, Fig. 1). The appearance of the beam plurality of sparks scattering flares "stars" - is nothing more than the visualization of superheated metal, removed through the outer shell. Oxide shell does not have time to merge into a spherical shape, since the exothermic oxidation



reaction terminated, cooling area is very large (due to the high level of dispersion), and the melting point of the oxide layer is great, and that it leads to rapid cooling and crystallization.

If there are no alloying elements and overheat the metal continues, then the metal break out, usually through a single hole. Metal and oxide shell scatter in different directions, according to the law of conservation of momentum - visually demonstrated in the bifurcation of the flares. Wherein metal instantly oxidized, that is occurs its autonomous combustion. The result of this process - the formation of two globules: oxide shell adopts a spherical shape with an explicit large-dendritic structure [6] and oxidized metal turns to a globule with small or medium-dendritic structure (Table. III, Fig. 2). Oxide shell have time to take spherical shape before crystallization, since it has a thick wall and contains a sufficient amount of heat, but sometimes there are shell with outer hole.

When grinding high-speed steel beam sparks is small and quantity of flares is insignificant. This is due to the very strong oxide shell, which is determined by the presence of tungsten. Metal inside the shell overheats and boils without break out to outside. The result is a globule with significant deviations from the spherical shape with a lumpy surface. In some cases, metal manages to break through the outer shell and then formed a thick-walled shell with a large hole (Table. III, Fig. 3) [7]. With an increase in the percentage of tungsten shells with holes is not observed. Molybdenum and nickel are also belong to alloying elements to significantly reinforcing oxide layer as well as tungsten.

When grinding tungstenfree cemented-carbide composition (such as TN20), we can see mainly combustion of nickel and molybdenum, wherein the sparks are few and globules are homogeneous or heterogeneous, due to titanium carbides. When grinding tungsten cemented-carbide composition (such as T5K10) mainly occurs combustion of cobalt wherein sparks are almost absent, and globules are homogeneous or heterogeneous, due to tungsten carbides (Table. III, Fig. 4).

Oxidation processes in grinding copper, lead, aluminum and some non-ferrous alloys are difficult [4] because of the low specific cutting force, directly affect the thermogenesis in the area microcutting ( $600 \text{ N/mm}^2$  - for duralumin,  $550 \text{ N/mm}^2$  - for brass,  $350 \text{ N/mm}^2$  - for lead, while for non-alloy steel, this

indicator is  $1500 \dots 1700 \text{ N/mm}^2$ , for high-temperature steel -  $2400 \text{ N/mm}^2$ ) and because of high thermal conductivity of material of workpiece ( $237 \text{ W/K}\cdot\text{mol}$  - for aluminum and  $401 \text{ W/mol}\cdot\text{K}$  - for copper). When grinding such metals sparks are not observed (Table. I).

Color change from red sparks - to a straw, from a straw - to white as they move (Table. I) can be explained by an increase of temperature of burning metal particles in the exothermic oxidation reaction.

#### IV CONCLUSION

1. Method of the determination of steel grade and other metals by spark is based on the features of oxidation (burning) of metal chips after it remove from the grinding area.
2. The emergence of single flashes in the beam sparks is a drop of superheated metal breaks out through the oxide shell.
3. The amount and nature of the demonstration of flashes depending on the characteristics of the outer shell and properties of metals, which are components of the alloy.
4. The main reasons affecting the presence of sparks in processing are specific cutting force and thermal conductivity of the material of the workpiece.

#### V REFERENCES

- [1] I.Y. Sitanov, *The determination of steel grade by spark*. Moscow: Machine building, 1968, 16 pp.
- [2] "Metal Identification by Spark Test with either a portable or stationary grinder" May 27, 2014. [Online]. Available: <http://www.weldingwire.com/Images/Interior/documentlibrary/metal%20id.pdf>. [Accessed: May 27, 2014]
- [3] S. Chandrasekar, T.N. Farris, R.R. Hebbbar, S.A. Hucker, and V.H. Bulsara, "Thermal Aspects of Surface Finishing Processes", *ASM Metals Handbook: Surface Engineering*, vol. 5, pp. 152-157, 1994
- [4] L. Lu, T.N. Farris, and S. Chandrasekar, "Sliding Microindentation Wear Particles: Spheres in Grinding Swarf", *Wear Particles: From the Cradle to the Grave*, D. Dowson, C.M. Taylor, T.H.C. Childs, M. Godet, and G. Dalmaz, Ed., Elsevier, pp. 257-263, 1992
- [5] D.V. Ardashev, "The photometric analysis of a shaving after grinding various steels", *Metalloobrabotka*, vol. 58, pp. 7-11, Aug. 2010
- [6] S. Malkin, "Grinding of Metals: Theory and Application", *Applied Metalworking*, vol. 3, pp. 95-109, 1984.
- [7] A.K. Tsokur, V.P. Tsokur, "Role of physical and chemical phenomena in thermal balance at grinding", *Scientific papers of Donetsk National Technical University Series: Machinebuilding and Mechanical Engineering*, vol. 124, pp56-61, 2007.

# **Physico-technical approach to design of composites from mineral and polymer technogenic resources**

**Gotfrīds Noviks**

*Rezeknes Augstskola, Faculty of Engineering*

**Abstract.** Artificial composite materials are currently being produced in large quantities, they are diverse and they are widely used in the economy. There have been extensive theoretical and experimental studies of different types of components, developed the calculation methods of composites production with predefined properties.

At the same time industry produces a lot of mineral and polymer waste, which are practically technogenic resources, but their use is currently at quite low levels. The paper examines the possibilities to use technogenic resources- mineral (such as ash and clay) and organic (polymers -PET containers) for producing qualitative composite materials. For this purpose theoretical analysis and calculations of the physical properties of components and process parameters that determine the operating characteristics of the composite material were carried out.

Composite-forming process efficiency determinative parameters were analysed: adhesion, the specific surface energy, specific free surface, adsorption capacity and the degree of dispersion of the particles.

The role of external factors in processing of composite were examined – temperature, concentration of components.

The characteristics of prepared samples of composites showed the possibility to use these waste for the development of qualitative products for different purposes.

**Keywords:** adhesion, composites, mineral waste, PET waste.

## I INTRODUCTION

A very significant part of the solid waste produced in the world is inorganic - mineral residues and waste. In literature a term „inorganic waste” often is used to determine not only really inorganic matter, but synthetic organic substances which do not originate in natural processes and are non-biodegradable also (e.g., plastic products) [1]. To avoid such misunderstanding in our study we used the term "mineral waste", i.e., all those materials, which are inorganic according to classical chemistry - the remnants of the construction and repair, debris and work off a building material, mineral extraction by-products, glass and glass-use industrial waste, ceramic waste, burning remnants, including ash, air and gas purification precipitated dust [2,3].

European Union statistics [4,5] shows that only during 5 recent years in 28 countries of the EU waste volumes increased by 10 million tons. (from 2505 million tons in year 2010 to 2515 million tons in year 2014), of which mineral solid waste constitutes 1780 million tons.

In general, in the EU as a whole is recycled only about 10÷12% of the waste. Latvia in 2014 produced

more than 2.3million tons of waste including mineral waste 0.68million tons.

Despite the fact that this waste is essentially valuable technogenic mineral resource, most of it is not currently fully utilized. One reason for this - there is no developed mineral waste recycling process optimization methodology. Most of the research is dedicated to the natural organic waste management.

At the same time mineral waste processing facilities, equipment and technology very differs from the organic waste treatment processes.

As was shown in our previous studies [2] the analysis of mineral waste recycling possibility must be carried out on the basis of their original features and compatibility with planned production quality. It prioritizes most perspective waste materials research directions. If the mineral waste basic properties meet the standarts for planned production, they can be directly or after minimal processing included in the production or manufacture of the reuse cycle.

However, such technogenic waste are quite a few (glass, metal scrap). Most of the waste have lost their original characteristics and the immediate return to the production process is technically cumbersome and uneconomical. So necessity to deeper processing of waste to produce a new product with a higher value to compensate the costs associated with recycling is

*ISSN 1691-5402*

actual task. Since most mineral waste are not biodegradable and can not be used as a fuel for thermal energy, the processing must be based on physical fields – mechanical treatment, thermal treatment, electromagnetic fields, thermo chemical processes. According to mineral waste composition and desired products may be selected one of two courses of their processing: disintegration or integration[2]. Disintegration means division raw materials in the respective components for the purpose to release of components for further use or distribute unfit (dangerous) components with a view to enhancing the quality of the residual components.

Disintegration technologies are quite widely used to waste water processing, rare elements extraction of coal ash, etc.

Integration is a composite formation process - in this case, a key factor is the optimal composition and structure of component finding (creation of compound -blend) and determination of necessary physical fields and modes of production, which can result in a final product designed in a previous forecast physical parameters. Solid waste recycling in this direction may prove to be effective. Components with different initial properties and their concentrations combination makes it possible to obtain materials with new properties.

Composite behaviour and its properties are not only determined by the properties and volume fractions of the components, but also appears certain new features due to the joint action of different components and external agent- so called synergetic effects.

For example, the Korea Advanced Institute of Science and Technology (KAIST) [6] developed a composite of only 4.10-5 % graphene inserted in metal. As a result the composite strength increased of more than 100 times. To get the desired properties of composite materials need to select the appropriate composite composition and treatment regime.

In fact, almost all naturally occurring objects are composites. Artificial most widely known composite is a concrete.

At present was created many modifications of concrete using as additional components liquid polymers, organic binders: polymer concrete, light-weight concrete, etc. Artificial composite materials (fiber-reinforced polymers, metal matrix composites, composite ceramic etc.) are currently produced in large quantities, they are diverse and they are widely used in the economy [7,23,25]. There have been extensive theoretical and experimental studies of different types of components, developed the methods of calculation predefined properties of composites [8].

Normally composite consists of two components - matrices and reinforcement material. Depending on the nature and structure of components may be various composites formed. Accordingly raw materials are specially selected and treated. For example, the

reinforcement (filling) material may be discrete (fiber) or continuous (threads, fabrics, netting), but matrix - polymers, oligomers, various binders.

The determining factors of composite properties can be combined into three groups:

The first group includes internal physical and chemical properties of composite-forming material:

- The physical properties of raw materials: mechanical, thermal, electromagnetic.

Minerals can be completely described by the physical parameters of a complex consisting of 12 basic indicators: density  $\delta$ , porosity  $P$ , compressive  $\sigma_c$  and tensile  $\sigma_t$  strength, Young's modulus  $E$ , Poisson's ratio  $\eta$ , specific thermal conductivity  $\lambda$ , specific heat  $c$ , thermal expansion coefficient  $\beta$ , specific electrical resistivity  $\rho$ , dielectric permeability  $\epsilon$ , specific permeability  $\mu$  [9]

- Physical-chemical and chemical properties - phase transition temperature  $T_{ph}$  and thermal effects, physico-chemical transformation enthalpy  $\Delta H$ , physico-chemical activity  $G$ , solubility  $S$ .
- Surface properties- specific surface energy  $\gamma$ , adhesion work  $w_a$  adsorption parameters  $F$ , diffusion coefficients  $D$ .

The second group include external parameters of the components changeable in the technological process:

- Physical geometrical parameters included in the composite structure components - the size of particles  $d$ , the shape, specific free surface  $S$ , mutual positions and orientations.
- Concentration of components  $C$ .

The third group includes the exposure factors on the basis of which is designed the composite production technology:

- Physical fields and physical-chemical processes.
- Operation modes: pressure, temperature, time, gradients, parameters of electromagnetic field, etc.

Since the creation of the composite material is carried out in order to obtain new materials with predetermined properties need to be predictable properties calculations. Composite theory develops a variety calculation methods of composite properties.

Percolation theory developed by Broadbent and Hammersley in 1957 currently is quite widely used approach to substance and energy transfer processes in the description of disordered systems (consisting mainly of two components) [10,11]. Theory determines the probability of the formation of clusters and predicts the composite flow properties (thermal conductivity, electrical conductivity, diffusion, dielectric and magnetic permeability, flexibility parameters). The decisive factor in the theory of percolation is critical threshold - critical probability  $p_c$  – in the case of two components  $p_c$  is equal to minimum filling component's (substrate) concentration  $x_c$  at which the composite properties

changes drastically – e.g., dielectrics turns into a conductor [12,13,14,15].

According to this theory, when one component (X1) property A value is a1 and volume concentration is x1 and the second component (X2) has the value a2 of the same property (and the concentration x2= 1-x1), the value of composite property ac can be calculated depending on the other components' threshold concentration xcr (or critical probability pcr) from the formulas:

$$ac = a_1 (x_{cr} - x_2)^{-q} \quad (1)$$

if  $x_2 < x_{cr}$

$$a_c = a_2 (a_1 / a_2)^s \quad (2)$$

if  $x_2 = x_{cr}$ .

$$ac = a_2 (x_2 - x_{cr})^t \quad (3)$$

if  $x_2 > x_{cr}$ .

Here q, s, t - critical indices.

The relationship between the critical indices can be described by formula [13].

$$q = t / (s - 1)$$

In the two-phase system critical probability is between about 1/3 and 2/3,  $s = 0.5$ ,  $q = t = 1.3$ .

In this theory a key parameter - the critical probability pc is quite variable. For most cases pc can not be calculated exactly, and is dependent on the components of the structure and their distribution (particle size, shape, orientation). In addition, there is no well-defined what it means to move from one position to the second, changes in characteristics occur even though at different speeds, but gradually.

For calculation outside the critical area can be used effective medium theory [16,17], which is based on the assumption that the two components are immersed in an effective homogeneous environment, the characteristic of which aef coincides with the composite real physical property a.

Effective medium theory pertains to analytical or theoretical modeling that describes the macroscopic properties of composite materials and is developed from averaging the multiple values of the constituents that directly make up the composite material.

$$[(a_2 - a_{ef})(x_2) / (a_2 + 2a_{ef})] + [(a_1 - a_{ef})(x_1) / (a_1 + 2a_{ef})] = 0 \quad (4)$$

Calculating statistical mixture properties ac containing only the two components with concentrations V1 and V2 and values of properties a1, a2 accordingly, quite widely is used V.I. Odelevsky equation [18]

$$ac = B + \sqrt{B^2 + a_1 \cdot a_2} \quad (5)$$

where:  $B = [(3V_2 - 1) + a_2(3V_1 - 1)]a_1$

Our analysis has shown [11] that the composite scalar (additives) physical parameters can be calculated by the formula arithmetic average weighted. Flow intensity parameters when the composite material is laminated and each layer consists of one component parallel to the layers may be most accurately calculated after the arithmetic average weighted also.

$$x // = \sum x_i V_i \quad (6)$$

but perpendicular to the layers - after the harmonic average weighted.

$$1 / x \perp = \sum (V_i / x_i) \quad (7)$$

The parameters which characterize the resistance of the flow, are calculated the contrary: the parallel layers - at the harmonic average weighed and perpendicular - by the arithmetic average weighted.

In other cases, the entire range of physical values change within the area limited by these two curves depending on the placement of components.

Statistically homogeneous environment where the content ratio of components in the mixture is close to 50/50 best fits the actual values of the parameters calculated using the weighted average logarithmic formula

$$\lg x = \sum V_i \lg x_i \quad (8)$$

When one of the components by volume becomes predominant changes the structure type - its component, which occupies a larger volume begins to play a decisive role and as a result properties of composite are nearer to equations 6 or 7. On the basis of investigation of natural composite materials - rocks [19] we obtained the regularities and nomograms, which can be also used in artificial composite properties forecasting (Fig.1).

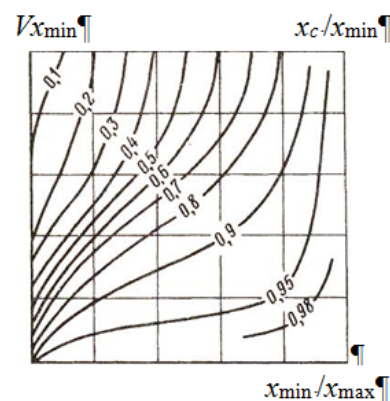


Fig.1. Nomogram for calculation physical property  $x_c$  of compounds consisting of two components :  $V_{x_{min}}$  - volume of component what physical parameter is  $x_{min}$ ;  $x_{max}$  - physical parameter of second component (larger).

Established that in the case of two statistically distributed components the relationship between the

concentrations of the components and properties may be approximated by a curve consisting of 6 different segments. But, as already mentioned, the developed calculation scheme for composite physical parameters is feasible only for flow characteristics- matter and energy transfer properties.

Calculation structurally sensitive tensor physical parameters of the composites is much more uncertain.

In all cases, the composite material is a monolithic whole, bringing together the components within them. So, the key here is the new links which are formed between the components, their physical nature and properties. This means that the mechanical links between the components calculations must take into account not only additives, but synergetic effects produced in the contact areas. In forecasting these ties major role have the interfacial layers properties between the matrix and the confinement (Fig.2).

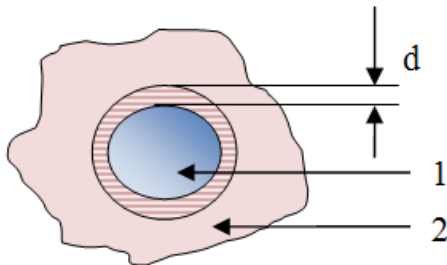


Fig.2. Interfacial layer d between inclusion 1 and matrix 2.  
d=0.01÷5 μm.

Studies [20] showed that the interfacial layer thickness is from 0.01 to 5 μm. This layer properties determine the specific components of the surface energy, adhesion and adsorption characteristics. Adhesion determines composite strength and crack formation and propagation in the processes [21]. Currently, there are several theories of adhesion [22,23]: mechanical theory of adhesion, adsorption theory, diffusion theory, electrostatic diffusion theory. They are based on the various interaction effects, such as:

- Lifshitz-van der Waals interactions,
- molecular interactions,
- adsorption,
- mechanical interlock,
- chemical bonding.

Molecular theory in addition to adhesion effect takes into account the physical chemical interaction between polymer and substrate, associated with catalysis, specific polymer transformations and polymer structure characteristics.

If there is no adhesion, any inclusion in matrix reduces the strength of the matrix due to stress concentration formed in the area around the inclusion, which leads to the destruction of the material.

Adhesion work  $w_a$  depends on components and the contact area specific surface energy, respectively,  $\gamma_1$ ,  $\gamma_2$ ,  $\gamma_{1-2}$  according to the equation:

$$w_a = \gamma_1 + \gamma_2 - \gamma_{1-2} \quad (9)$$

According to F.M.Fawkes [24,28] contact surface energy can be calculated by the following formula:

$$\gamma_{1-2} = \gamma_1 + \gamma_2 - 2(\gamma_1 \gamma_2)^{0.5} \quad (10)$$

A.W.Neumann [24,29] offers more precise equation:

$$\gamma_{1-2} = (\gamma_1^{0.5} - \gamma_2^{0.5}) / [1 - 0.015(\gamma_1 \gamma_2)^{0.5}] \quad (11)$$

Adhesion strength may be equaled to adhesion only if the connection have not defects and rupture occurs at low speed.

## II MATERIALS AND METHODS

This study examines the possibilities to recycle in useful product mineral waste- ash and clay combining them in composite with polymer waste-PET bottles. It is known that production of PET bottles in the world is increasing. [5,26,27]. Given into account that this waste is not biodegradable, its stock rises steadily.

In USA 32 million tons of plastic waste were generated in 2012, representing 12.7% of total municipal solid waste, among them almost 14 million tons of plastics as containers and packaging. And only 9 % of the total plastic waste generated in 2012 was recovered for recycling [30].

Our previous studies showed that there is an ash disposal problem also and it even does not solve using the renewable organic energy resources. For example, Finland produce annually 6.105 tons of ash, Sweden 8.105 tons, USA- 3.106 tons, China 2.106 tons. [31]

The aim was to find out in principle the possibility of creating a monolithic composite containing the matrix-forming fraction – thermoplastic polymer as a binder adhesive and substrate - a mineral filler components - ash or clay. Ash and especially wood ash characteristics were investigated during last 3 years [31,32].

Clay samples for experiments were taken from the largest Latvian Kupravas clay deposit.

The second component – used polyethylene terephthalate (PET) bottles.

PET bottles were shredded in slivers with size of 3-5mm, clay were dried and ground, ash were sieved to separate from unburned coarse coal particles.

Two types of clay were used - white and brown.

Ash samples were taken from household furnaces. Physical parameters of initial components shown in table 1.

Granulometric curves of mineral compounds are presented in fig.3.

Samples were set up as a two-component system, respectively:

- Clay + PET,

- Ash + PET.

PET concentration varied from 20 to 80 mass percent.

The components were mixed and with mixture were filled aluminum foil cups of 38 mm in diameter and 10 mm in height. Cups were placed in a muffle furnace and heated to temperatures in the range 230 0C - 310 0C, exposed at these temperatures for 10 minutes. During this time the melted material was mixed. Then it was cooled and investigated.

Measured properties of the resulting composite: density, hardness, conductivity wettability (table2).

Visual sample analysis results are displayed in Fig. (4-7).

TABLE 1.  
PROPERTIES OF COMPONENTS [31,33,34,35,36]

N	Property	PET	Clay	Ash
1.	Density ,g/cm <sup>3</sup>	1.38	2.6-2.8	1.74-1.87
2.	Specific area surface, m <sup>2</sup> /g	-	41-83; 61-346; 222; 18-30	2.2-2.9
3.	Specific surface energy, mJ/m <sup>2</sup>	44 (av)	60.2 74.4;75; 222	20 (av.)
4.	Adsorption, mg/g	0.05-0.8	15 (27-48% oil)	1.2 (metylen blue)
5.	Particle size (av.)	-	5.10 <sup>-3</sup>	3.10 <sup>-1</sup>
6.	Melting temperature, 0C	200-260	1200	1230
7.	Young Module, GPa	2,7-3.45	7.2	-
8.	Tensile strength, MPa	47-90 (79.3)	1.2	-

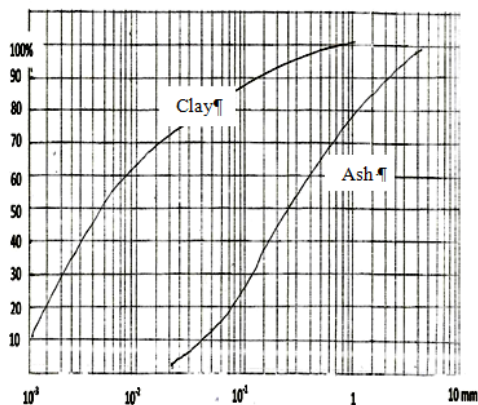


Fig.3. Granulometric curves of clay and ash

### III RESULTS AND DISCUSSION

Experiments show that, despite the fact that PET melting temperature according to the technical data is 260<sup>0</sup>C, at this temperature polymer is incapable to

coat evenly all substrate particles, due to the high viscosity of PET. Only at temperatures of 300 <sup>0</sup>C – 320 <sup>0</sup>C all particles overlap with the polymer film, and thanks to the adhesion forms the monolithic structure.

Polyethylene terephthalate (Polymer Thermoplastic resin) specific surface energy is in the range (32-80) mJ/m<sup>2</sup> according to literature data [35], the average 44 mJ/m<sup>2</sup>.

Clay specific surface energy depends on the mineral composition and can vary between 75 and 169.5 mJ/m<sup>2</sup> [36] and even 175mJ/m<sup>2</sup> for kaolinite [37].

For the previous calculations may take 150 mJ/m<sup>2</sup>.

Using this data specific surface energy according to Fawkes formula (10) for composite „Clay+PET” will be:

$$\gamma_{c-p} = 150 + 44 - 2(150 \cdot 44)^{0.5} = 31.5 \text{ mJ/m}^2$$

and adhesion work  $w_a = 150 + 44 - 31.5 = 162.5 \text{ mJ/m}^2$ . Wood ash specific surface energy to our previous studies may be accepted on average 20 mJ/m<sup>2</sup> and calculation using formula (10) for composite „Ash + PET” contact specific surface energy  $\gamma_{a-p}$  gives 4.7 mJ/m<sup>2</sup> and adhesion work  $w_a = 20 + 4.67 = 59.33 \text{ mJ/m}^2$ .

In accordance to Neumann equation (11) the contact surface energy can be calculated for composite „Clay + PET” as

$$\gamma_{c-p} = (150^{0.5} \cdot 44^{0.5}) / [1 - 0.015(150 \cdot 44)^{0.5}] = 25.4 \text{ mJ/m}^2$$

and  $w_a = 168.8 \text{ mJ/m}^2$ .

Composite „Ash + PET” accordingly  $\gamma_{a-p} = 3.9 \text{ mJ/m}^2$  and  $w_a = 60.1 \text{ mJ/m}^2$ .

As we see, the results of the calculations using formulas (10) and (11) are pretty close, and in both cases it shows that PET contact surface energy with clay is more than 6 times and adhesion work is around 2.7 times larger than the contact with ashes.

The experimental results also show that in order to achieve optimal mechanical parameters the proportions „Ash:PET” and „Clay:PET” in composites must be different.

In either case if PET content is less than 30% (mass) the components are poorly connected together and as a result we have mechanically weak , porous structure of composite (Fig 4.).



Fig. 4. Composite from mixture „Clay + PET”. PET content 30% (mass)

In composite "Clay + PET" starting from 50% PET content formed homogenous monolithic structure with high mechanical properties: hardness on the Mohs scale - 6-7, the average bulk density 1.79 g/cm<sup>3</sup> (white clay) and 1.77 g/cm<sup>3</sup>(brown clay). (Fig.5). In composite "Ash + PET" if there are 50% of ash, the most part of them (32% ash) remains free and are not bonded with the polymer. Sintered part is fragile and its density is only 1.44 g/cm<sup>3</sup>, which indicates the high porosity of the composite (Fig.6).

a)



b)



Fig. 5. Composite from mixture „Clay +PET". 50% (mass), a-white clay , b- brown clay



Fig . 6. Composite from mixture „ Ash+ PET"(volume of ash 50%)

And only by reducing the ash in the sample to 30-20% (mass) was achieved a complete mixing of the components and monolithic structure developed (Fig.7).

The properties of best composites examples are shown in table 2.

Since the determinant in formation this type of composite is a specific free surface of mineral

component, the amount of components in our experiments were converted into units of volume according to their density. PET density is of

1.38 g/cm<sup>3</sup>, ash - 1.82 g/cm<sup>3</sup>. Test sample was prepared by mixing 2.06 g PET and 2.02 g ash (about 50:50 mass). That is 42% (1.1cm<sup>3</sup>) ash and 58% (2.6 cm<sup>3</sup>) PET in a volume.



Fig 7. Composite from mixture „ Ash+ PET"(volume of ash 22% )

TABLE2  
PROPERTIES OF COMPOSITES

N	Properties	Clay +PET	Ash+PET
1	Density , g/cm <sup>3</sup>	1.70 (white), 1.77(brown)	1.59-1.44
2.	Adhesion work, mJ/m <sup>2</sup>	162.5-168.8	59.3-60.1
3.	Specific surface energy, mJ/m <sup>2</sup>	25.4-31.5	3.9-4.7
4.	Wettability(Water adsorption ), %	0.5-1.3	1.05-2

Since the investigated wood ash specific free surface [32] is 2.6 m<sup>2</sup>/g (average) total free surface of sample ash constitutes 5.25m<sup>2</sup>. According to [20], the interfacial layer thickness is of 0.01–5 μm. Calculations show that if the interfacial layer have minimum thickness of 0.01 μm, 1.5 cm<sup>3</sup> of the polymer may cover only 1.5 m<sup>2</sup> surface of the ash. This means that the creating effective homogeneous and strong composite require plastic volume of 5.25 cm<sup>3</sup>, or 83% of the total composite volume. Accordingly, the amount of ash 22%.

Our experiments approved that the best composite samples were obtained in this proportion (see Fig.7).

Analyzed composite "Clay+PET" samples showed that in the composite formation large role is playing adsorption capacity of the mineral part. Rough clay adsorption capacity of at least 15 mg/g (after methylene blue test), more than 30 times the ash adsorption ability 0.4 mg/g. As a result, for example, fusing a sample of PET and clay ratio by volume of 43.7:56.3 was obtained a homogeneous solid monolith (see Fig 5). Calculations show that in spite of the large clay specific free surface of

18 m<sup>2</sup>/g [37,38] it was enough the 2.17 cm<sup>3</sup> PET to coat 1.68 cm<sup>3</sup> clay. This means that the adsorptive

layer thickness of the contact between the phases constitute 0.026 μm. According adsorption thermodynamics best adhesion system forming conditions is when adhesive surface energy is less than the surface energy of the substrate [22].

In our case, the clay  $\gamma$  of at least 150 mJ/m<sup>2</sup>, but PET only 44mJ/m<sup>2</sup>, what also provides better performance composite "Clay+PET." Tested composite combines the brittle components - clay or ash - and elastic plastic PET matrix. Since in our case the clay confinement tensile strength is much less than PET, in the first place tensile strength stresses tear inclusion, but further crack propagation is blocked in the plastic matrix. The critical fracture stresses according to Griffiths - Orovan-Irvine equation, in the case when the crack formation occurs at the plastic deformation zone increase of the surface energy of plastic deformation  $\gamma_p$ :

$$\sigma = \sqrt{2E(\gamma_s + \gamma_{pl})/\pi} \quad (12)$$

Where  $E$  - plastic matrix Young's modulus,  $c$  - critical crack length. It is known that plastic deformation surface specific energy of approximately  $10^3\gamma_s$ . Since for the homogeneous matter:

$$\sigma = \sqrt{2E\gamma_s/\pi c}, \quad (13)$$

composite tensile strength theoretically can be increased to 30 times compared to the confinement strength.

$$\sigma_{comp} / \sigma_2 = \sqrt{(\gamma_s + \gamma_{pl}) / \gamma_s}. \quad (14)$$

This means that the composite „Clay+PET” tensile strength may reach 36 MPa.

Approximately such results (50 - 75 MPa) were achieved in industrial experiments of production composite of plastic and mineral waste [39].

But this is a case where the confinement ties with matrix components are ideal and elastic properties are not very different. But as inclusions in the matrix is a structural heterogeneity applying a load to composite in contact with the inclusions forms stress concentration, which depends on the confinement size, shape, its distribution in the matrix, the flexibility characteristics and type of links between them. So here is high importance of strong bonds between the inclusions and matrix, their quality and completeness. In the absence of adhesion any inclusion reduces the strength - especially tensile strength - inclusion do not perceive stresses and therefore it can be approximated as a crack or pores in composite. Our experiments found that the quality of those links in composite „Ash+PET” is lower than when the inclusions consists of clay particles. It means, that in order to obtain high quality composite material from mixture „Ash+PET” is necessity for additional procedures, such as ash adhesion capacity maximizing by adding modifiers, plasticizers, treatment with surfactants or temperature [40]. Thus, for example, is a patented technology of

composite creation where in the composition of thermoplastic and ash is added bridging agent - salune grafted polyethylene or grafted alpha olefic copolymer - substances that interact at the same time with thermoplastics as well as with the ashes [41].

#### IV CONCLUSIONS

1. Theoretically and experimentally founded in principle feasibility to produce composite material of thermoplastic waste (PET bottles) combined with mineral waste (ash, clay, debris), which can be used in different areas - civil engineering, hardware and various parts production.
2. Composite creation technology is thermophysical - based on plastic melting with mineral waste.
3. Determinants of creation homogeneous and mechanically durable composite are the specific surface energy, adsorption and adhesion characteristics of the components, the degree of dispersion, the content ratio of components and thermal exposure modes.
4. The experimentally determined the optimum conditions for the creation of composite. Clay and PET thermoplastic polymer composite component ratio is 50:50, ash and PET accordingly 20:80, the operating temperature of 300 to 320 °C, the heating time of 20min.
5. Better quality composite formed of PET alloy with clay. Ash and PET composite quality may be improved by reduction PET viscosity and raising components mutual adhesion ability and the increasing contact surface specific energy.

#### V REFERENCES

- [1] Inorganic waste. [Online] Available: <http://www.owp.csus.edu/glossary/inorganicwaste.php>. [Accessed May 5, 2015].
- [2] G.Noviks, "Basis of optimal mineral inorganic wasteprocessing methods", in *Environment. Technology. Resources: Proceedings of the 6-th International Scientific and practical conference, June 20-22, 2007*. Rezekne, pp. 87-101. Karen A.Hudson-Edwards and Bernhard Dold, "Mine waste Characterization, Management and Remediation", *Minerals*, 2015,5 pp. 82-85.
- [3] "Waste generation and treatment". [Online]. Available: <http://ec.europa.eu/eurostat/data/database> [Accessed May 5,2015].
- [4] D. Hoornweg and P. Bhada-Tata, *What a waste. A global review of solid waste management*. March 2012, No. 15. Urban development series – knowledge papers. Chapter 5. pp. 32-37. [Online]. Available: [siteresources.worldbank.org/INTURBANDEVELOPMENT/](http://siteresources.worldbank.org/INTURBANDEVELOPMENT/)[Accessed May 5,2015].
- [5] Y.Kim, J. Lee, Min Sun Yeom, Jae Won Shin, Hyungjun Kim, Yi Cui, Jeffrey W Kysar, James Hone, Yousung Jung and Seokwoo Jeon, "Strengthening effect of single-atomic-layer graphene in metal-graphene nanolayered composites", *Nature Communications*07/2013;4:2114.DOI:10.1038/ncomms3114, pp.1-7.[Online].Available: <http://www.researchgate.net/publication/244991748>. [Accessed March 7, 2015].
- [6] Krishan K. Chawla, *Composite Materials: Science and Engineering (Materials Research and Engineering)*, Springer, 2013.
- [7] Autar K. Kaw, *Mechanics of Composite Materials* (2nd ed.). CRC Taylor & Francis Group, 2005.
- [8] В.Ржевский. Г.Я.Новик, *Основы физики горных пород*, М.ЛЕНАНД, 2014.



- [9] Kim Christensen, *Percolation Theory*, London, 2002.
- [10] D. Austin. Percolation: Slipping through the Cracks. [Online]. Available: <http://www.ams.org/samplings/feature-column/fcarc-percolation#sthash.ulasL7vp.dpuf> [Accessed March 12, 2015]
- [11] Daniel Genin, Percolation: Theory and Applications. *NIST, 2007*. [Online]. Available: <http://www.pdfdrive.net/percolation-theory-and-applications4996426.html> [Accessed April 04, 2015].
- [12] “Теория перколяции”. [Online]. Available: <http://worldofmaterials.ru/spravochnik/composites/40-teoriya-perkolyatsii> [Accessed May 04, 2015].
- [13] John C. Wierman “Critical Percolation Probabilities”, North-Holland Mathematics Studies, Volume 118, 1985, pp. 349–359.
- [14] Dietrich Stauffer, Amnon Aharony, *Introduction in percolation theory*, CRC Press, 1994.
- [15] Tuck C. Choy, *Effective Medium Theory: Principles and Applications*, Oxford University Press, 1999.
- [16] Landauer, Rolf. "Electrical conductivity in inhomogeneous media", in *AIP Conference Proceedings, 40 American Institute of Physics. April 1978*, pp. 2–45. doi:10.1063/1.31150.
- [17] В.И.Оделевский, “Расчет обобщенной проводимости гетерогенных систем. Матричные двухфазные системы с невытянутыми включениями”, *Журнал Технической Физики*, 1951. Т. 21Б, No 6. с. 667-677.
- [18] Г.Я.Новик, М.Г.Зильбершмидт, *Управление физическими свойствами пород в процессах горного производства*, М.ЛКИ, 2010.
- [19] A.Baldan, “Adhesion phenomena in bonded joints”, *Turkey International Journal of Adhesion & Adhesives* 38, 2012, pp. 95-116.
- [20] А.В.Гордеев, *Моделирование свойств композиционных материалов, дисперсно армированных жесткими короткими волокнами*, 2010, 124с.
- [21] А.А.Берлин, В.Е.Васин, *Основы адгезии полимеров*, М., Химия, 1974.
- [22] Hong T. Hahn and Stephen W. Tsai, *Introduction to Composite Materials - Technology & Engineering*. CRC Press, 1980.
- [23] M.Zenkiewicz, „Methods for the calculation of surface free energy of solids”, *Journal of Achievements in Materials and Manufacturing Engineering*, Vol.24, Issue 1, September 2007, pp.137-145.
- [24] Г.И.Петрова, Э.Я.Бейдер, „Конструкционные материалы на основе армированных термопластов”, *Российский химический журнал* т.LIV,#1, 2010.с.1-16. [Online]. Available: <http://www.viam.ru/public> Accessed March 20, 2015.
- [25] Byung-Wan Jo, Seung-Kook Park, Jong-Chil Park „Mechanical properties of polymer concrete made with recycled PET and recycled concrete aggregates”, *Construction and Building Materials* 22, 2008.pp. 2281–2291.
- [26] Yun-Wang Choi, Dae-Joong Moon, Jee-Seung Chung, Sun-Kyu Cho „Effects of waste PET bottles aggregate on the properties of concrete” , *Cement and Concrete Research* 35, 2005, pp.776–781.
- [27] F. M. Fowkes, “Attractive Forces at Interfaces”, in: *Industrial and Engineering Chemistry* 56, 12 (1964), P. 40-52.
- [28] A.W. Neumann, *Applied Surface Thermodynamics*, CRC Press 2014 [ebook], Available: <https://www.crcpress.com/product/isbn/9780849396878>
- [29] “Common Waste and Materials” [Online]. Available: <http://www.epa.gov/osw/conservematerials/plastics.htm> [Accessed March 10, 2015].
- [30] Adrian K. James, Ronald W. Thring, Steve Helle and Harpuneet S. Ghuman. “Ash management review- application of Biomass Bottom Ash”, in *Energies*, 5, 2012, pp. 3856-3873.
- [31] G. Noviks, “Investigation of Biomass Ash Properties for their Utilization Assessment” in *Environment. Technology. Resources. Proceedings of the 9-th International Scientific and practical conference*, June 20-22, 2013. Rezekne, pp. 168-174.
- [32] “PET (polyethylene terephthalate)” [Online]. Available: <http://www.plastic-products.com/part12.htm> [Accessed March 15, 2015]
- [33] N. Torres, J.J. Robin, B. Boutevin. “Study of thermal and mechanical properties of virgin and recycled poly(ethylene terephthalate) before and after injection molding” in *European Polymer Journal* Volume 36, Issue 10, 1, 2000, pp. 2075–2080
- [34] “Surface Energy Data for PET: Poly(ethylene terephthalate)”. [Online]. Available: [www.accudynetest.com/polymer\\_surface\\_data/pet.pdf](http://www.accudynetest.com/polymer_surface_data/pet.pdf) [Accessed March, 24]
- [35] R. C. Mielenz, M.E. King Physical-Chemical Properties and Engineering Performance of Clays. [www.clays.org/journal/archive/volume%201/1-1-196.pdf](http://www.clays.org/journal/archive/volume%201/1-1-196.pdf)
- [36] Bronislaw Janczuk, Tomasz Bialo Piotrowicz, “Components of Surface Free Energy of some Clay Minerals” in *Clays and Clay Minerals*, Vol. 36, No. 3, 1.988, pp 243-248.
- [37] E. Chibowski, P. Staszczuk. Determination of Surface Free Energy of Kaolinite, in *Clays and Clay Minerals*, Vol. 36, No. 5, 455--461, 1988.
- [38] “Технология производства композиционных материалов на основе ПЭТ, переработка отходов”. [Online]. Available: <http://www.ecoteco.ru/?id=140> [Accessed March 20, 2015].
- [39] Chi-An Dai, Tai-An Tsui, Yao-Yi Cheng, “Adhesion of PET/PSMA Interfaces Reinforced with Plasma Treatment” in *Surface review and Letters*, Vol.13, No2&3, 2006, World Scientific Publishing Company, pp 265-271.
- [40] Maziyar Bolourchi, Roger W. Coupled fly ash filled polymer compounds. Patent WO 2013082047 A1 Nun 6, 2013 Nov 27 2012 Nov 29, 2011.

# **Accelerated method for the determination of freeze-thaw resistance of concrete**

**Sergey Nikolskiy, Olga Pertseva**

*St. Petersburg State Polytechnical University,  
Address: Polytechnicheskaya st.29, St. Petersburg, 195251, Russia*

**Abstract.** Main purpose of this research is to create the new reference method of determining the freeze-thaw resistance of concrete that is characterized by small labor input, high efficiency and a wide application scope. The offered method is based on measurement of long strength by nondestructive method. During this research, the theoretical analysis of concrete's specimen dependence on freeze-thaw resistance and energy, which is emitted by a specimen during destruction, has been carried out. Freeze-thaw resistance of a specimen is calculated as the mathematical relation of these energies, and the freeze-thaw resistance of concrete is calculated as an arithmetic mean value across specimens.

To prove the method correctness it was realized on 10 concrete specimens. Age of specimens consolidation is 88 days. Specimens of concrete mortar were prepared using a mix of portland cement 400 (12,3%), sand of dimensions 0.6-5 mm (24,7%), granite macadam of dimensions 5-20 mm (55,4%) and water (7,4%). Freeze-thaw resistance such mortar was determined earlier by method, approved national standard specification, it was equal 105 cycles. According dimensions by new offered method freeze-thaw resistance such mortar is equal 107 cycles and its confidence interval is equal 5,4 (probability  $P = 0,95$ ). Therefore, spread of results could be casual and the offered method is correct.

**Keywords:** concrete, freeze-thaw resistance, permanent set, durability, monitoring of strength, freeze-thaw cycling.

## **I INTRODUCTION**

Despite a variety of modern construction materials and technological research in this area, concrete remains more convenient material. It is a multipurpose and widespread material which is used during construction of buildings and facilities. The most important properties of concrete, which demonstrate themselves during the design phase of objects, are concrete's durability in terms of compression/stretching, waterproofing and freeze-thaw resistance. In climatic conditions of northern latitudes in which the North Western region is located as well, the last property is considered to be the most important one.

Freeze-thaw resistance of concrete is an ability of water-saturated concrete specimen to maintain repeated standard thermo cycles without noticeable damage. Different types of water pressure cause concrete's freeze-thaw deterioration, such as hydraulic and osmotic pressure [1], capillary pressure [2] and other types of water influence according to existing freeze-thaw resistance theory [3]. In order to determine the concrete mix composition, it is necessary to take into account freeze-thaw resistance.

## **II PROJECT SCOPE AND OBJECTIVES**

In order to keep comfortable microclimate inside of structure [4] measurement of durability of concrete is of grave importance [5]. The Worldwide experience offers a vast number of ways for determination of durability of the concrete structures [6], but accordingly to the European standard [7,8] there four main methods to determine the concrete frost resistance: Slab test, CDF, CIF-Test and Cube-Test. These test methods contain the following steps: curing and preparing the specimens, pre-saturation of the specimens and their thermo cycling. The test liquid simulates a deicing agent and contains 3% of NaCl weight and 97% weight of (demineralized) water in case of the freeze-thaw test and deicing salt resistance and demineralized water to test the freeze-thaw resistance of concrete respectively. Scaling of the specimens is measured after a well defined number of freeze-thaw cycles and leads to an estimate of the resistance of the tested concrete against freeze-thaw damage [9]. The test methods however differ in terms of their procedures and conditions [10]. Also CIF test shows determination of internal damage by measuring the relative dynamic modulus of elasticity (taking into account ultrasonic transit time) [11].

There are two different standard types of methods of determining the freeze-thaw resistance of concrete-basic [12] and reference [13] in the Russian Federation.

During the estimation of freeze-thaw resistance of concrete by the basic method, considerable random dispersion of values of concrete strength (variation coefficient  $\rho = 15 \dots 20\%$ ) [14] under invariable conditions of production and tests of specimens gives rise to a wide scatter of average values of strength and demands large volume test (quantity of test pieces 25 ... 50) as a proof that relative decreasing in strength of  $\Delta R/R = 0,05 \dots 0,15$  as a result of freezing and defrosting.

Therefore, the basic methods have two main weaknesses: high labour input and small operability. Determination of freeze-thaw resistance by basic methods takes long time intervals (from 1 to 6 months), so the reference methods are necessary.

One of the existing reference methods is a Dilatometric rapid method of determining the freeze-thaw resistance of concrete [13]. This method is a prototype for the method which has been offered by me. In this method concrete's freeze-thaw resistance is determined by the maximum relative difference of volume deformations of the tested concrete and standard specimens in accordance with tables provided in standard specification [12] taking into account concrete's type, its form and the size of specimens.

However, the results from the tables provided in state standard specification are acceptable only for Portland cement concrete and slag Portland cement concrete without surface-active additives (PEAHENS), such concretes are used extremely seldom now. In order to obtain new tables long labour-consuming experiences which imply using basic methods are needed [15].

The objectives of the project is expansion of methods of rapid determining the freeze-thaw resistance of concrete, decreasing labour input and increasing operability.

### III OFFERED METHOD OF DETERMINING THE FREEZE-THAW RESISTANCE OF CONCRETE

Suppositive solution belongs to test methods of porous water-saturated bodies and is intended for definition of a concrete brand in terms of freeze-thaw resistance. The main purpose has been reached both in the prototype by production of specimens' series from concrete mix, specimens sated with water, measure specimens, and freezing up to the standard temperature. However, the offered method includes the following important steps:

- Measurement of the relative tension set of a specimen  $\Theta_{ten}$  after the one cycle of freezing defrosting by dilatometer (here the DOD-100-K dilatometer has been used).

- Measurement of the greatest nondestructive loading  $L_0$  of a specimen in the conditions of stretching by acoustic methods for the nondestructive testing of concrete [16] (here AF-15 AE-complex by Kishenevskiy has been used) to determinate specimen's long-time strength  $R_{lt}$  in the conditions of stretching.
- Measurement of the short-term strength  $R$ .

At present the concept of greatest non-destructive loading  $L_0$  is usefully employed for express-monitoring of different kinds of long resistance, such as durability (mechanical [17] and exegetical [18], remaining life of the product [19], longevity [20, 21], freeze-thaw resistance [22,23] and cracking resistance [24]. Moreover, there are a wide scope of modern concrete mixtures, such as light-weighted concrete [25], vibropressed structures [26], high-performance concrete [27], concretes with additives [28, 29]. These are also porous materials and, therefore, should be tested for frost-resistance.

In time of freezing, development of concrete's damages is explained by subcritical cracks growth. In brittle solids cracks begin taking off by a shearing action [30], also the speed of their development is no more than 10-4m/s [31]. Therefore in conditions of freezing water, the filled crack in concrete captures the nearby closed pores. It stabilizes pressure in the water of the filled crack by about the value causing stretching tension in a material equal to long-time strength of a specimen in the conditions of stretching [32]. If the body's temperature changes from 78 K to 1493 K and the loading is as described earlier, the  $L_0$  value shifts inside of deviation determination of it, i.e.  $1 \div 3\%$ . This fact permits using the  $L_0$  value received at low temperature when the energy per unit of the specimen's volume which is disseminated in the course of freezing-defrosting is established.

If  $L_0$  is determined, it is possible to calculate a specimen's long-time strength  $R_{lt}$  in conditions of stretching:

$$R_{lt} = 2L_0/\pi S \quad (1)$$

where:  $S$  – area of a specimen's section perpendicular to compression planes;  $L_0$  – the greatest non-destructive loading of a specimen in the conditions of stretching;

Definition of a relative tension set and long-time strength of a specimen allows estimating the energy disseminated on processes destructions in the course of freezing-defrosting  $W_{tc}$  as per formula:

$$W_{tc} = \theta_{ten} R_{lt} \quad (2)$$

where:  $\theta_{ten}$  - relative tension set of a specimen;  $R_{lt}$  - specimen's long-time strength in the conditions of stretching.

Specimen's loading in the conditions of monoaxial compression to extreme loads, registration of these values of axial loads and axial strain is corresponding to loads, which allows calculating energy per unit of the specimen's volume which is disseminated in the course of its compression to extreme loads by numerical integration of dependence of axial loading from axial strain. Value of the energy disseminated in the unit of volume of a specimen in the course of its compression to extreme loads is in proportion to a square value of short-term strength [28]:

$$W_{com} = \alpha R^2 \quad (3)$$

where:  $R$  – short-term strength;  $\alpha$  – proportionality coefficient.

The logarithmation and differentiation of expression (3) allow calculating specimen's freeze-thaw resistance  $F_{sam}$  as per formula:

$$F_{sam} = 2[\Delta R/R] \cdot W_{com}/W_{tc} \quad (4)$$

where:  $[\Delta R/R]$  - standard relative decreasing in terms of strength ( $[\Delta R/R] = 0,05 \dots 0,15$  [4]);

Concrete's freeze-thaw resistance is found as an average of freeze-thaw resistance values for specimens.

#### IV REALIZATION OF THE OFFERED METHOD

Suppositive This method is realized as follows. First of all specimens in the form of cylinders or cubes with an edge of 10 cm from concrete mix of demanded structure are made. After that curing specimens are sated with water, and measured. Further greatest non-destructive loading of  $L_0$  is defined for each specimen by a non-destructive testing, for example, an acoustic emission method [29]. Without outreaching  $L_0$ , a specimen's crack doesn't develop yet in the conditions of stretching.  $R_{lt}$  is calculated as per formula (1). After specimen's freezing-defrosting up to the standard temperatures and definition  $\Theta_{ten}$  it is possible to calculate  $W_{tc}$  as per formula (2).

Further, a specimen is squeezed in the conditions of monoaxial compression to extreme loads, and current values of axial loading and relative tension corresponding to a specimen are registered. Freeze-thaw resistance for the  $F_{sam}$  concrete specimen is calculated by the received results as per formula (4). Concrete's freeze-thaw resistance is found as an average of values of freeze-thaw resistance for specimens. Confidential interval of concrete's freeze-thaw resistance is counted according to dispersion of values of freeze-thaw resistance for a series of specimens.

In particular, this way has been realized across 10 specimens cubes, an edge of 10 cm at the age of 88 days made of a concrete mix of such structure: Brand 400-1 Portland cement weight part, sand – 2 weight

parts, granite rubble 5 ... 20 mm – 4,5 weight parts, waters – 0,6 weight parts. It is experimentally established in two different ways for this concrete at the age of 88 days that after 105 freezing-defrosting corresponding to this concrete brand in terms of freeze-thaw resistance, average relative decreasing in strength makes 0,142 on an offered way and 0,16 on the basic way [12], that is both values lie within an error of the used ways. On the average relative decreasing in strength amounts to 15%.

Specimens have been sated with water according to the item's state standard specification, measured and registered volume. For each cube sated with water, splitting according to the item value of the greatest nondestructive load (without which excess of a crack in a specimen which doesn't develop yet is irreversible) have been defined. After each test the plane of compression of a specimen has been changed for the perpendicular plane to previous compression. Definition of the greatest nondestructive loading carried out by means of an acoustic emission way [30,31], using the AF-15 AE-complex by Kishenevskiy. Acoustic sensors with a frequency of 20-200 kHz have been established on the verge of a specimen, parallel to plane of compression. For creation of axial loading a hydraulic press has been used. Value of a specimen's long-time strength in the conditions of stretching has been counted by the received value of the greatest nondestructive loading, corresponding to it. Then average value of a long-time strength has been counted too. Results of calculating are given in the table.

The water-saturated specimens have been placed in the measuring camera of the DOD-100-K differential volume dilatometer and have been tested according to the standard [14]. According to the dependency diagrams of differences, relative volume tension set of a concrete and aluminum specimen have been calculated. Energy per unit of specimen's volume disseminated in the course of its freezing-defrosting as per formula (2) for each specimen.

Further average value of the specimen's long-time strength in the conditions of stretching has been defined as arithmetic average  $R_{lt}$  long-time strength values in the conditions of stretching.

Axial compression of specimens with a speed of 400 kg/sec. has been carried out on the hydraulic press equipped with the graph plotter of dependence of axial loading from axial strain. By the dependence received on the graph plotter the area under it has been determined, i.e. the energy disseminated per volume of a specimen in the course of its compression to extreme loads has been received.

Then for each brand of a concrete specimen freeze-thaw resistance values have been counted, (table 1) as number of freezing defrosting necessary for decrease in its strength by 15% is achieved by formula (4).

Further, an average  $\bar{F}_{15}$  for values of the  $F_{15i}$ , and an average square deviation of results of experience have been calculated:

$$S = \frac{\sqrt{\sum (F_{15i} - \bar{F}_{15})^2}}{3} \quad (5)$$

where: S – an average square deviation of experience results;  $F_{15i}$  – i-specimen concrete value in terms of freeze-thaw resistance at decreasing specimen's short-term strength in the conditions of compression by 15% have been received by the offered way; where i is changed since 1 to 10;  $\bar{F}_{15}$  –

concrete's freeze-thaw resistance equal to an arithmetic mean value of freeze-thaw resistance for series of concrete specimens at decreasing their short-term strength in the conditions of compression by 15%.

The average square deviation of  $F_{15i}$  values was equal 16. Taking this into account, a divergence of the average value of freeze-thaw resistance of concrete is considered to be 99,7 and the earlier experimentally found number of cycles is 105 (F15 brand) which is necessary for decreasing R for 15%. It is possible to consider these data casual, and the offered way is correct.

TABLE I  
DEFINITION OF THE CONCRETE'S TYPE IN TERMS OF THE FREEZE-THAW RESISTANCE AS PER OFFERED METHOD

№	$\bar{R}_R$ [MPa]	$\Theta_{TEN} \cdot 10^4$	$W_{TC} \cdot 10^4$ [MPa]	$W_{COM} \cdot 10^4$ [MPa]	$[\Delta W] \cdot 10^2$ [MPa]	$F_{15i}$
1	1,5	2,7	4,05	0,9990	2,997	74
2	1,7	3,1	5,27	1,7215	5,165	98
3	1,8	1,8	3,24	1,2312	3,694	114
4	1,9	2,6	4,90	1,6796	5,039	102
5	2,0	2,5	5,00	1,4333	4,300	86
6	2,1	1,9	4,00	1,4364	4,309	108
7	2,2	2,6	5,72	2,2308	6,692	117
8	2,3	2,1	4,83	1,3846	4,154	86
9	2,9	1,8	5,22	1,6008	4,802	92
10	3,1	1,5	4,65	1,8600	0,558	120
AVERAGE	2,15	2,1	4,69	1,5577		99,7

## V CONCLUSIONS

The offered way expands a list of technical means for the rapid method of determining the freeze-thaw resistance of concrete. Duration of determining the freeze-thaw resistance of concrete is caused by a long time of the specimen's water saturation (4 days according to standard specification [11]). At present this method was patented [33]. Detailed researches and pilot experimental studies are necessary to get more data and create new method of determining the freeze-thaw resistance of concrete in the future.

## VI REFERENCES

- [1] T.F. Rønning, "Freeze-Thaw Resistance of Concrete Effect of : Curing Conditions, Moisture Exchange and Material" Phd. thesis, Norwegian Institute of Technology, Norway, 2001.
- [2] V. Pukhkal, V. Murgul, S. Kondić, M. Živković, M. Tanić, N. Vatin, "The Study of Humidity Conditions of the Outer Walls of a "Passive House" for the Climatic Conditions of Serbia, City Nis", Applied Mechanics and Materials, vols. 725-726, pp. 1557-1563, 2015.
- [3] G.I. Gorchakov, M.M. Kapkin and B.G. Skramtaev, Povyshenie morozostojkosti betona v konstrukcijah promyshlennyh i gidrotehnicheskikh sooruzhenij. Moscow: Strojizdat, 1965.(rus)
- [4] D. Vuksanovic, V. Murgul, N. Vatin and V. Pukhkal, "Optimization of microclimate in residential buildings", Applied Mechanics and Materials, vol. 680, pp. 459-466, 2014.
- [5] T.N. Soldatenko, "Model identifikatsii i prognoza defektov stroitelnoy konstruksii na osnove nechetkogo analiza prichin ih povavljeniya", Magazine of Civil Engineering, vol. 25, pp. 52-61, 2011. (rus)
- [6] I.Garanzha and N. Vatin "Analytical methods for determination a load capacity of concrete-filled tubes under axial compression", Applied Mechanics and Materials, 633-634, pp. 965-971, 2014.
- [7] "Concrete. Specification, performance, production and conformity", EN 206:2013, 2013.
- [8] "Concrete testing – Hardened Concrete-Frost Resistance" SS 137244, Sweden, 2005.
- [9] RILEM TC 117-FDC, "TDC, CDF Test, Test Method for the Freeze-Thaw-Resistance of concrete with sodium chloride solution," RILEM Publications SARL, vol.29, pp. 523-528, 1996.
- [10] RILEM TC 176-IDC, "TDC, CIF Test, Test Method of frost resistance of concrete," RILEM Publications SARL, vol.37, pp. 743-753, 2004.
- [11] N. Bunke, "Prüfung von Beton – Empfehlungen und Hinweise als Ergänzung zu DIN 1048." Schriftenreihe des Deutschen Ausschusses für Stahlbeton, vol.422, pp.12-15, 1991.
- [12] Concretes. Basic method for the determination of frost-resistance, GOST 10060.1-95, 1995. (rus)
- [13] Concretes. Dilatometric rapid method for the determination of frost-resistance, GOST 10060.3-95, 1995. (rus)
- [14] Concretes. Methods for the determination of frost-resistance. General requirements, GOST 10060.0-95, 1995. (rus)

- [15] A.D. Dikun et al., "Opyt jekspressnogo opredelenija morozostojkosti betona transportnyh sooruzhenij." *Construction Materials*, vol. 8, pp.55-56, 2005.(rus)
- [16] T.S. Nikolskaya, Ispol'zovanie akusticheskoy jemissii dlja prognozirovanija dolgovechnosti izdelija. The IV international conference "Problemy prognozirovanija nadezhnosti i dolgovechnosti" October 14-17, 2009, St. Petersburg, Russia. St.Petersburg: Press of the St.Petersburg Polytechnical University, 2009.(rus)
- [17] T.S. Nikolskaya, "Particularity of Acoustic Emission in Ceramic Product under Partial Uploading." *Problems of Strength*, vol. 1, pp.140-147, 2002.
- [18] S.V. Akimov, T.S. Nikolskaya, S.G. Nikolskiy, "Sposob opredelenija morozostojkosti kamnja," RU Patent 2380681, July 1, 2008. (rus)
- [19] S.G. Nikolskiy, "Jekspress-kontrol' jerozii betona." *Magazine of Civil Engineering*, vol. 2, pp.39-44, 2008.(rus)
- [20] S.V. Akimov, T.S. Nikolskaya, S.G. Nikolskiy and U.G. Barabanthikov et al., "Sposob ocenki stojkosti izdelij pri nagruzenii," RU Patent 2442134, November 2, 2010. (rus)
- [21] S.V. Belyaeva et al., "Sposob ocenki korrozionnoj stojkosti betonnyh izdelij," RU Patent 2449266, November 15, 2010. (rus)
- [22] S.G. Nikolskiy, "Fracture Surface Analysis of Ceramic Bare under Short- and Long-term Bending." *Problems of Strength*, vol. 5, pp.133-140, 2009.
- [23] S.G. Nikolskiy, "Acoustic emission control of strength." *Problems of Strength*, vol. 6, pp.102-106, 1990.
- [24] A. Gorshkov, N. Vatin, D. Nemova and D. Tarasova, "Definition of the overturning and holding moments for floor-by-floor leaning walls made from aerated concrete blocks", *Applied Mechanics and Materials*, vols. 633-634, pp. 897-903, 2014.
- [25] N. Vatin, A. Gorshkov, D. Nemova, O. Gamayunova and D. Tarasova, "Humidity conditions of homogeneous wall from gas-concrete blocks with finishing plaster compounds", *Applied Mechanics and Materials*, vols. 670-671, pp. 349-354, 2014.
- [26] N.I. Vatin, I.I. Pestryakov, S.S. Kiski and Z.S. Teplova, "Influence of the geometrical values of hollowness on the physicotchnical characteristics of the concrete vibropressed wall stones", *Applied Mechanics and Materials*, vols. 584-586, pp. 1381-1387, 2014.
- [27] A. Ponomarev, M. Knezević, N. Vatin, S. Kiski and I. Ageev, "Nanosize scale additives mix influence on the properties of the high performance concretes", *Journal of Applied Engineering Science*, vol. 12, pp. 227-231, 2014
- [28] V. Korsun, N., Vatin, A. Korsun, and D. Nemova, "Physical-mechanical properties of the modified fine-grained concrete subjected to thermal effects up to 200°C", *Applied Mechanics and Materials*, 633-634, pp. 1013-1017, 2014.
- [29] L. Akimov, N. Ilenko, R. Mizharev, A. Cherkashin, N. Vatin and L. Chumadova, "Influence of Plasticizing and Siliceous Additives on the Strength Characteristics of Concrete", *Applied Mechanics and Materials*, vols. 725-726, pp. 461-468, 2015.
- [30] I.N. Ahverdev, *Osnovy fiziki betona*. Moscow: Strojizdat, 1981.(rus)
- [31] T.S. Nikolskaya, S.G. Nikolskiy and V.P. Terentiev, Jekspress-metody ocenki dlitel'noj stojkosti betona. The III international conference "Populjarnoe betonovedenie", February 27 - March 2, 2009, St. Petersburg, Russia. St.Petersburg: Press of the St.Petersburg Polytechnical University, 2009.(rus)
- [32] T.S. Nikolskaya, S.G. Nikolskiy, "Akusticheskaja jemissija pri jerozii melkozernistogo betona." *Nauchno-tehnicheskie vedomosti SPBGPU*, vol. 4, pp.242-248, 2008.(rus)
- [33] S.G. Nikolskiy, O.N. Pertseva, "Sposob opredelenya marki betona po morozostoykosti", RU Patent 2543669, July 4, 2013. (rus)

# **Experimental justification for sapropel and hemp shives use as a thermal insulation in Latvia**

**Stanislavs Pleiksnis<sup>1</sup>, Maris Sinka<sup>2</sup>, Genadijs Sahmenko<sup>2</sup>**

<sup>1</sup>*Rezekne Higher Education Institution, Atbrivosanas aleja str.115, LV -4600, Latvia*

<sup>2</sup>*Riga Technical university, Faculty of Civil Engineering, Institute of Materials and Structures, Kalku str. 1, Riga, LV-1658, Latvia.*

**Abstract.** Fossil energy resources in Latvia are imported from other countries, but at the same time, our country is rich in renewable energy resources and other raw materials, which are used very little. In the study it is proposed to create a thermal insulation material from hemp shives grown in Latvia as a filler material and lake sediment - sapropel as a binding agent. Both of the following materials are organic, renewable and locally available. Laboratory experiments show that ecological and complying with modern requirements thermal insulation material can be obtained from local, renewable raw materials: sapropel and hemp shives.

**Keywords:** sapropel, hemp shives, thermal insulation construction material.

## **I INTRODUCTION**

Latvian National Saeima accepted Latvian National Development Plan until 2020, which emphasizes the improvement of energy efficiency in all economic spheres. Great energy savings can be achieved in the construction sector by improving the energy efficiency of buildings by reducing energy consumption in construction output and simultaneously switching to renewable energy sources. [1]

In Latvia fossil energy resources are imported from other countries, but at the same time, our country is rich in renewable energy resources and other raw materials, which are used very little.

Renewable materials which contains natural fibers (e.g. jute, flax, hemp, cotton, cellulose) have many positive features: low thermal conductivity, low density, good specific tensile strength.[2,3,4] The natural fiber materials also have a low impact on the environment.[2,5]

In the study it is proposed to create a thermal insulation material from the hemp shives grown in Latvia as a filler material and lake sediment - sapropel as a binding agent. Both of the following materials are organic, renewable and domestic.

The industrial hemp (*Cannabis sativa*) has been positively regarded by its good thermal insulation and mechanical properties. Hemp stalk grows in 3.5 months and absorbs 4-5 times more CO<sub>2</sub> than a growing forest.[6,7]

Light-weight hemp concrete (hemp shives, lime and water) are used for filling the walls, floors and roof as

thermal insulation material.[8] Scientific literature has examined hemp concrete's thermal, physical, mechanical properties and moisture transfer as well as its use in construction. [9, 10, 11]

Hydraulic lime is commonly used as binding agent in hemp concrete. This research offers to use hemp shives in combination with organic binder agent derived from lake silt - sapropel.

Sapropel supplies are commonly found worldwide. It is a renewable resource. The most intense sapropel formation and accumulation is typical in Asian and European temperate climate zones (Russia, Scandinavian Peninsula, France, Germany, Poland, the Baltic States, Belarus and Ukraine) and in the North American continent in the Great Lakes region (Canada and United States).[12-17] Sapropel supplies and their chemical composition have been studied in several lakes in Russia. [18, 19] Significant sapropel supplies are also found in the Mediterranean. [20]

The first industrial use of hemp and hemp-lime composites as building insulation material in France took place in 1980s. [21] According to the Latvian National Development Plan creating a new composite material from local, renewable resources is actual task nowadays.

The objective of this study is to create a new constructive and insulation material from sapropel and hemp shives. The new construction material can be used as thermal insulation material in new building construction and to improve energy efficiency of old buildings.

## II MATERIALS

### **Sapropel**

The first studies of sapropel in Latvia started in the 1950's. This was carried out in the Latvian SSR Academy of Sciences, Institute of Chemistry and later in the Institute of Forestry Problems led by N.Brakse, B.Vimba and A.Kalnina. In the studies chemical composition and use of sapropel was found out. [22]

Sapropel are organogenetic lake sediments, which are derived from debris of aquatic plants and aquatic animals, which mixed with mineral particles (sand, clay, calcium carbonate and other compounds). It is mucilaginous jelly-like mass of colloidal structure with following undertones - brownish, black, gray, greenish or yellowish, which occurs in the majority of Latvian lakes and in more than third of the Latvian swamps.

Sapropel deposits thickness range from a few centimeters to about 20 m. [23]

Sapropel characterizing parameters are ash content, moisture, organic matter, as well as contents of iron and calcium. Ash content is characterized by mineral admixture quantity, which can vary in very large ranges from 5 to 85%. Natural moisture of sapropel ranges from 70 to 98%. Biological structure characterize organisms from which sapropel is formed. [23]

Total 1327 such lakes can be found in Latvia. As a result of work, an information was obtained on the lake sapropel deposits, which is summarized in the passports of findings. Forecasts stocks are laid down for each sapropel finding. Search works allow to select sapropel finding place by volume of stocks and by certain raw materials which have useful qualitative indicators for the further research which are needed before the industrial extraction of mineral resources. [23]

Predominantly studies of sapropel so far are related to the use in agriculture (as fertilizer), medicine (such as therapeutic mud) and chemical-technological processes (as fuel). The goal of this study is to look at the sapropel as construction material and especially, as a binder agent of sapropel-hemp shives insulation board and its production.

### **Hemp shives**

In production of sapropel and hemp shives insulation board it is intended to use residues (hemp shives) resulting from the processing of hemp. In hemp stalks about sixty-five percent are woody hemp part or the hemp shives which are not fully used. [24]

Hemp is an ancient crop, it has many and different use. Cultivation of hemp in Latvia has a very long history - the oldest hemp seeds were found in Talsu castle hill layers of 11-13th century, but it is likely that they might be cultivated already earlier. [25]

In Latvia from 2008 it is allowed to grow *Cannabis sativa* seed and to obtain the fiber. Consequently now hemp is cultivated in several Latvian regions

approximately in 600 ha, main products are fiber and seed.

According to the data of the Association of industrial hemp in 2013 in the European Union were grown approximately 14 000 ha of hemp. [26]

European Union Regulation of the common agricultural policy (CAP), for time period 2014- 2020 hemp is included in section on environment-enhancing factors. In addition, 1 ha of hemp each year absorbs four times more CO<sub>2</sub> than the same area of forest.

Hemp shives in practice are used as a raw material for building materials, animal bedding, gardening, firewood briquettes, in production of hemp panels and granule or in production of thermal insulation materials. [27]

In 2010 the total quantity of hemp shives was 44 000 t. In percentage distribution of the 44 000 tonnes of hemp shives 62% was used for animal bedding, 45% of them used in the horse stables. 15% of hemp shives were used in the construction area, namely in hemp shives and lime mixtures. Hemp shives lime lightweight concrete is cast in wooden frame during the construction of buildings, such an approach has been used for a couple of years for construction of private houses in France, UK and Ireland.[28] The European Eco-builders looks at this new product with great ambition for use it in ecological constructions.

The remaining 22% of hemp shives are used in many different places elsewhere, such as in cogeneration stations to generate heat / electricity, a small amount in particle board production and in other small productions.

Laboratory experiments show that from local, renewable raw materials; sapropel and hemp shives can be obtained high-quality, ecological and complying to modern requirements thermal insulation construction material.

For scientific studies natural raw materials were derived from a various local companies. Sapropel was extracted from the Ubogovas lake in Makonkalna parish, Rezeknes district. In turn hemp shives from "Latgale Agricultural Science Centre" Dr.agr. V. Stramkale, by processing them in Preiļu pretreatment workshop. In G. Liberta Innovative microscopy center of Daugavpils University collected sapropel samples with an electronic microscope VEGA were tested. Obtained results are summarized in Table I, where min and max measurements are % from weight.

Sapropel mass obtained from lake was 5.66% sapropel and 94.34% water. Shives with two different sizes were taken – one with large fraction of long and mechanically unbroken shives (L) and one with smaller fraction which has gone more processing cycles (S). Composition, density and thermal conductivity is visible in Table II.



Table I  
SAPROPEL CHEMICAL ELEMENT MIN AND MAX VALUES% BY WEIGHT

Chemical elements	C	O	Mg	Al	Si	S	K	Ca	Fe	Mo
Max	89,53	31,18	0,66	1,88	3,29	0,39	1,35	2,67	1,27	0,49
Min	53,06	35,40	0,66	1,55	2,86	0,40	0,52	1,07	0,94	0,49

TABLE II  
SIZE AND MECHANICAL PROPERTIES OF HEMP SHIVES

Name	Fibre	>20mm	10-20mm	0,63-10mm	Dust	Density, kg/m <sup>3</sup>	Thermal cond. W/m*K	Moisture, %
L	2,1%	16,9%	29,6%	48,3%	3,1%	62,53	0,051	9,72%
S	1,5%	4,9%	25,7%	65,3%	2,6%	78,43	0,053	8,96%

TABLE III  
COMPOSITIONS OF MIXTURES

	Shives type	Shives, g	Sapropel, g	Water, g	Sapropel: water ratio
L1	L	3673,6	5510,4	5510,4	1:1
S1	S	3149,2	4723,8	4723,8	1:1
S2	S	2830	5660	2830	2:1
S3	S	2237	6100	610	10:1

### III METHODS

#### A. Mould preparation

For the tests a moisture resistant plywood moulds were used, they are made of 28 mm thick plywood to withstand the applied pressure which is applied using four 10 mm diameter threaded rods at each corner of the mould. To ensure that the material doesn't stick to the mould, it is greased with formwork oil.

#### B. Preparation of ingredients

Before the mixing process all ingredients were prepared for the test. The hemp shives were weighted – the used amounts are shown in Table III. The ratio between shives and binder is 1:3 by mass, binder mass is sapropel with additional water. In the first part of the test - to ensure that sapropel fully mixes with the shives it is diluted with water to make it more workable, sapropel/water ratio 1:1 for L1 and S1 samples. The water is added to sapropel and then it is mixed together using electrical hand mixer.

In the second part of the test different sapropel/water ratio were taken to test the effect of additional binder addition on mechanical properties of the material. Binder/shives ratio wasn't changed,

water/sapropel ratio was 1:2 for S2 sample and 1:10 for S3 sample.

#### A. Mixing

Mixing was done using drum type concrete mixer, speed 22 rpm. First, the shives were placed in a working mixer, shortly after the binder mixture was poured in. The mixing process was continued for 3 minutes. No lumps formed in the mixing process, which is a difference from hemp-lime mixtures when prepared in drum mixer, that could be attributed to slightly wetter mix that of hemp-lime samples.

#### B. Moulding

For the first part of the test the moulding is done in three stages. First the mould with threaded rods is filled with the raw material to the top – 10 cm, then the pressure plate is put on and by tightening the nuts the sample is pressed from 10 cm thickness to 6 cm (Fig.1). Filing of the moulds is done in 4 to 5 cm layers by slightly tamping every layer. Samples are marked with letter P.

Second and another mould is filled with material until the 8 cm mark, a plywood plate is put on a top and concrete blocks with total weight of 50 kg, which makes the sample to shrink to around 6 cm in height. Samples are marked with letter K.

Third mould is filled with remaining material by filling in layers and tamping, a plywood plate is put on top, but no extra pressure is added. For the second part of the test only first two stages are used, as samples without any pressure showed poor results.



Fig. 1. Mould for compression

### C. Demoulding

Demoulding of the samples were done after two days of curing, they were demoulded and left to cure in horizontal positions for one more day. After that they were put in a vertical position and left to cure in laboratory conditions ( $20 \pm 2$  °C and  $40 \pm 10$  %RH). The weight of the samples were regularly checked to see if any changes occurs in mass, to assess the completeness of drying. The longest time necessary for complete drying was for sample S2P as it is the sample with the highest density.

### D. Testing

The testing was done in two stages, First, after the complete drying, sample dimensions and weight were measured, then – thermal conductivity. It was measured with a use of LaserComp FOX600 heat flow meter, following guidelines of LVS EN 12667, test settings  $0$  °C upper and  $20$  °C lower plate. After this test the samples were sawn into pieces for mechanical testing – two for compressive strength parallel to compaction direction, two for compressive strength crosswise the compaction direction and one for flexural strength. Dimensions –  $100 \times 100 \times$  height mm for compressive tests and  $350 \times 100 \times$  height for compressive strength. A layer of gypsum is spread over the interfaces to ensure even pressure application.

Tests were done according to LVS EN 826 on Zwick Z100 universal testing machine, with the pressure applied at 5mm/min, in the process a force-deformation diagram is recorded. The compressive strength test result is a value of pressure applied at 10% relative vertical deformations. Flexural test is continued until rupture, span between points – 200 mm, a 3 N prepressure is applied to the samples.

## IV RESULTS AND DISCUSSION

The summary of the test results can be seen in the Table IV. The type of mixture according to Table III is appended with corresponding type of compression during the moulding phase – P, K or N.

From the table it can be seen that compression during the preparation have direct impact on density, as P samples were pressed by 40% of height, K for 25% and N for 0%. But the differences in densities from the table doesn't match the differences of compaction, this is due to the fact, that all samples were slightly tamped during moulding and mixing of the material also made it to become more dense, so the effect of additional compression of the samples were not so great.

Densities also differed because of the sapropel/water ratio, as the hemp/binder ratio wasn't changed. Although the ratio differs 10 times for some samples, the density fluctuation is not so great. This is due to the fact that sapropel initially contained more than 95% water which, and by changing the ratio from 1:1 to 10:1 changes the amount of sapropel only less than two times, because the shives: binder ratio didn't change.

From the table it can also be seen that density have impact on thermal conductivity. This is because shives and sapropel have higher thermal conductivity than that of still air inclusions in thermal insulation materials, which means that by decreasing the amount of this air with addition of more sapropel and shives to volume, the thermal conductivity also gets higher. The correlation between density and thermal conductivity can be seen in Fig. 2.

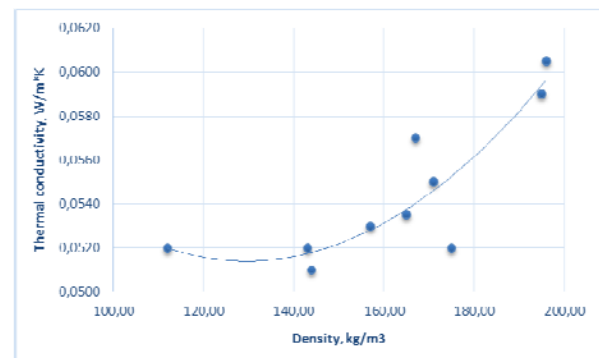


Fig.2. Thermal conductivity/density graph

This previous effect of increased density on thermal conductivity doesn't work on samples made without any pressure. This could indicate that when making samples with no pressure applied during curing the hemp shives are too far away from each other and doesn't create concealed volumes, which allows air to move more freely around and that makes the thermal conductivity of the samples to be higher. Because of

this effect, samples with no pressure applied weren't made in second part of the test.

From the results an effect of different shives on end properties of the material also can be seen. Large shives (L) shows slightly better thermal conductivity, which can be explained by more long and undamaged fiber tubes which has shown lower thermal conductivity than smaller, more processed fiber [29].

But mechanical properties of these long shives are worse, samples for compressive strength crosswise failed while they were sawn, compressive strength is even three times lower, the same for flexural strength. This could be explained by contact zone between the shives which is less for the long shives, this could attribute for the lower mechanical strength.

TABLE IV  
TEST RESULTS

Type	Sapropel: water ratio	Density, kg/m <sup>3</sup>	Thermal cond., W/m*K	Compr. strength, MPa	Compr. Strength crosswise, MPa	Flex. strength, MPa
L1P	1:1	165,00	0,0535	0,046	x	0,012
L1K	1:1	144,00	0,0510	0,019	x	0,007
L1N	1:1	112,00	0,0520	0,016	x	x
S1P	1:1	171,00	0,0550	0,089	0,027	0,022
S1K	1:1	157,00	0,0530	0,072	0,029	0,022
S1N	1:1	143,00	0,0520	0,033	0,011	x
S2P	2:1	196,00	0,0605	0,113	0,034	0,021
S2K	2:1	175,00	0,0520	0,094	0,015	0,015
S3P	10:1	195,00	0,0590	0,148	0,042	0,031
S3K	10:1	167,00	0,0570	0,087	0,025	0,016

The results also shows a correlation between density and mechanical strength – if the material is more dense then it also have greater mechanical strength. From the table it can be seen that the method how the density is raised isn't important, as both – with addition of more sapropel or with additional compression – achieves similar results, which also indicate that the mechanical strength is dependant on contact zone. Graphical correlation between compressive strength and density can be seen in Fig.3.

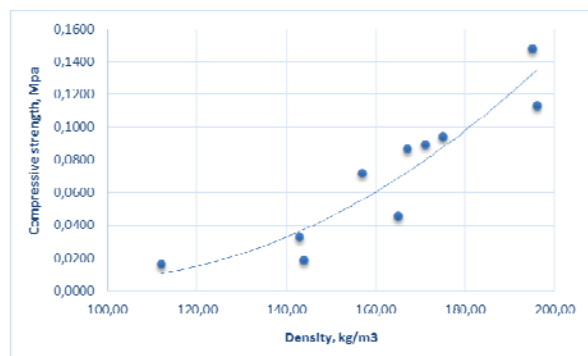


Fig.3. Compressive strength/density graph

If the results are compared to similar studies, then it can be seen that achieved thermal conductivity is adequate for sapropel thermal insulation materials as it is around 0,053 W/m\*K [30],[31]. But if compared to

other hemp materials, for example, a hemp lime concrete, then it has superior thermal conductivity as hemp-lime materials have it around 0,075 W/m\*K [32], although their mass is also larger.

Regarding the mechanical strength – the achieved result is equal to results from similarly made sapropel insulation material – around 0,15 MPa for compressive strength and 0,03 for flexural strength [31], but inferior to hemp-lime whose compressive strength is around 0,25 MPa, or sapropel insulation materials made with higher pressure and under temperature treatment, which activates natural binders in sapropel and hemp shives, with his method compressive strength from 0,35 to 1,85 MPa is achievable, without significant thermal conductivity losses.

## V CONCLUSIONS

1. Use of longer shives improves thermal conductivity because of more undamaged fiber, but worsens mechanical properties because of less contact zone between shives.
2. Samples should be compressed during the curing to ensure more closed air spaces between the shives, without compression thermal conductivity rises.
3. Density influences thermal conductivity of the material as well as mechanical strength, but is not important how the density is increased – with more binder or with additional compression.

4. Material showed results that are similar of other sapropel thermal insulation materials for conductivity, but worse for mechanical strength because the manufacture technologies differed.
5. Material shows better thermal conductivity than hemp-lime materials but has weaker mechanical strength.
6. Further tests should focus on improvement of mechanical strength which can be achieved using thermal treatment during the curing.
7. In the case of using the material as a thermal insulation - problems regarding fire protection and biological resistance should also be solved, as there are no mineral additives for the material at this moment.

## VI ACKNOWLEDGMENTS

The research leading to these results has received the funding from Latvia state research programme under grant agreement "INNOVATIVE MATERIALS AND SMART TECHNOLOGIES FOR ENVIRONMENTAL SAFETY, IMATEH".

## VII REFERENCES

- [1] Latvijas Nacionālais attīstības plāns 2014.–2020.gadam; 24.; 191.-194.punkti; [http://www.varam.gov.lv/lat/pol/ppd/ilgtsp\\_att/?doc=13858](http://www.varam.gov.lv/lat/pol/ppd/ilgtsp_att/?doc=13858).
- [2] A. Korjenic, V. Petránek, J. Zach, J. Hroudová, Development and performance evaluation of natural thermal-insulation materials composed of renewable resources, *Energy and Buildings* 43 (2011) 2518–2523.
- [3] J. Zach, J. Hroudová, Z. Brožovský Krejza, A. Gailius, Development of thermalinsulating materials on natural base for thermal insulation systems, *ProcediaEngineering* 57 (2013) 1288–1294.
- [4] H. Ku, H. Wang, N. Pattarachaiyakooop, M. Trada, A review on the tensile prop-erties of natural fiber reinforced polymer composites, *Composites: Part B* 42(2011) 856–873.
- [5] A.M. Papadopoulos, State of the art in the thermal insulation materials and aimsfor future developments, *Energy and Buildings* 37 (2005) 77–86.
- [6] A. Motori, S. Manzi, M. Montecchi, M. Canti, A preliminary study of the phys-ical and mechanical properties of sustainable hemp fibers based compositematerials for building insulated walls, in: *Proceedings of ECCM15-15th Euro-pean Conference on Composite Materials, Venice (Italy) 24-28 June, 2012*, pp. 1–8.
- [7] L. Zampori, G. Dotelli, V. Vernelli, Life cycle assessment of hemp cultivationand use of hemp-based thermal insulator materials in building, *EnvironmentalScience & Technology* 47 (2013) 7413–7420.
- [8] L. Arnaud, E. Gourlay, Experimental study of parameters influencing mechan-ical properties of hemp concretes, *Construction and Building Materials* 28(2012) 50–56.
- [9] R. Walker, S. Pavia, Moisture transfer and thermal properties of hemp–lime concretes, *Construction and Building Materials*, 64 (2014) 270–276.
- [10] Enrico Sassoni, Stefania Manzi, Antonio Motori, Matteo Montecchi, Max Canti, Novel sustainable hemp-based composites for application in thebuilding industry: Physical, thermal and mechanical characterization, *Energy and Buildings* 77 (2014) 219–226.
- [11] R. Walker, S. Pavia, R. Mitchell, Mechanical properties and durability of hemp-lime concretes, *Construction and Building Materials* 61 (2014) 340–348.
- [12] Jacqueline Süß, Kerstin Herrmann, Michael Seidel, Heribert Cypionka and Bert Engelen, et al; Two Distinct Photobacterium Populations Thrive in Ancient Mediterranean Sapropel <https://springerlink3.metapress.com/content/x6086hx271813h16/resource-secured/?target=fulltext.pdf&sid=hsk0h341jho04vresamjwsl&sh=www.springerlink.com>
- [13] Skrypnikova Marina, Uspenskaya Olga, Khokhlova Olga; Paleoclimate Study of Mountain Ecosystems by Multiple Group Biological Analysis <http://www.springerlink.com/content/yj4l47732967371x/fulltext.pdf>
- [14] V. I. Smetanin and A. V. Sogin, Use of hydraulic excavation for cleaning and construction of water bodies <https://springerlink3.metapress.com/content/c56j134131j72166/resource-secured/?target=fulltext.pdf&sid=hsk0h341jho04vresamjwsl&sh=www.springerlink.com>
- [15] G. A. Kovalenko, L. V. Perminova, G. V. Plaksin, O. V. Komova and T. V. Chuenko, et al.Immobilized Yeast Membranes as Biocatalysts for Sucrose Inversion <https://springerlink3.metapress.com/content/r7j0811674636373/resource-secured/?target=fulltext.pdf&sid=hsk0h341jho04vresamjwsl&sh=www.springerlink.com>
- [16] Saburo Sakai, Masaru Nakaya, Yoshikazu Sampei, David L. Dettman and Katsumi Takayasu Hydrogen sulfide and organic carbon at the sediment–water interface in coastal brackish Lake Nakaumi, SW Japan <http://www.springerlink.com/content/m5121r5740302555/fulltext.pdf>
- [17] W. Joe Lambert, Paul Aharon and Antonio B. Rodriguez, Catastrophic hurricane history revealed by organic geochemical proxies in coastal lake sediments: a case study of Lake Shelby, Alabama (USA) <https://springerlink3.metapress.com/content/v404184x01t22836/resource-secured/?target=fulltext.pdf&sid=hsk0h341jho04vresamjwsl&sh=www.springerlink.com>
- [18] Z. V. Semenova, D. F. Kushnarev, M. A. Litvintseva and A. V. Rokhin, Humic acids from the sapropel of Lake Ochaul <https://springerlink3.metapress.com/content/mw1u3020575432q7/resource-secured/?target=fulltext.pdf&sid=hsk0h341jho04vresamjwsl&sh=www.springerlink.com>
- [19] G. A. Leonova, V. A. Bobrov, E. V. Lazareva, A. A. Bogush and S. K. Krivonogov, Biogenic contribution of minor elements to organic matter of recent lacustrine sapropels (Lake Kirek as example) <https://springerlink3.metapress.com/content/g483632404795967/resource-secured/?target=fulltext.pdf&sid=hsk0h341jho04vresamjwsl&sh=www.springerlink.com>
- [20] Hilde F. Passier, Michael E. Böttcher and Gert J. De Lange, Sulphur Enrichment in Organic Matter of Eastern Mediterranean Sapropels: A Study of Sulphur Isotope Partitioning <https://springerlink3.metapress.com/content/xk482r7252x53321/resource-secured/?target=fulltext.pdf&sid=hsk0h341jho04vresamjwsl&sh=www.springerlink.com>
- [21] Boutin M-P, Flamin C, Quinton S, Gosse G, Inra L. Etude des caracteristiques environnementales du chanvre par l'analyse de son cycle de vie [Study of environmental characteristics of hemp by means of an analysis of its lifecycle]. *Ministere de l'Agriculture et de la Peche [Ministry of Agriculture and Fishery]*;2005.
- [22] Brakšes N., Vimbas B.un Kalniņa A., Par sapropelja īpašībām un pielietojumu Latvijas PSR, *Latvijas PSR Zinātņu Akadēmijas vēstis* Nr.8(133), 1958.
- [23] Lācis A., Sapropelis Latvijā, *Valsts ģeoloģijas dienests, Rīga*
- [24] Bolgzde, K., Ulme, A., Kaņepju šķiedru un stiebru īpašību un pārstrādes tehnoloģiju izpēte, to izmantošanas iespējas arhitektūras un interjera elementos, <http://web.ebscohost.com/ehost/pdfviewer/pdfviewer?sid=d715805e-838c-473d-939a-817e2d7b318c%40sessionmgr4002&vid=2&hid=4207> Sk.12.01.2015.
- [25] Kaņepes un to audzēšana, [http://www.laukunik.lv/lauksaimnieciba/zinas/2336-kanepes\\_un\\_to\\_audzšana](http://www.laukunik.lv/lauksaimnieciba/zinas/2336-kanepes_un_to_audzšana)

- [26] Carus. M., Market data on Industrial Hemp – fibres, shivs and seeds, European Industrial Hemp Association, 2013, [http://www.fibrafp7.net/Portals/0/Michael\\_Carus\\_Day\\_1.pdf](http://www.fibrafp7.net/Portals/0/Michael_Carus_Day_1.pdf)
- [27] Assoc. Prof., PhD. R., Réh, MSc. J., Vrtielka, Modification Effect of the Core Layer with Addition of Shives for Particleboard Manufacture, European Industrial Hemp Association, [http://www.eiha.org/attach/751/Reh\\_Vrtielka\\_EIHA\\_2012.pdf](http://www.eiha.org/attach/751/Reh_Vrtielka_EIHA_2012.pdf)
- [28] Carus, M., Karst, S., Kauffmann, A., Hobson, J., Bertucelli S., The European Hemp Industry: Cultivation, processing and applications for fibres, shivs and seeds, European Industrial Hemp Association, 2013, [http://www.eiha.org/attach/855/13-06\\_European\\_Hemp\\_Industry.pdf](http://www.eiha.org/attach/855/13-06_European_Hemp_Industry.pdf)
- [29] Vaitkus, S., Karpaviciute, R., Vėjelis, S., Lekunaite, L. Development and Research of Thermal Insulation Materials from Natural Fibres  
Conference: 22nd International Baltic Conference on Engineering Materials & Tribology (BALTMATTRIB) Riga, LATVIA Date: NOV 14-15, 2013  
ENGINEERING MATERIALS & TRIBOLOGY XXII Book Series: Key Engineering Materials Volume: 604 Pages: 285-288 Published: 2014
- [30] Balčiūnas, Giedrius; Žvironaitė, Jadvyga; Vėjelis, Sigitas The use of Sapropel in Development of Effective Thermal Insulating Materials; Key Engineering Materials;2014, Vol. 604, p313
- [31] Vaira Obuka, Aleksandrs Korjamins, Raitis Brencis, Ilmārs Preikšs, Oskars Purmalis, Karina Stankeviča, Māris Kļaviņš; Sapropēļa kūdras, sapropēļa kokskaidu siltumizolācijas plāksnes un to īpašības; Material Science and Applied Chemistry 2013/29
- [32] Sinka, M., Sahmenko, G.; Sustainable thermal insulation biocomposites from locally available hemp and lime; 9th International Scientific and Practical Conference on Environment, Technology and Resources; Rezekne; Latvia; 20 June 2013 through 22 June 2013.

# The simulation model of sliding contact with three degrees of freedom and distributed parameters of the transition layer

Igor Plohov, Alexander Ilyin, Oksana Kozyreva, Igor Savraev  
*Pskov State University, Faculty of Electromechanics.  
Address: pl.Lenina, 2, Pskov, 180000, Russia*

**Abstract.** The development of theoretical approaches to determining mechanical characteristics of sliding contacts by the creation of a simulation model of a sliding contact with three degrees of freedom and distributed parameters of the transition layer is considered. This model enables to obtain dynamic and integral characteristics of the sliding contact on design parameters given and characteristics of materials of contact pairs.

**Keywords:** sliding electrical contact, computation model, contact interaction, current device with sliding collecting.

## I INTRODUCTION

Many electromechanical systems have a current device with sliding collecting (CDSC) containing a single or a group of sliding contacts (SC). In the simplest case SC consists of two contact details pressed together which are moving relatively. The most common CDSC is a brush-contact device of an electrical machine, which consists of solid brushes installed in fixed brush holders and pressed against the surface of the rotating current collector (CC).

The work of CDSC is accompanied by mechanical vibrations of brushes arising from their interaction with a contact surface of CC. Surface irregularities the mathematical model of which is given in [19, 27] cause dynamic forces which modulate the contact pressure within a wide range. These forces can reach values which cause a breach of the contact resulting in short dead times [16, 19]. For high-speed CDSC (such as turbogenerators) mechanical factors are a major cause of sparking and an increased wear of contact pairs and can also cause "round light" which results in a long-term failure of a current device with sliding collecting.

So far it has not been a consensus regarding adequate modeling main features and characteristics of a sliding electrical contact. It is connected with a great variety and with the complexity of physical processes of electrofrictional interaction [2-25, 28-32]. Despite much research in this area a mathematical model of SC which must meet practical requirements has not been developed yet.

The rational choice of design parameters and materials of contact pairs [26] is made mainly experimentally which results in considerable time and cost consumption.

The subject of this research is the development of theoretical approaches to the determination of mechanical characteristics of SC by creating a distributed nonlinear dynamic model for receiving dynamic and integral characteristics of SC on the design parameters given and characteristics of materials of contacting pairs [19]. The modeling of dynamics of contacting with account of nonlinear distributed parameters in the transition layer will let predict the behaviour of the SC under various modes and search optimal design solutions at the design stage. This modeling will reduce the share of long-term expensive tests at the stage of designing SC and improve the quality of the development of CDSC.

## II SIMULATION MODEL

The simplest design of CDSC is shown in Fig. 1. The brush 1 placed in the guides brush holder 2 is pressed by the force  $F$  to the surface of the rotating current collector 3.

The dynamic model of SC shown in Fig. 2 has three degrees of freedom, unilateral mechanical connections and distributed nonlinear parameters of the contact layer [19]. The brush having mass  $m_b$  can perform radial oscillations  $Y(t)$  along the axis  $Y$ , tangential oscillations  $X(t)$  along the axis  $X$  and rotary oscillations  $\varphi(t)$  in the direction of the angle

*ISSN 1691-5402*

$\varphi$ . The brush body is considered to be absolutely rigid and the mass to be distributed evenly. The center of the mass of the brush is the point A which moves dynamically relatively the fixed coordinate system XOY. The structure of the dynamic model for axial oscillations is similar.

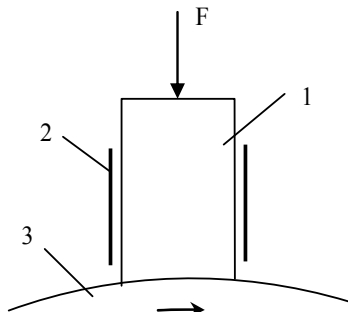


Fig. 1. Current device with sliding collecting.

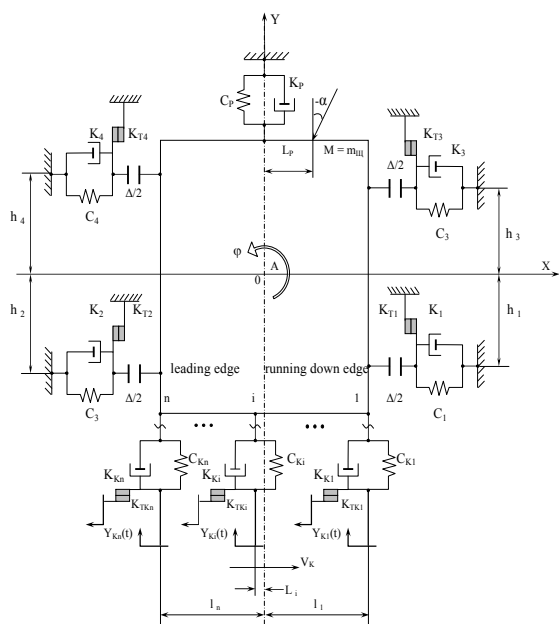


Fig. 2. Dynamic model of mechanical behaviour of a sliding contact.

The pressure spring with stiffness  $C_p$  and damping coefficient  $K_p$  affects on the brush with the force  $F_N$ , that can be applied at the angle  $\alpha$  and at the distance  $L_p$  relatively to the radial axis of the brush. The contact area "brush - current collector" (contact layer) is described mathematically with the distributed system of boundary element (BE), each of which is defined by the rheological model of Kelvin-Voigt [1] in the radial direction and the model of Coulomb- Amontons in the tangential direction. The parameters of these models are the following:  $C_{Ki}$  is a contact stiffness of i-BE;  $K_{Ki}$  is a damping coefficient contact GE;  $K_{TKi}$  is a boundary friction coefficient ET. Similarly the contact with the rails defined by four BE of the same type is simulated. The parameters of the model are the following:  $C_1, \dots, C_4, K_1, \dots, K_4$  are coefficients of

stiffness and contact damping active elements. Mechanical connections BE are unilateral and the brush has a tangential play  $\Delta$  in guides.

In accordance with the quasi-static principle of d'Alembert one can write the differential equations of the motion under the influence of kinematic disturbances  $Y_{Ki}(t)$ .

For coordinate Y:

$$m_u \frac{d^2 Y(t)}{dt^2} + \sum_{i=1}^n \left\{ C_{Ki}(\Delta Y_i) [Y(t) - Y_{Ki}(t) + l_i \varphi(t)] + K_{Ki}(C_{Ki}) \left[ \frac{dY(t)}{dt} - \frac{dY_{Ki}(t)}{dt} - l_i \frac{d\varphi(t)}{dt} \right] \right\} + \sum_{i=1}^4 F_{Yi}(t) + C_p Y(t) + K_p \frac{dY(t)}{dt} = -F_H(t) \cos \alpha; \quad (1)$$

for coordinate X:

$$m_u \frac{d^2 X(t)}{dt^2} + \sum_{i=1}^4 \left\{ C_i(\Delta X_i) [X(t) - \varphi(t) h_i] + K_i(C_i) \left[ \frac{dX(t)}{dt} - h_i \frac{d\varphi(t)}{dt} \right] \right\} = \sum_{i=1}^4 F_{Xi}(t) + F_H(t) \sin \alpha; \quad (2)$$

for coordinate  $\varphi$ :

$$J_u \frac{d^2 \varphi(t)}{dt^2} + \sum_{i=1}^n \left\{ C_{Ki}(\Delta Y_i) l_i [l_i \varphi(t) + Y(t) - Y_{Ki}(t)] + K_{Ki}(C_{Ki}) \left[ l_i \frac{d\varphi(t)}{dt} - \frac{dY(t)}{dt} - \frac{dY_{Ki}(t)}{dt} \right] \right\} + \sum_{i=1}^4 \left\{ C_i(\Delta X_i) h_i [X(t) - \varphi(t) h_i] + K_i(C_i) h_i \left[ \frac{dX(t)}{dt} - \frac{d\varphi(t)}{dt} h_i \right] + F_{Yi}(t) l_i \right\} = -\frac{h}{2} \sum_{i=1}^4 F_{Xi}(t) - F_H(t) (L_p \cos \alpha - \frac{h}{2} \sin \alpha), \quad (3)$$

where  $h$  is the height of the brush;  $Y(t)$ ,  $X(t)$ ,  $\varphi(t)$  are radial, tangential and angular values of the motion of the brush in the coordinate system given;  $l_i$ ,  $h_i$  are shoulders of BE of the contact layer and guides;  $F_{Yi}$ ,  $F_{Xi}$  are the friction forces in the BE of contact layer and in the guides:

$$F_{Yi}(t) = \left\{ C_i(\Delta X_i) [X(t) - \varphi(t) h_i] + K_i(C_i) \left[ \frac{dX(t)}{dt} - \frac{d\varphi(t)}{dt} h_i \right] \right\} K_{TKi} \text{sign} \frac{d\Delta Y_i(t)}{dt};$$

$$F_{Xi}(t) = \left\{ C_{Ki}(\Delta Y_i) [Y(t) - Y_{Ki}(t) + \varphi(t) l_i] + K_{Ki}(C_{Ki}) \left[ \frac{dY(t)}{dt} - \frac{dY_{Ki}(t)}{dt} + \frac{d\varphi(t)}{dt} l_i \right] \right\} K_{TKi}, \quad (4)$$

where  $\Delta Y_i$ ,  $\Delta X_i$  is a radial and tangential value of the convergence of interacting zones of microreliefs in i-BE:

$$\Delta Y_i = Y(t) - Y_{Ki}(t) + l_i \varphi(t), \quad (5)$$

$$\Delta X_i = X(t) - h_i \varphi(t).$$

After making the transition to the operator form we obtain after transformations the coordinates  $Y$ ,  $X$ ,  $\varphi$  respectively:

$$Y(p) = \frac{1}{pm_u} \left\{ \sum_{i=1}^n \left[ \frac{1}{C_{Ki}(\Delta Y_i)} (Y_{Ki}(p) - Y(p) - l_i \varphi(p)) + K_{Ki}(C_{Ki}) (Y_{Ki}(p) - Y(p) - l_i \varphi(p)) \right] + \sum_{i=1}^4 \left[ \frac{1}{F_{Yi}(p)} \right] - \frac{1}{C_p} Y(p) - K_p Y(p) - \frac{1}{p} F_H(p) \cos \alpha \right\} \quad (6)$$

$$X(p) = \frac{1}{m_u p} \left\{ \sum_{i=1}^4 \left[ \frac{1}{C_i(\Delta X_i)} (\varphi(p) h_i - X(p)) + K_i(C_i) (\varphi(p) h_i - X(p)) \right] + \frac{1}{p} F_H(p) \sin \alpha - \sum_{i=1}^n \frac{1}{C_{Ki}(\Delta Y_i)} \right\} \quad (7)$$

$$\varphi(p) = \frac{1}{J_{III} P} \left\{ \begin{aligned} & \left[ \sum_{i=1}^n \frac{1}{P} C_{Ki} (\Delta Y_i) l_i (Y_{Ki}(p) - Y(p) - \varphi(p) l_i) + \right. \\ & \left. + K_{Ki} (C_{Ki}) l_i (Y_{Ki}(p) h_i - Y(p) - \varphi(p) l_i) \right] + \\ & \left[ C_i (\Delta X_i) h_i \frac{1}{P} (\varphi(p) h_i - X(p)) + \right. \\ & \left. + K_i (C_i) h_i (\varphi(p) h_i - X(p)) + \frac{1}{P} F_{Yi}(p) l_i \right] - \\ & - \sum_{i=1}^n \frac{1}{P} F_{Xi}(p) \frac{h}{2} - \frac{1}{P} F_H(p) (L_p \cos \alpha + \frac{h}{2} \sin \alpha) \end{aligned} \right\} \quad (8)$$

According to the equations of motion, we will construct a generalized block diagram of the dynamic model (Fig. 3). According to the scheme the program was developed that allowed to study the influence of various factors on three coordinate oscillations of the brush. The study of tangential distributions of the contact instability, the contact pressure and the specific contact stiffness have been carried out.

To determine spatial distributions in the tangential direction of the contact pressure of the specific contact stiffness and a coefficient of a relative instability (CRI) we perform the following: 1) at each step of the calculation in each BE we determine the presence of the contact as a Boolean constant as well as a specific stiffness and pressure using the value of the contact convergence member; 2) the data are being collected during the period of the calculation then they are averaged over the time and given as graphs. Moreover on the data obtained we calculate the parameters that characterize the quality of contacting on the average over the entire contact area.

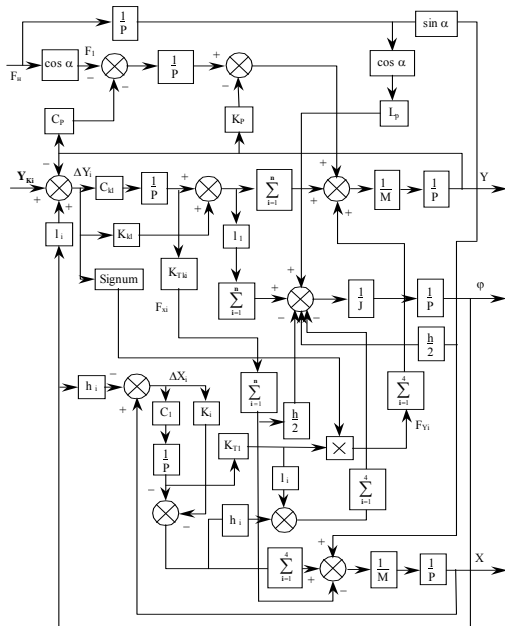


Fig. 3. Generalized block diagram of dynamic model.

Fig. 4 shows as an example the interconnected dynamic response to the standard kinematic perturbations obtained with the dynamic model.

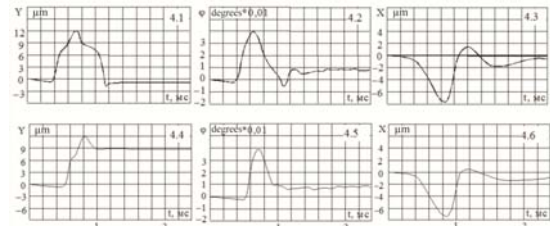


Fig. 4. Pulse response (top row) and unit-step response (bottom row) by  $\alpha = 0$ .

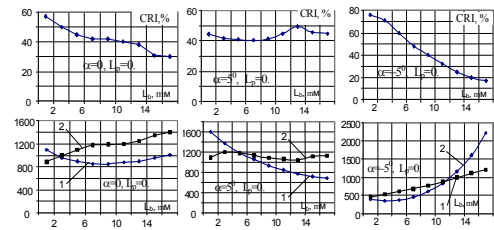


Fig. 5. Contact distributions for different values of  $\alpha$  and  $L_p$ . the top row of the graphs is the coefficient of relative instability, %; the bottom row of the graphs is the specific pressing N/m (curve 1), specific contact stiffness, MN/m/m (curve 2).

### III CONCLUSION

The analysis of the arrays of these characteristics obtained under different constant conditions and for different kinematic disturbances shows that: 1) generally the distributions of a contact are nonlinear; 2) by axial pressing force application the leading edge of the brush contact is more stable than the running down edge of the brush; 3) the contact pressure on the edges of the brush is more than in the middle; 4) the distribution of the contact stiffness is shaped qualitatively inversly in the relation to the distribution of CRI; 5) the increase of the linearity distribution of the stiffness and CRI can be achieved at positive values of the angle  $\alpha$  and arm  $L_p$ .

The analysis of the dynamic reactions shows that the loss time of the contact at the interaction of the brush with a single protrusion decreases when the pressure force is displaced or tilted in the direction of the leading edge. Practically all contact pressure is concentrated on the leading edge of the brush that works stably while CRI of running down edge of the brush increases significantly.

Now the dynamic model of the mechanics of the electrofrictional interaction is realized by means of the system of simulation Simulink MATLAB.

### IV REFERENCES

- [1] Рейнер М. Реология. М.: Наука. 1965, с.224.
- [2] Лившиц П.С. Справочник по щеткам электрических машин. М.: Энергоатомиздат. 1983.
- [3] Веселовский В. С, Угольные и графитовые конструкционные материалы, М., 1966.



- [4] Шулепов С. В. Физика углеграфитовых материалов, М., 1972.
- [5] Шулепов С. В. Рекристаллизованный графит, М., 1979.
- [6] Дёмкин Н.Б. Контактное шероховатых поверхностей. – М.: Наука, 1970. 227 с.
- [7] Мандельштам Л. И., Лекции по теории колебаний, М., 1972; Основы теории колебаний, 2 изд., М., 1988.
- [8] Анищенко В.С. Сложные колебания в простых системах: Механизмы возникновения, структура и свойства динамического хаоса в радиофизических системах. – М.: Либроком, 2009. 312 с.
- [9] Арнольд В.И. Математические методы классической механики. – М.: Наука, 1974. 432 с.
- [10] Белоцерковский О.М., Численное моделирование в механике сплошных сред. – М.: Физматлит, 1994. 442 с.
- [11] Рыжов Э.В. Контактная жесткость деталей машин. М.: Машиностроение. 1966. с.196.
- [12] Левина З.М., Решетов Д.Н. Контактная жесткость машин. М.: Машиностроение. 1971. с.264.
- [13] Пановко Я.Г., Губанова И.И. Устойчивость и колебания упругих систем, современные концепции, парадоксы, ошибки. М.: Наука. 1987.
- [14] Рыжов Э.В., Колесников Ю.В., Суслов А.Г. Контактное твердых тел при статических и динамических нагрузках. Киев: Наук. думка. 1982. с.172.
- [15] Кончиц В.В., Мешков В.В., Мышкин В.В. Триботехника электрических контактов. Минск: Наука и техника. 1986.
- [16] Механика скользящего контакта / В.И.Нэллин, Н.Я.Богатырев, Л.В.Ложкин и др. – М.:Транспорт. 1966.
- [17] Ilyin A., Plohov I., Isakov A. The simulation model of a sliding contact. *Environment. Technology. Resources: Proceedings of the 9th International Scientific and Practical Conference June 20-22, 2013. Volume II. Rezekne, 2013*, pp. 111-115.
- [18] Yip F.C., Venart J.E.S. Surface topography effects in the estimation of thermal and electrical contact resistance. – In: *Proc. Inst. Mech. Eng.*, 1968. V. 182. Pt. 3K. P. 81.
- [19] Плохов И. В. Комплексная диагностика и прогнозирование технического состояния узлов скользящего токосъема турбогенераторов. Диссертация доктора технических наук. – СПб: СПбГПУ. 2001.
- [20] Богатырев Н.Я. Исследование механики скользящего электрического контакта коллекторных машин малой мощности. Дис. на соиск. уч. степ. канд. техн. наук. – Томск: ТПИ. 1965. 22 с.
- [21] Гроссман М.И. Термические и механические факторы в работе скользящего контакта высокоиспользованных машин постоянного тока. Дис. на соиск. уч. степ. канд. техн. наук. Саратов. 1968. 21 с.
- [22] Давидович Я.Г. Исследование физико-механических и коллекторных характеристик щеток для электрических машин. Дис. на соиск. уч. степ. канд. техн. наук. – Омск: ОмИИТ. 1960. 19 с.
- [23] Дридзо М.Л. Оценка тангенциальных сил щеточно-коллекторного узла электрических машин постоянного тока // *Изв. вузов. Электромеханика*. – 1969. – №4. – С. 38–40.
- [24] Зиннер Л.Я., Скороспешкин А.И. Тангенциальные колебания щеток // *Известия ТПИ*. – 1968. – Т. 190. – С. 257–267.
- [25] Дридзо М.Л. Об условиях безотрывного движения скользящего контакта электрических машин постоянного тока // *Электротехника*. – 1967. – №6. – С. 37–41.
- [26] Стенд для исследования узла скользящего токосъема турбогенератора / Плохов И.В., Андрусич А.В., Ильин А.В. и др. // *Вестник Псковского государственного университета. Серия: Экономические и технические науки*. – Псков: ПсковГУ. 2012. № 1. С. 211-215.
- [27] Ильин А. В., Плохов И. В., Козырева О. И. Моделирование процессов электрофрикционного взаимодействия в узлах скользящего токосъема // *Научно-технический вестник Поволжья*. – Казань: Научно-технический вестник Поволжья. №4. 2013. С. 166–173.
- [28] Плохов И.В. Исследование сопротивления стягивания электрического контакта. *Электротехника*. №5. 2004. С. 13–18.
- [29] Плохов И.В., Козырева О.И., Ильин А.В. Определение компонент вектора состояния динамической модели электрофрикционного взаимодействия. *Вестник Псковского государственного университета*. 2013. № 3. С. 183-191.
- [30] Плохов И.В., Козырева О.И., Ильин А.В. Структура и алгоритмы имитационного моделирования динамики электрофрикционного взаимодействия. *Вестник Псковского государственного университета*. 2013. №3. С. 192-199.
- [31] Плохов И.В., Козырева О.И., Ильин А.В. Общие подходы к моделированию динамики электрофрикционного взаимодействия. *Вестник Псковского государственного университета*. 2013. №3. С. 134-142.
- [32] Ильин А. В., Плохов И. В., Козырева О. И. Моделирование микрорельефа поверхностей контактирующих деталей. // *Научно-технический вестник Поволжья*. – Казань: Научно-технический вестник Поволжья. №5. – 2013.– С. 180–183.

# **Impact of density and special features of manufacturing process on drying of autoclaved aerated concrete masonry blocks**

**Sanita Rubene, Martins Vilitis, Juris Noviks**  
*Riga Technical university, Faculty of Civil Engineering*

**Abstract.** Autoclaved aerated concrete (AAC) masonry blocks are construction material with high heat insulation parameters. In time of sustainable construction, this material can be used as a load bearing construction material for a range of buildings where it is necessary to obtain high heat insulation parameters of external delimiting constructions. The main problem of autoclaved aerated masonry constructions is the significant influence of relative humidity rate and its gradient on heat resistivity properties of the masonry constructions. Therefore it is important to monitor the drying process of AAC masonry constructions in order to avoid the sealing of moisture inside the masonry by early application of finishing layers on the construction. As there is a variety of manufacturers who offer AAC masonry blocks and the manufacturing process of the blocks slightly differ as well as the ingredients used for the manufacturing of the blocks this research has been done to determine the impact of manufacturing features and density of the blocks on their drying properties. The testing has been performed by non-destructive testing method – electrical impedance spectrometry (EIS) In the paper, there are included results of research of correlation between EIS and moisture content rate in masonry blocks provided by different manufacturers. All used blocks are with similar material density. As a result of the research correlation formulas between saturation rate of the material and EIS measurement result have been established and a graph of humidity migration throughout the cross section of the masonry construction has been determined.

**Keywords:** autoclaved aerated concrete, electrical impedance spectrometry, humidity distribution, non-destructive testing.

## I INTRODUCTION

Autoclaved aerated concrete (AAC) masonry blocks are construction materials with high heat insulation parameters. In time of sustainable construction, this material can be used as a load bearing construction material for a range of buildings where it is necessary to obtain high heat insulation parameters of external delimiting constructions. The main problem of autoclaved aerated masonry constructions is the significant influence of moisture content rate and its gradient on heat resistivity properties of the masonry constructions. Therefore, it is important to monitor the drying process of autoclaved aerated concrete masonry constructions in order to avoid sealing of the moisture inside the masonry by early application of finishing layers on the construction. As there is a variety of manufacturers who offer autoclaved aerated concrete masonry blocks and the manufacturing process of the blocks slightly differ as well as the ingredients used for the manufacturing of the blocks this research has been done to determine the impact of manufacturing features and density of the blocks on their humidity transfer properties and drying properties. The

measurements have been performed by non-destructive testing method – electrical impedance spectrometry (EIS). In the paper, there are included results of research of correlation between EIS and moisture content rate of masonry blocks provided by different manufacturers. All used blocks are with similar material density. As a result of the research correlation formulas between moisture content rate of the material and EIS measurement result have been established and a graph of humidity migration throughout the cross section of the masonry construction has been determined.

## II HUMIDITY DISTRIBUTION IN AUTOCLAVED AERATED CONCRETE CONSTRUCTIONS

Humidity distribution in AAC masonry construction depend on a range of different factors which include the technology of the manufacturing, ratio of the ingredients used for the material as well as the type and quality of the ingredients themselves. The porosity as well as the pores' structure and density of the AAC has significant impact on the drying properties of the material and its mass transfer properties.

ISSN 1691-5402

Humidity rate of the AAC masonry constructions has significant impact on its heat resistivity properties as well because heat transfer by conduction is affected by transfer of energy through molecular collision, therefore it follows that the thermal conductivity in liquids and solids is much greater than in gases (i.e. for water vapour at 10°C the conductivity  $\lambda$  is  $\approx 0.024$  W/mK, while for liquid water, the conductivity  $\lambda$  is  $\approx 0.6$  W/mK which is a factor 25 times greater) [1]. The Research of Barsotelli et.al [1] provides information that the porosity of the construction material has impact on its hygrometric properties and the research shows a low absorption velocity as a consequence of the large amount of macropores that slow down the capillary forces. Water vapour permeability is enhanced by the degree of connection among the pores and by the absence of condensation phenomena which are favoured by the presence of micropores. Therefore, a higher quantity of micropores should be envisaged favouring the condensation phenomena and hindering the water vapour diffusion.

The water transport phenomena are usually modelled by the diffusion type equation. The equation can have two basic forms. In the first case the driving potential at moisture transport is represented by the capillary pressure and the transport parameters in the equation are moisture capacity and moisture permeability, parameters as the moisture permeability and capacity can be modelled from the pore size distribution. In the second case the water flow driving potential is represented by the moisture content and the material transport parameter is the moisture diffusivity and the equation has so called diffusion form Bruce and Klute [2]. As the water transport parameters depend on the boundary conditions there is a difference between the moisture diffusivity during the water absorption, redistribution and drying.

In a case of drying the diffusivity is smaller (Kuenzel [3]). A detailed study on drying diffusivity and its determination is given by (Pel et al. [4-5]; Pel and Landman [6]) which present the approaches to diffusivity determination at the absorption and at the drying during different drying phases. Vu [29] realised the simulation experiments of drying process considering the variability of pore structure parameters expressed by theoretical pore size distributions and modelling the water transport coefficients of building materials represented as a bundle of capillaries, size distribution of which is based on their pore structure [7].

These statements will be used and developed in the particular research in order to determine the differences of hygrometric properties for several types of AAC masonry blocks by a non-destructive testing method, which can be applied on site conditions.

### III NON-DESTRUCTIVE METHODS FOR DETERMINATION OF HUMIDITY DISTRIBUTION IN MASONRY CONSTRUCTIONS

AAC masonry constructions are widely used for construction of buildings therefore the main field of application for the humidity distribution measurements would be buildings in construction stage or habitable buildings. Therefore, non-destructive measurement methods for detection of humidity distribution throughout the cross section of the AAC masonry construction are preferable.

Researches have been performed in order to detect the credibility of non-destructive test methods for the detection of relative humidity rate in constructions (mostly in concrete). So far, several methods for non-destructive detection of humidity rate in concrete constructions have been discussed.

Gamma densitometry is a nondestructive testing method commonly used to control the density of civil engineering materials [8], [9].

The principle of this method is based on a beam of gamma rays emitted by radioactive source and passing through the concrete (Fig. 1). The relative intensity of the transmitted particles is related to the mass of the traversed material  $m_c$ , the mass variation of the traversed points can thus be measured. Since chemical evolutions do not lead to significant losses of mass, the mass variation in these beams stem solely from water evaporation; and can be interpreted as the profile of water content variations [8], [10].

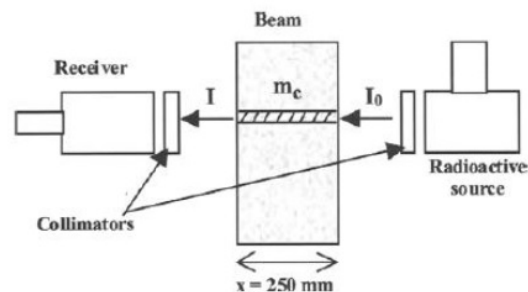


Fig. 1 Principle of the gamma densitometry technique [13], [15]

The gamma densitometry is based on absorption of the gamma ray emitted by a radioactive source of Cesium Cs137 [9]. The relation between intensity  $I$  of the flow of transmitted particles and traversed mass  $m_c$  is as follows is based on the Lambert's Law [10].

The mass variation of the volume intercepted by the gamma ray can be measured at different depths, so water content variation along the height of the concrete beam's cross section can be monitored. The calculation method assumes that at each measurement the flow intercepts the same volume of material [8], [10].

This method allows determining humidity distribution throughout the height of the cross section by non-destructible method, but it can hardly be used

in on-site conditions and is mostly laboratorial test method. Other restriction on this method is described in [8].

High quality relative humidity sensors are usually made of hair from horses or humans. The movement of the hair is converted into an electrical signal by a strain gauge. Similar sensors are made of a strip cellulose butyrate, a water absorbent polymer that likewise stretches and shrinks according to relative humidity.

There are two main types of relative humidity sensors, capacitive and resistive sensors. The capacitive sensor consists of a thin layer of water absorbent polymeric or inorganic material that is coated onto a conductive base. This layer is then covered with porous conductive layer material. With the increase of the relative humidity, the water content of the polymer increases too. Water has a high dielectric constant, which means that the combination of two electrodes with the water between can store a relatively high electric charge. This electrical capacity is measured by applying rapidly reversing (AC) voltage across the electrodes and measuring the current that passes. The polymer or inorganic material is usually aluminum oxide and just plays an indirect part of the measurement. The change of capacitance of these capacitive sensors is, however, small when even compared with the capacitance of few meters of cable. This means that the electronic process of data acquisition has to be completed close to the sensor. If one data logger is connected to several relative humidity sensors, each sensor will need its own power supply and relatively bulky electronics [8], [11].

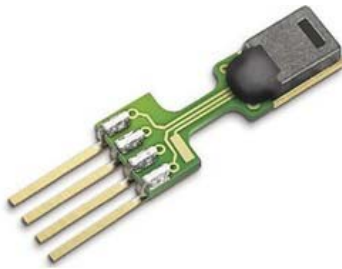


Fig. 2 (a) Capacitive sensor [8]



Fig. 2 (b) Resistivity Sensor [8]

Although capacitive sensors can have reduced accuracy at relative humidity values exceeding 90%,

they typically provide better linearity than resistive sensors. However, capacitive sensors can take several hours to reach equilibrium and provide valid readings [12]. They cannot also be directly exposed to fresh concrete. To solve this problem in the experiment, the sensors are mounted in plastic tubes with Gore-tex® caps and then embedded in fresh concrete. This material, protect the sensor from liquid water but allows vapor transmission. The vapor pressure within the airspace around the sensor and in the concrete pores will always be equal. This allowed the sensor to be permanently embedded in the concrete reaching its equilibrium and obtaining valid readings [8], [13].

Method of electrical impedance spectrometry (EIS) enables detection of the distribution of impedance or other electrical variables (such as resistivity, conductivity etc.) inside a monitored object, and thus the observation of its inner structure and its changes [14], [15]. This method ranks among indirect methods for detection of materials' properties through electrical measurements and it is used in measuring properties of organic and inorganic substances. So far, EIS is widely used in medicine as one of the most common testing methods in diagnostics where any kind of tissues are involved. It constitutes a very sensitive tool for monitoring phenomena that take place in objects (e.g. changes occurring in earth filled dams when loaded by water, in wet masonry sediments etc.), electrokinetic phenomena at boundaries (e.g. electrode/soil grain, between soil grains) or for describing basic ideas about the structure of an inter phase boundary (e.g. electrode/water) [16].

Rajabipour and Weiss have performed series of humidity detection and moisture gradient researches by application of EIS method [17]. The EIS method is based on the principle that a change in the water content of concrete alters the electrical response of the concrete (McCarter and Garvin [14], Weiss et al. [18]). On the other hand, Schießl and co-workers [19] have researched the moisture gradients that develop in drying concrete. Using a series of embedded stainless steel electrodes, they measured the electrical resistance of drying mortar samples as a function of distance from the drying surface [17]. As it is known from the approach of Matiasovsky, Mihalka, Pel, Landman [4-7] the water absorption, absorption after rewetting and the drying process have slightly different kinetics and should be considered separately.

EIS method with Z-meter [20] device allows using only one probe pair for multiple in-field measurements because the probes can be withdrawn from the construction after the measurement. Experiments with EIS method for the detection of humidity distribution throughout cross section of aerated concrete constructions have been performed in Riga Technical university by Z-meter III device and methodology for measurement process is being developed [21-23]. EIS method can be applied for non-destructive detection humidity level throughout

aerated concrete constructions. It is easily applicable for testing of relative changes of humidity level in construction. In such cases no prior calibration of the Z-meter III device is necessary [24].

The research performed by the authors display the influence of different aspects of the manufacturing process of AAC masonry blocks on their drying properties in aspect of hygrometrics.

IV DESCRIPTION OF THE EXPERIMENT

For the particular experiment, a set of five different types of AAC masonry blocks were used (Table 1).

TABLE 1  
TECHNICAL DATA OF AAC MASONRY BLOCKS USED FOR EXPERIMENT [25-28]

AAC block figure	Thermal conductivity in dry state stated by manufacturer $\lambda$ W/mK	Bulk density stated by manufacturer $\text{kg/m}^3$
<b>A</b>	0,090	375
<b>B</b>	0,105	375
<b>C</b>	0,11	500
<b>D</b>	0,12	500
<b>E</b>	0,096	400

There were chosen specimen with density in range from 375 to 500  $\text{kg/m}^3$  in order to determine the impact of density on speed of drying as well as on the accuracy of the EIS measurement results.

For the experiment a set of AAC masonry block samples were prepared, where four blocks of each type were taken. In each sample two bores were made for embedment of measurement probes (Fig.3).

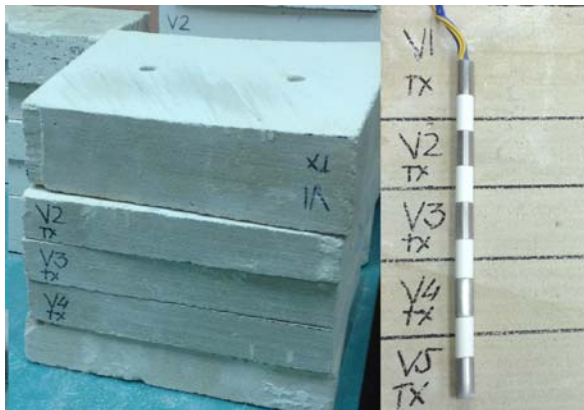


Fig.3 Autoclaved aerated masonry block sample with measurement probes

As the first step of the experiment the frequency analysis was performed on all samples in order to determine suitable EIS measurement frequency for all ACC masonry block types. The results of frequency analysis showed that there are different ranges of

frequencies which should be used for the EIS measurements on each type of the samples. But in order to acquire comparable data same frequency had to be chosen for all samples. So it was determined, that the frequency of 8000Hz is the most suitable for measurements on all samples.

One of the blocks from each type were split into several pieces according to the approach of Akita et al. [30] in order to determine the humidity rate of each segment in the masonry block by gravimetric method (Fig.4). The monitoring of the changes in humidity content of each sample was made by monitoring of mass changes in time for each specimen. Such approach allowed to determine the changes of moisture content in the samples.

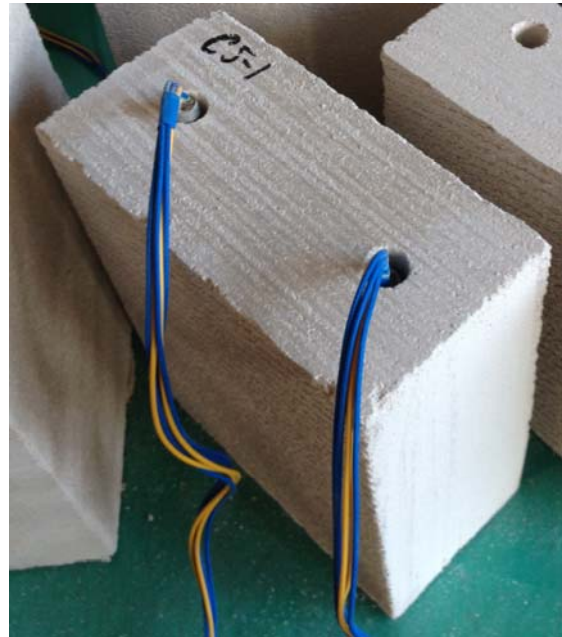


Fig.4 AAC masonry block samples for determination of humidity distribution by gravimetric method

The other three samples from each type were placed in laboratory premises (20°C, 85% Rh) for drying. Along the drying process regular EIS measurements were performed on all the experimental samples. Additional EIS measurements were performed on the cut samples in order to secure the obtained data of AAC masonry block relative humidity. Monitoring of samples' natural drying process was performed for four months. After the samples had reached the air dry state they were oven dried in order to determine the weight of samples in absolute dry state.

V RESULTS

From the obtained results it can be concluded that the density of the AAC does not have significant impact on samples' drying speed. The C and D samples (Table 1) had lost approximately the same

amount of moisture content (after 3 months of drying time in laboratory storage) in % as the other samples.

In the beginning of the experiment all samples had similar humidity distribution throughout the cross section although the humidity rate in the samples was significantly different (Fig.5). The initial humidity content of the AAC blocks depend on the specialties of the manufacturing process and storage conditions prior delivering the blocks to the construction site.

The data for Fig.5 was obtained by gravimetric measurement method for detection of moisture content in construction materials by the approach described by Akita et.al [30] and humidity content measurements by differences in mass. Further data concerning the moisture distribution throughout the cross section of the samples were obtained by EIS measurements. The gravimetric method was used for overall control of the experiment results and for preparation of correlation equation between the EIS measurement results and corresponding relative moisture content of the AAC.

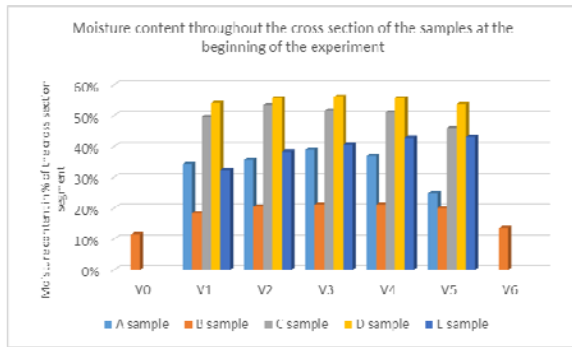


Fig.5 Moisture content throughout the cross section of the samples at the beginning of the experiment

In order to correlate values of EIS measurements with the absolute values of moisture content in cross section of the sample correlation graphs were prepared for each type of AAC samples (Fig.6a, 6b, 6c, 6d, 6e).

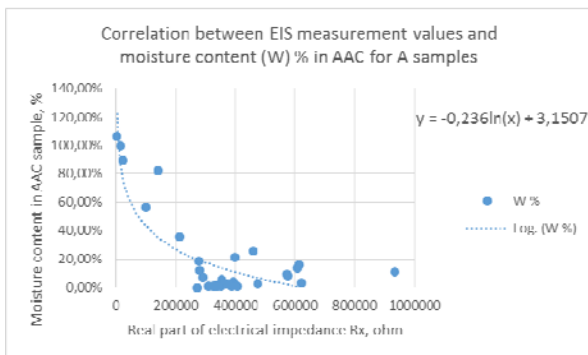


Fig.6a Correlation between EIS measurement values and moisture content of the samples of A series in %

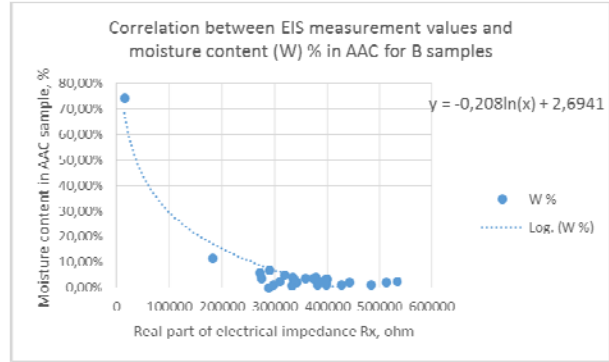


Fig.6b Correlation between EIS measurement values and moisture content of the samples of B series in %

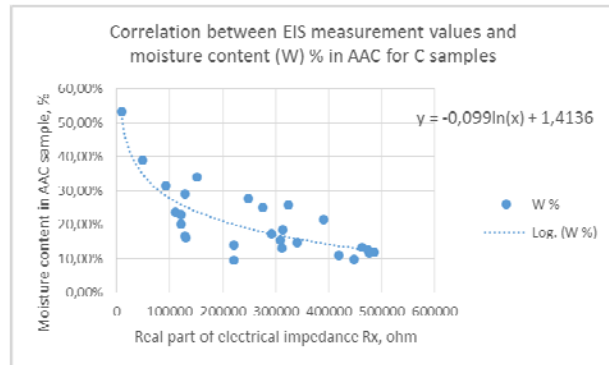


Fig.6c Correlation between EIS measurement values and moisture content of the samples of C series in %

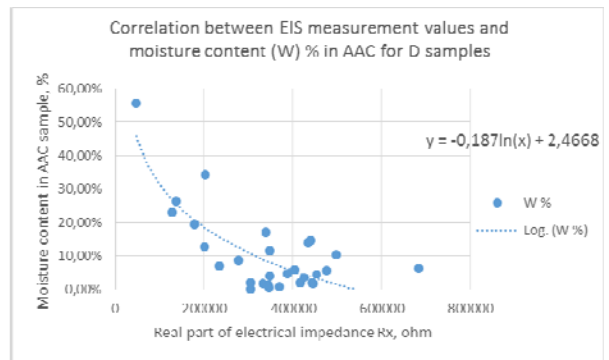


Fig.6d Correlation between EIS measurement values and moisture content of the samples of D series in %

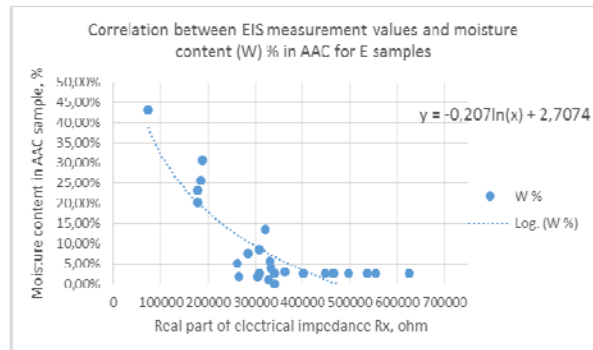


Fig.6e Correlation between EIS measurement values and moisture content of the samples of E series in %

The correlation equations have the same basic form:

$$y = a \ln(x) + C \quad (1)$$

where  $a$  varies from -0,099 to -0,236 and constant  $C$  varies from 1,4136 to 3,1507.  $A$  and  $C$  values from each particular equation can be used as a describing parameters of the respective type of AAC in aspect of drying speed and interaction with EIS measurement method.

The equation data (Fig.6a to 6e) was used to determine the changes of moisture content throughout the cross section of the AAC samples after 3 months drying time (Fig.7).

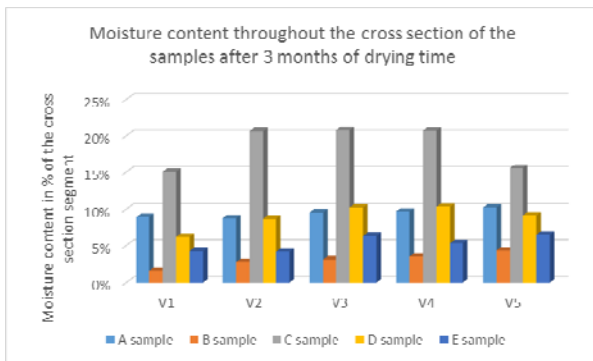


Fig.7 Moisture content throughout the cross section of the samples after 3 months of drying time

The measurement results show that the blocks with lower density have more regular humidity distribution throughout the cross section of the block than the samples with higher density.

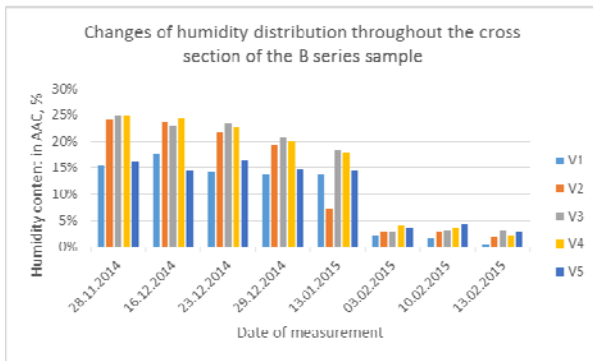


Fig.8 Changes of moisture content throughout the cross section of the samples during drying process

EIS measurement results can be transformed into moisture content rate of the AAC material and in such way the distribution of moisture content in the material sample can be determined by non-destructive method (Fig.8).

## VI CONCLUSIONS

From the obtained results, it can be concluded that the density of the AAC does not have significant impact on overall speed of samples' drying. It has impact on the speed of drying only in case the sample has high moisture content which is above 40%. In such case samples with higher density has lower drying speed for the central part of sample's cross section material.

However, the AAC density and structure of pores has significant impact on accuracy of EIS measurement interpretation. Therefore, prior using the EIS method by Z-meter device for humidity content measurements on-site, correlation equations between EIS measurement results and humidity content of the AAC sample should be determined in laboratory.

## VII REFERENCES

- [1] M. Barsottelli, G. F. Cellai, F. Fratini I and C. Manganeli Del Fa. The hygrometric behaviour of some artificial stone materials used as elements of masonry walls. *Materials and Structures/Matériaux et Constructions*, Vol. 34, May 2001, pp 211-216.
- [2] Bruce RR, Klute A The measurement of soil moisture diffusivity. *Soil Sci Soc Am Proc*, 1956, pp:458-462.
- [3] Kuenzel HM. *Simultaneous heat and moisture transport in building components*. IRB Verlag, Stuttgart, 1995.
- [4] Pel L, Brocken H, Kopinga K. Determination of moisture diffusivity in porous media using moisture concentration profiles. *Int J Heat Mass Transf* 39, 1996, pp:1273-1280.
- [5] Pel L, Landman KA, Kaasschieter EF. Analytic solution for the non-linear drying problem. *Int J Heat Mass Transf* 45, 2002, pp:3173-3180.
- [6] Pel L, Landman KA. A sharp drying front model. *Drying Technol* 22. 2004, pp:637-647
- [7] Matiasovsky P., Mihalka P. Pore Structure Parameters and Drying Rates of Building Materials. J. M. P. Q. Delgado (ed.), *Drying and Wetting of Building Materials and Components, Building Pathology and Rehabilitation 4*, DOI: 10.1007/978-3-319-04531-3\_4, © Springer International Publishing Switzerland 2014, pp. 71-90.
- [8] G.Quincot, M.Azenha, J. Barros, R.Faria. "State of the art – Methods to measure moisture in concrete" *Projetos De Investigação Científica E Desenvolvimento Tecnológico*, Portugal, 2011.
- [9] Villain, G. and M. Thiery. "Gammadensimetry: A method to determine drying and carbonation profiles in concrete." *NDT & E International* 39(4), 2006. p.328-337.
- [10] S. Multon, E. M. "Water distribution in beams damaged by alkali-silica reaction: global weighing and local gammadensimetry." *Materials and Structures* Vol. 37, 2004.
- [11] Physics, C. "Relative humidity sensors" 2010: 1-3.
- [12] Wiederhold, P. R. "Water vapor measurement, methods, and instrumentation." Marcel Dekker, Inc. New York, 1997. p. 384.
- [13] Zachary Grasley, D. A. L. "Relative humidity in concrete." *ACI Committee* 236, 2006. p.51-57.
- [14] McCarter, W.J.; Garvin, S. Dependence of Electrical Impedance of Cement-Based Materials on their Moisture Condition. In: *Journal of Applied Physics Series D: Applied Physics* 22 (1989), No. 11, S. 1773-1776.
- [15] Elsener, B. *Ion Migration and Electric Conductivity in Concrete*. Zürich: SchweizerischerIngenieur- und Architekten-Verein, 1990. - In: *Korrosion und Korrosionsschutz*. TI 5. Electrochemical Protection Process for Concrete Building Structures, Symposium 15. November 1990, S. 51-59.

- [16] Skramlik, J., Novotny, M. One-dimensional moisture transport monitored by a non-destructive method. *International Journal of Computers* Issue 4, Volume 2, 2008.
- [17] Farshad Rajabipour, Jason Weiss, John D. Shane, Thomas O. Mason, and Surendra P. Shah. A PROCEDURE TO INTERPRET ELECTRICAL CONDUCTIVITY MEASUREMENTS IN COVER CONCRETE DURING REWETTING. *Journal of Materials in Civil Engineering*, 2005. 17(5), pp:586–594.
- [18] Weiss, W. J., Shane, J. D., Mieses, A., Mason, T. O., and Shah, S. P. Aspects of monitoring moisture changes using electrical impedance spectroscopy. *Proceedings of the 2nd Symposium on Self-Desiccation and Its Importance in Concrete Technology*, Lund, Sweden. 1999.
- [19] Schießl, A., Weiss, W. J., Shane, J. D., Berke, N. S., Mason, T. O., and Shah, S. P. Assessing the moisture profile of drying concrete using impedance spectroscopy. *Concrete Science and Engineering*, 2, 2002. pp:106-116.
- [20] Parilkova, J. The EIS Method and a Z-meter III Device, a lecture within an event in Litice.
- [21] Rubene S. et al. Determination of Humidity Level in Aerated Concrete Constructions by Non Destructive Testing Methods, in Proc “Innovative Materials, Structures and Technologies” Riga, 2014 p.135-140.
- [22] Rubene S., Vilnītis M. Application of Electrical Impedance Spectrometry for Determination of Moisture Distribution in Aerated Concrete Constructions in Proc. “1st Conference and Working Session Eureka! 7614” Brno, Czech Republic, 2013. p. 124-130.
- Rubene, S., Vilnītis, M., Noviks, J. Monitoring of the Aerated Concrete Construction Drying Process by Electrical Impedance Spectrometry. In: *Proceedings of 4th International Conference "Advanced Construction 2014"*, Lithuania, Kaunas, 9-10 October, 2014. Kaunas: Kaunas University of Technology, 2014, pp.216-220. ISSN 2029-1213.
- [23] Rubene, S., Vilnītis, M., Noviks, J. Impact of Masonry Joints on Detection of Humidity Distribution in Aerated Concrete Masonry Constructions by Electric Impedance Spectrometry Measurements. *International Journal of Civil, Architectural, Structural and Construction Engineering*, 2015, Vol.9, No.1, pp.1089-1094. e-ISSN 1307-6892.
- [24] [http://aeroc.lv/index.php?page=938&lang=lat&cnt=AEROC\\_Universal](http://aeroc.lv/index.php?page=938&lang=lat&cnt=AEROC_Universal) site accessed on 17.03.2015.
- [25] <http://www.ytong-silka.pl/ru/content/756.php> site accessed on 17.03.2015.
- [26] [http://www.texoblock.lv/upload/buklets\\_lv.pdf](http://www.texoblock.lv/upload/buklets_lv.pdf) site accessed on 17.03.2015.
- [27] <http://roclite.lv/v2/tehniskie-parametri/fiziskas-un-tehniskas-ipasibas/> site accessed on 17.03.2015.
- [28] Vu TH. Influence of pore size distribution on drying behaviour of porous media by a vontinuous model. PhD thesis, Otto von Guericke University, Magdeburg. 2006.
- [29] Akita, H., Fujiwara, T. and Ozaka, Y.. " A practical procedure for the analysis of moisture transfer within concrete due to drying." *Magazine of Concrete Research* 48 (6), 1996, p.129-137.



# Ultra High Performance Concrete Reinforced with Short Steel and Carbon Fibers

Genadijs Šahmenko, Andrejs Krasnikovs, Artūrs Lukašenoks, Māris Eiduks  
Riga Technical University

**Abstract.** Fibers are usually used in High Performance Concrete with a purpose to increase bending strength and ductility. Important properties are the peak value of bearing stress (strength) and post-cracking behavior of bended element. In the framework of an experimental part, Ultra High Performance mix compositions were prepared using intensive mixer. Short steel fibers and carbon micro fibers in amount of 1% by volume, as well as its combination were used for cement matrix reinforcing. Results of compressive and bending tests proved an increase of strength value in the case of use both steel and carbon fibers. Carbon fibers were decreased the effect of explosive collapse of the UHPC cement matrix, at the same time still brittle bending behavior was take place. Steel fibers considerably improved bending ductility thanks to a pull-out mechanism of steel fibers. The best results were achieved in the case of combined application of both carbon and steel fibers.

**Keywords:** Steel fiber, carbon fiber, Ultra High Performance Concrete, bending behavior.

## I INTRODUCTION

Plain concrete is brittle material. Adding short fibers improves concrete ductility, bending strength and is minimizing crack formation risk [1]. The first fiber reinforced concrete (FRC) was patented in 1874 [2]. Researchers efforts during the last decades are focused on creating high strength fiber concrete having high bending strength and high ductility. The amount of steel fibers in modern FRC may reach up to 200 kg/m<sup>3</sup> and more. Steel fibers can be mentioned among the most effective, taking into account their mechanical properties and economical side of the problem. Simultaneously is observed high increase of non-metallic fibers use as a concrete disperse reinforcement during the last time. Advantages of the non-metallic fibers are high resistance against corrosion, chemical attack, light weight, high strength and easy mixing ability in fresh concrete statement. Tensile strength and tensile modulus (E-modulus) are the basic properties, which are determining fiber co-work with a cement matrix. The use of fibers having E-modulus lower then concrete E-modulus does not have any significant impact on bending strength (for example the polypropylene fibers). These types of fibers eliminate cracks formation on the early period of hydration and improve fire resistance of the hardened concrete [3][4]. Fibers, which have E-modulus higher than concrete one, are able to increase bending strength and to improve post-cracking behavior of the fiber concrete. Commonly

used fibers and their basic mechanical properties are summarized in the Table 1.

TABLE I  
PROPERTIES OF DIFFERENT FIBERS AND COMPARING WITH  
CONCRETE PROPERTIES

Material	Density, g/cm <sup>3</sup>	Elastic modulus, GPa	Tensile strength, MPa	Ultimate elongation, %
Steel	7.80	200	400-1200	5-20
Polypropilen	0.90	3.5-8.0	300-	10-25
Polyamid	0.90	1.9-2.0	720-750	24-25
Polyethilen	0.95	1.4-4.2	600-720	10-12
Acril	1.10	2.1	210-420	25-45
Neilone	1.10	4.2-2.5	770-840	16-20
Polyester	1.40	8.4-8.6	730-780	11-1
Carbon	1.63-2.00	200-650	1200-4500	1-2.1
Glass	2.60	70-80	1800-3850	1.5-3.5
Basalt	2.60-2.70	70-110	1600-3200	1.4-3.6
Typical concrete (C25/30)	2.40	34	3-5	< 1

Carbon fiber is high performance non-metallic reinforcing material, basic mechanical properties of a carbon fiber exceeds properties of a steel (Tab 1). Originally carbon fibers began to be used in the second part of 20<sup>th</sup> century producing high performance composite materials for aerospace and military applications.

At present, carbon fibers increasingly are used in concrete constructions. The most popular application is strengthening reinforced concrete constructions by composite carbon strips as well as replacing traditional steel reinforcement by carbon composite bars [5]. The use of carbon mesh and carbon knitted fabric are becoming more and more popular for creating highly aesthetic thin constructions [6]. Short carbon fibers are very rarely used in practice as concrete disperse reinforcement and only few publications may be find in this concern . Large part of information deals with carbon fibers use in traditional concrete mixes in order to improve their mechanical properties [7]. Author Akihama et al [8] used short carbon fibers in amount of 0.2 % by volume in Portland Cement concrete having water cement ratio equal to 0.5 and compressive strength up to 35 MPa. Increase of flexural strength up to 85 % was achieved. Study [9] was focused on bond improvement between carbon fibers and cement matrix with an aid of special covering.

High strength concrete as well as High (HPC) and Ultra high performance concrete (UHPC) are rapidly improving materials during last few decades [10]. UHPC is characterized by very high compressive strength as well as high bending strength. Short steel fibers usually are used in such material as disperse reinforcement. Non-metallic fibers may have some benefits comparing to steel one, but their use in UHPC haven't investigated properly. To use a combination of different types of fibers (so called *fiber cocktail*) is an interesting idea in order to achieve the best result. The aim of this study is to investigate the effect of combined use of carbon and steel fibers in UHPC concrete mixtures.

## II MATERIALS AND MIX DESIGN

In the experimental part typical UHPC basic mix composition was prepared. Main mix ingredients are the following: white Portland Cement CEM I 52.5 R (Aalborg), locally available quartz sand (combination of 2 fractions and quartz powder), pozzolanic admixture silica fume (Elkem, grade 920D), polycarboxilate based super plasticizer and water. Four mix compositions were produced: reference mix (REF), mix with carbon fibers (C), mix with steel fibers (S) and composite mix of carbon fibers together with steel fibers (C+S). Used TENAX® chopped carbon fibers are characterized by density 1.82 g/cm<sup>3</sup>, tensile strength 4275 MPa, tensile modulus 225 GPa and ultimate elongation 1.9%. Fiber length is 12 mm

and diameter 7 μm, therefore, aspect ratio of selected fiber is very high: 12000/7 = 1714.

Used steel fibers are fibers with hooked ends, having length 30 mm and diameter 0.5 mm, therefore aspect ratio of selected fibers are: 30/0.5 = 60. Long steel fibers was used to provide quasi-plastic behavior and crack bridging effect during bending test. At the same time, "wall effect" is possible, where the moulds walls direct the fibers, which are too long compared to the mould size (40 mm). Volumetric concentration of carbon and steel fibers in experimental mixes was provided 1 % from the total volume of concrete. Proportions between mix components were calculated in order to provide optimum grading curve which determines dense micro-structural packing. Mix compositions of experimental mixes are presented in the Tab II.

TABLE II  
UHPC MIX COMPOSITIONS, kg/m<sup>3</sup>

	Dens., kg/cm <sup>3</sup>	REF	C	S	S+C
Cements I 52.5 R	3.1	800	800	800	800
Sand Quartz 0.5/1 mm	2.65	800	800	800	800
Sand fine 0/0.3	2.65	300	300	300	300
Quartz powder	2.65	60	60	60	60
Silica Fume 920 D	2.2	140	140	140	140
Carbon micro fiber	1.82		18		18
Steel fiber 30 mm	7.8			78	78
Water	1	200	200	200	200
Superplasticizer	1.1	13	13	13	13
W/C		0.25	0.25	0.25	0.25
W/(C+SF)		0.21	0.21	0.21	0.21
Workability		flowable, plastic, good	flowable, plastic, good	plastic, too long fibers	plastic, too long fibers

## III SAMPLES PREPARATION AND TESTING

Mix ingredients were dozen with accuracy  $\pm 0.1\%$  and mixed using the highly intensive laboratory mixer Eirich. Carbon fibers were added during mixing and additionally mixed one minute in order to distribute fibers uniformly. Steel fibers were added at the end of mixing without intensive mixing effect in order to prevent fiber deformation during intensive mixing process.

Prismatic samples 40x40x160 mm were produced in steel moulds, then were demoulded after 1 day and cured in water environment (+20°C). Flexure and compressive test were performed after 1, 28 and 108 days of hydration. Force – deflection curves were obtained during three-point bending test using universal testing machine Zwick 150. The distance between supporting points 130 mm and rate of loading 5 mm/min was provided. Sample halves remaining after flexure test, were used to check compressive strength.

Compressive testing machine Controls Automax 5 was used, the rate of loading was 1.0 MPa/s.

SEM electronic microscope imaging was performed to investigate internal structure of produced material in details.

#### A. Compressive strength

Testing results of compressive strength (Fig. 1) shows continuous increase of strength values during hardening time, this effect may be described by long-term pozzolanic reactions between silica fume and calcium oxide (product of cement hydration) [11]. In the age of 7 days compressive strength values are approximately 80% from 28 day strength, but 108 days results demonstrates strength gain up to 20%, comparing to 28 day results. Reference mix has the least strength values, but adding carbon and steel fibers has beneficial effect on compressive strength. Compressive strength gain is observed up to 9% in the age of 28 days, comparing to reference mix (see Fig. 1). The biggest gain of compressive strength is observed in the case of steel fiber and steel fiber combination with carbon fiber in the age of 108 days.

Reference mix composition REF (without fibers) is characterized by explosive collapse when maximum force is achieved. Composition with carbon fibers also is characterized by brittle behavior, at the same time collapse process is not so brittle and associated with crack formation. Destroying process of mixes with steel fibers is much more ductile and development of multiply crack system took place before maximum force is achieved.

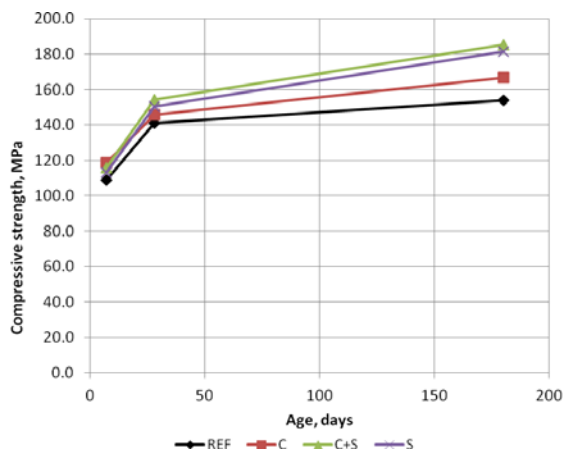


Fig. 1. Concrete compressive strength development.

#### B. Bending strength and ductility

Main task of adding fibers in concrete mix is increasing a bending strength and ductility. Analyzing peak values of bending strength (Fig. 2) in must be emphasized more positive influence of fibers on bending strength, comparing the effect on compressive strength. In the age of 28 days carbon fibers increases bending strength is up to 28% and for steel fibers up to 139%. The biggest improvement 186

% is achieved in the case of use carbon and steel fiber in combination (C+S).

Analyzing scattering of results, it must be stressed, that average squared deviation of compressive strength data in one series does not exceed 5% from the average result. The same deviation is found for bending strength of reference mix (REF) and composition with carbon fibers (C). Mix compositions with steel fibers (S and S+C) have the largest scattering of bending strength results (up to 15% from average result). High dispersion of bending strength results may be explained by non-homogeneous steel fiber distribution in the cross section of bended beam [12]. It must be stressed, that the length of used steel fibers (30 mm) is too big comparing to cross section dimension of sample (40 mm). In the future studies, shorter steel fibers ( $L < 15$  mm) should be used in order to prevent fiber unpredictable orientation and possible concentrations in local places.

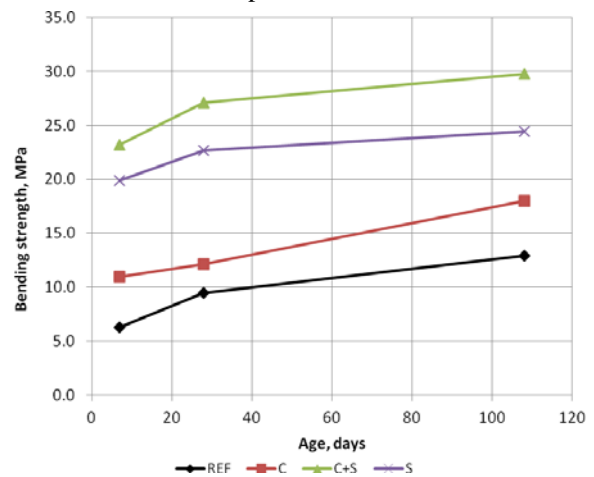


Fig. 2. Bending strength development.

Carrying out three-point bending test of mini beams, force – deflection curves were obtained. Curves give important information about bending behavior of material in the stage after crack formation as well as about ductility and bending energy. In order to compare bending curves, average curves for each mix composition were calculated, using experimental numerical data and Excel program. Curves related to 108 age samples are presented in the Fig. 3.

Obtained results shows huge difference between sample without steel fibers (REF and C) and sample containing steel fibers (S and C+S), which are characterized by higher maximum force peak and wide range of post-cracking curve. This effect may be explained by crack bridging with steel fibers and its pull-out mechanism [13][14].

Sample fracture energy may be determined as an area below bending curve. Taking into account numerical data of bending experiments, bending energies  $U$  ( $N \cdot mm$ , or  $mJ$ ) were calculated for 4 intervals corresponding maximum force and

deflections of 3, 4 and 5 mm correspondingly. The results are presented in the Fig. 4.

The first bars (corresponding maximum force) show that bending energy of mix containing carbon fibers is 70% higher than one of reference mix. At the same time, sample containing steel fiber has more than 10 times higher result. In the post-cracking stage bending energy determines pull-out work of mere long steel fibers.

The most interesting effect is considerable increase of energy (+15-20%) in the case of complex use both steel and carbon fibers. This difference (up to 5000 N\*mm) is much more than the total bending energy of C mix, containing only carbon fibers. This phenomenon makes possible to draw hypothesis about steel and carbon fiber synergy effect. Obtained results goes in accordance with results of pull-out behavior of single steel fiber from cement matrix with and without carbon fibers [15] [13] (Krasnikovs, Khabaz).

SEM pictures of UHPC cement matrix containing carbon fibers (after bending test) are presented in Fig. 5 and 6. Cement matrix is characterized by high density and big pores and cavities (Fig. 5). Taking into account very high aspect ratio of carbon fibers (1714), pull-out effect of all fiber is not possible. At the same time, free ends of carbon fiber and empty channels (Fig. 6) indicates that fiber is breaking inside channel and possible pull-out effect. This is evidenced by increased ductility and fracture toughness of carbon fiber reinforced sample, comparing to reference mix. In the Fig 6 can be seen carbon fiber channel crossing micro crack in cement matrix. This picture helps to explain bridging effect of carbon fiber, as well as synergy effect of steel and carbon fiber (carbon fiber prevents formation and expansion of micro-cracks in cement matrix).

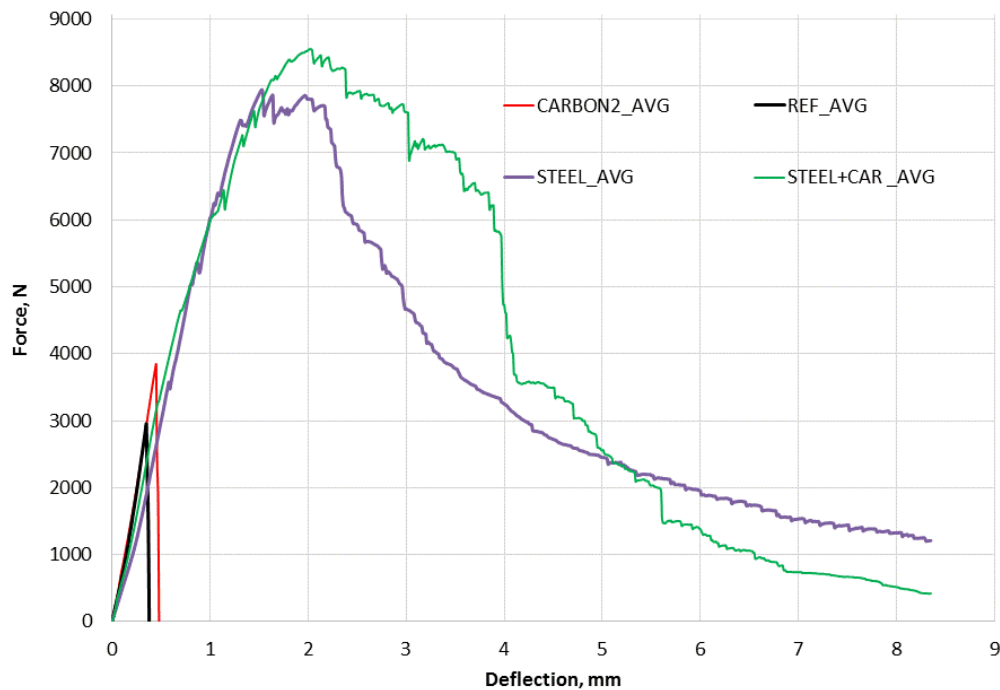


Fig. 3. Three-point bending force – deflection curves.

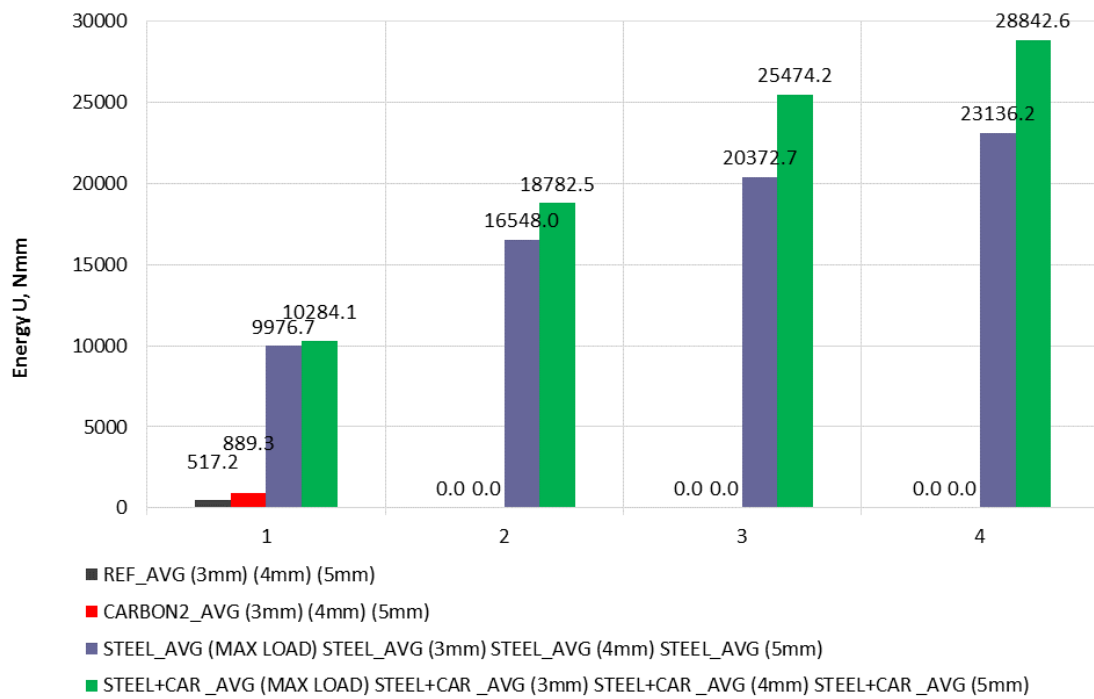


Fig. 4. Fracture energy – / Peak load; 2 crack opening 3mm; 3 crack opening 4mm; 4 crack opening 5mm.

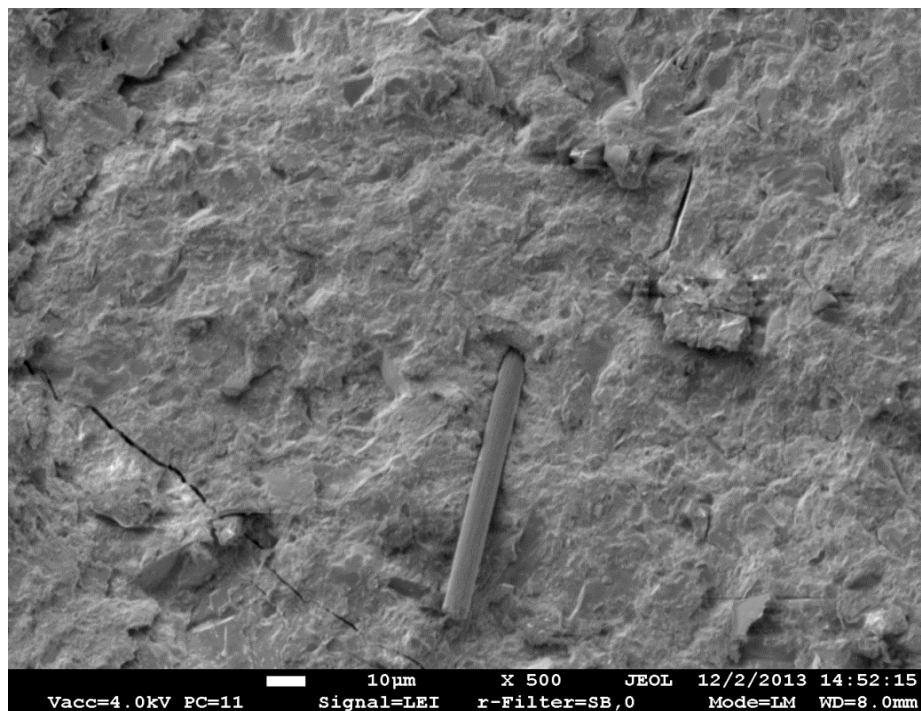


Fig. 5. SEM image of concrete microstructure, micro cracks and carbon fibers.

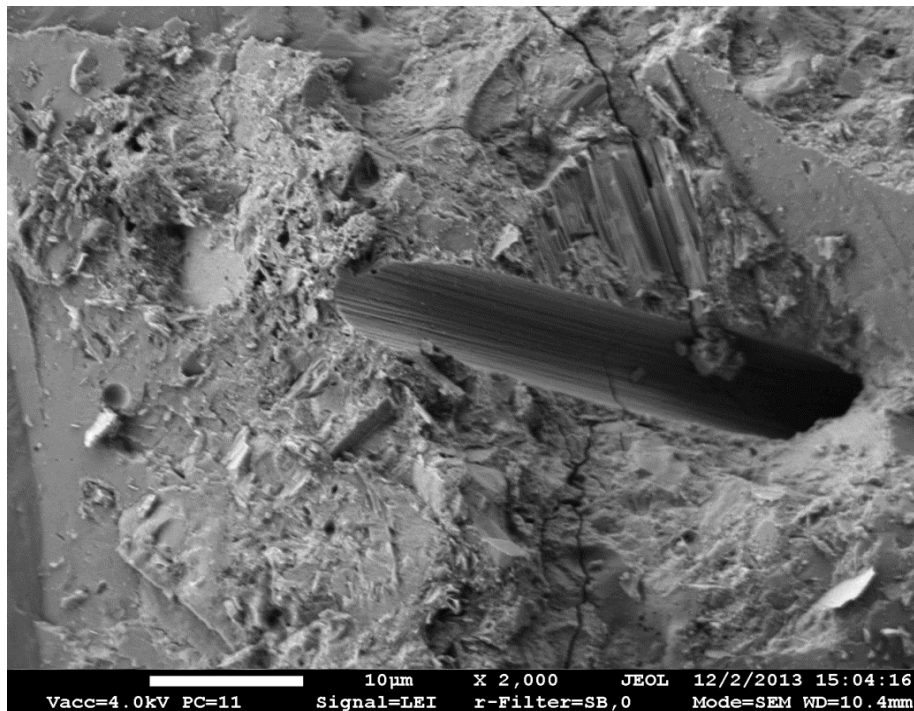


Fig. 6. SEM image of carbon fiber in concrete structure.

#### IV CONCLUSIONS

Use of intensive concrete mixer makes possible more uniformly distribute carbon fibers in the volume of the UHPC cement matrix. Introduction of carbon fibers in amount of 1% (by volume) improves bending strength of plain UHPC matrix up to 39% and compressive strength up to 9% and slightly compensates brittle behavior of collapse of ultra-high strength material.

Steel fibers are providing post-cracking bending behavior thanks to their pull-out hook mechanism. The best bending results was achieved in the case of combined use of both carbon and steel fibers. Considerable increase of the fracture energy in this case is explained by synergy work of two types of fibers. Carbon micro-sized fibers are reducing micro crack formation in the cement matrix and are improving steel fibers pull-out behavior. The task of future optimization UHPC mixes provides for finding optimum dosage of steel and carbon fibers, as well as its geometrical parameters in order to obtain the most economic mix composition, depending on used cement matrix.

#### V ACKNOWLEDGEMENTS

The support of the ESF project Nr. 1DP/1.1.1.2.0/13/APIA/VIAA/019 „New „smart” nanocomposite materials for roads, bridges, buildings and transport vehicle” is acknowledged.

#### VI REFERENCES

- [1] N. Banthia, V. Bindiganavile, J. Jones, and J. Novak, "Fiber-reinforced concrete in precast concrete applications: Research leads to innovative products.," *PCI J.*, vol. Summer 201, pp. 33-46, 2012.
- [2] B. R. Maidl, *Steel Fibre Reinforced Concrete*. Berlin: Ernst and Sohn, 1995, p. 292.
- [3] P. Lura and G. Pietro Terrasi, "Reduction of fire spalling in high-performance concrete by means of superabsorbent polymers and polypropylene fibers: Small scale fire tests of carbon fiber reinforced plastic-prestressed self-compacting concrete," *Cem. Concr. Compos.*, vol. 49, pp. 36-42, 2014.
- [4] P. Kalifa, G. Chene, and C. Galle, "High-temperature behaviour of HPC with polypropylene fibres: From spalling to microstructure," *Cem. Concr. Res.*, vol. 31, pp. 1487-1499, 2001.
- [5] D. Duthinh and M. Starnes, "Strength and ductility of concrete beams reinforced with carbon FRP and steel," 2001.
- [6] M. Kononova, O.; Krasnikovs, A.; Dzelzitis, K.; Kharkova, G.; Vagel, A. & Eiduks, "MECHANICAL PROPERTIES OF COMPOSITES REINFORCED BY COTTON KNITTED FABRIC," in *Proceedings of 7th International DAAAM Baltic Conference "INDUSTRIAL ENGINEERING" 22-24 April 2010, Tallinn, Estonia*, 2010, no. April, pp. 3-8.
- [7] P.-W. Chen and D. D. L. Chung, "Concrete reinforced with up to vol of short carbon fibers.pdf," *Composites*, vol. 1, pp. 33-51, 1993.
- [8] S. Akihama, M. Aya, and H. Ikeda, "Carbon fiber reinforced concrete," 1992.
- [9] Y. Xu and D. D. . Chung, "Carbon fiber reinforced cement improved by using silane-treated carbon fibers," *Cem. Concr. Res.*, vol. 29, no. 5, pp. 773-776, May 1999.
- [10] V. R. Falikman, Y. V. Sorokin, and O. M. Goryachev, "High-strength light-weight concrete: Technology and properties," *Bet. i Zhelezobet.*, no. 2, pp. 8-12, 2005.
- [11] I. Juhnevica and G. Shakhmenko, "The Influence of Different Pozzolanic Admixtures on Structure and Properties of Concrete," in *Proceedings of conference IbauSil-2012*, 2012, p. 8.

- [12] V. Lūsis and A. Krasnikovs, "Fiberconcrete with non-homogeneous fibers distribution," in *Vide. Tehnologija. Resursi - Environment, Technology, Resources*, 2013, vol. 2, pp. 67–71.
- [13] A. Krasnikovs, A. Khabaz, and I. Telnova, "Numerical 3D Investigation of Non-Metallic ( Glass , Carbon ) Fiber Pull-out Micromechanics ( in Concrete Matrix )," *Sci. J. Riga Tech. Univ. Transp. Eng. Mech.*, vol. 33, pp. 103–108, 2010.
- [14] O. Kononova, V. Lūsis, A. Galushchak, A. Krasnikovs, and A. MacAnovskis, "910. Numerical modeling of fiber pull-out micromechanics in concrete matrix composites," *J. Vibroengineering*, vol. 14, no. 4, pp. 1852–1861, 2012.
- [15] A. Krasnikovs, O. Kononova, A. Machanovsky, and A. Khabaz, "Pull-out micro-mechanism for fibers in concrete," in *ECCM 2012 - Composites at Venice, Proceedings of the 15th European Conference on Composite Materials*, 2012.

# **Alkali Activated Binders Based on Metakaolin**

**Laura Sele, Diana Bajare, Girts Bumanis, Laura Dembovska**

*Department of Building Materials and Products, Institute of Materials and Structures,  
Riga Technical University*

**Abstract.** According to research conducted in last 25 years, alkali activated binders have been considered as one of the most progressive alternative binders, which can effectively replace Portland cement. Production of alkali activated binders differs from the Portland cement production and is associated with lower CO<sub>2</sub> emissions. The use of recycled industrial by-products and wastes is also possible, what corresponds to the future guidelines and principles of sustainable binder production in the world.

The aim of this study was to create innovative alkali activated binders by using secondary raw materials, which will be different from the ones described in the scientific literature – alkali activated binders with porous structure. Raw materials used for the binders were metakaolin containing waste, waste from aluminium scrap recycling factory and recycled lead-silicate glass; solid contents were activated with modified sodium silicate solution with an addition of sodium hydroxide.

The physical properties of alkali activated binders, such as density, water absorption, open and total porosity, were determined and flexural and compressive strength of hardened alkali-activated binders were tested at the age of 28 days. Durability was examined by sulphate resistance test, which was performed according to SIA 262/1, appendix D: applicability and relevance for use in practice. 40x40x160 mm prismatic specimens were used for expansion measurement and determination of compressive strength.

The open porosity of obtained materials was up to 45%, density from 380 to 1720 kg/m<sup>3</sup>, compressive strength up to 29,8 MPa, water absorption 6 – 114 wt.%. After analysing the results from the sulphate test it was concluded that glass additive reduced the alkali activated binder resistance to sulphate attack.

**Keywords:** Alkali Activated Binder, Aluminium Recycling Waste, Waste Metakaolin.

## I INTRODUCTION

The production of different types of alkali activated binders results in a near zero-carbon dioxide emission, which is significantly less compared to the production of ordinary Portland cements (OPC) or lime binders [1]. For example, in case study of geopolymer concrete mixes based on typical Australian feed stocks, the results indicated a potential for a 44-64% reduction in greenhouse gas emissions while the financial costs varied from 7% lower to 39% higher compared with OPC [2]. It is clear that alkali activated binders can exhibit performance properties such as high compressive strength [3]; high level of resistance to a range of different acids and salt solutions [4]; high resistance to freeze-thaw [4]; not being subject to deleterious alkali-aggregate reactions [4]; low shrinkage [5]; effective solution for the stabilization of industrial by-products and the immobilization of heavy metals [6] as well as other important technologic and functional properties which depend from the chemical composition of raw materials used and the composition of mixes. Therefore alkali-activated binders (AAB) are receiving increased

attention as an alternative to OPC and lime because of their high functionality and low environmental impact.

Alkali activated binders traditionally are made by mixing powdered aluminosilicates based raw materials such as fly ash, metakaolin, slag or other materials rich with amorphous SiO<sub>2</sub> and Al<sub>2</sub>O<sub>3</sub> with an alkali activation solution [7] [8].

A key attribute of alkali activation technology is the robustness and versatility of their process of production; it enables products to be tailor-made from a range of aluminosilicate raw materials so that they have specific properties for a given application at a competitive cost [9]. Although several researchers demonstrated an excellent durability of alkali activated materials in their experiments, the major unsolved problem in the development and application of alkali activation technology is still related to the durability, because it seems to depend strongly on the application of adequate curing regimes and composition of mixes. Also carbonation can be quite problematic in these systems, as there is no reservoir of available calcium to provide a pH buffer; therefore durability performance is critically dependent on the development of a compact and refined pore structure

ISSN 1691-5402



[10]. The sulphate attack is a topical issue similarity as it is in systems made of OPC because of chemical reaction in wet media between sulphate ions and aluminate component of hardened cement paste [11]. A mineral formation increases internal stresses due to expansion of tricalciumaluminates (C3A) up to 227% from its initial volume [12]. This leads to irregular micro-crack pattern and degrades material durability. Similarities can be found with high calcium amount contained alkali activated systems, where sulphate salts can react with free lime and form ettringite and/or gypsum. Bakharev has reported that magnesium sulphate, compared to sodium sulphate, has more deleterious effect on sulphate resistance of concrete made of OPC or alkali activated slag. No visual signs of degradation were detected for alkali activated slag concrete while OPC specimens expanded significantly after long-term immersion in sodium sulphate solution [13]. El-Sayed has reported that compressive strength decreased up to 52% of alkali activated slag concrete when samples were exposed to magnesium sulphate attack for 6 months [14]. Also diffusion of alkali ions from structure of alkali activated materials to solution can cause stresses; deep vertical stresses can be observed [15]. However, using slag cements could lead to failure of material structure due to weakening and disintegration of structure before expansion could be observed [16].

Incorporation of pozzolans like fly ash, rice husk ash in OPC reduces the total calcium amount in cement system; therefore material, which is more durable to the sulphate attack, could be obtained [17]. The increased resistance to the sulphate attack of low-calcium alkali activated material could be sulphate caused by low calcium content available for reactions. AAB based on fly ash could reach superior sulphate resistance compared with OPC materials or high calcium amount contained AAB systems [18]. Bakharev has reported that specimens made of low-calcium AAB have increased durability to sulphate attack but it depends on type of activator used and cation type in sulphate media. At the end it was concluded that activator containing NaOH can lead to improved resistance of AAB to sulphate attack [15].

Resistance to the sulphate attack of alkali activated materials depends from polymerization degree of the material structure; highly cross-linked aluminosilicate polymer structure will be more stable even in comparison with OPC system [19]. Intensity of polymerization reaction and development of specimens' strength are affected by chemical composition of the system, ratio of solid raw material and activator, concentration of activator as well as curing conditions [14] [20] [21] [22]. There are many variables that could affect sulphate resistance of AAB but information on tried and tested solutions for the best performance is not available in literature.

The presented research focuses on a low-calcium alkali activated binders with high porosity and their

resistance to the sulphate attack. Porous binders were obtained from metakaolin containing waste (WMK) by incorporation of industrial wastes from aluminium scrap recycling (ASRW) as foam forming agent.

## II MATERIALS AND METHODS

### Materials

Low-calcium alkali activated binder (AAB) was obtained from industrial by-products and alkali activation solution. Waste metakaolin (WMK) was obtained from the expanded glass granule production plant "Stikloporas" UAB (Lithuania), where kaolinite clay is used as a substance for anti-agglutination in the final stage of expanded glass granule production and the obtained metakaolin containing material is defined as by-product. During processing WMK was calcined at 850 °C for about 40-50 minutes and fraction <0.25 mm was used as base material for alkali activation. Glass waste (GW) received from the glass recycling factory "Lampu Demerkurizācijas Centrs" Ltd. (Latvia) was used to modify the composition of AAB. Aluminium scrap recycling waste (ASRW) received from aluminium scrap recycling industry facility "Dilers" Ltd. (Latvia) was used as a foaming agent for creating of porous AAB structure [23]. The amount of ASRW in the mixture composition of AAB can define the final physical and mechanical properties of the obtained material. Chemical composition of the raw materials is given in Table 1. In order to increase homogeneity and fineness of ASRW and WG, both raw materials were ground in planetary ball mill Retsch PM 400 with speed 300 rpm for 30 minutes.

TABLE 1

CHEMICAL COMPOSITION OF RAW MATERIALS, W<sub>T</sub> %

CHEMICAL COMPONENT	ASRW	WMK	WG
Al <sub>2</sub> O <sub>3</sub>	63.2	51.7	1.0
SiO <sub>2</sub>	7.9	34.4	68.1
CaO	2.6	0.1	1.4
SO <sub>3</sub>	0.4	-	-
TiO <sub>2</sub>	0.5	0.6	-
MgO	4.4	0.1	-
Fe <sub>2</sub> O <sub>3</sub>	4.5	0.5	0.2
PbO	-	-	20.0
Na <sub>2</sub> O	3.8	0.6	8.0
K <sub>2</sub> O	3.8	-	1.2
Other	2.6	-	0.1
LOI, 1000°C	6.2	12.1	-

The activation of solid raw materials was done with modified sodium silicate solution. Commercially available sodium silicate solution from "Vincent's Polyline" Ltd. (Latvia) characterized by the silica modulus Ms 3.22 was modified with sodium hydroxide flakes from "Tianye Chemicals" (China) with 99% purity and alkali activation solution with silica modulus Ms 1.67 was obtained

Methods

Physical properties of AAB, such as density, water absorption, open and total porosity, were determined in accordance with EN 1097-6 and EN 1097-7. Flexural and compressive strength of hardened alkali-activated mortar bars were tested according to LVS EN 1015-11 at the age of 28 days. Sulphate resistance test was performed according to SIA 262/1, appendix D: applicability and relevance for use in practice. 40x40x160 mm prismatic specimens aged 28 days were used for expansion measurement and determination of compressive strength.

Sample preparation

The compositions of solid raw materials are given in Table 2. Two series of AAB were prepared: samples without WG in mixture composition (mixture composition with index G0) and samples with WG in mixture composition (with index G1, respectively). The incorporation of WG in the mixture composition of AAB increases the SiO<sub>2</sub> content; therefore the obtained AAB can possess different properties. The ASRW in both series were added from 0 to 1.0 mass ratio calculated from the amount of WMK resulting in materials with different porosity.

All dry components were weighted and mixed together to obtain homogenous powder, and alkali activation solution (AAS) was added to the mixture with a constant AAS/solid content ratio of 0.75. After mixing, the pastes were immediately poured into prismatic moulds measuring 4x4x16 cm. Moulds were covered to limit expansion of pastes and then placed in heating chamber at 80 °C for 24 h for the final setting in order to obtain porous AAB.

TABLE 2  
MIXTURE COMPOSITION OF AAB

MIXTURE COMPOSITION N	COMPOUND MASS RATIO			AAS/SOLID RATIO
	ASRW	WMK	WG	
0G1	0	1	1	0.75
0.1G1	0.1	1	1	
0.5G1	0.5	1	1	
1.0G1	1.0	1	1	
0G0	0	1	0	
0.1G0	0.1	1	0	
0.5G0	0.5	1	0	
1.0G0	1.0	1	0	

III RESULTS AND DISCUSSIONS

Physical properties of AAB

Due to the chemical reactions between ASRW and high alkalinity of the activation solution, gas evaporation was observed and porous structure of AAB was obtained (Fig.1). Highly porous AAB was obtained with the addition of ASRW even with 0.1 mass ratio to WMK in mixture composition. The pore volume, pore structure and density depend from the amount of ASRW and WG used in the AAB

composition. The physical properties of AAB are given in the Table 3.

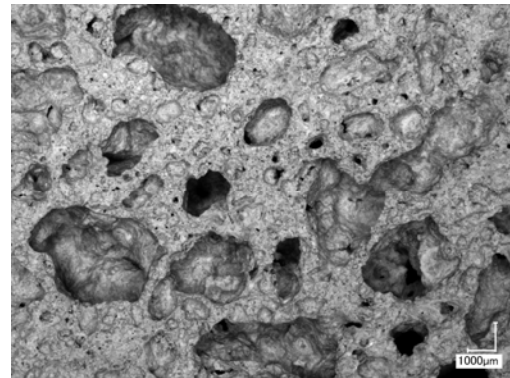


Fig. 1. Porous structure of AAB with ASRW (weight part 0.5) and without WG additives.

Samples without ASRW in the mixture composition provide the highest density and the density greatly depends from WG (1400 kg/m<sup>3</sup> for 0.0G0 and 1720 kg/m<sup>3</sup> for 1.0G1). Glass additive in mixture composition provides glassy and compact structure of AAB while structure of AAB without WG is more porous thus influencing porosity of the material (Table 3). All samples with glass additive in the mixture composition have higher density in comparison with samples without glass. Most likely glass additive dissolves in the alkali media and fills microporous of the material structure. This phenomenon also explains the difference of water absorption among samples with and without glass additive. Thus samples with glass in the composition have significantly lower water absorption compared with the rest. Water absorption for samples with glass in the mixture composition was from 6 to 93% while for the samples without glass additive in mixture composition – from 26 to 112%. Water absorption increases with the increase of open porosity of the samples which was determined by the amount of ASRW in the mixture composition. Porous AAB are characterized with high open porosity and it can be up to 44% (1.0G0). Glass additive in the mixture composition reduced open porosity which could be explained by the glassy structure of AAB.

TABLE 3  
PHYSICAL PROPERTIES OF AAB

MIXT. DESIGN	DENSITY KG/M <sup>3</sup>	WATER ABSORPTION %	OPEN POROSITY, %	TOTAL POROSITY, %
0.0G1	1720	6±0.4	10±0.6	20±0.5
0.1G1	770	17±0.7	12±0.4	64±0.3
0.5G1	490	78±0.9	36±0.8	78±0.2
1.0G1	390	93±2.0	37±0.3	83±0.4
0.0G0	1400	26±0.3	30±0.8	31±0.7
0.1G0	520	68±2.1	32±0.7	74±0.3
0.5G0	430	86±1.3	35±0.7	80±0.3
1.0G0	380	112±3.8	44±0.9	83±0.5

ASRW mass content increase in the mixture composition leads to significant decrease of density for all samples. Even 0.1 weight part of ASRW in the composition decreased density up to 60% (from 1720 to 770 kg/m<sup>3</sup> for samples with glass additive and from 1400 to 520 kg/m<sup>3</sup> without glass). By increasing the amount of ASRW in the composition to 1.0 weight part from the amount of WMK, the changes in sample density are less critical and it decreased to 390-390 kg/m<sup>3</sup>. By increasing amount of ASRW in the composition, influence of glass additive on the physical properties of obtained samples decreased but density of samples decreased below density of water.

Obtained samples with ASRW over 0.5 weigh part in mixture composition have total porosity around 80% and it is explained by the specific pore structure where more than 50% of pores are closed. This phenomenon ensures floating of samples in the water for unlimited time. Comparing porosity of denser samples without ASRW and samples with minimal amount of ASRW (0.1 with parts) in the composition, total porosity increased more than 2.5 times.

It can be concluded that WG and ASRW additives have great influence on the physical properties of samples made by alkali activation technology.

*Mechanical properties of AAB*

Compressive strength of hardened samples was in range from 0.5 MPa to 29.8 MPa and it strongly depends from composition (Table 4). Comparing series with and without WG in mixture composition, AAB samples with glass additive were with higher compressive strength compared (0.5 to 30 MPa) to AAB samples without WG (from 0.5 to 8 MPa).

By increasing the amount of ASRW in the mixture composition, compressive strength decreased to 0.5 MPa for both series of samples (Table 4). By incorporating ASRW even to 0.1 weight part to WMK, the compressive strength reduction was significant which can be explained by the increase of porosity for obtained material.

TABLE 4  
MECHANICAL PROPERTIES OF AAB

MIXT. DESIGN	FLEXURAL STRENGTH, MPA	COMPRESSIVE STRENGTH, MPA	REDUCTION OF COMPRESSIVE STRENGTH AFTER SULPHATE ATTACK, %
0.0G1	2.1	30.1	72
0.1G1	0.9	3.2	25
0.5G1	0.7	1.2	20
1.0G1	0.4	0.5	5
0.0G0	1.3	8.0	15
0.1G0	0.6	1.1	4
0.5G0	0.5	0.8	3
1.0G0	0.4	0.5	2

The flexural strength results were similar to the compressive strength and it strongly depends on WG content and ASRW ratio in the mixture composition.

As it is shown in Table 4, the flexural strength of samples with WG additive was from 0.4 to 2.1 MPa but without WG additive – 0.3 to 1.5 MPa. Porous structure obviously affects flexural strength and the results of flexural strength test show that samples without ASRW provide 3 times higher flexural strength.

The mechanical properties of AAB are strongly affected by physical properties of AAB. The mechanical properties of samples were defined with the amount of ASRW used in composition but influence of glass additive is essential in cases, when ASRW is not used or the amount of ASRW is low. The difference between series of samples with ASRW mass ratio to WMK from 0.5 to 1.0 was less significant and more comparable.

*Sulphate test*

Resistance to sulphate attack was tested for 28 days old samples (6 samples from each composition). Change of compressive strength after sulphate test is given in Table 4. The sulphate attack deteriorates the structure of AAB and the decrease of compressive strength was detected. Reduction of compressive strength was significant for AAB samples with WG in the mixture composition – compressive strength reduced even up to 72% (0.0G1) and the structure integrity of AAM was damaged. The strength loss of AAB made without WG and ASRW (0.0G0) was 15%.

Although ASRW provides porous structure and decreases compressive strength of AAB, the ASRW has significant effect on AAB resistance to sulphate attack. For sample series with WG in mixture composition the increase of ASRW reduced the compressive strength loss down to 5 % (1.0G1) while for samples with 0.1 and 0.5 mass ratio of ASRW to WMK was 25 and 20% respectively. Samples without WG in mixture composition provided low strength loss after sulphate test even with low ASRW content in mixture composition (4% for 0.1G0); therefore ASRW not only increases porosity and reduces initial compressive strength but also increases the AAB resistance to sulphate attack.

IV CONCLUSIONS

Alkali activated binders (AAB) were obtained by using industrial by-products such as aluminium scrap recycling waste (ASRW), lead-silicate glass waste (WG) from recycling of florescent lamps and waste metakaolin (WMK) after using as a substance for anti-agglutination in the final stage of expanded glass granule production as a secondary raw material.

The obtained material was characterized by density from 380 to 1720 kg/m<sup>3</sup>. The density can be controlled by ASRW mass ratio and WG additive. Because of wide range of density, all physical and mechanical properties were varied depending on the mixture

composition. Compressive strength up to 30.1 MPa and flexural strength up to 2.1 MPa can be achieved by selecting appropriate mixture composition.

Results of sulphate test evidently shows the effect ASRW and WG have on resistance to sulphate attack. Samples with higher proportion of ASRW have lower compressive strength changes. Samples with proportion of ASRW from 0.1 to 1.0 show 2-4% reduction of compressive strength after sulphate attack, while samples with the same proportion of ASRW and WG additives have 5-25% reduction.

In further research it would be essential to improve mixture composition for samples with high SiO<sub>2</sub> and low ASRW content to ensure high mechanical

properties of AAB (compressive strength 30 MPa) after sulphate attack. It would also be necessary to test such durability properties as freeze-thaw resistance.

## V ACKNOWLEDGEMENT

The research work was carried out in the frame of the Latvian Council of Science Project: "Development of sustainable effective lightweight construction materials based on industrial waste and local resources" (No. Z12.0412).

## VI REFERENCES

- [1] G. Habert, J. B. D'Espinose De Lacaillerie and N. Roussel, "An environmental evaluation of geopolymer based concrete production: Reviewing current research trends," *J. Clean. Prod.*, vol. 19, no. 11, pp. 1229–1238, 2011.
- [2] B. C. McLellan, R. P. Williams, J. Lay, A. Van Riessen and G. D. Corder, "Costs and carbon emissions for geopolymer pastes in comparison to ordinary portland cement," *J. Clean. Prod.*, vol. 19, no. 9–10, pp. 1080–1090, 2011.
- [3] W. K. W. Lee and J. S. J. van Deventer, "The effect of ionic contaminants on the early-age properties of alkali-activated fly ash-based cements," *Cem. Concr. Res.*, vol. 32, no. 4, pp. 577–584, Apr. 2002.
- [4] F. Pacheco-Torgal, Z. Abdollahnejad, a. F. Camões, M. Jamshidi and Y. Ding, "Durability of alkali-activated binders: A clear advantage over Portland cement or an unproven issue?," *Constr. Build. Mater.*, vol. 30, pp. 400–405, May 2012.
- [5] A. Elimbi, H. K. Tchakoute and D. Njopwouo, "Effects of calcination temperature of kaolinite clays on the properties of geopolymer cements," *Constr. Build. Mater.*, vol. 25, no. 6, pp. 2805–2812, Jun. 2011.
- [6] L. Zheng, C. Wang, W. Wang, Y. Shi and X. Gao, "Immobilization of MSWI fly ash through geopolymerization: effects of water-wash," *Waste Manag.*, vol. 31, no. 2, pp. 311–7, Feb. 2011.
- [7] M. C. G. Juenger, F. Winnefeld, J. L. Provis and J. H. Ideker, "Advances in alternative cementitious binders," *Cem. Concr. Res.*, vol. 41, no. 12, pp. 1232–1243, Dec. 2011.
- [8] D. Bajare, G. Bumanis and A. Korjakins, "New Porous Material Made from Industrial and Municipal Waste for Building Application," *Mater. Sci.*, vol. 20, no. 3, pp. 3–8, 2014.
- [9] P. Duxson, J. L. Provis, G. C. Lukey and J. S. J. van Deventer, "The role of inorganic polymer technology in the development of 'green concrete,'" *Cem. Concr. Res.*, vol. 37, no. 12, pp. 1590–1597, Dec. 2007.
- [10] R. R. Lloyd, J. L. Provis and J. S. J. van Deventer, "Pore solution composition and alkali diffusion in inorganic polymer cement," *Cem. Concr. Res.*, vol. 40, no. 9, pp. 1386–1392, Sep. 2010.
- [11] H. F. W. Taylor and R. S. Gollop, *Some chemical and microstructural aspects of concrete durability*. London: E & FN Spon, pp. 177–184, 1997.
- [12] S. E. Wallah and B. V. Rangan, "Research Report GC2," Australia, 2006.
- [13] T. Bakharev, J. G. Sanjayan and Y.-B. Cheng, "Sulfate attack on alkali-activated slag concrete," *Cem. Concr. Res.*, vol. 32, no. 2, pp. 211–216, Feb. 2002.
- [14] H. El-Sayed and E. Abo, "Resistance of Alkali Activated Water-Cooled Slag Geopolymer to Sulphate Attack," *Ceram.*, pp. 153–160, 2011.
- [15] T. Bakharev, "Durability of geopolymer materials in sodium and magnesium sulfate solutions," *Cem. Concr. Res.*, vol. 35, no. 6, pp. 1233–1246, Jun. 2005.
- [16] O. S. B. Al-Amoudi, S. N. Abduljawwad and M. Maslehuddin, "Magnesium-Sodium Sulfate Attack in Plain and Blended Cements," *J. Mater. Civ. Eng.*, vol. 6, no. 2, pp. 201–222, May 1994.
- [17] P. Chindaprasirt, P. Kanchanda, A. Sathonsaowaphak and H. T. Cao, "Sulfate resistance of blended cements containing fly ash and rice husk ash," *Constr. Build. Mater.*, vol. 21, pp. 1356–1361, 2007.
- [18] S. E. Wallah, D. Hardjito, D. M. J. Sumajouw and B. V. Rangan, "Sulfate and acid resistance of fly ash-based geopolymer concrete," in *Proceedings Australian structural engineering conference*, 2005.
- [19] V. Sata, A. Sathonsaowaphak and P. Chindaprasirt, "Resistance of lignite bottom ash geopolymer mortar to sulfate and sulfuric acid attack," *Cem. Concr. Compos.*, vol. 34, no. 5, pp. 700–708, May 2012.
- [20] D. L. Y. Kong and J. G. Sanjayan, "Damage behavior of geopolymer composites exposed to elevated temperatures," *Cem. Concr. Compos.*, vol. 30, no. 10, pp. 986–991, Nov. 2008.
- [21] G. Bumanis, D. Bajare and J. Locs, "The Effect of Activator on the Properties of Low-Calcium Alkali-Activated Mortars," *Key Eng. Mater.*, vol. 604, pp. 169–172, Mar. 2014.
- [22] G. Bumanis, D. Bajare and A. Korjakins, "Influence of the carbonate-free clay calcination temperature and curing conditions on the properties of alkali-activated mortar," *The International Scientific Conference „Innovative Materials, Structures and Technologies"*, pp. 24–28, 2014.
- [23] D. Bajare, A. Korjakins, J. Kazjonovs and I. Rozenstrauha, "Pore structure of lightweight clay aggregate incorporate with non-metallic products coming from aluminium scrap recycling industry," *J. Eur. Ceram. Soc.*, vol. 32, no. 1, pp. 141–148, Jan. 2012.

# Crack Development Research in Extra Fine Aggregate Cement Composites

Andina Sprince, Leonids Pakrastinsh, Bruno Baskers, Liga Gaile  
Riga Technical University, Department of Structural Engineering.  
Address: Azenes Street 16, Riga, LV-1048, Latvia.

**Abstract.** The cracking properties in cement-based composites widely influences mechanical behavior of construction structures. The challenge of present investigation is to evaluate the crack propagation near the crack tip. During experiments the tension strength and crack mouth opening displacement of several types of concrete compositions was determined. For each composition the Compact Tension (CT) specimens were prepared with dimensions 150x150x12mm. Specimens were subjected to a tensile load. Deformations and crack mouth opening displacement were measured with extensometers. Cracks initiation and propagation were analyzed using a digital image analysis technique. The formation and propagation of the tensile cracks was traced on the surface of the specimens using a high resolution digital camera with 60 mm focal length. Images were captured during testing with a time interval of one second. The obtained experimental curve shows the stages of crack development.

**Keywords:** cement-based matrix, fibre reinforced concretes, high performance concretes, PVA fibres.

## I INTRODUCTION

The development of new types of concrete focuses on Extra Fine Aggregate Cement Composites (with the largest aggregate dimension  $\leq 5$  mm) (EFACC). It is a composite material in which certain characteristics are developed for a particular application and environment. These characteristics are not only strength, but improved durability, increased resistance to various external agents, high rate of hardening, better aspect, etc. This concrete is characterized by an enhanced postcracking tensile residual strength, also defined as toughness in the following, due to the fiber reinforcement mechanisms provided by fibers bridging the crack surfaces. Fibers in concrete provide improved mechanical and physical properties of the material [1, 2].

The durability and deformation characteristics of a material are just as important as its strength properties. Therefore, designers and engineers need to know those properties of concrete and must be able to take them into account in the structure analysis [2, 3].

This paper reports on an experimental investigation of the cracking resistance of several types of EFACC using the Compact Tension test.

## II MATERIALS AND METHODS

The experimental work included the preparation of two EFACC compositions with polyvinyl alcohol (PVA) fibers constituting 2% of the total amount of cement with and without nanosilica. The EFACC mixtures consisted of cement, water, quartz sand

(grain size 0.3 - 1 mm), silica fume, nanosilica, microsilika, plasticizer Sikament and two types of PVA fibers. PVA fiber properties are listed in Table 1. For the purposes of this paper, the batches containing microsilica were designated MS PVA, and the ones containing microsilika and nanosilica - NS PVA [4].

TABLE 1  
PROPERTIES OF PVA FIBRES

Fibre type	$\emptyset$ [ $\mu\text{m}$ ]	L [mm]	$f_t$ [GPa]	E [GPa]
MC 40/8	40	8	1.6	42
MC 200/12	200	12	1.0	30

The testing procedure developed for the present work consisted of applying a tensile load to a single-edge notched specimen. The selected specimen shape resembles the one used for the evaluation of crack propagation behavior in metals (ASTM-E647 2005) [5], the so-called Compact Tension (CT) specimen, see Figure 1.

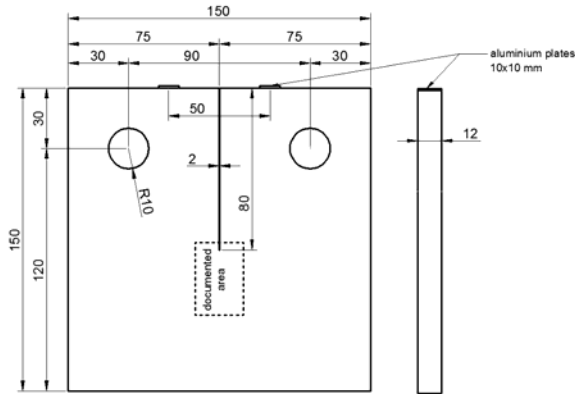


Fig. 1. Geometry of the Compact Tension (CT) specimen

With the purpose of maximizing the stress intensity at the tip of the notch, the notch thickness was reduced to 0.5 mm using a small diamond cutting disc. The depth of the specimen was also reduced, promoting the plain stress state. Summarizing, the dimensions adopted for the specimens were 150 mm by 150 mm (perpendicular and parallel to the notch) and 12 mm (thickness). The available path for progress of the initiated crack parallel to the notch was 30 mm. The distance between the loading axis and the tip of the notch was also 50 mm (see Figure 2).



Fig. 2. Preparation of Compact Tension specimens

The testing sequence consisted of subjecting the specimens to a tensile load at a constant displacement rate, transmitted by two rods with a diameter of 20 mm (see Figure 3). The use of the two rods allowed the transmission of the displacement while keeping

free the rotation of the specimen with respect to the rods. The adopted displacement rate was  $1\mu\text{m/s}$  [6].



Fig. 3. Determination of tensile strength and uniaxial tensile crack development research

The formation and propagation of the tensile crack was traced on the surface of the specimens using a high resolution digital camera positioned 70 mm away from the specimen. The lens with a 60 mm focal length allowed the observation of a 36 mm by 24 mm area on the surface of the specimen (see Figure 3). Shooting settings - lens aperture F11, shutter speed 1/30, ISO 200. Images with a 24 megapixel resolution were captured during testing at an interval of one second. These images were subsequently used for continuous interpolation of the strain fields at the inspected surface of the specimen. Optimal conditions for the strain field interpolation were met with the need of applying a speckle pattern on the surface of the specimen.

To experimentally measure the deformation during the CT tests, the ARAMIS software was used.

In the present case, fluorescent lights were used and positioned in such a way that the intensity of the light reflected by the specimen surface was even. The images of the surface of the specimens were analyzed prior to testing and sufficient image correlation was obtained. Each facet was composed of  $15 \times 15$  pixels. Each pixel covered a real area of  $6 \times 6 \mu\text{m}^2$ . The total area of  $36 \times 36 \text{ mm}^2$  was modeled by a facet mesh overlay composed of approximately  $400 \times 260$  facets [6].

Before testing, to measure crack mouth opening displacement (CMOD), the extensometer with precision  $\pm 2.5 \mu\text{m}$  was centrally and symmetrically positioned at the edge of the test plate's notch.

### III RESULTS AND DISCUSSION

Experimental durability tests clearly prove and confirm the hypothesis that by applying fiber "cocktail" higher material behavior and destruction

effectiveness is reached than when using only one type of fibers, as every length (type) of fibers has their own function: the short fibers strengthen cement matrix and perform clamping of long fibers, but long fibers connect large cracks, making a fiber bridge between edges of cracks [1] and does not allow brittle, instant failure of cement composite, which is extremely important in exploitation of load-bearing structures. Figure 4 and 5 show relationship of tension load and crack mouth opening displacement of several types of EFACC.

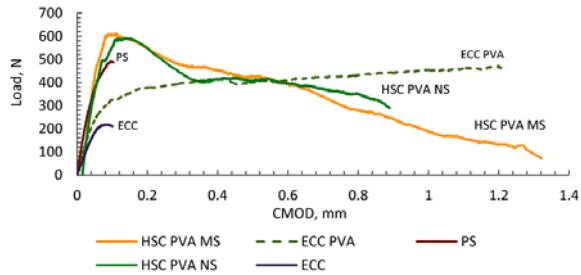


Fig. 5. Tensile strength and crack mouth opening displacement (CMOD) of different kind of cement composites

Several stages of EFACC behavior can be identified, (see Figure 4).

The Figure 6 shows the crack visibility to the human eye and by the system "Aramis". By human eye crack is visible when specimen is already collapsed but system "Aramis" allows the observation of how the cracks initiate and propagate in specimen. The crack becomes clearly visible, although their openings are very small. Detailed information about those experiments look for [4]

The first stage 0A (from zero to about 60-80% of peak load) corresponds to the ascending linear elastic portion of the curve where the section is not cracked. The second stage AB (from about 60-80% of peak load to peak load) corresponds to the portion of the curve where cracking starts and during which crack formation stabilizes and the specimen reaches its peak load. A peak point – B where the maximum resistance is attained. The third stage BC (from peak load to about 60% of peak load) correspond to the portions of the curve where strain softening starts and where the load–strain curve response is almost linear elastic and crack widths increase and the fourth stage (from C to the end) is a non-linear portion where either or both materials are in their non-linear range and crack widths continue to increase (according to Naaman [7]).

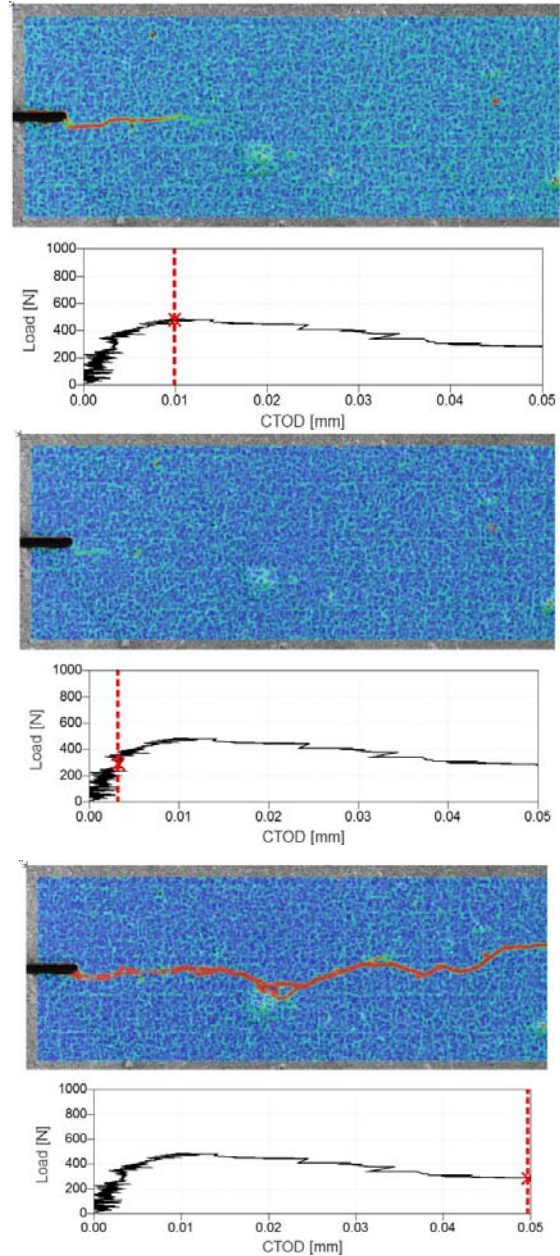


Fig. 4. Crack development of cement composite with nano silica mineral filler and the "cocktail" of two types of PVA fibers by using digital image-based monitoring system "Aramis"

#### IV CONCLUSIONS

Two Extra Fine Aggregate Cement Composites (EFACC) mixes with polyvinyl alcohol (PVA) fibers containing 2% of the total amount of cement by weight with and without nanosilica were prepared for a laboratory examination. The tensile load and the cracks mouth opening displacement (CMOD) were determined.

The experimental study indicates that nanosilica does not have significant influence on the EFACC tensile strength and on the CMOD properties.

Wider use of this material permit the construction of sustainable next generation structures with thin

walls and large spans that cannot be built using the traditional concrete.

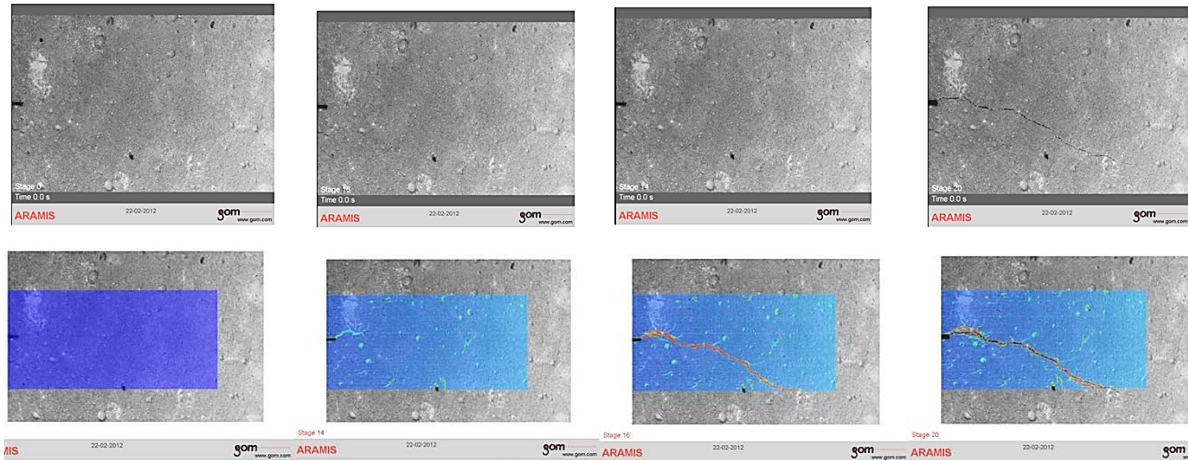


Fig. 6. Crack visibility to the human eye and by system "Aramis"

## V REFERENCES

- [1] Brandt A M 2008 Fibre reinforced cement-based (FRC) composites after over 40 years of development in building and civil engineering *Composite Structures* vol. 86 pp 3-9.
- [2] Prisco M, Plizzari G, Vandewalle L 2009 Fibre reinforced concrete: new design perspectives *Materials and Structures* vol. 42 pp 1261-1281.
- [3] Benin A V, Semenov A S, Semenov S G 2014 Fracture analysis of reinforced concrete bridge structures with account of concrete cracking under steel corrosion *Advanced Materials Research* vol. 831 pp 364-369.
- [4] Sprince A, Fischer G, Pakrastinsh L, Korjakins A 2014 Crack Propagation in Concrete with Silica Particles *Advanced Materials Research* vol. 842 (Switzerland: Trans Tech Publications) pp 470-476.
- [5] ASTM-E647 2005 Standard test method for measurement of fatigue crack growth rates ASTM Standard vol.03.01 (US: ASTM Standard)
- [6] Pereira E B, Fischer G, Barros J A O and Lepech M 2010 Crack formation and tensile stress-crack opening behavior of fiber reinforced cementitious composites (FRCC) *Proc. of Fra MCoS-7* pp 1638-1647
- [7] Naaman A E, Reinhardt H W 1996 Characterization of High Performance Fiber Reinforced Cement Composites *Proc. of 2nd Int. Workshop on HPRCC* (London: E. & FN Spon) chapter 41 pp 1-24.



# Materials Consumption Decrease for Long-Span Prestressed Cable Roof

Arturs Stuklis<sup>1</sup>, Dmitrijs Serdjuks<sup>2</sup>, Vadims Goremikins<sup>3</sup>

<sup>1</sup>Riga Technical University, Department of Structural Engineering,

<sup>2</sup>Riga Technical University, Department of Structural Engineering,

e-mail: Dmitrijs.Serdjuks@rtu.lv,

<sup>3</sup>Czech Technical University in Prague, Department of Steel and Timber Structures,

e-mail: goremikins@gmail.com

**Abstract.** Limited raw materials and energy resources are actual national economy problems which can be solved by the decrease of weight, increase of span and durability of load bearing structures. The largest structural spans were achieved by application of cable structures. The roofs are one of the most widely used in practice type of cable structures. However, increased deformability and necessity of the special methods of stabilizing are significant cable roofs disadvantages. The prestressing of one or several groups of cables is one of the probable methods for stabilizing of cable roofs. According to the recommendations available in the literature, all cables of the roof must be prestressed by the equal forces. But after applying of design vertical load, values of the forces, acting in the cables of the roof, changes within the wide limits. So, using of structural materials will not be rational in this case, taking into account, that the cables cross-sections are constant because the cables cross-sections were determined basing on the maximum axial force, acting in the all cables.

Possibility to decrease materials consumption by the changing of prestressing forces for cables of the roof was checked on the example of saddle-shaped cable roof with the rigid support contour and dimensions 60x60 m in the plan. Initial deflections of main suspension and stressing cables of the roof were equal to 7m. Suspension and stressing cables of the net were placed with the step equal to 2.828 m. Steel ropes with modulus of elasticity in 1.5·10<sup>5</sup> MPa were considered as a material of suspension and stressing cables of the roof. Suspension and stressing cables were divided into the groups, which are differed by the prestressing forces. Amount of cables groups changes within the limits from 1 to 27. Values of prestressing forces for cables groups change within the limits from 20 to 80% from the cables breaking force.

The dependences of material consumption and maximum vertical displacements of cable roof on the amount of cables groups and prestressing forces were determined as second power polynomial equations. It was stated, that division of suspension and stressing cables on the 18 groups enables to decrease cables material consumption by 19.2%. Values of prestressing forces for suspension and stressing cables of the roof were equal to 57 and 80 %, from it load-carrying capacity, correspondingly.

**Keywords:** Cable net, prestressing force, saddle-shaped cable roof.

## I INTRODUCTION

Limited raw materials and energy resources are actual problems of national economy at the present moment. The decrease of weight, increase of span and durability of load carrying structures are possible ways to fix the problem. The increase of structural efficiency could be achieved by the choice of prestressed tensioned structures, where stress distribution by cross-section is close to uniform [1], [2]. High strength structural materials are used in the full scale in this case. Prestressed saddle-shaped cable roofs take a special position among the prestressed long span structures (Fig. 1) because the saddle shape and prestressing enable to provide stability of the roof surface during the action of alternating loads and to

essentially decrease the ratio between applied load and structural dead weight (Fig. 1, c). The decreased ratio between applied load and structural dead weight save raw materials and energy resources [3], [4]. According to the recommendations available in the literature, all the cables of the load carrying net must be prestressed by the same force [5], [6].

But this recommendation is in the contradiction with the requirements to decrease structural materials consumption, because the difference between the axial forces, acting in the cables of the net after design vertical loads application, will be significant. Possibility to decrease structural materials consumption by 46% by the prestressing of each cable of the 30x30 m in the plan saddle-shaped roof

by the individual force was stated in the following investigations [3], [7]. But the considered cable roof was with the compliant contour, which is characterized by the increased displacements after application of design vertical load. Increased deformability is the main disadvantage of saddle-shaped cable roofs with compliant contour, which decrease the area of it application by the temporary buildings mainly. This disadvantage can be improved by using of the rigid contour [8], [9]. Amount of the cables groups in the net, which are differed by the level of prestressing and the level of prestressing of cables in the each group are the main parameters, of cables net prestressing. So, possibility to decrease materials consumption of saddle-shaped cable roof with the rigid contour by the prestressing of the cables by the different forces must be checked.

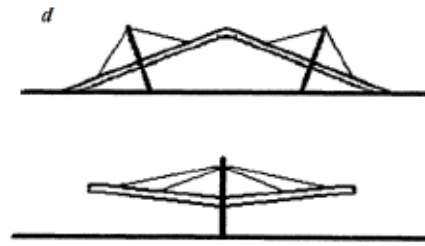
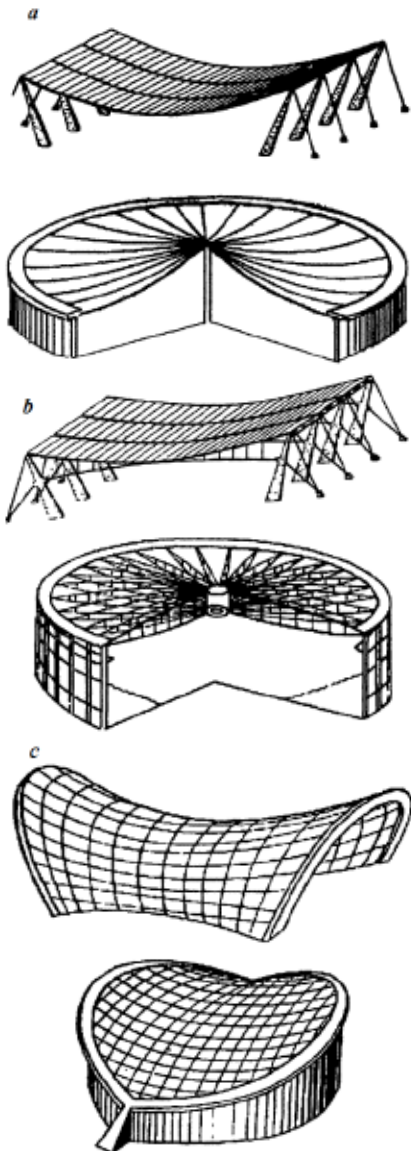


Fig. 1. Prestressed long-span cable structures: *a* – one-chord roofs, *b* – two-chord roofs, *c* – saddle-shaped roofs, *d* – combined roofs (Trushev, 1983; Ermolov, 1991).

Possibility to obtain a cable net, where stresses, acting in the all cables are the same also should be considered. Rational amount of the cables groups in the net, which are differed by the level of prestressing and the level of prestressing of cables in the each group, should be evaluated also.

## II APPROACH TO THE SOLUTION OF THE PROBLEM

### A. Structural solution of long-span prestressed cable roof

Prestressed saddle-shaped cable roof 60X60 m in plan was considered as an object of investigation. The initial deflections of catenary and stressing cables were equal to 7 and 5 m, correspondingly [5], [6]. So, the height of the prestressed saddle-shaped cable roof was equal to 12 m. The distance between the catenary and stressing cables in the plan was equal to 2.828 m. The span of main catenary and stressing diagonal cables was equal to 84.85 m (Fig. 2).

Supporting contour of the cable net was considered as a rigid one. The roofing consists from the two layers of timber boards, which were joined together by the nails, layer of heat insulation and layer of hydro insulation. Thickness of each layer of timber is equal to 33 mm and its strength class is C24. The two layers of timber boards can be created from the cross-laminated timber (CLT) panels, which must be placed so as the fiber direction of outer layers is parallel to the elements of supporting contour. The heat insulation is presented by the mineral wool PAROC ROS 30 with density equal to 100 kg/m<sup>3</sup> and thickness in 150 mm. The hydro insulation is presented by the three layers of prepared roofing paper with the surface density in 0.15 kPa.

Steel cables with an elastic modulus of  $1.5 \cdot 10^5$  MPa and ultimate tensile strength of steel wire of 1770 MPa [10], were assumed as a material for the catenary and stressing cables.

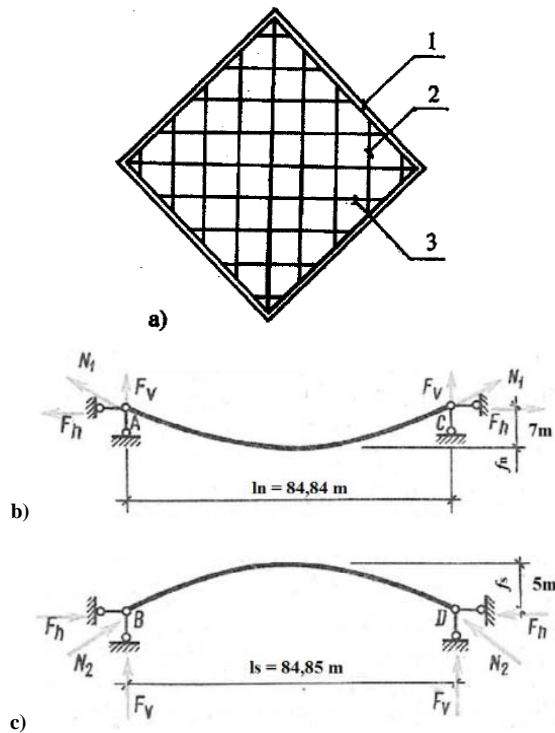


Fig. 2. Scheme of cable net for roof with rigid supporting contour a) and main diagonal catenary b) and stressing c) cables with support reactions: 1 – supporting contour, 2 – catenary cables, 3 – stressing cables,  $l_s$  and  $l_n$  spans of main suspension and stressing cables,  $f_s$  and  $f_n$  – initial deflections of suspension and stressing cables,  $F_v$  and  $F_h$  – vertical and horizontal support reactions,  $N_1$  and  $N_2$  – maximum axial forces in suspension and stressing cables of the net.

### B. Method of analysis

Possibility to decrease cable net's materials consumption for saddle-shaped cable roof with the rigid contour by the prestressing of the cables by the different forces is the major task of this paper. Possibility to obtain a cables net with decreased difference between the stresses, acting in the all cables [3], is considered as a condition, which must be satisfied to fix the problem.

Three variants of cable net with the different amount of cables groups with the different prestressing force were considered. The variants contain from 1 to 27 groups of cables. The level of cables prestressing changes within the limits from 20 to 80% from its load-carrying capacity.

Maximum axial forces, acting in catenary and stressing cables, were determined for the different stages of cable net loading. Maximum axial forces, acting in catenary cables were determined when the cable net is loaded by the dead weight and snow loads [11] in combination with prestressing. Maximum axial forces, acting in stressing cables and maximum vertical displacements of the cable net's nodes were determined by the ANSYS program for the stage, when cable net was loaded by the prestressing only.

Scheme of the cable net, which was created for it analysis by the ANSYS program, is shown in Figure 3. Design vertical load is applied as a point wise force to the nodes of the cable net.

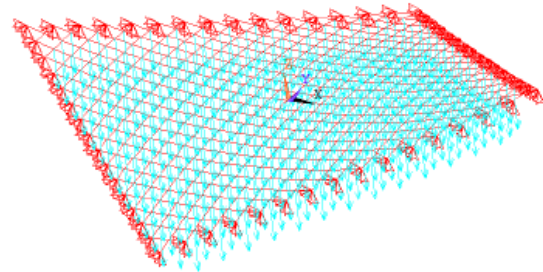


Fig. 3. Scheme of cable net loading.

Metallic cross-sections of catenary and stressing cables were determined by the following equation [12]:

$$A_{m,n(s)} \geq 1.5 \cdot \frac{n_{n,(s)} \cdot \gamma_R}{f_{uk}} \quad (1)$$

where  $A_{m,n,(s)}$  – metallic cross-section of catenary and stressing cables;

$n_{n,(s)}$  – maximum axial forces, acting in catenary and stressing cables;

$\gamma_R$  – partial factors;

$f_{uk}$  – characteristic value of tensile strength of steel wire.

Ultimate limit state (ULS) and serviceability limit state (SLS) were taken in to account during determination of cable's cross-sections and comparison of three mentioned variants of cable net prestressing.

Rational parameters of the cable net prestressing also must be evaluated in the work. Amount of the cables groups, which are differed by the level of prestressing ( $n$ ), prestressing levels of catenary ( $N_{0,n}$ ) and stressing ( $N_{0,s}$ ) cables were considered as the main parameters of the cable net prestressing.

The dependences of cable net materials' consumption ( $G$ ), coefficient of effectiveness of cable net materials using ( $\psi$ ), maximum vertical displacements of the cable net ( $\delta_{max}$ ) on the main parameters of the cable net prestressing were determined. Each from the mentioned above main parameters of the cable net prestressing has three values: maximum, minimum and mean. It means, that the total number of treated variants was equal to 27. The dependences were obtained as a second power polynomial equations on the base of numerical experiment, which was carried out using the software ANSYS.

$$G = b_0 + b_1 \cdot n + b_2 \cdot N_{0,n} + b_3 \cdot N_{0,s} + b_{12} \cdot n \cdot N_{0,n} + b_{13} \cdot n \cdot N_{0,s} + b_{23} \cdot N_{0,n} \cdot N_{0,s} + b_{11} \cdot n^2 + b_{22} \cdot N_{0,n}^2 + b_{33} \cdot N_{0,s}^2, \quad (2)$$

where  $G$  – cable net materials' consumption;  
 $n$  – amount of the cables groups, which are differed by the level of prestressing;  
 $N_{0,n}$  – prestressing level of catenary cables;  
 $N_{0,s}$  – prestressing level of stressing cables.

Rational from the point of view of materials consumption amount of the cables groups, which are differed by the level of prestressing, prestressing levels of catenary and stressing were determined by the systems of equations, which were analogous to the system (3), which was written for cable net materials consumption ( $G$ ).

$$\begin{cases} \frac{\partial G}{\partial n} = b_1 + b_{12} \cdot N_{0,n} + b_{13} \cdot N_{0,s} + 2 \cdot b_{11} \cdot n = 0, \\ \frac{\partial G}{\partial N_{0,n}} = b_2 + b_{12} \cdot n + b_{23} \cdot N_{0,s} + 2 \cdot b_{22} \cdot N_{0,n} = 0, \\ \frac{\partial G}{\partial N_{0,s}} = b_3 + b_{13} \cdot n + b_{23} \cdot N_{0,n} + 2 \cdot b_{33} \cdot N_{0,s} = 0, \end{cases} \quad (3)$$

The obtained results then were analysed and corrected by the inspection.

### III MATERIALS CONSUMPTION DECREASE FOR LONG-SPAN PRESTRESSED CABLE ROOF

Design value of dead weight of the roofings was equal to 1.239 kPa. Snow load was determined for Riga climatical conditions. The snow load is considered as uniformly distributed by the horizontal projection of the roof. Design value of snow load was equal to 1.80 kPa. So the value of pointwise forces applied to the nodes of the cable net was equal to 24.31kN.

The tension stresses distribution in the cables of the net for the variant with the four cables groups, which are differed by the prestressing level, is shown in Figure 4. The values of tension stress changes within the limits from 535.83 to 1470MPa. The values of tension stresses for variants with one and twenty seven groups of cables changes within the limits from 242.5 to 1129.6 MPa and from 104.9 to 1843.1MPa, correspondingly.

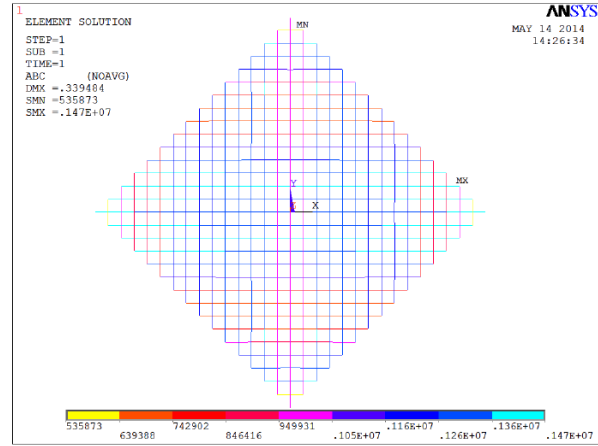


Fig. 4. Tension stresses distribution in the cables of the net for the variant with the four cables groups, which are differed by the prestressing level.

The dependence of cable net materials' consumption on the amount cables groups with the different prestressing force was obtained and shown in Figure 5.

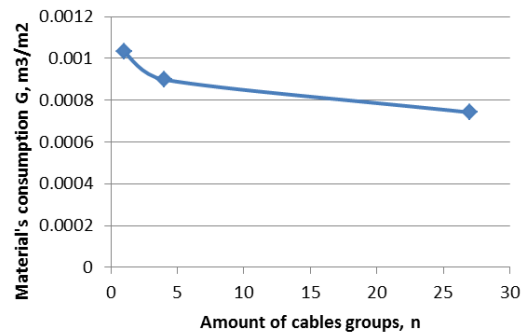


Fig. 5. The dependence of cable net materials' consumption on the amount cables groups with the different prestressing force.

It was stated, that materials volume was equal to 3.71, 3.24 and 2.67 m<sup>3</sup> for the variants which contains 1, 4 and 27 groups of cables, which are differed by the prestressing level, correspondingly. So, increase of cable groups amount with the different level of prestressing from 1 to 4 and 27 enables to decrease cable net materials consumption by 21.3 and 39.2%, correspondingly.

### IV EVALUATION OF RATIONAL PARAMETERS OF CABLE NET PRESTRESSING

The dependences of cable net materials' consumption ( $G$ ) coefficient of effectiveness of cable net materials using ( $\psi$ ), maximum vertical displacements of the cable net ( $\delta_{max}$ ) on the amount of cables groups ( $n$ ), which are differed by the levels of prestressing and this level for catenary ( $N_{0,n}$ ) and stressing ( $N_{0,s}$ ) cables, were determined basing on the

results of numerical experiment, which was carried out using the software ANSYS. Stresses decrease (%) in the cables of the net due to changing of groups amount which are differed by the level of prestressing is considered as the effectiveness of cable net materials using ( $\psi$ ). The variants contain 1, 4 and 27 groups of cables. The levels of catenary and stressing cables prestressing were equal to 0, 40 and 80% from its load-carrying capacity. The coefficients of second power polynomial equations for materials' consumption (G) coefficient of effectiveness of cable net materials using ( $\psi$ ) and maximum vertical displacements of the cable net ( $\delta_{max}$ ) are given in Table 1. The values of obtained coefficients allow to analyze level of influence of the amount of cable groups and prestressing level of catenary and stressing cables on the cable net materials' consumption, coefficient of effectiveness of cable net materials using, maximum vertical displacements of the cable net. The amount of cables groups is the factors which most significantly influence the

mentioned parameters of the cable net. Influence of prestressing level of catenary and stressing cables is significant also, but their levels of importance were form 7.17 to 6.21 times less than the same for the amount of cables groups. Absolute value of corresponding coefficients  $b_1$ ,  $b_2$ , and  $b_3$  are considered as the levels of importance for amount of cables groups and prestressing level of catenary and stressing cables, correspondingly.

Rational from the point of view of materials consumption, effectiveness of cable net materials using and maximum vertical displacements of the cable net amount of the cables groups, prestressing levels of catenary and stressing cables of the net were determined by the system of equations (3) and analogous systems. Rational values of the cables groups, prestressing levels of catenary and stressing cables of the net changes within the limits from 14 to 18 and from 49.6 to 57.3%, correspondingly.

TABLE 1  
THE COEFFICIENTS OF SECOND POWER POLYNOMIAL EQUATIONS

Coefficients of second power polynomial equations	Dependence for materials' consumption(G)	Dependence for coefficient of effectiveness of cable net materials using ( $\psi$ )	Dependence for maximum vertical displacements of the cable net ( $\delta_{max}$ )
$b_0$	$1.08 \cdot 10^{-3}$	374.70	489.52
$b_1$	$-5.14 \cdot 10^{-5}$	26.88	12.86
$b_2$	0	-8.89	-2.60
$b_3$	0	-6.92	2.07
$b_{11}$	$1.43 \cdot 10^{-6}$	-1.24	-0.36
$b_{12}$	0	0.11	0.01
$b_{13}$	0	0.07	0.03
$b_{22}$	0	0.04	-0.02
$b_{23}$	0	0.06	-0.02
$b_{33}$	$1.08 \cdot 10^{-3}$	0.03	-0.01

The dependences of the effectiveness of cable net materials using from the prestressing level of catenary and stressing cables of the net and the cable net materials consumption on the amount of cables groups are shown in Figure 6 and Figure 7. The dependence of the net prestressing level of the catenary and stressing cables on the maximal vertical deflection is shown on Figure 8.

The dependences which are shown on Figure 6 and Figure 8 were obtained for the amount of cables groups equal to 18. The both dependences have non-linear character. The dependences on Fig. 7 were obtained when the prestressing levels of catenary and stressing cables of the net were equal to 57 % and 80% from its load-carrying capacity, correspondingly. This result was obtained by the method of inspection basing on the values, which are numerically obtained and indicated on the Figure 6 and Figure 8. Character of obtained dependence did

not allow getting the maximum effectiveness of cable net materials using by the analytical approach only.

It was stated, that materials consumption for the cable net with 18 cables groups, prestressing levels of catenary and stressing cables of the net equal to 57% and 80%, correspondingly, is equal to  $6.22 \cdot 10^4$  m<sup>3</sup>/m<sup>2</sup>. So, materials consumption can be decreased by 16.17% in comparison with the variant of the net with 27 groups of cables, which are differed by its prestressing level.

The prestressing level of catenary cables should be maximal to obtain the minimum deflections. So, increase of levels of prestressing for catenary and stressing cables from 20 to 80 % from its load-carrying capacity enables to decrease the maximum vertical displacements from 600 till 200 mm for considered saddle-shaped cable roof with the rigid support contour and dimensions 60x60 m in the plan.

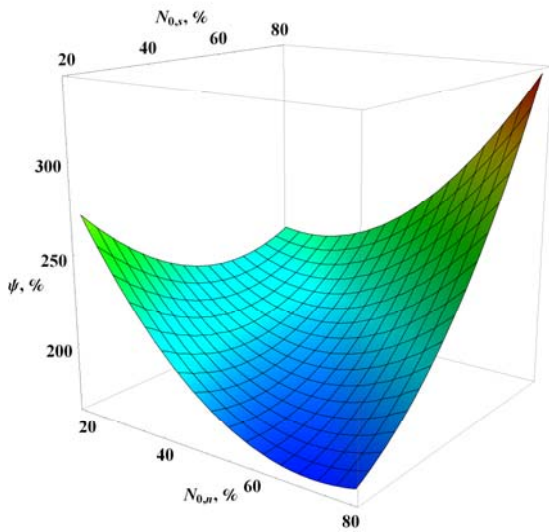


Fig. 6. The dependence of the effectiveness of cable net materials using from the prestressing level of catenary and stressing cables of the net.

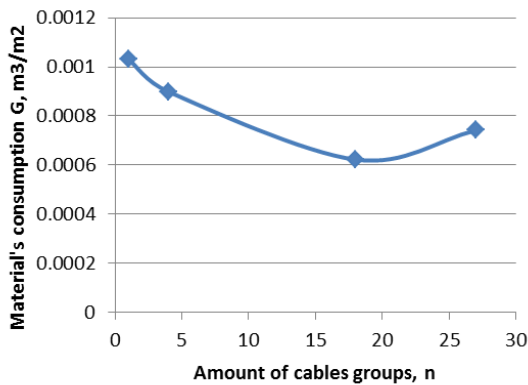


Fig. 7. The dependence of the cable net materials consumption on the amount of cables groups.

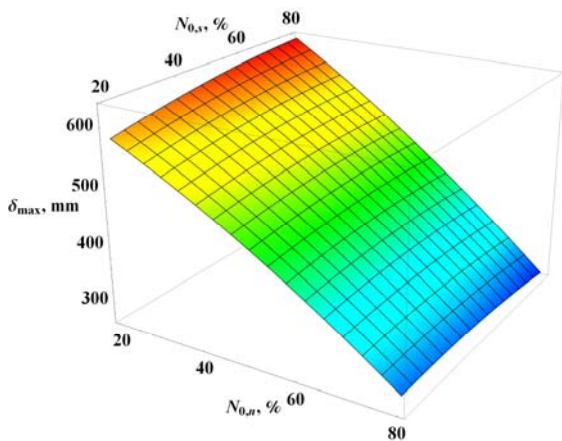


Fig. 8. The dependence of cable net prestressing level of catenary and stressing cables on maximal vertical deflection.

## V CONCLUSIONS

Possibility to decrease materials consumption by the changing of prestressing forces for cables of the roof was checked on the example of saddle-shaped cable roof with the rigid support contour and dimensions 60x60 m in the plan. So, increase of cable groups amount with the different level of prestressing from 1 to 4 and 27, enables to decrease cable net materials consumption by 21.3 and 39.2%, correspondingly. Values of prestressing forces, which were applied to the groups of cables, changes within the limits from 20 to 80% from the cables breaking force.

Rational from the point of view of cable net material's consumption amount of cables groups, which are differed by the levels of prestressing and prestressing level for catenary and stressing cables, were determined. It was stated, that division of suspension and stressing cables on the 18 groups enables to decrease cables material consumption by 19.2%. Values of prestressing forces for suspension and stressing cables of the roof were equal to 57 and 80 %, from it load-carrying capacity, correspondingly.

## VI ACKNOWLEDGEMENT

The research leading to these results has received the funding from Latvia state research programme under grant agreement "Innovative Materials and Smart Technologies for Environmental Safety, IMATECH". Project Nr.3, PVS ID1854, Task Nr.3.

## VII REFERENCES

- [1] V. Goremikins, "Rational Large Span Prestressed Cable Structure," Doctoral Thesis, Riga Technical University, Riga, 2013.
- [2] V. Goremikins, K. Rocens and D. Serdjusks, "Decreasing Displacements of Prestressed Suspension Bridge," *Journal of Civil Engineering and Management* vol. 18, no. 6, 2012, pp. 858–866.
- [3] D. Serdjusks, K. Rocens, L. Pakrastins, "Prestress Losses in the Stabilizing Cables of a Composite Saddle-Shaped Cable Roof," *Mechanics of Composite Materials*, vol. 39, no. 4, 2003, pp. 341-346.
- [4] V. Goremikins, K. Rocens, D. Serdjusks, "Cable Truss Analyses for Suspension Bridge," in *Proc. of 10th International Scientific Conference "Engineering for Rural Development", 24-25 May, 2012, Jelgava, Latvia*, vol. 11, 2012, pp. 228–233.
- [5] A. Trushev, *Spatial steel Structures*, Moscow, 1983.
- [6] V. Ermolov, *Engineering Structures*. Moscow, 1991.
- [7] D. Serdjusks, K. Rocens, "Decrease the Displacements of a Composite Saddle-Shaped Cable Roof," *Mechanics of Composite Materials*, vol. 40, no. 5, 2004, pp. 675-684.
- [8] V. Mihailov, *Predvariteljno naprjazennije kombinirovannije i vantovije konstrukciji*. Moskva: ACB, 2002.
- [9] L. Pakrastins, K. Rocens, D. Serdjusks, "Deformability of Hierarchic Cable Roof," *Journal of Constructional Steel Research*, vol. 62, 2006, pp. 1295-1301.
- [10] M. Liscicins, V. Lapkovskis, V. Mironovs, D. Serdjusks, "Composite Load-Bearing Element Based on the Perforated Steel Wastes," in *Proc. of 4th International Conference Advanced Construction, 9-10 October, 2014, Kaunas, Lithuania*, 2014, pp. 158–163.

- [11] European Committee for Standardization, *Eurocode 1: Actions on buildings*, Brussels, 2004.
- [12] European Committee for Standardization, *Eurocode 3: Design of steel structures – Part 1.11: Design of structures with tensile components*, Brussels, 2003.

# Effect of spray dryer settings on the morphology of illite clay granules

A.Stunda-Zujeva, V.Stepanova, L.Bērziņa-Cimdiņa

Riga Technical University Institute of General Chemical Engineering,  
P.Valdena Street 3, Riga, Latvia, e-mail of corresponding author:  
agnese.stunda-zujeva@rtu.lv

**Abstract.** Spray drying is an effective and common method for powder drying, e.g. clay. The morphology and properties of spray dried granules depend on properties of slurry and operational conditions of spray dryer. The aim of this study was to investigate the effect of spray dryer settings on the morphology of illite clay granules.

Laboratory scale spray dryer was used. Operational conditions: inlet temperature 190-220 °C, outlet temperature 70-96 °C, spray dispersion is obtained using two-fluid nozzle where the slurry feed was varied from 4.5 to 15 ml/min and gas pressure 15-40 mm. Slurry was prepared from clay fraction under 2 µm without additives. Latvian illite clay from Iecava, Pavāri and Laža deposits was studied. Slurries with concentration 1, 8 and 15 mass% was used. The size and morphology was investigated by scanning electron microscopy, surface area and porosity by liquid nitrogen sorption.

All obtained granules irrespective of spray dryer settings were well-rounded and dense without large pores or holes, however the surface was rough. The mean diameter of granules was in range of 2.6-5.4 µm, depending on slurry feed rate. The surface area of produced granules mostly depended on clay composition and was in a range of 70-92 m<sup>2</sup>/g. Inlet temperature in a range of 190-220 °C was found to be appropriate to produce well dried clay granules (moisture content <10 wt%).

**Keywords:** clay, illite, Latvian clay powder, spray-drying, slurry.

## I INTRODUCTION

Spray-drying is a convenient process for producing a granulated powder. It is an effective and fast method for slurry drying because of large surface area of sprayed droplets. The advantages of spray dried clays are uniform particle size [1] and randomly oriented particles in each granule and therefore in obtained powder. This is important e.g. in mineral analysis by X-ray diffraction [2]. The only disadvantage is mass losses due to small particles flying away with air flow. Conversion of fine powder to coarser makes the material less dusty that is safer for workers and makes easier to handle the material.

The most widespread clay mineral in Latvia is illite. The common use of illite clays is in building materials and pottery. However, it is worth to look for new applications, for example, as fillers in some composite materials or toners and thickeners in slurries, e.g. in cosmetics [3], in waste water purification from admixtures of organic dyes [4] and industrial waste treatment [5]. The influence of mineralogical composition, electrical conductivity and pH on the rheological properties of Latvian illite clays is described elsewhere [6], it was found that viscosity and plasticity can be influenced even

by small differences between mineralogical compositions of sample.

The morphology and properties of spray dried granules depends on slurry properties (e.g. surface tension, viscosity, density) and operational conditions of spray dryer (e.g. pressure and carrier gas velocity) [1]. The aim of this study was to investigate spray drying of some Latvian illite clay and the morphology of obtained clay granules.

## II MATERIALS AND METHODS

*Clay deposits.* Latvian illite clays from Laža, Pavāri and Iecava deposits were investigated. Iecava is Devonian clay that is a byproduct of refining dolomite from deposits in Bauska district, Laža is Quaternary clay deposit in Liepāja district 5 km to ZA from Aizpute. Pavāri is Devonian clay deposit in Cesvaine district. All deposits are economically feasible for use, they are under thin overburden layer or a byproduct in exploited deposit.

*Mineral composition.* The mineral composition of these clays has been investigated before [3] by X-ray diffraction and Quanto software, chemical composition was analysed by Scanning electron microscopy and chemical analysis. Fraction under

ISSN 1691-5402



63  $\mu\text{m}$  contained following minerals: Iecava – 51% illite, 11% quartz, 26% feldspar, 8% muscovite, 4% dolomite; Laža – 34% illite, 11% kaolinite, 8% chlorite, 13% quartz, 16% feldspar, 8% calcite, dolomite 5% dolomite, 5% muscovite; Pavāri – 35% illite, 4% kaolinite, 54% quartz, 7% feldspar. Pavāri clay did not contain carbonates that promotes aggregation and increase pH.

Iecava clay is gray, (5Y 7/1 after Munsell color chart), Laža clay – light brown (7,5YR 6/4), Pavāri clay – pink white (7,5YR 8/2). All clay contain iron ions, that can be dissolved using acid. [3].

*Slurry.* Clays were dispersed in distilled water, no additives (e.g. deflocculants) or other chemical treatment was used. Fraction under 2  $\mu\text{m}$  was separated by slurry centrifuge. Slurry with clay mass fraction of 7–9 % was obtained after first centrifugation and 1–2 % - after second centrifugation. The concentration was measured by evaporative moisture analyzer Kern MRS120-3. Viscosity was analyzed by reometer RheolabQC (Anton Paar) at 200 rpm speed.

*Spray drying.* Several operational conditions were tested. The criteria for suitable drying conditions were that no moist slurry droplets deposited in the lower part of drying chamber and dried particles reach cyclone and powder collecting chamber.

Slurry concentrations used in spray drying were ~ 1.5, 8, 15 and 20 %. Clays were spray dried in laboratory scale dryer - BUCHI Mini Spray Dryer B-290, spray dispersion was obtained in two-fluid nozzle, spray feed was ensured by peristaltic pump, aspirator worked in suction setting, so there was underpressure in the system. The yield of dryer is 50–1000 mL/h. Operational conditions that varied were inlet temperature (maximal for equipment is 225 °C), slurry feed rate, gas pressure. The constant settings were drying time and efficiency of cyclone that is determined by aspirator flow – 80% of power, fresh air humidity 32–40% and temperature 18–22 °C. Experimental parameters are shown in table 1.

*Sample names.* Sample names are made from Clay deposit (Iecava, Laža and Pavāri – Ie, La and Pa respectively), concentration and drying setting according to table I, e.g. Ie20%\_4 is Iecava clay slurry with a solid mass fraction 20 % dried in 4<sup>th</sup> setting.

*Clay granule analysis.* The size and morphology was investigated by high emission field electron microscopy Tescan Mira/LMU and microscopy image analyse software Image PRO. At least 1000 granules were measured for each sample.

The Surface area and porosity was measured by liquid nitrogen (77 K) absorption in automated analyser QuadraSorb SI. The analysed sample

weight was 0.2 g, before sorption it was outgassed at 100 °C for 24 h.

TABLE I  
SPRAY DRYER SETTINGS

Setting No.	Inlet temperature, °C	Slurry feed pump, %/ mL/min	Gas pressure, mm/normL/h
1	220	25/6.7	15/ 192
4	200	25/ 6.7	15/ 192
5	200	25/ 6.7	25/ 301
6	220	30/ 8.0	25/ 301
7	190	30/ 8.0	25/ 301
8	220	35/ 9.3	35/ 414
9	220	40/ 10.7	30/ 357
10	220	35/ 9.3	30/ 357
11	220	50/ 13.3	40/ 473
12	223	45/ 12.0	40/ 473
13	190	30/ 8.0	40/ 473
14	190	25/ 6.7	35/ 414

### III RESULTS AND DISCUSSION

*Viscosity of slurry.* Concentrated clay slurry is non-Newtonian fluid [6]. As it can be seen in Table II the viscosity of clay slurry strongly depends on mixing rate (or shear rate). At the beginning of measurement the viscosity of Ie15% at 200 rpm was 15.4 mPa·s, but after 100 s it stabilized at 13.8 mPa·s

TABLE II  
THE VISCOSITY (mPa·s) OF Ie20% AFTER MIXING AT CONSTANT RATE FOR 10 MIN

Repeat	40 rpm	60 rpm	80 rpm	200 rpm
1	189	131	100	22.8
2	182	127	99.5	22.4

The viscosity of all samples was different, the most viscous was Laža clay slurry, and the least viscous was Pavāri clay slurry (Fig. 1).

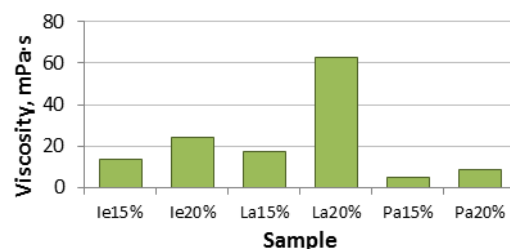


Fig. 1. The viscosity of investigated clay slurries (after 10 min, mixing rate 200 rpm).

The viscosity of La15% was 17.6 mPa·s at the beginning of measurement and after 65-115 s stabilized at 17.3 Pa·s that is 20% lower than Ie15%. The La20% was 3.6 times higher viscosity than La15%, 2.7 times higher than Ie20% viscosity and 7.3 times higher than Pa20%. First

measurement of La20% at the beginning showed the viscosity as high as 0.0873 Pa·s and after 10 min it decreased to 68.6 mPa·s, repeating measurement after few minutes did not showed so rapid decrease of viscosity 68.8 to 65.0 mPa·s and in next repeating it decreased from 65.3 to 62.8 mPa·s (the slopes are shown in Fig. 2).

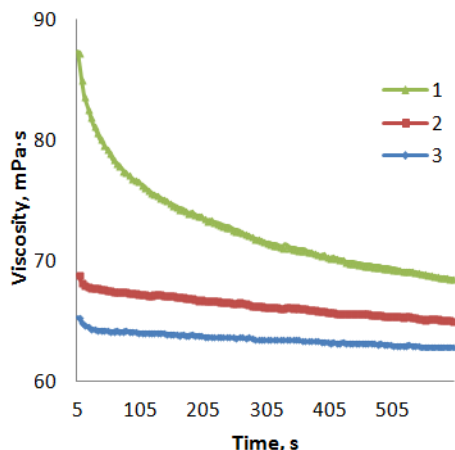


Fig. 2. The change of viscosity in time of La20% slurry in three following measurements

Other studies have shown that suspensions exhibit a rapid increase of apparent viscosity, if solid concentration (fraction < 63  $\mu\text{m}$ ) is raised from 30 to 35 wt% [6].

To ensure the homogeneity and lower viscosity in slurry feed tube of spray drier, the slurry is intensively mixed on magnetic mixer before feed.

*The effect of concentration and viscosity on spray dried particle surface area and size.* Surface area dependence on slurry concentration was observed for more viscous Laža slurry: La20% had the smallest average surface area 71  $\text{m}^2/\text{g}$ , La15% - 74 and La8% - 76  $\text{m}^2/\text{g}$ . Surface area was practically not affected by settings of spray drier for La20%. For less viscous slurry La15% and La8% the impact of feed rate and nozzle gas velocity increased. La8%\_13 surface area was 75  $\text{m}^2/\text{g}$  while La8% average surface area was 77  $\text{m}^2/\text{g}$ .

All Iecava and Pavāri samples showed significantly larger surface area, the average surface area of Iecava samples was 92  $\text{m}^2/\text{g}$  (StandardDeviation 2), Pavāri - 89  $\text{m}^2/\text{g}$  (StDev 3) while Laža - only 74  $\text{m}^2/\text{g}$  (StDev 2). For Iecava and Pavāri samples definite relationship between the investigated spray dryer parameters and surface area of granules was not found (Fig. 3).

*The role of inlet temperature.* Inlet temperature in a range of 190-220  $^{\circ}\text{C}$  was found to be appropriate to produce dry clay granules (moisture content 3–10 wt%). The outlet temperature was 70–96  $^{\circ}\text{C}$ . For the inlet temperature as low as 190  $^{\circ}\text{C}$  maximal slurry feed rate was 30% or 8 mL/min to achieve dry sample.

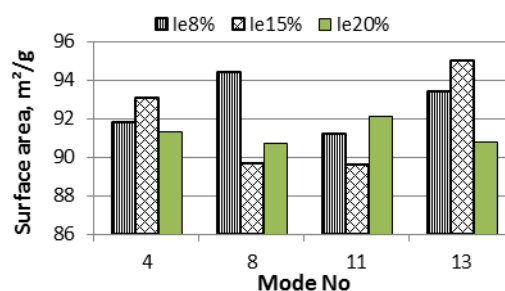


Fig. 3. Surface area of Iecava clay granules obtained from slurries with various concentrations and spray dried at various settings.

*Sorption isotherms and porosity.* The sorption isotherm of all samples was between Type II and type IV isotherms (Fig. 4) after IUPAC classification; that corresponds to "high surface energy solids" [7]. Type II isotherms typically characterise non-porous or macroporous materials. Other authors have obtained similar sorption data of natural illite clay [5].

The inflection point or knee of the isotherm (called point B) that indicates the stage at which monolayer coverage is complete and multilayer adsorption begins to occur was detected at relative pressure  $p/p_0$  was less than 0.04 for all samples. The absorbed volume at  $p/p_0$  0.04 was 18  $\text{cm}^3/\text{g}$ .

The obtained clay granules mostly contain macropores (> 50 nm) as the adsorption isotherm rose rapidly near  $p/p_0 = 1$  and in the limit of large macropores exhibit an essentially vertical rise.

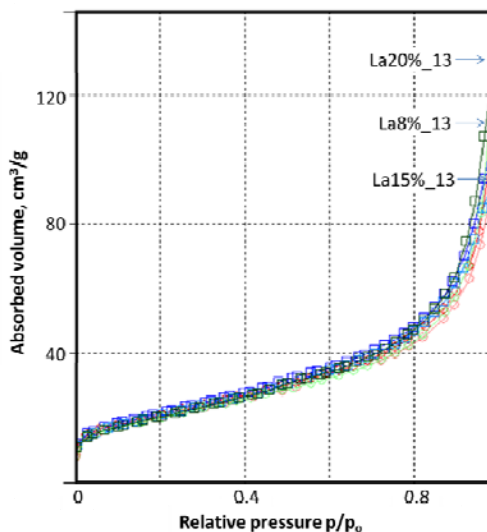


Fig. 4. Adsorption-desorption isotherms of nitrogen on some Laža clay granules.

A narrow hysteresis loop that is characteristic mesopores (pore diameter 2–50 nm) was observed (Fig. 5). The size and shape of hysteresis loop was similar within the same clay type irrespective to spray drying conditions, but slightly differed for

each clay deposit. This can be due to flocculation of clay particles.

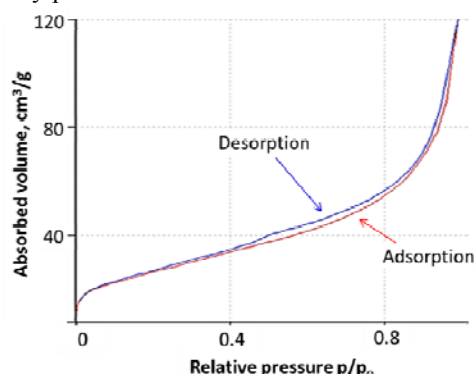


Fig. 5. Hysteresis loop of adsorption isotherms on Pavāri clay granules.

Total pore volume for pores with radius less than 83.8 nm at  $p/p_0 = 0.988418$  was greater for less viscous samples: Ie8% - average is  $0.3 \text{ cm}^3/\text{g}$ , more viscous Ie20% is around 0.2 and all Laža samples fit in range 0.1–0.2. The porosity and pore size depends on median diameter of primary particles, solid mass concentration and flocculation state; it does not depend on ambient air and initial droplet volume [8]. In studied case it can be concluded that porosity of clay granules is determined by mineral composition, e.g. impurities like iron containing minerals that increase flocculation of clay minerals.

*Size and shape of granules.* The size of granules varied from operational conditions (Fig. 6.). The largest granules were obtained in setting of drying No 4 that had lowest air flow and slurry feed rate, for Ie15%\_4 size reached  $5.2 \mu\text{m}$  (StDev 4.1) and the smallest was for La8%\_8 and La8%\_13 –  $2.6 \mu\text{m}$  (StDev 1.4). The mean diameter of granules correlate with maximal diameter, the correlation coefficient was 0.992. The size distribution was similar for all samples (Fig. 7 and Fig. 8a and 8b).

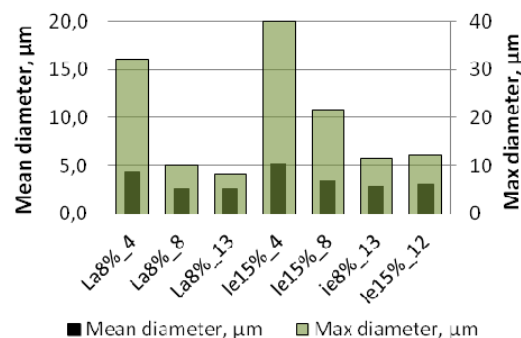


Fig. 6. The size of spray dried granules. Different clay types dried in various conditions.

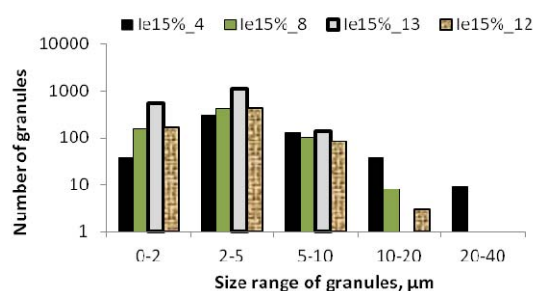
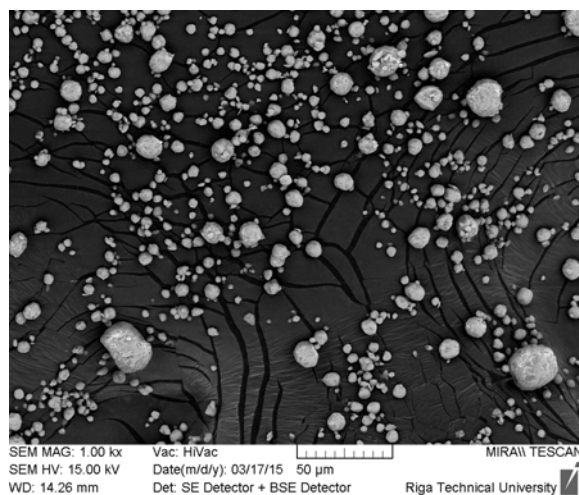


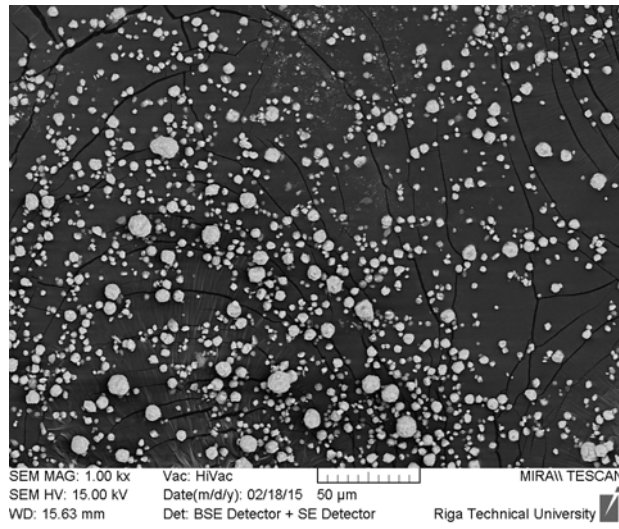
Fig. 7. The size distribution of granules. Iecava clay 15% slurry dried in different conditions.

All obtained granules were dense without large macropores or holes (Fig. 8), however the surface was rough. Most of granules were well-rounded, but not all was ideally spherical. The size and shape of granules were similar irrespective of clay type or concentration or spray dryer settings (Fig. 8c, 8d and 8e). Plate-like surface structure can be seen especially for Iecava clay granules (Fig. 8c), however the plates are not a single clay particles (Fig. 8f).

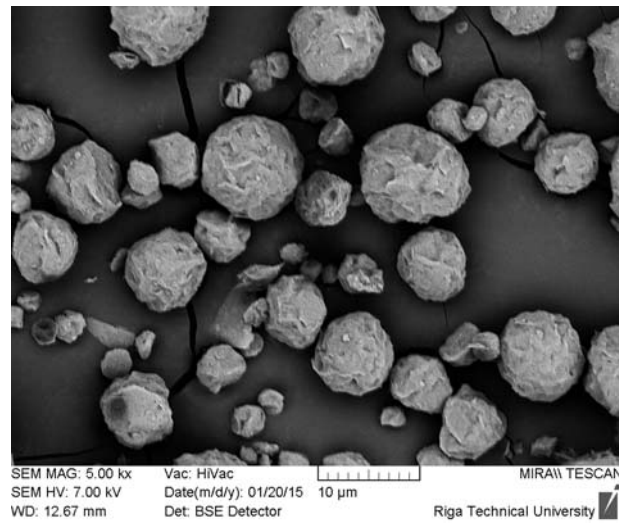
a) Pa20%\_4



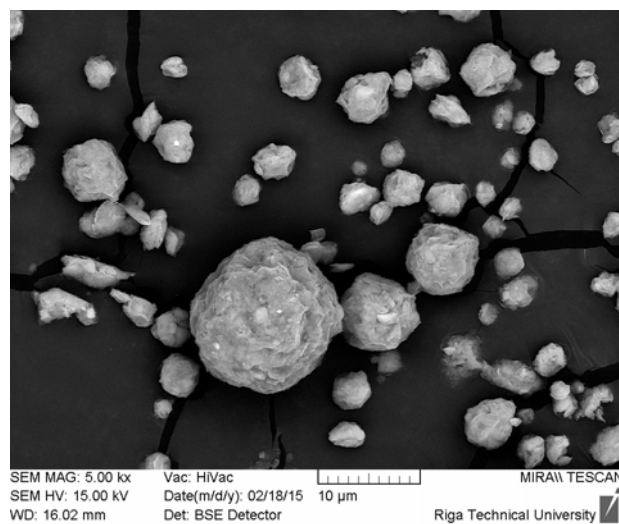
b) La15%\_4



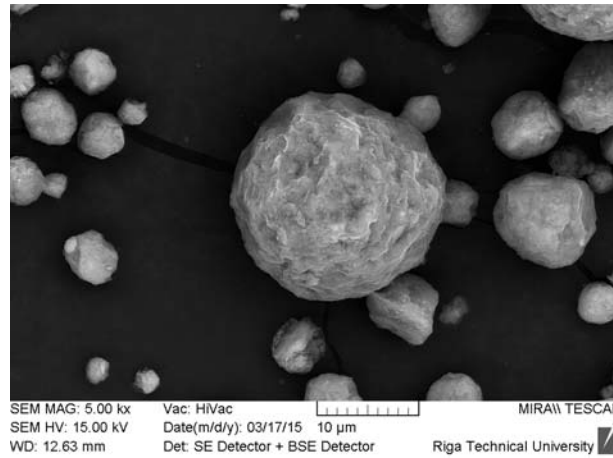
c) Ie15%\_14



d) La15%\_14



e) Pa15%\_14



f) Pa15%\_14

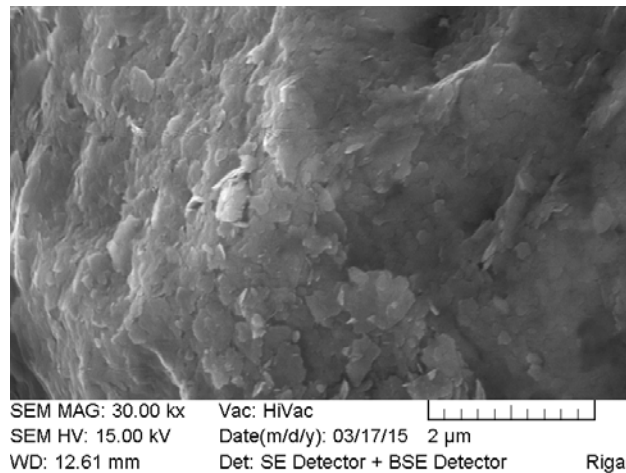


Fig. 7. Clay granules, SEM images

#### IV CONCLUSIONS

The morphology of clay granules are not sensitive to operational conditions of spray dryer. The surface area depends mostly of clay composition while the mean diameter is significantly affected by slurry feed rate and air flow. The mean diameter of granules was 2.6. Inlet temperature in a range of 190-220 °C was found to be appropriate to produce well dried clay granules (moisture content <10 wt%). All obtained spray dried samples had well-rounded granules.

#### V ACKNOWLEDGMENTS

This work has been supported by the National Research Program of Latvia 2014-2017 within the project No.4.4. (Y8099) „Zemes dzīļu resursu izpēte dabisko izejvielu dažādošanai un jaunu tehnoloģiju izstrādei (GEO)” (Investigation of underground resources to obtain different natural

raw materials and to develop new technologies (GEO)).

#### VI REFERENCES

- [1] A. B. D. Nandiyanto and K. Okuyama, “Progress in developing spray-drying methods for the production of controlled morphology particles: From the nanometer to submicrometer size ranges,” *Adv. Powder Technol.*, vol. 22, no. 1, pp. 1–19, Jan. 2011.
- [2] R. Hughes and B. Bohor, “Random clay powders prepared by spray-drying,” *Am. Mineral.*, vol. 55, pp. 1780–1786, 1970.
- [3] I. Dušenkova, “Latvijas mālu sagatavošanas tehnoloģijas izstrāde un īpašību pētījumi izmantošanai kosmētiskajos produktos,” Rīgas Tehniskā universitāte, 2014.
- [4] V. Lakevičs, V. Stepanova, I. Skuja, I. Dušenkova, and A. Ruplis, “Influence of Alkali and Acidic Treatment on Sorption Properties of Latvian Illite Clays,” *Key Eng. Mater.*, vol. 604, pp. 71–74, Mar. 2014.
- [5] R. a. Alvarez-Puebla, D. S. Dos Santos, C. Blanco, J. C. Echeverria, and J. J. Garrido, “Particle and surface characterization of a natural illite and study of its copper retention,” *J. Colloid Interface Sci.*, vol. 285, pp. 41–49, 2005.

- [6] I. Dusenkova, "Rheological properties of Latvian illite clays," *Acta Geodyn. Geomater.*, vol. 10, no. 4, pp. 459–464, Nov. 2013.
- [7] F. Wypych and K. G. Satyanarayana, Eds., *Clay Surfaces. Fundamentals and Applications*. London: Elsevier Academic Press, 2004, p. 567.
- [8] R. Mondragon, J. C. Jarque, J. E. Julia, L. Hernandez, and A. Barba, "Effect of slurry properties and operational conditions on the structure and properties of porcelain tile granules dried in an acoustic levitator," *J. Eur. Ceram. Soc.*, vol. 32, no. 1, pp. 59–70, Jan. 2012.

# RESEARCH INTO BIOLOGICAL CHARACTERISTICS OF DRIED SAPROPEL

Rasma Tretjakova<sup>1</sup>, Jūlija Grebeža<sup>2</sup>, Andris Martinovs<sup>1</sup>

<sup>1</sup>Rezeknes Augstskola, Faculty of Engineering,  
Atbrivosanas aleja 115, Rezekne, LV-4601, Latvia.

<sup>2</sup>Institute of Food Safety, Animal Health and Environment BIOR,  
Liepu iela 33b, Rēzekne, LV-4600, Latvia.

**Abstract.** Microbiological characteristics of dried sapropel of Lake Rušona and Lake Ubagova and concrete containing sapropel and hemp sheaves (Ubagova Lake) have been studied. The antimicrobial activity was studied by the reference test cultures *Staphylococcus aureus* ATCC 25923, *Salmonella enteritidis* ATCC 13076, *Enterococcus faecalis* ATCC 29212, *Bacillus cereus* ATCC 10876, *Escherichia coli* ATCC 25922, *Candida albicans* ATCC 10231. Antibacterial activity on *Staphylococcus aureus* reference test cultures is stated in Rušona Lake sample before treatment with UV rays. Antibacterial activity is not stated in Ubagova Lake sapropel sample. 20 minutes' long UV ray treatment is not long enough to prevent the growth of sapropel materials. Both Rušona Lake and Ubagova Lake samples contain microorganisms that start growing and intensively reproducing in favourable conditions. When in contact with humidity, at the temperature from 18 to 37± 1 °C, mold colonies form on concrete containing sapropel and hemp sheaves, for this reason this material should not get in contact with humidity when used in construction.

**Keywords:** bacteria, fungi, mold.

## I INTRODUCTION

Sapropel is the sediment of freshwater lake mud, which is made up of more than 95% organic substances and is formed on the bottom of the body of water as a result of incomplete decomposition (oxidation) of dying and sunken biomass (different aquatic plants, phytoplankton and zooplankton, living organisms, pollen and spores of highest plants) under conditions of oxygen deprivation. The sapropel is strategic natural resources, numerous studies have shown the possibility of the effective use of sapropels in bio-energy, food industry, chemical industry, agriculture, cattle-breeding, forestry, construction industry, medicine (balneology, pharmacology, mud therapy) and cosmetics [1] – [9]. There are noticeable resources of sapropel in Latvia but insufficient study prevents the use of it. Latvia has 2256 lakes with a total area of 1001 km<sup>2</sup> or 1.5 % of the country. The total area of mires is 6401 km<sup>2</sup> or 9.9 % of Latvia. Most lakes and bogs contain sapropel deposits. The State Geology Office of Latvia states that there are more than 750 million m<sup>3</sup> of lake sapropel resources and about 1.5 billion m<sup>3</sup> of sapropel reserves. There are about 2 billion m<sup>3</sup> of joint sapropel resources in

Latvia [10]. Nowadays issues concerning ecological construction and production of environmentally friendly materials are getting even more important. A noticeable part of social resources has to be invested in construction materials, thus it is very important to produce effective and environmentally friendly materials by using local resources. Development of ecological construction materials and increasing application of them in construction expands because it gives an opportunity to save resources during production and does not pollute environment. These materials are fully recyclable and decompose in relatively short period of time after the exploitation. As the interest in economics that uses local natural resources increases, the study of sapropel use in construction material production is getting more topical. Several scientists [8], [10], [11], [12] point on use of sapropel in construction. Gružāns [13] economical calculations show that sapropel-concrete could become one of the cheapest and most available construction materials in the whole Latvia. But solid sapropel is a new, almost unused material yet. To find maximally effective application for sapropel, its mechanical, physical, chemical and biological

characteristics should be known. The aim of this study is to determine the biological activity of solid sapropel materials.

## II MATERIALS AND METHODS

In experiments Nr 1 to Nr 5 two samples were tested – the 1st sample is sapropel from Diunoklis gulf of Lake Rušona, collected from upper layer (0.3 - 0.5 m in depth), the 2nd sample is Lake Ubagova sapropel, collected from deeper layer. The samples were dried at the temperature of 20 - 23 °C and preserved in laboratory conditions for 3 months. Experiments were carried based on CLSI M100-S23 Performance standards for antimicrobial susceptibility testing [14]. In assessing of the antibacterial agents were used the following criteria: absence of zones around the wells for microbial growth inhibition or occurrence of zone areas.

For the evaluation of antimicrobial activity in experiments 1 to 4 were used the following test strains: *Staphylococcus aureus* ATCC 25923, *Salmonella enteritidis* ATCC 13076, *Enterococcus faecalis* ATCC 29212, *Bacillus cereus* ATCC 10876, *Escherichia coli* ATCC 25922, *Candida albicans* ATCC 10231. Reference test cultures were planted on PCA (Plate Count Agar) and incubated for 24 h in 37 ± 1 °C temperature.

In Experiment Nr 1 sapropel samples are divided into small pieces. MHA (Mueller-Hinton agar) is melted in boiling water bath, then cooled to the temperature of ~ 40 °C, obtained broth is poured in sterile 90 mm Petri dishes. The mixture is allowed to solidify for 20 minutes. Reference cultures are inoculated in TSB (Tryptone Soya Broth), to 0.5 McFarland (the turbidity is evaluated by comparing to 0.5 McFarland standard). Sterile cotton swab is soaked in inoculant, pressed against the inner wall of test tube, then densely draw stripes on the surface of MHA, this action is repeated two times turning Petri dish for 60 degrees each time. The Petri dish is left to dry for 15 minutes. Then small sapropel material sample is put and pressed in the dish using sterile pincers.

In Experiment Nr 2 after incubation reference cultures from PCA are inoculated in TSB, till 0.5 McFarland (the turbidity is evaluated by comparing to 0.5 McFarland standard) and incubated in thermostat for 1 h at 37 °C temperature in order to get "refresh" substance. Sapropel samples are milled put into laminar and treated with UV rays. Sterile test tubes filled with MHA are melted in boiling water bath, then cooled to the temperature of ~ 40 °C, add reference cultures 1 ml (incubated in TSB), mixed with electrical mixer (Vortex), obtained broth is poured in sterile 90 mm Petri dishes. The mixture is allowed to solidify for 20 minutes. Using sterile instrument a hole in the broth is made. Using sterile instrument the hole is filled with sapropel.

In Experiment Nr 3 reference cultures are disseminated on PCA. Sapropel samples are milled put into laminar and treated with UV rays for 20 minutes. MHA is melted in boiling water bath, then cooled to the temperature of ~ 40 °C, obtained broth is poured in sterile 90 mm Petri dishes. Agar is allowed to solidify for 20 minutes. Reference cultures are inoculated in TSB, 0.5 McFarland (the turbidity is evaluated by comparing to 0.5 McFarland standard). Sterile cotton swab is soaked in inoculated TSB, pressed against the inner wall of test tube, then densely draw stripes on the surface of MHA, this action is repeated two times turning Petri dish for 60 degrees each time. The Petri dish is left to dry for 15 minutes. Using sterile instrument a hole in the broth is made. Using sterile instrument ½ of the hole is filled with sapropel.

In Experiment Nr 4 broth and reference cultures are made as in experiment Nr. 3. Preparatory procedure of sapropel material is different - after treating with UV rays for 20 minutes, milled sapropel sample is poured out in sterile Petri dishes, saline is added, mixed, put in thermostat at 37 °C and is allowed to "maturate" for 30 minutes. Using sterile instrument a hole in the broth is made. Using sterile instrument the hole is filled with matured in the thermostat sapropel.

In experiment Nr 5 two microorganisms reference cultures have been used: *Staphylococcus aureus* ATCC 25923, *Escherichia coli* ATCC 25922. Reference cultures were planted on PCA and incubated for 24h at 37 °C temperature. Sapropel samples are milled, put into laminar and treated with UV rays for 20 minutes. Reference cultures are inoculated in TSB, 0.5 McFarland (the turbidity is evaluated by comparing to 0.5 McFarland standard). 9 ml of inoculant with sterile pipette is taken into 3 test tubes. To the 1<sup>st</sup> test tube 1g of the 1<sup>st</sup> sapropel sample is added, to the 2<sup>nd</sup> test tube 1g of the 2nd sapropel sample is added, the 3<sup>rd</sup> test tube – control. All test tubes substance is mixed. Test tubes are incubated in for 24 h at 37 °C temperature. Dilution from incubated TSB is made till 10<sup>-10</sup> degree. 90 mm Petri dishes are filled with 1 ml dilution from 10<sup>-6</sup> till 10<sup>-10</sup>. It is melted on PCA, cooled to the temperature of ~ 40 °C. Dilution is poured with PCA, mixed and agar is allowed to solidify for 20 minutes. It is incubated for 24 h at 37 ± 1 °C temperature. Then colonies are counted.

In experiments Nr 6 – 9 concrete containing sapropel and hemp sheaves have been tested.

Experiments are carried out based on standard LVS EN ISO 4833-1:2014 – enumeration of microorganisms.

In experiments Nr 6 and 7 10 ± 0.01 g of sample in a sterile bag is weighed out, then add 90 sodium chloride peptone solution. Substance is being mixed with electrical mixer Stomaher™ for 3 minutes, then



allow the biggest parts to settle. From the obtained solution dilution from  $10^{-3}$  - to  $10^{-10}$  is made (with sterile pipette suspensions are taken into another test tube with 9 ml sodium chloride peptone solution). 1 ml of tested sample dilution (from  $10^{-2}$  - $10^{-10}$ ) is taken on each of 2 sterile Petri dishes, then about 12 - 15 ml PCA is poured on each dish, when cooled till 44 - 47 °C, is carefully mixed and allowed to solidify. Incubate for  $72 \pm 4$  h at  $30 \pm 1$  °C and  $22 \pm 1$  °C. Calculate colonies (for calculating are chosen the dishes which contain less than 150 colonies).

Calculate the number N of mesophilic aerobic and facultative anaerobic microorganisms using the equation:

$$N = \frac{\sum C}{V \cdot (n_1 + 0.1 \cdot n_2) \cdot d} \quad (1)$$

where C- sum of the colonies counted, V- the volume of inoculum applied on each dish (1 ml),  $n_1$ - the number of dishes retained at the first dilution,  $n_2$  - the number of dishes retained at the second dilution, d - the dilution factor - 1.

In experiment Nr 8  $2 \pm 0.01$  g of sample is weighed out on 4 sterile Petri dishes. 2 ml of sterile water is poured on each dish, then mixed. Incubate at  $22 \pm 1$  °C,  $30 \pm 1$  °C,  $37 \pm 1$  °C, at room temperature which fluctuates from 18 °C till 23 °C. Every 24 h growth control is made, in order to avoid material desiccation, 1ml sterile water is added.

In experiment Nr 9  $2 \pm 0.01$  g of sample is weighed out on 4 sterile Petri dishes. 2 ml of sterile water is poured on each dish, then mixed. Dishes are taken into "Whril-pack" sterile bags, closed hermetically. Incubate at  $22 \pm 1$  °C,  $30 \pm 1$  °C,  $37 \pm 1$  °C, at room temperature. Growth control is made every 24h.

### III RESULTS AND DISCUSSION

In experiment Nr 1 checking the antibacterial activity of sapropel materials on *Staphylococcus aureus*, *Salmonella enteritidis*, *Enterococcus faecalis*, *Bacillus cereus*, *Escherichia coli*, *Candida albicans* it

has been noticed that Rušona Lake sapropel materials have *Staphylococcus aureus* 2 mm growth delay, in other reference cultures - *Salmonella enteritidis*, *Enterococcus faecalis*, *Bacillus cereus*, *Escherichia coli*, *Candida albicans* growth delay has not been stated. In its turn, the development of growth delay zone has not been noticed in any of Ubagova Lake sapropel material of applied reference cultures. Intense growth on broth of both studied materials has been noticed, colonies are large, with rugged edges, tarnished, white and cream-coloured.

In experiment Nr 2, in order to evaluate growth delay and suppress the growth of sapropel natural microflora, sapropel was pulped and treated with UV rays; as a result, the development of delay zone has not been noticed neither in Rušona Lake sapropel materials, nor in Ubagova Lake sapropel materials with any of applied reference cultures. Findings are difficult to be read and interpreted, as sapropel has matured and increased its volume ~2 times. Part of materials has been electrified and stuck to Petri dishes covers. Growth of both studied materials on broth has been noticed, colonies are large, with rugged edges, tarnished, white and cream-coloured.

In experiments Nr 3 and 4, in order to prevent volume increasing, which disturbs to evaluate results effectively, moistened material has been used and the hole ½ filled with studied material. As a result the development of delay zone has not been noticed neither in Rušona Lake sapropel materials, nor in Ubagova Lake sapropel materials with any of applied reference cultures. Findings are clearly to be read. Growth of both samples on broth has been noticed, colonies are large, with rugged edges, tarnished, white and cream-coloured.

In experiment 5, adding Rušona Lake sapropel material and Ubagova Lake sapropel material to *Staphylococcus aureus* and *Escherichia coli* suspensions, after 24 h period of incubation a number of microorganisms has not decreased, is observed the decreasing of the number of microorganisms comparing to control sample. Results of the study of antibacterial activity of test samples, presented in the Table 1.

TABLE 1.  
ANTIBACTERIAL ACTIVITY OF TEST SAMPLES

Reference test cultures	Rušona Lake sapropel sample (kvv/1ml)	Ubagova Lake sapropel sample (kvv/1ml)	Control (kvv/1ml)
<i>Staphylococcus aureus</i>	$14 \times 10^8$	$15 \times 10^8$	$10 \times 10^8$
<i>Escherichia coli</i>	$16 \times 10^8$	$14 \times 10^8$	$12 \times 10^8$

In experiment Nr 6, studying concrete containing sapropel and hemp sheaves after 72 h of incubation at  $30 \pm 1$  °C temperature, the number of mesophilic aerobic and facultative anaerobic microorganisms is  $7.5 \times 10^6$  kvv/1g (Table 2).

In experiment Nr 7, after 72h of incubation at  $22 \pm 1$  °C temperature, the number of mesophilic aerobic and facultative anaerobic microorganisms is  $6.3 \times 10^6$  kvv/1g (Table 2).

In experiment Nr 8, incubating concrete containing sapropel and hemp sheaves without

broth with added water, at all checked temperatures ( $22 \pm 1^{\circ}\text{C}$ ,  $30 \pm 1^{\circ}\text{C}$ ,  $37 \pm 1^{\circ}\text{C}$ , room temperature, which fluctuates from  $18^{\circ}\text{C}$  till  $23^{\circ}\text{C}$ ), after 7 days is observed the increasing of mold colonies (Table 2).

In experiment Nr 9, incubating concrete containing sapropel and hemp sheaves without

broth with added water in a sterile polyethylene bag, the increasing of mold colonies is observed at all checked temperatures ( $22 \pm 1^{\circ}\text{C}$ ,  $30 \pm 1^{\circ}\text{C}$ ,  $37 \pm 1^{\circ}\text{C}$ ), room temperature, which fluctuates from  $18^{\circ}\text{C}$  till  $23^{\circ}\text{C}$  after 5 days (Table 2).

TABLE 2.

BIOLOGICAL CHARACTERISTICS OF CONCRETE CONTAINING SAPROPEL AND HEMP SHEAVES

Microorganisms	$22 \pm 1^{\circ}\text{C}$	$30 \pm 1^{\circ}\text{C}$	$37 \pm 1^{\circ}\text{C}$	Room temperature $18^{\circ}\text{C} - 23^{\circ}\text{C}$
Number of mesophilic aerobic and facultative anaerobic microorganisms	$6.3 \times 10^6$	$7.5 \times 10^6$	not checked	not checked
Mold colonies (Pates "Whril-pack")	positive	positive	positive	positive
Mold colonies (Plate)	positive	positive	positive	positive

Platonov *at al.* [2] states that sapropel protective antibiotic activity against *E.coli*, *St.aureus*, *C.diphtherie* and fungi *Candida* was demonstrated. Strus *at al.* [15] studies have shown a slight antibacterial activity of sapropel against selected test cultures (*Escherichia coli* ATCC 25922, *Pseudomonas aeruginosa* ATCC 27853, *Bacillus subtilis* ATCC 6633, *Proteus vulgaris* ATCC 4636, *Candida albicans* ATCC 885/ 653). However, in this study, antibacterial activity of Rušona Lake sapropel sample has been observed only on *Staphylococcus aureus*, but Ubagova Lake sapropel sample has not shown anti-bacterial effect on any of applied microorganisms reference cultures. Stankeviča, Kļaviņš [10] point out that anti-bacterial effect is characteristic of fresh sapropel. Also Marčenko and Gurinovich [16] mention that microorganisms that educe antibiotics, which are antagonistic chain of pathogenic saprophilic microorganisms have been found in fresh sapropel. In this study dried sapropel has been studied.

The research shows that sapropels contain an extremely large amount of microorganisms – in 1 g of fresh sapropels there are 12 billion microorganisms in its top layer. In the lower layers, starting from around 0.6 - 1.0 m from the lake bed surface the amount of microorganisms decreases [17]. In Latvia, in 1965 Stūris [18] in his research of Kaņiera Lake and Babītes Lake stated that microorganisms distribution and biochemical activity directly depend on the depth of sapropel layer and season.

In this study sapropel samples have been taken from different lakes and depths, as a result its biological activity is different.

Also Stankeviča and Kļaviņš [10] point out that content and characteristics of sapropels from various deposits are very different and depend on the productivity of the water body, characteristics of the aboveground water flow, and climatic conditions. Before using concrete containing sapropel in

construction, its biological characteristics and chemical content must be studied. Specific features of biological activity correlate with chemical content of substances [2]. Antibiotics and sulphanilamide in sapropels are synthesized by fungus and actinobacteria.

Possibly, chemical characteristics of fresh and dried sapropel are different, natural microflora changes and it does not show typical antibacterial characteristics. In order to approve this hypothesis, chemical characteristics of fresh and dried sapropel at different depths from several lakes must be studied.

While incubating Rušona and Ubagova Lakes sapropel samples on broth the growth has been noticed, which points out that not only fresh sapropel, but also dried samples have microorganisms that are able to grow. This characteristic has been observed after treatment with UV rays, so 20 minutes' treatment with UV rays do not eliminate all natural microflora of samples.

Studying concrete containing sapropel and hemp sheaves construction materials it has been stated that they contain a big number of microorganisms. When in contact with humidity, at the temperature from  $18^{\circ}\text{C}$  to  $37^{\circ}\text{C}$ , mold has developed on sapropel and hemp sheaves construction materials. The mold is a significant risk factor for health, especially in relation to the diseases affecting the human respiratory and immune system. Overall four types of health problems are observed in relation to moisture and mold exposure - allergic diseases, respiratory irritation, infections and toxicological effects [19].

#### IV CONCLUSION

1. Both Rušona Lake and Ubagova Lake dried sapropel samples contain microorganisms, which begin to grow and reproduce intensively in enabling circumstances.

2. 20 minutes' treatment with UV rays is not enough to eliminate the growth of sapropel made samples.
3. Rušona Lake sapropel test sample has antimicrobial activity on *Staphylococcus aureus* reference culture before it is treated with UV rays.
4. Ubagova Lake sapropel test sample does not have antimicrobial activity.
5. When in contact with humidity, at the temperature from  $22 \pm 1$  °C,  $30 \pm 1$  °C,  $37 \pm 1$  °C, room temperature ( $18$  °C till  $23$  °C), mold colonies form on concrete containing sapropel and hemp sheaves, for this reason this material should not get in contact with humidity when used in construction.

## V REFERENCES

- [1] Nikolaeva L. A., Latyshev V. G. and Burenina O. N. Fuel Briquettes from Brown Coals of Yakutia. ISSN 0361-5219, Solid Fuel Chemistry, vol. 43, No. 2, pp. 109–112, 2009.
- [2] Platonov V.V., Khadartsev A.A., Chunosov S.N. and Fridzon K.Y. The biological effect of sapropel. *Fundamental research*, vol. 9 (11), 2474 – 2480, 2014. [Платонов В.В., Хадартцев А.А., Чуносков С.Н., Фридзон К.Я. Биологическое действие сапропеля. *Фундаментальные исследования*, 9 (11), 2474 - 2480, 2014].
- [3] Kireicheva L.V. and Khokhlova O.B. Sapropels: composition, properties, applications. Moscow, pp. 124, 1998. [Кирейчева Л.В., Хохлова О.Б. Сапропели: состав, свойства, применение. М. 124 с., 1998].
- [4] Ostrovskij M. V. Testing HUMIN PLUS Microfertilizer. *European Agrophysical Journal*, vol. 1(2), pp. 77 – 83, 2014.
- [5] Tsukanov S. V., Owayski F., Zeidan I., Zeidan A., Uptis I., Apse J. and Ostrovskij M. V. Application of Organic Fertilizers Based on Sapropel and Peat in Countries of Middle East. *European Agrophysical Journal*, vol. 1(3), pp.118 – 128, 2014.
- [6] Kitapova R.R. and Ziganshin A.U. Biologic Activity of Humic Substances from Peat and Sapropel. *Kazanskiy meditsinskiy zhurnal*, vol. 1, pp. 84-89, 2015.
- [7] Schepetkin I., Khlebnikov A., Kwon B.S. Medical drugs from humus matter: Focus on mumie. *Drug Development Research*, vol. 57(3), pp. 140 - 159, 2002.
- [8] Pleiksnis S. and Teirumnieka E. „Concrete containing sapropel and hemp sheaves for insulation of buildings,” L. R. Patent 14869, C04B18/18, C04B18/24, June 20, 2014.
- [9] Obuka V., Korjamins A., Brencis R., Preikšs I., Purnalis O., Stankeviča K., Kļaviņš M. Sapropel/Peat-Wood Chip Insulation Materials and Their Properties. *Materials Sciences and Applied Chemistry*, vol. 29, pp.127-136, 2013.
- [10] Stankeviča K. and Kļaviņš M. Sapropel and its application possibilities. *Materials Sciences and Applied Chemistry*, vol. 29, pp.109-126, 2013. Available from: file:///C:/Users/user/Desktop/pub18075.pdf
- [11] Vimba B. "Thermal dissolution of sapropel and chemical characteristics of obtained material", Vimba B. „Sapropela termiskā šķīdināšana un iegūto produktu ķīmiskais raksturojums”. Disertācija, Latvijas Lauksaimniecības Akadēmija, Rīga, 1956.
- [12] Kurzo B.V. Regularity of development and problems in using sapropel. Minsk, [Курзо Б. В. Закономерности формирования и проблемы использования сапропеля. Минск, 224 с. 2005].
- [13] Gružāns A. Sapropelbetons. *LLA raksti*, Nr.9, 547 – 561. lpp., 1960, in Stankeviča K. and Kļaviņš M. Sapropel and its application possibilities. *Materials Sciences and Applied Chemistry*, vol.29, pp.109-126, 2013.
- [14] Performance standards for antimicrobial susceptibility testing. 23rd informational supplement. CLSI M100-S23. Clinical Microbiologie Procedures Handbook. American Society for Microbiology, Washington, USA. 2004.
- [15] Strus O.E., Polovko N.P., Maloshtan L.M. and Solodchenko T.P. The study of the properties of sapropel deposits of Pribich. *Problems of ecological and medical genetics and clinical immunology*, vol. 3 (123), 2014.
- [16] Marchenko L.O., Gurinovich E.S. Microbiological research into sapropel of Belorussian lakes. Problems in using sapropel in national economy. Minsk, Science and Engineering, [Марченко Л.О., Гуринович Е. С. *Микробиологические исследования сапропелей Белорусских озер. Проблемы использования сапропелей в народном хозяйстве*. Минск, Наука и техника, с. 74–81., 1976].
- [17] Kuznesov S. I. The microflora of lakes and its geochemical activity. 440 pp., 1970. [Кузнецов С. И. Микрофлора озёр и её геохимическая деятельность. Л., изд. Наука, 440 с., 1970].
- [18] Sturis T. Researches into sapropel microflora of Kaņiera and Babītes Lakes. Dissertation summary. Riga, Institute of experimental and clinical medicine of Latvia, Sturis, T. *Kaņiera un Babītes ezera sapropela dūņu mikrofloras pētījumi*. Disertācijas kopsavilkums. Rīga, Latvijas eksperimentālas un klīniskas medicīnas institūts, 1965.
- [19] Sahakian N.M., Park J.H., Cox-Ganse J.M. Dampness and Mold in the Indoor Environment: Implications for Asthma. *Immunology and Allergy Clinics of North America*, vol. 28 (3), pp. 485-505, 2008.

# Laser Effect on Spherical Nanoparticles with Thin Surface Layer

A. I. Vanin, V. G. Solovyev

Department of Physics, Faculty of Physics and Mathematics, Pskov State University,  
Lenin Square 2, 180000 Pskov, Russia  
E-mail: a.ivanin@mail.ru

**Abstract.** It is shown that metal nanoparticles with thin atomic surface layer can be used as laser active medium. Significant narrowing of the emission band in the spectrum of the particle with a surface layer was found.

**Keywords:** nanoparticles, lasers, radiation.

## I INTRODUCTION

The relevance of the study is conditioned by the need to create materials for lasers on nanoparticles. The possibility of laser design based on nanoparticles coated with dielectric shells was demonstrated, for example, in [1], [2]. The purpose of this work is to suggest a way of fabrication of nanolaser active medium including nanoparticles with thin atomic surface layers.

## II THEORETICAL APPROACH

We consider surface excitations of a spherical metal particle with inverse population of atoms in a thin surface layer (one or two layers of atoms on the particle surface) as an active medium. The possibility of significant deformation of the surface collective excitations' spectrum of spherical particles with a thin surface layers was shown in our work [3]. The atoms of the surface layer directly interact with the radiation and the particle (see details in [3]). Dielectric layer is not formed in a thin surface layer of atoms. If one examines surface dielectric layer, the spectrum of surface excitations of the particle is weakly deformed.

In the presence of a thin surface layer (one or two atomic layers) polarizability  $R^3 A(\omega)$  of a spherical particle can be represented in the following form [3]:

$$A(\omega) = \frac{\operatorname{tg}(K(\omega))}{\sqrt{2}} + \frac{1}{\cos^2(K(\omega))} \cdot \frac{\alpha(\omega)}{1 - \sqrt{2} \cdot \alpha(\omega) \operatorname{tg}(K(\omega))},$$

where the particle radius  $R$  is much smaller than the characteristic absorption wavelength in the particle's material and in the atoms of the surface layer,

$$\alpha(\omega) = \frac{\varepsilon(\omega) - 1}{\varepsilon(\omega) - 2}.$$

Here  $R^3 \alpha(\omega)$  represents polarizability of a spherical particle in vacuum,  $\varepsilon(\omega)$  is the dielectric constant of the particle substance. The surface layer is described by the function

$$K(\omega) = \sum_a \frac{\sqrt{2} \cdot \alpha_a(\omega) N_a}{R^3},$$

where  $N_a$  is the population of the state number  $a$  in the atoms of the surface layer,  $\alpha_a(\omega)$  represents polarizability of an atom in  $a$ -state with regard to its short-wavelength interaction with the particle surface. If the atoms of the surface layer are described in three-level approximation, the function  $K(\omega)$  can be represented in the form

$$K(\omega) = \frac{a_0 \omega_0^2}{\omega_0^2 - \omega^2 - i\gamma\omega} + \frac{a_1 \omega_1^2}{\omega_1^2 - \omega^2 - i\gamma\omega},$$

where  $\omega_0$ ,  $\omega_1$  are the transition frequencies in the atoms of the surface layer; these values can be shifted as compared with the transition frequencies of the free atom due to the short-wavelength interaction (e.g., chemisorption) with the particle;  $\gamma$  represents the attenuation frequency of the transition,  $a_0, a_1$  are parameters, which are proportional to the difference between the populations of the transition levels in the atoms of the surface layer.

### III RESULTS AND DISCUSSION

An example of the absorption (or radiation) spectrum (imaginary part of  $A(\omega)$ ) of the particle with a thin surface layer is shown in Fig. 1.

The emission spectrum of atoms in the surface layer of the particle (imaginary part of the first term in the expression for  $A(\omega)$ ) is shown in Fig. 2. The parameters of the surface layer

are  $\frac{\omega_0}{\omega_p} = 0.54$ ,  $\frac{\omega_1}{\omega_p} = 1$ ,  $\frac{\gamma}{\omega_p} = 0.05$ ,  $a_0 = -0.0125$

(population inversion),  $a_1 = 0.025$ . The choice of parameters is made for the sake of the clarity of the demonstration effect. The dielectric constant of the substance of the particle is described in the hydrodynamic approximation:

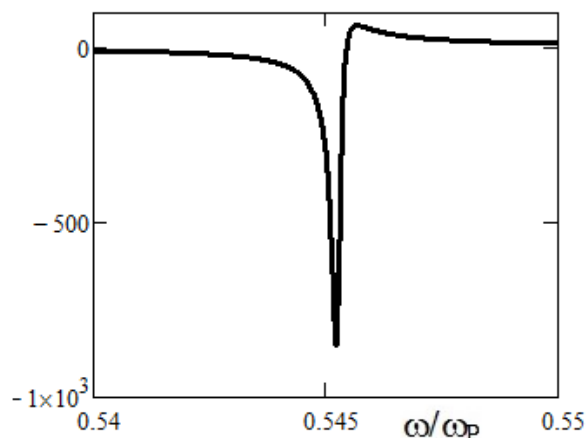


Fig. 1. Absorption (or radiation) spectrum of the particle with a thin surface layer.

$$\varepsilon(\omega) = 1 - \frac{\omega_p}{\omega(\omega + ig\omega_p)},$$

where  $\omega_p$  is the plasma oscillation frequency,  $g\omega_p$  represents the damping frequency of the plasma oscillations in the substance of the particle ( $g = 0.1$ ).

From the spectra in Figs. 1 and 2 one can observe significant narrowing of the emission band in the spectrum of the particle with a surface layer by many orders of magnitude as compared with the width of the

emission band of the atoms in the surface layer as well as with a typical absorption bandwidth of the particle without the surface layer. The lifetime of collective surface excitations in the particle with the surface layer also significantly increases. Narrow radiation band (long lifetime) of surface excitations in the particle demonstrates the possibility of lasing by nanoparticles possessing thin surface layers of atoms with inverse population.

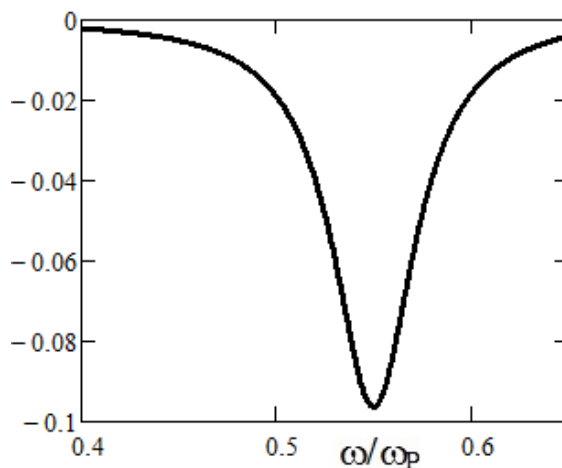


Fig. 2. The surface layer contribution to emission spectrum.

### IV CONCLUSIONS

The possibility of radiation generation and amplification by metal particles with thin surface layers has been theoretically demonstrated.

### V REFERENCES

- [1] M. A. Noginov, G. Zhu, A. M. Belgrave, R. Bakker, V. M. Shalaev, E. E. Narimanov, S. Stout, E. Herz, T. Suteewong, and U. Wiesner, "Demonstration of a spaser-based nanolaser", *Nature*, vol. 460, pp. 1110–1112, 2009.
- [2] M. A. Noginov, G. Zhu, M. Mayu, B. A. Ritzo, N. Noginova, and V. A. Podolskiy, "Stimulated emission of surface plasmon polaritons", *Physical Review Letters*, vol. 101, pp. 226806, 2008.
- [3] А. И. Ванин, "Влияние поверхностного слоя на мелкодисперсных включениях на оптику среды", *Журнал технической физики*, том 64, с. 115–118, 1994.

# Optical Properties of Nanostructured Silver Embedded by Electro-Thermo-Diffusion in Opal Photonic Crystal

V. L. Veisman<sup>1</sup>, S. G. Romanov<sup>2</sup>, V. G. Solovyev<sup>1</sup>, M. V. Yanikov<sup>1</sup>

<sup>1</sup>Department of Physics, Faculty of Physics and Mathematics, Pskov State University,  
Lenin Square 2, 180000 Pskov, Russia;

<sup>2</sup>Institute of Optics, Information and Photonics, University of Erlangen-Nuremberg,  
Haber Str. 9a, 91058 Erlangen, Germany;

Ioffe Physical Technical Institute,  
Polytechnicheskaya Street, 26, 194021 St. Petersburg, Russia

**Abstract.** Novel nanocomposite materials *Ag / opal* have been prepared by electro-thermo-diffusion of silver in opal template. Optical properties of these photonic crystals have been studied by angle-resolved reflectance spectroscopy. Interpretation of the observed optical spectra has been made on the basis of the Bragg diffraction and the Fano resonance between diffracted in *Ag / opal* composite photonic crystal electromagnetic waves and those resonantly scattered by silver dendrites.

**Keywords:** Fano resonance, nanostructured silver, opal photonic crystals.

## I INTRODUCTION

Architectures combining conductive network and photonic crystal functionality pave a way for novel generation of efficient solar cells and lighting devices. To meet this demand we prepared the respective nanocomposite *Ag / opal* by electro-thermo-diffusion of silver in opal template.

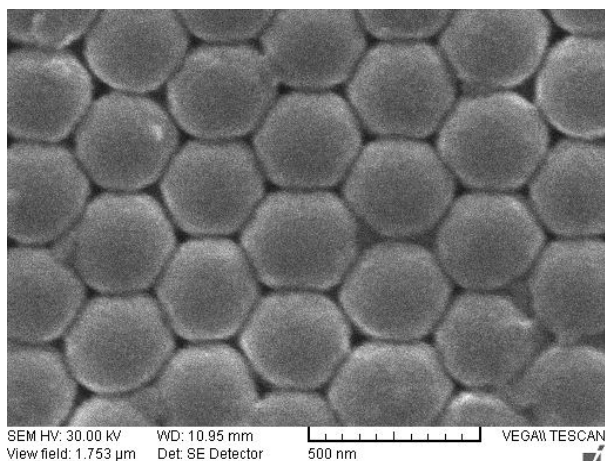


Fig. 1. SEM image of the opal matrix under study.

Self-assembled synthetic opals consist of silica or polymer beads that are assembled in closely packed face centered cubic (FCC) lattice [1] (Fig. 1). Since

the diameters  $D$  of beads are in the range of hundreds nanometers, opals and opal-based metal-dielectric composites are widely used as 3-dimensional photonic [2] and hybrid plasmonic-photonic crystals [3] for the visible light.

## II MATERIALS AND METHODS

Silica opal samples were characterized by «VEGA // LMU Tescan» Scanning Electronic Microscope in the Daugavpils University. According to SEM images (Fig. 1), the mean sphere diameter of the bare opal under study is  $D \approx 288$  nm.

The electro-thermo-diffusion of silver in the opal matrix ( $10 \times 10 \times 2$  mm<sup>3</sup> slab) has been carried out under electric field of  $E=1.7$  kV/cm at temperature of  $T=(664 \pm 2)$  K. The electrolysis process lasted for 2.5 hours. During this time the electric current was increased from 2.6  $\mu$ A up to the saturation value of 1.3 mA. Therefore one can estimate the silver ion concentration after electrolysis as  $\sim 10^{20}$  cm<sup>-3</sup>.

Angle-resolved reflectance spectra of the parent opal matrix as well as those of the opal-based nanocomposite *Ag / opal* have been measured under illumination by white light from a tungsten lamp. Reflection spectra have been acquired by USB650 Red Tide spectrometer (Ocean Optics).

ISSN 1691-5402

### III RESULTS AND DISCUSSION

Normalized to the maximum value reflectance spectra of opal template and those of nanocomposite *Ag / opal* at two different angles of light incidence are shown in Fig. 2.

Reflectance spectra of all the samples demonstrate the zero order diffraction resonance that depends on the angle of light incidence  $\theta$ . The shift of the central wavelength  $\lambda$  of the Bragg resonance (Fig. 3) obeys the combined Bragg  $2a \cos \beta = \lambda / n_{eff}$  and Snell's ( $n_{eff} \sin \beta = \sin \theta$ ) laws:

$$\lambda^2 = 4a^2 n_{eff}^2 - 4a^2 \sin^2 \theta,$$

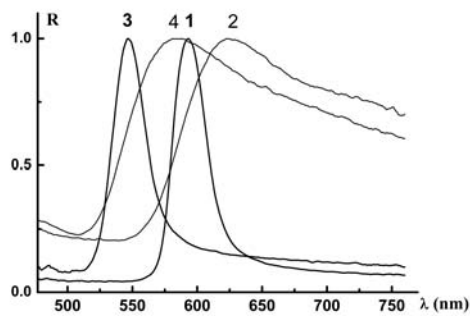


Fig. 2. Normalized reflectance spectra of opal template (1, 3) and those of nanocomposite *Ag / opal* (2, 4) at the angles of incidence 15° (1, 2) and 35° (3, 4).

where  $a = 0.816D$  is the interplane distance for (111) planes of the FCC lattice and  $n_{eff}$  represents the effective refractive index of the photonic crystal.

The reflectance maxima in the *Ag / opal* nanocomposite spectra are shifted to the longer wavelengths as compared with those in the spectra of parent opal matrix, because the effective refractive index of composite ( $n_{composite} \approx 1.44$ ) is higher than that of the opal template ( $n_{opal} \approx 1.33$ ).

The striking observation is the pronounced distortion of diffraction resonance band in the reflectance spectra of *Ag / opal* composite (Fig. 2, curves 2, 4) that contrasts to quite symmetric Bragg resonance shape in the spectra of bare opal (Fig. 2, curves 1, 3). To our opinion, this phenomenon is the manifestation of the Fano resonance [4] – [7] between diffracted in *Ag / opal* composite photonic crystal electromagnetic waves and those resonantly scattered by silver dendrites.

Under this assumption, the resonance profile could be approximated by Fano formula

$$R = \frac{(\varepsilon + q)^2}{\varepsilon^2 + 1}, \text{ where } \varepsilon = \frac{D}{\lambda}$$

is the reduced energy (wavenumber or frequency),  $q$  represents the phenomenological parameter describing the relative strength of the Bragg resonance and the

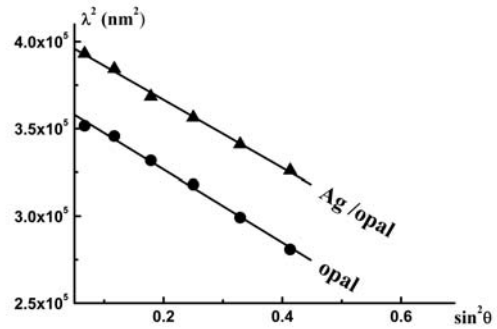


Fig. 3. Angular dispersions of the (111) Bragg resonances in the opal template and in the *Ag / opal* photonic crystal.

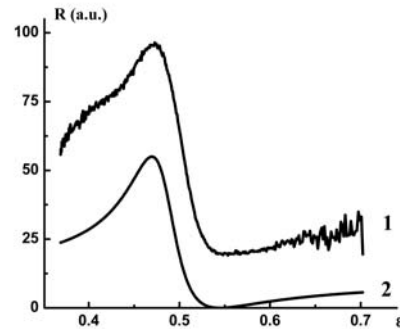


Fig. 4. Reflectance spectrum of composite *Ag / opal* at the angle of incidence 15° and its approximation with Fano formula ( $q=-2$ ).

broadband dendrite plasmon scattering.

Fig. 4 demonstrates rather good agreement between the Fano theory and our experimental results.

### IV CONCLUSIONS

The light diffraction in *Ag / opal* photonic crystals prepared by electro-thermo-diffusion of silver in opal matrix is affected by the light scattering at silver dendrites. This interaction leads to Fano-type distortion of the Bragg resonance shape.

### V ACKNOWLEDGEMENTS

The authors wish to thank M. I. Samoilovich for providing high-quality bulk opal matrices, V. I. Gerbreder and A. S. Ogurcov for having taken the SEM images, G. S. Cema and A. A. Gonyan for their assistance in some experiments, A. I. Vanin and S. I. Grashchenkov for fruitful discussions.

This work was supported by the Ministry of Education and Science of Russian Federation under the project 2.4128.2011 “Complex Investigation of

Physical Properties of Nanocomposites Based on Regular Porous Matrices”.

#### VI REFERENCES

- [1] V. G. Balakirev, V. N. Bogomolov, V. V. Zhuravlev, Y. A. Kumzerov, V. P. Petranovskii, S. G. Romanov, L. A. Samoilovich, "Three-dimensional superlattices in opals", *Crystallography Reports*, vol. 38, pp. 348–353, 1993.
- [2] K. Busch, S. Lölkes, R. B. Wehrspohn, H. Föll, Eds., *Photonic crystals: Advances in design, fabrication, and characterization*. Weinheim: Wiley-VCH, 2004.
- [3] S. G. Romanov, A. V. Korovin, A. Regensburger, U. Peschel, "Hybrid colloidal plasmonic-photonic crystals", *Advanced Materials*, vol. 23, pp.2515–2533, 2011.
- [4] U. Fano, "Effects of configuration interaction on intensities and phase shifts", *Phys. Rev.*, vol. 124, pp. 1866–1878, 1961.
- [5] A. E. Miroschnichenko, S. Flach, Yu. S. Kivshar, "Fano resonances in nanoscale structures", *Reviews of Modern Physics*, vol. 82, pp. 2257–2298, 2010.
- [6] M. Yanikov, V. Veisman, A. Gonyan et al., "Experimental investigation of physical properties of nanostructured silver, embedded by electro-thermo-diffusion into opal porous matrix", *Vestnik PskovSU. Series "Natural Sciences, Physics and Mathematics"*, issue 5, pp. 196–201, Pskov, 2014.
- [7] M. Yanikov, V. Veisman, S. G. Romanov, V. Solovyev, "Experimental study of Fano resonance in university course of physics", *The Problems of Educational Physical Experiment*, 25<sup>th</sup> Collection of Articles, pp. 96-98, Moscow, 2015.



# **Overview of tuned liquid dampers and possible ways of oscillation damping properties improvement**

**Jans Veļičko, Līga Gaile**

*Riga Technical University, Department of Structural Mechanics*

**Abstract.** Nowadays liquid tuned dampers are used in high-rise buildings and many others “dynamically sensitive” engineering structures. Liquid damper properties can be widely changed using different shapes of water containers, additional barriers inside, different types of liquid etc. Different types of liquid dampers exist or are proposed by researchers. Main types of liquid dampers are observed and compared in the paper.

One of the main disadvantages of the majority of liquid dampers is that only one main oscillation frequency is damped, that is not enough for the structures, where different vibrations modes are essential simultaneously. Existing solutions of this problem are examined in the paper.

**Keywords:** tuned mass dampers, tuned liquid dampers, damping, oscillation.

## I INTRODUCTION

Nowadays tuned dampers are the essential part of high-rise buildings and many others “dynamically sensitive” engineering structures. They are widely used in the world’s highest buildings for the damping of wind and seismic induced mechanical vibrations and improvement of building dynamic behavior. As a result, higher and more flexible engineering structures can be built.

Main idea of vibration damper is that damper mass oscillates in counter phase to main structure. As a result amplitudes of main structure oscillations are reduced due to summation with damper oscillations.

So called tuned mass dampers – dampers where main mass is solid body elastically or viscoelastically connected with the main structure – are more widely distributed in engineering structures [31]. Connection stiffness is specially adjusted (tuned) to the particular structure vibration frequency to obtain the damping effect. The most straightforward type of tuned mass damper – a heavy sphere suspended on a cable at the top of the tower. This type of damper is widely used in high-rise building.

In the last decades, the idea of tuned liquid dampers (TLD) got an extension and development. Liquid – mainly water – is used as damping mass in this type of dampers. TLD is a cheap, simple in construction and environmental friendly damper type. Such dampers also can be used as an additional water reserve for the building water supply and the fire-fighting systems.

The use of TLD in high-rise building started to increase in the last decade. Main types and ways of improvement of TLD are observed in consequent sections.

## II OVERVIEW OF TUNED LIQUID DAMPERS

Liquid motion is a complex process with many parameters and effects that generally is described with the fluid dynamics laws. TLD properties can be widely changed using different shapes of water tanks with or without additional barriers inside.

Usually liquid dampers are strictly connected to the main structure. Liquid motion inside the damper causes oscillations in counter phase to main structure and corresponding damping effect.

### *A. Tuned liquid column dampers (TLCD)*

One of the most widespread types of liquid dampers is tuned liquid column damper (TLCD). TLCD is U-shaped tube filled with liquid. Liquid flows from one vertical column to the other creating horizontal damping force due to impact on vertical walls and friction between liquid and tube in horizontal part. Liquid motion in TLCD can be well described by hydraulic laws. Due to this TLCD are well investigated and used in engineering practice.

For some time similar dampers are used in naval architecture for ship stability and are called antiroll tanks. In this case, special pipes connect two tanks along sides of the ship.

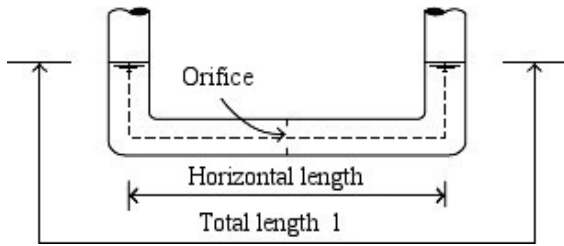


Fig. 1. Principal structure of TLCD [25].

Natural oscillation frequency of tuned liquid column damper is

$$\omega = \sqrt{2g/l} \quad (1)$$

where  $l$  is total length of a water column. Therefore, the adjustment of such dampers to particular structure is simple, by adding or draining some water from it.

However, this simple damper type also has its disadvantages. Firstly, TLCD is planar structure that works only in one direction. Therefore, for real structures that oscillate in all directions improvements should be made. Secondly, TLCD produces relatively small damping force to their own mass comparing to other damper types. Thirdly, TLCD oscillates and creates a significant damping effect in only one frequency. Studies have shown that considerable TLCD damping effect is obtained only if damper and main structure oscillation frequencies ratio does not exceed 0,9...1,1 interval [3].

Therefore, TLCD are suitable for wind turbines, simple geometry towers and other structures with one dominating oscillation frequency.

Consequently, researchers propose different modifications of TLCD to improve its effectiveness.

### B. Modified Tuned Liquid Column Dampers

Theoretical proposal of TLCD modification is offered by many researchers to raise its effectiveness and range of application.

Placing two TLCD in orthogonal directions damping effect in both main vibration directions will be assumed. Such system is called double tuned liquid column damper (DTLCD) [11].

Circular/torsional tuned liquid column dampers (CTLCD/TTLCD) are proposed for the torsional movement of eccentric structures [1]. In this case damper tube is shaped in circle and should be combined with DTLCD to provide damping effect for all types of main construction motion.

The problem of unidirectional effectiveness of TLCD also can be solved by placing one TLCD on rotating platform that is controlled by electronics. This electronic control provides right orientation of TLCD to ensure damping in the largest oscillation direction. Such damper is called hybrid tuned liquid column damper (HTLCD) [11].

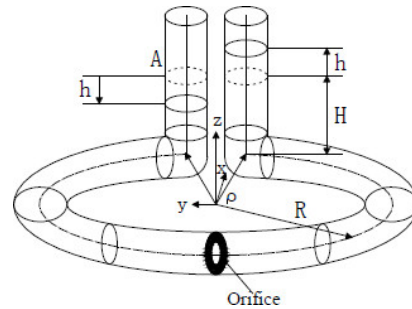


Fig. 2. Scheme of Circular/Torsional TLCD [1].

Of course even more complex shapes of TLCD can be developed and used. Dampers can consist not only from one tube, but from 2 containers connected with different cross section tubes. In this case oscillation frequency depends not only on liquid column length, but on containers and connecting tube geometry. Such dampers sometimes are called liquid column vibration absorbers (LCVA).

To increase the horizontal damping force obtained from liquid motion TLCD can be supplemented with orifices – additional barriers (fig. 1 and fig. 2). These barriers can be fulfilled not only as a plate with openings, but also as a steel ball inside damper [20] or in the other ways.

Valve that changes free tube cross section can be used instead of an orifice. Such valve allows easy to control damper parameters. The valve can be made with computer control which will change damper parameters according to the dominating structure oscillation mode at the moment [30]. Computer controlled dampers with variable properties are called semi-active dampers, opposite to the passive dampers without real time control.

If we hermetically seal both TLCD ends, we will ensure air pressure changes in the end zones during oscillations. Practically additional gas spring to water column in the damper is provided. Such dampers are called pressurized tuned liquid column dampers (PTLCD) or tuned liquid column gas dampers (TLCGD) [13]. This damper type extends frequency range of TLCD.

Some researchers propose to replace tight connection between damper and main structure to elastic. It can be fulfilled by hanging platform with TLCD with ropes to main structure. In this case, pendulum type liquid dampers are obtained [12]. Actually, it is a combination of TLCD and mass damper and it functions according to the more complex motion laws.

To provide effective damping at many frequencies multiple tuned liquid column dampers (MTLCD) are proposed – a series of liquid column dampers of different sizes simultaneously connected to the main structure. It is an unsophisticated approach to multi-frequency problem and it corresponds with multiple mass damper idea, which is fulfilled in some high-rise

buildings. In this case, several different dampers can be located along height of building on different levels. Size of each damper can be consequently reduced and their parameters can be optimized for the particular structure oscillation mode.

Some researchers offer to use magneto-rheological fluid or electro-rheological fluids in TLCD [5, 11, 19]. In this case, electromagnetic field generating devices can be placed around TLCD tube. Electromagnetic field can cause changes of rheological properties of fluid and as a result changes of damper mechanical properties. This process under computer control allows adjusting damper properties to most critical structure oscillations at the particular moment. These types of dampers are called magneto-rheological dampers (MR-TLCD) or electro-rheological dampers (ER-TLCD). Similar idea of the damper properties adjustment is used in modern top class vehicle semi-active suspensions.

Mentioned examples show that there are many different routes for TLCD development. At the moment it is hard to predict, what approach will be most effective and which will get practical application in construction industry.

### C. Sloshing liquid dampers (SLD)

Sloshing dampers have the simplest construction comparing to the other types of liquid dampers. Generally, it is a rectangular or barrel-shaped container with commensurable all three dimensions that is partly filled with liquid. Liquid impacts sidewalls of container generating damping force. Due to simple construction, sloshing dampers are often meant by the term tuned liquid dampers in literature and papers.

However, simple damper construction does not lead to the simple understanding of its mechanic. In SLD happens sloshing - liquid has free surface where waves can arise. Effects of waves, sloshing viscous damping and suppression, sloshing-structure interaction and others occur in this case. Considering that liquid sloshing dynamics is complex developing discipline, precise solution of SLD movement can be hardly obtained in practical case [2].

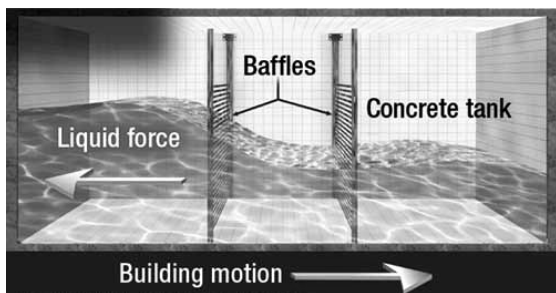


Fig. 3. SLD with additional slat screens (baffles) [23].

As a result, investigations of SLD often are based on experimental studies or simplified calculation models. Widespread SLD simplified calculation model is a tuned mass damper analogy – water in container is represented as solid body suspended on cable (simple pendulum). Such pendulum motion model is well known, but it roughly describes liquid motion.

Development of more accurate practical calculation methods of SLD is an actual objective for researchers and civil engineers [21].

SLD can be divided into shallow or deep dampers according to their dimensions. Liquid motion mechanic differs in these cases. Generally damper effectiveness significantly decreases if water depth to tank length ratio is less than 0,10...0,15 [10, 16].

Natural water oscillation frequency in shallow rectangular SLD without barriers according to the linear water wave theory is [15, 16]

$$\omega = \sqrt{\frac{\pi g}{l} \cdot \tanh\left(\frac{\pi \cdot h}{l}\right)} \quad (2)$$

where  $l$  is length of damper in the direction of oscillations,  $h$  is water depth and  $g$  is acceleration of free fall. Any changes of damper geometry accordingly changes oscillations frequency.

To improve SLD effectiveness and enlarge damping force construction can be supplemented by additional slat screens (baffles) – additional barrier in the container, which receives a part of liquid motion force. Such baffles make liquid motion in damper even more complex, but its effectiveness is generally proved [9, 24, 27]. Additional barriers can increase energy dissipation up to 60% [2].

Most suitable structures for SLD practical application are high-rise towers, where damper is also additional water tank for fire-fighting system.

### D. Bi-directional liquid dampers (BLD)

For TLCD it is possible to use U-shaped tank with considerable dimension transverse to damper working plane instead of a tube (fig. 4). In this case in TLCD transversal direction sloshing effect occurs. Such damper works in one direction as TLCD, but in other as SLD. This construction is called a bi-directional liquid damper (BLD) or combined liquid damper [6, 29].

Main practical advantage of this damper is that one damper ensures practical effect in both directions and effectively uses space.

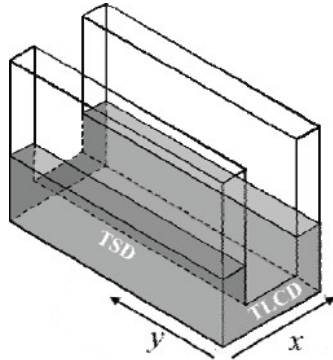


Fig. 4. Bi-directional liquid dampers (BLD) [6].

Additionally, to use space even more effectively, in the middle of BLD can be placed one more rectangular liquid container – sloshing damper. Practically it will be one big liquid rectangular container divided by inner walls into separated different type dampers.

### III WAYS OF IMPROVEMENT OF TUNED LIQUID DAMPERS

One of the main disadvantages of currently examined liquid dampers is that only one main oscillation frequency is damped. This is not enough for the structures, where simultaneously different vibration modes are essential. Even for structures with one main oscillation mode multi-frequency dampers should be useful, because structure oscillation frequency can be variable in some range due to different factors and it can be hard to perfectly tune damper for specific structure. Therefore, creating an effective multi-frequency liquid damper is a relevant problem.

Some authors offer using multiple liquid dampers – simple incensement of damper amount with different properties. Consequently size of one damper and it effectiveness reduces, but total required space increases. This is a main disadvantage for this approach, especially noting that damper mass and structure mass ratio should reach definite values to provide considerable damping effect (3...4% [4, 18]). In addition, it is important to notice that the damper, which has positive effect on one frequency, could create negative oscillations increasing effect on the other frequencies. This feature obliges to choose MTLCD separate damper parameters especially carefully.

Other way to multiply oscillation frequencies damping is semi-active damper creation – damper with computer adjustable properties at any particular moment for the most critical oscillations. Properties adjustment can be done by changing orifices or slat screen dimensions or position, or using magneto-rheological / electro-rheological fluids with variable electromagnetic field. It is complicated to fulfill this elegant idea technically in practice. Semi-active damper should have interconnected oscillation sensors

strictly strengthened to main structure in different places, movable or variable details in damper and computer control with corresponding software. Practical realization of such damper would be a serious task in any particular case.

Using more complex shapes of water dampers, with special barriers, could be one of the ways to solve the problem and create multi-frequency dampers.

Sloshing damper divided with significant slat screens (baffles) into several partitions combines different liquid motions – a part of motion energy causes waves inside each partition, but another part causes waves along whole damper [24]. Choosing relevant shape and amount of barriers inside SLD dampers could help to develop passive multi-frequency damper.

Impact of sloshing damper container and barrier shape changes on damping properties is less investigated. Some researcher investigated influence of SLD slope bottom on its properties. It was found that slope bottom decreases waves and makes liquid motion more uniform [14, 28]. This example shows how even small changes of damper container shape significantly affects oscillation parameters.

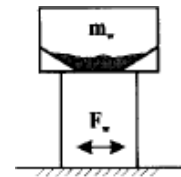


Fig. 5. SLD with sloped bottom [14].

Developing of dampers and barrier shapes could help in using more complex liquid motion modes for oscillation energy dissipation and damping of main structure. This approach would demand complex investigation of new forms of damper containers and barriers using fluid dynamics computational and experimental studies together with structural dynamics studies.

Also, one additional disadvantage of all liquid dampers should be noted – water, liquid that is mainly used in dampers, freezes at negative temperatures. This problem is not essential in heated rooms or can be solved using other liquids or antifreeze additives, but this measure reduces practical advantages of liquid dampers.

Generally, effectiveness of a damper increases together with damper and structure masse ratio. Some studies show that dampers mass must be at least 3-4% of structure mass to provide significant effect [4, 18]. This factor limits application area of liquid dampers – for example, for heavy reinforced concrete high-rise building large damper, which that requires a lot of space and produces additional load on columns and foundation, is necessary. On the other hand, relatively small damper will be enough for light structures –

steel masts and lattice towers, footbridges etc. Damper most effective mass ratio investigation would be a relevant research aim.

Practical application of TLD to different structures – high-rises [22, 23], bridges [8], wind turbines [26], floating platforms [17] etc. is investigated. However, less attention is paid to light lattice towers vibration damping, where oscillation problem is relevant. Such towers often are used as communication or observation towers and correspondingly have high allowable deformation requirement from telecommunication industry or human comfort viewpoint [7]. Simple and reasonably cheap TLD for light lattice tower would find wide practical application.

Generally two main approaches for liquid damper development can be marked out – creation of more complex semi-active or active dampers with parameters adjustable for instant moment oscillations and development of more effective shapes of simple passive dampers.

#### IV CONCLUSIONS

Nowadays liquid oscillation dampers are in active development stage. Researchers and engineers seek for optimal form and construction of liquid dampers.

Comparing large amount of research articles dedicated to liquid dampers it is possible to claim, that more attention is given to tuned liquid column dampers and their development, than to sloshing dampers. I suppose, that it can be explained with more simple and clear TLCD functioning principles.

Two main liquid damper development directions that could provide multi-frequency damping can be marked out. First is - creating more complex semi-active or active dampers under computer control with parameters adjustable to most critical oscillations mode at instant moment. In this case, different techniques to adjust damper parameters are proposed and examined.

Second way is developing effective shapes of containers and inner barriers of passive dampers, which provide more complex liquid motion modes for oscillation energy dissipation and damping of main structure. This approach is not investigated well and seems perspective; however, it demands complex studies of dampers with fluid dynamics and structural dynamics methods as well as development of practical but precise calculation procedure.

Passive liquid dampers could be effective solution for excessive vibration reduction in light lattice towers.

#### V REFERENCES

- [1] Linsheng Huo and Hongnan Li, *Seismic Response Reduction of Eccentric Structures Using Liquid Dampers, Vibration Analysis and Control - New Trends and Developments*, Dr. Francisco Beltran-Carbajal (Ed.), InTech, 2011, ISBN: 978-953-307-433-7.
- [2] Raouf A. Ibrahim, *Liquid Sloshing Dynamics*, Cambridge University Press, 2005.
- [3] A. Farshidianfar, P. Oliazadeh, H.R. Farivar, "Optimal Parameter's Design in Tuned Liquid Column Damper", *17th. Annual (International) Conference on Mechanical Engineering – ISME2009*, May, 2009, University of Tehran, Iran.
- [4] P. Banerji, *Tuned liquid dampers for control of earthquake response, 13th World Conference on Earthquake Engineering*, Vancouver, B.C., Canada, August 1-6, 2004, Paper No. 1666.
- [5] H. Masuda, T. Oyamada and T. Sawada, *Experimental study on damping characteristics of the tuned liquid column damper with magnetic fluid, 13th Int. Conf. on Electrorheological Fluids and Magnetorheological Suspensions*. Journal of Physics: Conference Series 412 (2013) 012049.
- [6] H.R. Lee and K.W. Min, *Reducing Acceleration Response of a SDOF Structure with a Bi-Directional Liquid Damper, The Proceedings of the Twelfth East Asia-Pacific Conference on Structural Engineering and Construction – EASEC12*. Procedia Engineering, vol. 14, pp. 1237–1244, 2011.
- [7] L. Gaile, *Analysis of Dynamic Parameters of Observation Towers in Latvia, Environment, Technology, Resources: Proceedings of the 9th International Scientific and Practical Conference*. Vol.II, Latvia, Rēzekne, 20-22 June, 2013. Rēzekne: RA Izdevniecība, 2013, pp.58-64.
- [8] M. Reiterer, *Control of pedestrian-induced bridge vibrations by tuned liquid column dampers, Proceedings of the Third European Conference on Structural Control, 3ECSC, 12-15 July 2004*, Vienna University of Technology, Vienna, Austria.
- [9] S.H. Crowley, R. Porter, *Optimal screen arrangements for a tuned liquid damper*, *International workshop on water waves and floating bodies 26*, 2011, Athens.
- [10] Sheng Dong, Hua Jun Li, Tomotsuka Takayama, *Characteristics of Tuned Liquid Damper For Suppressing Wave-Induced Vibration, Proceedings of the Eleventh (2001) International Offshore and Polar Engineering Conference*, 17-22 June, Stavanger, Norway.
- [11] B. Nanda, "Application of tuned liquid damper for controlling structural vibration" M.S. thesis, National Institute of Technology, Rourkela, India, 2010.
- [12] A. Sarkar A, O.T. Gudmestad, "Pendulum type liquid column damper (PLCD) for controlling vibrations of a structure – Theoretical and experimental study", *Engineering Structures*, vol. 49, pp. 221–233, 2013.
- [13] Ch. Fu and F. Ziegler, "Vibration prone multi-purpose buildings and towers effectively damped by tuned liquid column-gas dampers", *Asian journal of civil engineering (building and housing)*, vol. 10, pp. 21-56, no. 1, January 2009.
- [14] D.E. Olson and D.A. Reed, "A nonlinear numerical model for sloped-bottom tuned liquid dampers", *Earthquake Engineering & Structural Dynamics*, vol. 30, Issue 5, pp. 731–743, May 2001.
- [15] D. Reed, J. Yu, H. Yeh and S. Gardarsson, "Investigation of Tuned Liquid Dampers under Large Amplitude Excitation", *Journal of Engineering Mechanics*, vol. 124, Issue 4, pp. 405–413, April 1998.
- [16] E. Bhattacharjee, L. Halder, R.P. Sharma, "An experimental study on tuned liquid damper for mitigation of structural response", *International Journal of Advanced Structural Engineering (IJASE)*, vol. 5, Issue 1, December 2013.
- [17] H.H. Lee, S.-H. Wong, R.-S. Lee, "Response mitigation on the offshore floating platform system with tuned liquid column damper", *Ocean Engineering*, vol. 33, Issues 8–9, pp. 1118–1142, June 2006.
- [18] Jong-Cheng Wua, Ming-Hsiang Shihb, Yuh-Yi Lina, Ying-Chang Shenc, "Design guidelines for tuned liquid column damper for structures responding to wind", *Engineering Structures*, vol. 27, Issue 13, pp. 1893–1905, November 2005.
- [19] J.Y. Wang, Y.Q. Ni, J.M. Ko, B.F. Spencer Jr, "Magneto-rheological tuned liquid column dampers (MR-TLCDs) for vibration mitigation of tall buildings: modelling and analysis

- of open-loop control”, *Computers & Structures*, vol. 83, Issues 25–26, pp. 2023–2034, September 2005.
- [20] K.A. Al-Saif, K.A. Aldakkan, M.A. Foda, “Modified liquid column damper for vibration control of structures”, *International Journal of Mechanical Sciences*, vol. 53, Issue 7, pp. 505–512, July 2011.
- [21] K.M. Shum, “Closed form optimal solution of a tuned liquid column damper for suppressing harmonic vibration of structures”, *Engineering Structures*, vol. 31, Issue 1, pp. 84–92, January 2009.
- [22] K.-W. Min, H.-S. Kim, S.-H. Lee, H. Kim, S.K. Ahn, “Performance evaluation of tuned liquid column dampers for response control of a 76-story benchmark building”, *Engineering Structures*, Volume 27, Issue 7, Pages 1101–1112, June 2005.
- [23] M. Nadine, “A Sleek Skyscraper in San Francisco Raises the Profile of Performance-Based Design”, *Architectural Record*, June 2008.
- [24] O. M. Faltinsen, R. Firoozkoobi, A. N. Timokha, “Analytical modeling of liquid sloshing in a two-dimensional rectangular tank with a slat screen”, *Journal of Engineering Mathematics*, vol. 70, Issue 1-3, pp 93-109, July 2011.
- [25] P. Ahadi, M. Mohebbi and K. Shakeri, “Using Optimal Multiple Tuned Liquid Column Dampers for Mitigating the Seismic Response of Structures”, *ISRN Civil Engineering*, vol. 2012, Article ID 592181, 6 pages.
- [26] S. Colwell, B. Basu, “Tuned liquid column dampers in offshore wind turbines for structural control”, *Engineering Structures*, vol. 31, Issue 2, pp. 358–368, February 2009.
- [27] S. Crowley, R. Porter, “An analysis of screen arrangements for a tuned liquid damper” *Journal of Fluids and Structures*, vol. 34, pp. 291–309, October 2012.
- [28] S. Gardarsson, H. Yeh and D. Reed, “Behavior of Sloped-Bottom Tuned Liquid Dampers”, *Journal of Engineering Mechanics*, vol. 127, No. 3, pp. 266-271, March 2001.
- [29] S.-K. Lee, K.-W. Min, H.-R. Lee, “Parameter identification of new bidirectional tuned liquid column and sloshing dampers”, *Journal of Sound and Vibration*, vol. 330, Issue 7, Pages 1312–1327, 28 March 2011.
- [30] S.K. Yalla, A. Kareem, J.C. Kantor, “Semi-active tuned liquid column dampers for vibration control of structures”, *Engineering Structures*, vol. 23, pp. 1469–1479, 2001.
- [31] T. Tanaka, M. Yamamoto, T. Katayama, K. Nakahira, K. Yamane, Y. Shimano, K. Hirayama, “Recent Applications of Structural Control Systems to High-Rise Buildings”, *Earthquake Engineering and Engineering Seismology*, Vol. 4, No. 1, pp. 75-93.

## **PRINCIPLES OF PUBLICATION USE AND ETHICS**

*The Publisher states the following principles of publication use and ethics:*

1. Only original works, that have not been previously published and in which the data do not infringe the copyright of another person or organization, are accepted for publishing.
2. Every submitted paper is reviewed anonymously by 2 reviewers.
3. Publisher has the right to use plagiarism detection software to screen submitted papers.
4. Authors retain copyright over their work, while allowing the conference to place this unpublished work under a Creative Commons Attribution License, which allows others to freely access, use.
5. Publisher undertakes to publish articles accepted after reviewing and, according to the scientific quality of an article, publish them electronically and include them in various international scientific paper data bases.
6. Publisher undertakes to use author's personal data only for the needs of identification of authors and co-authors, as well as to preserve data in accordance with the restrictions determined in the current regulations of the Republic of Latvia.

*The author (-s) of original article confirms and guarantees that:*

1. A paper has been written by the Author (s) who has (have) been stated in the Paper and in this statement and there is no any other person who would have any rights to this Paper.
2. The Paper is original; it has not been previously published and is not under simultaneous consideration by another publications.
3. The Paper will not later be submitted elsewhere.
4. There are references for all the pictures, data and other materials used in the Paper.
5. The results of the Paper are genuine; they do not infringe on the original work of another person or organisation. The Author (-s) have taken all the necessary measures to ensure the requirements of the sponsors' who finance the Paper.
6. If author finds a significant error after the publishing of the paper, it is the author's obligation to promptly notify the editor.
7. The Author (-s) has (have) been authorised to submit the Paper for publication; the intellectual property rights will not be infringed according to the 14th, 15th articles of the Copyright law and other normative acts of the Republic of Latvia and international normative acts binding for the Republic of Latvia.
8. The Author (-s) take (-s) the sole responsibility related to the third parties' objections and demands concerning the publishing or using the Paper.
9. The Author (s) take (-s) all the responsibility and promptly, irrevocably and unconditionally undertakes to independently at his (their) own expenses and risk if there will be objections or demands from the third parties' concerning the publishing or using the Paper.

*Publication editor:*

1. Ensures double-blind peer-review of the submitted paper.
2. Until the publishing, ensures the confidentiality of information concerning the submitted article.
3. Strives to prevent any possible conflict of interests between authors and reviewers or editors.

*Reviewer:*

1. Evaluates the content of the article according to the scientific article criteria, without regard to ethnic origin, gender, sexual orientation, citizenship, religious beliefs or political views of the authors.
2. Keeps confidential all the information related to submitted paper.
3. Notifies the editor if there is a suspicion of plagiarism or copyright infringement.
4. If the reviewer feels unqualified to review or knows that it is impossible to provide review in time, he should notify the Editor-in-Chief and ask to exempt him from reviewing.

